Design and Modelling of Small Scale Low Temperature Power Cycles

Wronski, Jorrit; Haglind, Fredrik; Elmegaard, Brian; Skovrup, Morten Juel

Publication date:
2015

Document Version
Publisher's PDF, also known as Version of record

Design and Modelling of Small Scale Low Temperature Power Cycles

PhD Thesis

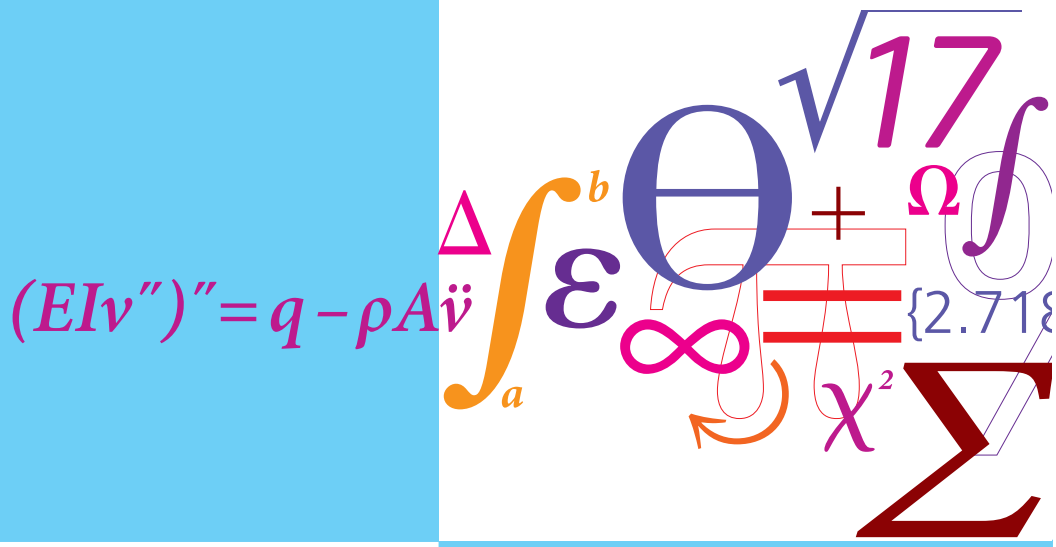

Jorrit Wronski
DCAMM Special Report No. S190
May 2015

DTU Mechanical Engineering
Department of Mechanical Engineering

PhD Thesis

Design and Modelling of Small Scale Low Temperature Power Cycles

Jorrit Wronski

Kongens Lyngby 2015

Design and Modelling of Small Scale Low Temperature Power Cycles
Jorrit Wronski, May 2015

PhD Thesis
ISBN: 978-87-7475-432-9
DCAMM Special Report No. S190

DTU Mechanical Engineering
Section of Thermal Energy
Technical University of Denmark

Nils Koppels Allé, Building 403
2800 Kongens Lyngby, Denmark
Phone +45 4525 4131
www.mek.dtu.dk

This thesis is written in British English using LaTeX 2_ε and `Biber`. It is set in Adobe MinionPro and Adobe MyriadPro for text and headlines. Mathematic symbols are provided by MnSymbol and code is printed in `Latin Modern Mono`. The overall layout is heavily inspired by Laursen's template.

Summary

The work presented in this report contributes to the state of the art within design and modelling of small scale low temperature power cycles. The study is divided into three main parts: (i) fluid property evaluation, (ii) expansion device investigations and (iii) heat exchanger performance.

The traditional approach to fluid property modelling requires users to choose between computational efficiency and high accuracy since the complexity of many of the modern equations of state makes the evaluation of fluid properties time consuming. This work contributed to the new fluid property library CoolProp that provides automated routines for fluid property evaluations based on Taylor series expansion and bicubic interpolation. The internal structure was redesigned completely to include mixtures and the library currently contains binary interaction parameters for many refrigerants and natural working fluids. It also includes more than 100 pure and pseudo-pure fluids as well as over 100 pure and binary secondary heat transfer fluids. The reformulation of the equations for the incompressible fluids allowed the calculation of a full thermodynamic state, including entropy and selected partial derivatives. The accelerated property evaluation by means of table-based interpolation was shown to be up to 120 times faster than solving the full equation of state (EOS) for enthalpy and pressure as inputs, which enhanced the simulation experience significantly while keeping the associated relative error below 10^{-4} at all times and below 10^{-7} away from the phase boundaries.

Regarding expansion devices for small scale organic Rankine cycle (ORC) systems, this work focussed on reciprocating machines. A prototype of a reciprocating expander with a swept volume of 736 cm^3 was tested and modelled. The model was written in object-oriented Modelica code and was included in the ThermoCycle framework for small scale ORC systems. Special attention was paid to the valve system and a control method for variable expansion ratios was introduced based on a cogeneration scenario. Admission control based on evaporator and condenser conditions was found to be suitable for an optimisation of the expander operation. During the experiments, the machine ran with n-pentane as working fluid and delivered up to 2.5 kW of shaft power. Operating with variable admission valve timing, the expander exhibited a stable isentropic efficiency around 70 % for expansion ratios from 8 to 15. The simulation code could predict the expander efficiency within 6 % points, larger deviations of up to

30 % occurred for the produced work per revolution. An analysis of the heat transfer occurring in the expansion chamber showed that also large heat losses only had a limited impact on the work output of the expander.

The final part of this report deals with the performance of plate heat exchangers. Several plate heat exchanger correlations were reviewed focussing on their applicability to ORC systems. A framework for dynamic heat exchanger modelling was developed that includes both single-phase and two-phase flow in pipes and plate heat exchangers. Four different pairs of heat transfer correlations were compared based on a test case with a dynamic heat source suggesting that a simplified modelling approach could be sufficient to model the dynamic response of a small scale plate heat exchanger. Working towards a validation of heat transfer correlations for ORC conditions, a new test rig was designed and built. The test facility can be used to study heat transfer in both ORC and high temperature heat pump systems.

Resumé

Denne afhandling bidrager til forskningen indenfor design og modellering af små kraftprocesser til udnyttelse af lavtemperaturkilder. Arbejdet er delt op i tre hoveddele: (i) fluidegenskabsberegning, (ii) undersøgelse af ekspansionsmaskiner og (iii) varmevekslereffektivitet.

Den traditionelle tilgang til fluidegenskabsmodellering kræver at man, på grund af den høje kompleksitet af tilstandsligningerne, enten vælger en metode til hurtig beregning eller en metode med høj nøjagtighed. En del af denne arbejde er indgået i udviklingen af et nyt bibliotek til beregning af termodynamiske tilstandsstørrelser, CoolProp, hvilket indeholder metoder til automatisk og hurtig interpolation af fluidegenskaber. Den interne struktur af biblioteket er blevet nyudviklet for at inkludere arbejdsmiddelblandinger og i dag indeholder biblioteket mange binære interaktionsparametre for kølemidler og naturlige arbejdsmidler. Derudover findes der også flere end 100 rene og pseudo-rene stoffer såvel som over 100 sekundære varmetransportmedier. Nye ligninger til disse inkompressible medier tillader en beregning af en termodynamisk tilstand inklusiv entropi og udvalgte partielle afledede. Interpolationsmetoderne er op til 120 gange hurtigere end den egentlige tilstandsligning når man bruger tryk og entalpi som tilstandsvariabler. Dette gavner mange slags systemberegninger mens den nyintroducerede relative fejl er mindre end 10^{-4} på alle tidspunkterne og mindre end 10^{-7} den største del af enfaseområdet.

Med hensyn til ekspansionsmaskiner til små ORC-anlæg fokuserer arbejdet på stempelmaskiner. En prototype med en arbejdsvolumen på 736 cm^3 er blevet testet og modelleret. Modellen er skrevet i det objektorienterede sprog Modelica og er blevet integreret i ThermoCycle-biblioteket, hvilket har modellering af små ORC-anlæg som formål. Ventilsytemerne er blevet analyseret i forbindelse med udviklingen af et styringskoncept for variable ekspansionsforhold og dens implementering i en model af et kraftvarmeanlæg. Indsprøjtningsstyring baseret på fordamper- og kondensatortemperatur er blevet brugt til at optimere ekspanderdriften. Maskinen kørte med n-pentan som arbejdsmiddel og leverede en effekt på op til 2.5 kW. Den variable ventilstyring kunne holde effektiviteten på omkring 70 % under drift med ekspansionforhold fra 8 til 15. Modellen kunne forudsige effektiviteten indenfor 6 %-points, men beregningen af det producerede arbejde per omdrejning havde en fejl på op til 30 %. En analyse

af varmetabet fra ekspansionsmaskinen har vist, at også et stort varmetab kun har begrænset betydning for maskinens kraftproduktion.

Den sidste del af rapporten omhandler pladevarmeveksler. Arbejdet leverer en oversigt over korrelationer til pladevarmeveksler med fokus på anvendelsen i ORC-processer. En ramme for simulering af både enfase- og tofasevarmeoverførsel er blevet implementeret, som kan bruges til pladevarmeveksler og rørstrømning. Fire par af korrelationer er blevet sammenlignet ved hjælp af en dynamisk varmekilde og en forenklet model, baseret på masseflow og dampindhold, kunne genskabe resultaterne af de avancerede korrelationer. Den store usikkerhed der ligger i brugen af korrelationer kræver en eksperimentel validering af resultaterne. En ny testopstilling er blevet designet og bygget til dette formål samt tests af varmeoverførsel i systemer med højtemperaturvarmepumper. Opstillingen presenteres til sidst i rapporten.

Preface

This PhD thesis was prepared at the Department of Mechanical Engineering, Technical University of Denmark, Denmark (DTU) in fulfilment of the requirements for acquiring a PhD degree in Mechanical Engineering.

The work has been conducted at the Section of Thermal Energy from late 2011 to spring 2015 and included a visit to the Thermodynamics Laboratory at the University of Liège, Belgium in spring 2013. The main advisor was Associate Professor Fredrik Haglind, DTU, and Associate Professor Brian Elmegaard, also DTU, and PhD Morten Juel Skovrup, IPU, acted as co-supervisors. The project has been financed by the Technical University of Denmark and by a donation from IPU. The stay in Belgium has been supported by a travel grant from the Otto Møensted Foundation.

Kongens Lyngby, May 2015

Jorrit Wronski

Acknowledgements

This thesis is the outcome of a few years of work and many people have contributed to it on a professional level or on a personal motivational level or both.

The support I received from my three advisers Fredrik Haglind, Brian Elmegaard and Morten Juel Skovrup is also acknowledged. You did your best to minimise my sidetracking and to help me stay focused while giving me the freedom to define my own goals.

The ongoing cooperation among VHE[1], IPU[2] and DTU[3] was the driver behind the work on the reciprocating expander and I would also like to acknowledge the funding provided by IPU. The component design and experimental work of Kristian Fredslund Jensen and Nikolas Aulin Paldan were crucial for this project and I would like thank them, as well as Harald Nes Rislå for the permission to publish the results and for the many fruitful discussions. I am also very grateful for all the help I received from my colleagues at the Section of Thermal Energy at DTU. Especially my office mates Christian, Lasse, Elham, Abid, Tuong-Van, Leonardo, Andrea and Hafþór for creating a professional but warm atmosphere. I also have had the privilege to spend some of my time at ULg[4] and I would like to express my gratitude for welcoming me in the lab. Ian, Adriano, Sylvain and Vincent, you have made the work on CoolProp and ThermoCycle much more fun. There were also numerous student projects during the past years and many of them contributed to the experimental work described in this thesis. Thank you, dear students, for your commitment and for taking part in our research work.

Special thanks go to my friends and family for being there to remind me of the things that really matter. Sophie, I am looking forward to catch up on all the hours we have not spent together recently.

[1] Viking Heat Engines AS, Kristiansand Norway

[2] IPU, Kongens Lyngby, Denmark

[3] Technical University of Denmark, Department of Mechanical Engineering, Kgs. Lyngby, Denmark

[4] University of Liège, Thermodynamics Laboratory, Liège, Belgium

Contents

Chapter 1

Introduction

1.1 Background

Driven by political, environmental and economic concerns, energy efficiency experienced increased attention over the last decades. Public discussions about dependency on fossil fuels, CO_2 emissions as well as rising prices for heat and electricity lead to a number of efforts in the fields of energy usage and conversion. At the same time, technical development and advancing industrialisation are accompanied by a world-wide increase in power consumption. Low temperature power cycles can contribute to the political goals of increased energy efficiency that many countries have published. The action plans for energy efficiency and renewable energy like the Danish Energy Strategy 2050 [56] or the German Climate Action Programme 2020 [30] are two examples that show that many countries work on improving energy production and on reducing energy consumption.

Heat at low temperatures is considered an energy form of limited value. It can be generated relatively cheap, but is difficult to convert to other forms of energy and is therefore often rejected from a process. The organic Rankine cycle (ORC) technology provides a way to convert low temperature heat into electricity by evaporating a low-boiling working fluid at high pressures and extracting work from a subsequent expansion process. The theoretical thermodynamic limits, *i.e.* the Carnot efficiency, make it a technology with an inherently low efficiency. Within these limits, it is one of the best-performing cycles and it is an established conversion path for the production of electricity from low temperature heat sources such as industrial waste heat, geothermal sources and the exhaust streams from combustion-driven power cycles [51]. Compared to water, typical ORC working fluids have higher saturation pressures at the same temperatures. Thus, plants generally do not operate much below atmospheric pressures and the post-expansion volume flow rate per produced unit of power is lower. Using simple cycle layouts, ORC systems can be very compact and employ less components than steam cycles. Hence, ORC systems are well-suited for small scale applications that often are economically challenged by the unfavourable ratio between investment costs and power production rate [197]. For small scale systems, Colonna et al. [51] and Quoilin et al. [197] mention mobile applications, biomass-based systems and combined heat and power (CHP) in general as promising fields for the application of ORC plants.

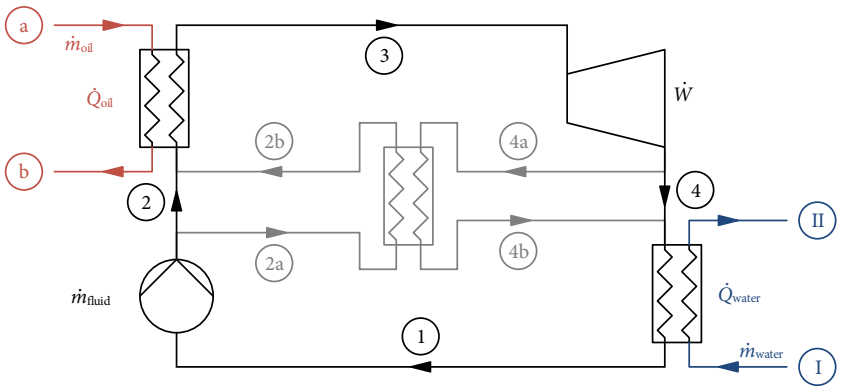

Figure 1.1: The system layout of a basic organic Rankine cycle configuration showing the optional regenerative heat exchanger in the middle.

1.2 Organic Rankine Cycle Technology

The system layout of the ORC is similar to that of a simple steam Rankine cycle. A pump pressurises the working fluid in the condensed liquid state from (1) to (2) in Figure 1.1 before it enters the evaporator. The high pressure vapour passes the expander from (3) to (4) producing mechanical work at rate of $\dot{W}$. Afterwards, the fluid enters the condenser and leaves it in liquid form returning to state (1). The heat input often comes from an oil-based heat carrier fluid while heat is rejected to a cooling water loop, thus the subscripts 'oil' and 'water' in Figure 1.1. The heat flow rate $\dot{Q}_{oil}$ is added in the evaporator, cooling the heat transfer medium from state (a) to state (b) on the left hand side of Figure 1.1. The condenser removes the heat flow rate $\dot{Q}_{water}$ from the working fluid by heating the water stream at $\dot{m}_{water}$ from state (I) to state (II).

Heat source and heat sink are typically realised as once-through heat exchangers operating with a liquid heat transfer medium on the secondary side. The absence of boiler drums and reheat sections makes the ORC simpler and more compact than its steam counterpart. The only system modification regularly used in practical applications is the inclusion of an additional regenerative heat exchanger transferring heat from the expanded vapour to the pressurised liquid as indicated by the states (4a)/(4b) and (2a)/(2b) in Figure 1.1. Such a heat exchanger is also referred to as 'recuperator' and is a particular feature of ORC systems. A plot in reduced entropy and reduced temperature is presented in Figure 1.2 that helps to understand the effect of the different shapes of the saturation bell, which can make the installation of a regenerative heat exchanger beneficial. Some of the working fluids used for ORCs have a positive inclination of

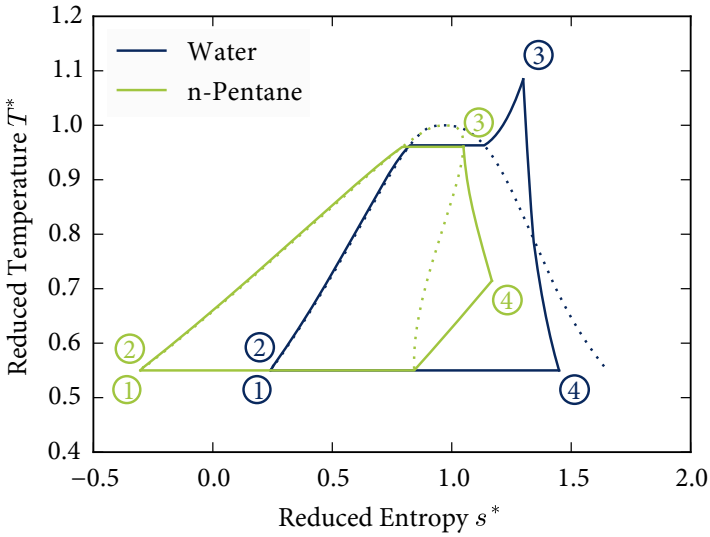

Figure 1.2: Two power cycles drawn in reduced properties with respect to the critical point using water and n-pentane as working fluids.

the partial saturation derivative $\partial T''/\partial s$ on the dew line causing large amounts of superheat after the expansion. The dew lines on the right hand side of the dotted phase boundaries in Figure 1.2 have different inclinations for water and n-pentane. This has implications for the design of a power cycle since expansion devices can be sensitive to the presence of droplets in the working fluids.

The darker line shows a typical steam Rankine cycle based on water and the expansion process from ③ to ④ enters the two-phase domain due to the negative inclination of the dew line $\partial T''/\partial s$. Furthermore, the temperature in point ④ is very close to the temperature of state ②, *i.e.* there is no heat transfer potential. This is different for the ORC shown in lighter colour in Figure 1.2. Here, the state ④ is further away from saturation conditions enabling an exchange of heat between the fluid coming from the pump in state ② and the expander exhaust stream ④.

To reduce the partial condensation during expansion, the steam cycle requires a noticeable amount of superheat at the expander inlet and the temperature in state ③ is higher than the evaporation temperature. Most of the fluids used in ORC systems have a larger inclination of the dew line than water. This does not mean that $\partial T''/\partial s$ is positive in all cases, but the general trend is that ORC plants do require less superheat

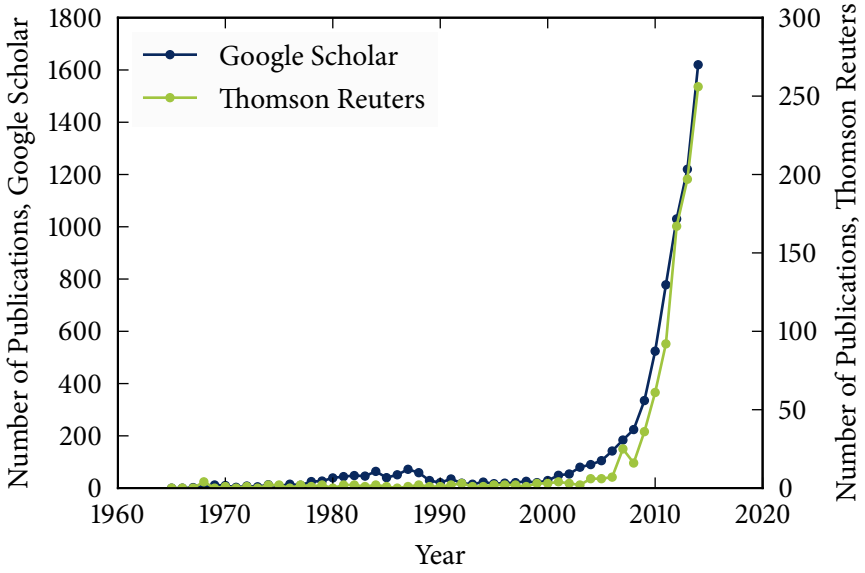

Figure 1.3: Annual number of publications matching the phrase 'organic rankine cycle' obtained from two research-oriented databases.

than steam cycles and that there often is no need to install a dedicated heat exchanger to superheat the working fluid prior to expansion.

The flexible application of ORCs and efficiency improvements, especially for small scale systems, have led to an increased growth of the installed ORC capacity. David, Michel and Sanchez [58] report an increase in the total installed capacity of 1.3 GW_{el} for the period from 1995 to 2007. Even though Colonna et al. [51] only count new installations for 0.7 GW_{el}, which is almost half of the other figure for the same period, both studies observe a sharp increase in the growth rate around year 2005. After 2007, the annual increase in installed power continues linearly for both data sets at rates of 0.3 GW_{el} and 0.2 GW_{el}, respectively.

Inspired by the approach of Colonna et al. [51] and David, Michel and Sanchez [58], an analysis of the number of ORC-related publications is presented in Figure 1.3. Searching for the exact phrase 'organic rankine cycle' on Google Scholar and in the Thomson Reuters Web of Science returned the annual number of new publications plotted in Figure 1.3. Both graphs show a large growth rate after year 2010 following a transition phase from year 2000 to year 2010. The large increase in publications can only be partly attributed to a general increase in published papers. The main part of

this increase reflects the high level of attention the ORC research received during the last years. According to Colonna et al. [51], ORCs also gain an above-average share of attention within the currently booming field of energy engineering.

1.3 Current State & Motivation

There is a large number of low-boiling working fluids that are suitable for ORC plants and many studies have been conducted to find the optimal working fluid for a given ORC application. Most approaches either compared a group of selected fluids [22, 47, 72, 95, 131, 192, 202] or optimised a binary fluid mixture [7, 8, 35, 100, 212, 245] to find the best working fluid. Until today, no general procedure for a structured fluid selection has been presented, but the integration of cycle and fluid optimisation is progressing with publications on molecular design [130, 177, 178], evaporation temperature optimisation [98] and fluid-based figures of merit [128].

The large amount of publications is also reflected by the rising number of review papers. While Hung, Shai and Wang [106] and Tchanche et al. [227] published general reviews of ORC publications, most of the recent review papers have a narrower scope. Chen, Goswami and Stefanakos [47] review the working fluid selection papers and the different methods proposed to find a suitable fluid for a given application. Another component-oriented review is presented by Qiu, Liu and Riffat [193] who review a collection of studies on small scale expanders. However, the majority of reviews focusses on the application of ORC systems like biomass-fuelled CHP [69], bottoming cycles for exhaust heat recovery [251], trigeneration plants [222], solar desalination facilities [61] and industrial waste heat [134]. There are also techno-economic studies that review both the technology and the market [51, 197, 244]. Out of this number of reviews, the most recent material has been presented by Colonna et al. [51] and Quoilin et al. [197]. Both works cover the history and current trends of the field of ORC and Colonna et al. [51] discuss larger installations and turbine development while Quoilin et al. [197] pay special attention to smaller systems and volumetric expanders. Both reviews conclude that smaller system still require research and further development.

The low price of refrigeration and air compressors makes these devices a prominent starting point for experimental work on ORCs [60]. Scroll devices clearly dominate the experimental studies conducted on small scale ORC, for example are 16 out of the 22 experimental studies reviewed by Quoilin et al. [197] dedicated to scroll devices. Also screw and vane-type devices were discussed, but experiments with reciprocating devices were not mentioned. A possible drawback of piston-based devices is that they have more moving parts than scroll devices and friction and wear have to be studied closely before a potential product can be launched. Furthermore, the oscillatory

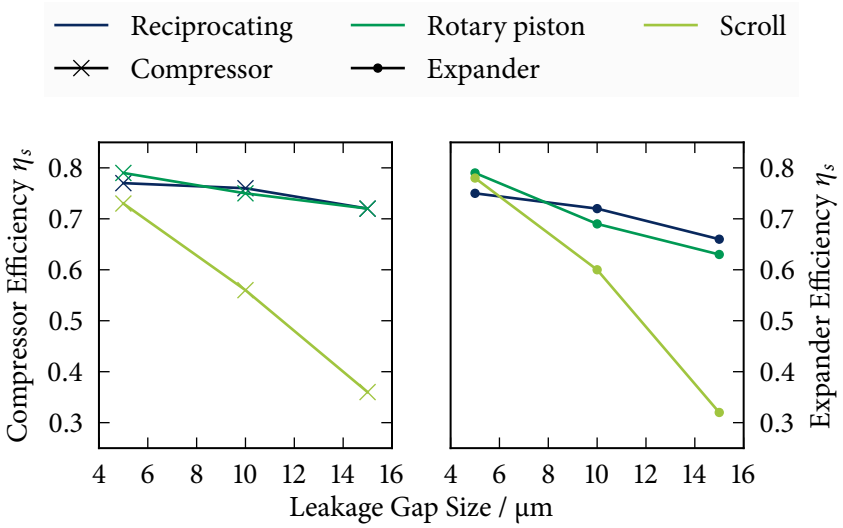

Figure 1.4: Isentropic compressor and expander efficiencies as reported by Huff and Radermacher [103] for CO_2 systems.

movement of the mechanical parts of a reciprocating machine causes vibrations, which often require a damper construction making the system larger and appear more bulky. Piston expanders are nevertheless an option that should be considered for small scale ORC. Mathie, Markides and White [160] compiled a number of papers on reciprocating compressors and expanders and concluded that many researchers expect theoretical efficiency values for well-working piston machines. They further pointed out that such values are unlikely to be reached by mass-produced low-cost machines. According to Huff and Radermacher [103], the approximate efficiencies of reciprocating machines mainly depend on the leakage gap size. They examined reciprocating, rotary piston and scroll machines with respect to their efficiency in CO_2 cycles and Figure 1.4 compiles their results for compressors and expanders.

While the performance of scroll, rotary piston and reciprocating machines was similar for high precision devices with gaps sizes of 5 µm, scroll devices were more sensitive to leakage and their efficiency dropped more with increasing gap size [103]. Piston machines suffered less from increased manufacturing tolerances, which makes them an interesting candidate for the economically challenging field of small scale ORC [197]. Leakage had a similar impact on the the performance of refrigeration compressors and expanders, which suggests that the trade-off between manufacturing

costs and efficiency could be similar to current refrigeration systems for high-volume production units. Reciprocating devices are also expected to be a better match for ORC systems running at elevated temperatures. Volumetric expansion devices are limited to a built-in volume ratio and the expansion ratio of reciprocating machines can be as high as 25 while scroll machines normally operate at ratios of three to four. The increased expansion ratio range and the potentially higher efficiencies motivate further studies of the reciprocating machines as expansion devices in low capacity ORCs.

The processes taking place inside a reciprocating expander are more complicated than the expansion of working fluid in a closed chamber. Modelling the dynamic gas exchange processes during the exhaust and during the admission of new working fluid requires an integration in time. Accurate fluid property evaluation is often a bottleneck in dynamic simulation. In models for small systems or for single components, even highly optimised fluid property code typically consumes more than half of the computational time [205] to calculate the properties of pure and pseudo-pure fluids. For real mixtures, the situation gets worse as the computational effort often increases exponentially with the number of components in a mixture. The most commonly used fluid property software is today provided by Lemmon, Huber and McLinden [135] and is a scientific tool that has not been designed for the needs of contemporary modelling approaches. It is thus common practice to divide the property space into different regions and to provide efficient formulations for the each of them. The industry standard for water [108] is probably the most well-known member of this group of accelerated calculation routines. Other implementations for refrigerants based on hand-crafted polynomials [211] or specific splines [207] further document the need for efficient formulations. Due to the large number of possible ORC working fluids, a general procedure that accelerates the calculation of fluid properties is needed. Implementing such a routine would not only benefit the expander simulations mentioned but also facilitate other advanced modelling approaches like Monte Carlo sampling, genetic optimisation algorithms and the implementation of control systems similar to the work of Tegethoff et al. [230].

Besides the accurate calculation of the thermophysical properties of potential working fluids, many models also require information on the secondary heat transfer fluids, typically oil-based heat recovery media or aqueous solutions in cooling loops. Since numerous software packages are used to model thermodynamic systems, a contribution in this field is thus required to provide an accessible interface that can be used with many of the established tools.

Before a control system for a small scale ORC unit can be designed, the dynamic behaviour of the system has to be analysed. Low capacity installations often have a different dynamic response than larger systems or power plants. The reduced inertia of volumetric expansion devices and the small generators practically removes their

influence on the system response to load changes [195]. The thermal inertia plays a larger role and especially the heat exchangers contribute to the dynamic behaviour of smaller systems [45]. The simplicity of ORC systems, notably the absence of steam drums and reheaters causes a concentration of the inertia effects in evaporator and condenser, which often are single once-through devices. Their low price and their compactness make plate type heat exchangers a ubiquitous component in industrial processes and refrigeration and heat pump systems as well as in small scale ORC and they are thus considered the most relevant type of heat exchanger to study in this context.

In a typical system, heat exchangers are the only means to provide thermal energy to the cycle and to reject heat from it. The performance of the heat transfer equipment thus directly impacts the grade of the supplied energy and the system performance. There is a need for further research on heat transfer equipment since many heat exchanger correlations are not validated in the temperature and pressure ranges that are relevant for ORC applications. The existing correlations, especially the ones developed for refrigeration applications, have rarely been compared to experimental data recorded at ORC working conditions. Also review papers covering the single-phase and two-phase heat transfer in plate heat heat exchangers [122] mostly focus on refrigeration application. The above suggests that there is a need for a systematic review of the application of plate heat exchangers in small scale ORCs. Besides the associated static modelling methods, such a work should also involve means to validate the dynamic operation to facilitate the prestudies required for the development of control algorithms.

1.4 Objectives

The overall objective of this work is to contribute to the design and modelling of small scale ORC systems by providing tools and models that facilitate the analysis of such systems including their dynamic behaviour This thesis covers three major aspects of the design and modelling of small scale low temperature power cycles. The multitude of working fluids used in low temperature power cycles makes (i) fluid property evaluation a topic that deserves special attention. The second aspect deals with the work-generating (ii) expansion process and focusses on reciprocating machines, which have not received much attention from the scientific community so far. The last point is the assessment of the (iii) heat exchanger performance. The list at the end of this section summarises the objectives in seven specific tasks.

The methods developed within this project shall be applied to the components of a small scale power cycle and the results are to be compared to reference data obtained from either established models or experimental campaigns. The findings from the

modelling studies and the comparisons provide a contribution to the design of low capacity power cycles running on low grade heat. This work shall advance the state of the art in modelling of small scale low temperature power cycles by providing reusable and accessible models. In short, this study aims at contributing by accomplishing the following tasks:

- Provide routines for an accelerated evaluation of working fluid properties (i).
- Make the different secondary heat transfer media properties available (i).
- Create a flexible and validated modelling tool for reciprocating devices (ii).
- Define and quantify losses that occur in reciprocating expansion machines (ii).
- Review existing heat transfer correlations for ORC working fluids (iii).
- Build a framework to include heat transfer correlations into dynamic plate heat exchangers models (iii).

1.5 Thesis Outline

Besides this introductory chapter, the thesis consists of three main chapters that cover the aspects (i) through (iii). Detailed results and lengthy, less important equations have been moved to the chapters in the appendix. The individual contents of the chapters can be summarised as follows:

Chapter 2 describes the architecture of the new fluid property library CoolProp for compressible fluids and incompressible heat transfer media. It also presents new equations that provide means of calculating a full state record, including entropy, from data provided in technical data sheets and from published polynomial coefficients. The implementation is verified for and and the computational performance of CoolProp is compared to another fluid property software, REFPROP.

Chapter 3 describes the expansion technologies used in small scale organic Rankine cycles. A prototype of a reciprocating expanders is presented and experimental and modelling results are presented. The model is validated and used to optimise the control of the admission valve based on cogeneration scenario with varying condenser pressure and a fixed heat source. A theoretical investigation of the expansion assesses the impact of heat losses on the expander performance.

Chapter 4 starts with a review of the published literature on plate heat exchangers from an ORC perspective. Four pairs of heat transfer correlations are selected and implemented as replaceable components in a distributed heat transfer model. A preliminary comparison of the correlations is presented for an ORC evaporator with a dynamic heat source. To facilitate the experimental validation, the design of a new heat transfer test rig for ORCs and heat pumps is presented.

Chapter 5 summarises results and contributions from the present thesis. The objectives from the current chapter are revisited and suggestions for future work are given in the last section of this thesis before the appendix.

Appendix A provides an overview of the articles and conference contributions that have been published during the work on this thesis.

Appendix B contains graphs that compare the performance of CoolProp and REFPROP based on average execution times. It also holds additional figures for the performance mapping of the equation of state (EOS) and the incompressible fluids for implicit and explicit calls.

Appendix C explains details about the fitting algorithm for the coefficients for the incompressible fluids. The tables presented in this chapter list the limits for the implemented incompressible fluids and a collection of fitting reports can be consulted for a visual inspection of the fit quality for the different fluids.

Appendix D holds a collection of additional modelling results for the dynamic heat transfer that occurs in an air-filled gas spring and the n-pentane expander from Chapter 3.

Appendix E lists the equations from the heat transfer correlations used in Chapter 4. It also provides detailed figures on the results discussed in Section 4.2.

Appendix F contains the procedures used to analyse the preliminary heat transfer data and a description of the modified expander test rig, the measured data and the data sheets for the employed heat exchangers. It also holds temperature-entropy diagrams for the new heat exchanger test rig described in Section 4.3, lists of the employed sensors as well as data sheets for the new heat exchangers.

Chapter 2

Fluid Property Modelling

This part covers the calculation of thermophysical fluid properties. It describes the structure of the new fluid property library CoolProp, which is based on state-of-the-art formulations using high-accuracy equations of state. Besides the Helmholtz free energy formulations for compressible fluids, which have previously been described in Bell et al. [29], the library also contains a framework to fit equations for incompressible fluids. This chapter presents new functions that provide means of calculating a full state record, including entropy, from data provided in technical data sheets and from published polynomial coefficients. Furthermore, it describes the updated architecture of the database and gives an overview of the computational effort required to calculate fluid properties and thus continues our work presented in Pierobon et al. [185].

2.1 Computer Aided Cycle Design

Simulation of thermodynamic systems has become one of the main pillars of engineering work, university education as well as public and private research. Many software products are tightly integrated with existing workflows and increasing simulation quality has led to decreasing experimental efforts while accelerating the pace of implementation and development of new and optimised thermodynamic processes. Such processes involve a number of non-linear phenomena, *e.g.* the phase change of a working fluid or transitions between laminar and turbulent flow regimes, calling for robust solution strategies and integrators.

Software for modelling thermo-fluid systems typically involves an ecosystem of at least three interacting software components. First, a system interpreter (i) converts the users' input and creates a modified system of equations along with bindings to external libraries. These equations are then processed by a numerics component (ii) containing solvers and integrators, which typically consist of custom-made special-purpose algorithms and modified versions of popular mathematics libraries like the Basic Linear Algebra Subprograms [132] (BLAS), its high-level companion the Linear Algebra Package [6] (LAPACK) and the Harwell Subroutine Library [208] (HSL). The third component is the fluid property package (iii) whose calculations often are the bottleneck of the entire solving procedure while discontinuities in the thermophysical

properties and their derivatives challenge the solvers' stability. For dynamic simulations, a fourth functional (iv) unit can be introduced to provide access to data for varying operating conditions including controller inputs. Common software packages in the field of thermo-fluid simulations implement one or more of the four aspects, (i) through (iv), mentioned above. If needed, missing features are often supplemented by accessing an independent library.

There are a number of software solutions for steady-state simulation. Many customised solutions are based on the general purpose computing packages SciPy [113] and MATLAB [231], exploiting their powerful solvers and data treatment facilities. A popular equation-based application for static modelling is Engineering Equation Solver [123] (EES). Another package for similar purposes is CycleTempo [13], which also comes with its own fluid property database, representing the component-based modelling environments. Dynamic problems formulated in systems of differential equations require other approaches such as the ones implemented in Ascend [5], AspenONE [15], Dynamic Network Analysis [77] (DNA) and the different implementations of the Modelica language[165], for example Dymola [57] and OpenModelica [172].

Fluid property calculations are usually delegated to external libraries that are accessed on a per-call basis extending a small group of built-in fluid property correlations. A commonly used library for this purpose is the REFPROP fluid property database [135] version 9.1 (REFPROP), developed by the National Institute of Standards and Technology of the United States of America (NIST). It can handle pure and pseudo-pure fluids as well as a large amount of mixtures of common working fluids. Another commercial software for a similar purpose is FluidProp [14], the property calculation engine behind CycleTempo. Furthermore, the TIL Media Suite [241] provides access to optimised routines tailored for dynamic simulations.

The only freely-available high-accuracy property libraries for mixtures, known to the author are Thermodynamic Reference and Engineering Data [216] version 1.1 (TREND) and the CoolProp fluid property database version 5.0.8 (CoolProp). Both are also competitive free fluid property libraries for pure and pseudo-pure fluids since they contain a large selection of relevant working fluids with CoolProp offering the unique features of tabulated property interpolation. The other open-source alternatives FPROPS [190] from the Ascend project and the Modelica-based packages ModelicaMedia [242] and HelmholtzMedia [236] only have a limited number of working fluids. Many software packages include their own routines for a number of fluids. Dynamic Network Analysis [77] (DNA) for example includes water/steam [246], real gases and mixtures of ideal gases [154] and refrigerants [211]. Other pieces of software like EES also have custom-made fluid properties tailored for rapid calculation and stability with a slightly reduced accuracy.

While REFPROP from NIST is the industry standard for fluid property calculations, it has not been designed to run as a property provider for involved simulations. It occasionally crashes or gives erroneous results, especially with mixtures like ammonia-water, and it requires some effort to include it in a custom simulation software. NIST only supports a Microsoft Windows operating system (Windows) and provides a limited number of wrappers for numerous environments that have been contributed by users.

Focussing on computational performance, it is important to provide well integrated wrappers for a number of possible programming languages and simulation environments. The users are expected to be engineers, scientists and students of related disciplines who do not necessarily bring a strong background in computer science. Providing plug-in solutions and a simple interface minimises the possible performance deterioration caused by flaws in custom wrapper code. Besides supporting all major platforms from Windows to an Apple Macintosh operating system (OS X) and a system with Linux kernel and GNU tools (Linux), it also runs on embedded systems like the National Instruments CompactRIO controller (cRIO) and mobile phones as well as in web browsers. The effort to provide high performance extensions for many platforms and tools has, until now, lead to wrapper packages for EES, Microsoft Excel, LibreOffice, ANSYS Fluent, National Instruments LabView, MathWorks MATLAB, Maplesoft Maple, PTC Mathcad, Scilab, Wolfram Mathematica, GNU Octave and SMath. Libraries are available for the languages C#, Delphi, Fortran, Java, Javascript, Julia, Lua, Modelica, PHP, Python and VB.NET. Being written in portable C++, the code can be compiled with many different compilers for even more platforms and systems, if needed.

The demand for a comprehensive fluid property library that supports the state-of-the-art routines for a number of relevant working fluids has been met by version 4 of CoolProp, which has been introduced to the public by Bell et al. [29]. In this publication, we describe the equation of state (EOS) used for compressible fluids and provide reference values for the extended corresponding states method by Huber, Laesecke and Perkins [102]. Version 4 of CoolProp could not handle mixtures and the next section describes the redesign of the internal structure, which was necessary to include mixtures in the next major release, CoolProp 5. Afterwards, the thermodynamics of incompressible fluids and their integration into the fluid property library are described. This part includes a new set of equations to calculate a full state record and a subset of partial derivatives using only basic information on thermal expansion and heat capacity polynomials.

2.2 Designing a Fluid Property Database

Initially, CoolProp was not intended to be a stand-alone software library for thermophysical fluid properties. It was an integrated part of a compressor simulation code developed at the Ray W. Herrick Laboratories [26] to simulate scroll compressors for CO_2 applications. Since then, more and more fluids have been included and the development gained momentum due to the support of the University of Liège, Thermodynamics Laboratory, Liège, Belgium (ULg) and the Technical University of Denmark, Department of Mechanical Engineering, Kgs. Lyngby, Denmark (DTU). Being decoupled from the rest of the simulation code, it became the first open-source fluid property software to include the extended corresponding state method to calculate transport properties by Huber, Laesecke and Perkins [102].

Many solution strategies for larger systems of equations benefit from analytical partial derivatives. To facilitate the construction of such analytical Jacobians, CoolProp provides access to all homogeneous phase first and second order partial derivatives of thermophysical properties implementing the general ideas presented by Crawford [54] and Carroll [42] and reviewed by Thorade and Saadat [238].

Besides this outer interface, the internal structure also has to be well-defined to provide a unified interface for the inclusion of other fluid property packages. Such an integration serves two purposes: (i) low-level access to other libraries is extremely helpful to verify results of internal calculations and (ii) it allows the users to exploit the infrastructure of CoolProp to access other fluid property libraries.

Helmholtz-energy-based EOS provide the most accurate source of thermodynamic data for many relevant working fluids [218], but evaluating state points based on random inputs is a computationally expensive task. The EOS is usually provided in a temperature-density-explicit form and those two properties are not very common iteration variables for a simulation software. The described software uses two different interpolation methods: (i) Tabular Taylor Series Expansion[164, 253] (TTSE) and (ii) bicubic interpolation, which has been published in the work of Keys [117]. Instead of accessing a calculation routine and a solver, fluid properties are now provided as interpolated values from a regularly spaced grid [29, 185].

The concept explained above is best summarised by means of a Unified Modelling Language (UML) diagram. Taking a thermodynamic state as the basic element, the most important components of the new library design can be explained with the basic elements listed in Figure 2.1. In this context, a state is an object that is able to provide all thermophysical properties directly or as a result of a calculation without access to an external data source or object. Using formulations based on the dimensionless Helmholtz energy α that are explicit in the reciprocal reduced temperature τ and the reduced density δ, a state contains τ, δ and the first three orders of partial derivatives

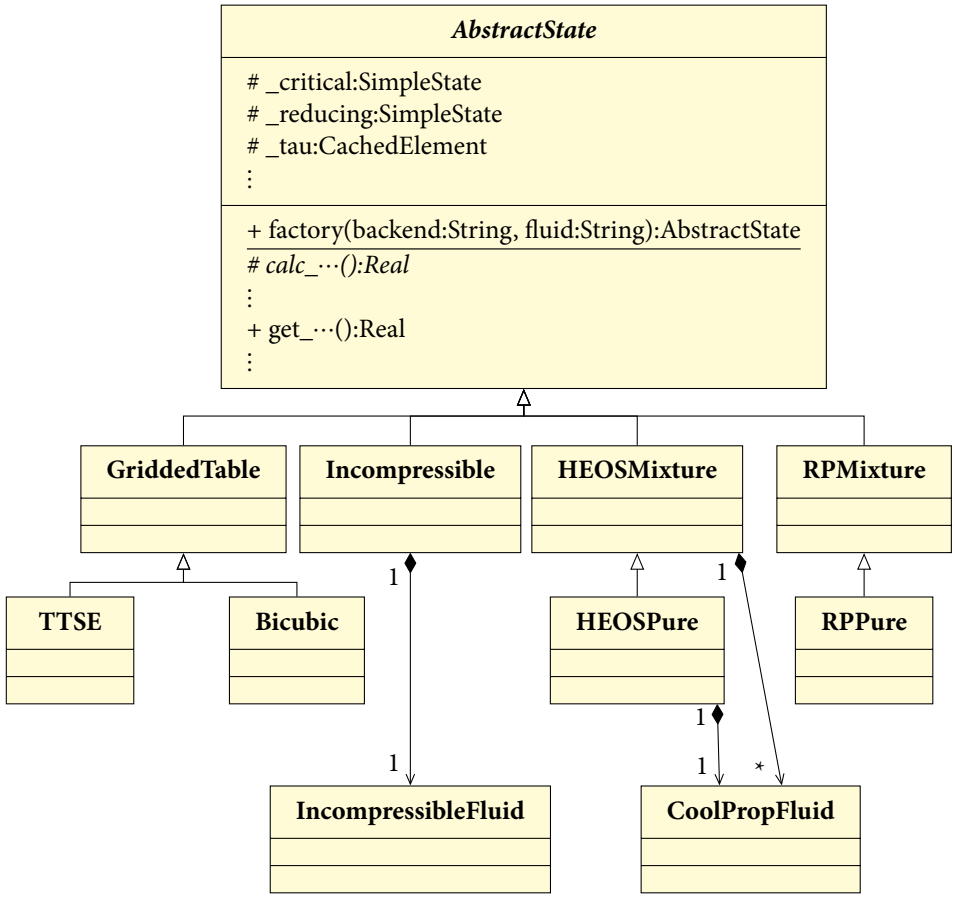

Figure 2.1: The internal structure of the different data sources in CoolProp.

of the ideal contribution α^0 and the real or residual part α^r with respect to τ and δ. Subsequently, analytical expressions can be used to provide any thermophysical property or its first or second order derivative.

The reducing and the critical properties are represented by 'SimpleState' objects, which only contain a few values that can be read from the outside: molar density ρ_m, temperature T, pressure p and molar specific enthalpy h_m. In many cases, the critical and reducing state are the same, but they can also differ, for example for many pseudo-pure fluids.

The 'AbstractState' class in CoolProp saves all calculated properties in cached elements. Caching intermediate results speeds up the calculation because many of

the property calculations involve similar terms. For example both the procedures to calculate pressure and enthalpy involve the partial derivative of the residual part of α with respect to δ. For the pressure equation

$$p = \rho RT(1 + \delta\alpha^{\mathrm{r}}_{\delta}), \tag{2.1}$$

it is the only partial derivative, while calculating enthalpy requires a total of three partial derivative of either the ideal or residual dimensional Helmholtz energy

$$h = RT\left((1 + \delta\alpha^{\mathrm{r}}_{\delta}) + \tau(\alpha^{0}_{\tau} + \alpha^{\mathrm{r}}_{\tau})\right) \tag{2.2}$$

with $\alpha^{\mathrm{r}}_{\delta} = (\partial\alpha^{\mathrm{r}}/\partial\delta)_{\tau}$. The number of possible combinations of derivatives increases with order, but so does the overlap of required intermediate results, which effectively decreases the computational effort. More details regarding the use of Helmholtz energy formulations in equations of states can be found in the the the International Association for the Properties of Water and Steam (IAPWS) release [107], the corresponding publication by Wagner and Pruss [246] and the book by Span [220]. Thorade and Saadat [238] provide additional information covering the application to dynamic modelling and the two-phase domain.

Access to the cached elements is controlled by the 'get_…' and 'calc_…' functions. The state object only exposes the former, which internally calls the latter or returns the variable directly from the cache. Access to other software libraries and different calculation routines is implemented through the 'calc_…' methods. The different backends used to provide fluid all implement their own set of functions to provide the functionality defined in the 'AbstractState'. The instantiation of the different backend objects is managed by a factory method. This method takes string variable that determines the calculation backend to be used as well as the fluid name. The factory function initialises an object that is derived from the 'AbstractState' class and returns a shared pointer to that object.

Figure 2.1 shows four different calculation backends. The 'GriddedTable' defines common functions for the interpolation routines like table generation and file system access functions. The actual interpolation is implemented in the subclasses 'TTSE' and 'Bicubic', which provide two alternative ways to calculate properties from the same tabular material. The first one uses a truncated Taylor series to evaluate fluid properties at a given point. To obtain density from pressure and enthalpy inputs, the Taylor expansion

$$\rho(h,p) = \Delta h\left(\frac{\partial\rho}{\partial h}\right)_{p} + \frac{\Delta h^2}{2}\left(\frac{\partial^2\rho}{\partial h^2}\right)_{p} + \Delta p\left(\frac{\partial\rho}{\partial p}\right)_{h} + \frac{\Delta p^2}{2}\left(\frac{\partial^2\rho}{\partial p^2}\right)_{h} + \Delta h\Delta p\left(\frac{\partial^2\rho}{\partial p\partial h}\right) + \rho_{i,j} \tag{2.3}$$

illustrates the calculation procedure. The derivatives are evaluated at the point i, j, and the differences are given by $\Delta p = p - p_j$ and $\Delta h = h - h_i$. The nearest state points j and i in p and h direction can be found directly due to the regular spacing of the grid of points. For an improved representation of the p-v-T surface and first order continuous derivatives, bicubic interpolation can be used. In the bicubic interpolation method, the state variable and its derivatives are known at each neighbouring grid point. This information is used to generate a bicubic representation for the property in the interpolation range, which could be expressed as

$$\rho(x, y) = \sum_{i=0}^{3} \sum_{j=0}^{3} a_{ij} x^i y^j \tag{2.4}$$

where a_{ij} are constants based on the cell boundary values and x and y are normalized values for the enthalpy and pressure, for instance. The constants a_{ij} in each cell are cached for additional computational speed.

The only external fluid property library supported so far is REFPROP. The 'RPMixture' class manages access to the REFPROP library and uses the exposed functions of that library to update its own internal variables. To carry out all calculations internally, one has to use the 'HEOSMixture' backend. This class implements different kinds of Helmholtz-energy-based EOS as well as the mixing rules required to calculate the fluid blends described by the formualtions described by the Groupe Européen de Recherches Gazières (GERG) [126, 127] and the NIST models [136, 139, 142]. Both mixture backends have derived subclasses, 'RPPure' and 'HEOSPure', that simplify parts of the expressions and internal calculations by skipping mixture-specific terms.

The 'Incompressible' backend support the calculation of a thermodynamic state based on functions for density and heat capacity. It supports only liquid fluids and provide access to a subset of properties, namely h, u and s, and uses T and p as state variables. The next part, Section 2.3, covers the internal calculations of this backend.

2.3 Thermodynamics of Incompressible Fluids

Liquid heat transfer fluids are used in many installations. In refrigeration plants, aqueous solutions are often employed to distribute the cooling while minimising the amount of refrigerant needed in the cooling plant. For warmer systems, heat supply is typically implemented as transfer loop with on an oil-based intermediate liquid. It is common practice to regard these intermediate fluids as incompressible to simplify the calculations. Even though density is not affected by pressure, it is often considered to be a function of temperature. Knowledge of the thermal expansion behaviour then links measured volume flow and mass flow. Since these fluids are used as heat

transfer media, technical data sheets typically contain information on viscosity and thermal conductivity besides the required information covering thermal expansion and specific heat capacity. In most cases, suppliers provide either tabulated data or simple parametrised equations, often polynomials, that describe the thermophysical and transport properties as functions of temperature.

During the following analysis, temperature T and pressure p are used as state variables for pure fluids with an additional state variable concentration x for brines and binary mixtures. In this work, incompressible mixtures with different compositions are regarded as independent fluids, which should be kept in mind when comparing properties for different compositions since there is no unified approach to include the composition in the definition of the reference states. Entropy and enthalpy values obtained for mixtures with different compositions should not be used in an energy balance without further precautions.

The evaluation of the thermodynamic properties of incompressible fluids is usually based on the assumption that the specific volume is constant at all times. Forcing a constant specific volume v then leads to two simplifications. The specific heat capacity at constant volume c_v becomes equal to the specific heat capacity at constant pressure c_p, as proven in textbooks like the one by Çengel and Boles [46] or by Moran et al. [168]. Equating the specific heat capacities

$$c_p = c_v = c \tag{2.5}$$

makes the internal energy u a function of temperature only. The second aspect deals with the definition of enthalpy h and cancels out the last term term from

$$dh = du + v\,dp + \cancelto{0}{p\,dv} = c\,dT + v\,dp \tag{2.6}$$

due to the constant volume condition $dv = 0$. Furthermore, textbooks often assume that pumping processes are isothermal $dT = 0$ and thus $du = 0$, which leads to a new simplified equation for the pump work of incompressible fluids

$$\Delta h = v_0\,(p_1 - p_0). \tag{2.7}$$

Another application of Equation (2.7) is the computation of an enthalpy correction term that can be used to approximate the properties of subcooled liquid based on tabulated saturation data for v' at the same temperature.

Kostic [125], however, claimed that the errors introduced by Equation (2.7) render it less suitable to approximate such an isothermal process. Using water as an example, Kostic [125] showed that an isothermal compression has to lead to a decrease in internal energy and that also enthalpy has to decrease at temperatures above 300 °C. Kostic

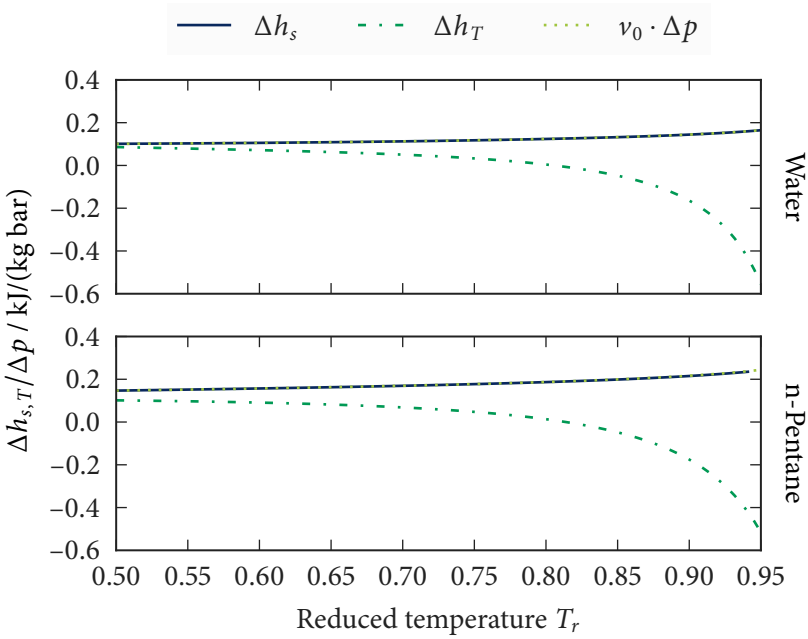

Figure 2.2: Enthalpy change per unit pressure increase as calculated for a compression from 1 bar above saturation conditions to 11 bar above saturation conditions. The lines show the change in enthalpy that occurs for an isentropic process (Δh_s), an isothermal process (Δh_T) and for the approximation described by Equation (2.7) for water and n-pentane.

[125] stressed that Equation (2.7) is well suited to compute an isentropic process instead, which can be proven from basic thermodynamic relations.

The exact same formulation as in Equation (2.7) is obtained from a combination of Equation (2.6) and $du = T\,ds - p\,dv$. In this case, the differential volume terms cancel each other out and the assumption of an isothermal and isochoric state change can be replaced by assuming an isentropic process: $dT \neq 0$, $dv \neq 0$ and $ds = 0$.

One practical aspect of this issue is the inaccuracy of the basic incompressibility assumption. This aspect has been partly discussed by Kostic [125] with the help of property tables for water, but also other fluids behave similarly as shown in Figure 2.2, which compares water and n-pentane. For both fluids, the full EOS has been used to calculate the average change in enthalpy for a pressure increase by 10 bar starting at 1 bar above saturation conditions. n-pentane exhibited a behaviour similar to water.

Regarding the differences between Δh_s and Δh_T in Figure 2.2, the approximation of the properties of the subcooled phase from saturation data can only be carried out with caution. However, employing an isentropic efficiency η_s together with Equation (2.7) can define the required specific pump work w_{pump} from

$$\eta_{\text{is}}\, w_{\text{pump}} = v_0\, (p_1 - p_0). \tag{2.8}$$

One way to simplify the calculations is to circumvent some of the initial assumptions and to provide means to calculate a full thermodynamic state from the simplified equations for density and specific heat capacity. This removes possible sources for errors and allows users to stick to their well known concepts of isentropic, polytropic and isothermal state changes without requiring additional knowledge about certain assumptions and limitations when using incompressible media.

With enthalpy depending on pressure and a variable density, the correct set of equations that satisfies the definition of enthalpy $h = u + pv$ and only uses temperature and pressure as state variables had to be found. The first step was to assume that the supplier information on heat capacity relates to enthalpy. Afterwards, the incompressibility assumption $(\partial v/\partial p)_T = 0$ could be used instead of the constant specific volume, since density information was available to calculate $(\partial v/\partial T)_p$. Having a direct link between density and temperature, all other properties could be defined from T, ρ and p. Internal energy was defined based on enthalpy by the basic relation $u = h - p/\rho$, which left only entropy s and enthalpy h as undefined properties.

Based on the partial derivatives with respect to the state variables and the fourth Maxwell relation, the entropy formulation in T and p could be simplified to

$$ds = \left(\frac{\partial s}{\partial T}\right)_p dT + \left(\frac{\partial s}{\partial p}\right)_T dp = \left(\frac{\partial h}{\partial T}\right)_p T^{-1} dT - \left(\frac{\partial v}{\partial T}\right)_p dp. \tag{2.9}$$

The impact on enthalpy was derived by rewriting the equation in terms of the state variables p and T employing $h = u + pv$:

$$dh = \left(\frac{\partial h}{\partial T}\right)_p dT + \left(\frac{\partial h}{\partial p}\right)_T dp = \left(\frac{\partial h}{\partial T}\right)_p dT + \left(v - T\left(\frac{\partial v}{\partial T}\right)_p\right) dp. \tag{2.10}$$

Rearranging Equation (2.9) and Equation (2.10) in T,ρ-notation yielded the final formulations for changes in entropy and enthalpy

$$ds = cT^{-1} dT + \qquad \rho^{-2}\left(\frac{\partial \rho}{\partial T}\right)_p dp \text{ and} \tag{2.11}$$

$$dh = c \qquad dT + \rho^{-1} dp + T\rho^{-2}\left(\frac{\partial \rho}{\partial T}\right)_p dp. \tag{2.12}$$

Hence, the absolute values for the caloric properties were defined as

$$\Delta s = \int_{T_0}^{T_1} \frac{c}{T} dT + \frac{p_1 - p_0}{\rho_1^2} \left(\frac{\partial \rho}{\partial T} \right)_p \text{ and} \tag{2.13}$$

$$\Delta h = \int_{T_0}^{T_1} c dT + \frac{p_1 - p_0}{\rho_1} \left(1 + \frac{T}{\rho} \left(\frac{\partial \rho}{\partial T} \right)_p \right). \tag{2.14}$$

Equation (2.13) and Equation (2.14) were able to describe changes in entropy and enthalpy. However, some prefer absolute values to define states and, just like the compressible fluids, also incompressible fluids have to have a reference state that sets an arbitrary value for enthalpy and entropy. Setting a reference enthalpy of 0 kJ/kg and an entropy of 0 kJ/(kg K) in the vicinity of the expected operating temperature and pressure avoids very large numerical values, a potential source of confusion. The reference values of the state variables T and p are also the starting points for the integration Equation (2.13) and Equation (2.14), $T_0 = T_{\text{ref}}$ and $p_0 = p_{\text{ref}}$. By default, the reference state is defined at a temperature of 20 °C and a pressure of 1 atm:

$$T_{\text{ref}} = 293.15\,\text{K} \quad = 68\,^\circ\text{F} \tag{2.15}$$

$$p_{\text{ref}} = 101\,325\,\text{Pa} = 14.696\,\text{psi} \tag{2.16}$$

$$h_{\text{ref}} = 0\,\text{J/kg} \tag{2.17}$$

$$s_{\text{ref}} = 0\,\text{J/(kg K)} \tag{2.18}$$

2.4 Data Fitting & Coefficients

In the last section, the relations used to construct all thermodynamic properties from temperature and pressure information was described. This work relied on the possibility to evaluate the the integral functions in Equation (2.13) and Equation (2.14). Fitting the provided data sets for heat capacity and density by means of ordinary power polynomials made it possible to calculate these integrals without further problems. The polynomial functions for density

$$\rho = \sum_{i=0}^{n} x^i \cdot \sum_{j=0}^{m} \boldsymbol{C}_\rho[i,j] \cdot T^j \text{ and} \tag{2.19}$$

and for specific heat capacity at constant pressure

$$c = \sum_{i=0}^{n} x^i \cdot \sum_{j=0}^{m} \boldsymbol{C}_c[i,j] \cdot T^j \tag{2.20}$$

defined both their partial derivatives and their integrals directly from the matrix of fitted coefficients $\boldsymbol{C}$. The resulting equations were

$$\left(\frac{\partial \rho}{\partial T}\right)_p = \sum_{i=0}^{n} x^i \cdot \sum_{j=1}^{m} \boldsymbol{C}_\rho[i,j] \cdot j \cdot T^{j-1}, \tag{2.21}$$

for the partial derivative of density with respect to temperature and

$$\int_{T_0}^{T_1} c\,dT = \sum_{i=0}^{n} x^i \cdot \sum_{j=0}^{m} \frac{\boldsymbol{C}_c[i,j]}{j+1} \cdot \left(T_1^{j+1} - T_0^{j+1}\right) \text{ and} \tag{2.22}$$

for the integrated specific heat capacity. Reducing the exponent by one and integrating in terms of temperature yielded the entropy term

$$\int_{T_0}^{T_1} \frac{c}{T} dT = \sum_{i=0}^{n} x^i \cdot \left(\boldsymbol{C}_c[i,0] \cdot \ln\left(\frac{T_1}{T_0}\right) + \sum_{j=0}^{m-1} \frac{\boldsymbol{C}_c[i,j+1]}{j+1} \cdot \left(T_1^{j+1} - T_0^{j+1}\right) \right), \tag{2.23}$$

Equations (2.19) to (2.23) were the last missing parts to compute Equations (2.13) and (2.14).

Data provided by manufacturers of heat transfer fluids are not always provided in the International System of Units from French 'Le Système International d'Unités' (SI units). Temperatures are often given in the local units °F and °C. An offset had to be introduced to enable the use of coefficients obtained from formulations in °C in thermodynamic relations that exclusively employ K for temperatures. Additionally, some scientific publications, like the one by Melinder [163], use a centred approach for fitting polynomials, which can enhance the fit quality. This also requires a base temperature, *i.e.* an offset, and a base concentration at which the value passed to the internal functions changes sign. The new variables were thus defined as

$$x_{\text{in}} = x - x_{\text{base}} \text{ and} \tag{2.24}$$

$$T_{\text{in}} = T - T_{\text{base}}. \tag{2.25}$$

This modification did not affect the linear combinations in Equations (2.21) and (2.22), but the integration of the first term of Equation (2.11) required some changes due to the logarithm in Equation (2.23). Besides that, the base temperature must not be equal to the reference temperature to avoid a division by zero in the logarithm of Equation (2.23). To enable the direct use of coefficients from publications based on centred fits, a new formulation for the integral $\int (\partial s/\partial T)_p \, dT$ had to be found, which is able to use the polynomial coefficient $\boldsymbol{C}_c$ from centred fits together with the modified temperature input as defined by Equation (2.25).

As a first step for simplification, the two binomial expressions $(T - T_{\text{base}})^{(j+1)}$ from the right hand side of Equation (2.23) had to be expanded to a series. Only containing j and T and being independent from x_{in}, the whole sum of temperature differences could be moved out of the inner loop to improve computational efficiency. The integration of this new function $f(j, T)$ then yielded the final factor F to be multiplied with the other coefficients and the concentration. The new expression for the integrated partial derivative of entropy with respect to temperature at constant pressure was obtained, which reads

$$\int_{T_0}^{T_1} \left(\frac{\partial s}{\partial T}\right)_p dT = \sum_{i=0}^{n} x_{\text{in}}^i \cdot \sum_{j=0}^{m} \boldsymbol{C}_c[i,j] \cdot F(j, T_{\text{in},0}, T_{\text{in},1}) \text{ with} \tag{2.26}$$

$$F = (-1)^j \cdot \ln\left(\frac{T_{\text{in},1}}{T_{\text{in},0}}\right) \cdot T_{base}^j + \sum_{k=0}^{j-1} \binom{j}{k} \cdot \frac{(-1)^k}{j-k} \cdot \left(T_{\text{in},1}^{j-k} - T_{\text{in},0}^{j-k}\right) \cdot T_{\text{base}}^k. \tag{2.27}$$

While polynomial functions, with or without offset, were sufficient to describe density and specific heat capacity, they are not the optimal choice for transport properties, the vapour pressure or the freezing temperature. Sticking to lower order terms, the fitting results for pure power polynomials were not satisfactory and other functions had to be employed. Especially exponential-like functions are difficult to approximate with ordinary polynomials, but the following three alternative formulations provide some variety and enabled the selection of more appropriate functions for each of the other properties. All of the additional formulations contained an exponential term, with the simplest one being

$$f(T) = \exp\left(\frac{\boldsymbol{C}[0]}{T + \boldsymbol{C}[1]} - \boldsymbol{C}[2]\right), \tag{2.28}$$

which required three coefficients to be fitted. A slightly different shape could be produced by stretching and shifting a logarithmic term by means of multiplication and addition of coefficients as in

$$f(T) = \exp\left(\log\left(\sum_{i=0}^{l} (T + \boldsymbol{C}[0])^{-i-1}\right) \cdot \boldsymbol{C}[1] + \boldsymbol{C}[2]\right). \tag{2.29}$$

The last alternative was created by

$$f(T, x) = \exp\left(\sum_{i=0}^{n} x^i \cdot \sum_{j=0}^{m} \boldsymbol{C}[i,j] \cdot T^j\right). \tag{2.30}$$

Out of the three presented equations, only Equation (2.30) was suitable for mixtures as it contained the input parameter x denoting the fraction of component other than

water besides the temperature T. Following the works of Melinder [163] and Skovrup [210], the exponents for both the standard polynomials and the exponential version were arranged in a triangular matrix to avoid overfitting. Formally, these conditions satisfied $0 \leq i \leq n$, $0 \leq j \leq m$ and $i + j \leq \max(n, m)$. For mixtures, $m = 5$ and $n = 3$ were assigned as default values. Omitting the composition term with $n = 0$ yielded the pure fluid formulations for which $l = 1$ and $m = 4$ were selected.

The standard polynomials were used for the density ρ, heat capacity c and thermal conductivity λ functions, while dynamic viscosity μ, vapour pressure p_{sat} and freezing temperature T_{freeze} were exponential functions. For exponential functions of only one variable, $\mu(T)$, $p_{\text{sat}}(T)$ and $T_{\text{freeze}}(x)$, the procedure started by fitting Equation (2.28). If the fit quality was poor, the second exponential function Equation (2.29) wast tested. The exponential polynomial Equation (2.30) was used as a fall-back function for single variable fits and it was the only function used for multivariate fits, for example $\mu(T, x)$. All the data fitting has been compiled in an easy-to-use Python package `CPIncomp`, which can be downloaded together with the CoolProp software.[1] This piece of Python software is organised around three interacting objects, which are all part of Figure 2.3: 'SolutionData', 'IncompressibleData' and 'IncompressibleFitter'.

The 'SolutionData' class acts a container for the input to the fitting routines. Its main purpose is to provide a common interface to access the data coming from all different kinds of sources. It holds data in protected variables and exposes means of testing data integrity as well as functions to calculate properties from fitted coefficients. The three subclasses 'DigitalData', 'PureData' and 'CoefficientData' do not provide any specialised functions. They are merely equipped with internal routines to make different data formats digestible for their base class. 'DigitalData' autonomously samples hard-coded property functions and converts the output to the correct format. To allow the input of univariate data sets, 'PureData' redefines parts of the internal functions of 'SolutionData', which normally requires two-dimensional (2D) matrices in temperature and concentration as input. The last class, 'CoefficientData' is able to convert coefficient matrices, like the ones from [163], to the correct format and thus disables the data fitting procedures for properties that already have fitted equations. Note that Python supports multiple inheritance and that combinations of the aforementioned can be created if necessary, for example 'DigitalData' and 'PureData' are needed to support a pure with a custom set of property functions.

Each 'SolutionData' object contains eleven instances of the 'IncompressibleData' class. It holds two instances that represent the input in temperature and concentration and six more for the different properties of interest: (i) density, (ii) specific heat capacity, (iii) dynamic viscosity, (iv) thermal conductivity, (v) saturation pressure and (vi)

[1] https://github.com/CoolProp/CoolProp

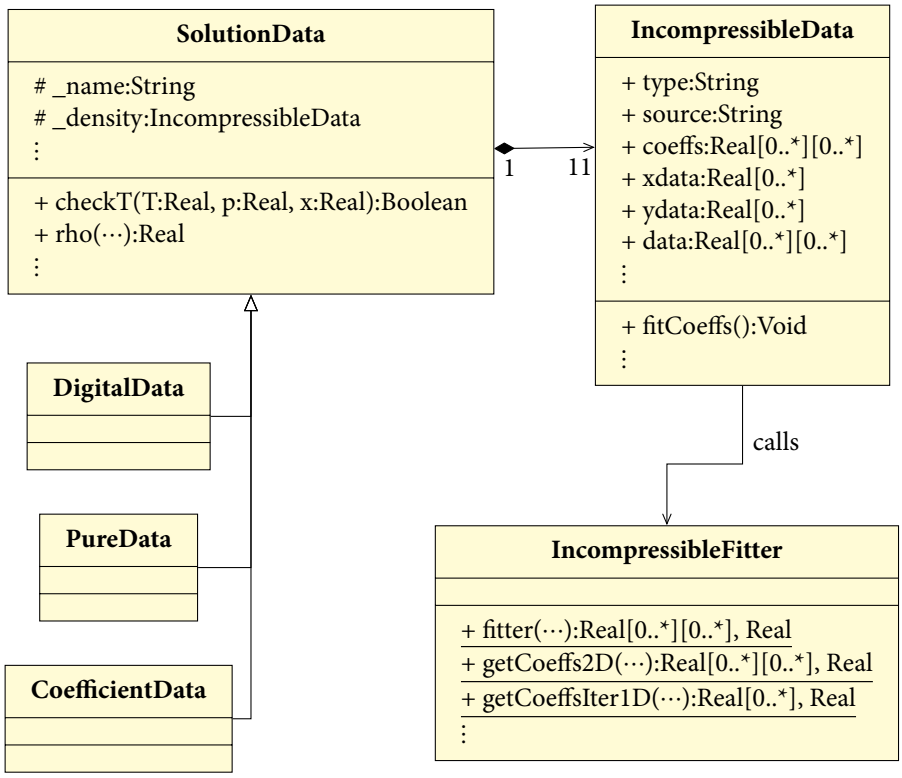

Figure 2.3: Python objects and their most important functions used during the data fitting procedure.

freezing temperature. The last three objects are needed to convert data between the different domains in which mixture information is stored: (i) mass-based, (ii) volume-based or (iii) mole-based. Each 'IncompressibleData' is filled with the coordinates of the data points in temperature, 'xdata', and concentration, 'ydata', before it calls the static functions in the 'IncompressibleFitter' object. The 'fitter' function determines whether the data should be represented by an exponential function or a normal polynomial and returns the fitted coefficients to the 'IncompressibleData' object together with information on the fit quality. If the function is of the exponential type, the fit is conducted on the logarithm of the input data since the values for such functions often span several orders of magnitude.

The beauty of using polynomials is that the coefficients can be found by solving a system of linear equations, as done in 'getCoeffs2D'. This guarantees to deliver the optimal solution in terms of the sum of squared errors. For more details, please have a

look at Appendix C.1 where the decomposition of the triangular coefficient matrix is described with an example and annotated code. The non-polynomial functions are fitted iteratively by 'getCoeffsIter1D' using the Levenberg-Marquardt algorithm [156], Powell's method [187] or the Broyden-Fletcher-Goldfarb-Shanno approach [189], which are available from MINPACK [169] and SciPy [113].

2.5 The Incompressible Fluid Database

The difficulties arising from the exponential nature of some inputs, especially viscosity data, are illustrated by Figure 2.4. Using an oil-based heat transfer fluid by Eastman Chemical Company [232] (Therminol 72) as an example, the curvature of the original data could not be matched by the normal exponential function from Equation (2.28). In fact, Therminol 72 is one of the fluids that made it necessary to include a new equation into the fitting procedure, which led to the introduction of Equation (2.29). This new form represents the data better than the other ones and produced an error that was one order of magnitude lower. Furthermore, Figure 2.4 shows why polynomials should be used with caution. Without further stabilisation at the boundaries, the resulting function tends to diverge from the original data at low and high temperatures.

The problem of polynomial fitting becomes even more obvious when comparing the derivatives of the newly constructed functions. In the derivatives shown in Figure 2.4, the real data exhibited a convex behaviour and so did Equations (2.28) and (2.29). However, Equation (2.30) introduced a new artificial inflection point and thus did not comply with the required monotonicity to reproduce a convex graph. At around 250 °C, the first derivative had a minimum and the second derivative changed sign. Note that negative values of the derivatives are omitted in Figure 2.4 to enable the logarithmic scaling of the ordinate. Such a difference in the evolution of dynamic viscosity is expected to be large enough to give misleading results in a pressure drop calculation.

In CoolProp, the incompressible fluids are divided into three major groups: (i) pure fluids, (ii) mass-based binary mixtures and (iii) volume-based binary mixtures. Until now, no mole-based mixtures have been added to the database, but the facilities are there to handle them. The pure fluids and mass-based binary mixtures are by far the most common fluids in this library. While the group of pure fluids contains data for many different kinds of incompressible liquids, almost all of the binary mixtures are aqueous solutions. For these liquids, the concentration always denotes the added component ranging from 0.0 for pure water to 1.0 for no water at all. Please refer to the tables in Appendices C.2 to C.4 for more details regarding the temperature and concentration ranges for each fluid. The sections in the appendix also contain one

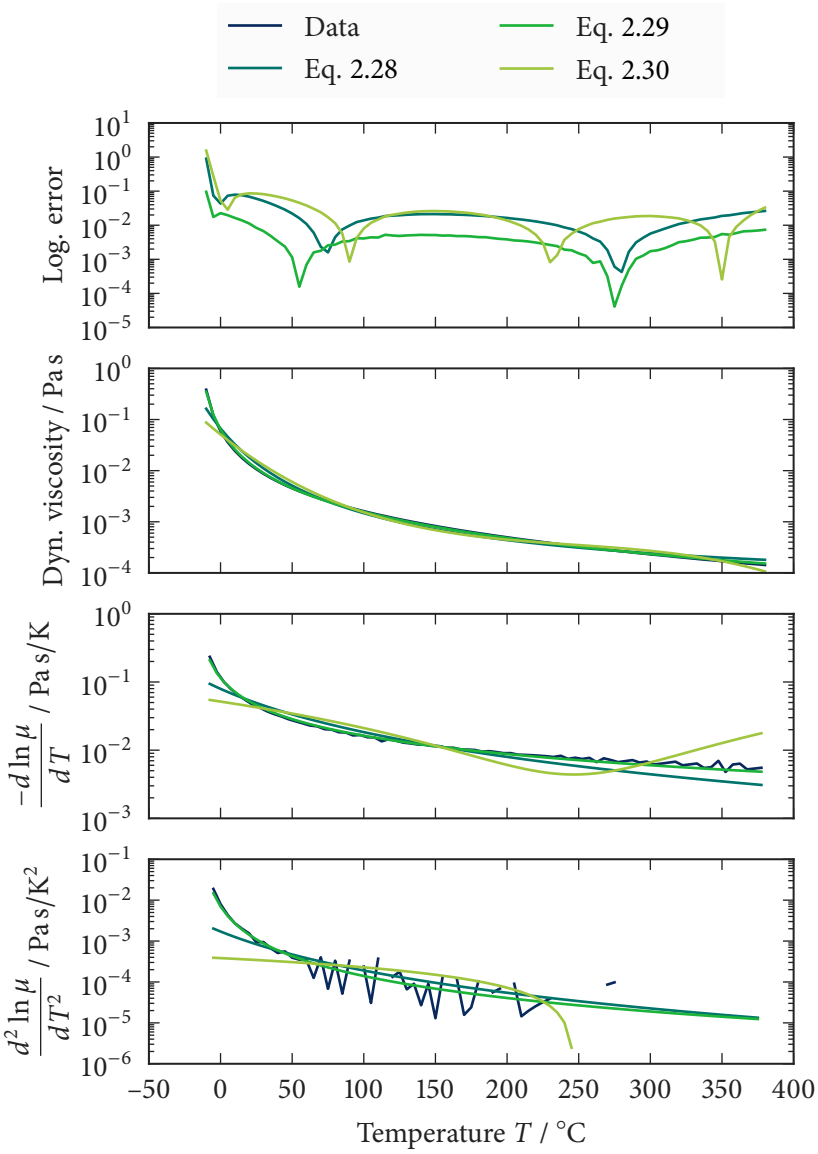

Figure 2.4: Error of the fit of the dynamic viscosity of T72 as a function of temperature approximated by the three different exponential functions and the first and second derivative thereof with respect to temperature calculated from data points and the three fitted functions.

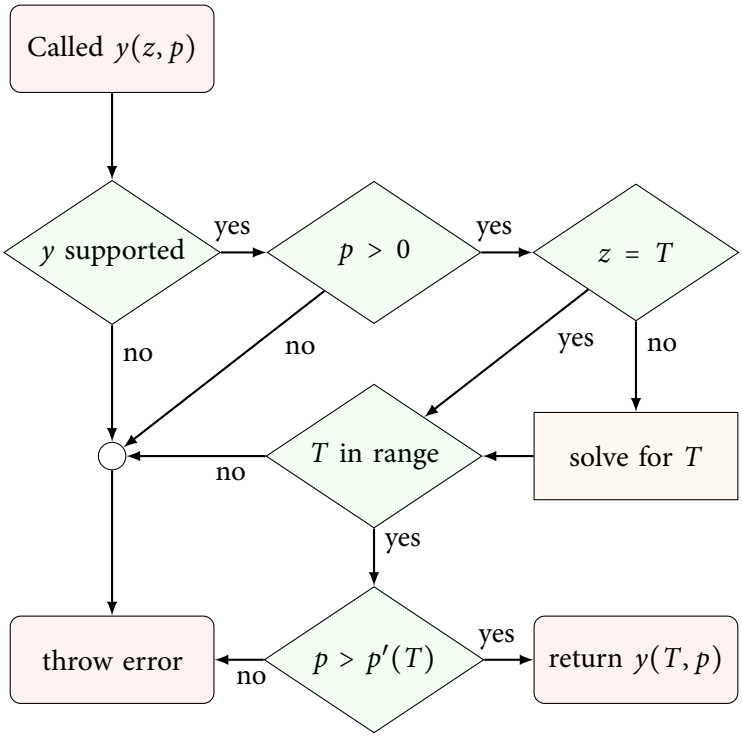

Figure 2.5: Procedure to calculate the properties of an incompressible liquid.

report page per fluid that holds information on the data source, the chosen fitting functions and fit quality for each of the 104 different data sets.

As mentioned already in Section 2.3, temperature T and pressure p are the preferred state variables for incompressible fluids since the equations are explicit in T and p. Figure 2.5 outlines the computational flow that is used to calculate the other quantities. Pressure has to be one of the provided inputs and the first test that is performed makes sure that only positive pressures are provided. If the second input is not temperature, a slightly modified bounded version of Brent's method [37, 38] is employed to obtain it from the provided input. If the fluid contains vapour pressure information, the pressure is compared to the saturation conditions before the final output is computed from temperature and pressure.

The secondary input pairs to calculate the state of an incompressible fluid are (ρ, p), (h, p) and (s, p). To assure that the algorithm finds the correct solution, it requires a bijective mapping $f : T \rightarrow y$: The property function has to describe a unique relationship between input and output. To satisfy this condition, the function

```
In [ 1]: from CoolProp.CoolProp import PropsSI
# A round-trip in properties to demonstrate accuracy and integrity
In [ 2]: T_init = 500.0
In [ 3]: P_init = 101325
In [ 4]: D_init = PropsSI('D','T',T_init,'P',P_init,'INCOMP::T72')
In [ 5]: S_init = PropsSI('S','D',D_init,'P',P_init,'INCOMP::T72')
In [ 6]: H_init = PropsSI('H','S',S_init,'P',P_init,'INCOMP::T72')
In [ 7]: T_init = PropsSI('T','H',H_init,'P',P_init,'INCOMP::T72')
In [ 8]: T_init
Out[ 8]: 500.0000000000001
# Some more code to demonstrate the mixture syntax:
# Density of a lithium bromide solution at 300 K and 1 atm.
In [ 9]: PropsSI('D','T',300,'P',101325,'INCOMP::LiBr[0.23]')
Out[ 9]: 1187.5438243617214
# Use different inputs to obtain the specific heat capacity with
# an alterntive mixture composition expression.
In [10]: PropsSI('C','D',1188,'P',101325,'INCOMP::LiBr-23%')
Out[10]: 3097.6976716141344
```

Listing 2.1: IPython example for using the incompressible fluid T72 and a lithium bromide solution

has to be strictly monotonic. Hence, its derivative is not allowed to have any roots. Transport properties cannot be used as inputs even though the functions might respect the aforementioned criterion.

The incompressible fluids are tightly integrated with the rest of the fluid property library. The prefix `INCOMP::` tells the factory function to select the incompressible backend for property calculations. Since all incompressible fluids are either pure substances or water-based mixtures, there is only one composition parameter, as shown in the second half of Listing 2.1. This parameter denotes the fraction of the fluid other than water. For pure fluids, providing compositional information throws an error. Composition fraction can be provided in a decimal notation from 0.0 to 1.0 in square brackets or alternatively as a decimal number in percent preceded by a hyphen, both cases are shown in Listing 2.1.

An example session in the IPython console illustrates the use of the incompressible fluids in Python. Based on an initial temperature of 500 K and a pressure of 1 atm, density, entropy and enthalpy were calculated. Using the last result as input to the next calculation the procedure verified the accuracy of the implementation since the final temperature equalled the initial temperature to numerical precision.

2.6 Verification & Computational Performance

To verify the implemented equations, this section compares the equations described above to the full EOS of water and another set of functions for the incompressible LiBr (aq). The first comparison will be based on the partial derivatives, while the second case directly compares the calculated properties h and s.

Figure 2.6 shows the partial derivatives of entropy and enthalpy with respect to the state variables for water in the liquid phase at 20 bar. Only the evolution of the properties with temperature is shown since neither Equation (2.9) nor Equation (2.10) depend on pressure. The approximated values, INC, were obtained from the equations described above and functions for density $\rho(T)$ and specific heat capacity $c_p(T)$ that were fitted to the respective values of the EOS for liquid water from 0 °C to 200 °C. For both, entropy and enthalpy, the changes with respect to pressure were about six orders of magnitude lower than the changes with temperature. This means that a pressure change of up to 10 bar has the same impact on enthalpy and entropy as a temperature change of 1 K, given that the overall behaviour does not change much during the integration.

The influence of pressure on entropy behaved in the opposite way compared to the influence on enthalpy. The absolute value of $(\partial s/\partial p)_T$ increased with temperature, while the pressure sensitivity of the enthalpy decreased with an increasing temperature. This situation changed for the derivatives with respect to temperature. The term $(\partial s/\partial T)_p$ decreased and $(\partial h/\partial T)_p$ increased with higher temperatures.

Over the last twenty years, a group from the Czech Republic has published a number of thermophysical property calculations codes for incompressible matter. Focussing on Gibbs energy formulations, they derived tailored high-accuracy equations for binary aqueous systems relevant for absorption refrigeration cycles using (i) NH_3 (aq), (ii) LiBr (aq) and (iii) LiCl (aq). Their publication on LiBr (aq) [179] also contains calculation routines for liquid water, while steam properties and the solid-liquid transition data for the salts, LiBr (aq) and LiCl (aq), are provided separately [180, 182].

Below, the LiBr (aq) properties from Pátek and Klomfar [179] are compared to the data calculated from the polynomial fits described above. It has to be mentioned that Pátek and Klomfar [179] were so kind to provide the C code to reproduce the data from their publication. Their code has been used without alterations to produce the graphs shown in Figure 2.7. Focussing on absorption systems, the reference equations always assume saturation conditions, which defines the pressure and removes one degree of freedom. The pressure dependency of the properties is not neglected, but included implicitly in the formulae for enthalpy and entropy. To prepare the comparison in Figure 2.7, density, specific heat capacity and saturation pressure of LiBr (aq) were approximated by polynomial functions. Afterwards, the procedure from Section 2.3

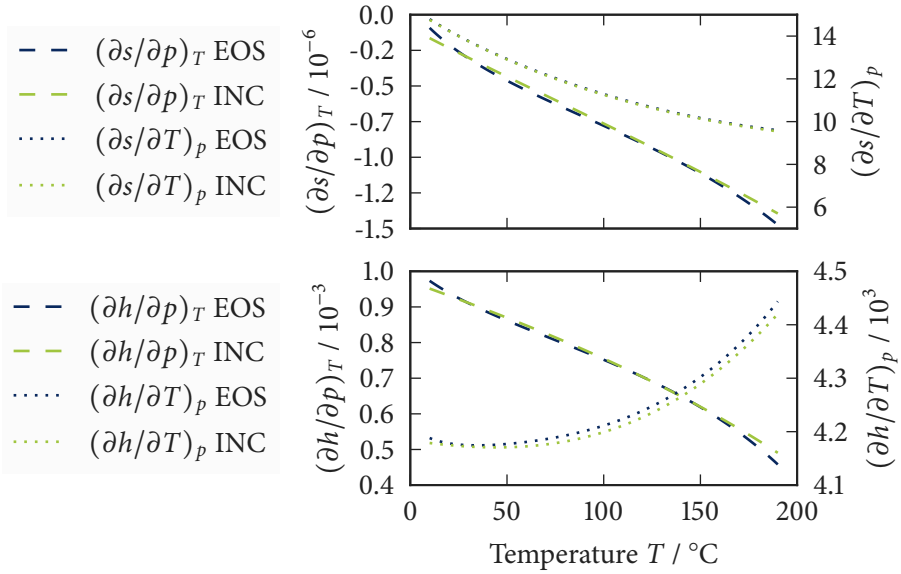

Figure 2.6: Partial derivatives of entropy s (upper graph) and enthalpy h (lower graph) with respect to pressure p and temperature T in SI units.The figure compares values calculated with the full equation of state (EOS) to values obtained from the simplified functions assuming incompressibility (INC) for pure water at a constant pressure of 20 bar. The derivatives with respect to pressure are shown as dashed lines and belong to the axis on the left side, while derivatives with respect to temperature are dotted lines and follow scale on the right hand side.

was employed to obtain entropy and enthalpy for three different mass fractions x of lithium bromide.

The three lines in Figure 2.7 correspond to increasing lithium-bromide mass fractions of 0.10, 0.35 and 0.60 from top to bottom for s, h, p' and c_p and from bottom to top for ρ. Pure water from Wagner and Pruss [246] is shown for comparison. Note that the p' for water is almost completely covered by the $x = 0.10$ line. The dotted lines that were produced with the new implementation lie on top of the solid ones, indicating that the data fitting was successful. A quantification of the deviation from the reference data for the incompressible fluids is presented in Table 2.10 in the next section.

The simple functions for the incompressible fluids did not require further optimisation to achieve satisfactory performance. This was different for the compressible

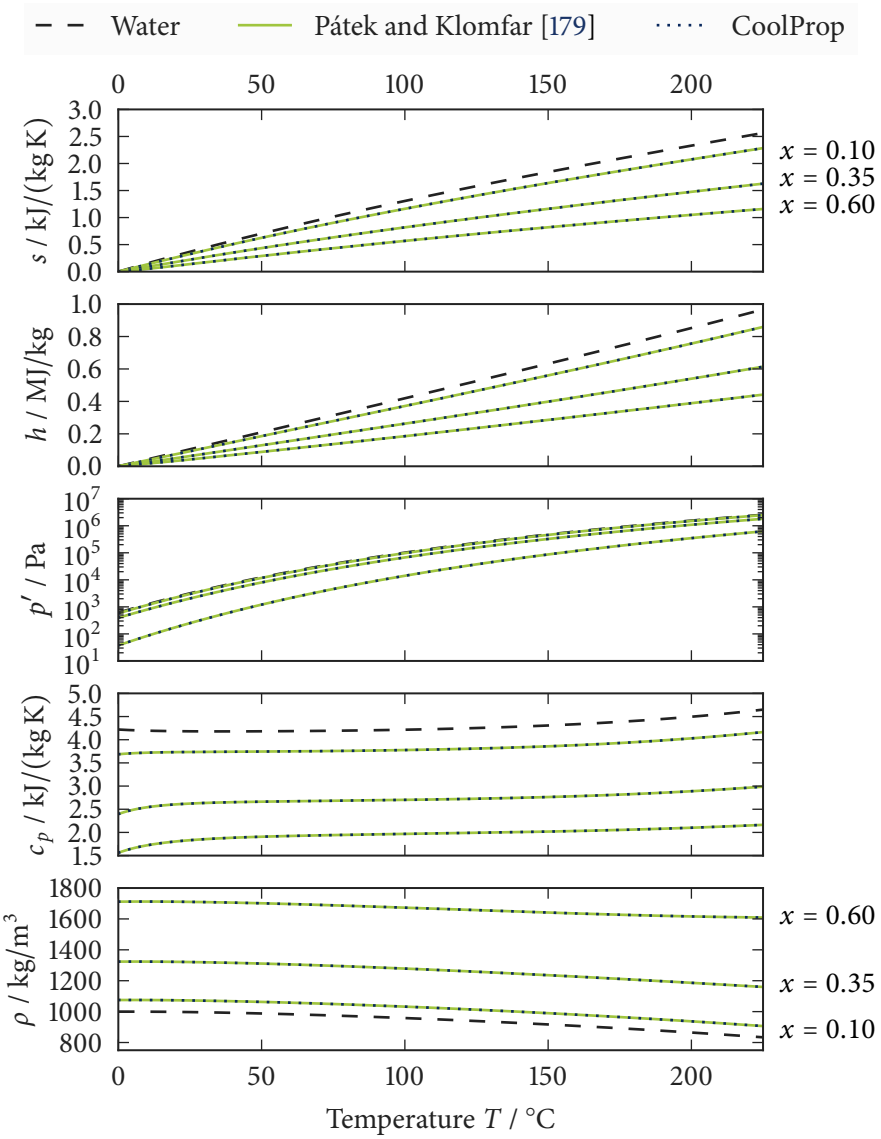

Figure 2.7: Entropy s, enthalpy h, saturation pressure p', specific heat capacity c_p and density ρ of a saturated LiBr (aq) solution calculated with the reference equations [179] and the implementation in CoolProp.

```
h_min = PropsSI('H','T',T_min,'Q',0,fluid)
h_max = PropsSI('H','T',T_min,'Q',1,fluid)
h_max = max(PropsSI('H','T',T_crit,'D',D_crit,fluid),h_max)
h_max = (h_max-h_min)*2.0+h_min
```

Listing 2.2: Determining minimum and maximum enthalpy for a test data set.

fluids. As written above, some EOS involve computationally expensive calculations. All the performance data shown in this report were recorded with CoolProp using the same desktop computer[2] for all calculations. Where possible, performance was compared to the current standard implementation from REFPROP. The range for property evaluations has been determined based on the triple point and the hard-coded limits for maximum pressure and temperature for each fluid.

The p, T-range was transferred to the h, p-domain by using the steps from Listing 2.2, which find the minimum and maximum enthalpy for the test data by comparing the critical enthalpy to the enthalpy of the saturated liquid and vapour phase at the triple point. Calculations for incompressible fluids cover the liquid region only and minimum and maximum enthalpy were obtained directly from the temperature and pressure limits.

Using a uniform distribution function, one thousand random points were selected from the enthalpy and pressure range. A full state record containing ρ, h, p, s and T was then populated for each point and checked for consistency. If any errors occurred, the whole record was discarded and new data points were picked with the distribution function. Errors might occur, for example, because the h, p-data ranges do not match totally with the ρ, T-space used for the internal calculations, which is described in more detail at the end of this section.

With data from fifty repetitions of the procedure described above, the bar graphs in Figure 2.8 could be generated. Each of the bars shows the average execution time calculated from the 50 000 data points. The bars are arranged in groups of three. On the left is a bar without hatching pattern. It represents the average time per call to a fit for the liquid phase according to Appendix C.1 using pressure p and temperature T as state variables. The central columns with forward diagonal hatching pattern were calculated from calls to CoolProp, while the rightmost bar of each group of three was taken from REFPROP-calls. It is shown here with a backward diagonal pattern. The columns are arranged in three groups that represent the expected computational effort required to obtain the requested property. The dark blue bars correspond to calls to a constant in the database. In our case, this was a call to the constant T_{max}, the highest

[2] Stationary computer running a 64 bit Debian system with Linux kernel 3.16.0, 8 GiB DDR2 memory at 800 MHz and an Intel Core2 Quad CPU Q6600 with 8 MiB L2 cache operating at 2.4 GHz

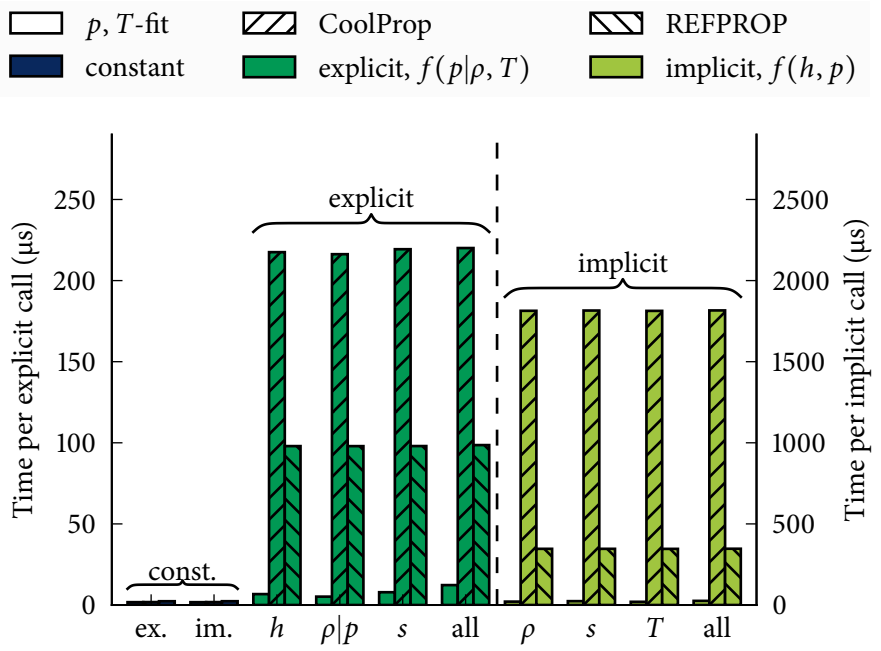

Figure 2.8: Average execution times of calls to the constant $T_{\max}$, properties as $f(\rho|p, T)$ and as a function $f(h, p)$ for water from CoolProp and REFPROP for 50 000 randomly distributed points.

valid temperature for the implemented EOS. Obtaining these values did not involve any calculation and was a measure of the overhead related to accessing the fluid properties. As expected, the values were returned much faster than in all other cases, regardless of the input parameters. Both the explicit 'ex.' and implicit 'im.' calls exhibited the same response time of 1.5 µs to 2.5 µs. The explicit calls used a combination of either p and T, for the incompressible fit, or ρ and T, for CoolProp and REFPROP, as inputs and did not require any iteration. The implicit calls used h and p as inputs and involved an internal iteration on the different state variables to calculate the requested property. The label below the abscissa of the four graphs for the explicit and implicit calls shows the property to be calculated.

Explicit calls to the polynomial fit of the incompressible region were only slightly slower than the first two calls to the constant values. The results were returned after approximately 5 µs to 12 µs with a small penalty for the calculation of all outputs compared to a single property. This penalty vanished for the implicit calls and all results

were available after 20 µs. Note that the explicit calls are related to the ordinate on the left hand side, while the implicit state evaluations were depicted with respect to the ordinate on the right, which was scaled by a factor of ten. For the two implementations of the full EOS, there was almost no penalty for calculating more than one output. In fact, REFPROP returned a fully populated thermodynamic state record by default to avoid multiple calls with the same inputs. Even though CoolProp does not determine all properties by default, it still saves temporary values for the different derivatives of the Helmholtz energy with respect to reduced temperature and pressure. Reusing these figures effectively limited the effort to calculate more than one output.

Comparing the values for the EOS by Wagner and Pruss [246], the CoolProp implementation was about two times slower than REFPROP for explicit calls: 220 µs versus 100 µs per call. For the implicit function calls, the ratio increased to a value close to five. It took CoolProp 1800 µs to determine the state from enthalpy and pressure, while REFPROP only needed 350 µs on average. Looking at other fluids, for example n-pentane in Figure 2.9, the picture becomes more diverse. The EOS by Span and Wagner [219] for n-pentane requires less computational work and direct calls to CoolProp and REFPROP yielded results after 35 µs and 50 µs, respectively. Even though CoolProp was faster for the direct evaluation of the EOS, the results for the implicit calls show and advantage for REFPROP.

The interpolation methods mentioned in Section 2.2 resulted in an execution time similar to the polynomial evaluation for the incompressible region. Being independent from the original EOS, the increase in computational speed obviously varied with the complexity of the EOS. For water, using IAPWS 1995 [246] in the subcooled region, both interpolation methods yielded an acceleration by a factor of more than 120 when calculating density from p and h based on the implementation described in our publications [29, 185]. Out of the time used to process one property call, the computational time for the actual calculation was as low as 1 µs per $\rho(p, h)$-call, the rest was used for string comparisons and object generation. The figure of 1 µs per call is in good agreement with the numbers reported by Johansen [112] for the same fluid. Johansen [112] also provides an in-depth comparison of numerous interpolation schemes, but limits his investigation to water as working fluid.

The relative error in density that was introduced from the approximations could be kept below 1×10^{-4} for the tested fluids water, R245fa and air. This error was observed to be largest in the two-phase region and in the vicinity of the critical point. Further away from the phase boundaries, the relative difference in density between EOS and tabular interpolation typically dropped to values between 1×10^{-7} and the numerical precision of the employed computer system.

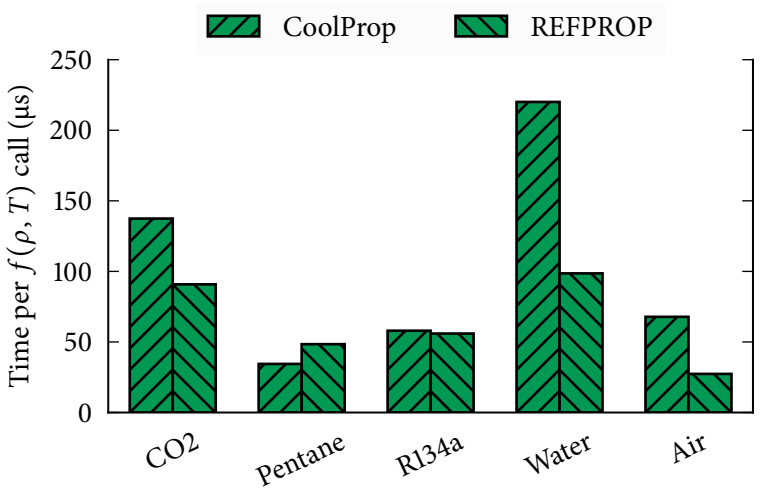

(a) Average time per ρ, T-call to CoolProp and REFPROP for five different fluids.

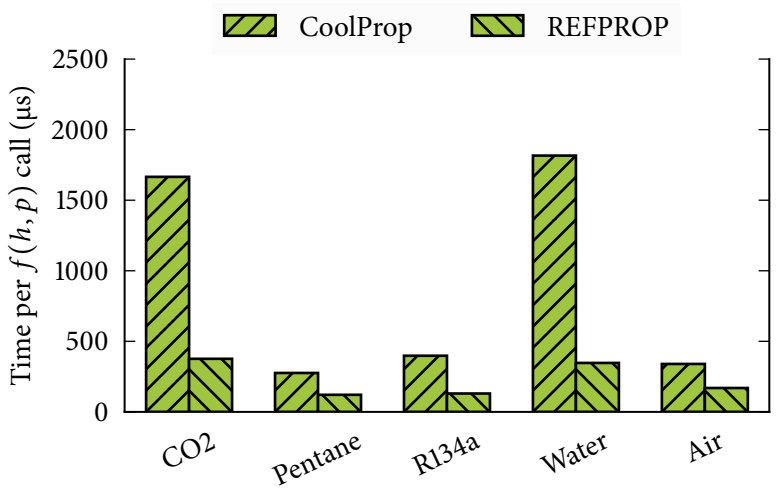

(b) Average time per h, p-call to CoolProp and REFPROP for five different fluids.

Figure 2.9: Average execution times of explicit and implicit calls to two different fluid property libraries calculated from 50 000 random points.

2.7 Accuracy & Performance Mapping

A summary of all the data fits carried out for CoolProp is given in Table 2.10. Rows containing minimum, average and maximum error in percent are shown for each of the fluid groups. A page number behind the smallest and the largest number refers to the detailed fitting report, which can be consulted for further details. The number in parentheses behind the average error shows the number of fluids that have coefficient for a certain equation. This number also includes the fluids that directly use coefficients from other publications and does therefore not reflect the number of fitted equations. All incompressible fluids have coefficients for density, heat capacity, viscosity and thermal conductivity. Many of the mixtures have information on the freezing temperature as a function of temperature and a fourth of the fluids have a function for the vapour pressure. The is the only mixture with a vapour pressure correlation.

The error was calculated as a normalised root-mean-square of a difference of two values (RMS) ϵ_0 from

$$\epsilon_0 = \sqrt{\frac{\sum_{i=1}^{n} \left(z_i - z_{\mathrm{ref},i}\right)^2}{n}} \left(\max(z_{\mathrm{ref}}) - \min(z_{\mathrm{ref}})\right)^{-1} \tag{2.31}$$

with n denoting the number of data points and z as the property to be fitted. The maximum normalised errors were all below 5 % and the average ϵ_0 was typically below 1 %. Only the saturation pressure p' had an average error above 1 %.

The relatively larger errors for c_p occurred typically for fluids that have a non-monotonic heat capacity function. The low order of a maximum of four coefficients in terms of temperature, a third order function, made it difficult to reproduce a function with inflection points. This was the case for the pure fluid in Appendix C.1 on page 239 and in Appendix C.1 on page 319. The large error for the viscosity in Appendix C.1 on page 242 occurred due to the discontinuities in the original data, which prevented the minimisation routines from working well. However, it also illustrates the benefits of fitting less flexible functions with an appropriate basic shape. Even though the data fit is not ideal, the shape of the curve still resembled the original data.

In general, it is difficult to make a fair comparison of software performance and this work is by no means a comprehensive study of computational efficiency. The results presented in Figure 2.9 should be interpreted with caution. There are many factors that influence the performance of a piece of software and especially if it involves mathematical solution procedures and different compilers. Solvers might have different criteria to determine the accuracy of a solution leading to different numbers of iterations. Compilers from different manufacturers and for different languages carry out a variety of optimisations regarding the mathematical procedures. At this point, also very basic

Table 2.10: Minimum, average and maximum normalised root mean square deviation in percent of the property fits divided into pure fluids, mass-based mixtures and volume-based mixtures. The full fitting report is on the page given after the minimum and maximum value. Parentheses behind the average value indicate how many data sets exist for this property.

Property		Pure	Mass-based	Volume-based
ρ	min.	0.00 % p. 262	0.00 % p. 285	0.00 % p. 315
	avg.	0.14 % (57)	0.10 % (34)	0.30 % (13)
	max.	0.51 % p. 221	0.61 % p. 306	0.99 % p. 319
c_p	min.	0.00 % p. 233	0.00 % p. 293	0.02 % p. 311
	avg.	0.87 % (57)	0.13 % (34)	0.59 % (13)
	max.	4.06 % p. 239	0.89 % p. 304	3.09 % p. 319
μ	min.	0.00 % p. 271	0.00 % p. 303	0.03 % p. 318
	avg.	0.61 % (57)	0.19 % (34)	0.46 % (13)
	max.	3.17 % p. 242	1.67 % p. 306	1.09 % p. 312
T_{freeze}	min.	%	0.00 % p. 281	0.00 % p. 323
	avg.	% (0)	0.11 % (30)	0.14 % (13)
	max.	%	1.42 % p. 306	0.63 % p. 318
λ	min.	0.00 % p. 261	0.00 % p. 287	0.08 % p. 318
	avg.	0.52 % (57)	0.24 % (34)	0.21 % (13)
	max.	2.03 % p. 224	2.43 % p. 308	0.56 % p. 322
p'	min.	0.01 % p. 257	0.21 % p. 279	%
	avg.	1.21 % (26)	0.21 % (1)	% (0)
	max.	4.79 % p. 259	0.21 % p. 279	%

functions play a significant role and an advantage in terms of performance might boil down to a superior implementation of the exponential function approximation. In addition to that, CoolProp and REFPROP also calculate different partial derivatives internally. REFPROP only calculates what is needed to provide the most common thermophysical properties, while CoolProp caches all derivatives of the reduced state variables that are required to compute any other partial derivative as summarised by Thorade and Saadat [238].

Discarding the absolute values, computational performance evaluation can still be used to identify areas for improvements of a piece of software and to find and map challenging application cases. Following the suggestions above, Figures 2.11(a) and 2.11(b) should not be compared to each other, but looked at individually. Hence the different scales for the coloured bars. Both graphs show the average execution time per call from 50 000 randomly distributed points. The darker colours indicates a faster execution for calls with the h and p inputs according to the coordinate system.

In addition to the execution times, Figures 2.11(a) and 2.11(b) also contain lines for easier inspection of the different regions. In both cases, the critical isobar, the critical isenthalp, the critical isotherm, the critical isentrop and the critical isochor are printed on top of the figures. Phase changes are also highlighted by another line around the two-phase dome and a line in the top left corner marking the liquid-solid transition.

The performance of both CoolProp and REFPROP degraded in the vicinity of the critical point. The vanishing of the differences between the vapour and the liquid phase challenged the solving procedure. As did alignment of isobars and isotherms, the critical isotherm runs horizontally through the critical point together with the critical isobar. The procedures used in Figure 2.11(b) exhibited a clear dependency on pressure and density. Shades of lighter colours follow the critical isochor and isobar indicating an increased number of iterations. The patterns occurring on Figure 2.11(b) also suggest that there are pronounced regions, which might be related to different procedures to obtain an initial guess for the iteration on density and temperature. Both fluid libraries performed well in the ideal gas region at low pressures and supercritical temperatures. CoolProp only had one defined region, which lies between 300 bar and 1000 bar. The solver performed worst in this pressure range and the influence of the critical isotherm was less pronounced. The smooth changes in the execution time distribution also indicate that the guess value generation in CoolProp employed less conditional statements that made the algorithm switch between different formulations based on clearly defined pressure and enthalpy values. This trend could also be observed for other fluids, more information on CO_2, n-pentane, R134a, air and incompressible water can be found in Appendix B.2.

Looking at the incompressible LiBr (aq) implementation in Figure 2.12, the bounded solver performed well in the full range for the data fit. The time distribution was almost

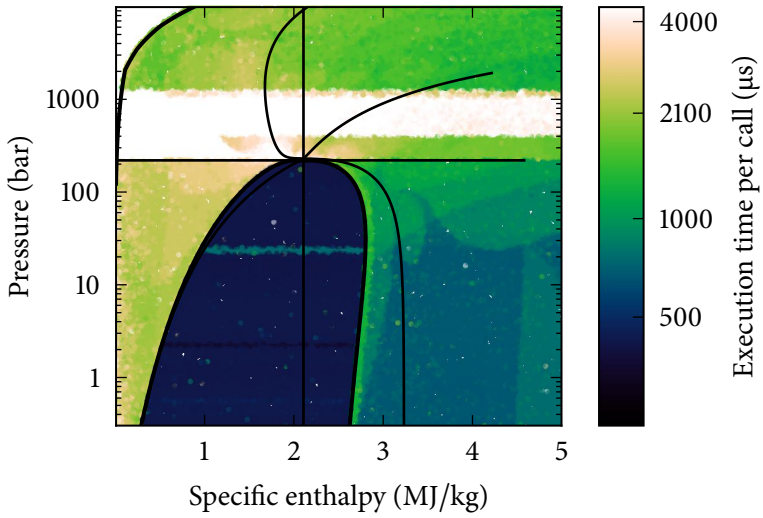

(a) Water from CoolProp using Wagner and Pruss [246].

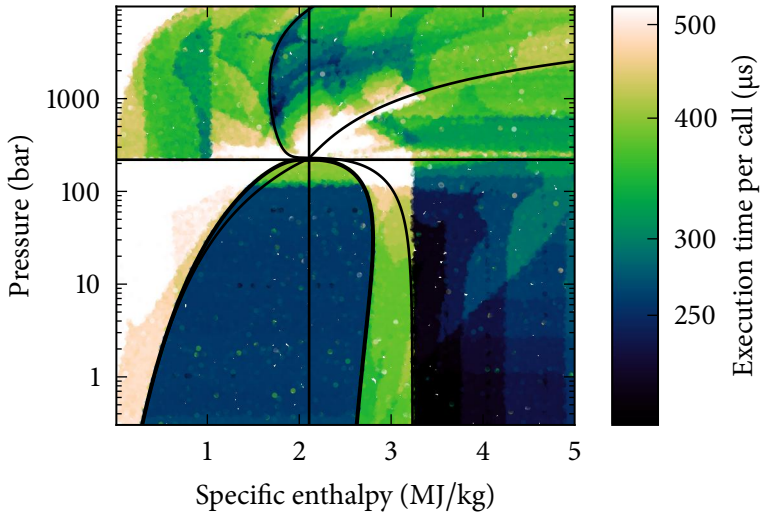

(b) Water from REFPROP using Wagner and Pruss [246].

Figure 2.11: Execution times of calls to $f(h, p)$ for water using different implementations of the same EOS by Wagner and Pruss [246].

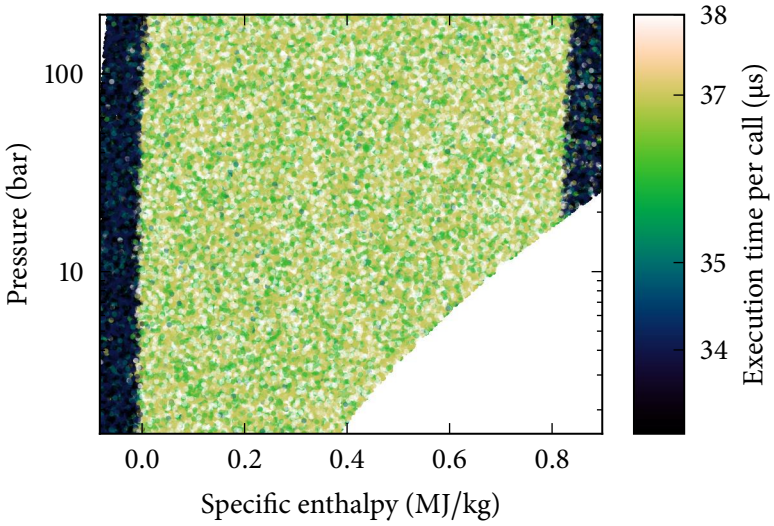

Figure 2.12: Execution times of calls to $f(h, p)$ for LiBr (aq) using the polynomial data fits.

uniform with slightly improved calculation speed close to the boundaries. Compared to the full EOS, the functions for the liquid region were rather well-behaved and did neither challenge the solver's stability nor did they require extensive iterations.

Despite the poorer performance of CoolProp for many of the tested cases, optimising the solvers and guess value generation is not a high priority task. Being able to precalculate data for the interpolation backends removes the need for fast evaluations of the EOS. Users that require fast execution times will most probably employ the interpolation routines. For lighter applications, calculation times of 2.5 ms are acceptable.

In order to employ the interpolation techniques discussed above, tabulated data has to be generated from the EOS. The current implementation uses gridded data sets in terms of enthalpy h and logarithmic pressure $\ln p$ and logarithmic specific volume $\ln v$ and temperature T, respectively. The minimum enthalpy h_{min} is the enthalpy of the saturated liquid state at the minimum temperature defined by the employed EOS T_{min}. The maximum enthalpy for the table data h_{max} is found in a fashion similar to the procedure described in Listing 2.2. The minimum pressure p_{min} is defined by the saturated vapour state at T_{min}. p_{max} is obtained from doubling the reducing pressure of the EOS, which often is the critical pressure. T_{max} is defined in the same way, while minimum and maximum specific volume are extracted from the previously

generated tables in h and $\ln p$. The resulting regularly spaced grids for water are shown in Figure 2.13.

It is obvious from Figure 2.13 that the two ranges of tabulated data do not cover the same regions. Therefore, additional calculation steps are required to assure that the calculation stays within the bounds of both data sets. Note that the overlap between the regular grid in enthalpy and pressure, shown with a lighter colour, and the gridded properties in terms of v and T, shown with darker lines, is rather large for water. For other fluids, especially man-made refrigerants, only a small portion of both tabular sets overlaps.

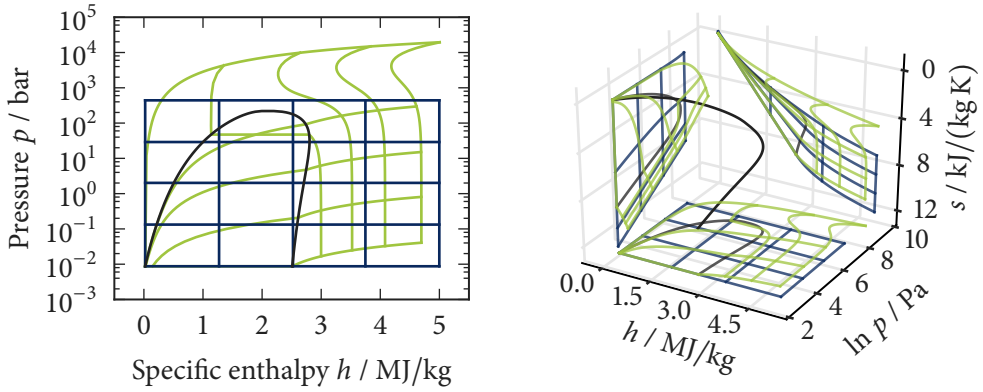

(a) Water with pressure and enthalpy as reference properties.

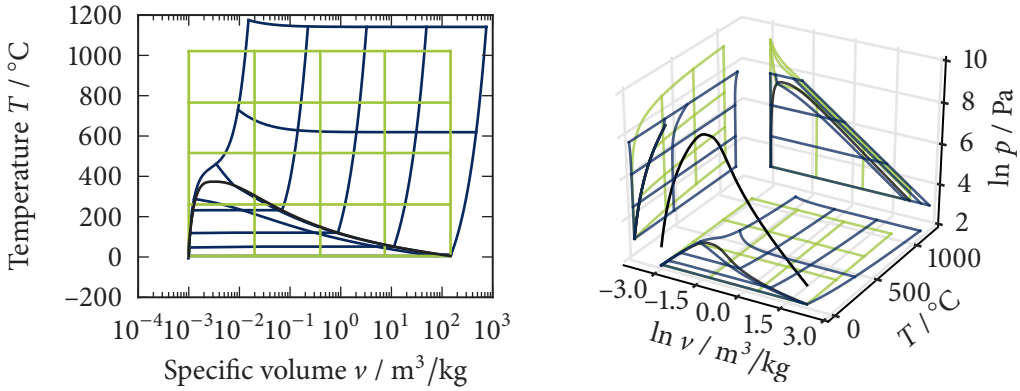

(b) Water with temperature and volume as reference properties.

Figure 2.13: Gridded water properties with (p, h) and (T, v) as reference systems. The darker coloured grid is spaced regularly in the logarithmic pressure and in enthalpy, while the lighter coloured grid is constructed from logarithmic specific volume and temperature.

2.8 Conclusions & Outlook

The design of a new fluid property library was introduced and described. The new CoolProp heavily uses inheritance and other features of object-oriented programming. The redesign of the software lead to a clearer structure and is expected to simplify maintenance tasks. The reorganisation of the code was carried out because the old structure could not deal with mixtures. The new version now contains binary interaction parameters for a number of refrigerant and natural working fluids.

Many thermodynamic relations could be implemented in a general way providing access to analytical derivatives for all thermodynamic properties. In additional to that, new equations for incompressible fluids were implemented that allow the calculation of all thermodynamic properties and some partial derivatives. A new fitting framework was developed and applied to more than one hundred datasets for incompressible heat transfer fluid including binary mixtures. The coefficients obtained from the fitting routines were used to validate the implemented functions via a comparison to published data calculated with different sets of equations. New equations were presented to obtain entropy from heat capacity polynomials that use an offset.

The new library has not been optimised for efficiency and it currently performs worse than the industry standard in terms of computational efficiency. Depending on the EOS in use, the average execution time per property call as required by CoolProp was between 0.8 and 2.5 times the computational time needed by REFPROP for explicit evaluations based on density and temperature. For implicit calls based on pressure and enthalpy, the aforementioned ratio increased up to a value of 5 while the accelerated calculation methods based on interpolation provided a speedup up by a factor of 120 and thus reduce the need for very responsive equations and solvers. The distribution of execution times in the property space nevertheless suggests that there are regions with a significant optimisation potential, especially at supercritical pressures.

Due to the high accuracy of these interpolation methods [29], the next version of CoolProp will cover the whole T, p and h, p space for an EOS with the same number of data points, currently 200×200. The maximum enthalpy is then obtained from $T_{\max}$ in the low pressure limit. Besides the obvious boundaries given by T, p and h, p, a melting curve based on the Simon-Glatzel equation can be used to further reduce the area that has to be covered. However, special cases with a negative inclination of the melting curve in h, p coordinates, like water, will still require the evaluation of the EOS in some cases. With those two reference data sets, a one-dimensional search in the tables would allow for twelve different input pairs. Only the combinations s, u and s, v and u, v will not be covered. Transport properties will be tabulated in T, p with numerical derivatives instead of T, v to play well together with the other tabulated data and to avoid the computationally expensive extended corresponding states method.

Chapter 3

Reciprocating Expander

This chapter describes the expansion technologies used in small scale organic Rankine cycles and reciprocating machines are discussed in detail. Continuing the work of Wronski et al. [258], a prototype of a reciprocating expanders is presented and studied with both experimental and modelling work. Measurements obtained from different operating conditions are used to validate a dynamic model that also has been described by Wronski, Skovrup and Haglind [259]. Afterwards, this model is employed to study different admission valve control schemes for a cogeneration system presented by Wronski, Oudkerk and Haglind [257]. A theoretical investigation of an expansion process and ideal reference cases suggests that the work output is less affected by the heat loss from the expander.

3.1 Volumetric Expanders for ORC Systems

Various expansion machines are used in mini and small scale organic Rankine cycle (ORC) installations. Among these, volumetric machines are the most popular with published work on, for example, vane-type [20, 21, 55, 59, 167, 194], screw [16, 213, 214, 252, 264], reciprocating [87, 162, 221] and scroll expanders [4, 27, 28, 49, 60, 86, 143, 145, 148, 173, 174, 243, 248, 265]. Even though there is experimental research on flow machines for cycles with capacities down to 1 kW_{el} [62, 149, 184], the review of Qiu, Liu and Riffat [193] for power cycles with less than 10 kW of electrical output recommends vane-type air motors or dedicated vane-type expanders and scroll machines. Also Quoilin et al. [197] expect displacement expanders to remain the most common expansion devices.

As indicated by the number of references given above, scroll machines dominate in the literature, but they have some noticeable drawbacks that motivate research within the field of reciprocating machines. Scroll machines have a relatively low built-in volume ratio, or expansion ratio $\Upsilon = v_{out}/v_{in}$, and operating at high pressure ratios Π requires two machines in series [195]. Such a more complex assembly could operate with an expansion ratio of up to twelve, which still is less than what can be achieved with single stage reciprocating machines. Reciprocating devices can reach ratios well above twenty being limited only by the clearance volume, which is the volume between the piston at top dead centre (TDC) and the cylinder head.

Employing their experience within small scale refrigeration plants, Quoilin et al. [198] draw operational regimes for scroll and screw machines concluding that neither of them can cover the high expansion ratios required for biomass combined heat and power (CHP) and high temperature waste heat recovery. In their publication, Quoilin et al. [198] give a maximum expansion ration of four for scroll machines and five for screw machines. Furthermore, the authors of [198] define a volumetric performance indicator VC to be

$$VC = \frac{\dot{V}_{\text{in}}}{\dot{W}} = \frac{v_{\text{in}}}{\delta h} \tag{3.1}$$

based on either volumetric flow rate $\dot{V}$ and power $\dot{W}$ or on specific volume v and enthalpy change δh, which should have a maximum value of $0.5\,\text{m}^3/\text{MJ}$ based on their experience with refrigeration compressors.

A similar method has been used before by Brunin, Feidt and Hivet [40] to define the operating regimes of compression heat pumps. Even though Quoilin et al. [198] do not refer to the earlier work [40], the used volumetric indicator is the same: $0.5\,\text{m}^3/\text{MJ}$ in [198] and $2.0\,\text{MJ}/\text{m}^3$ in [40]. The other limiting factor of the operational regime is the desirable isentropic efficiency η_s of not less than 0.9. Figure 3.1 illustrates how the aforementioned criteria are used to create the operational space for a certain expansion machine running at subcritical conditions.

The two darkest solid lines cut the figure into four pieces at the critical temperature of the working fluid. The second solid line limits the left hand side of the operating domain and indicates the saturation temperatures and which the isentropic efficiency is equal to 0.9. Left of this line, underexpansion losses make the efficiency drop below the chosen threshold value. Running the expander in the space on the right of the efficiency line yields efficiencies above 0.9 and it is the volumetric performance indicator that forms the boundary here. Until now all calculations have been carried out with the maximum expansion ratio, but at lower expansion ratios, the maximum VC calculation extends the operating map further to the right. The dotted line shows the limiting VC for the lower limit of the expansion ratio, which is set to 2.5. The space that is confined by the boundaries discussed above forms the possible operational regime within which a given technology performs according to the defined limits or better forming the area indicated with the light dashed line in Figure 3.1. Note that the procedure described here deviates from the approach of Quoilin et al. [198] in one point. The extension of the operating regime at low expansion ratios is not considered in the original work and thus the operational enveloped described here is larger than that described in the cited publication.

To draw a similar map for reciprocating machines, a volume flow range has to be defined on the low pressure side of the expander. Assuming a possible rotational speed

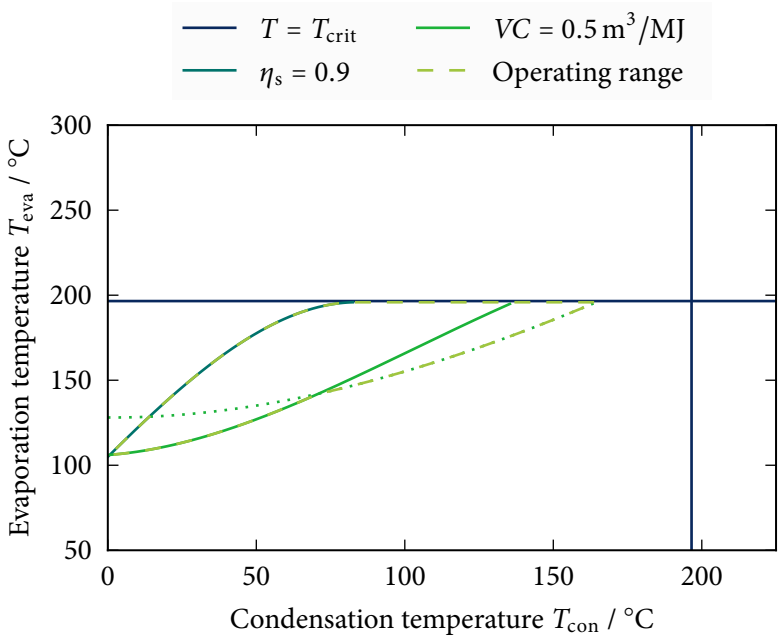

Figure 3.1: Construction of the operating domain of volumetric expanders.

Table 3.2: Limitations for the operation of different volumetric expanders.

	$\dot{V}_{out}$		Υ		η_s	VC_{max}
Scroll	1.1	49	2.5	4	0.9	0.5
Screw	25.0	1100	2.5	5	0.9	0.5
Piston	0.2	80	2.5	10	0.9	0.5

from 240 rpm to 2400 rpm and a swept volume of 50 cm^3 to 2000 cm^3 the minimum and maximum volume flow rates can be calculated as presented in the last row of Table 3.2. Regarding the inlet and outlet conditions, one can assume that the expander operates with an expansion ratio of up to ten, which still is a rather conservative choice and higher expansion ratios are possible if needed.

ORCs operate with different fluids and numerous studies have been conducted that describe different approaches to select an appropriate working fluid for a given application. Therefore the operating maps are drawn for several fluids and thus provide a simple tool for a preliminary fluid selection, if the number of possible working fluids

can be reduced beforehand by other criteria like flammability or health concerns. Selecting R134a, R245fa, R123, n-pentane, toluene and MDM makes the graphs cover some of the most common working fluids.

Based on the volume and efficiency constraints, the fluid properties link evaporation and condensation temperature that form the axes of Figure 3.3(a) and of Figure 3.3(b). The maps for scroll expander and reciprocating machine have a similar shape and the overall position is determined by the working fluid. The low expansion ratio volume constraint is more visible in Figure 3.3(b) where the right hand branch of *VC* extends the map to higher condensation temperatures. The flexibility that comes with higher maximum expansion can be found in the larger area covered by the reciprocating machines compared to the scroll. The operational regimes for the scroll lie within the boundaries for the reciprocating machines, which covers approximately twice the area in Figure 3.3.

Running at high expansion ratios requires accurate timing of the admission and exhaust process. Especially the intake phase has to be controlled carefully because minor differences in the amount of admitted fluid have a large impact due to the large density differences between compressed and expanded vapour. The valves used for admission and exhaust of the working fluid are thus a potential source of losses. In their recent work, Antonelli et al. [12] investigate timing effects for the working fluids isobutane and R152a in a rotary piston device and Badami and Mura [18] present a study for a small scale reciprocating steam engine that investigates losses associated with the gas exchange in the expansion chamber.

However, the sensitivity to valve timing can theoretically also be an advantage of piston expanders. The operational regime of a single machine can be extended by applying a variable valve control scheme. The valves in the cylinder head of reciprocating machines are often easily accessible, which makes design of control mechanisms less cumbersome than in other volumetric devices. Installing several admission lines in very compact devices of the scroll or rotary piston type is often more complicated.

Despite such promising perspectives, volumetric ORC expanders with a variable expansion ratio are not discussed extensively in the literature. Even though they might exist, no papers published on reciprocating ORC expanders with variable expansion ratios could be found in the literature search conducted for this thesis.

The following sections briefly introduce the experimental facilities used to record operational data from tests of a reciprocating ORC expander delivering up to 2.5 kW at six different operating conditions running with n-pentane as working fluid. The single-cylinder single-stage expander prototype was developed by the project partners involved in this project and has been tested collaboratively at the Technical University of Denmark, Department of Mechanical Engineering, Kgs. Lyngby, Denmark (DTU).

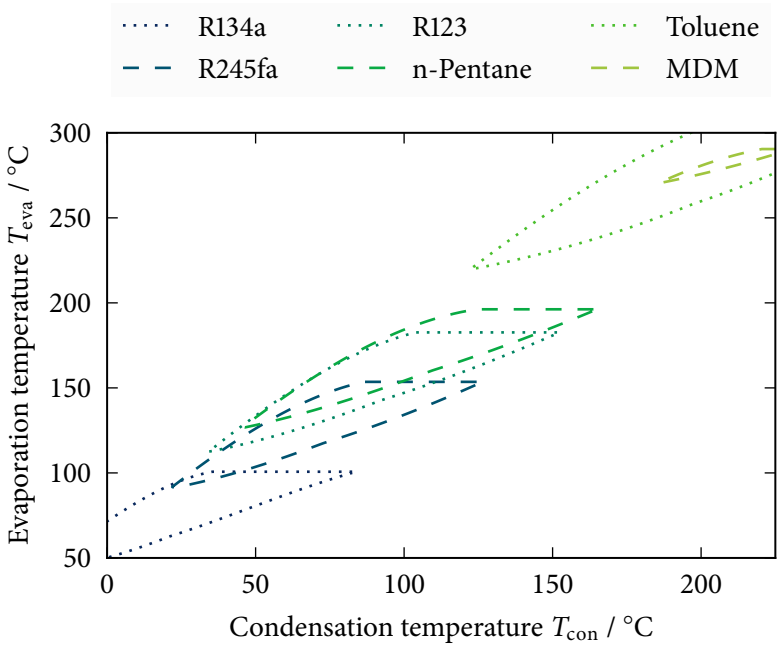

(a) Operational regime for a scroll expander.

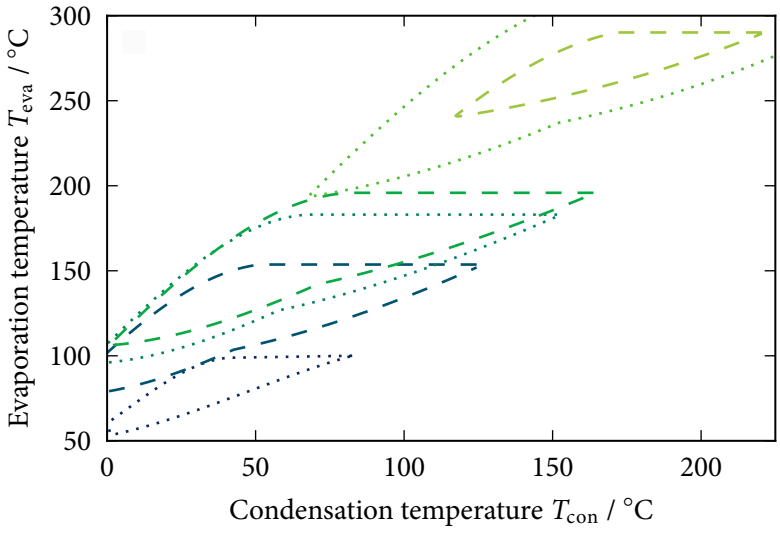

(b) Operational regime for a reciprocating expander.

Figure 3.3: Typical operational regime for volumetric expanders using different working fluids.

To improve the performance at varying operating conditions, the machine uses a variable admission valve timing and two sets of exhaust valve profiles.

Based on the experimental data, a dynamic model is formulated in the Modelica language. Special attention is paid to the robust modelling of the valve actuation to avoid computational inefficiencies caused by singularities of state variables or their derivatives. Based on this modelling work, an isentropic expansion efficiency is calculated and presented together with other results describing the special features of the discussed system. The model and the experimental data are compared for six steady-state operating points. High resolution pressure and torque traces are presented as well as figures showing the isentropic expander efficiency and amount of produced work per revolution. Eventually, the differences between the model and the measurements are discussed providing explanations for most significant differences. Using fixed valve operation, this model can be used to identify the losses associated with non-optimal valve characteristics for a given operating range. Considering variable valve control, the efficiency model can be used to formulate a control strategy and to identify the correct control input parameters.

3.2 Design, Tests & Modelling

Studied Machine & System

Initial tests of the proof-of-concept design of a reciprocating ORC expander shown in Figure 3.4(a) have been conducted in 2011 and were described briefly by Wronski et al. [258]. In this machine, a double-acting piston connects two expansion spaces resulting in a compounding configuration where the working fluid starts to expand in a small high pressure chamber. During the second half of the stroke, this volume gets connected to another chamber yielding a final expansion step that uses the combined volume of both chambers.

The successful initial tests motivated the commercial partners to design a more production-oriented second version of the machine. The new design is more conventional and features two 'ordinary' single-acting pistons that only produce work during the half of one crankshaft revolution each. Also here, the cylinders are connected by a valve allowing for either two-stage operation in series or as a parallel configuration for increased power output. The data presented here were, however, recorded during operation with one cylinder only.

Following the structure of the physical device, the reciprocating machine is described on a per-component basis. The most relevant parts are shown in Figure 3.5 and will be discussed in more detail below. A bearing holds the crankshaft, which is connected to the crank arm of the length l_{cr}. A connecting rod with length l_{ro} links the

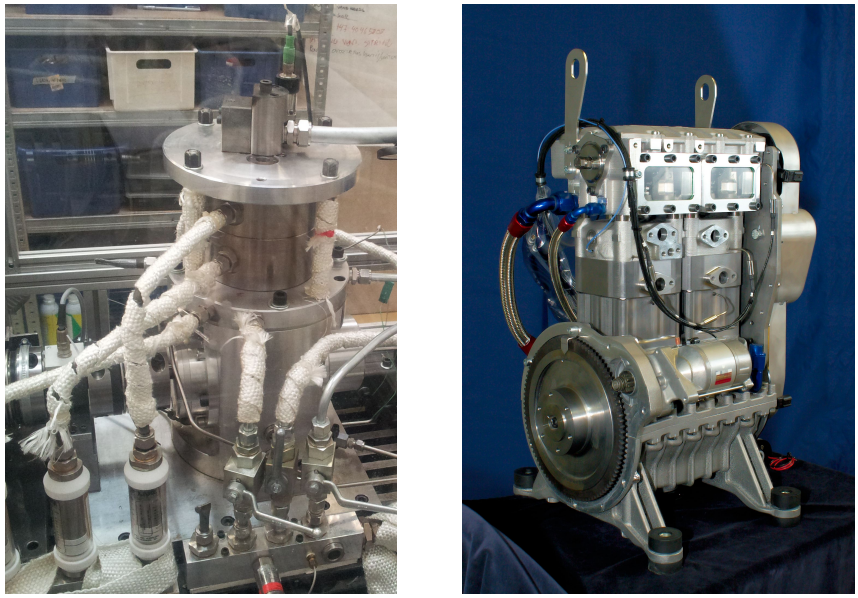

(a) Proof-of-concept design. **(b)** Second expander prototype.

Figure 3.4: Photographs of the two tested reciprocating expanders.

piston pin to the crank arm. Since the piston pin is not necessarily located right above the crankshaft, there is a piston pin offset, which is denoted by δ_{pi}. The piston itself has a bore of d_{pi} and its movement is limited to the vertical direction by a cylindrical wall of a mass m_{w} and a temperature T_{w}. All mechanical parts shown in Figure 3.5 are regarded as ideally stiff and with their mass distributed evenly along their main axis.

The fluid-related indices 'in', 'cyl' and 'out' used in Figure 3.5, refer to the thermodynamic states in supply pipe, expansion chamber and exhaust line, respectively. Mass can enter and leave the control volume through three ports: (i) inlet valve, (ii) outlet valve and (iii) the leakage gap of equivalent diameter δ_{w} between piston and cylinder wall. Energy exchange with the control volume takes place by means of heat transfer to and from the walls at temperature T_{w} and by the amount of work extracted or added via the piston. Since the piston is located directly above the crankshaft δ_{pi} is 0 m. The clearance volume, which is left in the expansion chamber when the piston reaches TDC, is 36 cm^3. All other geometric details are listed in Table 3.6. Here, the masses of the bearings at each end of the connecting rod are added to the piston and the crankarm, respectively. Since the latter is a lumped quantity accounting for the rotating masses below the cylinder, it is an estimated value. The dagger symbol † indicates

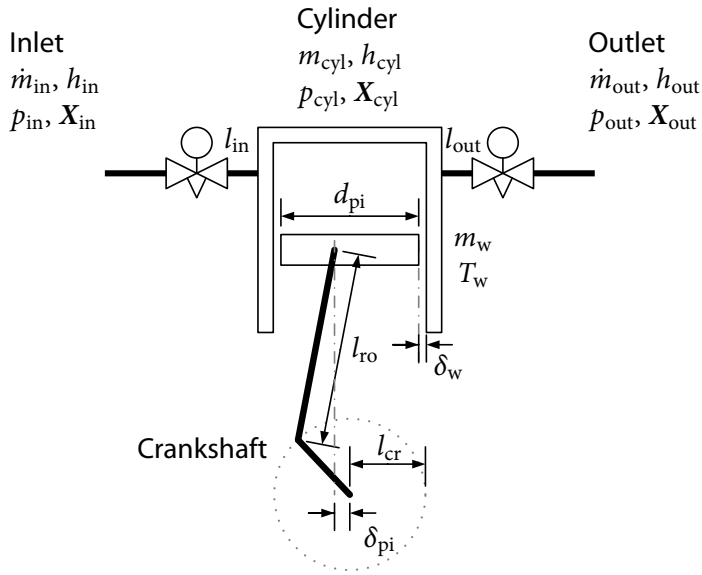

Figure 3.5: Control volume and geometry of the reciprocating machine.

Table 3.6: Properties of the different mechanical parts.

Piston	$d_{pi} = 46\,\text{mm}$	$m_{pi} = 400\,\text{g}$
Conrod	$l_{ro} = 163\,\text{mm}$	$m_{ro} = 423\,\text{g}$
Crankarm	$l_{cr} = 55\,\text{mm}$	$m_{cr} = 750\,\text{g}^{\dagger}$
Wall	$\delta_w = 0\,\text{mm}^{\dagger}$	$m_w = 25\,\text{kg}^{\dagger}$
Inlet	$d_{in} = 25.6\,\text{mm}$	$l_{in} = 0\,\text{mm}^{\dagger}$
Outlet	$d_{out} = 22\,\text{mm}$	$l_{out} = 0\,\text{mm}^{\dagger}$

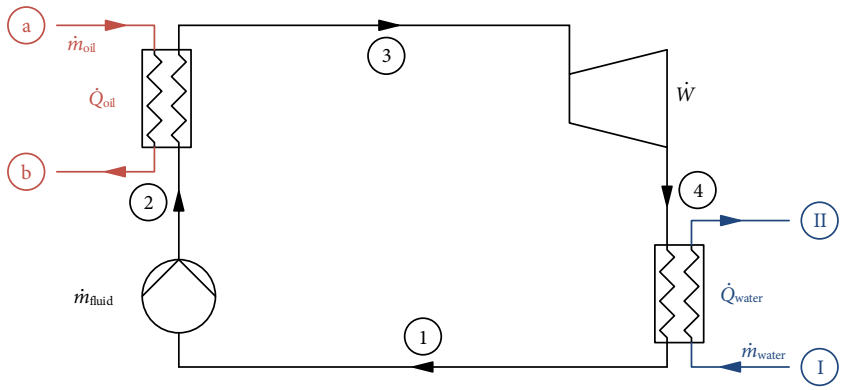

Figure 3.7: A simplified sketch of the investigated power cycle.

that the mass could not be measured directly. The crankarm weight is found from a simplified geometric sketch assuming an approximate density of 7600 kg/m^3. Using an average density of 2700 kg/m^3, the same method was applied to find the total jacket mass attributed to one cylinder. While the crankarm is made from stainless steel, the expander jacket is made of aluminium, hence the different density figures. Both values are rounded to account for the inaccuracy of the weight estimation. Leakage is neglected by setting the gap size δ_w to 0 mm. The lengths of 0 mm for l_{in} and l_{out} are used since the valves are located in the cylinder head and no additional pressure drop occurs due to a piece of pipe mounted between the valves and the expansion chamber.

Based on a modified version of Figure 1.1, the process diagram in Figure 3.7 shows the main components that were used during the experiments. Besides the expander, the experimental rig includes an air-driven piston pump to pressurise the working fluid from (1) to (2) before it enters the evaporator. The evaporated fluid passes the expander from (3) to (4) and reaches the water-cooled condenser leaving it in state (1). Both heat exchangers are brazed plate type devices. An oil loop with 400 l of heat transfer fluid and five 12 kW electrical heaters supplies the heat flow rate $\dot{Q}_{oil}$ to the evaporator, while cooling the heat transfer medium from state (a) to state (b). The cooling water loop removes the heat flow rate $\dot{Q}_{water}$ from the condenser by heating the water flow rate $\dot{m}_{water}$ from state (I) to state (II).

Figure 3.7 does not include the receiver vessel for the working fluid which has an approximate volume of 5 l and is placed between the condenser and the pump covering the height difference of 70 cm between condenser outlet port and pump inlet. The second system feature missing from Figure 3.7 is the heat supply to the expander. Both prototypes have connectors for the heat transfer fluid loop that have been used to

preheat the engine jacket reducing the time needed to reach steady state operating conditions.

Operating Points

The performance of the expansion machine is described by two series of experiments named 'S' and 'L' covering a total of six operating points that differ in both evaporation and condensation temperature and pressure. Each series of measurements consists of two high temperature tests (S1, S2, L1 and L2) with an evaporator outlet temperature T_{eva} of around 150 °C and one low temperature case, S4 and L4, with a T_{eva} close to 125 °C. Heat rejection took place with condenser temperatures T_{con} of 20 °C for the low temperature case and one of the high temperature cases. The second high temperature case ran at a higher condenser temperature of 40 °C, which also reduced the expansion ratio.

Experiments were carried out with two different camshaft designs for the exhaust valve and variable timing for the injection system. The first cam design 'S' had a short exhaust opening period of 75°. The solid line in Figure 3.9(a) shows the operation of the exhaust valve, which was the same for all 'S' cases, and the dotted line shows the specific inlet port control for the case S4. The early exhaust closing angle of −97° before TDC resulted in a high recompression ratio. Hence, more mass remained in the chamber leading to a higher cylinder pressure at the beginning of the admission of a new batch of working fluid. Compressing a large amount of gas before injection can yield an increased efficiency at high pressure ratios. The throttling losses occurring in the early injection phase are minimised because the pressure difference between the supply line and the expansion chamber is reduced. However, at low pressure ratios, a high recompression ratio can cause an overshoot in cylinder pressure which in turn decreases efficiency. Therefore, a second, less aggressive, exhaust valve timing scheme 'L' with a longer opening period of 115° was implemented to allow for testing of lower pressure ratios and hence lower evaporator temperatures. Comparing the two valve operation profiles in Figure 3.9(a) and Figure 3.9(b), visualises the impact of the different exhaust valve timings. Both systems opened the exhaust shortly after the bottom dead centre (BDC), but the longer opening in Figure 3.9(b) lead to a period with a fully opened exhaust line while the exhaust in Figure 3.9(a) started to close again shortly after reaching the fully opened position.

The timing for the admission valve in Table 3.8 was found experimentally by minimizing the length of the admission period $\theta_{in,open} - \theta_{in,close}$. Starting with a long opening interval, the cutoff angle $\theta_{in,close}$ and the inlet opening angle $\theta_{in,open}$ were carefully moved towards TDC. The angles documented in Table 3.8 represent the shortest possible admission period at which the expander ran reliably. No stable valve

Table 3.8: Operating points for the experiments in terms of valve timing, temperatures and pressures at the outlet of evaporator and condenser.

Case	S1	S2	S4	L1	L2	L4
$\theta_{\text{in,open}}$ / °	−11	−10	−10	−2	−5	−19
$\theta_{\text{in,close}}$ / °	7	15	25	16	27	10
T_{eva} / °C	153	145	125	155	157	126
p_{eva} / bar	15.4	14.2	10.1	14.7	15.3	9.8
T_{con} / °C	19.4	37.5	19.5	20.0	39.2	20.4
p_{con} / bar	0.9	1.4	0.9	0.9	1.6	0.9

configuration with an acceptable performance is found for the missing cases S3 and L3, which were supposed to operate between 125 °C and 40 °C. The other values in Table 3.8 are the exact evaporator and condenser outlet temperatures, T_{eva} and T_{con}, and pressures, p_{eva} and p_{con}, for all six cases.

Measurements

A high speed data acquisition running at 10 kHz was used to record cylinder pressure, torque and crankshaft position. The cylinder pressure was obtained from a strain gage sensor with a full scale value of 35 bar and a maximum combined uncertainty of ±0.25 % thereof. Also the torque sensor is based on strain gages and has a nominal torque of 200 N m and a maximum deviation of ±0.3 % of the rated value. This sensor recorded the torque applied to a hydraulic brake mounted at the end of the crank shaft. Before that brake, the shaft position was measured with an incremental magnetic pulse generator allowing to calculate and store the average rotational speed of the crank shaft. A slower sampling rate of 1 Hz was used to acquire averaged temperature data in the pipes connecting the expander to the evaporator and to the condenser. The 25 bar version of a piezoresistive pressure transducer was used to record the corresponding pressures with an uncertainty of ±0.5 %. Temperatures at evaporator outlet, condenser outlet and expander outlet were measured using thermocouples with an uncertainty of ±0.5 K.

Based on the measured crankshaft position and the valve control setpoints, two high accuracy servo drives controlled a rotary admission valve presented in Figure 3.10. Using separate drives to control the opening and the closing of the admission line made it possible to close the inlet before the maximum opening degree was reached.

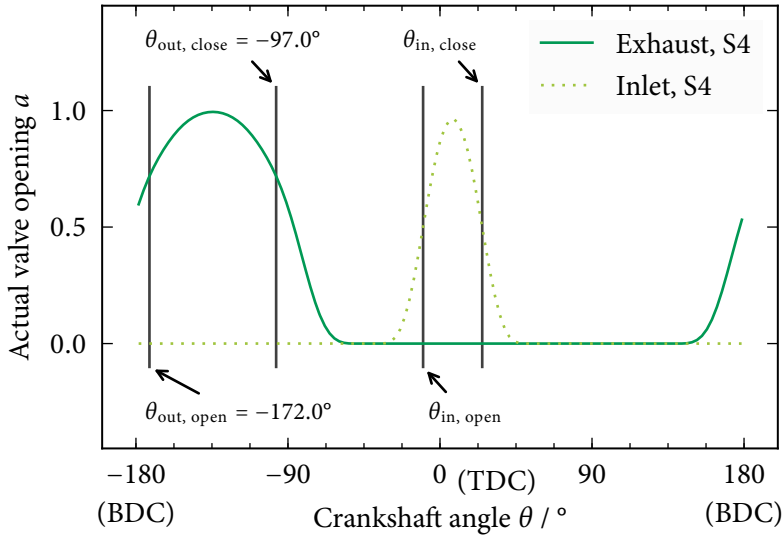

(a) Short exhaust valve opening profile.

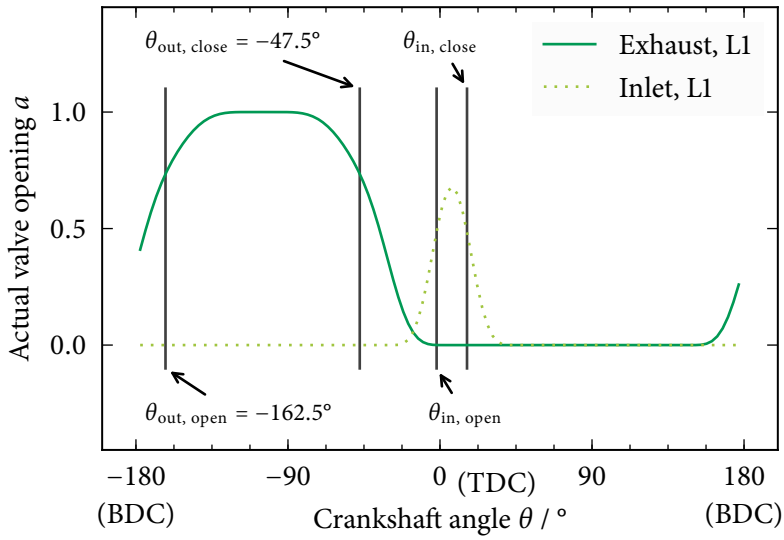

(b) Long exhaust valve opening profile.

Figure 3.9: Valve operation during one crankshaft revolution with long and short exhaust valve opening.

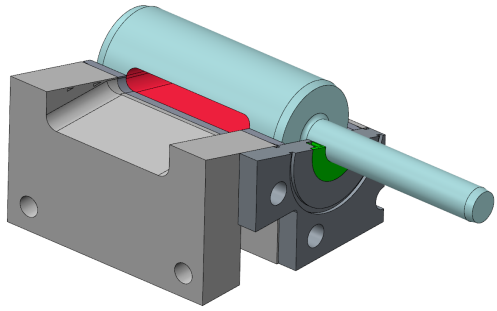

Figure 3.10: Rotary admission valve of the tested expander.

This explains the relative admission valve opening of less than unity occurring in Figure 3.9(b).

On the cooling water side, two energy meters from accuracy class 2 of EN1434[79] were employed to measure $\dot{V}_{\text{water}}$ with a minimum accuracy of ±5 % of the permanent flow rate values of 16 m^3/h and 3 m^3/h, respectively. Inlet and outlet temperatures of the secondary side of the condenser have been measured with two PT100 class A resistance thermometers with an uncertainty of approximately 0.25 K in the cooling water temperature range.

Fluid Modelling

Based on meaningful initial guesses for the confined mass $m_0 = \rho_0\ V_{\text{cyl}}$ and the total internal energy $U_0 = m_0\,(h_0 - p_0/\rho_0)$, energy and mass balances were calculated for the expansion chamber according to a slightly modified version of the established `Modelica.Fluid` standards presented by Franke et al. [83]. The energy balance equation has the form

$$dU/dt = \sum(\dot{m}_i\ h_i) + \sum \dot{E}_i + \dot{W} + \dot{Q} \tag{3.2}$$

with U being the internal energy in the control volume and $\dot{E}_i$ denoting the kinetic energy flow rates over the system boundaries

$$\dot{E}_i = \dot{m}_i\ 0.5 w_i^2. \tag{3.3}$$

The rate of work exchange with the surroundings was described by

$$\dot{W} = -\dot{l}_{\text{pi}}\ p_{\text{cyl}}\ A_{\text{pi}} \tag{3.4}$$

using the piston-fluid interface area A_{pi} and the piston position l_{pi}. This position did not include the clearance at TDC, which had to be added in

$$V_{\text{cyl}} = V_{\text{TDC}} + A_{\text{cyl}}\ l_{\text{pi}}. \tag{3.5}$$

Note that the leakage gap defined the difference between the two circular areas A_{cyl} and A_{pi} via $d_{\mathrm{cyl}} = 2\delta_{\mathrm{w}} + d_{\mathrm{pi}}$. The piston pin connected the fluid model to the other mechanical parts via the force

$$F_{\mathrm{cyl}} = A_{\mathrm{cyl}} \left(p_{\mathrm{amb}} - p_{\mathrm{cyl}} \right) \tag{3.6}$$

and the motion described by $\dot{l}_{\mathrm{cyl}}$.

These energy flow rates were defined by temperature and static pressure and could include a dynamic part based on the fluid velocity in the ports, in cases where detailed knowledge about the flow losses in the valves is available. The absolute values for mass and internal energy defined the state of the working fluid and were obtained from the relations $m = V\ \rho$ and $U = \int \dot{U} dt$, which connected thermophysical properties obtained from an equation of state (EOS) by Span and Wagner [219] via CoolProp fluid property database version 5.0.8 (CoolProp) with the balance equations. The heat transfer rate to and from the cylinder wall $\dot{Q}_{\mathrm{w}}$ was calculated according to Adair, Qvale and Pearson [2]. This correlation has been developed for ammonia compressors and belongs to the family of Nusselt number (Nu) correlations, which are based on the Reynolds number (Re) and the Prandtl number (Pr). The computation of

$$\mathrm{Nu} = \frac{\bar{\alpha}\ \Gamma}{\lambda} = 0.053\ \mathrm{Re}^{0.8}\ \mathrm{Pr}^{0.6}\ \text{with} \tag{3.7}$$

$$\mathrm{Re} = \frac{\rho\ \Lambda\ \Gamma}{\mu} \tag{3.8}$$

requires the characteristic velocity $\Lambda = 0.5 d_{\mathrm{e}}\ \Omega_{\mathrm{e}}$ and the characteristic length $\Gamma = 0.5 d_{\mathrm{e}}$. To account for a high degree of turbulence after admission of the working fluid, the equivalent swirl velocity used by Adair, Qvale and Pearson [2] $\Omega_{\mathrm{e}} = f(\Omega, \theta)$ decreases from working fluid admission to exhaust employing an equivalent diameter $d_{\mathrm{e}} = \frac{6\mathrm{volume}}{\mathrm{surface}}$. Section 3.5 holds more details different the heat transfer and figures illustrating the evolution of the heat transfer coefficient over one crankshaft revolution are presented there and in Appendix D.

Eventually, the total mass balance equation was expressed in terms of

$$\dot{m}_{\mathrm{cyl}} = \dot{m}_{\mathrm{in}} + \dot{m}_{\mathrm{out}} + \dot{m}_{\mathrm{leak}}, \tag{3.9}$$

which was coupled with a vectorised component mass balance to provide the possibility of using mixtures as working fluids by means of a composition vector $\boldsymbol{X}$

$$\dot{m}_{\mathrm{cyl}}\ \boldsymbol{X}_{\mathrm{cyl}} = \dot{m}_{\mathrm{in}}\ \boldsymbol{X}_{\mathrm{in}} + \dot{m}_{\mathrm{out}}\ \boldsymbol{X}_{\mathrm{out}} + \dot{m}_{\mathrm{leak}}\ \boldsymbol{X}_{\mathrm{leak}}. \tag{3.10}$$

A crucial part of the system are the valves since pressure drops during admission and exhaust have a major influence on the operation. The system studied here is

equipped with a rotary admission valve and a poppet-type exhaust system. Admission is controlled electrically and can therefore operate with different opening and cut-off timings. However, being triggered by the crankshaft rotation, the process of opening and closing is fixed in terms of crank angle degrees. At a given crankshaft angle θ, the nominal opening x_0 of both valve types was calculated from

$$x_0 = \max(0, g(\theta, \theta_{\text{open}}) - g(\theta, \theta_{\text{close}})) \tag{3.11}$$

using a smooth transition for the opening and the closing angles. For both angles $\theta_{\text{act}} \in \{\theta_{\text{open}}, \theta_{\text{close}}\}$ the equation

$$g(\theta, \theta_{\text{act}}) = \begin{cases} 0 & \text{if } -\pi/2 \geq \theta_{\text{rel}} \\ \psi & \text{if } +\pi/2 < |\theta_{\text{rel}}| \\ 1 & \text{if } +\pi/2 \leq \theta_{\text{rel}} \end{cases} \tag{3.12}$$

was solved, which involves the definition of

$$\psi(\theta_{\text{rel}}) = 1 + \frac{1}{4}\left(\cos(\theta_{\text{rel}})^2 + 2\right)\sin(\theta_{\text{rel}}) - \frac{1}{2} \tag{3.13}$$

and the relative crank angle position $\theta_{\text{rel}} = \pi(\theta - \theta_{\text{act}})/\Delta\theta_{\text{act}}$. This implementation provides a continuous transition up to the second order and originates from smoothing functions presented by Richter [200]. The transition durations $\Delta\theta_{\text{open}}$ and $\Delta\theta_{\text{close}}$ of 55° and 100° were constant for all cases.

Based on the nominal opening a_0, the actual opening a was calculated by a characteristic function. This function translated the opening signal a_0 to a factor a that could be multiplied with the maximum flow area to obtain the instantaneous flow area. Figure 3.11 illustrates the differences between the rotary valve used for admission control and the exhaust valve of the traditional poppet type. The rotary system mapped nominal opening to actual opening linearly, while the second curve in Figure 3.11 exhibited a typical poppet valve behaviour that sometimes is referred to as quick opening characteristic. It can be described by

$$a = 1 - (b - 0)(1 - a_0) + (b - 1)(1 - a_0)^c \tag{3.14}$$

with the parameter $b = 0.5$ and the exponent $c = 5$.

The valve implementation in the Modelica standard follows the standard EN 60534 [81]. Hence, the mass flow was calculated from a nominal throat area A_{t} defined by the hydraulic inlet and outlet diameters in Table 3.6 and the upstream density ρ_1 and pressure p_1. The equation

$$\dot{m} = a\ Y\ A_{\text{t}}\sqrt{\Delta p_{1,\text{t}}\ \rho_1} \tag{3.15}$$

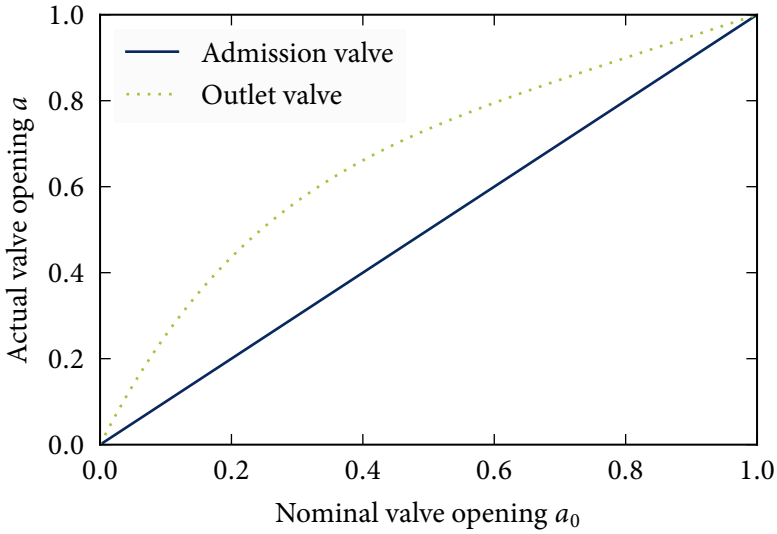

Figure 3.11: Opening characteristics of inlet and outlet valve.

employed a flow expansion factor Y and a modified throat pressure difference $\Delta p_{1,t} = x\ p_1$ to account for pseudo choking conditions. The pressure differential ratio factor x was obtained from the total pressure difference $x = \Delta p_{1,2}/p_1$, but was limited to $x \leq 0.5\ a_0$ yielding $Y = 1 - 2x/3$.

An orifice flow equation was used to approximate the pressure drop in the pipes between the heat exchangers and the expander. As suggested by Franke et al. [83], the equation

$$\Delta p_{1,2} = 0.5\ \zeta\ \rho_1\ w^2 \tag{3.16}$$

simplified the pressure drop calculation assuming a $\zeta = 1.5$ for a homogeneous fluids velocity w in supply and exhaust pipes.

Mechanical Component Modelling

The modelled system consisted of the mechanical components attached to the expander and the internal mechanism displayed in Figure 3.5. The internal components of the slider-crank mechanism were regarded as ideally stiff with their mass distributed evenly along the gravitational symmetry line. In addition to the parts described in Table 3.6, there were also the external mechanical components, which are described below. The whole crankshaft assembly is shown in Figure 3.12, which also contains

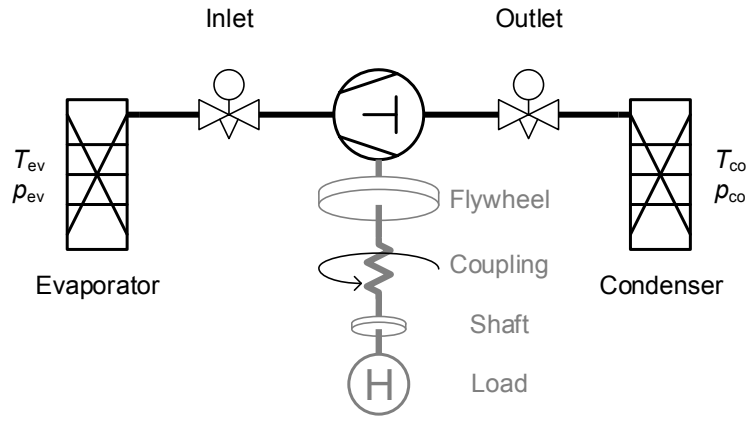

Figure 3.12: Modelled system assembly.

the heat exchangers and valves. The crankshaft itself had a mass of 1 kg, an idealized cylindrical shape with a radius of 2 cm and a length of 20 cm. The flywheel was directly connected to the crank shaft and the model concentrated almost all rotational inertia in a bulk value of 120 g m^2. The total rotational inertia was approximately four times the inertia of the installed flywheel, which is equal to 30.6 g m^2. A stiff rotational spring described by the constant of 8 kN/rad accounted for the flexibility of the shaft connectors and the deformation of the shaft itself. At the end of the model assembly, an additional rotational inertia of 12 g m^2 represented the last part of the shaft and the hydraulic brake used to dissipate the generated energy. As in the experimental installation, torque was measured directly at the load making the dynamic behaviour of the shaft visible in the torque measurements. Mechanical losses were lumped in an artificial quadratic friction term that dissipated energy by imposing a torque M_{fr} that acts against the direction of rotation according to the equation

$$M_{fr} = M_0 \left(\omega/\omega_0\right)^2 \tag{3.17}$$

with a nominal friction M_0 of 2.5 N m at a nominal rotational speed ω_0 of 1000 rpm.

Additional Calculations

Combining the measured cooling water volume flow rate and temperatures on the secondary side of the condenser with the working fluid temperature and pressure measurements, the heat uptake of the cooling water could be used to calculate the average working fluid mass flow rate $\dot{m}_f$. The incompressible volume flow rate of water $\dot{V}_{water}$ at a constant density ρ_{water} was multiplied with the constant specific heat

capacity $c_{p,\text{water}}$ and the temperature difference ΔT_{water} to obtain the heat flow rate in the condenser

$$\dot{Q}_{\text{water}} = \dot{V}_{\text{water}}\, \rho_{\text{water}}\, c_{p,\text{water}}\, \Delta T_{\text{water}}. \tag{3.18}$$

Using the energy balance on the primary side, dividing the heat flow rate by the enthalpy difference defined the mass flow rate of working fluid

$$\dot{m}_{\text{f}} = \dot{Q}_{\text{water}} / \left(h_{\text{out}} - h_{\text{con}}\right) \tag{3.19}$$

based on the expander outlet enthalpy h_{out}, as obtained from the measured temperatures and pressures, and the condenser outlet enthalpy h_{con}.

Multiplying this value with the specific work obtainable from an isentropic expansion from evaporation pressure p_{eva} to condensing pressure p_{con} yielded the reference power $\dot{W}_s$. To find the isentropic efficiency η_s, the actual shaft power $\dot{W}$ was calculated from the measured torque M and the rotational speed ω and divided by $\dot{W}_s$. The isentropic efficiency was calculated in the same way for the experimental data and in the simulations. Both formulations were based on an average value for the rotational speed during one revolution.

The uncertainties mentioned in Section 3.2 have been processed with Engineering Equation Solver [123] (EES) resulting in slightly different values for the different operating conditions. This allowed us to calculate the measurement-related absolute error ϵ of a derived quantity Z from the partial derivatives with respect to all involved measurements X_i and their respective uncertainties ϵ_{X_i}:

$$\epsilon_Z = \sqrt{\sum_i \left(\frac{\partial Z}{\partial X_i}\right)^2 \epsilon_{X_i}^2}. \tag{3.20}$$

The partial derivatives needed for this procedure were computed numerically for each operating point. Since EES does not include uncertainties for the fluid property functions, those had to be included manually adding more elements to the calculation of the final uncertainty ξ_Z. In their publications covering the employed EOS, Span and Wagner [219] and Wagner and Pruss [246] mention a maximum acceptable uncertainty of ±1 % for the caloric properties of gaseous n-pentane and ±0.2 % for those of liquid water. These values were combined with Equation (3.20) using the equation

$$\frac{\xi_Z}{Z} = \sqrt{\left(\frac{\epsilon_Z}{Z}\right)^2 + 0.01^2\ j + 0.002^2\ k} \tag{3.21}$$

where j and k were the total number of fluid property calls for n-pentane and water required to compute the dependent variable Z. Applying the above to the subsequent determination of $\dot{Q}_{\text{water}}$, $\dot{m}_{\text{f}}$ and η_s, one obtains the corresponding (j, k) pairs of $(0, 2)$, $(2, 2)$ and $(5, 2)$. This additional step increases the absolute uncertainty of the determination of η_s by approximately 0.3 %.

3.3 Expander Test Results & Discussion

Recorded & Calculated Data

A comparison between the dynamic model and the experimental results is presented in Figures 3.13 and 3.14. Both figures show scatter plots of measured data from 20 subsequent revolutions at steady state operation for each of the operating points S1 through L4. Recorded at a sampling frequency of 10 kHz, each series contains more than 35 000 samples. The solid line above the scattered points represents a single revolution of the modelled operation at the same evaporator and condenser conditions. Running in steady state, the modelled data does not change from revolution to revolution and there is no need to show more than one revolution.

Figure 3.13 shows the torque measured at the hydraulic load as a function of crankshaft angle. The abscissa values of −180° and 180° denote the BDC while the TDC is located at 0°. Due to the absence of a piston pin offset, the top position of the crankarm-conrod connection coincided with the TDC. The exhaust and admission periods are marked by the area enclosed by the grey lines that are labelled with 'out' and 'in', respectively. Starting from the BDC on the left hand side of Figure 3.13, the torque decreased while fluid left the expansion chamber. After the exhaust valve was closed, more energy was extracted from the rotating masses to recompress the fluid left in the expansion chamber. New working fluid was injected close to TDC and the fluid performed work on the piston making the torque curves rise sharply.

The pressure-volume graphs in Figure 3.14 display the pressure inside the cylinder with respect to the volume of the expansion chamber. The evaporator pressure is indicated by a line marked with p_{eva}, while the condenser pressure is annotated with p_{con}. The piston moved between BDC and TDC causing a change in trapped volume from 770 cm^3 to 36 cm^3. Hence, the presented design could operate with a theoretical maximum expansion ratio of more than 21 in the low mass flow limit. Following the lower branch of the pressure curve from right to left, the exhaust process took place until the valve closes and the remaining gas was compressed as the piston travels towards TDC. The cylinder pressure peaked around the minimum clearance volume and the process continued with fluid intake and expansion along the high pressure branch of the cycle until it reached BDC again.

The experimental campaign produced similar results for the isentropic expansion efficiency regardless of the operating conditions. Only run L4, with little precompression and a low expansion ratio yielded an efficiency of below 55 %. All other operating conditions from Table 3.8 resulted in an expansion efficiency around 0.7, as listed in Table 3.15. These figures also make up the abscissa of Figure 3.16, which indicates the difference between calculated and measured isentropic efficiency. The errorbars

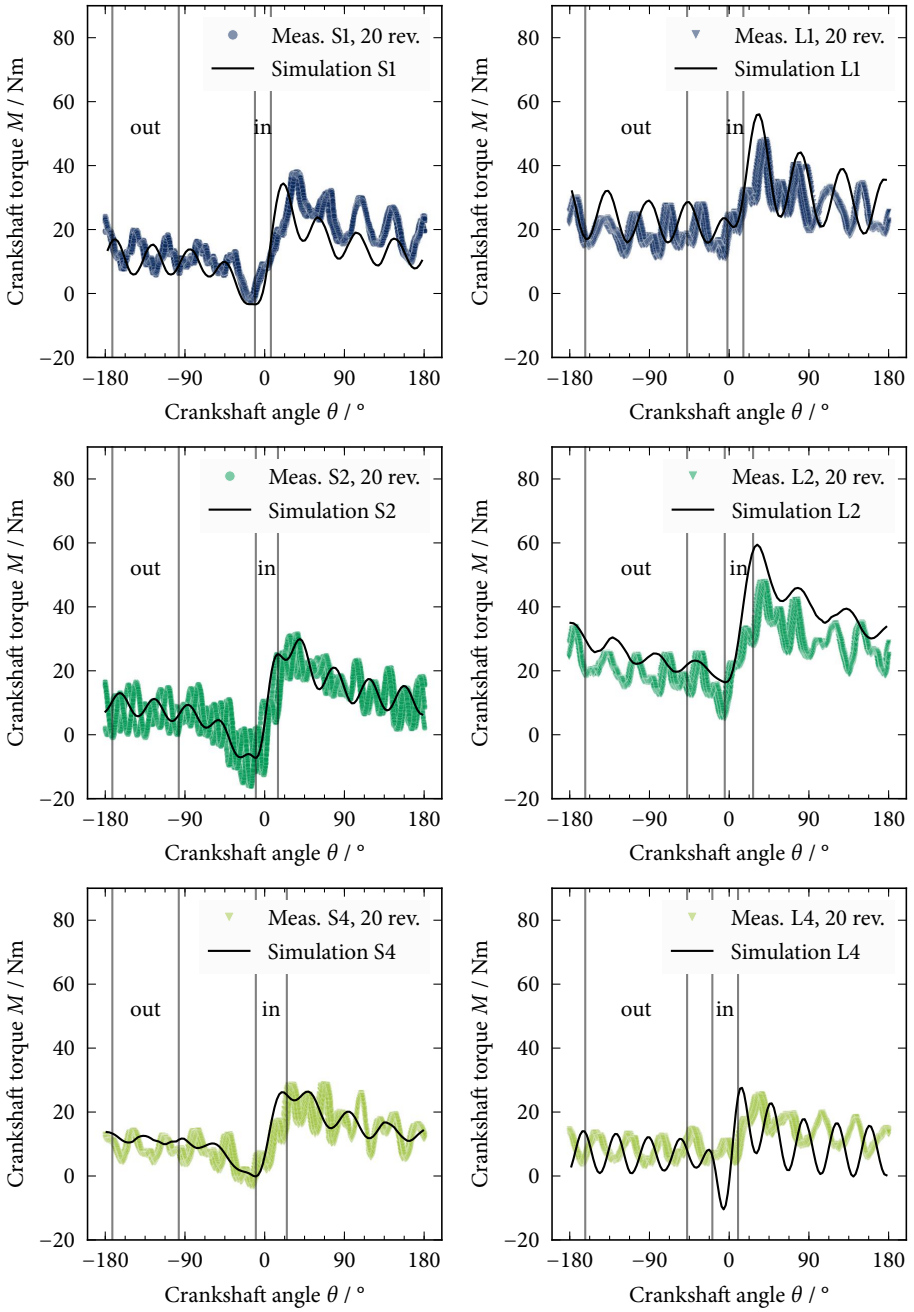

Figure 3.13: Measured torque data from 20 revolutions and simulation results for one revolution versus crankshaft angle at six operating points.

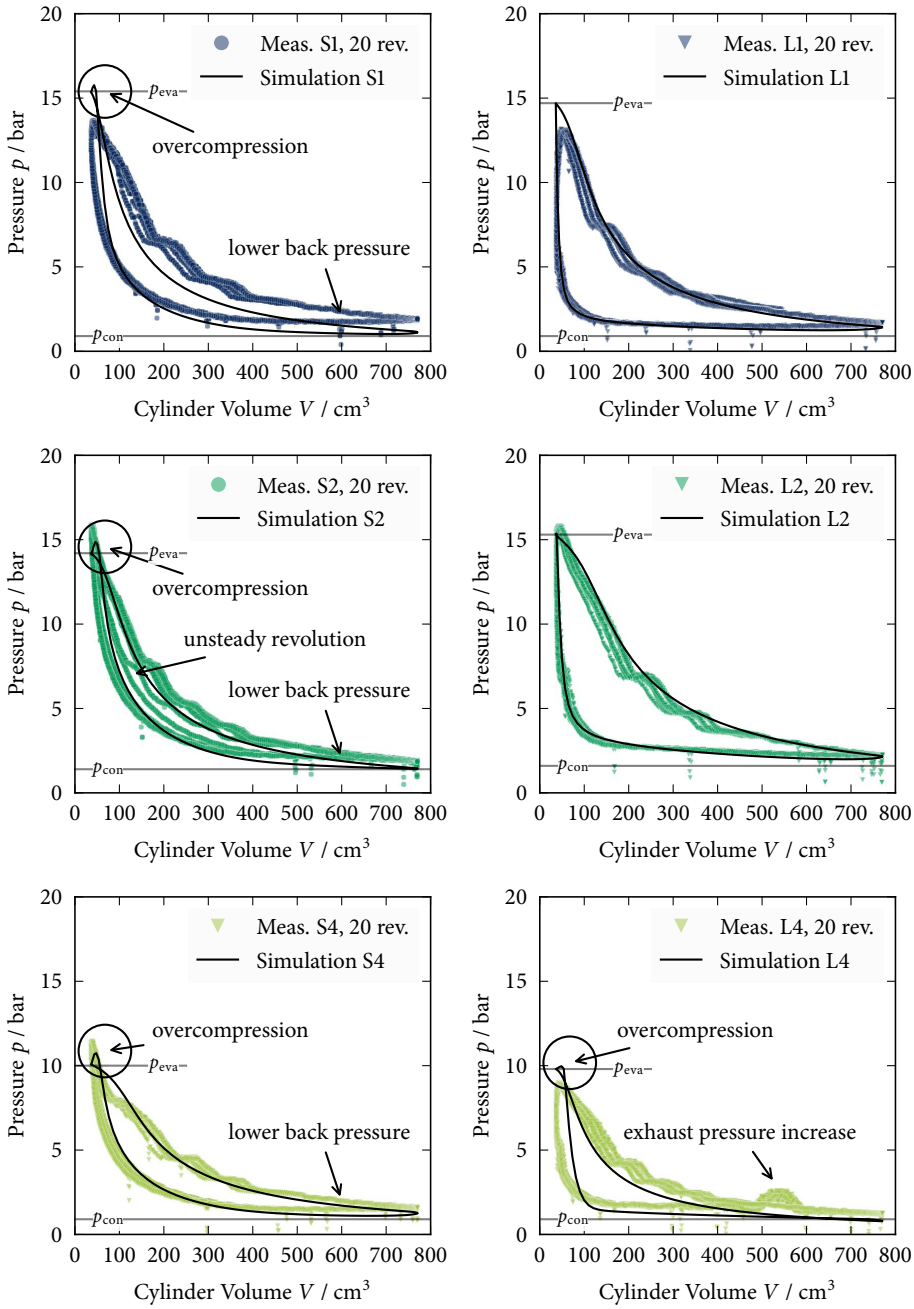

Figure 3.14: Measured pressure data from 20 revolutions and simulation results for one revolution versus cylinder volume at six operating points.

Table 3.15: Additional dependent figures obtained from the experimental data including their uncertainties

	$\dot{Q}_{\text{water}}$ (kW)	$\dot{m}_{\text{f}}$ (g/s)	η_s (%)	$\dot{W}$ (kW)
S1	11.4 ± 0.58	22.3 ± 1.18	72.5 ± 5.4	1.8 ± 0.07
S2	5.6 ± 0.27	11.7 ± 0.58	74.0 ± 4.9	0.8 ± 0.05
S4	7.7 ± 0.39	16.6 ± 0.88	70.5 ± 5.7	1.1 ± 0.06
L1	15.2 ± 0.77	30.2 ± 1.58	70.8 ± 5.3	2.4 ± 0.06
L2	18.6 ± 0.89	38.8 ± 1.95	68.0 ± 4.3	2.4 ± 0.07
L4	10.8 ± 0.55	22.6 ± 1.20	53.0 ± 4.3	1.1 ± 0.06

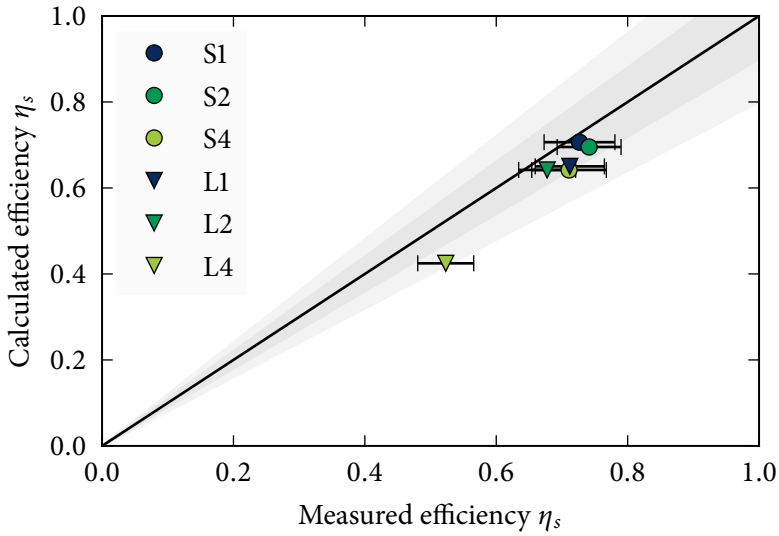

Figure 3.16: Calculated and measured isentropic expander efficiencies, the filled areas indicate a difference of ±10 % and ±20 %.

show the total uncertainty ξ_{η_s} from measurements and the employed equations of state according to Equations (3.20) and (3.21). No errors are shown for the simulated data sets. The two shaded spaces around the central line are drawn at ±10 % and ±20 % relative difference between simulation and measurements. All points are within the ±10 % band except for L4, which approaches the ±20 % margin.

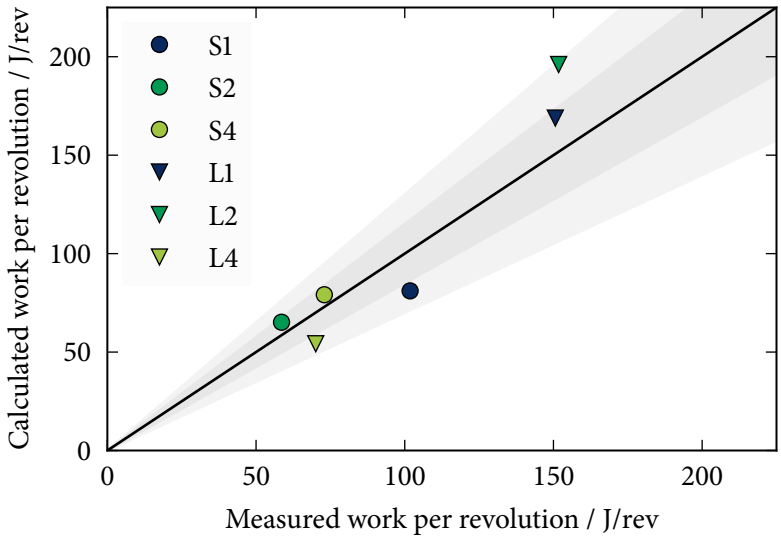

Figure 3.17: Calculated versus measured expander output, the filled areas indicate a difference of ±15 % and ±30 %.

Dividing the power output in last column of Table 3.15 by the average rotational speed yielded the work that was extracted per revolution. Figure 3.17 compares the work per revolution from the measurements and from the simulations in a similar fashion as Figure 3.16 compares the efficiencies. Due to the larger differences between modelled output and the experiments, the shaded areas were extended to cover 15 % and 30 %, respectively. The runs with a short valve opening 'S' delivered between 55 J/rev and 100 J/rev, while the simulations predicted between 60 J/rev and 75 J/rev. Allowing more mass to enter the cylinder increases the output to approximately 150 J/rev for L1 and L2 while L4 produces less work per revolution than S4.

Experimental Campaign

In the section above, measurements of six different experiments have been presented. The plots in Figure 3.13 suggest that all measurements were taken at steady state conditions. The scattered points form a single line and only in limited parts of case S2, there is one revolution out of twenty that does not lie directly on top of the other ones.

The reoccurring torque oscillation in the measurements in Figure 3.13 were of an amplitude of approximately 30 % of the maximum torque for all cases. This behaviour was attributed to the periodical application of force to the crankshaft and the accompa-

nying deformations. The three upper series in Figure 3.13 exhibit a minimum torque below 0 N m shortly before TDC. At those points of the revolutions, work has to be performed on the trapped gas in the cylinder. This causes a measurable deceleration of the hydraulic equipment reversing the sign of the torque for a short period in S1, S2 and S4.

Comparing S2 in Table 3.8 and Figure 3.14, we can see that the peak pressure of almost 16 bar was higher than the evaporator pressure of 14.2 bar. This overcompression of the remaining gas before injection consumed a significant amount of energy from the flywheel. In addition to that, it increased flow losses since a part of the working fluid charge had to leave the cylinder in the direction of the evaporator and enter it again before the actual injection process could start, which also reduced the average mass flow rate per cycle. In fact, S2 produced the lowest measured power of all test cases. However, the recompression pressure was not high enough to cause a large efficiency penalty since case S2 also exhibited the highest isentropic expander efficiency. Also case S4 suffered from too much recompression, but the lower pressure levels reduced the forces on the piston and thereby limited the impact on the measured torque.

The large pressure ratios and high mass flow rates produced the most power. From S1 to L1, power output increased by a third from 1.8 kW to 2.4 kW. The lower efficiency in case L1 is expected to be related to the throttling losses caused by large pressure differences occurring in the early admission phase due to an incomplete precompression in the expansion chamber.

The measured isentropic expander efficiency of test L4 was worse than in all other cases, see Table 3.15. This indicates that shifting the admission window forward by approximately 15° had a negative impact on efficiency. An early opening of the admission valve avoided large pressure differences at TDC, but at the same time it required larger amounts of fluid to travel back and forth through the admission valve. In addition to the early opening, the PV-diagram of L4 in Figure 3.14 also exhibited a peculiarity in the exhaust phase. There was an increase in pressure in the low pressure branch at around 540 cm^3 that occurred in all plotted revolutions. This indicates that either there was a problem with the exhaust system causing flow resistance or a problem with the inlet valve creating a temporary connection from evaporator to condenser. High frequency condenser pressure measurements could be used to determine the cause of this 'bump'. A blocked exhaust would lead to a decreased pressure in the pipe towards the condenser and a shortcut to the evaporator would cause a pressure peak to occur in that pipe. However, the low maximum sampling frequency supported by the pressure transducers did not allow for this kind of analysis. Recording the inlet pressure with a higher resolution is expected to be beneficial as well. Pressure variations are expected to occur in the evaporator and the admission system due to the relatively large swept volume of the piston pump. It operates at a lower frequency than the fluid injection

and the actual injection pressure is likely to be different from the average supply line pressure.

Modelling Results

A dynamic modelling approach has been presented alongside the experimental data from six test runs. Figure 3.13 shows measurements and calculated data points for the instantaneous crankshaft torque. The spring constant of 8 kN m/rad that approximated the crankshaft stiffness captured parts of the dynamic behaviour. Higher order phenomena were not reproduced by the model, but the fluctuations in torque occured with a magnitude similar to the measured one. However, the model is not suited for a mechanical analysis of the whole assembly, but additional spring and damper components could be used to obtain a better match with the experimental data.

The measured and calculated pressure in the cylinder in Figure 3.14 did not match equally well at all operating conditions. The modelled exhaust of working fluid, decreasing chamber volume at low pressures, took place at a lower pressure than what was observed in the experiments. The flow resistance in the pipes connecting expander and condenser might have been underestimated in the model. Despite the lower modelled back pressure in the exhaust pipes, chamber pressure peaked at the same or higher values as the piston reached TDC on the left hand side of the PV-diagrams. Additionally, the pressure also decreased faster in cases with a short admission period like S1 and S2. Such effects could be attributed to a delayed valve operation in the model. Increased pressure drop over the exhaust valve started the recompression in the cylinder earlier while a high pressure difference in the early admission phase kept the fluid from leaving the chamber and thus lead to an overshoot at the end of the recompression. This is also one possible explanation for the notable overcompression in case L4, which had the earliest admission opening at −19°.

A detailed flow analysis of the inlet valves could also help explaining the fast decay in chamber pressure, which might be also caused by an overestimated flow resistance in the partly opened admission valve. Accumulation effects related to the flow back and forth through the supply valve were not taken into account. The fluid pushed out of the cylinder at TDC would increase the pressure in the supply line, which can result in more flow into the cylinder in the late admission phase, effectively 'widening' the PV-curve in the cases S1 and S2 in Figure 3.14.

Using the average mass flow rate per cycle, the model calculated a lower efficiency than the one calculated based on the laboratory tests, see Figure 3.16. Both, flow losses and thermal losses occurred in the model. As discussed above, the calculated flow resistance in the partially opened valves might be too high, which also decreased the overall efficiency. Another possibility is that the heat transfer rate was lower than

predicted by Equation (3.48). For steady state operation, the wall temperature has to be between the evaporator and condenser temperature. At high pressures and temperatures, heat is transferred from the working fluid to the wall. At the end of the expansion, this heat flow is reversed causing an additional entropy generation. However, due to the major impact of the flow losses on performance, the first step towards a thorough analysis should be a dedicated valve study to determine flow loss parameters more accurately.

Even though efficiency is predicted within an accuracy of 10 %, the produced power from the model deviates from the measurements by up to 30 %. Running the dynamic model at steady state amplified the effect small differences in efficiency had on the produced shaft work. Flow losses impact mass flow rates and that affected the produced work per revolution even further.

3.4 Variable Cut-off Angle

Application to Cogeneration

Small scale combined heat and power systems are already available based on combustion engines, but other technologies like fuel cells and Stirling engines still have to prove their maturity. An ORC can be used as a bottoming cycle to extract electricity from various types flue gasses as decribed by Badami et al. [19] for a reciprocating steam expander connected to a combustion engine. Another possible heat source for small scale cogeneration is biomass [69] and a simple biomass-based system has been proposed by Qiu et al. [194]. Micro-scale ORC cogeneration units are expected to save more than 10 % of the primary energy consumption [175] and have gained a lot of attention in the recent scientific literature [204, 265]. Also experimental research systems are under development and Colonna et al. [51] expect improved designs to occur within the next years. However, many of the investigated expansion devices suffer from an inflexible design that leads to significant losses when operating with changing expansion ratios [144]. This section provides an analysis of the potential benefits associated with the implementation of an advanced admission valve control for reciprocating expanders.

The domestic demand for space heating and hot water was assessed based on a European standard [80] and a Danish standard [73] forming the basis for an annual performance comparison. Assuming a fixed temperature heat source, the ORC condenser provides all heating required by a multi-family utility system. The geometry of the expander matches the tested prototype from Section 3.2 and also the working fluid, n-pentane, is the same as in the experimental campaign discussed in Section 3.3. These data are then used to assess the annual performance of a CHP plant with and without adaptive admission control. Besides the expander related performance indicators, the annual operating time and the annual electricity production are compared for different valve timings.

Heat Demand Assessment

According to the medium temperature scenario in EN 14825:2012 [80], the required temperature of heat supply for space heating was calculated for the average European reference temperatures covering the range from −10 °C to 15 °C. Figure 3.19 contains a plot of the aforementioned temperature of heat demand as a function of the outdoor temperature. The associated annual heat demand for Danish homes was taken from Markussen et al. [155] and will be explained briefly. A house with 95 m^2, which is inhabited by three persons, was expected to have an annual heat demand of 2400 kWh_{th}

Table 3.18: DHW and SH capacity per house and year for a system serving five houses.

Quantity	Unit	Amount
SH capacity	kW_{th}	3.0
DHW capacity	kW_{th}	4.8
SH consumption	MWh_{th}	3.7
DHW consumption	MWh_{th}	2.4
Heat losses	MWh_{th}	0.3

for domestic hot water (DHW) generation and 3700 kWh_{th} for space heating (SH). Furthermore, the authors of the study [155] conclude that a nominal capacity of 3 kW_{th} is enough to provide comfortable space heating. For single house DHW systems, the Danish Standard 439 (DS439) [73] defines a peak demand of approximately 40 kW_{th}. Considering a utility system for five houses with a central storage and annual distribution losses of 300 kWh_{th}, the installation had to be designed for eight Danish standard apartments, which meant that one house had to be calculated as 1.6 standard apartments. DS439 recommends an installed storage volume of 25 l per standard apartment for the chosen capacity of 3 kW_{th} per standard apartment.

Table 3.18 summarises the above and allows to calculate the total heating capacity of 39 kW_{th}, which is needed to cover a consumption of 32 MWh of heat at different temperature levels. The space heating demand scales linearly with outdoor temperature. The average DHW demand is constant throughout the whole year. For hot water production, the system operates with a condenser temperature of 50 °C while the space heating temperature requirements are defined by the medium temperature scenario from EN 14825:2012 [80]. The solid line in Figure 3.19 shows the linear heat demand characteristic. The European average temperature scenario assumes a heating period with temperature between −10 °C and 15 °C. There are no hours with an average temperature below that range and no heating is needed above 15 °C. For these temperatures, EN 14825:2012 [80] provides the heat supply temperatures 43 °C, 37 °C, 33 °C and 28 °C for outdoor temperatures of −7 °C, 2 °C, 7 °C and 12 °C, respectively. Using these support points, a linear function defines the demand temperatures from −10 °C and 15 °C. The annual temperature distribution during the heating season is also provided by EN 14825:2012 [80] in the form of temperature bins. Each of the 25 temperature steps in full °C is assigned a number of hours based on the hourly average temperature.

Following this linear approach, the total heat load was calculated as a function of outdoor temperature. The heat loss coefficient *UA* for the considered indoor space was found from an annual energy balance yielding an average of 395 W/K. Assuming that

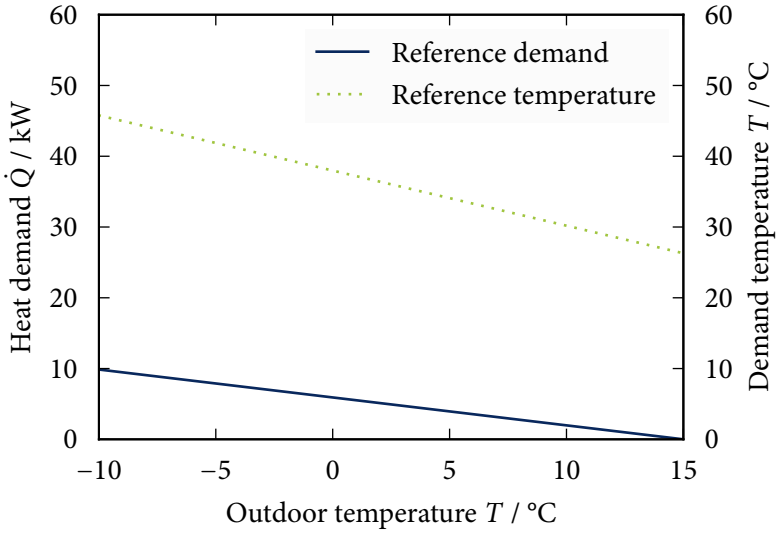

Figure 3.19: Temperatures of heat demand for the different scenarios described in EN 14825:2012.

the function $\dot{Q} = UA\ \Delta T$ describes the space heating demand in the range of −10 °C to 15 °C, the maximum average heating load that occurs at −10 °C was approximately 10 kW_{th}. The resulting function could be multiplied with the temperature bins to obtain the annual heat consumption at different outdoor temperatures, as shown in Figure 3.20. Since this study employs the average reference conditions from EN 14825:2012 [80], the heating period covered only 4910 h while the domestic hot water consumption was constant throughout the year. This means that the sum of the DHW values shown in Figure 3.20 is less than the total demand of 12.75 MWh_{th} since the Figure 3.20 only covered the heating period and not the 3850 h that did not require space heating.

Expander Model

This work focusses on the operation of the inlet valves for a reciprocating expander to avoid the losses caused by a mismatch between built-in volume ratio and system pressure [144]. Figure 3.21 shows the pressure inside the expansion chamber of a reciprocating machine with a fixed valve timing. The valves lock the expansion ratio to match a condenser temperature of T_{con} = 50 °C, but only the dotted curve matches these conditions. A condenser temperature of 25 °C leads to an underexpansion and the lower part of the solid curve is no longer horizontal during the exhaust. The pressure

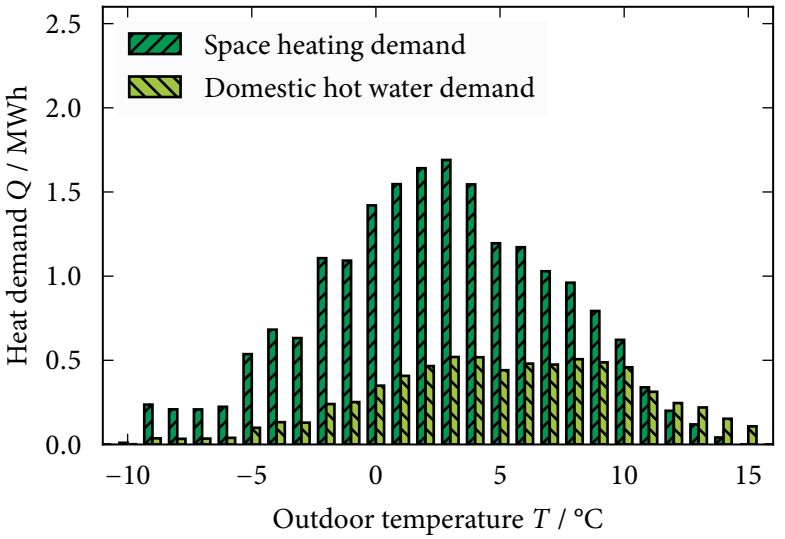

Figure 3.20: Heat demand at different outdoor temperatures.

keeps decreasing while the fluid leaves the expansion chamber, which is an indicator of unexploited potential for work extraction. At a higher condenser temperature of 75 °C, overexpansion can be observed on the right hand side of the dashed graph. The low pressure in the cylinder makes fluid from the condenser entering the expansion chamber to lift the pressure to condenser conditions causing additional losses.

The same model as in the previous Section 3.2 was used to implement the valve control. Note that Figure 3.22 contains the same components as Figure 3.12 and additional lines indicating the control input variables for the valves as described later in this section. The swept volume was defined by the bore of 46 mm and the stroke of 110 mm. The piston oscillated between its top dead center position with a clearance volume of 36 cm^3 and the bottom position at approximately 770 cm^3.

A system consisting of fluid source, admission valve, expansion chamber, exhaust valve and fluid sink represented the flow path of the working fluid travelling from evaporator to condenser as shown in Figure 3.22. The source held an infinite amount of fluid at approximately 16 bar and 150 °C. Limiting the inlet temperature allowed the utilization of water as intermediate heat transfer fluid with temperatures of up to 175 °C at pressures below 12 bar. Practical limitations for small scale installations have led to similar limits in biomass-based cogeneration systems [194] and solar CHP installations [203] presented in the literature. Compressible flow occurred in both, the

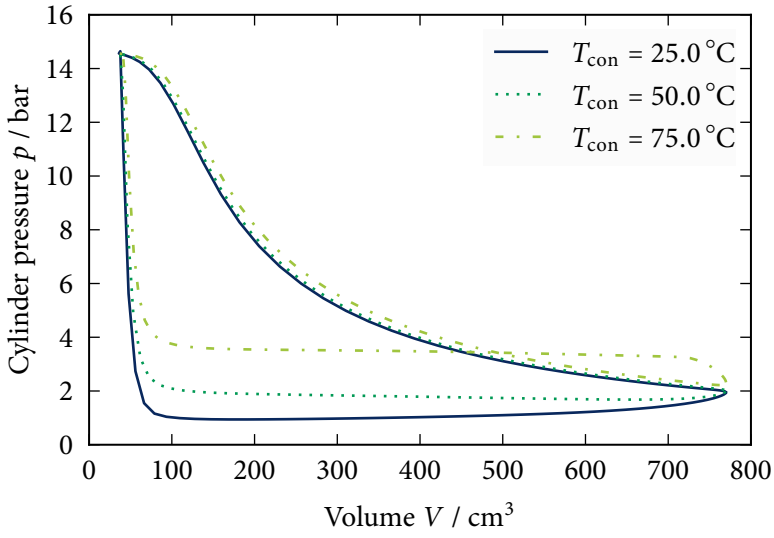

Figure 3.21: PV-diagram for different condenser pressures with fixed admission timing.

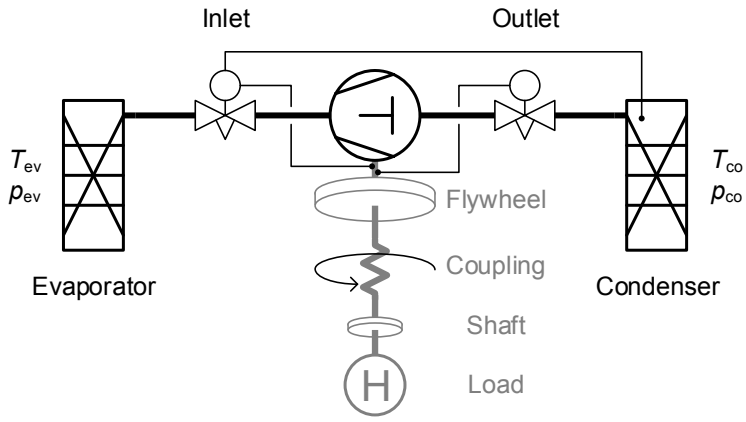

Figure 3.22: An overview of fluid-related parts of the modelled system and crankshaft assembly.

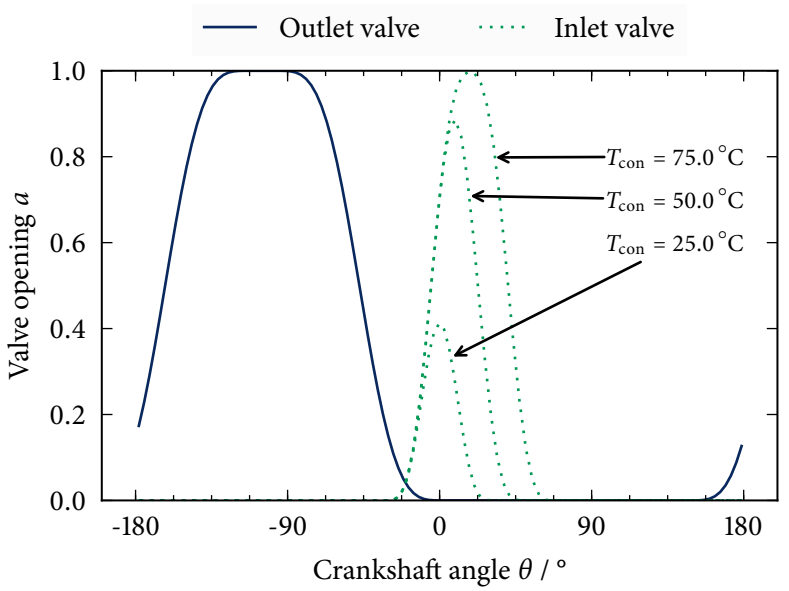

Figure 3.23: Operation of the exhaust valve and the inlet valve for three different setpoint temperatures.

inlet and outlet valves accounting for flow losses and the possibility of choked flow. As described earlier, the Modelica language was used to model the described system and valves from the standard library were employed. The valves were modified with custom opening curves, but still complied with the original formulation based on the standard EN 60534 [81]. According to Equation (3.12) *et seq.*, the valve operation could be described by modified opening and closing angles.

As shown in Figure 3.23, the operation of the exhaust valve was fixed by defining its opening angle as −162.5° before TDC and the middle of the closing action as −47.5°. The transition from fully closed to fully open or the other way was set to 100° of crankshaft rotation. The inlet valve was set to open at −5° and the switching process took 55°. The cutoff angle, which is the closing angle of the inlet valve, was determined by a controller based on the condenser temperature to avoid over- and underexpansion as described below yielding the dotted curves Figure 3.23. Note that the inlet valve did not open completely for most condenser temperatures. The long transition phase of 55° lead to a significant overlap between the opening and closing procedures. This required the cutoff to overrule the opening. The experiments presented in Section 3.2 suggest

that such a control scheme could be realised with a valve assembly using components similar to the rotor shown in Figure 3.10.

Besides the fluid related components, Figure 3.22 also shows the mechanical part of the model. A speed-dependent load was attached to a flywheel, $I = 0.125\,\mathrm{kg\,m^2}$, and the crankshaft of the reciprocating machine. Crankshaft dynamics were neglected and the whole system was regarded as ideally stiff. However, the most important difference between the two models was the new admission control concept, which is described in the next paragraph.

Operating with a fixed exhaust valve timing, the expander was controlled by the injection system only. Hence, the injection cutoff angle θ_{cut} had to be determined as a function of condenser conditions. This cutoff angle describes the crankshaft position θ at which the volume in the cylindrical expansion chamber corresponds to the optimal expansion ratio Υ for a given operating condition. Assuming saturation conditions in the heat exchanger, the condenser pressure changes with temperature in a well-defined way as $p'(T)$. This enabled the calculation of the pressure ratio between vapour with 5 K of superheat at an evaporator outlet temperature T_{eva} of 150 °C and the pressure associated with condenser temperatures T_{con} of 25 °C to 75 °C. To find the correct cutoff angle, the needed ratio of specific volumes Υ was translated to the correct pre-expansion volume of the cylinder and the associated distance l_{pi} between piston and cylinder head. The equations

$$\Upsilon = \frac{V_{\mathrm{max}}}{V_{\mathrm{cut}}} = f(T_{\mathrm{eva}}, T_{\mathrm{con}}), \tag{3.22}$$

which relates the trapped volume at BDC to the volume at which the inlet valve closes, and

$$\theta_{\mathrm{cut}} = f(l_{\mathrm{pi,cut}}) = f(V_{\mathrm{cut}}) \tag{3.23}$$

summarise this procedure yielding $\theta_{\mathrm{cut}} = f(T_{\mathrm{con}})$ for a given geometry based on an isentropic expansion process from p_{eva} to p_{con}. To illustrate the impact of the concept described above, four simulations were carried out for the whole range of condenser temperatures. One expander model was equipped with a variable valve control according to Equations (3.22) and (3.23) while the other simulations employed a fixed θ_{cut} from a setpoint temperature T_{set} that matches a T_{con} of 30 °C, 50 °C and 70 °C. Within this work, the variable valve control is going to be referred to as active valve control (AV), while the fixed timings are abbreviated with a reference to the temperature set points in °C in the condenser: fixed valve control for 30 °C (FV30), fixed valve control for 50 °C (FV50) and fixed valve control for 70 °C (FV70).

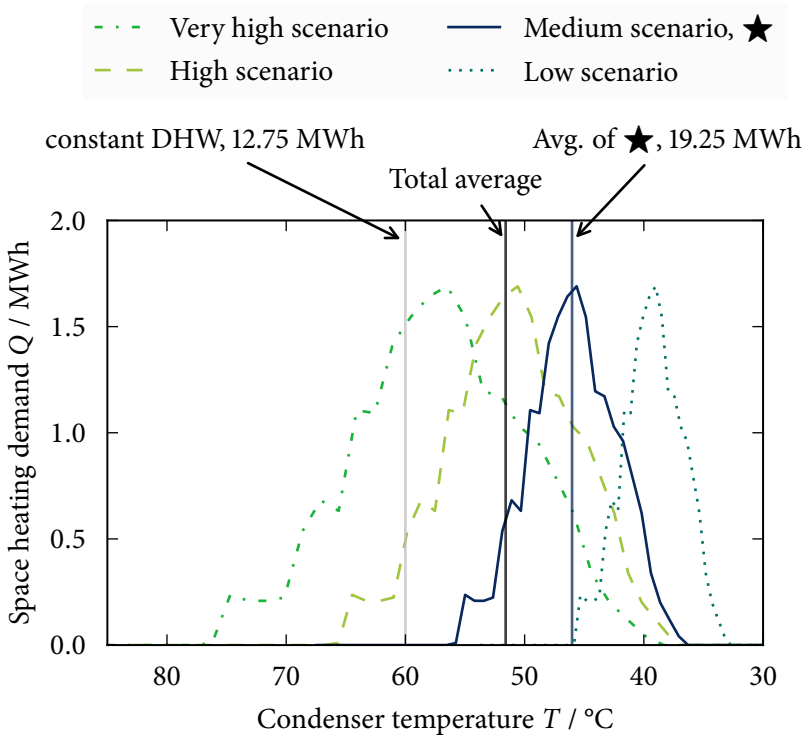

Figure 3.24: Heat demand at different condenser temperatures with average values indicated for the medium scenario, the DHW and the resulting value from combining those two.

Heat Demand & ORC Operation

Figure 3.24 shows the amount of required space heating as a function of the condenser temperature for the four different scenarios given in EN 14825:2012 and can therefore be regarded as a combination of Figures 3.19 and 3.20. The vertical lines indicate the average temperature in the condenser for the medium temperature scenario, the domestic hot water production and the total average based on the amount of heat produced at the respective conditions. For the given pinch point temperature difference in the condenser of 10 K, the average ORC working fluid condensation temperature was determined to 51.6 °C. Note that the abscissa, which shows the condenser temperature, has been inverted. This makes it easier to compare the figures on the different graphs

since the low outdoor temperatures on the left correspond to a higher temperature of heat demand.

Knowing the demand profile, the next step was to carry out an annual performance calculation based on the four different valve control schemes. Performance data from the dynamic model from Section 3.2 were used to obtain the internal working fluid mass flow rate $\dot{m}_\mathrm{f}$ and the isentropic expander efficiency η_s for each condenser temperature. Assuming that there was no subcooling after the condenser and that the liquid pump operated with an isentropic efficiency of 0.5, the whole power cycle could be calculated. This yielded the heat release from the condenser at the different temperature levels, which afterwards could be used to obtain the operating time from dividing the thermal energy demand in kWh by the heat flow rate from the condenser in kW. This study does not include a detailed investigation of the time distribution of heat availability and demand. Following the suggestions by Markussen et al. [155] for the space heating and DS439 [73] for the hot water generation, the storage capacity was expected to suffice both systems.

The equations used for the annual calculations are based on the definition of the enthalpy-based isentropic expander efficiency

$$\eta_s = \frac{h_\mathrm{in} - h_\mathrm{out}}{h_\mathrm{in} - h\left(p_\mathrm{out}, s_\mathrm{in}\right)} \tag{3.24}$$

and pump efficiency

$$\eta_{s,\mathrm{pump}} = \frac{h\left(p_\mathrm{out}, s_\mathrm{in}\right) - h_\mathrm{in}}{h_\mathrm{out} - h_\mathrm{in}}. \tag{3.25}$$

All cycle calculations were carried out with the same parameters for the pump efficiency $\eta_{s,\mathrm{pump}} = 0.5$, the amount of subcooling after the condenser $\Delta T_\mathrm{subcool} = 0\,\mathrm{K}$, the superheat at the expander inlet $\Delta T_\mathrm{superheat} = 5\,\mathrm{K}$ and the evaporation temperature $T_\mathrm{eva} = 145\,^\circ\mathrm{C}$. The cycle efficiency η_th is defined as

$$\eta_\mathrm{th} = \frac{\dot{W} - \dot{W}_\mathrm{pump}}{\dot{Q}_\mathrm{in}}. \tag{3.26}$$

Results & Discussion

An illustrative result of the first steps of this analysis is displayed in Figure 3.25. Here, the changes in saturation pressure and specific volume are expressed in terms of Π and Υ, respectively. Both ratios decreased as the condenser temperature approached evaporator conditions. To meet the desired expansion ratio, the cutoff angle had to behave in the opposite way, stopping admission of working fluid between 5° and 40° crankshaft angle after top dead center.

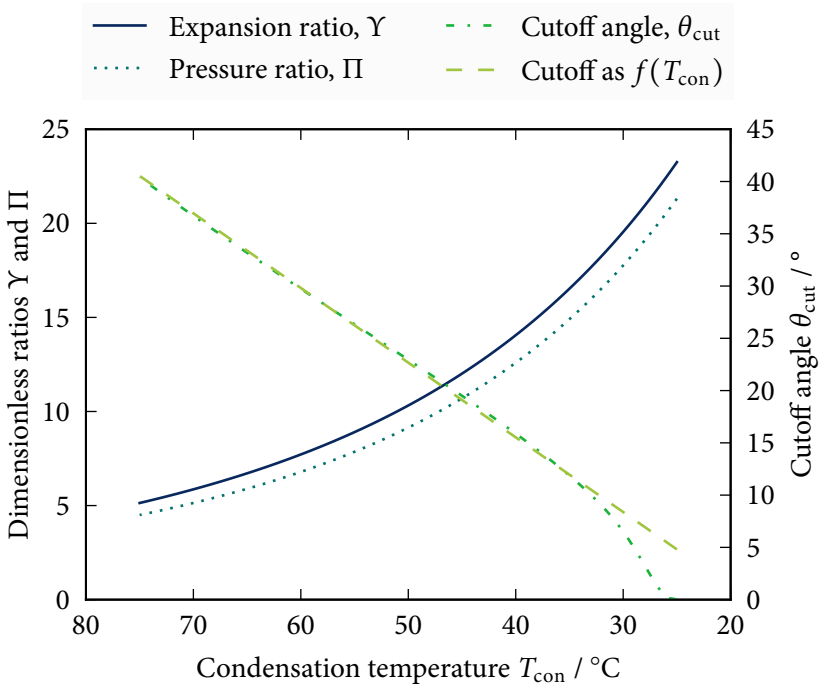

Figure 3.25: Linearized cutoff angle as a function of expansion ration Υ.

The data from Figure 3.25 could be used to derive a simple linear relation between condenser temperature in Kelvin and cutoff angle in radians

$$\theta_{cut} = b + z_0 + c\ z_1\ T_{con} \tag{3.27}$$

with $b = -3.634$ and $c = 0.01247$. While b and c are functions of the cylinder geometry and the fluid properties at the expander inlet as well as the crank mechanism, z_0 and z_1 depend on the valves and the inlet and exhaust pipe systems. The presented linearisation implicitly employed the fact that the shape of the exponential-like vapour pressure curve matched the close-to-sinusoidal piston displacement curve in the range from 10° to 40°.

When implementing Equation (3.27) in a controller, z_0 and z_1 can be used to compensate for flow losses occurring before and after the expansion chamber. The maximum pressure in the expansion chamber might not reach the evaporator pressure during admission. Adding an offset to the calculation of the cutoff angle compensates for this problem. In case of a lossy pipe connection from expander to condenser, the

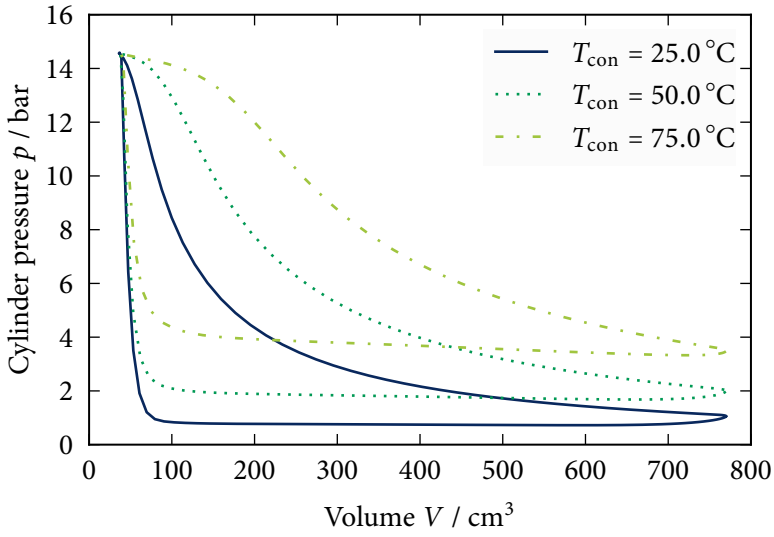

Figure 3.26: PV-diagram for different condenser pressures with variable admission timing.

z variables can also be used to assure a certain amount of underexpansion, which facilitates a faster mass exchange during the exhaust phase.

Figure 3.26 shows the cylinder pressure during one revolution at the same operating conditions as in Figure 3.21. Adjusting the cutoff according to Equation (3.27) with $z_0 = 0.0$ and $z_1 = 1.0$ controlled the amount of mass inside the cylinder and the expansion ratio resulting in different pressures at the end of expansion. The valve opening curves in Figure 3.23 have been generated with the same settings and the employed cutoff angles were approximately 5°, 23° and 41°. Translating the angles to cylinder volumes resulted in cutoff chamber volumes close to 38 cm^3, 74 cm^3 and 151 cm^3.

At lower condenser pressures, the selected control scheme produces in an increasing amount of underexpansion since the chamber pressure at BDC is higher than the exhaust pressure, which is indicated by the horizontal part of the curve. Compared to Figure 3.21, overexpansion could be avoided and the general mismatch in terms of pressure at BDC and in the condenser is reduced.

The solid curve for variable timing in Figure 3.27 meets the three dotted lines for fixed valve control at their respective design temperatures. The actively controlled valves allowed the expander to maintain an elevated efficiency over the whole operating

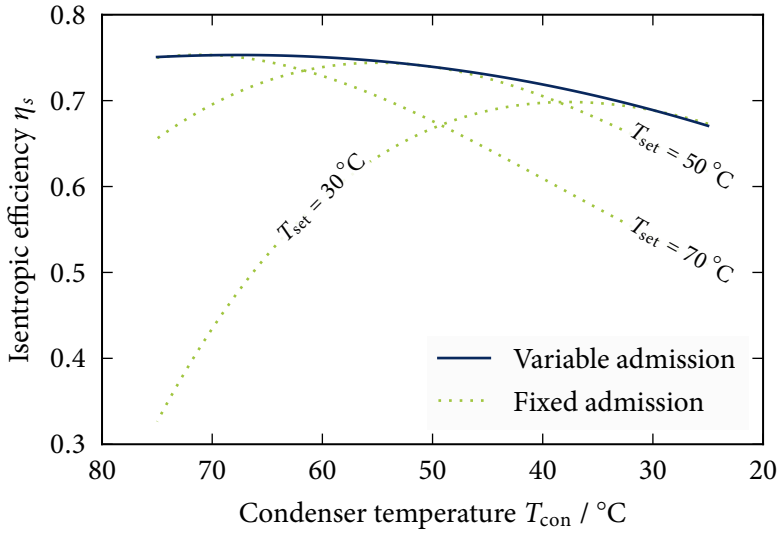

Figure 3.27: Isentropic expander efficiency with variable admission control and different fixed controller setpoints.

range. The efficiency line for the controlled injection system connects the maxima of the dotted lines yielding the highest obtainable efficiency. The admission schemes with the three different setpoint temperatures of 30 °C, 50 °C and 70 °C performed almost as well as the variable control within a range of ±5 °C around their setpoint. Outside of this range, the efficiency decayed.

This decay was more pronounced for temperatures above the setpoint temperature. The overexpansion caused by a T_{set} below T_{con} had a higher impact on the performance than the same temperature difference with the opposite sign causing underexpansion. The general trend towards higher expander efficiencies with increasing condenser temperature in Figure 3.27 is related to the better match between recompression and volume ratio. The sharp edge in bottom left corner of Figures 3.21 and 3.26 illustrates the low level of recompression. Following the lower part of the pressure curve throughout the exhaust stroke from right to left, the cylinder pressure did not increase before the internal volume passed 100 cm^3. The result was a large difference between chamber pressure and evaporator pressure, which caused a lossy inrush during the early admission phase to compress the remaining fluid in the chamber. Such losses can be avoided by adjusting the exhaust valve system to make the pressure after recompression match the evaporator pressure.

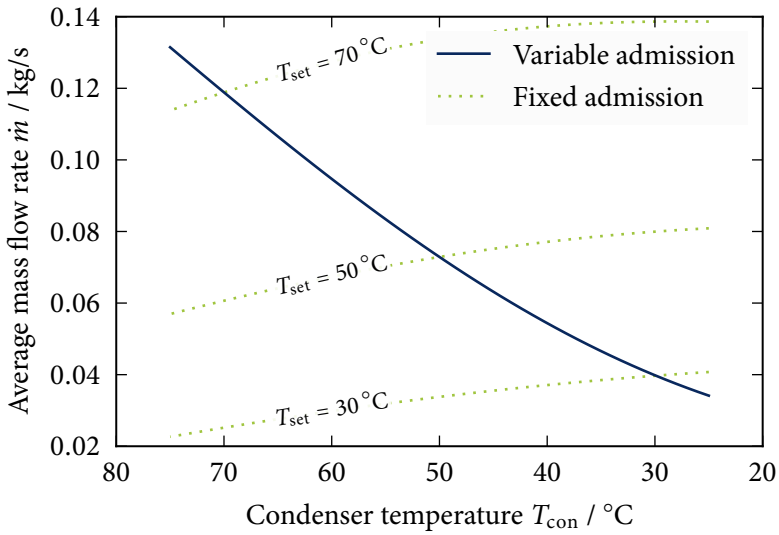

Figure 3.28: Mass flow rates with variable admission control and different fixed controller setpoints.

The mass flow rates associated with the operating conditions described above are shown in Figure 3.28. Also here, the curve for variable admission design met the dotted lines for the fixed admission systems at the setpoint temperatures. The mass flow rate through the system increased with increasing condenser temperature for a variable valve timing while the average mass flow rate decreased monotonically for the cases with a fixed timing. Here, the higher pressure during the exhaust lead to more mass in the cylinder at the end of the exhaust stroke. With otherwise constant settings, more remaining mass in the expansion chamber only allowed a decreased amount of mass to enter the cylinder per stroke thus reducing the average mass flow rate. For the variable admission system, the extended inlet period had the opposite effect by allowing more fluid into the expander on a per cycle basis. This had a much larger influence on the average mass per cycle causing the increasing mass flow rate shown in Figure 3.28.

From the analysis of the annual heat demand in Figure 3.24, it was found that the energy-averaged condenser temperature was 51.6 °C. The central reference case FV50 assumed a condenser temperature 50 °C and is therefore expected to be the closest competitor to the variable valve timing in an annual performance assessment.

Recalling the 10 K pinch point temperature difference and the heat demand temperatures from Figure 3.19, the number of operating hours per outdoor temperature

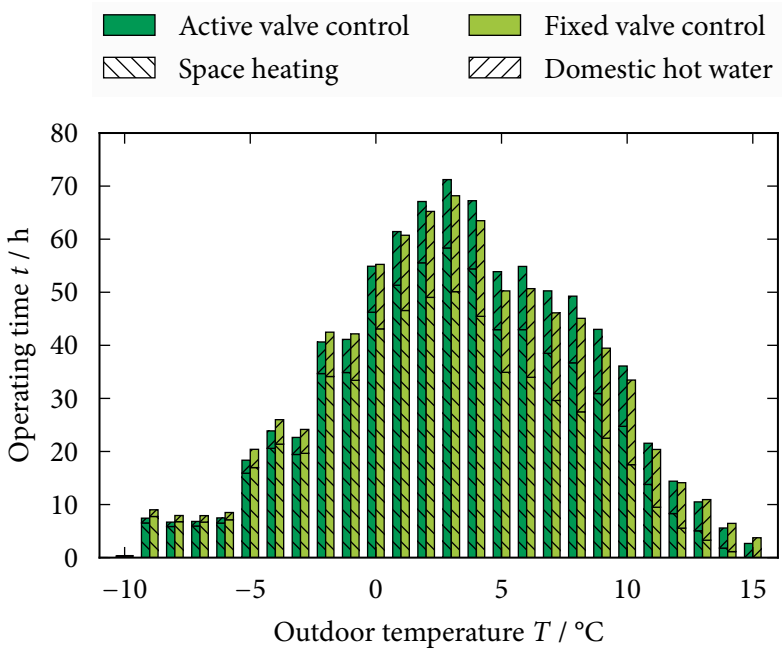

Figure 3.29: Annual operating hours required to cover the heat demand with variable valve timing, darker bars, and a fixed cutoff defined by a setpoint temperature of 50 °C shown as lighter bars.

bin was calculated. Figure 3.29 compares the annual operating hours for the variable valve timing system with the FV50 reference case. The height of the darker bars represents the full load operating hours for a system with variable valve timing while the lighter bars refer to the central reference case with a fixed timing. Note that the bars are divided into an upper part with forward hatching for the time of domestic hot water production and a lower part with a backward hatching pattern calculated from space heating demand. The temperature required to satisfy the space heating demand changes with outdoor temperature, while domestic hot water was always produced at a condenser temperature of 60 °C. At low outdoor temperatures, the CHP plant mostly produced space heating, while high ambient temperatures reduced the need for space heating, which lead to an operation governed by the domestic hot water consumption. Hence, the internal division of the bars in Figure 3.29 moves from the top, only SH, to the bottom, only DHW, with increasing outdoor temperatures. A comparison of the two sets of graphs suggests that the operating times were similar for the actively

controlled system and the fixed valve scheme. The latter operated a little longer for very low and very high ambient temperatures, while the system with variable timing ran longer for outdoor temperatures between 1 °C and 12 °C. The upper part of the bars, which is related to the domestic hot water production is always longer for the fixed valve timing. The elevated condenser temperatures for this case lead to a reduced mass flow rate in the fixed system, see Figure 3.28, which in turn reduced the thermal output of the system requiring a longer operating period. Generally, the differences in mass flow rate governed the overall changes in both electrical and thermal output. The opposite trends, *i.e.* lower power at higher condenser temperatures for fixed timing and higher power for higher temperatures for the variable control, can also be found in the differences in operating hours to cover the space heating demand, the lower part of the bars in Figure 3.29. Below a condenser temperature of 50 °C, or above an outdoor temperature of approximately −2.5 °C, the actively controlled systems delivered less heat, thus the extended operating period.

The overall results for the four different cases are shown in Figure 3.30. Also here, the lower (left) part of the bars relates to operation in SH mode and the last part is contributed by DHW production. This time, the hatching patterns do not illustrate the difference between SH (darker color) and DHW (lighter color), but are used to highlight the different reference conditions for the admission control. All data were normalised with respect to the variable admission system, which always has the value of unity. The axis on the left provides information regarding the absolute values for the different quantities. The results suggest that the third case with a fixed valve timing tuned to a condenser temperature of 50 °C performs similarly to the variable admission system. The annual hours of operation required to cover the heat demand of 12.75 MWh for domestic hot water and 19.25 MWh for space heating only differed by 39 h. However, the distribution between DHW and SH production is slightly different. The fixed FV50 system ran for more hours to produce the hot water. Since the heat release basically follows the mass flow rate, the operating hours express the same ratios as the average mass flows calculated from the data in Figures 3.28 and 3.29. The low mass flow caused by the short admission for the FV30 case required the system to run much longer. The difference between AV and FV50 disappears in the next category that covers the amount of produced electricity. The system with variable valve control had an annual electricity production of 2700 kWh from SH operation and 1560 kWh from DHW production and FV50 produced 2680 kWh and 1535 kWh, respectively. Covering the same heat demand, all of the investigated system consumed a similar amount of heat, which was close to 36 MWh per year. The average annual electrical efficiency was above 10 % for all systems, but AV and FV50 outperformed FV30 and FV70. The two best cases had a similar annual electricity production at electrical efficiencies of 11.8 % and 11.6 %, respectively.

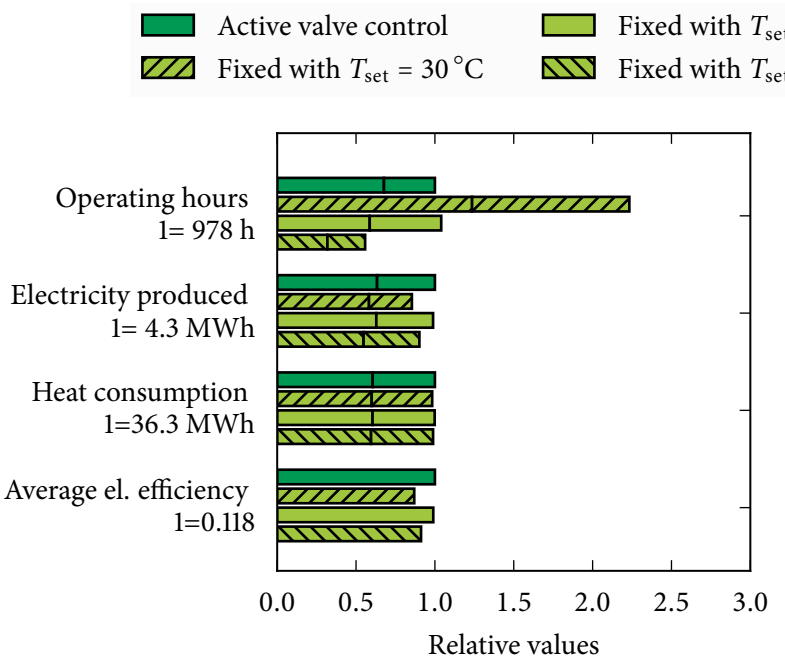

Figure 3.30: Summarising figures for CHP operation with a variable valve timing and a fixed set point with three different reference temperatures, the length of the left hand side of the bars refers to space heating operation and the length of the right hand side is related to the domestic hot water production.

Translating the expander efficiencies from Figure 3.27 to cycle efficiencies yields Figure 3.31. Here, the differences are less pronounced and the performance of FV50 was closer to the one of AV. The increasing temperature difference from high to low condenser temperatures yielded a higher theoretical efficiency that overrules the decreasing expander performance and the overall cycle efficiency increases.

It is important to note that the total operating hours only covered a small share of the year. If the heat that drives the power cycle is available at a low price, for example as waste heat from other processes or from locally available biomass, these hours could be used for producing electricity. This would have a major impact on the average operating temperature of the condenser. Assuming that the system rejects heat to the environment, the annual average condenser temperature was estimated to 25 °C from the average annual outdoor temperature of 11 °C.

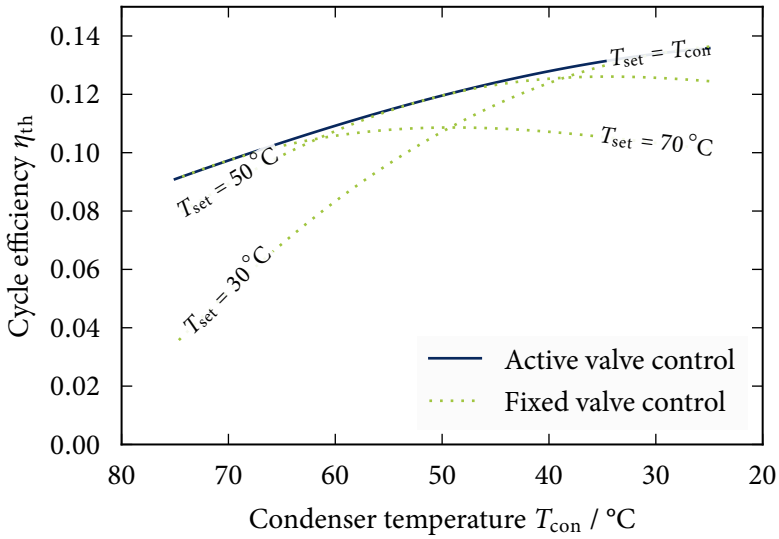

Figure 3.31: Cycle efficiency with $\eta_{s,pump} = 0.5$, $\Delta T_{subcool} = 0\,K$, $\Delta T_{superheat} = 5\,K$ and $T_{eva} = 145\,°C$.

Table 3.32: Power production without heat demand at $T_{con} = 25\,°C$.

Quantity	Unit	AV	FV30	FV50	FV70
Operating time	h	7782	6576	7743	8215
El. produced	MWh	20.3	20.5	43.8	64.8
Heat consumed	MWh	149	151	352	640
El. efficiency	%	13.6	13.6	12.5	10.1

Table 3.32 compiles the figures for the possible additional operation for electricity generation only. The operating time reflects the hours that are not needed to satisfy the heat demand discussed above. Due to the low average condenser temperature, the variable valve timing performed similar to the FV30 case instead of the FV50 case. The active valve control reached a heat-to-electricity conversion efficiency of 13.6 %. FV30 had the same electrical efficiency, which is 1.1 % points higher than for the FV50 and outperformed FV70 by 3.5 % points. Despite the lower mass flow rates, the AV case produced a similar amount of electricity as FV30 does due to the longer operating time. The even higher mass flow rates for FV50 and FV70 lead to an electricity production and heat consumption that was more than two and three times higher than for FV30.

Based on these numbers, the average annual electrical efficiencies are found to be 13.2 %, 13.0 %, 12.4 % and 10.2 % for the AV, FV30, FV50 and FV70 case. Considering continuous operation all year round thus leads to an advantage for the flexible valve timing. This performance is close to the efficiencies shown in Tab. 3.32 since this operating mode accounts for more than 75 % of the operating time in all cases.

Further investigations of the different operating modes and possible benefits from implementing a variable valve control have to involve a more detailed assessment of the heat source, which is not carried out in this study. Actively controlling the admission system allows the system to run at an optimal efficiency at all times. However, the differences in efficiency are not large enough to promote an unconditional implementation. Running with a fixed evaporator temperature and pressure, the new control variable does not require additional sensors, but the valve actuation mechanism is certainly going to be more advanced due to the required flexibility. The test machine describe earlier[259] used high precision servo motors to achieve this flexibility. To reduce cost and complexity of a potential product, a purely mechanical solution should be considered.

Another option that has not been discussed here is the variable control of the exhaust valve. The ability to reach the evaporator pressure by recompressing a different amount of working fluid after the exhaust phase is expected to lift the isentropic expander efficiency to values around 0.9, but further work is required to document this is detail. Also this enhancement would not require more sensors and the additional parts needed for such a solutions are very similar to the ones for the adaptive admission system. One could argue that installing both a flexible admission and exhaust valve mechanism does not make the system much more complicated compared to only one variable valve timer.

Besides a generally higher efficiency, two variable valves also increase the change in mass flow rate and power output. The decrease in average mass flow rate with increasing expansion ratio is amplified, which also reduces the electrical output. Considering only underexpansion and insufficient recompression as internal sources of losses, the produced work per swept volume decreases with increasing efficiency. A reciprocating expander working with the ideal expansion ratio also requires the same volume ratio during recompression to avoid in-rush losses during the early admission phase. Running under these conditions, the expander resembles a gas spring. Mass exchange cannot take place without either underexpansion or insufficient recompression. The correct design decision regarding the device's power density in terms of mean work output per average volume flow rate is therefore also influenced by the mechanical losses. Such losses typically scale with rotational speed, which is roughly proportional to the volume flow rate for a fixed mechanical design.

The final issue to be mentioned in this discussion is the working fluid, especially because domestic cogeneration applications have to comply with high safety standards. Using a flammable working fluid might be a problem and other fluids should be considered in future studies. However, this is not expected to change the overall results of this work. Being able to adjust the expansion ratio by controlling the cutoff angle allows the reciprocating machine to run with different working fluids without modifications. Only the produced power and the mass flow rate will change depending on the enthalpy drop in the expansion chamber.

3.5 Heat Transfer During Expansion

Heat Loss From Expanders

Depending on the circumstances, heat transfer in reciprocating machines can be either desired or unwanted. Devices that primarily apply work to a fluid, especially compressors, are often cooled to reduce the amount of work needed to reach a certain pressure. Expansion devices on the other hand run on compressed fluid and heat losses reduce the amount of extracted work and such devices are thus insulated. In this section, theoretical reference processes are introduced and evaluated based on simplified single step processes and by discretising the process numerically. Focussing on the heat loss from expanders, the reference processes are compared to results obtained from heat transfer correlations for reciprocating machines.

The ideal limits for expansion and compression processes are the reversible adiabatic process found in Rankine and Joule cycles and the reversible isothermal process known from Ericsson and Stirling cycles [25]. A reversible adiabatic state change takes place at a constant entropy and is thus the standard reference process for an expansion. Assuming ideal cooling capabilities, the isothermal compression work is the lower limit for the work required to compress a gaseous working fluid. Even though a heated expansion with temperature increase is theoretically possible, this work also refers to the isothermal process as the limiting case for maximum achievable work extraction from a given pressure difference.

In most studies, the expansion process is considered adiabatic assuming that there is only a low rate of heat loss from the expander to the environment. Even if the expander does not exchange thermal energy with the environment, the cyclic nature of the expansion process in volumetric machines causes heat transfer between the confined fluid and the surrounding walls. At steady state operation, the temperature of the wall will reach an average value depending on the working fluid, the machine type (expander or compressor) and the inlet conditions. The relatively high thermal conductivity of the wall material and its mass dampen the temperature fluctuations

over one cycle and such variations are typically neglected [34]. Experimental work on small scale ORC systems supports the general assumption of limited heat loss. Glavatskaya et al. [87] concluded from parameter estimations based on measurements and modelling work that their reciprocating machine had an overall heat transfer coefficient UA_∞ of 2.5 W/K that connected the expander shell to the environment. A less insulated scroll machine was found to loose heat at a rate of 6.38 W/K and 3.4 W/K by Lemort, Declaye and Quoilin [143] and Lemort, Quoilin and Lebrun [146]. For an uninsulated small turbine, Li et al. [148] reported 3.2 $\mathrm{W/(m^2\,K)}$, 7.0 $\mathrm{W/(m^2\,K)}$ and 7.0 $\mathrm{W/(m^2\,K)}$ for radiative, convective and conductive losses per unit surface area, respectively. There is a large difference between those studies since the heat loss rate per unit of produced power is orders of magnitude larger for displacement machines. The data presented by Lemort, Declaye and Quoilin [143], allows to calculate the heat loss rate to more than 15 % of the produced power, whereas Li et al. [148] measured around 3 %. Both investigations were carried out with machines operating between 80 °C and 130 °C with a maximum shaft power of 2 kW and 3.3 kW, respectively. The internal heat transfer resistances for the transfer of thermal energy from the working fluid to the shell UA_f were approximately five times higher than the outer heat transfer coefficients and Lemort, Quoilin and Lebrun [146] estimates those values to be in the range of 20 W/K to 35 W/K for small scroll expanders.

In general, two different approaches are considered when assessing the efficiency of an expansion machine. There is a thermodynamic approach (i) based on the change in specific enthalpy Δh of the working fluid and the mechanical approach (ii) that uses a measured or calculated work output W. For simple adiabatic cases without leakages, Δh and the power $\dot{W}$ are directly related via the mass flow rate $\dot{m}$. With an increasing amount of heat transfer during expansion, the change in specific enthalpy and the specific work output $w = \dot{W}/\dot{m}$ diverge since the heat flow $\dot{Q}_\mathrm{f} = \dot{m} q_\mathrm{f}$ directly expresses the difference between these terms in the energy balance

$$0 = (h_\mathrm{in} - h_\mathrm{out})\,\dot{m} - \dot{Q}_\mathrm{f} - \dot{W}. \tag{3.28}$$

To include this heat transfer in the reference processes, the definition of the isentropic efficiency can extended to

$$\eta_s = \frac{w}{w_\mathrm{rev}} = \frac{h_\mathrm{in} - h_\mathrm{out} + q_\mathrm{f}}{h_\mathrm{in} - h_\mathrm{out,rev}}, \tag{3.29}$$

which adds the transferred heat to the enthalpy difference. To match the sign in the equation above, a heat flow out of the expanding fluid has to have a negative sign. Modifying up the lumped isentropic expansion efficiency by amplifying the heat-transfer-related effects provides a new figure of merit, which shall be called the adiabatic

efficiency η_{s^+}. The isentropic and isothermal expansions were investigated based on a theoretical approach that was recommended for steam expansion calculations by Bejan [25]. His simplified equations were applied to the expansion of an organic working fluid, n-pentane, and compared to a step-wise calculation procedure. The results of the calculations presented below provide insight into the impact of heat losses on the expansion processes in small scale machines. The change in produced work is described and associated change of η_s is compared to that of η_{s^+}.

Beside the theoretical approach, detailed equations were employed to capture the effect of the cyclic heat transfer to and from the wall. The first heat transfer correlations for reciprocating machines date back to the early twentieth century and were related to combustion engines, see for example the works by Nusselt and Eichelberg [74–76, 171]. These early equations employed mean piston speed, pressure and temperature as parameters and were completely empirical. They provided a straight forward way to model the heat transfer in a simple way yielding results in the right order of magnitude. Later, Elser [78] improved the modelling approach by introducing relations based on Re and Pr [186], which greatly enhanced the applicability. Equations of this kind are still recommended for compressor modelling [188] and have recently been compared to advanced numerical models by Disconzi, Pereira and Deschamps [66] with good agreement for R134a.

Reference Processes

According to Bejan [25], there is a general function to approximate the reversible work

$$W_{\text{rev}} \approx \frac{p_1 V_1}{k-1}\left(1-\left(\frac{V_1}{V_2}\right)^{k-1}\right), \tag{3.30}$$

which is valid for processes with a constant value for k. Thus, the only difference to calculate an isentropic and an isothermal expansion is the value used for coefficient k, which is expressed by either k_s or k_T, respectively. Bejan [25] provides equations for both variables based on partial derivatives with respect to specific volume v. These equations could be transferred to the density domain yielding

$$k_s = -\frac{v}{p}\left(\frac{\partial p}{\partial v}\right)_T \frac{c_p}{c_v} = \frac{\rho}{p}\left(\frac{\partial p}{\partial \rho}\right)_s \text{ and} \tag{3.31}$$

$$k_T = -\frac{v}{p}\left(\frac{\partial p}{\partial v}\right)_T = \frac{\rho}{p}\left(\frac{\partial p}{\partial \rho}\right)_T = \frac{1}{\kappa\, p} \tag{3.32}$$

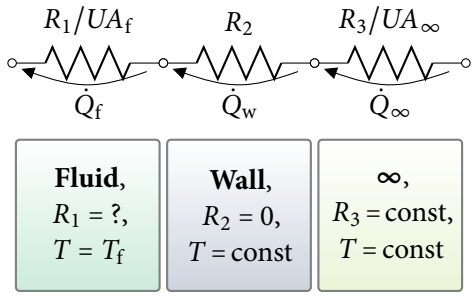

Figure 3.33: Heat transfer from fluid to environment.

with the isothermal compressibility κ, which can be employed for a direct calculation of Equation (3.32). $(\partial p/\partial \rho)_s$ could be solved with the tables from Bridgman [39] through

$$\left(\frac{\partial p}{\partial \rho}\right)_s = \left(\frac{\partial p}{\partial \rho}\right)_u + \left(\frac{\partial p}{\partial u}\right)_\rho \left(\frac{\partial u}{\partial \rho}\right)_s \text{ with} \tag{3.33}$$

$$\left(\frac{\partial u}{\partial \rho}\right)_s = \left(\frac{\partial u}{\partial v}\right)_s \left(\frac{\partial v}{\partial \rho}\right)_s = \frac{p}{\rho^2} \text{ from} \tag{3.34}$$

$$du = T\,ds - p\,dv \tag{3.35}$$

or by employing the definition of the speed of sound $a^2 = (\partial p/\partial \rho)_s$. Dividing Equation (3.30) by the mass involved in a state change per unit time yielded the reference cases of reversible work for the denominator of Equation (3.29) for isentropic and isothermal expansion. Recalling the original assumption of a constant expansion coefficient k, the validity of Equation (3.30) had to be documented. Since this work targets ORC expanders, n-pentane was employed as example fluid to determine the impact of the changing thermodynamic properties on k_s and k_T. This was done by evaluating Equation (3.31) and Equation (3.32) on a grid in terms of entropy and pressure as well as temperature and pressure to find the regions where Equation (3.30) can be applied.

Equation (3.30) has been recommended for steam processes and the results for another working fluid might be different, even for constant expansion coefficients. An alternative definition of the reversible work that does not assume ideal gas behaviour, as implied by the constant k, could be found by splitting the state change into sufficiently small steps. The general description below shall be the basis for the assessment of the reference processes as well as other, less ideal, state changes.

The heat transfer calculations involved working fluid temperature T_f, the expander housing temperature T_w and external conditions defined by T_∞. Assuming steady state operation simplified the heat transfer problem by defining T_w and T_∞ as constant values.

Consequently, the overall heat transfer coefficient UA_∞ on the outside of the expander was constant as well. To satisfy these conditions, the heat flow $\dot{Q}$ had to be constant throughout the series of elementary nodes shown in Figure 3.33. Furthermore, the metal wall was expected to have a very high thermal conductivity decreasing its thermal resistance R_2 to a value close to 0 K/W. The wall in contact with the fluid thus had a spatially uniform temperature distribution. This implied that a changing temperature during expansion inside a machine did not impact the local wall temperature due to the steady state assumption. Compiling the above in Equation (3.36) and Equation (3.37) lead to six unknowns in

$$\dot{Q}_\infty = UA_\infty \left(T_\infty - T_\mathrm{w}\right) = \text{const} \quad \text{and} \tag{3.36}$$

$$\dot{Q}_\mathrm{f} = UA_\mathrm{f} \left(T_\mathrm{w} - T_\mathrm{f}\right). \tag{3.37}$$

The steady state condition imposed a net zero heat transfer to the wall for an integration in time and eliminated the heat flow $\dot{Q}_\mathrm{f}$ through $0 = Q_\mathrm{f} - Q_\infty$ yielding

$$0 = \int_{t_0}^{t_1} \dot{Q}_\mathrm{f}\, dt - \dot{Q}_\infty \left(t_1 - t_0\right). \tag{3.38}$$

Expanding a constant mass flow rate $\dot{m}$ in a continuous process, the total heat transfer that all fluid portions experienced had to be equal to the outer heat transfer. At any point in time, the integrated specific heat transfer was defined by

$$\dot{Q}_\infty = \dot{Q}_\mathrm{f} = \dot{m} \int_{p_\mathrm{in}}^{p_\mathrm{out}} q_\mathrm{f}/dp. \tag{3.39}$$

Equation (3.39) uses the pressure as integration variable for the instantaneous heat flow rate, while Equation (3.38) was time based. Dividing the whole continuous expansion process into n steps in terms of pressure with a constant step efficiency of η_s localised heat transfer in terms of temperature. For every step j, the equations

$$h^*_{\mathrm{f},j} = \left(h\left(p_{\mathrm{f},j}, s_{\mathrm{f},j-1}\right) - h_{\mathrm{f},j-1}\right)\eta_\mathrm{s} + h_{\mathrm{f},j-1}, \tag{3.40}$$

$$q_{\mathrm{f},j} = UA_\mathrm{f}\left(T_\mathrm{w} - T^*_{\mathrm{f},j}\right) / \left(n\, \dot{m}_\mathrm{f}\right) \quad \text{and} \tag{3.41}$$

$$h_{\mathrm{f},j} = h^*_j + q_j \tag{3.42}$$

were evaluated, which eventually yielded the final enthalpy $h_{\mathrm{f},j=n} = h_{\mathrm{f,out}}$. The total heat transfer rate $\dot{Q} = \dot{m}_\mathrm{f} \sum_{j=1}^{n} q_{\mathrm{f},j}$ and work transfer rate $\dot{W} = \dot{m} \sum_{j=1}^{n} w_{\mathrm{f},j}$ were the

sum of all simultaneously occurring specific terms multiplied with the mass flow rate. The specific work was defined by the first expansion step only

$$w_{\mathrm{f},j} = h_{\mathrm{f},j-1} - h^*_{\mathrm{f},j}. \tag{3.43}$$

The unknown heat transfer resistances had to be found from correlations or defined by further assumptions. For the reference cases, these values are already defined as $UA_\mathrm{f} = 0$ for the adiabatic cases and as $UA_\mathrm{f} = \infty$ for the isothermal case. The isentropic expansion efficiency η_s is equal to unity for the reversible reference processes. While Equation (3.41) describes the heat transfer inside the cylinder, an alternative definition could used for cases that employed the combined overall working fluid heat transfer coefficient to directly connect working fluid and ambient temperature

$$q_{\mathrm{f},j} = UA_{\mathrm{f},\infty} \left(T_\infty - T^*_{\mathrm{f},j} \right) / \left(n\, \dot{m}_\mathrm{f} \right). \tag{3.44}$$

Even without internal entropy generation, the entropy in the control volume changed due to the transfer of heat. To isolate the effect of heat transfer from other loss mechanisms, a new definition of the reference work was needed. The efficiencies calculated from Equation (3.29) did not reflect the performance of an expander compared to an ideal process. One particular problem is that the adiabatic expansion efficiency is coupled to heat transfer by superimposing constant control volume entropy. The more heat loss occurs, the more entropy has to be generated internally resulting in an increasingly non-ideal expansion. Using such a reference process can therefore lead to biased efficiency values.

Following the aforementioned reasoning, an attempt was made to develop an alternative efficiency definition that considers heat transfer to determine the available work expressed in the denominator of Equation (3.29). The new formulation

$$\eta_{s^+} = \frac{w}{h_\mathrm{in} - h_{\mathrm{out},s^+}} \text{ with} \tag{3.45}$$

$$s^+ = s_\mathrm{in} + q\ T_{\mathrm{f},\infty}{}^{-1} \tag{3.46}$$

satisfied this criterion by adjusting the reference entropy s^+. It was found by including the entropy removed or added by means of heat transfer in Equation (3.46). Since the expansion process was not necessarily isothermal, attention had to be paid to the definition of $T_{\mathrm{f},\infty}$. The average temperature of heat transfer could be approximated from a logarithmic temperature difference between the environment and the isentropic process

$$T_{\mathrm{f},\infty} = T_\infty + \frac{\left(T_\mathrm{in} - T_\infty \right) - \left(T_{\mathrm{out},s} - T_\infty \right)}{\ln\left(\frac{\left(T_\mathrm{in} - T_\infty \right)}{\left(T_{\mathrm{out},s} - T_\infty \right)} \right)}. \tag{3.47}$$

Table 3.34: Parameters for example expansion process.

Parameter	Value	Description
$\eta_{s,j}$	70 %	Expansion efficiency
p_{in}	15 bar	Inlet pressure
p_{out}	1.5 bar	Outlet pressure
T_{in}	150 °C	Inlet temperature
$\dot{m}_{\text{f}}$	50 g/s	Mass flow n-pentane

For the basic case of adiabatic operation, the contribution from heat loss to the reference process vanishes and Equation (3.45) becomes Equation (3.29). The proposed equations thus provide an extension of the established efficiency definitions and do not replace it. The reference processes and the step-wise expansion were compared for the expander inlet and outlet conditions listed in Table 3.34, which are similar to the conditions that were used in Section 3.4. In addition to the ideal processes, the combined overall working fluid heat transfer coefficient $1/UA_{\text{f},\infty} = 1/UA_{\text{f}} + 1/UA_{\infty}$ was varied from 0 W/K to 10 W/K, which is in the same range as the values proposed by Lemort, Declaye and Quoilin [143], Lemort, Quoilin and Lebrun [146] and Li et al. [148].

In-cylinder Heat Transfer

Annand [9] and Woschni [256] and others continued the work of Eichelberg [75] and Nusselt [171] and established the new basic in-cylinder heat transfer equation in the form of the right hand side of Equation (3.48) in scientific literature. The new equations were based on dimensionless numbers and fitting parameters achieving better agreement with measurements. In the publications Annand [9], Annand and Ma [10] and Annand and Pinfold [11], parameter a was combined with the last term Pr^c since Pr was almost constant reducing Equation (3.48) to $\text{Nu} = a\ \text{Re}^b$. Introducing a characteristic length Γ and a characteristic speed Λ created even more flexibility and eventually lead to formulations similar to Equation (3.7) and Equation (3.8) from Section 3.2

$$\text{Nu} = \frac{\tilde{\alpha}\,\Gamma}{\lambda} = a\ \text{Re}^b\ \text{Pr}^c \quad \text{and} \tag{3.48}$$

$$\text{Re} = \frac{\Lambda\,\Gamma}{\nu} = \frac{\rho\,\Lambda\,\Gamma}{\mu} \tag{3.49}$$

Table 3.35: Parameters from different heat transfer correlations.

a	b	c	Γ	Λ	Ref.
0.575	0.7	0.00	d_{pi}	$\bar{\bar{l}}$	[a] [9]
0.053	0.8	0.60	d_{e}	$0.5 d_{\mathrm{e}}\, \omega_{\mathrm{e}}$	[b] [2]
0.600	0.8	0.60	d_{pi}	$\bar{\bar{l}}$	[c] [64]

[a] Combustion engine models employ different coefficients for the different strokes.
[b] Equivalent diameter $d_{\mathrm{e}} = \frac{6\mathrm{volume}}{\mathrm{surface}}$ and swirl velocity $\omega_{\mathrm{e}} = f(\omega, \theta)$
[c] simplified, recommended for general compressors

with heat transfer coefficient $\bar{\alpha}$, kinematic viscosity ν and dynamic viscosity μ. Many correlations employed the cylinder bore $d$pi as characteristic length and the mean piston speed

$$\bar{\bar{l}}_{\mathrm{pi}} = 2\left(\hat{l}_{\mathrm{pi}} - l_{\mathrm{pi},0}\right)\, \omega \tag{3.50}$$

for the characteristic velocity. Due to the number of different correlations and their high degree of similarity, only a few were implemented here to provide an impression of the different values and parameters. The Nu-based equations were rearranged to meet the form given in Equation (3.48) and Table 3.35 holds the corresponding parameters and references.

The old equations proposed by Woschni [256] and Annand [9] are still used today and Pinkernell and Bargende [186] concluded that $b = 0.78$ and $c = 0.33$, as obtained from pipe flow, were also valid for diesel engines. The same holds true for spark-ignition engines and a recent comparison by Mohammadi and Yaghoubi [166] also supported the applicability of the work by Woschni [256]. Due to the related processes, modern compression ignition engines behave similarly to diesel engines according to Soyhan et al. [215]. For refrigeration compressors and ORC expanders, gas properties do not change as drastically as in combustion engines. Therefore, a piece-wise definition of the parameters, as done for most internal combustion engines, was omitted in Table 3.35. Demuynck et al. [63] and Annand [9] mentioned a range of 0.35 to 0.8 for coefficient a and this study used the middle of that interval.

Later work on combustion engines by Lawton [133] incorporated thermal diffusivity $\widetilde{\alpha}$ and an expression for the expansion speed. Detailed studies of the occurring phase difference between heat flux and gas-to-wall temperature difference were conducted by Kornhauser and Smith [124]. Their definition of a complex Nu explicitly accounted for an observed thermal impedance. For large Peclet numbers (Pe) of $100 < \mathrm{Pe}_{\omega} < 10000$

calculated from crankshaft angular velocity, Kornhauser and Smith [124] derived a close match of imaginary and real part of the Nu approximately equal to

$$\mathrm{Nu} = 0.56\ \mathrm{Pe}_{\omega}^{0.69} = \frac{\tilde{\alpha}\ d_{\mathrm{pi}}}{\lambda} \tag{3.51}$$
$$\text{with}\ \ \mathrm{Pe}_{\omega} = \frac{\omega\, d_{\mathrm{h}}^2}{4\widetilde{\alpha}}\ \text{and}\ d_{\mathrm{h}} = \frac{4\text{volume}}{\text{area}} = 4l.$$

Kornhauser and Smith [124] are also one of the few to consider general compression and expansion processes whereas most other papers either focus on combustion engines or compressors.

Since there are similarities between pipe flow and the in-cylinder phenomena, the well-know Dittus-Boelter, or McAdams, correlation [67, 161, 254, 255]

$$\mathrm{Nu} = 0.023\ \mathrm{Re}^{0.8}\ \mathrm{Pr}^{(\ )} \tag{3.52}$$

with $\mathrm{Pr}^{0.4}$ for heating and $\mathrm{Pr}^{0.33}$ for cooling resembles Equation (3.48). Consequently, a third approach to model in-cylinder heat transfer could be based on pipe flow correlations. In the recent work by Irimescu [110], a Nu correlation for undeveloped flow in short pipes from Gnielinski [88] was adapted to be used for spark ignition and compression ignition engines. Independently, Gnielinski [89] confirmed the general validity of the equations, but at the same time proposed some revisions of his original correlation in the form of a factor K on the right hand side in

$$\mathrm{Nu} = \frac{(\zeta/8)\ (\mathrm{Re}-1000)\ \mathrm{Pr}}{1 + 12.7\sqrt{\zeta/8}\ \left(\mathrm{Pr}^{2/3}-1\right)} \left(1 + \left(\frac{D}{L}\right)^{2/3}\right) K \tag{3.53}$$

$$\text{with}\ K = \begin{cases} \left(\frac{\mu_{\mathrm{f}}}{\mu_{\mathrm{w}}}\right)^{0.14} & \text{in reference [110],} \\ \left(\frac{\mathrm{Pr}}{\mathrm{Pr}_{\mathrm{w}}}\right)^{0.11} & \text{for liquids [89],} \\ \left(\frac{T_{\mathrm{f}}}{T_{\mathrm{w}}}\right)^{\sigma} & \text{for gasses [89].} \end{cases} \tag{3.54}$$

Irimescu [110] further stressed the applicability of his equations to different cases using different fluids and even mixtures. However, there should still be room for improvement according to the problems and challenges pointed out by Gregorig [91, 92] regarding the appropriate definition of the correction term K. As explained by Hufschmidt and Burck [104] and Hufschmidt, Burck and Riebold [105] and Gnielinski [89] and Gnielinski [90], the altered K in Equation (3.54) improved Equation (3.53) notably. It reduced the overcompensation of varying fluid properties when using the viscosity ratio $\mu_{\mathrm{f}}/\mu_{\mathrm{w}}$ only. For cooling applications, Gnielinski [90] recommended to set $\sigma = 0$ and for $T_{\mathrm{f}} < T_{\mathrm{w}}$, the exponent σ had to be found from experiments and the

referenced publications only contained values for air (0.45) [89], steam (-0.18) and CO_2 (0.12), both from Gnielinski [90]. However, Gregorig [91, 92] provided background information that enable the interested reader to obtain a sensible value for σ and the exponent of the Pr ratio allowing for a determination of K over a wide range of temperatures for liquid and gaseous fluids. Given these information, the remaining parameters of Equation (3.53) were the friction factor ζ determined from

$$\zeta = \begin{cases} (1.82 \log(\mathrm{Re}) - 1.64)^{-2} & \text{in [88, 110] or} \\ (1.80 \log(\mathrm{Re}) - 1.50)^{-2} & \text{from [89, 90]} \end{cases} \tag{3.55}$$

and the pipe diameter D and length L. As in Irimescu [110], d_{pi} and clearance height l_{pi} were used for those parameters and Γ was equal to the mean piston speed. Together with the fluid and the wall temperature, the heat transfer coefficients could be used to calculate a heat transfer rate to the wall. All data was obtained from steady state operation without heat losses to the environment, which means that the net heat transfer for one revolution was 0 J in all cases.

Results & Dicusssion

When Bejan [25] introduced Equation (3.30), he stressed that it only is applicable for sufficiently small state changes so that the exponents k_s and k_T are constant. It was thus necessary to map the values of these exponents to find the regions where Equation (3.30) can be applied. Equation (3.31) and Equation (3.32) have been evaluated on a grid that covers temperatures and pressures from the triple point of n-pentane up to 500 °C and 80 bar including the ranges in which an ORC with n-pentane would operate.

Starting with the isentropic reference process, the values for k_s are presented in Figure 3.36(a). The two-phase domain was excluded from the calculation because there is no directly applicable expression for the derivatives needed to calculate k_s and k_T. Even though Thorade and Saadat [238] deliver many explicit formulations that can be used to overcome the computational challenges, the general concerns regarding the use of quantities like the speed of sound in multiphase systems remain. To comply with the initial assumptions for Equation (3.29), an expansion from 50 bar to 40 bar at 2.3 kJ/(kg K) was selected as example process for Equation (3.30) since the contour lines for k_s are almost horizontal on that range.

Applying the same strategy to visualise the evolution of k_T resulted in Figure 3.36(b). In the liquid phase, the overall impression is the same as in Figure 3.36(a). The k_T values peaked exponentially in the vicinity of the triple point and the numerical values above the saturation curve were lower than in Figure 3.36(a). Furthermore, a more

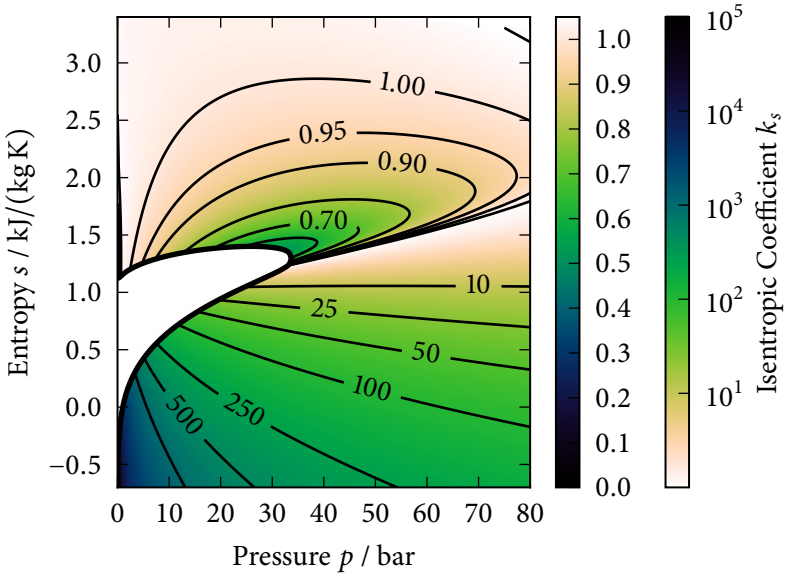

(a) Lines of constant isentropic exponent in a s-p diagram of n-pentane.

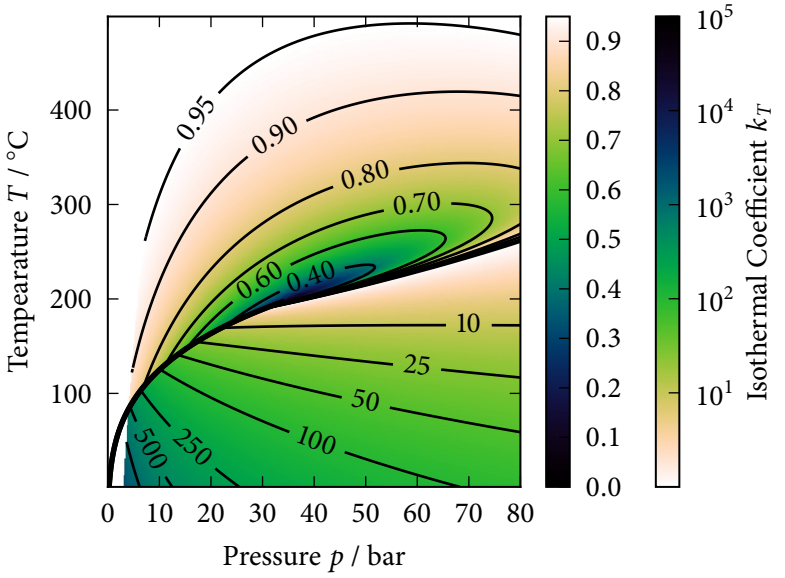

(b) Lines of constant isothermal exponent in a T-p diagram of n-pentane.

Figure 3.36: Mapping of expansion exponents for Equation (3.30).

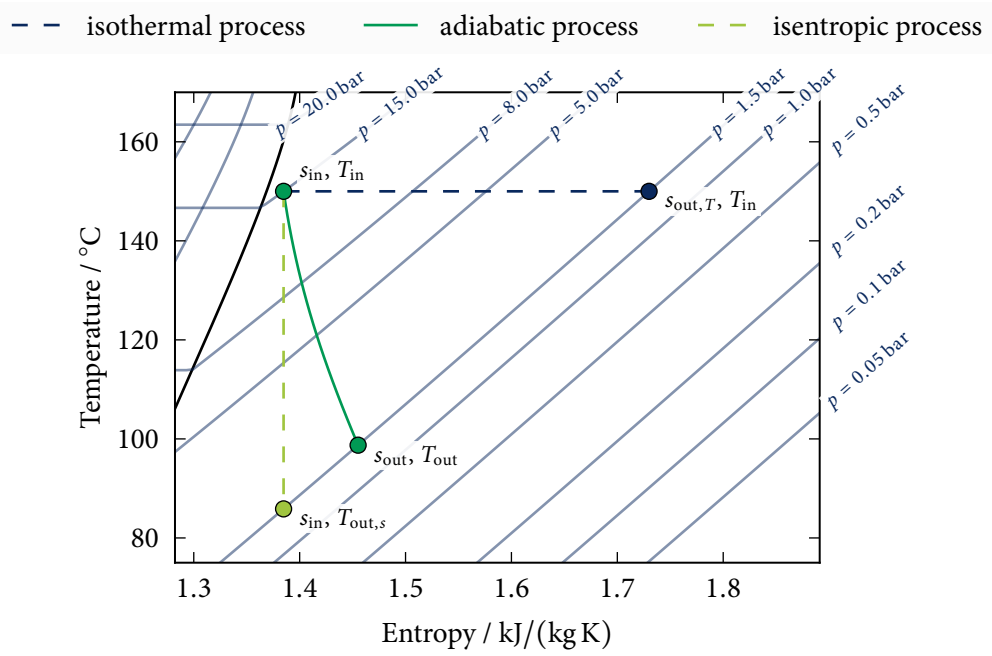

Figure 3.37: Example expansion processes for the limiting cases and an adiabatic state change.

distinct nadir was found at the critical point around 33.7 bar and 197 °C. Horizontal contour lines occur at higher pressures than for k_s, which resulted in a different region for the direct application of Equation (3.30) for isothermal expansion. The comparison is going to be carried out for an expansion from 70 bar to 60 bar at 400 °C.

The specific work obtained from the simplified isentropic expansion was 13.49 kJ/kg and for the isothermal process the result was 10.09 kJ/kg. Both of the selected processes calculated from Equation (3.30) were compared to their respective numerical counterpart from Equations (3.40) to (3.43). In both cases, the step-wise procedure produced values that were higher than estimated but the deviations did not exceed 7 % and 12 %. However, the contour lines in Figures 3.36(a) and 3.36(b) indicate that the ranges with constant expansion coefficients were limited. In both cases, gas phase expansion processes with constant k would require supercritical temperatures and pressures. Looking at the typical ORC operation with a relatively low amount of superheat, Equation (3.30) is not applicable due to the variations k in the vicinity of the dew line.

Table 3.38: Work and heat flow rates for expansion processes with heat loss.

$UA_{f,\infty}$ (W/K)	10.0	7.5	5.0	2.5	0.0
$-\dot{W}$ (kW)	3.15	3.17	3.19	3.21	3.23
$-\dot{Q}_w$ (kW)	1.00	0.76	0.51	0.26	0.00
η_s (%)	69.9	70.3	70.7	71.1	71.5
η_{s^+} (%)	58.4	61.1	64.2	67.6	71.5

A representative expansion process starts close to the two-phase region at a subcritical pressure. Figure 3.37 shows the limiting cases and a lossy expansion in a temperature-enthalpy diagram for an expansion of n-pentane. The dark dashed line depicts a reversible isothermal process and the light dashed line shows a reversible isentropic expansion. The solid line drawn between the two limiting cases depicts an adiabatic expansion with losses, which is one of the most common approaches to calculate an adiabatic and lossy expansion. Employing the parameters from Table 3.34, produced a larger difference between the simplified single-step approach and the multi-step calculation. Equation (3.30) predicted a produced work of 112 kJ/kg for the isentropic process and 153 kJ/kg for the isothermal expansion while the numerical procedure yielded 90 kJ/kg and 101 kJ/kg. To achieve an isothermal expansion, 146 kJ/kg of thermal energy have to be added to the control volume. The adiabatic expansion process produced 65 kJ/kg.

Until now, the amount of heat transferred was imposed either by the isothermal or by the adiabatic assumption. Including the combined overall working fluid heat transfer coefficient $UA_{f,\infty}$ and Equation (3.44) delivered an estimation of the impact of gradual heat losses during the expansion process. The rightmost column in Table 3.38 holds a summary of the expander performance for the adiabatic lossy expansion shown in Figure 3.37. In the table, the heat loss increases from right the right column to the left left column until it reached 1 kW. The amount of extracted work decreased gradually from 3.23 kW to 3.15 kW causing a drop in efficiency. As expected, an increase in heat loss made the different efficiency figures diverge since η_{s^+} amplifies the impact of the heat transfer. Using the same step efficiency, the resulting η_s followed the decrease in work output while η_{s^+} dropped faster indicating that energy is lost from the process.

A detailed view of the stepwise calculation is given in the upper right corner of Figure 3.39. The resulting expansion connected the state points (s_j, T_j) at every pressure p_j after the heat q_j had been removed from the enthalpy h_j^* that was obtained from an adiabatic expansion. An ideal expansion at constant entropy is shown as the vertical line connecting inlet conditions as in Figure 3.37. The second dashed line,

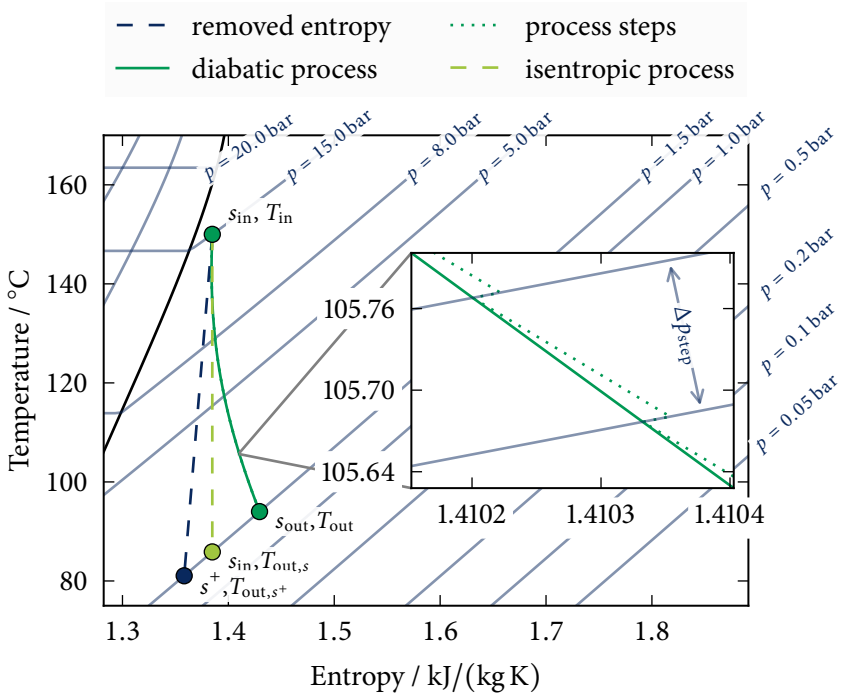

Figure 3.39: T-s diagram of the expansion process.

which has a positive inclination, refers a process with decreasing in entropy to s^+ as described by Equation (3.46) with $T_{f,\infty}$ of 114 °C. The solid line for the diabatic process indicates the progression of the expansion for a $UA_{f,\infty}$ value of 5.0 W/K and refers to the central column in Table 3.38.

Figure 3.40 shows the calculated heat transfer coefficients $\bar{\alpha}$ for the n-pentane expander used in Section 3.4 based on the different Nu correlations and Equation 3.48. The correlation of Destoop [64] resulted in values much higher than the other equations, as expected from the parameters in Table 3.35. Annand [9] and Kornhauser and Smith [124] both produced similar curves, but with much lower amplitudes of less than a third of the values calculated according to Destoop [64]. Values obtained from Gnielinski [90] were located between the other curves with high values at small crankshaft angles and low heat transfer coefficients at the end of expansion. Since no experimental data could be used to obtain a correction coefficient σ, the correction factor K from Equation 3.54 is set to unity. The Adair, Qvale and Pearson [2] correlation is the only one that lead to an increase in heat transfer coefficient while the piston approaches

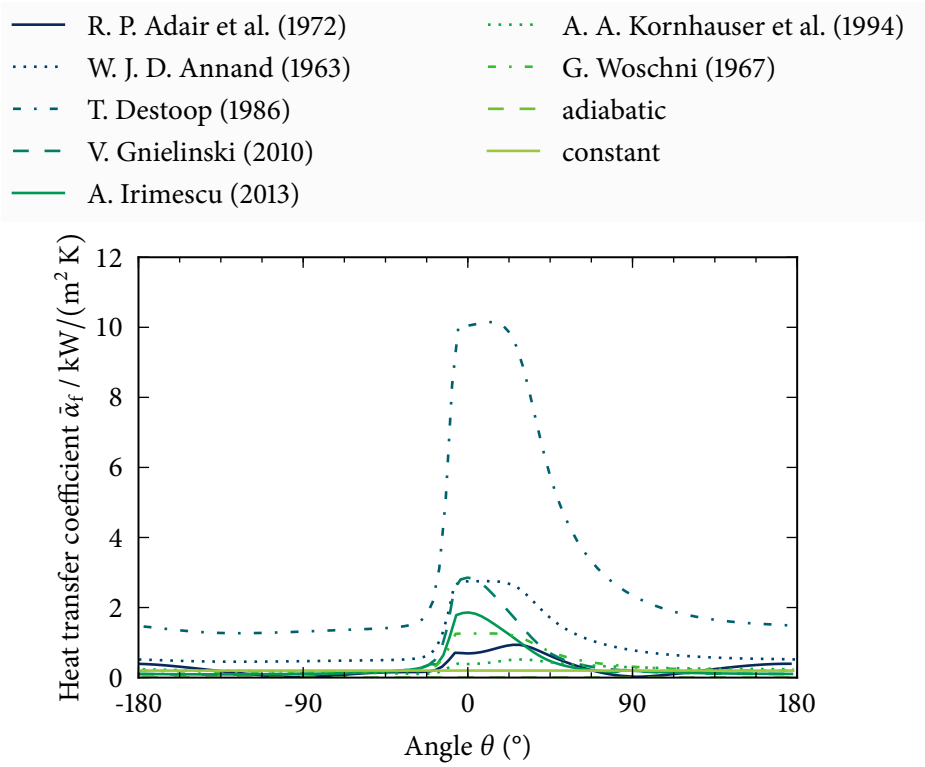

Figure 3.40: Wall heat transfer coefficient during one revolution of an n-pentane expander.

BDC at 180°. The resulting heat transfer rates had values in the range from −1 kW to 3.5 kW. The corresponding shaft power output is shown by the curves in Figure 3.41, which was not affected much by the different heat transfer rates. In fact, even the highest heat transfer rates from the correlations did not lead to a noticeable difference in terms of power output. A larger impact could be seen for a gas spring with air and more graphs for both cases are compiled in Appendix D. The closed volume of the gas spring operated between 5 bar and 45 bar and temperatures from 100 °C to 500 °C. The correlations predicted heat transfer rates of −3 kW to 9 kW, which lead to a difference of up to 10 % in terms of power required to drive the crankshaft.

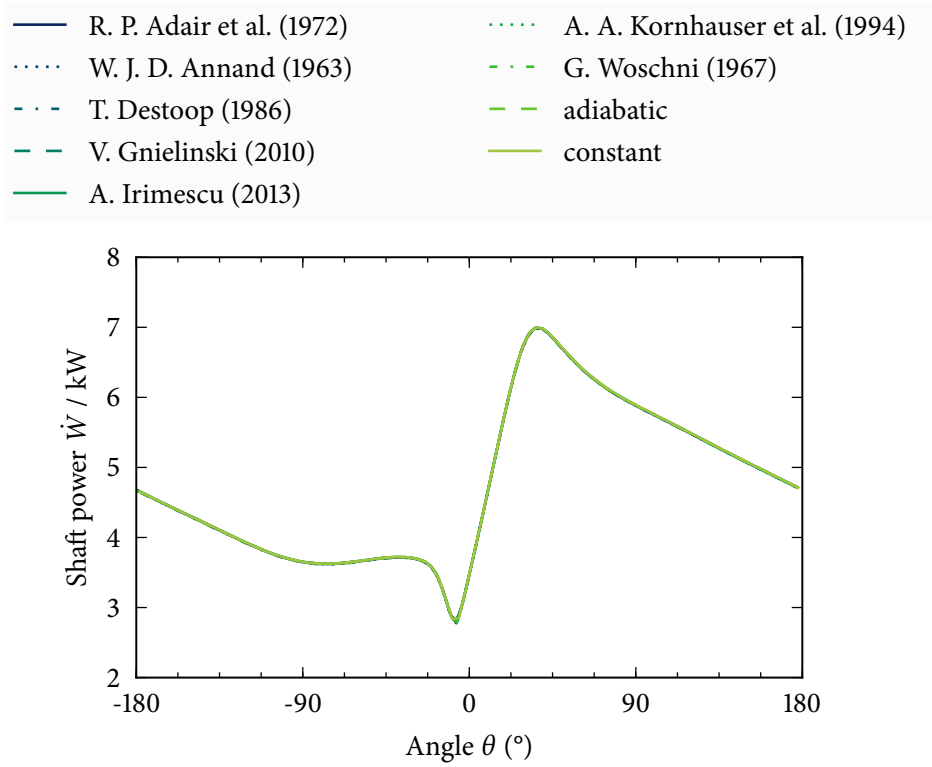

Figure 3.41: Crankshaft power during one revolution of an n-pentane expander.

3.6 Concluding Remarks on Reciprocating Expanders

Model Validation

A new design of a reciprocating expander has been presented running in an organic Rankine with n-pentane as working fluid. The test rig was described and the expected uncertainty of the measured figures was presented. Experimental data showed that variable injection valve timing can be used to operate a reciprocating machine at an almost constant isentropic efficiency of 70 % for pressure ratios of approximately 16.5 (S1, L1), 9.7 (S2, L2) and 11 (S4). The negative impact of non-ideal valve operation was observed in case L4. The valve characteristics play a major role for the efficient operation of a reciprocating machine. Switching quickly between fully closed and fully opened is essential to minimize throttling losses during injection and exhaust. This

proof-of-concept suggests that a rotary valve system can be used to design a machine with a variable expansion ratio.

The experimental data was compared to a dynamic model that predicted the expander efficiency within 10 % without extended parameter tuning, if case L4 is discarded. Produced work could be calculated within a range of less than 30 % deviation between the model and the measurements for all cases. Following the suggestions in this work, it is possible to refine the presented model and adapt the object-oriented code to other designs. The implemented equations have been published as an integrated part of the ThermoCycle library [199], which is available at `https://github.com/thermocycle/Thermocycle-library` and a parametrised version of the model can be found as a digital attachment to Wronski, Skovrup and Haglind [259]. Using the open standard libraries of the Modelica language, others may create new components that seamlessly integrate with the presented code to refine certain aspects of the model to meet the user's requirements in terms of both accuracy and computational performance.

Variable Valve Timing

The possibility to change the expansion ratio of the expander during operation is potentially advantageous for applications that require flexibility. This work documented the development of a control method for reciprocating ORC expanders based on a variable cutoff. Domestic cogeneration was selected as an example since it is one of the applications that require varying condenser temperatures. Small scale ORC units are considered a promising candidate to enter the cogeneration market for domestic installations in the near future [51]. This work contributes an analysis of the performance of a cycle based on a reciprocating expander. Based on standards for space heating demand and domestic hot water production, EN 14825:2012 [80] and DS439 [73], the performance of an expander with a variable cutoff control was compared to systems with a fixed cutoff.

The change in expansion ratio with varying condenser temperature was found to be similar to the evolution of the trapped volume inside a reciprocating expanding machine. This similarity could be exploited to implement a cutoff valve control for a system operating with a fixed evaporator state based on temperatures only.

According to the performed simulations, the adaptive control could keep the isentropic expander efficiency between 68 % and 75 % while the best-performing reference case with a fixed valve scheme varies between 62 % and 73 %.

The expander used for this study had the same swept volume of 734 cm^3 in all cases. Running with different cutoff angles had a large impact on the average mass flow rate. The absolute change in average mass flow rate with varying condenser temperature was

highest for the variable admission control system. The calculated mass flow rate of AV ranged from 0.13 kg/s to 0.03 kg/s while it changed from below 0.06 kg/s to 0.08 kg/s for the 50 °C case FV50 with decreasing condenser temperatures.

Running with a fixed inlet period, the average mass flow rate increased with decreasing condenser temperature due to the lower fluid density at the beginning of the recompression phase. The reduced admission of working fluid from the dynamically controlled valves resulted in a decreased average mass flow rate at lower condenser pressures.

Electrical power output and heat release from the cycle were mainly governed by the mass flow rate. This results in differences in operating time required to meet the same heat demand of more than 100 % between the case with the lowest output, FV30, and the variable control case.

For the examined European cogeneration scenario, the variations in condenser temperature do not result in significant advantages for the variable admission control system compared to a well-tuned fixed valve operation system. Selecting a fixed set point close to the average operating conditions, like in the FV50 case, yields similar figures in terms of average annual electrical efficiency for variable and fixed valve control.

Diabatic Expansion

The simplified approach described by Equation (3.30) could estimate the work produced from an isentropic and an isothermal expansion with an error of approximately 10 % for constant k-values throughout the process. At realistic expander operating conditions, k_s and k_T are not constant and the error associated with Equation (3.30) rose to more than 20 % for the isentropic process and more than 30 % for the isothermal state change. To employ Equation (3.30), graphs like Figures 3.36(a) and 3.36(b) should be consulted to determine whether the simplifications can be applied or if a numerical procedure should be used.

Heat loss from expansion devices is often neglected and the results presented here indicate that the work output is not affected much, which justified the general assumption of an adiabatic process. The new efficiency figure was introduced η_{s^+} to capture the effects of both lossy expansion and heat loss in one number. At heat loss rates that were about twice the value of what can be expected from a small scale machine, the work output decreased by less than 3 % while the heat loss rate approached one third of the work output rate.

The same conclusions can be drawn from the dynamic analysis. Even in cases with a large amount of heat transfer, the power produced by the expander operation did not change notably. The curves in Figure 3.41 are all very similar, which indicates that

the gas exchange process reduced the impact of heat transfer. The steady state fluid temperatures were influenced less by the heat transfer since new fluid always entered the machine with the same temperature.

Chapter 4

Plate Type Heat Exchangers

This chapter reviews the published literature on plate heat exchangers, which often refers to refrigeration applications. A framework for distributed heat transfer calculations is introduced and is included in a modelling library [199]. A preliminary comparison of different correlations is presented for an organic Rankine cycle (ORC) evaporator connected to a variable heat source. The results suggest that a simplified modelling approach with constant heat transfer coefficients for liquid, two-phase and vapour region can produce results similar to those obtained from correlations. Experimental data is needed to validate the correlations and the last part of this chapter describes the design of a new heat exchanger test facility for small scale power cycles and heat pumps.

4.1 Introduction

Application & Design

Efficient heat transfer devices are needed in many places, not only in ORC plants, and typical designs are based on either shell-and-tube constructions or stacked plate devices. While the first is common in heavy duty applications with high pressures and temperatures or corrosive substances, plate heat exchangers (PHEs) provide a cost-efficient alternative for plants operating at limited pressures and temperatures. Their compact and scalable design and the ease of cleaning makes these devices very popular, especially in the food industry [1]. PHEs are also less prone to fouling due to the unsteady flow conditions that occur due to the internal structure of the devices [31].

The heat transfer in PHEs has been subject to scientific investigations since their invention in the late 19^{th} century. However, the early devices could only be used for low pressure applications, which limited their market penetration and there was only a minor incentive for advanced heat transfer studies. Additionally, the early gasket-type heat exchangers had leakage problems at elevated pressures, which had to avoided at all costs for systems with incompatible or hazardous fluids. Over the last decades, improved manufacturing processes have led to new plate designs that constantly increased efficiency and lowered the costs. Here, the introduction of brazed plate heat exchangers (BPHEs) has been a leap forward in terms of material economy [176]. This

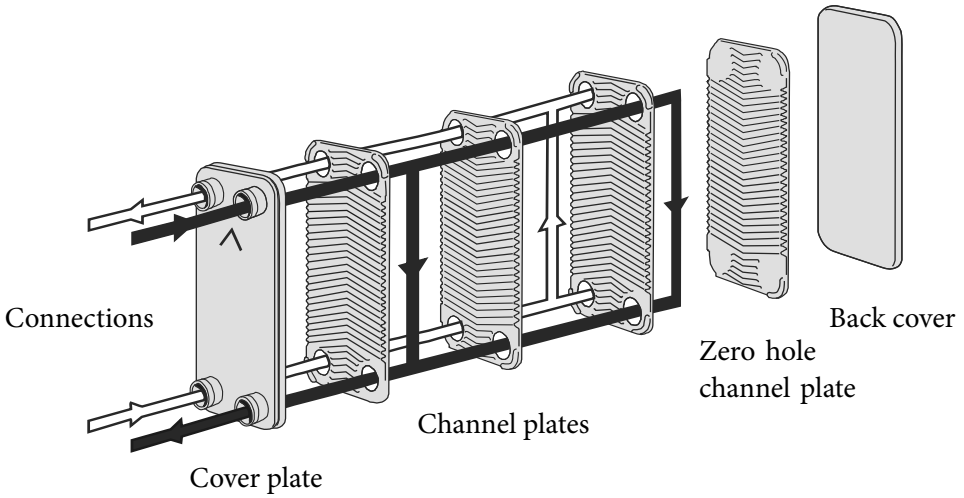

Figure 4.1: Schematic of a BPHE in single-pass counter-flow configuration, adapted from SWEP International AB [223].

new design abolishes the need for tension rods and stiff end plates or frames to keep the components in place. Figure 4.1 sketches the assembly of a BPHE in counter-current configuration. The stacked plates are assembled with opposing patterns forming the characteristic flow channels. The shape of the plates guides the two heat transfer fluids to the right channels and no additional sealing or bolts are needed. The rigid cover plates provide the needed stiffness, but are less bulky than the compression plates required for sealed devices.

New off-the-shelve devices, like the ones discussed in Section 4.3, can handle up to 50 bar and 150 °C at a very low production cost. In his latest review Abu-Khader [1] suggests that gasket type plate heat exchanger models can be used up to 150 °C and 20 bar, while models with lamella plates withstand up to 800 °C and 40 bar.

During the brazing process, the whole device is heated in an oven, which causes the thin copper or nickel sheets between the plates to melt. At sufficiently high temperatures, the viscosity of the molten brazing agent decreases enough to allow capillary forces to displace the material between the rigid steel plates. The molten metal gathers at the joints and connects the plates.

The flow inside the channels of a PHE can be either co-current or counter-current, but also more exotic configurations with multiple inlets are possible. This flexibility assures an efficient heat transfer for processes with very different heat capacity flow rates, which can occur in part-load operation. The simplest possible configuration is

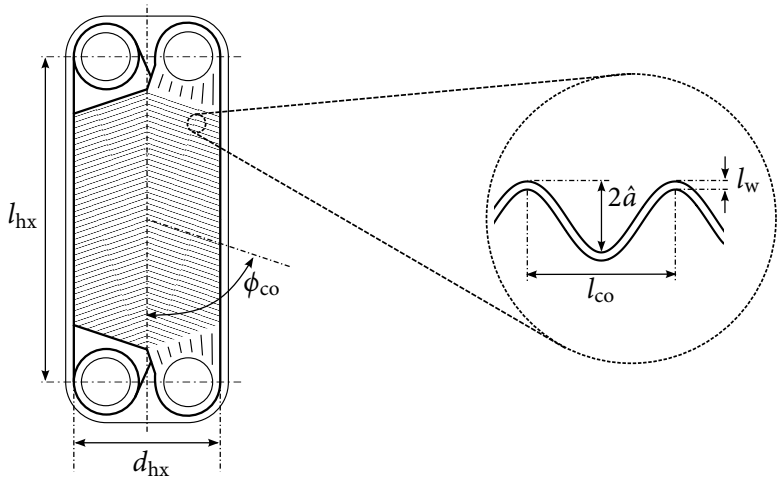

Figure 4.2: Geometry of a chevron-type plate heat exchanger, adapted from Thorade [237] and Martin [159].

shown in Figure 4.1. On the left hand side, the primary fluid, shown in white, and the secondary fluid, black arrows, enter the heat exchanger. In this counter-current design, the primary fluid flows upwards and the secondary side flows downwards. Hence, the shown device is used to heat the primary fluid taking advantage of the change in density that accompanies a temperature change. The outermost channels are typically filled with the secondary fluid, which implies that there is one more secondary channel than primary channels N_f. For the shown single-pass configuration, the number of secondary channels N_{sf} is always half of the number of plates, which in turn has to be an even number. Heat transfer capacity scales linearly with the number of plates and size limitations only occur due to the manufacturing process. The heat exchanger is already assembled before the brazing process starts, which leads to large temperature gradients during the final heating step. This is an obvious conflict with the uniform temperature distribution that is required for a a high-quality brazed joint and thus limits the size of these components.

The channel plates are not flat, but have a characteristic shape to enhance the heat transfer. The most common type is the herringbone or Chevron pattern [31], which has already been shown in Figure 4.1. Such plates are characterised by their geometrical features as illustrated in Figure 4.2. The macroscopic properties are the length and width of the flow path, which are named l_{hx} and d_{hx}. The inclination of the corrugation pattern is denoted with ϕ_{co}. This angle increases from 0° for corrugations parallel to the flow path to 90° for corrugations normal to the main flow direction. Typical

values for ϕ_{co} are in the range of 40° to 75°. The corrugations themselves are wavy and are often described as sinusoidal patterns with an amplitude $\hat{a}$ and a phase of l_{co}. Some publications also refer to the latter also as the pattern wavelength Λ. A flow channel is confined by two similar plates which are mounted in opposite directions. The last figure indicated on Figure 4.2 is the plate thickness l_w. Some other derived dimensionless quantities that are going to be used in Section 4.2 are the wave number

$$X = 2\pi\hat{a}/l_{co} \tag{4.1}$$

and the surface enhancement factor

$$\Phi \approx \left(1 + \sqrt{1 + X^2} + 4\sqrt{1 + X^2/2}\right)/6, \tag{4.2}$$

which approximates the ratio between the real heat transfer area per plate and its rectangular projection given by the term $l_{hx} \cdot d_{hx}$. From the flow arrangement in Figure 4.1, we see that the heat transfer area per plate is defined as the total area A_{hx} divided by twice the number of primary channels.

Depending on which convention is used, the dimensionless numbers that characterise the heat exchanger can be calculated differently. The definitions for the Reynolds number (Re) and the Nusselt number (Nu)

$$\mathrm{Re} = \rho\ \Lambda\ \Gamma/\mu \text{ and } \mathrm{Nu} = \tilde{\alpha}\ \Gamma/\lambda$$

both contain a characteristic length Γ and a characteristic velocity Λ, which do not have mutually agreed definitions, but often are part of heat transfer correlations.

Research Overview

The traditional application for PHEs is liquid-liquid heat transfer [1], for example in district heating stations or the dairy industry. Hence, the majority of scientific publications covers the single-phase case, mostly using water as heat transfer fluid on both sides of the heat exchanger. Among the established correlations for single-phase heat transfer and pressure drop in PHEs, the early works by Focke, Zachariades and Olivier [82], Wang and Vanka [247], Martin [157], and Muley and Manglik [170] have received a lot of scientific attention and are heavily cited. All of these papers present experimental data and correlations that approximate the average heat transfer over the whole length of a single plate in the heat exchanger. Maldistribution is not often included in heat transfer studies even though analytical models for the flow distribution between the different plates have already been introduced by Bassiouny and Martin [23, 24]. The more recent works by Wang [249, 250] unify the aforementioned approach

with other theories and deliver a comprehensive design strategy that focusses on the distribution of the fluid between the stacked channels.

The single-phase heat transfer in PHEs is normally described by semi-empirical equations that resemble the equations for pipe flow heat transfer. Some of them are built around additional correction terms to reproduce the behaviour of PHEs while others only employ modified constants for the same purpose [82]. A comprehensive theoretical approach has been proposed by Martin [157]. Comparing several data sources, Martin [157] reviews different publications and provides corrected and consistent coefficients for the equations initially presented by Heavner, Kumar and Wanniarachchi [99]. Even though Martin [157] links the pressure gradient to the heat and mass transfer within the theoretical framework of Lévêque [147], the actual pressure drop calculation remains semi-empirical.

Ayub [17] reviewed more than twenty single-phase correlations for PHEs and recommend, among others, to use a correlation developed by Muley and Manglik [170] even though it has been developed for water. They argue that the dimensionless numbers included in the correlation are sufficient to apply the correlation to different refrigerants. Also Palm and Claesson [176] mention the same correlation as a good choice for liquid-phase heat transfer. However, both reviews stress that the correlation only includes a limited number of geometric parameters, which might lead to unexpected results for PHEs with special, non-chevron type plates. As an alternative, Palm and Claesson [176] refer to the semi-theoretical approach by Martin [157]. Muley and Manglik [170] use the corrugation angle and the surface enhancement factor to define the geometry, while Martin [157] calculates the enhancement factor based on the patter wavelength, amplitude and corrugation angle. In later publications, Martin [157–159] compares the correlation to experimental data for many different geometries and found that a slightly revised form agrees best with the measurements he had access to [159]. Dović, Palm and Švaić [71] present work on a general correlation for arbitrary geometries. Also here, the same works [157, 170] are used as reference cases, which underlines their importance. Other attempts to generalise the calculation of arbitrary flow configurations, like the ones proposed by Gut and Pinto [96] and Qiao et al. [191], are not considered here since the majority of heat exchangers for small scale systems of of the single-pass type.

Advanced sealing materials and the introduction of the BPHEs eventually solved the existing leakage problems and PHEs entered additional fields of application including the air-conditioning, refrigeration and heat pump sectors [97]. In these fields, the legislative charge restrictions for the established man-made working fluids accelerated the implementation of PHEs due to their low hold-up volume [17]. The increased interest in PHEs also lead to an increasing number of scientific publications that document and analyse heat exchanger performance under operating conditions

that resemble those of evaporators and condensers in heat pumps and refrigeration systems. Despite the popularity of PHEs in the ORC community, literature covering the heat exchanger performance at temperatures and pressures suitable for ORCs is scarce. During the last years, only the theoretical work by Karellas, Schuster and Leontaritis [116] focusses on the performance of PHEs in an ORC, but covers exclusively supercritical systems. However, the similarities in terms of working fluids and system layouts indicate that results obtained from refrigeration studies can be transferred to ORC conditions.

The latest reviews published on the use of PHEs in refrigeration systems by Ayub [17], García-Cascales et al. [84], Khan et al. [122] and Palm and Claesson [176] do not come to a mutual conclusion regarding the performance in the two-phase regime. The comparisons made by García-Cascales et al. [84] for n-propane and R22 illustrate the large differences between the published correlations for evaporation and condensation. One possible cause for this is that most correlations are developed with data of only a few different fluids. Such models tend to disagree with data recorded for other fluids.

Fluid-specific PHE correlations for boiling heat transfer have been developed for the man-made refrigerant R134a [68, 70, 261] and the blend R410A [97, 101, 152]. Within the field of flow boiling of natural refrigerants, NH_3 has been studied as pure fluid [68, 118, 119, 121] and as a binary mixture with water [225, 226] as well as with a lubricant [120]. Furthermore, data has been published on n-propane [84, 151], propene [151] and isobutane [151].

Heat transfer during condensation has been studied less. Besides the general review by García-Cascales et al. [84], there are mostly specific publications for certain fluids. The same fluids as for evaporation dominate the literature with works on R410A [129] and R134a [150, 153, 262]. The last publication by Longo and Zilio [153] also includes data on R1234yf. The comprehensive work of Thonon and Bontemps [233] covers the hydrocarbons n-pentane, n-butane and n-propane as well as mixtures of n-butane and n-propane. Additional data for condensing n-heptane has been published by Würfel and Ostrowski [260].

4.2 Heat Transfer Calculations

Selection of Correlations

Building on the long history of liquid-liquid applications with PHEs, modelling of the single phase heat transfer has been studied well over the last decades. The two correlations by Martin [157] and Muley and Manglik [170] have been recommended and validated by various sources and are thus selected for implementation. However, a lot of thermal energy is transferred during the phase change of the working fluid. Thus

the prediction of boiling and condensation heat transfer rates plays an important role in the design process.

Out of the refrigeration studies mentioned above, more publications deal with the evaporation than with the condensation of working fluid. Also for ORCs, the evaporation of the working fluid is considered more important. Evaporators normally operate further away from ambient conditions, which are typically used as heat sink in both refrigeration and ORC plants. A well-working heat transfer on the evaporator side does not only minimise the entropy production caused by heat transfer, but also leads to higher expander inlet temperatures that directly impact the systems efficiency.

Due to the size constraints in smaller systems, such installations typically employ once-through heat exchangers that cover the phase transition and the adjacent single phase regimes. A comprehensive analysis of the heat transfer process therefore has to combine the liquid region, the phase change process and the vapour domain.

Boiling and evaporation occur when heat is transferred to a liquid triggering an intermediate or permanent phase change. For moderate superheat at the solid-liquid interface, the heat flux increases with increasing wall temperature. This changes at very high heat fluxes and temperature differences, but phenomena like the critical heat flux and the Leidenfrost-point are not discussed here since heat transfer from a liquid heat carrier medium hardly occurs with sufficiently high temperature differences in the boundary layer. Focussing on the technical application in plate heat exchangers with low temperature heat sources, the predominant boiling regime is saturated flow boiling [48]. In this process, vapour is generated at the channel walls and certain flow patterns develop based on the heat flux and the vapour fraction. In addition to the convective heat transfer that also occurs in single-phase systems, nucleate boiling heat transfer describes the amount of thermal energy transferred by means of bubble formation. Vapour formation is assumed to enhance the convective heat transfer, which in turn suppresses the nucleation. Until now, different explanations for the interrelation of these mechanisms exist since the problem is not fully understood.

Even though many publications cover the two-phase heat transfer in PHE, no mutually agreed modelling approach has been presented. Equations of several forms and with a large number of different coefficients have been published and most of them are able to reproduce the data that were used to develop the correlations. However, comparing calculated results from one equation to measurements for another working fluid does not always yield satisfying results [84].

Evaporation in heat exchangers includes a convective part and a nucleate boiling contribution. The interaction of both parts has been characterised by the Thonon boiling criterion [234, 235], which is the product of the Boiling number (Bo) and the Lockhart-Martinelli parameter X. Experiments with R22 and different operating conditions by Thonon et al. [234] suggest that (i) corrugated plate heat exchangers

are dominated by convective boiling and (ii) the importance of the nucleate boiling contribution increases with pressure.

Recalling that the pressure level in ORC evaporators is higher than in refrigeration system, nucleate boiling is expected to contribute significantly to the total heat transfer. This assumptions is also supported by Palm and Claesson [176], who conducted experiments for R134a in heat pump cycles and found that the nucleate boiling correlation by Cooper [53] could reproduce their data if multiplied with a factor of 1.5. Also Longo [151] recommends the same correlation for the hydrocarbons isobutane, n-propane and propene and the results reported in the aforementioned work suggest that the heat transfer is underestimated by more than 20 %. Hence the Cooper [53] correlation is selected for further studies and is implemented with the correction factor 1.5 as proposed by Palm and Claesson [176].

The basic heat transfer mechanisms known from pipe flow can also be applied to PHEs, if the characteristic length Γ and velocity Λ are selected carefully [82]. Depending on the correlation, the equivalent diameter

$$d_\mathrm{e} = 2\hat{a} \tag{4.3}$$

or the hydraulic diameter

$$d_\mathrm{hyd} = 4\hat{a}/\Phi \tag{4.4}$$

are used to calculate Re and the heat transfer coefficient (HTC) from Nu, while the real cross-sectional area has to be used to determine the superficial flow velocity. Since the enhancement factor Φ for real PHEs is most likely between 1.1 and 1.5, d_h is typically 1.3 to 1.8 times larger than d_e.

To illustrate the performance of PHEs, two different sets of unmodified heat transfer correlations for pipes are implement alongside a model using constant heat transfer coefficients for the single-phase and two-phase flow domains. All the implemented correlations are listed in Table 4.3, which provides an overview of the different combinations of correlations and the references used to obtain the equations.

For single-phase flows in pipes, the correlation by Dittus and Boelter [67] is a popular reference case and is part of the established family of Re and Nu correlations. It is thus selected together with the Gnielinski [88] and Gnielinski [90] equations, which are considered a comprehensive modelling approach, which covers the whole flow regime while Dittus and Boelter [67] assume fully turbulent conditions. However, the increased applicability comes at the price of a more involved calculation.

Also the evaporation heat transfer in pipes is evaluated with two approaches of different degrees of complexity. The correlation introduced by Gungor and Winterton [93] and simplified in Gungor and Winterton [94] is formulated by means of an additional factor to be multiplied with a calculated single-phase heat transfer following

Table 4.3: Pairs of implemented plate heat exchanger correlations.

Type	Single-phase (sp)	Two-phase (tp)
All	constant	constant
Pipe	DB: Dittus-Boelter [67] Equation (E.11), $\Gamma = d_e$ G: Gnielinski [90] Equations (E.12) to (E.19), $\Gamma = d_e$	GW: Gungor-Winterton [94] Equations (E.22) to (E.23), $\Gamma = d_e$ S: Shah [209] Equations (E.24) to (E.31), $\Gamma = d_e$
PHE	MM: Muley-Manglik [170] Equations (E.1) and (E.2), $\Gamma = d_h$ MA: Martin [159] Equations (E.3) to (E.10), $\Gamma = d_h$	C: Cooper [52, 53] Equation (E.21), no Γ C: Cooper [52, 53] Equation (E.21), no Γ

the superposition theory of convective and nucleate boiling. The authors used a large database of experimental data points that includes refrigerants and organic fluids to find a single expression for the whole vapour quality range. They also compared other boiling models to the same data set and found that the piecewise-defined correlation by Shah [209] produced the second best results besides their own formulation, which also is chosen for further investigations.

The actual implementation if the correlations from Table 4.3 can be found in Appendix E.1. These equations are afterwards used to model the heat transfer in the distributed model presented in the next section.

Distributed Models

The heat transfer models implemented in this work exploit the framework of the the ThermoCycle Modelica library [199] (ThermoCycle). In this library, the heat exchanger models are built from interconnected cells. These cells are the basic structure for both heat and mass transfer. The way in which the individual cells are connected determines the flow configuration of the heat transfer device. Currently, there are four different configurations available: (i) counter-current, (ii) co-current, (iii) cross-flow, (iv) fixed heat flux and (v) semi-isothermal. The first three configurations are used to model heat transfer between two fluids while the fourth option has been designed to model solar applications in the works of Ireland et al. [109] and Dickes et al. [65]. The fifth option facilitates modelling of heat transfer to and from an isothermal reservoir as it occurs in heat exchangers with unbalanced heat capacity flow rates like dry coolers or air conditioning systems with phase change.

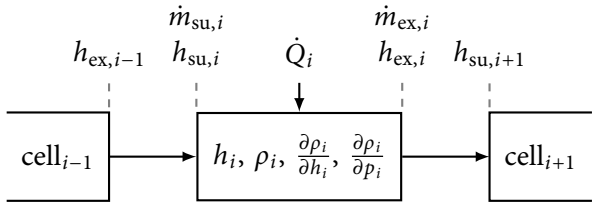

Figure 4.4: Cell structure in the ThermoCycle heat exchangers.

The generic structure of the cell models facilitates the automated connection of control volumes and flow models by linking the mass balance

$$\dot{m}_{ex} - \dot{m}_{su} = V\frac{d\rho}{dt} = V\left(\frac{\partial \rho}{\partial h}\frac{dh}{dt} + \frac{\partial \rho}{\partial p}\frac{dp}{dt}\right) \tag{4.5}$$

and energy balance

$$V\rho\frac{dh}{dt} = \dot{m}_{su}(h_{su} - h) - \dot{m}_{ex}(h_{ex} - h) + \dot{Q} + V\frac{dp}{dt} \tag{4.6}$$

of the different cells through nodes [195]. The current state of the finite volume approach in ThermoCycle only considers ideal homogeneous flows. There is no pressure gradient in flow direction, no inter-cell pressure drop and multi-phase flow is always regarded as ideally mixed [199].

Based on the design flow direction, each cell is connected to an inlet node labelled 'su' and an outlet node labelled 'ex'. In Figure 4.4, the arrows indicate the nominal flow direction and also represent the nodes that determine the enthalpy and mass of the fluid that enters and leaves the control volume. Transfer of thermal energy is considered positive, $\dot{Q} > 0$, when it enters the cell as well.

The bulk state inside the control volume is determined by the state variables h and p. The CoolProp fluid property database version 5.0.8 (CoolProp) library provides the partial derivatives $\partial\rho/\partial h$ and $\partial\rho/\partial p$ to be used in Equation (4.5). Five different calculation schemes are available in ThermoCycle. Two of these schemes are based on the central difference approach, $h = (h_{su} + h_{ex})/2$, and three schemes use the upwind formulation $h = h_{su}$.

The piecewise definition of the node enthalpy for the central difference approach

$$h_{su} = \begin{cases} h_{ex,i-1} & \text{if } \dot{m}_{su,i} \geq 0 \\ h_i & \text{if } \dot{m}_{su,i} < 0 \text{ and } \dot{m}_{ex,i} \geq 0 \\ 2h_i - h_{ex,i} & \text{if } \dot{m}_{su,i} < 0 \text{ and } \dot{m}_{ex,i} < 0 \end{cases} \tag{4.7}$$

allows the models to handle flow reversals. The upwind scheme uses a simplification of Equation (4.7), which eliminates the dependency on $\dot{m}_{\mathrm{ex},i}$. It also disables the last of the three cases presented in Equation (4.7) and can handle zero flow situations efficiently by using an optional smoothing function for the enthalpy at very low fluid flow rates. Thus the five implemented discretisations are: (i) basic central difference, (ii) central difference with flow reversal, (iii) basic upwind, (iv) upwind with flow reversal and (v) upwind with smooth flow reversal.

Scheme (v) is one out of seven different methods that have been implemented and tested by Quoilin et al. [196] to enhance model robustness. The second enthalpy-related method has been proposed by Schulze, Gräber and Tegethoff [206] and uses a limiter function for the enthalpy entering the control volume

$$h_{\mathrm{su}} > h + \rho \left(\partial\rho/\partial h\right)^{-1}, \tag{4.8}$$

which makes sure that the resulting system of equations can be solved.

Switching between different equation sets and other discontinuities can cause chattering, which leads to problems during the integration process an can be responsible for simulation failures [111]. When entering the two-phase regime from saturated liquid, a discontinuity occurs in the density function, which is a well-know but challenging issue in two-phase flow calculations with finite volume models [32].

Therefore, the five remaining methods focus on the fluid density and its derivatives. Here the tight integration with CoolProp opens up for new possibilities to counteract the negative impact of non-continuous fluid properties. CoolProp provides means to use a spline approximation for the density derivatives on the bubble line to avoid such singularities. However, decoupling the density and its derivative introduces an error in the mass balance in Equation (4.5). This is addressed by the second low-level robustness measure, which calculates a smoothed density with matching partial derivatives.

On the cell-level, Bonilla, Yebra and Dormido [33] and Casella [43] promote the use of mean densities, which can be regarded as an extension of the central difference scheme to the fluid density. This established technique is also used in the popular ThermoPower library [44]. The last two methods do not have a physical meaning, but they can be implemented easily. One is to introduce an artificial damping term by applying a first order filter to the calculated density and the second one is a simple truncation of the density derivative. Both methods have to be used with caution and the mass balance should be monitored closely.

The general formulation of the one-dimensional flow equations facilitates an automated discretisation by splitting a given flow path into an arbitrary number of segments. Each cell solves its own mass and energy balance based on the discretisation schemes introduced above. Heat transfer can only occur to and from the wall component that

connect primary and secondary side of the heat exchanger, all other walls are considered adiabatic. Since all cells are generated in a similar fashion, the heat transfer model has to be flexible enough to handle liquid, two-phase and vapour flows and the corresponding heat transfer calculations. Taking advantage of the object-oriented Modelica language, an inheritance tree is presented in Figure 4.5 to visualise the relations of the different heat transfer models that support automated discretisation. Building on the experiences gained by Quoilin [195], the cell heat transfer has been described by three abstract, or partial, objects, which have two different implementations each.

ThermoCycle defines a basic interface called '*PartialHeatTransfer*', which is realised by an 'Ideal' heat transfer component without any thermal resistance and a component with a 'Constant' heat transfer resistance. The base object requires the homogeneous bulk state of the enclosed fluid as input and returns the resulting heat flow rate per wall area. The wall itself is represented by a thermal port that absorbs the calculated heat flux and provides access to the wall temperature data. The next level of detail is reached in the '*PartialHeatTransferZones*' model. This abstract model has to be fed with additional information, namely the nominal mass flow rate $\dot{m}_{\mathrm{nom}}$, the actual mass flow rate $\dot{m}$ and the vapour quality x as well as constant nominal values for the HTC for each of the working fluid phases, $\bar{\alpha}_{\mathrm{l}}$, $\bar{\alpha}_{\mathrm{tp}}$ and $\bar{\alpha}_{\mathrm{g}}$. The two models that implement this interface modify the HTC either based on the mass flow rate

$$\bar{\alpha} = \bar{\alpha}_{\mathrm{nom}} \left(\dot{m}/\dot{m}_{\mathrm{nom}}\right)^{0.8} \tag{4.9}$$

or as a function of the vapour quality

$$\bar{\alpha} = \begin{cases} \bar{\alpha}_{\mathrm{l}} & \text{if } x < -\Delta x/2 \\ \bar{\alpha}_{\mathrm{l}} + \left(\bar{\alpha}_{\mathrm{tp}} - \bar{\alpha}_{\mathrm{l}}\right)\left(1 + \sin\left(x\ \pi/\Delta x\right)\right)/2 & \text{if } x < \Delta x/2 \\ \bar{\alpha}_{\mathrm{tp}} & \text{if } x < 1 - \Delta x/2 \\ \bar{\alpha}_{\mathrm{tp}} + \left(\bar{\alpha}_{v} - \bar{\alpha}_{\mathrm{tp}}\right)\left(1 + \sin\left(\left(x-1\right)\ \pi/\Delta x\right)\right)/2 & \text{if } x < 1 + \Delta x/2 \\ \bar{\alpha}_{\mathrm{g}} & \text{if } x \geq 1 + \Delta x/2 \end{cases} \tag{4.10}$$

with $\Delta x = 0.1$, which differs from the original version [195] that uses $\Delta x = 0.05$.

The most advanced heat transfer interface is the last abstract class shown in Figure 4.5, '*PartialHeatTransferSmoothed*'. Here, the functionality of 'VaporQualityDependance' and 'MassFlowDependence' are already included in the base class. The vapour quality-based smoothing is based on the transition function in Equation (3.12), which is smooth and continuous up to the second derivative. Additionally, the heat transfer coefficients for the different zones do not longer have to be constant, which means that correlations can be used to calculate those values. While 'Smoothed' only implements the interface, 'SmoothedInit' adds additional functionality by preparing

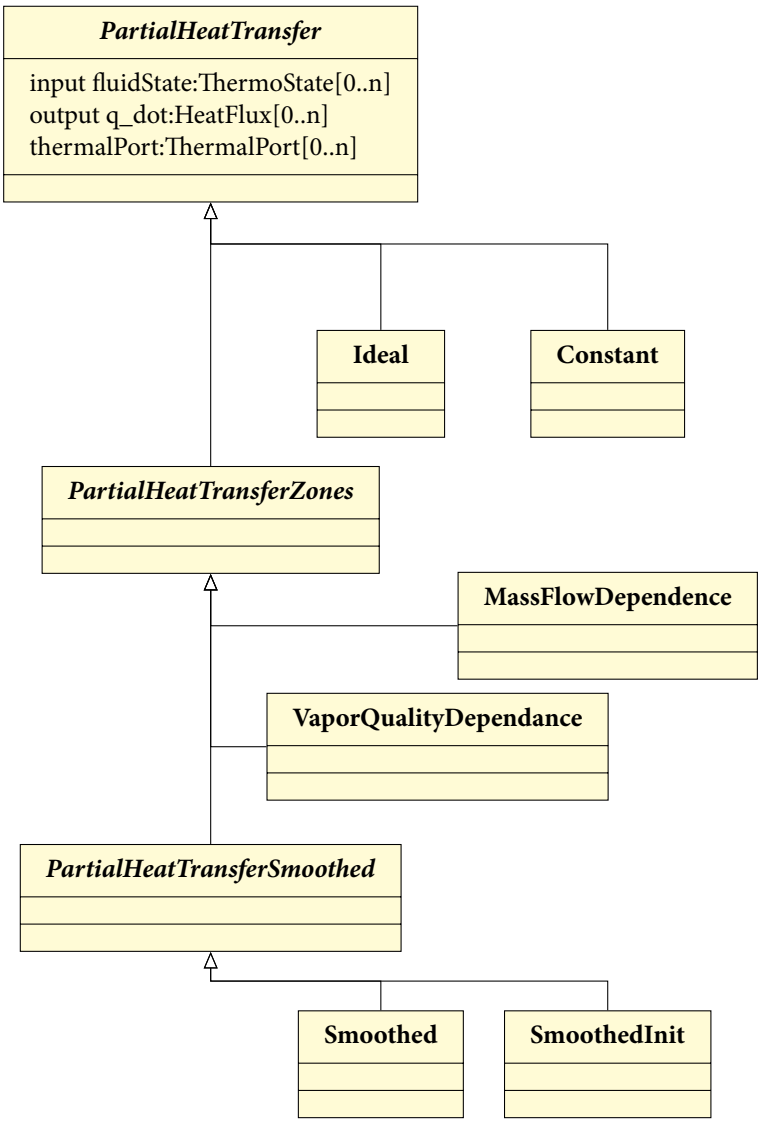

Figure 4.5: Software structure of the heat exchanger cells in ThermoCycle.

fluid states for the different zones that can be passed to heat transfer correlation. Later, more details follow on the specific aspects of the implementation of the correlations. Besides that, model robustness can be enhanced by introducing a first order filter for the HTC and by limiting its slop $d\tilde{\alpha}/dt$ in a similar fashion to what has been done with the enthalpies to stabilise the cell balance equations described at the beginning of this chapter. If the system is known to be in a certain state, complexity can be reduced by forcing a the heat transfer to be calculated for one region only. This also disables the smoothing and is particularly useful for heat transfer media that are known to be in the liquid state at all times, but still require a heat transfer correlation instead of the mass flow-based approach discussed earlier.

To implement heat transfer correlations instead of the constant values used in Figure 4.9, an additional group of objects is required. Using abstract classes to distinguish between single-phase and two-phase correlations allows the centralisation of correlation independent tasks and makes sure that the correlations are used in the correct region. The last element from Figure 4.5, 'SmoothedInit', occurs also in Figure 4.6, which shows the object structure of the implemented HTC correlations.

The heat transfer cell holds three references to heat transfer calculation models. Two of them are limited to single-phase calculations and one is exclusively for two-phase models. All correlation models take mass flow rate and heat flow rate as inputs and provide the HTC as output as shown for '*PartialHeatTransferCorrelation*' in Figure 4.6. In addition to the fluid state, which also is part of the '*PartialSinglePhaseCorrelation*', the '*PartialTwoPhaseCorrelation*' calculates the bubble and dew states of the working fluids since most correlations require such information. A second pair of specialisations of the basic correlation interface is related to the cell geometry, which is either of the pipe-type or part of a plate heat exchanger. The former only requires the hydraulic diameter as parameter, while the latter takes corrugation depth, pattern inclination, corrugation wave length and flow width as parameters. Exploiting the multiple inheritance mechanism of the Modelica language, these four interfaces are enough to implement the correlation matrix from Table 4.3 by creating the nine objects in the bottom of Figure 4.6.

To illustrate the impact of the different smoothing methods and correlations, a fictitious heat transfer process in an R134a evaporator is presented below. The test cell varies the working fluid enthalpy based on the heat of evaporation at a given pressure, which not necessarily is constant. At each time step of the integrator, bubble and dew state enthalpy, h' and h'', are evaluated for the current pressure p. The initial and final

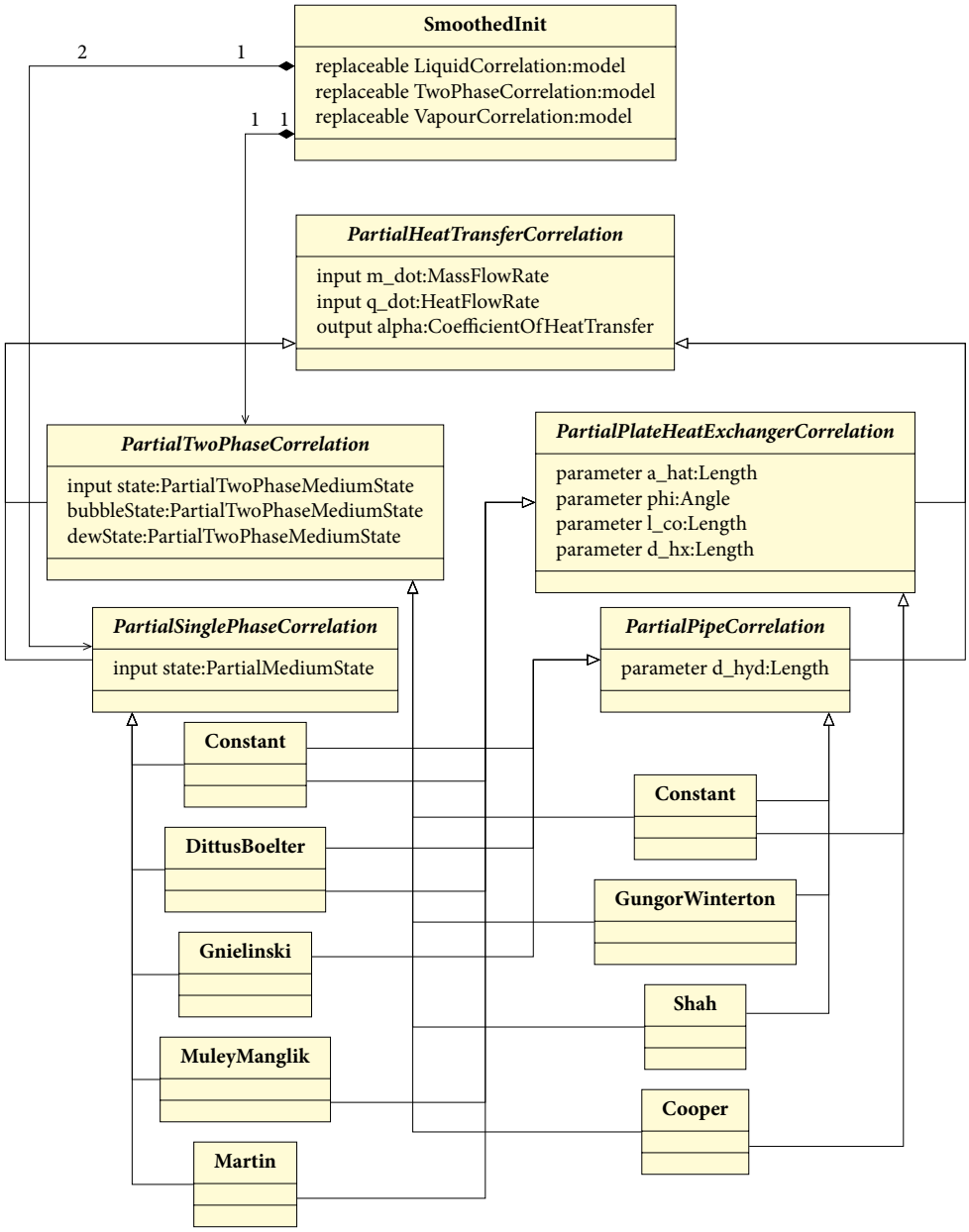

Figure 4.6: Software structure of the heat exchanger correlations in ThermoCycle.

enthalpy for the two-phase sweep are defined by a margin around the two-phase dome Δx, which can be summarised by

$$h_0 = h' - \Delta x \left(h'' - h'\right) \text{ and} \tag{4.11}$$

$$h_1 = h'' + \Delta x \left(h'' - h'\right). \tag{4.12}$$

The heat source temperatures are calculated based on the assumption of a linear temperature profile with a defined pinch point temperature difference ΔT at the bubble line and at the end of the superheated region, which implies that studied process has to be an evaporation. The minimum and maximum temperatures of the secondary fluid can be computed by

$$T_0 = T' - \Delta T - \frac{\Delta x}{\Delta x + 1} \left(T_1 - \Delta T - T''\right) \text{ and} \tag{4.13}$$

$$T_1 = T\left(p_1, h_1\right). \tag{4.14}$$

Afterwards, the variables $\dot{m}$, p and h can be varied linearly using the same scaling variable running from 0 to 1. For the examples given below, R134a evaporates at a constant pressure of 6.75 bar and with a constant mass flow rate. The temperature profiles calculated from Equations (4.11) to (4.14) for the working fluid and the secondary fluid are shown in Figure 4.7.

In addition to these basic tests, a full dynamic simulation of a real small scale plate heat exchangers is performed. The dynamic data used for this analysis is based on the vehicle exhaust gas measurements that are published as part of ThermoCycle. The data set comprises 30 min of temperature and mass flow rate figures from a heat recovery system connected to a combustion engine in dynamic operation.

The example is based on the heat exchanger 'B8Tx10' by SWEP International AB, Landskrona, Sweden (SWEP). To roughly match the design conditions provided by the supplier, the mass flow rate function and the temperature profile are scaled and shifted to swing around the heat exchanger design operating point. The resulting profile in Figure 4.8 covers a temperature range between 150 °C and 170 °C and a mass flow rate that varies between 50 g/s and 150 g/s. The design specifications of the simulated heat exchanger were fixed to an inlet temperature of 160 °C and an outlet temperature of 140 °C for a mass flow rate of 87 g/s of the secondary fluid, an oil-based heat transfer fluid by Chevron [229] (Texatherm 22). The primary side of the heat exchanger has been dimensioned to operate as an evaporator for isobutane at a constant mass flow rate of 19.3 g/s. The selected evaporation temperature of 115 °C defines the pressure as 26 bar. During the simulation, the counter flow heat exchanger operates with the design mass flow rate and pressure for the saturated liquid on the primary side. The

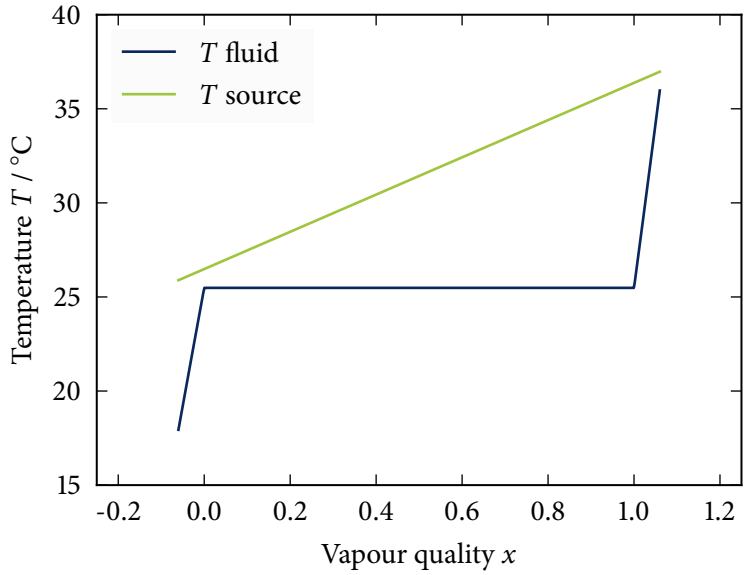

Figure 4.7: Vapour quality and temperatures in the R134a evaporator example.

inlet conditions on the secondary side are varied according to the profile shown in Figure 4.8 and the pressure is kept constant at a value of 10 bar.

The heat exchanger geometry is not fully specified in the product data sheet, which only provides the flow length $l_{\mathrm{hx}} = 27.8$ cm, the flow width $d_{\mathrm{hx}} = 7.6$ cm, and the weight of 1.56 kg. The other plate specifications have been measured manually. The estimated values are the corrugation angle $\phi_{\mathrm{co}} = 65°$, the corrugation depth $\hat{a} = 1.0$ mm and the corrugation wavelength $l_{\mathrm{co}} = 7.5$ mm. The plate material is assumed to be standard stainless steel with a specific heat capacity of 500 J/(kg K). The total hold-up volume on the primary side and the secondary side are 0.156 l and 0.195 l. These numbers illustrate the symmetrical design of the plate heat exchanger since both sides have the same hold-up volume per channel of 0.039 l for this device with four primary flow passages and five secondary channels.

The total flow entering the heat exchanger is divided by the number of channels neglecting all distributional effects and the pressure drop in the manifolds. Assuming an adiabatic system, heat transfer is calculated for one plate only using a series of two thermal resistances. Transferring heat from the bulk of the secondary fluid to the primary fluid only involves the convectional resistances calculated as the reciprocal values of the HTC. The conductive resistance occurring inside the plate itself is neg-

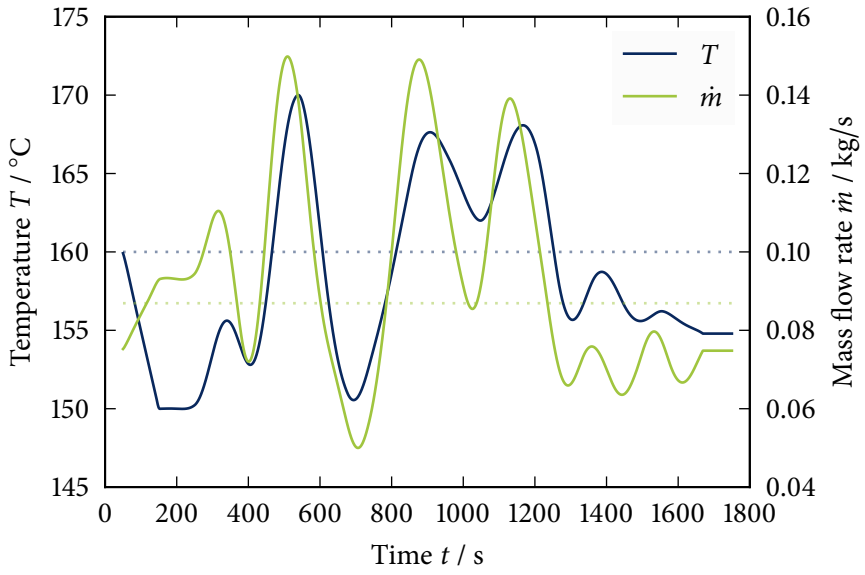

Figure 4.8: Heat source temperature and mass flow rate for the dynamic modelling study. Dotted lines show the design point values.

lected as is the heat transfer in the wall in flow direction. Together with the adiabatic assumption, the above simplifies the heat exchange process to a one-dimensional (1D) heat transfer problem with a capacitive term that accounts for the thermal capacity of the wall. The results presented below have been obtained from a calculation based on eighteen cells in flow direction. Mean values are calculated based on the amount of heat transferred, not based on the area

$$\bar{\alpha}_{\text{mean}} = \frac{\sum_{i=0}^{17} \dot{Q}_i \, \bar{\alpha}_i}{\dot{Q}_{hx}}. \tag{4.15}$$

Modelling Results

Implementing '*PartialHeatTransferSmoothed*' with constant HTC models for the different zones shows the effect of the robustness measures mentioned above, as can be seen in Figure 4.9. A symmetrical smoothing of the HTC at the transition from liquid to two-phase to vapour is shown with the darkest solid line. The next solid line in a medium-dark colour shows the effect of an applied first order filter. The test run was set to take 10 s in total and a filter constant of 0.5 s was chosen. The lightest solid line shows

the evolution of the HTC with an applied derivative limiter of $|d\bar{\alpha}/dt| \leq 5\,\mathrm{kW/(m^2\,K\,s)}$. For the present figures, the limiter has a reduced impact and the first and the last line are close to each other. The most obvious differences between these curves occur on the right hand side of Figure 4.9 at a vapour quality around unity. In that region, the smoothed HTC decreases faster than the limited one, which continues to drop at the maximum rate until both lines meet again at the end of the figure. The second graph experiences delays compared to the first one. The smoothed and the limited HTC reach the constant nominal values for the two-phase region, which is drawn with a dotted line, at a vapour quality of 0.1 while the filtered one approaches it later at around $x = 0.3$. The nominal values applied in this calculation are $1.5\,\mathrm{kW/(m^2\,K)}$ for the liquid region, $6\,\mathrm{kW/(m^2\,K)}$ in the two-phase domain and $1\,\mathrm{kW/(m^2\,K)}$ in the vapour phase. The smoothing range used here is larger than the range for the plotted, which keeps all three graphs from reaching the nominal values on the left for pure liquid and for pure vapour on the right. The plotting stops at $x = 1.075$ and also here the delay caused by the filter causes the largest difference between the normally smoothed function and the modified one in Figure 4.9.

From a physical point of view, it could make sense to shift the smoothing range forward in terms of vapour quality. Subcooled boiling starts at bulk temperatures lower than the boiling point due to temperature differences between the bulk fluid and the boundary layer at the wall. A similar effect could also occur at the end of the evaporation. Here, dry-out occurs and the incomplete coverage of the wall leads to a decrease in heat transfer coefficient. However, the current implementation only uses symmetrical smoothing to avoid a dependency on the direction of heat transfer since the same phenomena would require a shift towards higher vapour qualities when calculating condensation heat transfer.

Using the same geometrical parameters as for the advanced simulations ($\hat{a} = 1.0\,\mathrm{mm}$, $\phi_{\mathrm{co}} = 65°$, $l_{\mathrm{co}} = 7.5\,\mathrm{mm}$ and $d_{\mathrm{hx}} = 76\,\mathrm{mm}$) makes it possible to draw a graph for the PHE correlations that matches Figure 4.9. The characteristic length for the pipe correlations is set to the equivalent diameter $d_{\mathrm{e}} = 2\hat{a}$ while the same cross-sectional area is used to calculate the flow velocities in the PHE and pipe models. The results shown in Figure 4.10 have been obtained for a fixed mass flow rate of 5 g/s.

Heat transfer coefficients calculated from the four combinations of correlation introduced in Table 4.3 are shown as functions of the vapour fraction. The keys in the legend refer to the correlation used for for liquid, two-phase and gaseous region (l-tp-g). The transition from one correlation to another takes place in the ranges from −0.1 to 0.1 and from 0.9 to 1.1. The region between 0.1 and 0.9 shows the unmodified value of the two-phase correlation. The pipe correlations by Gungor and Winterton [94] and by Shah [209] yield similar values for the chosen process with maximum heat transfer coefficients of approximately $2\,\mathrm{kW/(m^2\,K)}$. Both approaches result in a HTC

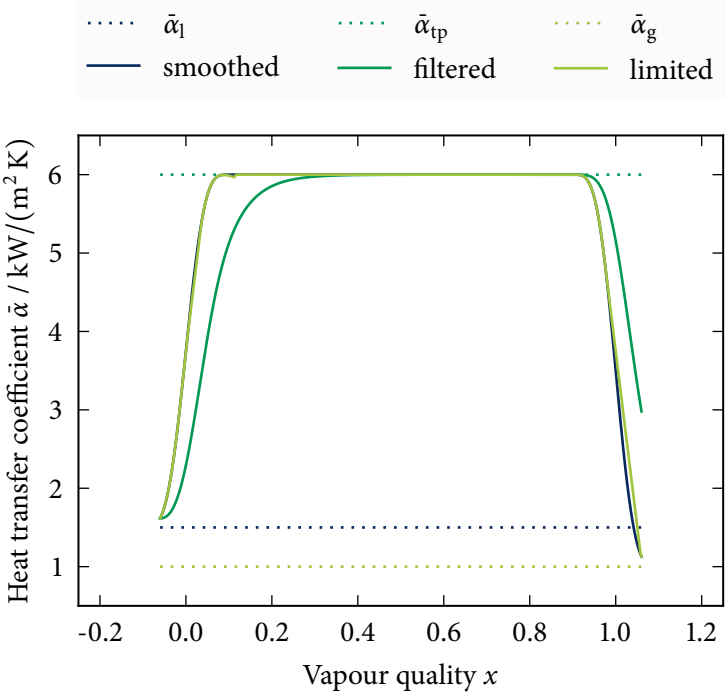

Figure 4.9: Vapour quality and three different smoothed heat transfer coefficients from a simple test cell. Nominal values are indicated with dotted lines.

that is more than one order of magnitude lower than the values calculated for plate heat exchangers, which peak close to 50 kW/(m² K). Nucleate boiling correlations, like the two-phase heat transfer model by Cooper [52, 53] (C), are linked with the heat flux and the increasing HTC values at higher vapour qualities can be attributed to the larger temperature differences occurring in that region. The interrelation between heat transfer coefficient, temperature difference and heat flow rate makes the HTC rise at a rate higher than the linearly growing temperature difference during evaporation in Figure 4.7.

A second set of data is calculated for an extended temperature range to show the behaviour of the single-phase correlations. Providing a Δx of 0.55 to the Equations (4.11) to (4.14) results in a heat source temperature range from −50 °C to 125 °C. This linear profile is used as the abscissa in Figure 4.11, which shows the single-phase HTC and omits the much higher values during evaporation. The pipe correlations by Dittus and Boelter [67] and by Gnielinski [90] result in $\bar{\alpha}$-values between 50 W/(m² K)

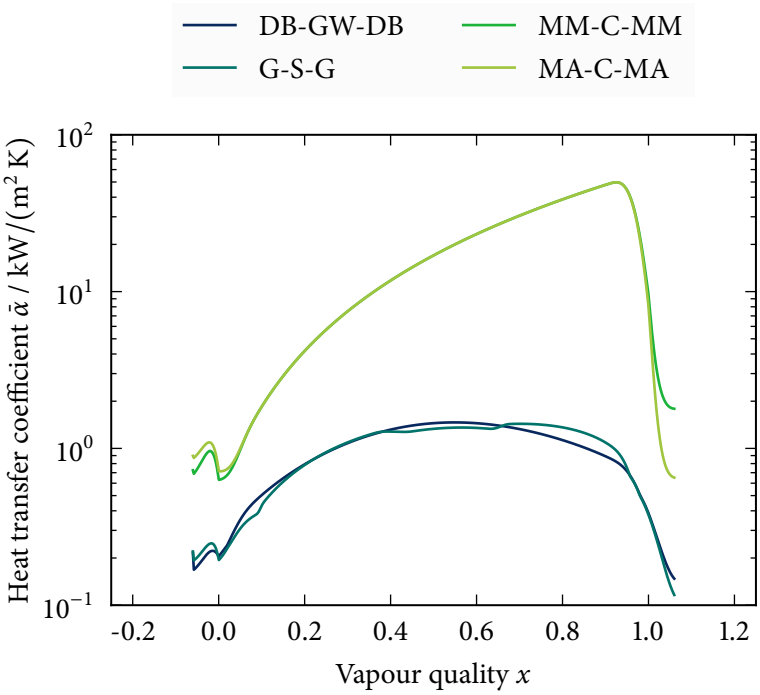

Figure 4.10: Vapour quality and smoothed heat transfer correlations for a pipe case and a simple plate heat exchanger geometry for R134a.

to 300 W/(m² K). In this range, the single-phase heat transfer model by Dittus and Boelter [67] (DB) increases monotonically in the liquid and the gaseous region while the single-phase heat transfer model by Gnielinski [90] (G) decreases in the liquid region as it approaches the bubble line. For plate heat exchangers, the single-phase heat transfer model by Martin [159] (MA) predicts an approximate heat transfer coefficient of 0.7 kW/(m² K) for the full liquid and gaseous phase. The other PHE correlation, the single-phase heat transfer model by Muley and Manglik [170] (MM), increases from 0.6 kW/(m² K) to 2.6 kW/(m² K) in the liquid region. This particular behaviour can be observed because the variation in temperature at a constant flow rate yields a Re range that coincides with the transition from laminar to turbulent flow for this particular correlation as described in Appendix E.1. The gaseous region is turbulent at all times and the the increase of the HTC with increasing temperature is less pronounced.

Using the same correlations as in Figure 4.10 and Figure 4.11, the dynamic cell model has been used to calculate the heat transfer in the example device using the

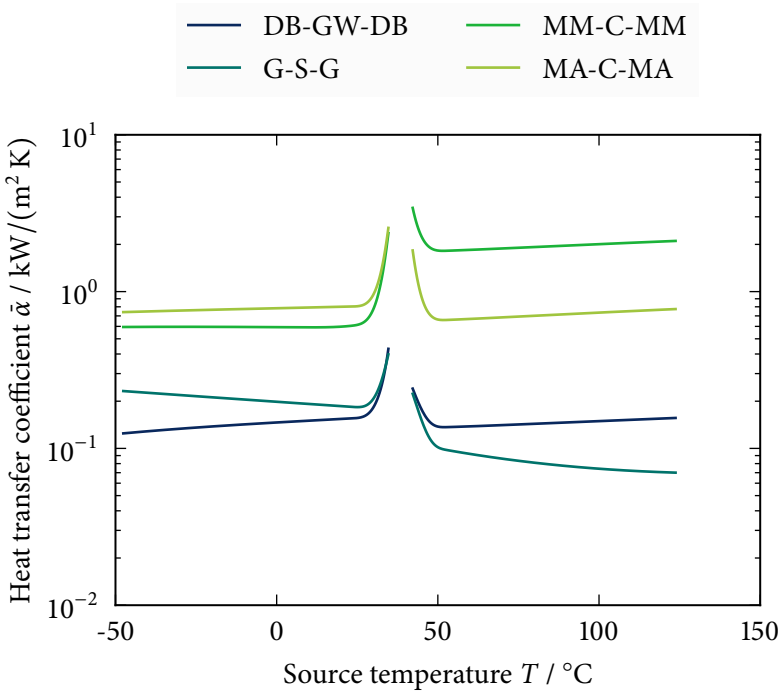

Figure 4.11: Heat source temperature and smoothed heat transfer coefficients for the extended single-phase region of the R134a test case.

dynamic data from Figure 4.8. The twelve lines presented in Figure 4.12 show the mean heat transfer coefficient on the primary side $\bar{\alpha}_f$ and on the secondary side $\bar{\alpha}_{sf}$. The value for the total heat transfer process $\bar{\alpha}_{hx}$ is calculated as the reciprocal value of the sum of the heat transfer resistances.

Recalling that the working fluid inlet is saturated liquid and that the system has been designed as evaporator, it is no surprise to see that the mean heat transfer coefficient on the working fluid side $\bar{\alpha}_f$, which is shown as a solid line in Figure 4.12, is close to the value calculated for $x = 0.5$ in Figure 4.10. Most cells are in the two-phase domain and the boiling heat transfer thus dominates the total mean value for all eighteen cells. The evaporation heat transfer correlations for pipes predict a value between 2.5 kW/(m² K) and 5 kW/(m² K), which is lower than the 20 kW/(m² K) to 30 kW/(m² K) calculated for plate heat exchangers. The amplitude of the changes in HTC during the modelled period is also larger for the PHE equations. The two-phase heat transfer model by

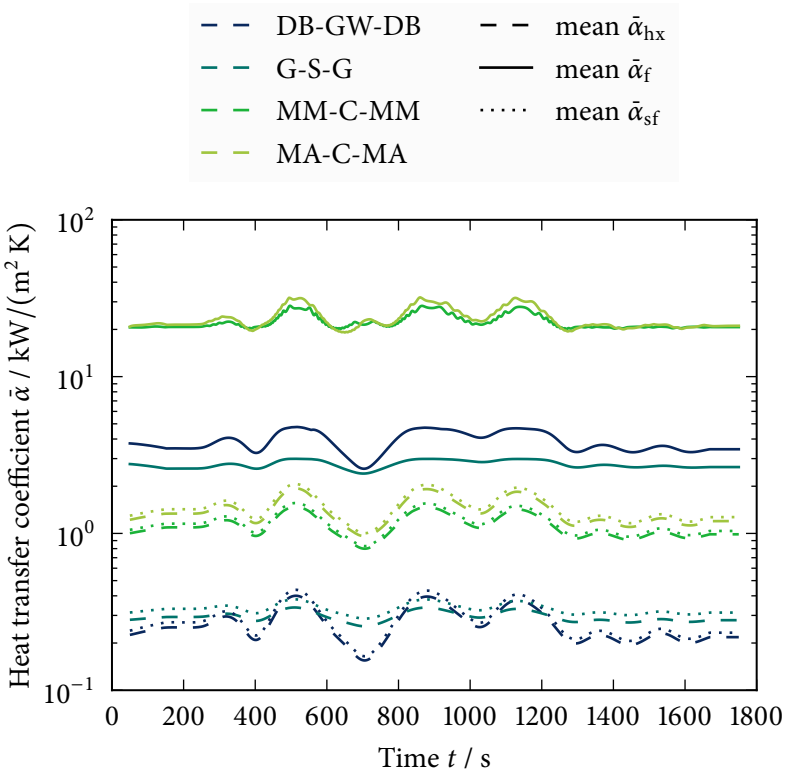

Figure 4.12: Mean heat transfer coefficients for the whole example heat exchanger, the working fluid side with isobutane and the secondary side with Texatherm 22.

Gungor and Winterton [94] (GW) exhibits minor changes in $\bar{\alpha}$ while the two-phase heat transfer model by Shah [209] (S) stays close to 3 kW/(m² K) at all times.

The difference between the two boiling models based on Cooper [52, 53] are attributed to two effects. The solid line in the lightest colour shows the value calculated with the derivative limiter introduced above, which reduces the oscillations that occur at the periods with high mass flow rates and temperatures around 500 s, 900 s and 1200 s. At the same time, the heat flux dependency in the nucleate boiling term amplifies the influence of the HTC on the secondary side on $\bar{\alpha}_{f}$.

The dotted line in Figure 4.12 refers to the secondary fluid heat transfer coefficient. Here, the mean value is calculated exclusively from the liquid correlation since the heat transfer medium is far from its boiling point. The pipe models by Dittus and

Boelter [67] and by Gnielinski [90], DB and G, result in HTCs from 0.15 kW/(m^2 K) to 0.5 kW/(m^2 K) while the graphs for the PHE formulations, MM and MA, cover the range between 0.75 kW/(m^2 K) and 2 kW/(m^2 K). The general shape of the graphs is similar for all functions. However, DB and MM are more sensitive to the temperature and mass flow rate variations than G and MA.

The dashed line shows the combined heat transfer coefficient for the whole heat exchanger calculated with the four different correlation pairs. Having the primary heat transfer resistance on the liquid side, the overall HTCs are close to the values for the secondary side and follows their evolution closely.

The heat transfer rate that results from the calculated HTCs is shown in Figure 4.13 and Figure 4.14. Both figures show the basic 'SmoothedInit' implementation with constant values for the different zones as already presented in Figure 4.9. In addition to the smoothing described above, also the mass flow correction from Equation (4.9) is applied, which explains why the heat transfer rate from the 'smoothed' model also exhibits a dependency on the mass flow rate on the secondary side. The dotted line on Figure 4.13 and Figure 4.14 indicates the design heat transfer rate of 4.1 kW for the isobutane evaporator.

The reduced heat transfer coefficients for the pipe models in Figure 4.12 also lead to lower heat transfer rates. The pipe correlations in Figure 4.13 predict a heat transfer rate lower than the 'smoothed' model, while the PHE equations in Figure 4.14 result in higher values. The approach with constant HTCs reaches or exceeds the design heat flow rate three times during the simulated period. The models based on MM, C and MA on the other hand estimate a heat transfer rate above the design value for most of the time range.

The general impression of the change of the HTCs with time is similar for all five cases. Modifying the heat transfer coefficients based on the fixed reference values and a smooth transition function captured many of the dynamic features that occurred for the calculations based on the full correlations. However, only the heat transfer rates obtained from the 'smoothed' and the second pipe approach link the drop in mass flow rate on the secondary side at 1050 s to a prominent decrease in HTC. The other correlation pairs, especially the ones for the PHE, exhibit a damped response to this change.

Figures 4.13 and 4.14 only cover the heat release from the secondary side, which is different from the heat received by the primary fluid. A general change in temperatures also requires the temperature of the heat exchanger walls to rise or fall introducing a capacitive damping in the heat transfer subject to a varying temperature level. According to Figure 4.15, the average wall temperature of the discretised PHE lies between 117 °C and 125 °C for the tested heat source profile. The two darker curves show the total heat release from the secondary side $\dot{Q}_{sf}$, the total heat uptake of the primary side $\dot{Q}_{f}$

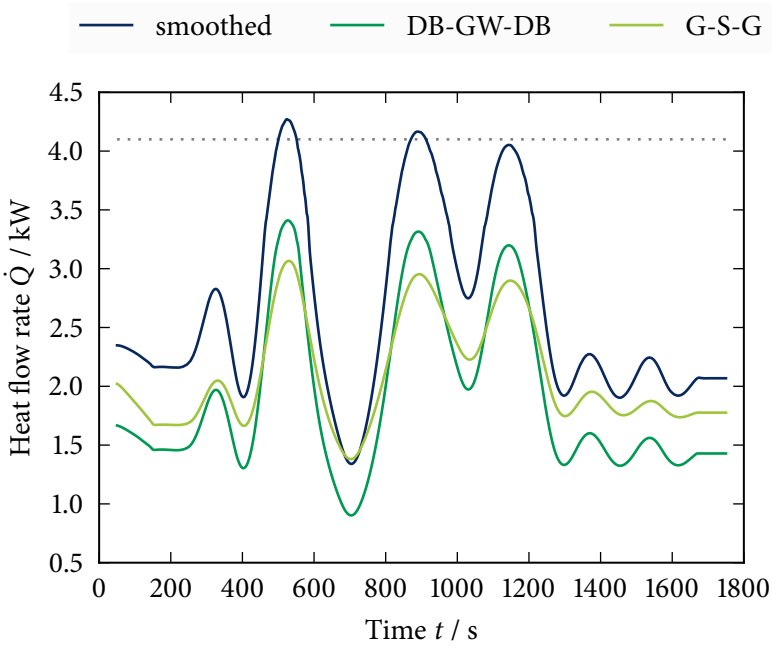

Figure 4.13: Heat release from the secondary side of the heat exchanger using smoothed constant heat transfer coefficients and the two sets of pipe correlations, the design capacity is shown with a dotted line.

and the wall average temperature T_w is presented in a lighter colour. The latter is the direct result of the differences between the heat flow rates since the heat exchanger is considered adiabatic and there are no other heat flows that contribute to the energy balance. However, the limited amount of metal in the brazed plate heat exchanger does have limited total heat capacity, which reduces the impact of the of the mass of the wall on the overall heat exchange. Scaling the abscissa to show the full series of calculated data makes the two darker line graphs in Figure 4.15 follow each other closely and the peaks and nadirs of the heat flow rate occur not more than 10 s to 50 s before the corresponding feature of the lighter wall temperature graph.

The average $\tilde{\alpha}$ values calculated from the different correlation pairs for the whole device in Figure 4.12 do not vary several orders of magnitude because most of the primary side remains in two-phase conditions and the secondary side is liquid-only at all times. Looking at the first and the last cell in working fluid flow direction from the eighteen-cell discretisation, larger changes in HTC occur. The differences between the

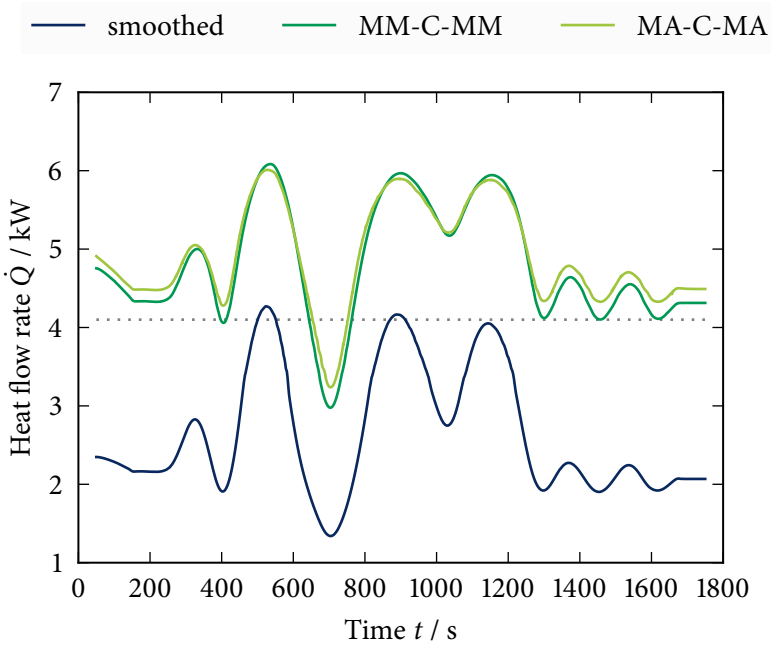

Figure 4.14: Heat release from the secondary side of the heat exchanger using smoothed constant heat transfer coefficients and the two sets of plate heat exchanger correlations, the design capacity is shown with a dotted line.

single-phase and the two-phase correlations that are bridged by the vapour fraction-based interpolation become obvious in Figure 4.16 even though the heat transfer coefficients in the first cell and the last cell stay in the proximity of 3 kW/(m^2 K) for a long period. Around 500 s, 900 s and 1100 s, the HTC drops to values close to 0.5 kW/(m^2 K) because there is only gaseous fluid present in the last cell. At other times, the low heat transfer predicted by the first set of pipe correlations, DB-GW-DB, causes an incomplete evaporation keeping the HTC on a high level since all cells are filled with boiling liquid.

The generally higher HTCs predicted by the MA-C-MA equations yield a superheated flow of working fluid out of the evaporator for the whole simulated period except for the time around 700 s where the outlet approaches the dew point resulting in a peak of the HTC in the last working fluid cell in Figure 4.17 above the otherwise constant value of 2.5 kW/(m^2 K). Due to the saturated liquid at the inlet, the first cell

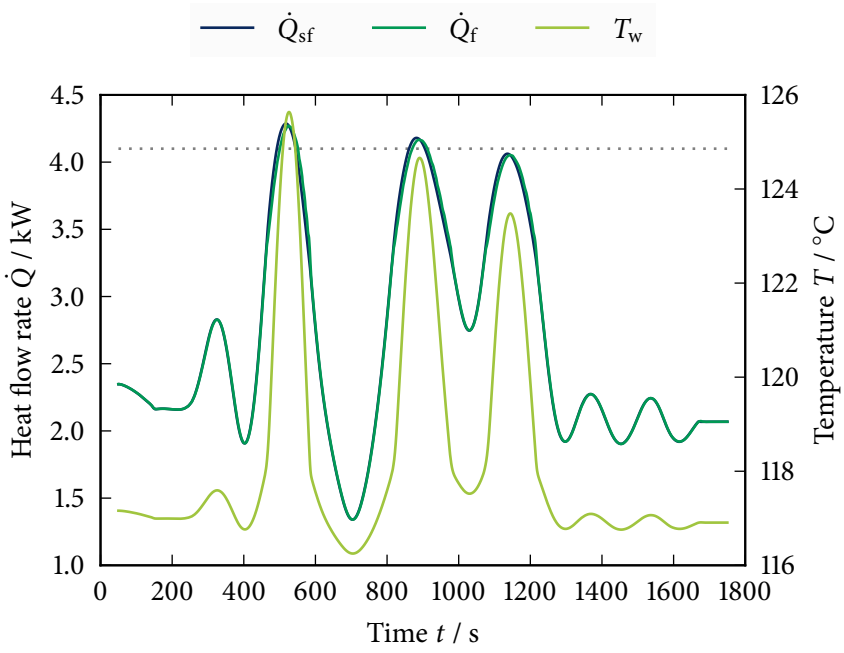

Figure 4.15: Heat flow rates from the secondary side to the wall and from the wall to the primary side together with the wall temperatures as calculated from the 'smoothed' model.

remains in two-phase conditions during the simulated period with HTCs that mostly exceed 10 kW/(m^2 K).

The HTC in the first working fluid cell follows the changes on the development on the secondary side in Figure 4.16 and Figure 4.17. The correlations by Gungor and Winterton [94] and Cooper [52] both depend on the heat flux, which is connected to the total heat transfer resistance. This quantity is in turn influenced by the low HTCs on the secondary side.

The included robustness measures have not been tested thoroughly and the benefits associated with them cannot be quantified at this stage. It is nevertheless expected to be beneficial to include a term that counteracts the abrupt changes in HTC that can occur. Especially implicit correlations that include the heat flux in the determination of the convective heat transfer rate can oscillate like the upper two graphs for the correlation by Cooper [52] in Figure 4.12.

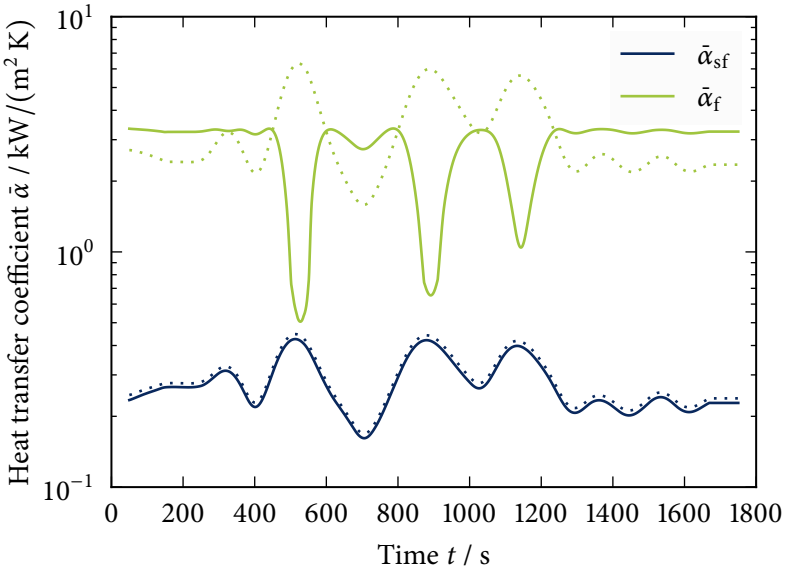

Figure 4.16: Heat transfer coefficients for the secondary and the primary side of the heat exchanger in the cells at the working fluid inlet and outlet shown with dotted and solid lines, respectively. The values are calculated from the DB-GW-DB correlation ensemble.

Other aspects that have not been studied in detail are thermal diffusion and pressure drop caused by fluid acceleration, gravity or friction. The cell models developed in this work are tailored for heat exchanger simulations and diffusion has been neglected because the mass fluxes that typically occur in pipes and PHEs suppress the impact of internal thermal conduction in the fluid. In addition to that, the modelled convective heat transfer rates are several orders of magnitude higher than the possible contribution from a diffusional term. While diffusion can have a stabilising effect on the mass and energy balance [36, 112], pressure drop can destabilise the system of equations, especially in the vicinity of the bubble line where a decrease in pressure may cause spontaneous flash evaporation of the working fluid. The small pressure drop that occurs in PHEs under normal operating conditions can justify the simplification of lumping the pressure drop for the whole heat exchanger in an artificial downstream flow resistance [195]. However, for pipe-based heat exchangers, Kærn [114] discusses several correlations showing impact of frictional pressure drop on the distribution of refrigerant in an air-conditioning evaporator.

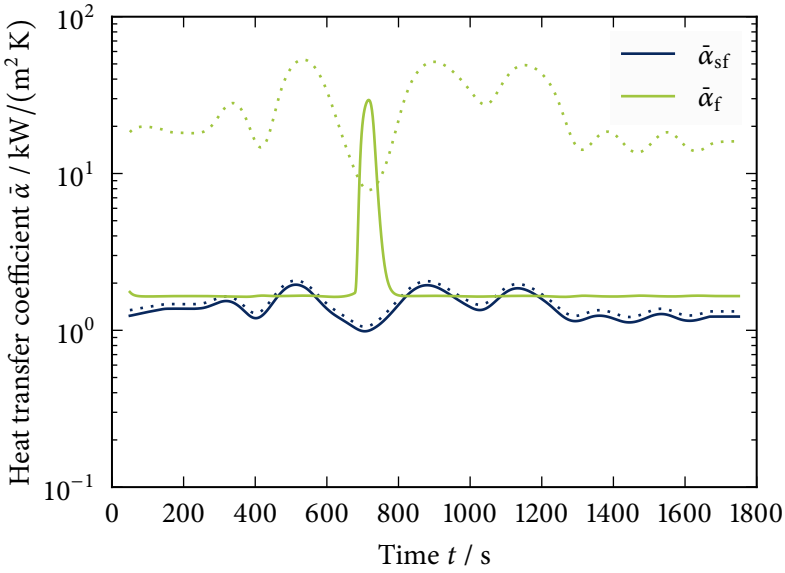

Figure 4.17: Heat transfer coefficients for the secondary and the primary side of the heat exchanger in the cells at the working fluid inlet and outlet shown with dotted and solid lines, respectively. The values are calculated from the MA-C-MA correlation ensemble.

4.3 Heat Transfer Experiments

Dedicated Heat Exchanger Test Rig

Due to the need of experimental validation of the heat transfer models, the expander test facilities described in Section 3.2 were modified to record data on PHEs. The expander was removed from the test bench and two small plate heat exchangers were installed together with a mass flow meter and additional temperature and pressure sensors. The old system has been designed to handle flammable fluids and the formerly used working fluid n-pentane was also used for the heat transfer measurements. After initial tests with the modified installation, it was concluded that the present installation could not be used for accurate heat transfer measurements. Constructing a Wilson-plot and a modified Wilson-plot as described above produced data points that did not correlate well with the tested equations, see also Table F.4. The unbalanced heat transfer that is documented in detail in Appendix F.2, especially in Figure F.5, did not allow for a calibration of the secondary side heat transfer characteristics. Since recording

experimental data was considered an important part of the work on small scale plate heat exchangers, it was decided to abandon the old installation. The rest of this section thus covers the design and of a new dedicated heat exchanger test rig.

To serve multiple purposes, the new heat transfer test installation was designed to simulate both ORC-like operation and conditions occurring on the high pressure side of a high temperature heat pump. These devices are also subject to an increasing number of scientific studies and can operate with the same working fluids, which is why one installation should be able to handle both operating schemes. R134a, isobutane, R407c and R1234yf were identified as relevant working fluids for both cases and were selected as reference media for the design of the new plant.

The new system was built to study heat transfer, which made large temperature differences and pinch points desirable to simplify the validation and design of correlations. In many installations, the heat transfer equipment is oversized, which leads to a very small temperature differences and thereby amplifies measurement uncertainty effects. Bearing the above in mind, the heat exchange capacity of the rig was designed to be much lower than the capacity of the heat and cold supply facilities. At the same time, many small and long plates should be preferred over a few very wide ones since correlations often neglect the influence of the outer plates and the more plates there are, the better is this assumption.

To assure a sufficient heat supply capacity, the design mass flow rate was limited to 50 kg/s. At similar mass flow rates, the heat of evaporation for isobutane is almost twice that of the other fluids. A low heat of evaporation might lead to flashing effects in the inlet manifold, which effectively disturbs the flow distribution. Comparing the thermal requirements for subcritical isobutane and supercritical R407c, the total capacities of the evaporator and condenser sections are expected to be around 10.5 kW each. Dimensioning the rig for maximum pressure operation means that the design calculations involve transcritical operation for all fluids. However, most of the operating is expected to be used at subcritical conditions, which is also used to describe the process in the next paragraph.

Figure 4.18 gives a visual impression of the process in terms of temperature T and entropy s, the numbers mentioned in the text below correspond to the different state points highlighted in Figure 4.18. The actual design and the installed equipment is shown in Figure 4.19. In both figures, the process starts on the left hand side and the working fluid moves clockwise through the different components as described below. Liquid working fluid leaves the receiver in ⓪ and gets pressurised by the working fluid pump reaching state ①. The first heat exchanger delivers a part of the required heat elevating the fluid temperature to saturation conditions at high pressure in state point ②. Afterwards, the evaporator provides the thermal energy needed to produce vapour in state ③. The exit of the evaporator is indicated by point ④ and the

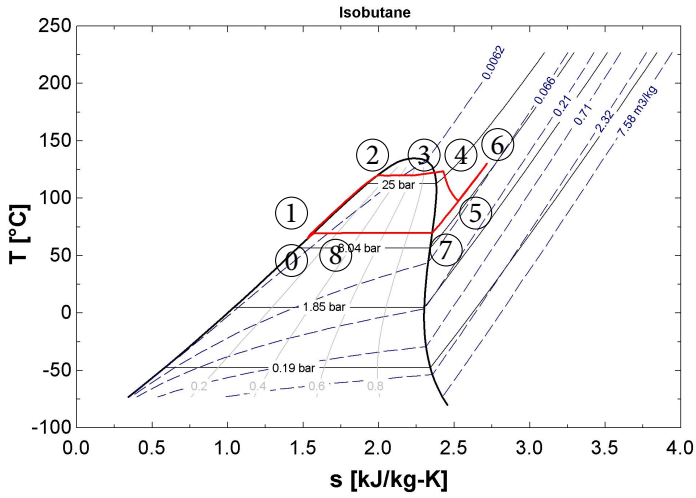

Figure 4.18: Temperature-entropy diagram of the targeted process with subcritical isobutane.

working fluid passes the expansion valve with very little superheat reaching state ⑤. An additional heat supply assures sufficient superheat in state ⑥ to simulate heat pump operation and with a desuperheater, from ⑥ to ⑦, and a condenser being operated with cooling water like the thermal load for a heat pump system covering the transition from state ⑦ to ⑧ and back to ⓪. The cycle is closed when the working fluid enters the receiver vessel in liquid state. The four main heat exchangers are equipped with pressure difference sensors to record the flow resistance under varying conditions. Since the system only has a limited working fluid charge, accumulation is neglected and only a single mass flow measurement is considered sufficient. To calculate the amount of transferred heat all inlet and outlet temperatures of the heat exchangers are measured. With water and thermal oil being almost incompressible, simple volume flow sensors can provide the last piece of data needed for a heat balance evaluation.

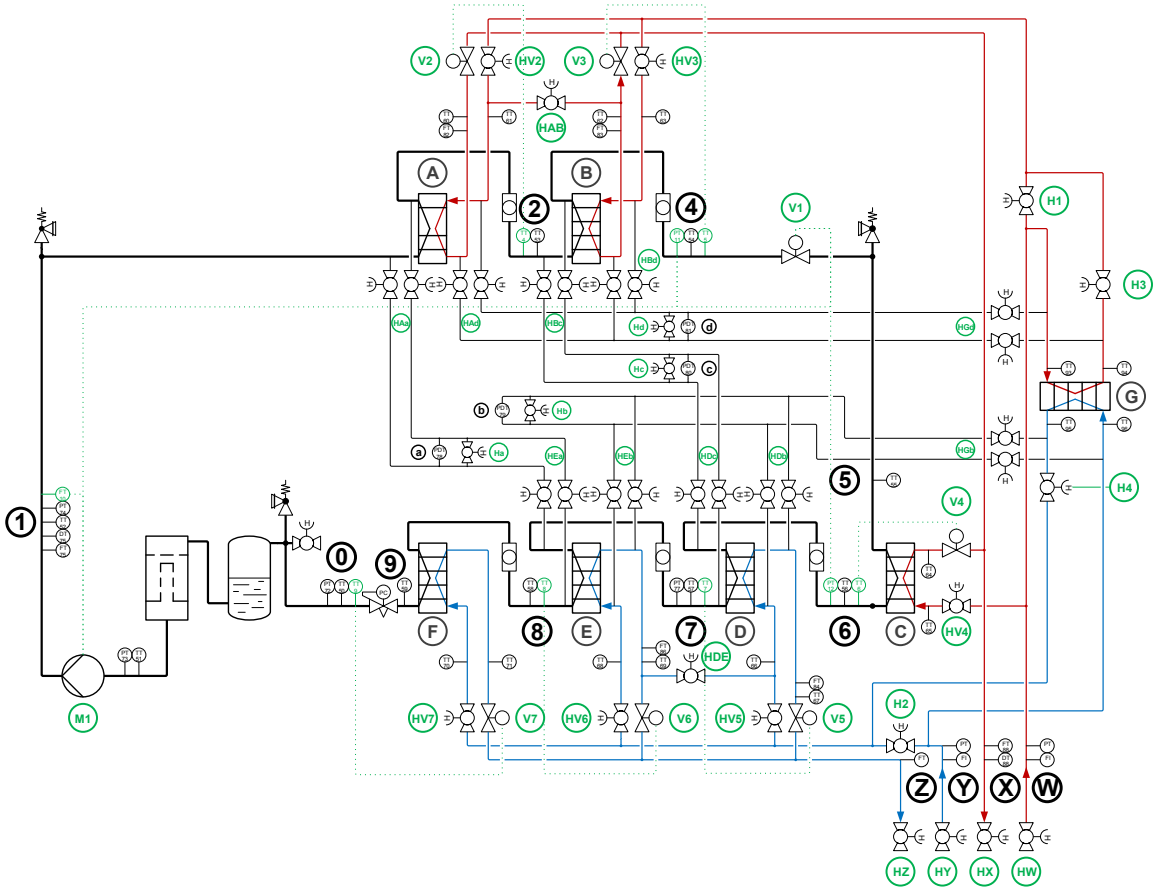

Figure 4.19: Process and instrumentation diagram of the heat exchnager test facilities.

Reliable and accurate control of the flow and the heat transfer was one of the major challenges with the initial heat exchangers test rig. To avoid such problems in the future, the new design includes automatic controls for all relevant properties. The dotted green connections in Figure 4.19 represent the inputs to the PID-controllers and the security switches. The pump motor M1 on the left hand side is operated according to the mass flow rate in ① and has emergency shutoff switches triggered by the pressures in point ④ and ⑥, which overrule the mass flow control. The pressure in point ④ and ⑥ also controls the opening of the expansion valve V1. The valves that can regulate the flow rates of the secondary media are located downstream from the heat exchangers. The pumps for the secondary media operate at a constant frequency while the flow rates get adjusted via the valves. Only the working fluid temperature is used as input to determine the flow on the secondary side. The above only applies to parallel operation in which the heat exchangers are individually connected to the hot and cold sources. In serial mode, the ball valves HAB and HDE are opened and HV2 and HV5 are closed to force the same portion of secondary fluid through preheater Ⓐ and evaporator Ⓑ as well as through condenser Ⓔ and desuperheater Ⓓ. In this case, V3 and V6 are closed manually and the secondary side flow is only controlled by V2 and V5, respectively.

To simplify the calculations, the same plates (B8T [224]) are used in all heat exchangers. Based on the design heat load calculations, three different PHEs were selected for the hot ORC side. Table 4.20 summarises the properties of the devices, which only differ in the number of plates.

The desired operational flexibility lead to a large amount of pipes the assembly is shown in Figure 4.21. The left hand side of Figure 4.21 shows the front view of the final design with the secondary fluid pipes. The two upper boxes on the left are the heat exchangers Ⓐ and Ⓑ. The subcooler Ⓕ and the condenser Ⓔ are mounted directly below. Desuperheater Ⓓ and superheater Ⓒ are located on the bottom of the right hand side of the rig and single-phase device Ⓖ was placed in the top right. All components in contact with the working fluid are on the front side, which is separated from the environment by an acrylic containment. The confined space can be attached to a ventilation system if the system runs with flammable working fluids. To comply with safety regulations, the sensors and valve for the secondary fluids are all located on the back of the assembly, which is shown on the right hand side of Figure 4.21. The large boxes on the drawing are the cabinets for the data acquisition system on the left and the programmable controllers on the right. An overview of the installed sensors on the working fluid side can be found in Table F.10 and Table F.11 holds the corresponding information for the secondary sides.

Table 4.20: Plate heat exchanger specifications for the new test rig.

Property	Preheater	Evaporator	Desuperheater
Number of plates	8[a]	10[a]	16[a]
Primary channels	3[a]	4[a]	7[a]
Secondary channels	4[a]	5[a]	8[a]
Flow length in mm	278[b]	278[b]	278[b]
Flow width in mm	76[b]	76[b]	76[b]
Total area in m^2	0.138[a]	0.184[a]	0.322[a]
Weight in kg	1.41[a]	1.56[a]	2.01[a]
Plate thickness in mm	0.24[b]	0.24[b]	0.24[b]
Wave length in mm	7.5[c]	7.5[c]	7.5[c]
Corrugation depth in mm	1.0[b]	1.0[b]	1.0[b]
Chevron angle in °	65[c]	65[c]	65[c]

[a] Based on design calculations, see also Appendix F.3.
[b] Based on the product data sheet for B8T [224].
[c] Based on manual measurements.

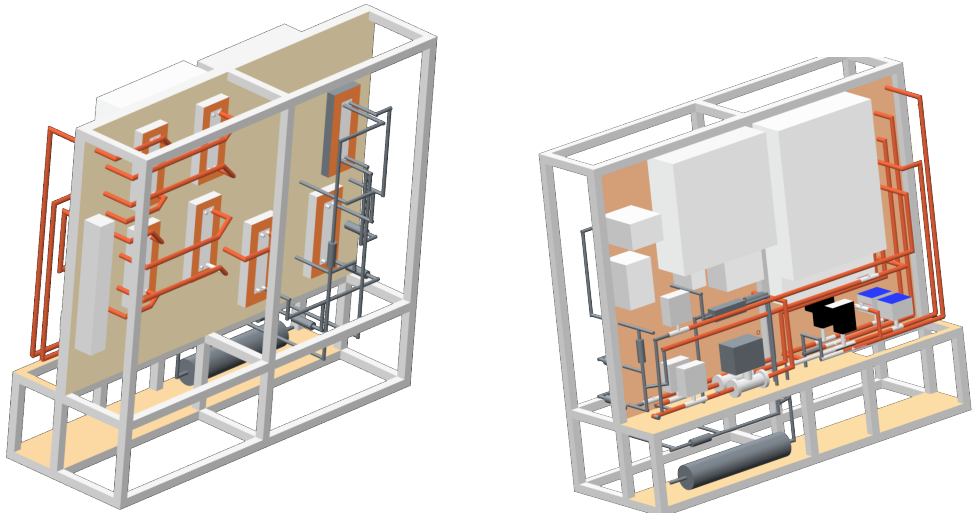

Figure 4.21: Enthalpy-based vapour quality and the smoothed heat transfer coefficients from a simple test.

State of the Work

The heat exchanger test rig has been built with assistance from the Copenhagen School of Marine Engineering and Technology Management and is currently being tested with R134a at Technical University of Denmark, Department of Mechanical Engineering, Kgs. Lyngby, Denmark (DTU). Initial tests indicate that the installation works as expected, but more work is needed to tune the controllers. The valves on the secondary fluid side could be used to control the working fluid temperatures, but the temperature-based control scheme is challenged in the vicinity of the two-phase region. Low mass flow rates and high pressure differences between the low and the high pressure side of more than 20 bar caused unstable pump operation, which limits the operating range.

The data acquisition system has been tested successfully up to sampling rates of 2 kHz. The installed sensors have not been calibrated yet. A manual calibration of temperature and pressure sensors can be carried out at DTU to reduce the measurement uncertainties, which should be quantified after such a procedure has been carried out.

4.4 Conclusions

The research on heat transfer correlations for relevant ORC working fluids has been reviewed for pipe flow and plate heat exchangers. The scarcity of experimental data that match ORC applications suggests that there could be large uncertainties associated with the heat transfer performance predicted from refrigeration correlations. However, the influence of the single phase heat transfer on the secondary side of a heat exchanger reduces the impact of this uncertainty on the overall performance, especially for correlations that have a strong link to the surface heat flux.

A generalised interface has been developed to include heat transfer correlations in a distributed plate heat exchanger model. The results of a modelling study with four pairs of single phase and boiling correlations suggested that the dynamic response can be approximated with a simplified function based on nominal values for liquid, two-phase and gaseous flow and the mass flow rate. Such a simplification drastically reduces the computational effort since the current correlation framework relies on the evaluation of two single-phase correlations and one two-phase correlation for each calculation cell.

The reviewed material has been prepared for implementation in a dynamic modelling framework and facilities for validation of the models have been designed. Earlier measurements with a modified expander test facility did not produce satisfying results, which motivated the development of a new experimental setup. A dedicated plate heat exchanger test rig has been built and the details of the design have been described.

Chapter 5

Final Remarks

This chapter summarises the results and the findings of the previous chapters are repeated in a condensed form. The objectives formulated in Section 1.4 are addressed and the chapter ends with suggestions for future work that provide hints for the improvement of the methods presented in this thesis.

5.1 Conclusions

The objectives formulated in Chapter 1 are repeated here together with a condensed description of the results of this work.

- Provide routines for an accelerated evaluation of working fluid properties (i): Contributions have been made to the open-source project CoolProp, which contains more than 100 compressible fluids. The software provides access to interpolation routines that evaluate thermophysical properties approximately more than 100 times faster than the equations of state. The property library has been extended to handle mixtures of selected components at arbitrary compositions. Attention has been paid to the flexibility of the produced code and it has been integrated with most of the relevant computational tools for thermodynamic systems.

- Make the different secondary heat transfer media properties available (i): More than 100 incompressible pure fluids and aqueous solutions have been included in CoolProp. New equations have been developed for fluids with a temperature offset including analytical derivatives and integrals to provide all relevant thermodynamic properties including entropy and selected partial derivatives to enhance the modelling experience.

- Create a flexible and validated modelling tool for reciprocating devices (ii): The implemented model of a reciprocating device takes advantage of many components from the Modelica standard library. Interoperability is guaranteed by relying on standardised connectors only. The model can operate as expander and compressor and has been released as part of ThermoCycle.

- Define and quantify losses that occur in reciprocating expansion machines (ii): Focussing on operation at variable expansion ratios, this work documents a stable expander efficiency of 70 % for a reciprocating machine prototype. Control schemes for a rotary valve system are proposed and have been applied to a cogeneration case documenting the potential of actively controlled valves. Furthermore, it was found that the increased heat loss from smaller systems only had a limited impact on the produced power. For a system with 3.2 kW of electrical output, 1 kW of heat loss reduced the produced work by less than 0.1 kW.

- Review existing heat transfer correlations for ORC working fluids (iii): Several heat transfer correlations have been reviewed concluding that there is a need for additional experimental validation. A new test facility has been designed to test working fluids for ORC systems.

- Build a framework to include heat transfer correlations into dynamic plate heat exchangers models (iii): A framework for heat transfer correlations has been added to ThermoCycle, which is available online including a selection of heat transfer correlations. The dynamic behaviour of a simplified method to dynamically calculate heat transfer based on vapour fraction, mass flow rate and fixed reference values could approximate the values calculated from full correlations.

5.2 Future Work

This section provides starting points that can be used to continue the work presented in this report. Based on the challenges and results that were encountered, the following paragraphs can guide the interested reader to the areas where additional research is required:

(i): The automated generation of property tables for interpolation has shown to be a useful feature. However, the phase boundaries are difficult to estimate during interpolation and the results, especially those from the bicubic scheme, occasionally hit the wrong phase for evaluations based on, for example, T and p. A reliable routine could improve the performance here. Another interesting feature could be the generation of fully differentiable functions for selected regions. Fitting simple functions like polynomials can be one way to facilitate the development of embedded models for control algorithms that have to work close to real-time speed. Considering the incompressible fluids, the consistency of the implemented models should be documented. The binary solutions do not account for the heat of mixing, which might cause confusion in some

cases. As a last point, the integration between the different calculation routines should be improved. Currently, aqueous solutions do not yield the same property values as pure water and the humid air calculations do neither meet the water properties nor the dry air properties at the end of the concentration ranges.

(ii): The experimental and modelling studies with reciprocating machines presented here do not cover an investigation of the influence of the pressure losses during the gas exchange. It is thus suggested to conduct a dedicated valve study that takes the analysis of the flow in inlet and exhaust valves to a higher level of detail. The challenging task to construct components that allow large volume flow rates to enter and leave the cylinder while not compromising on opening time is considered a major obstacle for further improvements of reciprocating expanders. As an extension to the efficiency-focussed valve control conducted in this study, future work should also investigate the operating regime in terms of power output. Higher rotational speeds lead to an increased work production rate, which is accompanied by larger pressure drops in the valves. The presented work only describes rotary design and more traditional poppet-type valves should also be studied. They are expected to provide better sealing characteristics, but their durability might prove to be a challenge due to the large forces arising from the pressure differences and the fast operation.

(iii): An obvious next task regarding the heat exchanger modelling is the validation of the implemented heat transfer correlations. In case of a mismatch, new correlations should be developed based on the data recorded with the test rig designed as part of this project. A comprehensive review of the existing single-phase and two-phase correlations can be carried out providing guidelines for the selection of correlations depending on the working fluid. Furthermore, supercritical operation has not been discussed in this work. Assuming a sufficiently large heat transfer area, evaporation-less transcritical operation can beneficial for ORCs due to the non-isothermal heat addition. The dynamic behaviour of the heat transfer equipment is expected to play a larger role for small scale systems. Experimental work with the dynamic operation of off-the-shelf heat exchangers can contribute to the understanding of the dynamics of low capacity power cycles.

Bibliography

[1] M. M. Abu-Khader. 'Plate heat exchangers: Recent advances'. In: *Renewable and Sustainable Energy Reviews* 16.4 (2012), pp. 1883–1891. DOI: 10.1016/j.rser.2012.01.009.

[2] R. P. Adair, E. B. Qvale and J. T. Pearson. 'Instantaneous Heat Transfer to the Cylinder Wall in Reciprocating Compressors'. In: *Proceedings of the International Compressor Engineering Conference*. 86. 1972, pp. 521–526.

[3] R. Akasaka, Y. Zhou and E. W. Lemmon. 'A Fundamental Equation of State for 1,1,1,3,3-Pentafluoropropane (R245fa)'. In: *Journal of Physical and Chemical Reference Data* 44.1 (2015), pp. 013104-1–013104-11. DOI: 10.1063/1.4913493.

[4] M. Ali Tarique, I. Dincer and C. Zamfirescu. 'Experimental investigation of a scroll expander for an organic Rankine cycle'. In: *International Journal of Energy Research* (2014). DOI: 10.1002/er.3189.

[5] B. Allan, K. Chittur, L. Cisternas, J. Pye, V. Rico-Ramirez, J. Shao et al. *ASCEND modelling environment v4*. 2014.

[6] E. Anderson, Z. Bai, C. Bischof, S. Blackford, J. Demmel, J. Dongarra et al. *LAPACK Users' Guide*. Third. Philadelphia, PA: Society for Industrial and Applied Mathematics, 1999.

[7] J. G. Andreasen, U. Larsen, T. Knudsen, L. Pierobon and F. Haglind. 'Selection and optimization of pure and mixed working fluids for low grade heat utilization using organic Rankine cycles'. In: *Energy* 73 (2014), pp. 204–213. DOI: 10.1016/j.energy.2014.06.012.

[8] G. Angelino and P. Colonna. 'Multicomponent working fluids for organic Rankine cycles (ORCs)'. In: *Energy* 23.6 (1998), pp. 449–463.

[9] W. J. D. Annand. 'Heat transfer in cylinders of reciprocating internal combustion engines'. In: *Proceedings of the Institution of Mechanical Engineers* 177.36 (1963), pp. 973–996.

[10] W. J. D. Annand and T. H. Ma. 'Instantaneous Heat Transfer Rates To The Cylinder Head Surface Of A Small Compression-ignition Engine'. In: *Proceedings Of The Institution Of Mechanical Engineers* 185.71-72 (Nov. 1971), pp. 976–987.

[11] W. J. D. Annand and D. Pinfold. *Heat Transfer In The Cylinder Of A Motored Reciprocating Engine*. Technical Paper 800457. Society of Automotive Engineers (SAE), Feb. 1980. DOI: 10.4271/800457.

[12] M. Antonelli, A. Baccioli, M. Francesconi and L. Martorano. 'Experimental and Numerical Analysis of the Valve Timing Effects on the Performances of a Small Volumetric Rotary Expansion Device'. In: *Energy Procedia* 45 (2014). ATI 2013 - 68th Conference of the Italian Thermal Machines Engineering Association, pp. 1077–1086. DOI: 10.1016/j.egypro.2014.01.113.

[13] Asimptote bv and Propulsion and Power group at Delft University of Technology. *Cycle-Tempo*. 2014.

[14] Asimptote bv and Propulsion and Power group at Delft University of Technology. *FluidProp v3.0*. 2014.

[15] Aspen Plus. 'Release AspenONE, Aspen Technology'. In: *Inc., Cambridge, MA, USA* (2004).

[16] V. K. Avadhanula and C.-S. Lin. 'Empirical Models for a Screw Expander Based on Experimental Data From Organic Rankine Cycle System Testing.' In: *Journal of Engineering for Gas Turbines and Power* 136.6 (2014), p. 1.

[17] Z. H. Ayub. 'Plate Heat Exchanger Literature Survey and New Heat Transfer and Pressure Drop Correlations for Refrigerant Evaporators'. In: *Heat Transfer Engineering* 24.5 (2003), pp. 3–16. DOI: 10.1080/01457630304056.

[18] M. Badami and M. Mura. 'Preliminary design and controlling strategies of a small-scale wood waste Rankine Cycle (RC) with a reciprocating steam engine (SE)'. In: *Energy* 34.9 (2009), pp. 1315–1324. DOI: 10.1016/j.energy.2009.04.031.

[19] M. Badami, M. Mura, P. Campanile and F. Anzioso. 'Design and performance evaluation of an innovative small scale combined cycle cogeneration system'. In: *Energy* 33.8 (2008), pp. 1264–1276. DOI: 10.1016/j.energy.2008.03.001.

[20] O. Badr, S. Naik, P. W. O'Callaghan and S. D. Probert. 'Expansion machine for a low power-output steam Rankine-cycle engine'. In: *Applied Energy* 39.2 (1991), pp. 93–116. DOI: 10.1016/0306-2619(91)90024-R.

[21] O. Badr, P. W. Ocallaghan, M. Hussein and S. D. Probert. 'Multi-vane Expanders As Prime Movers For Low-grade Energy Organic Rankine-cycle Engines'. In: *Applied Energy* 16.2 (1984), pp. 129–146. DOI: 10.1016/0306-2619(84)90060-6.

[22] O. Badr, S. D. Probert and P. W. O'Callaghan. 'Selecting a working fluid for a Rankine-cycle engine'. In: *Applied Energy* 21.1 (Jan. 1985), pp. 1–42. DOI: 10.1016/0306-2619(85)90072-8.

[23] M. K. Bassiouny and H. Martin. 'Flow distribution and pressure drop in plate heat exchangers—I U-type arrangement'. In: *Chemical Engineering Science* 39.4 (1984), pp. 693–700. DOI: 10.1016/0009-2509(84)80176-1.

[24] M. K. Bassiouny and H. Martin. 'Flow distribution and pressure drop in plate heat exchangers—II Z-type arrangement'. In: *Chemical Engineering Science* 39.4 (1984), pp. 701–704. DOI: 10.1016/0009-2509(84)80177-3.

[25] A. Bejan. 'Single-Phase Systems'. In: *Advanced engineering thermodynamics*. 3rd Editio. Hoboken, N.J, USA: John Wiley & Sons, Inc., 2006. Chap. 4, pp. 145–203.

[26] I. H. Bell. 'Theoretical and Experimental Analysis of Liquid Flooded Compression in Scroll Compressors'. PhD thesis. Purdue University, 2011.

[27] I. H. Bell, V. Lemort, E. A. Groll, J. E. Braun, G. B. King and W. T. Horton. 'Liquid flooded compression and expansion in scroll machines – Part II: Experimental testing and model validation'. In: *International Journal of Refrigeration* 35.7 (2012), pp. 1890–1900. DOI: 10.1016/j.ijrefrig.2012.07.008.

[28] I. H. Bell, V. Lemort, E. A. Groll, J. E. Braun, G. B. King and W. T. Horton. 'Liquid-flooded compression and expansion in scroll machines – Part I: Model development'. In: *International Journal of Refrigeration* 35.7 (2012), pp. 1878–1889. DOI: 10.1016/j.ijrefrig.2012.07.010.

[29] I. H. Bell, J. Wronski, S. Quoillin and V. Lemort. 'Pure- and Pseudo-Pure Fluid Thermophysical Property Evaluation and the Open-Source Thermophysical Property Library CoolProp'. In: *Industrial & Engineering Chemistry Research* 53.6 (2014), pp. 2498–2508. DOI: 10.1021/ie4033999.

[30] BMUB, Division KI I 1, ed. *The German Government's Climate Action Programme 2020*. Federal Ministry for the Environment, Nature Conservation, Building and Nuclear Safety, 2014.

[31] U. Bolmstedt. 'HEAT EXCHANGERS'. In: *Encyclopedia of Dairy Sciences*. Ed. by H. Roginski. Oxford: Elsevier, 2002, pp. 1313–1321. DOI: 10.1016/B0-12-227235-8/00198-X.

[32] J. Bonilla, L. J. Yebra and S. Dormido. 'Chattering in dynamic mathematical two-phase flow models'. In: *Applied Mathematical Modelling* 36.5 (May 2012), pp. 2067–2081. DOI: 10.1016/j.apm.2011.08.013.

[33] J. Bonilla, L. J. Yebra and S. Dormido. 'Mean densities in dynamic mathematical two-phase flow models'. In: *CMES: Computer Modeling in Engineering & Sciences* 67.1 (2010), pp. 13–38. DOI: 10.3970/cmes.2010.067.013.

[34] J. Bonjour and A. Bejan. 'Optimal distribution of cooling during gas compression'. In: *Energy* 31.4 (2006), pp. 409–424. DOI: 10.1016/j.energy.2005.04.004.

[35] A. Borsukiewicz-Gozdur and W. Nowak. 'Comparative analysis of natural and synthetic refrigerants in application to low temperature Clausius-Rankine cycle'. In: *Energy* 32.4 (Apr. 2007), pp. 344–352. DOI: 10.1016/j.energy.2006.07.012.

[36] D. Bouskela and B. E. Hefni. 'A physical solution for solving the zero-flow singularity in static thermal-hydraulics mixing models'. In: *Proceedings of the 10th International Modelica Conference*. Vol. 96. 88. Lund, Sweden, Mar. 2014, pp. 847–855. DOI: 10.3384/ecp14096847.

[37] R. P. Brent. 'Algorithms for Minimization without Derivatives'. In: Englewood Cliffs: Prentice-Hall, 1973. Chap. Chapter 4: An Algorithm with Guaranteed Convergence for Finding a Zero of a Function, pp. 47–60.

[38] R. P. Brent. 'An algorithm with guaranteed convergence for finding a zero of a function'. In: *The Computer Journal* 14.4 (1971), pp. 422–425.

[39] P. Bridgman. 'A Complete Collection of Thermodynamic Formulas'. In: *Physical Review* 3.4 (Apr. 1914), pp. 273–281. DOI: 10.1103/PhysRev.3.273.

[40] O. Brunin, M. Feidt and B. Hivet. 'Comparison of the working domains of some compression heat pumps and a compression-absorption heat pump'. In: *International Journal of Refrigeration* 20.5 (1997), pp. 308–318. DOI: 10.1016/S0140-7007(97)00025-X.

[41] D. Bücker and W. Wagner. 'Reference Equations of State for the Thermodynamic Properties of Fluid Phase n-Butane and Isobutane'. In: *Journal of Physical and Chemical Reference Data* 35.2 (2006), pp. 929–1019. DOI: 10.1063/1.1901687.

[42] B. Carroll. 'On the use of Jacobians in thermodynamics'. In: *Journal of Chemical Education* 42.4 (1965), pp. 218–221. DOI: 10.1021/ed042p218.

[43] F. Casella. 'Object-oriented modelling of two-phase fluid flows by the finite volume method'. In: *Proceedings 5th MATHMOD Vienna*. ARGE Simulation News, 2006, pp. 6–8.

[44] F. Casella and A. Leva. 'Modelica open library for power plant simulation: design and experimental validation'. In: *Proceedings of the 3rd international Modelica conference*. 2003, pp. 41–50.

[45] F. Casella, T. Mathijssen, P. Colonna and J. van Buijtenen. 'Dynamic Modeling of Organic Rankine Cycle Power Systems'. In: *Journal of Engineering for Gas Turbines and Power* 135.4 (Mar. 2013), p. 042310. DOI: 10.1115/1.4023120.

[46] Y. A. Çengel and M. A. Boles. *Thermodynamics, An Engineering Approach*. 6th edition. New York: McGraw-Hill, 2007.

[47] H. Chen, D. Y. Goswami and E. K. Stefanakos. 'A review of thermodynamic cycles and working fluids for the conversion of low-grade heat'. In: *Renewable and Sustainable Energy Reviews* 14.9 (Dec. 2010), pp. 3059–3067. DOI: 10.1016/j.rser.2010.07.006.

[48] J. Claesson. 'Thermal and Hydraulic Performance of Compact Brazed Plate Heat Exchangers Operating as Evaporators in Domestic Heat Pumps'. PhD Thesis. Royal Institute of Technology, 2004.

[49] S. Clemente, D. Micheli, M. Reini and R. Taccani. 'Energy efficiency analysis of Organic Rankine Cycles with scroll expanders for cogenerative applications'. In: *Applied Energy* 97 (Sept. 2012), pp. 792–801. DOI: 10.1016/j.apenergy.2012.01.029.

[50] P. Colonna, N. R. Nannan and A. Guardone. 'Multiparameter equations of state for siloxanes: [(CH3)3-Si-O1/2]2-[O-Si-(CH3)2]i=1,...,3, and [O-Si-(CH3)2]6'. In: *Fluid Phase Equilibria* 263.2 (2008), pp. 115–130. DOI: 10.1016/j.fluid.2007.10.001.

[51] P. Colonna, E. Casati, C. Trapp, T. Mathijssen, J. Larjola, T. Turunen-Saaresti et al. 'Organic Rankine Cycle Power Systems: From the Concept to Current Technology, Applications, and an Outlook to the Future'. In: *Journal of Engineering for Gas Turbines and Power* 137.10 (2015), pp. 100801-1–100801-19. DOI: 10.1115/1.4029884.

[52] M. G. Cooper. 'Flow boiling—the 'apparently nucleate′ regime'. In: *International Journal of Heat and Mass Transfer* 32.3 (1989), pp. 459–464. DOI: 10.1016/0017-9310(89)90133-6.

[53] M. G. Cooper. 'Heat Flow Rates in Saturated Nucleate Pool Boiling—A Wide-Ranging Examination Using Reduced Properties'. In: *Advances in Heat Transfer* 16 (1984), pp. 157–239. DOI: 10.1016/S0065-2717(08)70205-3.

[54] F. H. Crawford. 'Jacobian Methods in Thermodynamics'. In: *American Journal of Physics* 17.1 (1949), pp. 1–5. DOI: 10.1119/1.1989489.

[55] F. F. O. Daminabo. 'A NOVEL 2kWe BIOMASS-ORGANIC RANKINE CYCLE MICRO COGENERATION SYSTEM'. PhD thesis. University of Nottingham, 2009.

[56] Danish Ministry of Climate and Energy. *Energy strategy 2050: from coal, oil and gas to green energy*. Copenhagen, Denmark: Danish Government, 2011.

[57] Dassault Systèmes AB. *Dymola 2014*. Lund, Sweden, 2013.

[58] G. David, F. Michel and L. Sanchez. 'Waste heat recovery projects using Organic Rankine Cycle technology—Examples of biogas engines and steel mills applications'. In: *Proceedings of the World Engineers' Convention*. Geneva, Switzerland, Sept. 2011.

[59] T. A. Davidson. 'Design and anlysis of a 1 kw ORC employing a multi-vane expander, for use with a low temperature solar collector'. Bachelor Thesis. Massachusets Institute of Technology, 1977.

[60] S. Declaye, S. Quoilin, L. Guillaume and V. Lemort. 'Experimental study on an open-drive scroll expander integrated into an ORC (Organic Rankine Cycle) system with R245fa as working fluid'. In: *Energy* 55 (2013), pp. 173–183. DOI: 10.1016/j.energy.2013.04.003.

[61] A. M. Delgado-Torres and L. García-Rodríguez. 'Design recommendations for solar organic Rankine cycle (ORC)-powered reverse osmosis (RO) desalination'. In: *Renewable and Sustainable Energy Reviews* 16.1 (2012), pp. 44–53. DOI: 10.1016/j.rser.2011.07.135.

[62] J. Demierre, S. Henchoz and D. Favrat. 'Prototype of a thermally driven heat pump based on integrated Organic Rankine Cycles (ORC)'. In: *Energy* 41.1 (May 2012), pp. 10–17. DOI: 10.1016/j.energy.2011.08.049.

[63] J. Demuynck, M. De Paepe, H. Huisseune, R. Sierens, J. Vancoillie and S. Verhelst. 'On the applicability of empirical heat transfer models for hydrogen combustion engines'. In: *International Journal of Hydrogen Energy* 36.1 (2011), pp. 975–984. DOI: 10.1016/j.ijhydene.2010.10.059.

[64] T. Destoop. 'Compresseurs volumetriques'. In: Techniques de l'ingénieur, 1986. Chap. B4220, pp. 1–27.

[65] R. Dickes, A. Desideri, I. Bell, S. Quoilin and V. Lemort. 'Dynamic modeling and control strategy analysis of a micro-scale CSP plant coupled with a thermocline system for power generation'. In: *Proceedings of EuroSun 2014*. International Solar Energy Society, 2014.

[66] F. P. Disconzi, E. L. Pereira and C. J. Deschamps. 'Development of an In-Cylinder Heat Transfer Correlation for Reciprocating Compressors'. In: *Proceedings of the International Compressor Engineering Conference*. Paper 1342. 2012, pp. 1–10.

[67] F. W. Dittus and L. M. K. Boelter. 'Heat transfer in automobile radiators of the tubular type'. In: *University of California Publications in Engineering* 2 (1930), pp. 443–461.

[68] E. Djordjevic and S. Kabelac. 'Flow boiling of R134a and ammonia in a plate heat exchanger'. In: *International Journal of Heat and Mass Transfer* 51.25–26 (2008), pp. 6235–6242. DOI: 10.1016/j.ijheatmasstransfer.2008.01.042.

[69] L. Dong, H. Liu and S. Riffat. 'Development of small-scale and micro-scale biomass-fuelled CHP systems – A literature review'. In: *Applied Thermal Engineering* 29.11-12 (2009), pp. 2119–2126. DOI: 10.1016/j.applthermaleng.2008.12.004.

[70] V. D. Donowski and S. G. Kandlikar. 'Correlating evaporation heat transfer coefficient of refrigerant R134a in a plate heat exchanger'. In: *Proceedings of Boiling 2000: Phenomena and Emerging Applications*. 2000, Paper 154.

[71] D. Dović, B. Palm and S. Švaić. 'Generalized correlations for predicting heat transfer and pressure drop in plate heat exchanger channels of arbitrary geometry'. In: *International Journal of Heat and Mass Transfer* 52.19–20 (Sept. 2009), pp. 4553–4563. DOI: 10.1016/j.ijheatmasstransfer.2009.03.074.

[72] U. Drescher and D. Brüggemann. 'Fluid selection for the Organic Rankine Cycle (ORC) in biomass power and heat plants'. In: *Applied Thermal Engineering* 27.1 (Jan. 2007), pp. 223–228. DOI: 10.1016/j.applthermaleng.2006.04.024.

[73] DS 439:2009. *Code of Practice for domestic water supply installations*. Charlottenlund, Denmark: Danish Standards, 2009.

[74] G. Eichelberg. 'Some new investigations on old combustion engine problems–Study of heat flow in cylinder walls and pistons'. In: *Engineering* 148.3850 (1939), pp. 547–550.

[75] G. Eichelberg. 'Temperaturverlauf und Wärmespannungen in Verbrennungsmotoren'. PhD thesis. Eidgenössische Technische Hochschule Zürich, 1922. DOI: 10.3929/ethz-a-000097573.

[76] G. Eichelberg. 'The temporal course of heat transfer in diesel engines'. In: *Zeitschrift des Vereines Deutscher Ingenieure* 72 (1928), pp. 463–464.

[77] B. Elmegaard and N. Houbak. 'DNA–a general energy system simulation tool'. In: *Proceedings of SIMS 2005*. Trondheim, Norway, Oct. 2005, pp. 1–10.

[78] K. Elser. 'Der instationäre Wärmeübergang in Dieselmotoren: Theoretische und experimentelle Untersuchungen'. PhD thesis. Eidgenössische Technische Hochschule Zürich, 1954.

[79] EN 1434-1:2007. *Heat meters – Part 1: General requirements*. Charlottenlund, Denmark: Danish Standards, 2007.

[80] EN 14825:2012. *Air conditioners, liquid chilling packages and heat pumps, with electrically driven compressors, for space heating and cooling – Testing and rating at part load conditions and calculation of seasonal performance*. Charlottenlund, Denmark: Danish Standards, 2012.

[81] EN 60534-2-1:2011. *Industrial-process control valves – Part 2-1: Flow capacity – Sizing equations for fluid flow under installed conditions*. Charlottenlund, Denmark: Danish Standards, 2011.

[82] W. W. Focke, J. Zachariades and I. Olivier. 'The effect of the corrugation inclination angle on the thermohydraulic performance of plate heat exchangers'. English. In: *International Journal of Heat and Mass Transfer* 28.8 (1985), pp. 1469–1479.

[83] R. Franke, F. Casella, M. Sielemann, K. Proelss, M. Otter and M. Wetter. 'Standardization of Thermo-Fluid Modeling in Modelica.Fluid'. In: *Proceedings of the 7th International Modelica Conference*. Como, Italy: Modelica Association, 2009, pp. 122–131.

[84] J. R. García-Cascales, F. Vera-García, J. M. Corberán-Salvador and J. Gonzálvez-Maciá. 'Assessment of boiling and condensation heat transfer correlations in the modelling of plate heat exchangers'. In: *International Journal of Refrigeration* 30.6 (2007), pp. 1029–1041. DOI: 10.1016/j.ijrefrig.2007.01.004.

[85] H. Gedanitz, M. J. Dávila and E. W. Lemmon. 'Speed of sound measurements and a fundamental equation of state for cyclopentane'. In: *J. Chem. Eng. Data* (To be published, preprint provided by Eric Lemmon).

[86] A. Giuffrida. 'Modelling the performance of a scroll expander for small organic Rankine cycles when changing the working fluid'. English. In: *Applied Thermal Engineering* 70.1 (2014), pp. 1040–1049. DOI: 10.1016/j.applthermaleng.2014.06.004.

[87] Y. Glavatskaya, P. Podevin, V. Lemort, O. Shonda and G. Descombes. 'Reciprocating Expander for an Exhaust Heat Recovery Rankine Cycle for a Passenger Car Application'. In: *Energies* 5.6 (June 2012), pp. 1751–1765. DOI: 10.3390/en5061751.

[88] V. Gnielinski. 'New Equations For Heat And Mass-transfer In Turbulent Pipe And Channel Flow'. In: *International Chemical Engineering* 16.2 (1976), pp. 359–368.

[89] V. Gnielinski. 'On heat transfer in tubes'. In: *International Journal of Heat and Mass Transfer* 63 (2013), pp. 134–140. DOI: 10.1016/j.ijheatmasstransfer.2013.04.015.

[90] V. Gnielinski. 'VDI Heat Atlas'. In: ed. by P. Stephan. 2nd. Berlin Heidelberg: Springer, 2010. Chap. G1 Heat Transfer in Pipe Flow, pp. 691–700. DOI: 10.1007/978-3-540-77877-6_34.

[91] R. Gregorig. 'The effect of a nonlinear temperature dependent Prandtl-number on heat transfer of fully developed flow of liquids in a straight tube'. In: *Wärme- und Stoffübertragung* 9.2 (1976), pp. 61–72. DOI: 10.1007/BF01589459.

[92] R. Gregorig. 'Verallgemeinerter Ausdruck für den Einfluß temperaturabhängiger Stoffwerte auf den turbulenten Wärmeübergang'. In: *Wärme- und Stoffübertragung* 3.1 (1970), pp. 26–40. DOI: 10.1007/BF01881220.

[93] K. E. Gungor and R. H. S. Winterton. 'A general correlation for flow boiling in tubes and annuli'. In: *International Journal of Heat and Mass Transfer* 29.3 (1986), pp. 351–358. DOI: 10.1016/0017-9310(86)90205-X.

[94] K. E. Gungor and R. H. S. Winterton. 'Simplified general correlation for saturated flow boiling and ccomparison of correlations with data'. In: *Chemical Engineering Research and Design* 65 (1987), pp. 148–156.

[95] T. Guo, H. Wang and S. Zhang. 'Comparative analysis of natural and conventional working fluids for use in transcritical Rankine cycle using low-temperature geothermal source'. In: *International Journal of Energy Research* 35.6 (2011), pp. 530–544. DOI: 10.1002/er.1710.

[96] J. A. Gut and J. M. Pinto. 'Modeling of plate heat exchangers with generalized configurations'. In: *International Journal of Heat and Mass Transfer* 46.14 (July 2003), pp. 2571–2585. DOI: 10.1016/S0017-9310(03)00040-1.

[97] D.-H. Han, K.-J. Lee and Y.-H. Kim. 'Experiments on the characteristics of evaporation of R410A in brazed plate heat exchangers with different geometric configurations'. In: *Applied Thermal Engineering* 23.10 (2003), pp. 1209–1225. DOI: 10.1016/S1359-4311(03)00061-9.

[98] Y.-L. He, D.-H. Mei, W.-Q. Tao, W.-W. Yang and H.-L. Liu. 'Simulation of the parabolic trough solar energy generation system with Organic Rankine Cycle'. In: *Applied Energy* 97 (2012), pp. 630–641. DOI: 10.1016/j.apenergy.2012.02.047.

[99] R. L. Heavner, H. Kumar and A. S. Wanniarachchi. 'Performance of an industrial plate heat exchanger: effect of chevron angle'. In: *AIChE symposium series* 89.295 (1993), pp. 262–267.

[100] F. Heberle, M. Preißinger and D. Brüggemann. 'Zeotropic mixtures as working fluids in Organic Rankine Cycles for low-enthalpy geothermal resources'. In: *Renewable Energy* 37.1 (Jan. 2012), pp. 364–370. DOI: 10.1016/j.renene.2011.06.044.

[101] Y. Y. Hsieh and T. F. Lin. 'Saturated flow boiling heat transfer and pressure drop of refrigerant R-410A in a vertical plate heat exchanger'. In: *International Journal of Heat and Mass Transfer* 45 (2002), pp. 1033–1044.

[102] M. L. Huber, A. Laesecke and R. A. Perkins. 'Model for the Viscosity and Thermal Conductivity of Refrigerants, Including a New Correlation for the Viscosity of R134a'. In: *Industrial & Engineering Chemistry Research* 42.13 (2003), pp. 3163–3178. DOI: 10.1021/ie0300880.

[103] H.-J. Huff and R. Radermacher. *CO_2 Compressor-Expander Analysis*. Tech. rep. March. Arlington, Virginia: Air-Conditioning and Refrigeration Technology Institute, 2003, pp. 1–77.

[104] W. Hufschmidt and E. Burck. 'Der Einfluss temperaturabhängiger Stoffwerte auf den Wärmeübergang bei turbulenter Strömung von Flüssigkeiten in Rohren bei hohen Wärmestromdichten und Prandtlzahlen'. In: *International Journal of Heat and Mass Transfer* 11.6 (1968), pp. 1041–1048.

[105] W. Hufschmidt, E. Burck and W. Riebold. 'Die Bestimmung örtlicher und mittlerer Wärmeübergangszahlen in Rohren bei hohen Wärmestromdichten'. In: *International Journal of Heat and Mass Transfer* 9.6 (1966), pp. 539–565.

[106] T. C. Hung, T. Y. Shai and S. K. Wang. 'A review of organic rankine cycles (ORCs) for the recovery of low-grade waste heat'. In: *Energy* 22.7 (July 1997), pp. 661–667. DOI: 10.1016/S0360-5442(96)00165-X.

[107] IAPWS. *Revised Release on the IAPWS Formulation 1995 for the Thermodynamic Properties of Ordinary Water Substa nce for General and Scientific Use*. Tech. rep. Doorwerth, The Netherlands: International Association for the Properties of Water and Steam, 2009.

[108] IAPWS. *Revised Release on the IAPWS Industrial Formulation 1997 for the Thermodynamic Properties of Water and Steam*. Tech. rep. Lucerne, Switzerland: International Association for the Properties of Water and Steam, 2007.

[109] M. K. Ireland, M. S. Orosz, J. Brisson, A. Desideri and S. Quoilin. 'Dynamic Modeling and Control System Definition for a Micro-CSP Plant Coupled With Thermal Storage Unit'. In: *ASME Turbo Expo 2014: Turbine Technical Conference and Exposition*. American Society of Mechanical Engineers. 2014, V03BT26A016–V03BT26A016. DOI: 10.1115/GT2014-27132.

[110] A. Irimescu. 'Convective heat transfer equation for turbulent flow in tubes applied to internal combustion engines operated under motored conditions'. In: *Applied Thermal Engineering* 50.1 (2013), pp. 536–545. DOI: 10.1016/j.applthermaleng.2012.06.051.

[111] J. M. Jensen. 'Dynamic Modeling of Thermo-Fluid Systems'. PhD Thesis. Technical University of Denmark, 2003.

[112] A. O. Johansen. 'Numerical study of evaporators in power plants for improved dynamic flexibility'. PhD thesis. Technical University of Denmark, 2013.

[113] E. Jones, T. Oliphant, P. Peterson et al. *SciPy: Open source scientific tools for Python*. 2001.

[114] M. R. Kærn. 'Analysis of Flow Maldistribution in Fin-and-tube Evaporators for Residential Air-conditioning Systems'. PhD thesis. Technical University of Denmark, 2011.

[115] A. Kamei, S. W. Beyerlein and R. T. Jacobsen. 'Application of Nonlinear Regression in the Development of a Wide Range Formulation for HCFC-22'. In: *International Journal of Thermophysics* 16.5 (1995), pp. 1155–1164.

[116] S. Karellas, A. Schuster and A.-D. Leontaritis. 'Influence of supercritical ORC parameters on plate heat exchanger design'. In: *Applied Thermal Engineering* 33-34 (Feb. 2012), pp. 70–76. DOI: 10.1016/j.applthermaleng.2011.09.013.

[117] R. G. Keys. 'Cubic Convolution Interpolation for Digital Image Processing'. In: *Ieee Transactions On Acoustics, Speech, And Signal Processing* 29.6 (1981), pp. 1153–1160.

[118] M. S. Khan, T. S. Khan, M.-C. Chyu and Z. H. Ayub. 'Evaporation heat transfer and pressure drop of ammonia in a mixed configuration chevron plate heat exchanger'. In: *International Journal of Refrigeration* 41 (2014), pp. 92–102. DOI: 10.1016/j.ijrefrig.2013.12.015.

[119] M. S. Khan, T. S. Khan, M.-C. Chyu and Z. H. Ayub. 'Experimental investigation of evaporation heat transfer and pressure drop of ammonia in a 30deg chevron plate heat exchanger'. In: *International Journal of Refrigeration* 35.6 (2012), pp. 1757–1765. DOI: 10.1016/j.ijrefrig.2012.05.019.

[120] T. S. Khan, M. S. Khan, M.-C. Chyu and Z. H. Ayub. 'Ammonia evaporation in a mixed configuration chevron plate heat exchanger with and without miscible oil'. In: *International Journal of Refrigeration* 51 (2015), pp. 120–134. DOI: 10.1016/j.ijrefrig.2014.12.002.

[121] T. S. Khan, M. S. Khan, M.-C. Chyu and Z. H. Ayub. 'Experimental investigation of evaporation heat transfer and pressure drop of ammonia in a 60deg chevron plate heat exchanger'. In: *International Journal of Refrigeration* 35.2 (2012), pp. 336–348. DOI: 10.1016/j.ijrefrig.2011.10.018.

[122] T. S. Khan, M. S. Khan, M.-C. Chyu, Z. H. Ayub and J. A. Chattha. 'Review of Heat Transfer and Pressure Drop Correlations for Evaporation of Fluid Flow in Plate Heat Exchangers (RP-1352)'. In: *HVAC&R Research* 15.2 (2009), pp. 169–188. DOI: 10.1080/10789669.2009.10390832.

[123] S. Klein and F. L. Alvarado. *EES – Engineering Equation Solver v9.616*. Madison, Wisconsin, USA: F-Chart Software, 2014.

[124] A. A. Kornhauser and J. L. Smith. 'Application of a complex Nusselt number to heat transfer during compression and expansion'. In: *Transactions of the ASME. Journal of Heat Transfer* 116.3 (1994), pp. 536–542. DOI: 10.1115/1.2910904.

[125] M. M. Kostic. 'Analysis of Enthalpy Approximation for Compressed Liquid Water'. In: *Journal of Heat Transfer* 128.5 (2006), pp. 421–426. DOI: 10.1115/1.2175090.

[126] O. Kunz, R. Klimeck, W. Wagner and M. Jaeschke. *The GERG-2004 Wide-Range Equation of State for Natural Gases and Other Mixtures*. English. GERG Technical Monograph 15. Groupe Européen de Recherches Gazières, 2007, pp. 3032–3091.

[127] O. Kunz and W. Wagner. 'The GERG-2008 Wide-Range Equation of State for Natural Gases and Other Mixtures: An Expansion of GERG-2004'. English. In: *Journal of Chemical & Engineering Data* 57.11 (2012), pp. 3032–3091. DOI: 10.1021/je300655b.

[128] C.-R. Kuo, S.-W. Hsu, K.-H. Chang and C.-C. Wang. 'Analysis of a 50kW organic Rankine cycle system'. In: *Energy* 36.10 (Oct. 2011), pp. 5877–5885. DOI: 10.1016/j.energy.2011.08.035.

[129] W. S. Kuo, Y. M. Lie, Y. Y. Hsieh and T. F. Lin. 'Condensation heat transfer and pressure drop of refrigerant R-410A flow in a vertical plate heat exchanger'. In: *International Journal of Heat and Mass Transfer* 48.25-26 (Dec. 2005), pp. 5205–5220. DOI: 10.1016/j.ijheatmasstransfer.2005.07.023.

[130] M. Lampe, J. Groß and A. Bardow. 'Simultaneous process and working fluid optimisation for Organic Rankine Cycles (ORC) using PC-SAFT'. In: *22nd European Symposium on Computer Aided Process Engineering*. Ed. by I. D. L. Bogle and M. Fairweather. Vol. 30. Elsevier, 2012, pp. 572–576. DOI: 10.1016/B978-0-444-59519-5.50115-5.

[131] U. Larsen, L. Pierobon, F. Haglind and C. Gabrielii. 'Design and optimisation of organic Rankine cycles for waste heat recovery in marine applications using the principles of natural selection'. In: *Energy* 55 (2013), pp. 803–812. DOI: 10.1016/j.energy.2013.03.021.

[132] C. L. Lawson, R. J. Hanson, D. R. Kincaid and F. T. Krogh. 'Basic Linear Algebra Subprograms for Fortran Usage'. In: *ACM Transactions on Mathematical Software* 5.3 (Sept. 1979), pp. 308–323.

[133] B. Lawton. 'Effect Of Compression And Expansion On Instantaneous Heat-transfer In Reciprocating Internal-combustion Engines'. In: *Proceedings Of The Institution Of Mechanical Engineers Part A—Journal Of Power And Energy* 201.3 (1987), pp. 175–186. DOI: 10.1243/PIME_PROC_1987_201_022_02.

[134] S. Lecompte, H. Huisseune, M. van den Broek, B. Vanslambrouck and M. De Paepe. 'Review of organic Rankine cycle (ORC) architectures for waste heat recovery'. English. In: *Renewable and Sustainable Energy Reviews* 47 (2015), pp. 448–461. DOI: 10.1016/j.rser.2015.03.089.

[135] E. W. Lemmon, M. L. Huber and M. O. McLinden. *NIST Standard Reference Database 23: Reference Fluid Thermodynamic and Transport Properties-REFPROP, Version 9.1*. Tech. rep. Gaithersburg: National Institute of Standards and Technology, Standard Reference Data Program, 2013.

[136] E. W. Lemmon and R. T. Jacobsen. 'A Generalized Model for the Thermodynamic Properties of Mixtures'. In: *International Journal of Thermophysics* 20.3 (1999), pp. 825–835.

[137] E. W. Lemmon, U. Overhoff, M. O. McLinden and W. Wagner. 'Equation of state for propylene'. Personal communication with Eric Lemmon. 2010.

[138] E. W. Lemmon. 'Pseudo-Pure Fluid Equations of State for the Refrigerant Blends R-410A, R-404A, R-507A, and R-407C'. In: *International Journal of Thermophysics* 24.4 (2003), pp. 991–1006.

[139] E. W. Lemmon and R. T. Jacobsen. 'Equations of State for Mixtures of R-32, R-125, R-134a, R-143a, and R-152a'. In: *Journal of Physical and Chemical Reference Data* 33.2 (2004), pp. 593–620. DOI: 10.1063/1.1649997.

[140] E. W. Lemmon, M. O. McLinden and W. Wagner. 'Thermodynamic Properties of Propane. III. A Reference Equation of State for Temperatures from the Melting Line to 650 K and Pressures up to 1000 MPa'. In: *Journal of Chemical and Engineering Data* 54 (2009), pp. 3141–3180.

[141] E. W. Lemmon and R. Span. 'Short Fundamental Equations of State for 20 Industrial Fluids'. In: *Journal of Chemical & Engineering Data* 51.3 (May 2006), pp. 785–850. DOI: 10.1021/je050186n.

[142] E. Lemmon, R. T. Jacobsen, S. G. Penoncello and D. Friend. 'Thermodynamic properties of air and mixtures of nitrogen, argon, and oxygen from 60 to 2000 K at pressures to 2000 MPa'. In: *Journal of Physical and Chemical Reference Data* 29 (2000), pp. 331–385. DOI: 10.1063/1.1285884.

[143] V. Lemort, S. Declaye and S. Quoilin. 'Experimental characterization of a hermetic scroll expander for use in a micro-scale Rankine cycle'. In: *Proceedings of the Institution of Mechanical Engineers, Part A: Journal of Power and Energy* 226.1 (Nov. 2011), pp. 126–136. DOI: 10.1177/0957650911413840.

[144] V. Lemort and S. Quoilin. 'Designing scroll expanders for use in heat recovery Rankine cycles'. In: *Proceedings of the International Conference on Compressors and their Systems 2009*. London: Institution of Mechanical Engineers, Sept. 2009, pp. 3–12.

[145] V. Lemort, S. Quoilin, C. Cuevas and J. Lebrun. 'Testing and modeling a scroll expander integrated into an Organic Rankine Cycle'. In: *Applied Thermal Engineering* 29.14-15 (Oct. 2009), pp. 3094–3102. DOI: 10.1016/j.applthermaleng.2009.04.013.

[146] V. Lemort, S. Quoilin and J. Lebrun. 'Numerical Simulation of a Scroll Expander for Use in a Rankine Cycle'. In: *Proceedings of the International Compressor Engineering Conference at Purdue 2008*. Lafayette, Indiana, 2008.

[147] A. Lévêque. 'Les lois de la transmission de chaleur par convection'. In: *Annales des Mines ou Recueil de Mémoires sur l'Exploitation des Mines et sur les Sciences et les Arts qui s'y Rattachent* XIII.13 (1928), pp. 201–239.

[148] J. Li, G. Pei, Y. Li and J. Ji. 'Evaluation of external heat loss from a small-scale expander used in organic Rankine cycle'. In: *Applied Thermal Engineering* 31.14-15 (2011), pp. 2694–2701. DOI: 10.1016/j.applthermaleng.2011.04.039.

[149] J. Li, G. Pei, Y. Li, D. Wang and J. Ji. 'Energetic and exergetic investigation of an organic Rankine cycle at different heat source temperatures'. In: *Energy* 38.1 (Feb. 2012), pp. 85–95. DOI: 10.1016/j.energy.2011.12.032.

[150] G. A. Longo. 'Heat transfer and pressure drop during HFC refrigerant saturated vapour condensation inside a brazed plate heat exchanger'. In: *International Journal of Heat and Mass Transfer* 53.5–6 (Feb. 2010), pp. 1079–1087. DOI: 10.1016/j.ijheatmasstransfer.2009.11.003.

[151] G. A. Longo. 'Hydrocarbon Refrigerant Vaporization Inside a Brazed Plate Heat Exchanger'. In: *Journal of Heat Transfer* 134 (2012), pp. 101801–1–101801–10. DOI: 10.1115/1.4006817.

[152] G. A. Longo and A. Gasparella. 'HFC-410A vaporisation inside a commercial brazed plate heat exchanger'. In: *Experimental Thermal and Fluid Science* 32.1 (Oct. 2007), pp. 107–116. DOI: 10.1016/j.expthermflusci.2007.02.004.

[153] G. A. Longo and C. Zilio. 'Condensation of the low GWP refrigerant HFC1234yf inside a brazed plate heat exchanger'. In: *International Journal of Refrigeration* 36.2 (2013), pp. 612–621. DOI: 10.1016/j.ijrefrig.2012.12.018.

[154] B. Lorentzen. 'Power Plant Simulation'. PhD thesis. Laboratory for Energetics: Technical University of Denmark, 1995.

[155] M. Markussen, B. Elmegaard, T. S. Ommen, M. Brand and J. E. Thorsen. *Heat Pumps for Domestic Hot Water Preparation in Connection with Low Temperature District Heating*. Tech. rep. J. nr. 64011-0076. Energiteknologisk Udviklings- og Demonstrationsprogram (EUDP), 2013.

[156] D. W. Marquardt. 'An Algorithm for Least-Squares Estimation of Nonlinear Parameters'. In: *Journal of the Society for Industrial and Applied Mathematics* 11.2 (1963), pp. 431–441.

[157] H. Martin. 'A theoretical approach to predict the performance of chevron-type plate heat exchangers'. In: *Chemical Engineering and Processing: Process Intensification* 35.4 (1996), pp. 301–310. DOI: 10.1016/0255-2701(95)04129-X.

[158] H. Martin. 'The generalized Lévêque equation and its practical use for the prediction of heat and mass transfer rates from pressure drop'. In: *Chemical Engineering Science* 57.16 (2002), pp. 3217–3223. DOI: 10.1016/S0009-2509(02)00194-X.

[159] H. Martin. 'VDI Heat Atlas'. In: ed. by P. Stephan. 2nd. Berlin Heidelberg: Springer, 2010. Chap. N6 Pressure Drop and Heat Transfer in Plate Heat Exchangers, pp. 1515–1522. DOI: 10.1007/978-3-540-77877-6_109.

[160] R. Mathie, C. N. Markides and A. J. White. 'A Framework for the Analysis of Thermal Losses in Reciprocating Compressors and Expanders'. English. In: *Heat Transfer Engineering* 35.16-17 (2014), pp. 1435–1449. DOI: 10.1080/01457632.2014.889460.

[161] W. H. McAdams. *Heat Transmission*. 2nd. New York: McGraw-Hill, 1942.

[162] S. McKenna, G. McCullough and R. Douglas. 'Thermodynamic Modelling Of A Reciprocating Expander In An Organic Rankine Cycle'. In: *Proceedings of SEEP2012*. Dublin, Ireland, 2012, pp. 357–362.

[163] Å. Melinder. *Properties of Secondary Working Fluids for Indirect Systems*. International Institute of Refrigeration, 2010.

[164] K. Miyagawa and P. G. Hill. 'Rapid and accurate calculation of water and steam properties using the tabular taylor series expansion method'. English. In: *Journal of Engineering for Gas Turbines and Power* 123.3 (2001), pp. 707–712. DOI: 10.1115/1.1367340.

[165] *Modelica—A Unified Object-Oriented Language for Physical Systems Modeling*. Language Specification Version 3.2 Revision 2. Modelica Association. Linköping, Sweden, July 2013.

[166] A. Mohammadi and M. Yaghoubi. 'Estimation of instantaneous local heat transfer coefficient in spark-ignition engines'. In: *International Journal of Thermal Sciences* 49.7 (2010), pp. 1309–1317. DOI: 10.1016/j.ijthermalsci.2009.12.010.

[167] M. Mohd, N. Y. Tahir and T. Hoshino. 'Efficiency of Compact Organic Rankine Cycle System with Rotary-Vane-Type Expander for Low-Temperature Waste Heat Recovery'. In: *International Journal of Environmental Science And Engineering* 2.1 (2010), pp. 11–16.

[168] M. J. Moran, H. N. Shapiro, D. D. Boettner and M. B. Bailey. *Principles of Engineering Thermodynamics*. 7th edition. New York: Wiley, 2012.

[169] J. J. Moré, B. S. Garbow and K. E. Hillstrom. *User Guide for MINPACK-1*. Tech. rep. Report ANL-80-74. Argonne, USA: Argonne National Laboratory, 1980.

[170] A. Muley and R. M. Manglik. 'Experimental Study of Turbulent Flow Heat Transfer and Pressure Drop in a Plate Heat Exchanger With Chevron Plates'. In: *Journal of Heat Transfer* 121.1 (1999), pp. 110–117. DOI: 10.1115/1.2825923.

[171] W. Nusselt. 'Der Wärmeübergang in der Verbrennungskraftmaschine'. In: *Forschungsarbeiten auf dem Gebiete des Ingenieurwesens*. Vol. 264. Verlag des Vereines deutscher Ingenieure, Julius Springer, 1923.

[172] Open Source Modelica Consortium. *OpenModelica*. 2014.

[173] E. Oralli, M. A. Tarique, C. Zamfirescu and I. Dincer. 'A study on scroll compressor conversion into expander for Rankine cycles'. In: *International Journal of Low-Carbon Technologies* 6.3 (June 2011), pp. 200–206. DOI: 10.1093/ijlct/ctr008.

[174] M. S. Orosz. 'Geometric Design of Scroll Expanders Optimized for Small Organic Rankine Cycles'. In: *Journal of Engineering for Gas Turbines and Power* 135.4 (Mar. 2013), p. 042303. DOI: 10.1115/1.4023112.

[175] J.-F. Oudkerk, S. Quoilin, S. Declaye, L. Guillaume, E. Winandy and V. Lemort. 'Evaluation of the Energy Performance of an Organic Rankine Cycle-Based Micro Combined Heat and Power System Involving a Hermetic Scroll Expander'. In: *Journal of Engineering for Gas Turbines and Power* 135.4 (Mar. 2013), p. 042306. DOI: 10.1115/1.4023116.

[176] B. Palm and J. Claesson. 'Plate heat exchangers: Calculation methods for single and two-phase flow'. In: *Heat Transfer Engineering* 27.4 (2006), pp. 88–98. DOI: 10.1080/01457630500523949.

[177] A. I. Papadopoulos, M. Stijepovic and P. Linke. 'On the systematic design and selection of optimal working fluids for Organic Rankine Cycles'. In: *Applied Thermal Engineering* 30.6-7 (May 2010), pp. 760–769. DOI: 10.1016/j.applthermaleng.2009.12.006.

[178] A. I. Papadopoulos, M. Stijepovic, P. Linke, P. Seferlis and S. Voutetakis. 'Toward Optimum Working Fluid Mixtures for Organic Rankine Cycles using Molecular Design and Sensitivity Analysis'. In: *Industrial & Engineering Chemistry Research* 52.34 (2013), pp. 12116–12133. DOI: 10.1021/ie400968j.

[179] J. Pátek and J. Klomfar. 'A computationally effective formulation of the thermodynamic properties of LiBr-H2O solutions from 273 to 500 K over full composition range'. In: *International Journal of Refrigeration* 29.4 (2006), pp. 566–578. DOI: 10.1016/j.ijrefrig.2005.10.007.

[180] J. Pátek and J. Klomfar. 'A simple formulation for thermodynamic properties of steam from 273 to 523 K, explicit in temperature and pressure'. In: *International Journal of Refrigeration* 32.5 (2009), pp. 1123–1125. DOI: 10.1016/j.ijrefrig.2008.12.010.

[181] J. Pátek and J. Klomfar. 'Simple functions for fast calculations of selected thermodynamic properties of the ammonia-water system'. In: *International Journal of Refrigeration* 18.4 (1995), pp. 228–234. DOI: 10.1016/0140-7007(95)00006-W.

[182] J. Pátek and J. Klomfar. 'Solid-liquid phase equilibrium in the systems of LiBr-H2O and LiCl-H2O'. In: *Fluid Phase Equilibria* 250.1–2 (2006), pp. 138–149. DOI: 10.1016/j.fluid.2006.09.005.

[183] J. Pátek and J. Klomfar. 'Thermodynamic properties of the LiCl-H2O system at vapor-liquid equilibrium from 273 K to 400 K'. In: *International Journal of Refrigeration* 31.2 (2008), pp. 287–303. DOI: 10.1016/j.ijrefrig.2007.05.003.

[184] G. Pei, J. Li, Y. Li, D. Wang and J. Ji. 'Construction and dynamic test of a small-scale organic rankine cycle'. In: *Energy* 36.5 (May 2011), pp. 3215–3223. DOI: 10.1016/j.energy.2011.03.010.

[185] L. Pierobon, J. Wronski, I. H. Bell, F. Haglind and B. Elmegaard. 'DNA–an integrated open-source optimization platform for thermofluid systems'. In: *Proceedings of the 55th Conference on Simulation and Modelling (SIMS 55)*. Ed. by A. R. Kolai, K. Sørensen and M. P. Nielsen. Aalborg, Denmark: Linköping University Press, 2014, pp. 197–210.

[186] D. Pinkernell and M. Bargende. 'Handbook of Diesel Engines'. In: ed. by K. Mollenhauer and H. Tschoeke. Berlin: Springer, 2010. Chap. 7 Engine Component Loading, pp. 195–220. DOI: 10.1007/978-3-540-89083-6_1.

[187] M. J. D. Powell. 'An efficient method for finding the minimum of a function of several variables without calculating derivatives'. In: *The Computer Journal* 7.2 (1964), pp. 155–162.

[188] B. G. S. S. Prasad. 'Heat Transfer in Reciprocating Compressors—A Review'. In: *Proceedings of the International Compressor Engineering Conference*. Paper 1349. 1998, pp. 857–863.

[189] W. H. Press, S. A. Teukolsky and W. T. Vetterling. *Numerical recipes in C: The art of scientific computing*. 2nd edition. Cambridge University Press, 1999.

[190] J. Pye, S. Muratet, K. Chittur, H. Ke, R. Towers, S. Ranganadham et al. *FPROPS*. 2014.

[191] H. Qiao, V. Aute, H. Lee, K. Saleh and R. Radermacher. 'A new model for plate heat exchangers with generalized flow configurations and phase change'. In: *International Journal of Refrigeration* 36.2 (2013), pp. 622–632. DOI: 10.1016/j.ijrefrig.2012.11.020.

[192] G. Qiu. 'Selection of working fluids for micro-CHP systems with ORC'. In: *Renewable Energy* 48 (Dec. 2012), pp. 565–570. DOI: 10.1016/j.renene.2012.06.006.

[193] G. Qiu, H. Liu and S. Riffat. 'Expanders for micro-CHP systems with organic Rankine cycle'. In: *Applied Thermal Engineering* 31.16 (Nov. 2011), pp. 3301–3307. DOI: 10.1016/j.applthermaleng.2011.06.008.

[194] G. Qiu, Y. Shao, J. Li, H. Liu and S. B. Riffat. 'Experimental investigation of a biomass-fired ORC-based micro-CHP for domestic applications'. In: *Fuel* 96.January (June 2012), pp. 374–382. DOI: 10.1016/j.fuel.2012.01.028.

[195] S. Quoilin. 'Sustainable energy conversion through the use of Organic Rankine Cycles for waste heat recovery and solar applications'. en. PhD thesis. University of Liège, Oct. 2011, pp. 1–183.

[196] S. Quoilin, I. Bell, A. Desideri, P. Dewallef and V. Lemort. 'Methods to Increase the Robustness of Finite-Volume Flow Models in Thermodynamic Systems'. In: *Energies* 7 (2014), pp. 1621–1640. DOI: 10.3390/en7031621.

[197] S. Quoilin, M. V. D. Broek, S. Declaye, P. Dewallef and V. Lemort. 'Techno-economic survey of Organic Rankine Cycle (ORC) systems'. In: *Renewable and Sustainable Energy Reviews* 22 (June 2013), pp. 168–186. DOI: 10.1016/j.rser.2013.01.028.

[198] S. Quoilin, S. Declaye, A. Legros, L. Guillaume and V. Lemort. 'Working fluid selection and operating maps for Organic Rankine Cycle expansion machines'. In: *Proceedings of the 21st International Compressor Conference at Purdue*. 2012.

[199] S. Quoilin, A. Desideri, J. Wronski, I. H. Bell and V. Lemort. 'ThermoCycle: A Modelica library for the simulation of thermodynamic systems'. In: *Proceedings of the 10th International Modelica Conference*. Lund, Sweden: Modelica Association, 2014.

[200] C. C. Richter. 'Proposal of New Object-Oriented Equation-Based Model Libraries for Thermodynamic Systems'. PhD thesis. Technical University Carolo-Wilhelmina Braunschweig, 2008.

[201] M. Richter, M. O. McLinden and E. W. Lemmon. 'Thermodynamic Properties of 2,3,3,3-Tetrafluoroprop-1-ene (R1234yf): Vapor Pressure and p-rho-T Measurements and an Equation of State'. In: *Journal of Chemical and Engineering Data* 56.7 (2011), pp. 3254–3264. DOI: 10.1021/je200369m.

[202] B. Saleh, G. Koglbauer, M. Wendland and J. Fischer. 'Working fluids for low-temperature organic Rankine cycles'. In: *Energy* 32.7 (July 2007), pp. 1210–1221. DOI: 10.1016/j.energy.2006.07.001.

[203] S. Schimpf and R. Span. 'Simulation of a solar assisted combined heat pump-Organic rankine cycle system'. In: *Energy Conversion and Management* (2015). DOI: 10.1016/j.enconman.2015.01.083.

[204] S. Schimpf and R. Span. 'Techno-economic evaluation of a solar assisted combined heat pump-Organic Rankine Cycle system'. In: *Energy Conversion and Management* 94 (2015), pp. 430–437. DOI: 10.1016/j.enconman.2015.02.011.

[205] C. Schulze. 'A Contribution to Numerically Efficient Modelling of Thermodynamic Systems'. PhD thesis. Technical University Carolo-Wilhelmina Braunschweig, 2013.

[206] C. Schulze, M. Gräber and W. Tegethoff. 'A limiter for preventing singularity in simplified finite volume methods'. In: *Mathematical Modelling*. Vol. 7. 1. 2012, pp. 1095–1100.

[207] C. Schulze and J. Köhler. 'Spline Based Interpolation Of The Two Phase Region Of Binary Mixtures Using Multiparameter Equations Of State'. In: *Proceedings of the 4th IIR Conference on Thermophysical Properties and Transfer Processes of Refrigerants*. Delft, The Netherlands, 2013.

[208] Scientific Computing Department and UK Science and Technology Facilities Council. *HSL – A collection of Fortran codes for large scale scientific computation*. 2013.

[209] M. M. Shah. 'Chart Correlation For Saturated Boiling Heat Transfer: Equations And Further Study'. In: *ASHRAE Transactions* 88 (1982), pp. 185–196.

[210] M. J. Skovrup. *SecCool Properties v1.33*. IPU Refrigeration and Energy Technology. 2013.

[211] M. J. Skovrup. *Thermodynamic and Thermophysical Properties of Refrigerants – Package in Borland Delphi for the refrigerants*. Tech. rep. Version 3.10. Technical University of Denmark, Oct. 2001.

[212] I. K. Smith and R. Pitanga Marques da Silva. 'Development of the trilateral flash cycle system. Part 2: Increasing power output with working fluid mixtures'. In: *Proceedings of the Institution of Mechanical Engineers, Part A: Journal of Power and Energy* 208.2 (1994), pp. 135–144.

[213] I. K. Smith, N. Stosic and C. A. Aldis. 'Development of the trilateral flash cycle system Part 3: the design of high-efficiency two-phase screw expanders'. In: *Proceedings of the Institution of Mechanical Engineers, Part A: Journal of Power and Energy* 210.1 (1996), pp. 75–93.

[214] I. K. Smith and N. Stosic. 'Prospects for Energy Conversion Efficiency Improvements by the use of Twin Screw Two-Phase Expanders'. In: *Centre for Positive Displacement Compressor Technology*. Vol. 35263. 2002.

[215] H. S. Soyhan, H. Yasar, H. Walmsley, B. Head, G. T. Kalghatgi and C. Sorusbay. 'Evaluation of heat transfer correlations for HCCI engine modeling'. In: *Applied Thermal Engineering* 29.2-3 (2009), pp. 541–549. DOI: 10.1016/j.applthermaleng.2008.03.014.

[216] R. Span, T. Eckermann, J. Gernert, S. Herrig, A. Jäger and M. Thol. *TREND – Thermodynamic Reference and Engineering Data v1.1*. Lehrstuhl für Thermodynamik, Ruhr-Universität Bochum. 2014.

[217] R. Span and W. Wagner. 'A New Equation of State for Carbon Dioxide Covering the Fluid Region from the Triple Point Temperature to 1100 K at Pressures up to 800 MPa'. In: *Journal of Physical and Chemical Reference Data* 25.6 (1996), pp. 1509–1596. DOI: 10.1063/1.555991.

[218] R. Span, W. Wagner, E. W. Lemmon and R. T. Jacobsen. 'Multiparameter equations of state—recent trends and future challenges'. English. In: *Fluid Phase Equilibria* 183 (2001), pp. 1–20.

[219] R. Span and W. Wagner. 'Equations of State for Technical Applications. II. Results for Nonpolar Fluids'. In: *International Journal of Thermophysics* 24.1 (2003), pp. 41–109.

[220] R. Span. *Multiparameter equations of state : an accurate source of thermodynamic property data*. Berlin: Springer, 2000. DOI: 10.1007/978-3-662-04092-8.

[221] M. Steffen, M. Löffler and K. Schabera. 'Efficiency of a new Triangle Cycle with flash evaporation in a piston engine'. In: *Energy* 57 (2013), pp. 295–307. DOI: 10.1016/j.energy.2012.11.054.

[222] F. A. Al-Sulaiman, F. Hamdullahpur and I. Dincer. 'Trigeneration: A comprehensive review based on prime movers'. In: *International Journal of Energy Research* 35.3 (Mar. 2011), pp. 233–258. DOI: 10.1002/er.1687.

[223] SWEP International AB. *Installation and Maintenance Manual for BPHEs*. 2013.

[224] SWEP International AB. *Technical Information on B8T*. http://www.swep.net/en/products_solutions/productfinder/Pages/B8T.aspx. [Online; accessed 2015-5-9].

[225] F. Táboas, M. Vallès, M. Bourouis and A. Coronas. 'Assessment of boiling heat transfer and pressure drop correlations of ammonia/water mixture in a plate heat exchanger'. In: *International Journal of Refrigeration* 35.3 (2012). Refrigeration and Heat Pumping with Sorption Processes, pp. 633–644. DOI: 10.1016/j.ijrefrig.2011.10.003.

[226] F. Táboas, M. Vallès, M. Bourouis and A. Coronas. 'Flow boiling heat transfer of ammonia/water mixture in a plate heat exchanger'. In: *International Journal of Refrigeration* 33.4 (June 2010), pp. 695–705. DOI: 10.1016/j.ijrefrig.2009.12.005.

[227] B. F. Tchanche, G. Lambrinos, A. Frangoudakis and G. Papadakis. 'Low-grade heat conversion into power using organic Rankine cycles – A review of various applications'. In: *Renewable and Sustainable Energy Reviews* 15.8 (Oct. 2011), pp. 3963–3979. DOI: 10.1016/j.rser.2011.07.024.

[228] *Technical Data Sheet*. The Dow Chemical Company. 1997.

[229] *Technical Data Sheet*. Chevron Products Company. 2004.

[230] W. Tegethoff, C. Schulze, M. Gräber, M. Huhn, N. Stulgies, C. Kaiser et al. *TEMO–Thermische Echtzeitfähige Modelle*. Tech. rep. 01IS08013A, 01IS08013B, 01IS08013C. TLK-Thermo GmbH, TU Braunschweig, TU Clausthal, 2011.

[231] The MathWorks. *Matlab R2013b*. 2013.

[232] *Therminol Heat Transfer Reference Disk v5.1*. Eastman Chemical Company. 2014.

[233] B. Thonon and A. Bontemps. 'Condensation of Pure and Mixture of Hydrocarbons in a Compact Heat Exchanger: Experiments and Modelling'. In: *Heat Transfer Engineering* 23.6 (2002), pp. 3–17. DOI: 10.1080/01457630290098718.

[234] B. Thonon, A. Feldman, L. Margat and C. Marvillet. 'Transition from nucleate boiling to convective boiling in compact heat exchangers'. In: *International journal of refrigeration* 20.8 (1997), pp. 592–597. DOI: 10.1016/S0140-7007(97)00049-2.

[235] B. Thonon, R. Vidil and C. Marvillet. 'Recent research and developments in plate heat exchangers'. In: *Journal of Enhanced Heat Transfer* 2.1-2 (1995), pp. 149–155. DOI: 10.1615/JEnhHeatTransf.v2.i1-2.160.

[236] M. Thorade. *HelmholtzMedia – A fluid properties library*. 2014.

[237] M. Thorade. 'Entropy-based assessment criteria for the heat transfer in power cycles theiAnwendungen for practical applications (in German: Entropiebasierte Bewertungskriterien für den Wärmeübergang in Kraftwerksprozessen und ihre Relevanz für praktische Anwendungen)'. PhD thesis. Department of Mechanical Engineering, Hamburg University of Technology, 2014. DOI: 10.15480/882.1207.

[238] M. Thorade and A. Saadat. 'Partial derivatives of thermodynamic state properties for dynamic simulation'. In: *Environmental Earth Sciences* 70.8 (Apr. 2013), pp. 3497–3503. DOI: 10.1007/s12665-013-2394-z.

[239] R. Tillner-Roth and H. D. Baehr. 'A International Standard Formulation for the Thermodynamic Properties of 1,1,1,2-Tetrafluoroethane (HFC-134a) for Temperatures from 170 K to 455 K and Pressures up to 70 MPa'. In: *Journal of Physical and Chemical Reference Data* 23 (1994), pp. 657–729. DOI: 10.1063/1.555958.

[240] R. Tillner-Roth, F. Harms-Watzenberg and H. D. Baehr. 'Eine neue Fundamentalgleichung fur Ammoniak (A new Fundamental Equation of State for Ammonia, in German)'. In: *Tagungsband Deutscher Kälte- und Klimatechnischer Verein*. 1993.

[241] TLK Thermo GmbH. *TIL Media Suite*. 2014.

[242] H. Tummescheit, J. Eborn, F. J. Wagner, M. Otter, M. Tiller, H. Elmqvist et al. *Modelica.Media v3.1*. Modelica Association. 2013.

[243] B. Twomey, P. A. Jacobs and H. Gurgenci. 'Dynamic performance estimation of small-scale solar cogeneration with an organic Rankine cycle using a scroll expander'. In: *Applied Thermal Engineering* 51.1–2 (2013), pp. 1307–1316. DOI: 10.1016/j.applthermaleng.2012.06.054.

[244] F. Vélez, J. J. Segovia, M. C. Martín, G. Antolín, F. Chejne and A. Quijano. 'A technical, economical and market review of organic Rankine cycles for the conversion of low-grade heat for power generation'. In: *Renewable and Sustainable Energy Reviews* 16.6 (Aug. 2012), pp. 4175–4189. DOI: 10.1016/j.rser.2012.03.022.

[245] R. A. Victor, J.-K. Kim and R. Smith. 'Composition optimisation of working fluids for Organic Rankine Cycles and Kalina cycles'. In: *Energy* 55 (2013), pp. 114–126. DOI: 10.1016/j.energy.2013.03.069.

[246] W. Wagner and A. Pruss. 'The IAPWS Formulation 1995 for the Thermodynamic Properties of Ordinary Water Substance for General and Scientific Use'. In: *Journal of Physical and Chemical Reference Data* 31 (2002), pp. 387–535. DOI: 10.1063/1.1461829.

[247] G. Wang and S. P. Vanka. 'Convective heat transfer in periodic wavy passages'. In: *International Journal of Heat and Mass Transfer* 38.17 (1995), pp. 3219–3230. DOI: 10.1016/0017-9310(95)00051-A.

[248] H. Wang, R. B. Peterson, K. Harada, E. Miller, R. Ingram-Goble, L. Fisher et al. 'Performance of a combined organic Rankine cycle and vapor compression cycle for heat activated cooling'. In: *Energy* 36.1 (Jan. 2011), pp. 447–458. DOI: 10.1016/j.energy.2010.10.020.

[249] J. Wang. 'Pressure drop and flow distribution in parallel-channel configurations of fuel cells: U-type arrangement'. In: *International Journal of Hydrogen Energy* 33.21 (2008), pp. 6339–6350. DOI: 10.1016/j.ijhydene.2008.08.020.

[250] J. Wang. 'Pressure drop and flow distribution in parallel-channel configurations of fuel cells: Z-type arrangement'. In: *International Journal of Hydrogen Energy* 35.11 (2010). 3rd Argentinean and 2nd Latin American Congress inHydrogen and Sustainable Energy Sources 3rd Argentinean and 2nd Latin American Congress inHydrogen and Sustainable Energy Sources, pp. 5498–5509. DOI: 10.1016/j.ijhydene.2010.02.131.

[251] T. Wang, Y. Zhang, Z. Peng and G. Shu. 'A review of researches on thermal exhaust heat recovery with Rankine cycle'. In: *Renewable and Sustainable Energy Reviews* 15.6 (2011), pp. 2862–2871. DOI: 10.1016/j.rser.2011.03.015.

[252] Z. G. Wang, S. He, J. X. Li and G. J. Song. 'Modeling and Testing a Screw Expander Integrated into a Trilateral Flash Cycle'. In: *Advanced Materials Research* 383-390 (Nov. 2011), pp. 727–733. DOI: 10.4028/www.scientific.net/AMR.383-390.727.

[253] K. Watanabe and R. B. Dooley. *Guideline on the Tabular Taylor Series Expansion (TTSE) Method for Calculation of Thermodynamic Properties of Water and Steam Applied to IAPWS-95 as an Example*. Tech. rep. Vejle, Denmark: The International Association for the Properties of Water and Steam, Aug. 2003.

[254] W. C. Williams. 'If the Dittus and Boelter equation is really the McAdams equation, then should not the McAdams equation really be the Koo equation?' In: *International Journal of Heat and Mass Transfer* 54.7-8 (2010), pp. 1682–1683.

[255] R. H. S. Winterton. 'Where did the Dittus and Boelter equation come from?' In: *International Journal of Heat and Mass Transfer* 41.2-3 (1998), pp. 809–810.

[256] G. Woschni. *A Universally Applicable Equation for the Instantaneous Heat Transfer Coefficient in the Internal Combustion Engine*. Technical Paper 670931. Society of Automotive Engineers (SAE), Feb. 1967. DOI: 10.4271/670931.

[257] J. Wronski, J. F. Oudkerk and F. Haglind. 'Reciprocating Expanders for Small-scale Organic Rankine Cycles—Part B: Variable Valve Timing and Cogeneration'. In: *submitted* (2015).

[258] J. Wronski, M. J. Skovrup, B. Elmegaard, H. N. Rislå and F. Haglind. 'Design and Modelling of a Novel Compact Power Cycle for Low Temperature Heat Sources'. In: *Proceedings of ECOS 2012*. Ed. by U. Desideri, G. Manfrida and E. Sciubba. Perugia, Italy: Firenze University Press, June 2012.

[259] J. Wronski, M. J. Skovrup and F. Haglind. 'Reciprocating Expanders for Small-scale Organic Rankine Cycles—Part A: Modelling and Experiments'. In: *submitted* (2015).

[260] R. Würfel and N. Ostrowski. 'Experimental investigations of heat transfer and pressure drop during the condensation process within plate heat exchangers of the herringbone-type'. In: *International Journal of thermal sciences* 43.1 (2004), pp. 59–68. DOI: 10.1016/S1290-0729(03)00099-1.

[261] Y. Yan and T. Lin. 'Evaporation heat transfer and pressure drop of refrigerant R-134a in a plate heat exchanger'. English. In: *Journal of Heat Transfer* 121.1 (1999), pp. 118–127. DOI: 10.1115/1.2825924.

[262] Y. Yan, H. Lio and T. Lin. 'Condensation heat transfer and pressure drop of refrigerant R-134a in a plate heat exchanger'. English. In: *International Journal of Heat and Mass Transfer* 42.6 (1999), pp. 993–1006. DOI: 10.1016/S0017-9310(98)00217-8.

[263] B. A. Younglove. 'An International Standard Equation of State for the Thermodynamic Properties of Refrigerant 123 (2,2-Dichloro-1,1,1-Trifluoroethane)'. In: *Journal of Physical and Chemical Reference Data* 23.5 (1994), pp. 731–779. DOI: 10.1063/1.555950.

[264] H. G. Zhang, H. Liang, X. Liu, B. Liu, Y. Chen, Y. T. Wu et al. 'Research of Two Stage Single Screw Expander Organic Rankine Cycle System Scheme Based on the Waste Heat Recovery of Diesel Engine's Exhaust Gas'. In: *Advanced Materials Research* 201-203 (Feb. 2011), pp. 600–605. DOI: 10.4028/www.scientific.net/AMR.201-203.600.

[265] D. Ziviani, A. Beyene and M. Venturini. 'Design, Analysis and Optimization of a Micro-CHP System Based on Organic Rankine Cycle for Ultralow Grade Thermal Energy Recovery.' In: *Journal of Energy Resources Technology* 136.1 (2014), p. 1.

List of Symbols

Throughout this work, variables are printed in italics, and vectors and matrices are written in bold face italics: a (index or superscript), a (variable), $\boldsymbol{a}$ (vector). Furthermore, dots above letters denote a derivative with respect to time: thermal energy Q becomes the heat flow rate $\dot{Q}$.

Acronyms

1D one-dimensional.

2D two-dimensional.

3D three-dimensional.

4D four-dimensional.

air a mixture of N_2, O_2 and Ar or R729 [142].

NH_3 ammonia [240].

AV active valve control.

AVL AVL Schrick GmbH, Remscheid, Germany.

BDC bottom dead centre.

BLAS Basic Linear Algebra Subprograms [132].

BPHE brazed plate heat exchanger.

n-butane C_4H_{10} or R600 [41].

C two-phase heat transfer model by Cooper [52, 53].

CHP combined heat and power.

CIA Central Intelligence Agency of the United States of America.

CO_2 carbon dioxide or R744 [217].

CoolProp CoolProp fluid property database version 5.0.8.

c-pentane C_5H_{10} or cyclopentane [85].

cRIO National Instruments CompactRIO controller.

DB single-phase heat transfer model by Dittus and Boelter [67].

desktop computer stationary computer running a 64 bit Debian system with Linux kernel 3.16.0, 8 GiB DDR2 memory at 800 MHz and an Intel Core2 Quad CPU Q6600 with 8 MiB L2 cache operating at 2.4 GHz.

DHW domestic hot water.

DNA Dynamic Network Analysis [77].

Dowtherm Q oil-based heat transfer fluid by The Dow Chemical Company [228].

DTU Technical University of Denmark, Department of Mechanical Engineering, Kgs. Lyngby, Denmark.

EES Engineering Equation Solver [123].

EOS equation of state.

FV30 fixed valve control for 30 °C.

FV50 fixed valve control for 50 °C.

FV70 fixed valve control for 70 °C.

G single-phase heat transfer model by Gnielinski [90].

GDP gross domestic product.

GERG Groupe Européen de Recherches Gazières.

GW two-phase heat transfer model by Gungor and Winterton [94].

HFE7000 1-methoxyheptafluoropropane or $C_3F_7OCH_3$.

HSL Harwell Subroutine Library [208].

HTC heat transfer coefficient.

IAPWS International Association for the Properties of Water and Steam.

IPU IPU, Kongens Lyngby, Denmark.

isobutane C_4H_{10} or R600a [41].

isopentane C_5H_{12} or R601a [141].

LAPACK Linear Algebra Package [6].

laptop portable computer running a 32 bit Debian system with Linux kernel 3.16.7, 4 GiB DDR3 memory at 1333 MHz and an Intel Core i5-2520M with 3 MiB cache operating at 2.5 GHz.

LiBr (aq) aqueous lithium bromide solution [179].

LiCl (aq) aqueous lithium chloride solution [183].

Linux system with Linux kernel and GNU tools.

MA single-phase heat transfer model by Martin [159].

MDM octamethyltrisiloxane or $C_8H_{24}O_2Si_3$ [50].

MM single-phase heat transfer model by Muley and Manglik [170].

nD multi-dimensional.

NH_3 (aq) aqueous ammonia solution [181].

NIST National Institute of Standards and Technology of the United States of America.

ORC organic Rankine cycle.

OS X Apple Macintosh operating system.

n-pentane C_5H_{12} or R601 [219].

PHE plate heat exchanger.

n-propane C_3H_8 or R290 [140].

propene propylene, C_3H_6 or R1270 [137].

R123 $C_2Cl_2F_3H_1$ [263].

R1234yf 2,3,3,3-tetrafluoroprop-1-ene or $C_3H_2F_4$ [201].

R134a 1,1,1,2-tetrafluoroethane or CH_2FCF_3 [239].

R152a 1,1-difluoroethane or $C_2H_4F_2$.

R22 chlorodifluoromethane or $CHClF_2$ [115].

R245fa 1,1,1,3,3-pentafluoropropane or $C_3F_5H_3$ [3].

R407c a blend of R32, R125 and R134a.

R410A a mixture of R32 and R125 [138].

REFPROP REFPROP fluid property database [135] version 9.1.

RMS root-mean-square of a difference of two values.

S two-phase heat transfer model by Shah [209].

SH space heating.

SI units International System of Units from French 'Le Système International d'Unités'.

sp single-phase.

SSP G7 SSP G7 heat transfer calculation software version 7.0.3.

SWEP SWEP International AB, Landskrona, Sweden.

TDC top dead centre.

Texatherm 22 oil-based heat transfer fluid by Chevron [229].

Therminol 72 oil-based heat transfer fluid by Eastman Chemical Company [232].

ThermoCycle ThermoCycle Modelica library [199].

toluene C_7H_8 [141].

tp two-phase.

TREND Thermodynamic Reference and Engineering Data [216] version 1.1.

TTSE Tabular Taylor Series Expansion[164, 253].

U.S. United States of America.

UK United Kingdom.

ULg University of Liège, Thermodynamics Laboratory, Liège, Belgium.

UML Unified Modelling Language.

VHE Viking Heat Engines AS, Kristiansand Norway.

water H_2O or R718 [246].

Windows Microsoft Windows operating system.

Roman Letters

a relative valve lift or speed of sound, m/s.

A area, m^2.

$\hat{a}$ corrugation amplitude, m.

c specific heat capacity, $J/(kg\,K)$.

C a coefficient.

$\boldsymbol{C}$ a coefficient matrix.

d thickness or diameter, m.

f specific Helmholtz energy, J/kg.

F force, N.

g gravitational acceleration, $9.806\,65\,kg\,m/s^2$.

G mass flux, kg/m^2.

h specific enthalpy, J/kg.

H enthalpy, J.

k expansion coefficient.

K nusselt number correction factor.

l thickness or length, m.

m mass, kg.

M molar mass in kg/mol or torque in N m.

N number of items.

p pressure, Pa.

q specific heat or thermal energy, J/kg.

Q heat or thermal energy, J.

R heat transfer resistance, K/W.

R_m molar gas constant, 8.314 46 J/(mol K).

R_p peak surface roughness, m.

R_s specific gas constant, J/(kg K), $R_\mathrm{s} = R_\mathrm{m}/M$.

s specific entropy, J/(kg K).

S entropy, J.

t time, s.

T temperature, K.

u specific internal energy, J/kg.

U internal energy, J.

UA total heat transfer coefficient, W/K.

v specific volume, m^3/kg.

V volume, m^3.

VC volumetric performance indicator, $\dot{V}_\mathrm{in}/\dot{W}$.

$\boldsymbol{V}$ Vandermonde matrix, $\boldsymbol{V}(x)_{i,j} = x_i^{j-1}$ or $\boldsymbol{V}(x)_j = \boldsymbol{x}^{j-1}$.

$\boldsymbol{V}_2$ 2D Vandermonde matrix, $\boldsymbol{V}_2(x, y)_{i,j} = x^{i-1}, y^{j-1}$.

w specific work or mechanical energy, J/kg.

W work or mechanical energy, J.

w flow velocity, m/s.

x differential ratio factor.

X wave number, Lockhart-Martinelli parameter.

$\boldsymbol{X}$ composition vector.

x enthalpy-based vapour fraction.

Y nozzle flow expansion factor.

Greek Letters

α reduced Helmholtz energy, $\alpha = f/(RT)$.

$\bar{\alpha}$ heat transfer coefficient, $\mathrm{W/(m^2\,K)}$.

$\widetilde{\alpha}$ thermal diffusivity, $\mathrm{m^2/s}$.

δ gap size in m and reduced density, $\delta = \rho/\rho_\mathrm{r} = \nu_\mathrm{r}/\nu$.

Δ difference.

ϵ absolute error of another variable, like ϵ_x.

η efficiency.

Γ characteristic length, m.

κ isothermal compressibility, 1/Pa.

λ thermal conductivity, $\mathrm{W/(m\,K)}$.

Λ characteristic velocity, m/s.

μ dynamic viscosity, Pa s.

ω rotational speed, rpm.

ϕ chevron angle, °.

Φ surface enhancement factor.

π circumference to diameter ratio of a circle, 3.141 59….

Π pressure ratio.

ψ ratio of two-phase to single-phase heat transfer coefficient and relative crank angle position.

ρ density, kg/m^3.

τ reciprocal reduced temperature, $\tau = T_r/T$.

θ crankshaft angle.

Υ expansion ratio.

ξ friction coefficient.

ζ flow friction coefficient.

Subscripts and Superscripts

act valve actuation angle.

amb at ambient conditions.

avg average value.

base central value for centred fits.

bs referring to bubble suppression.

cb referring to convective boiling.

close valve closing.

co heat exchanger plate corrugation.

cold cold stream or side.

con at the condenser.

cr referring to the crankshaft.

crit property the value at the critical point.

cut cutoff angle.

cyl inside the cylinder.

e equivalent.

el electricity-based.

eva at the evaporator.

ex exit or exhaust.

exp experiment related.

f referring to the working fluid.

fr friction related.

g referring to the gaseous phase.

h isenthalpic.

hot hot stream or side.

hx referring to the whole heat exchanger or heat exchange process.

hyd hydraulic, based on wetted perimeter.

in at the inlet.

∞ distant ambient property.

l referring to the liquid phase.

lam laminar.

leak leakage flow.

lm logarithmic.

max maximum value.

min minimum value.

nb referring to nucleate boiling.

nom nominal value.

open valve opening.

out at the outlet.

p isobaric.

pi referring to the piston.

pump pumping process.

r reducing property, often the value at the critical point.

rec at the recuperator.

ref reference conditions, reference value.

rel relative value or position.

rev reversible.

ro referring to the piston connection rod.

s isentropic.

set setpoint value.

sf referring to the secondary fluid.

sim simulation related.

su suction or supply.

t at the throat of a nozzle.

T isothermal.

th thermal energy-based.

tp referring to the two-phase domain.

turb turbulent.

v isochoric.

w referring to the wall.

0 ideal contribution term as superscript and normalised value or initial value as subscript.

+ modified property.

″ saturated vapour quantity or flux value.

′ saturated liquid quantity.

r real or residual contribution term.

* reduced property.

Characteristic Numbers

Bo Boiling number .

Co Convection number .

Fr Froude number .

Hg Hagen number .

Nu Nusselt number .

Pe Peclet number .

Pr Prandtl number .

Re Reynolds number .

Appendix A

List of Publications

Articles

[2] I. H. Bell, J. Wronski, S. Quoillin and V. Lemort. 'Pure- and Pseudo-Pure Fluid Thermophysical Property Evaluation and the Open-Source Thermophysical Property Library CoolProp'. In: *Industrial & Engineering Chemistry Research* 53.6 (2014), pp. 2498–2508. DOI: 10.1021/ie4033999.

[5] U. Larsen, L. Pierobon, J. Wronski and F. Haglind. 'Multiple regression models for the prediction of the maximum obtainable thermal efficiency of organic Rankine cycles'. In: *Energy* 65 (2013). DOI: 10.1016/j.energy.2013.10.026.

[13] J. Wronski, J. F. Oudkerk and F. Haglind. 'Reciprocating Expanders for Small-scale Organic Rankine Cycles—Part B: Variable Valve Timing and Cogeneration'. In: *submitted* (2015).

[15] J. Wronski, M. J. Skovrup and F. Haglind. 'Reciprocating Expanders for Small-scale Organic Rankine Cycles—Part A: Modelling and Experiments'. In: *submitted* (2015).

Refereed Conferences

[1] I. H. Bell, S. Quoillin, J. Wronski and V. Lemort. 'Coolprop: An Open-source Reference-quality Thermophysical Property Library'. In: *ASME-ORC 2013 – 2nd International Seminar on ORC Power Systems*. 2013.

[3] L. Bennov, J. Wronski, W. B. Markussen and F. Haglind. 'Experimental And Numerical Analysis Of Brazed Plate Heat Exchangers For Organic Fluids'. In: *ASME-ORC 2013 – 2nd International Seminar on ORC Power Systems*. 2013.

[4] A. Desideri, B. Dechesne, J. Wronski, S. Quoilin and V. Lemort. 'Comparison of Moving Boundary and Finite-volume Heat Exchanger Models in the Modelica Language'. In: *Submitted to ASME ORC 2015 the 3rd International Seminar on ORC Power Systems*. Brussels, Belgium, 2015.

[6] L. Pierobon, J. Wronski, I. H. Bell, F. Haglind and B. Elmegaard. 'DNA–an integrated open-source optimization platform for thermofluid systems'. In: *Proceedings of the 55th Conference on Simulation and Modelling (SIMS 55)*. Ed. by A. R. Kolai, K. Sørensen and M. P. Nielsen. Aalborg, Denmark: Linköping University Press, 2014, pp. 197–210.

[7] S. Quoilin, A. Desideri, I. H. Bell, J. Wronski and V. Lemort. 'Robust And Computationally Efficient Dynamic Simulation Of ORC Systems: The Thermocycle Modelica Library'. In: *ASME-ORC 2013 – 2nd International Seminar on ORC Power Systems*. 2013.

[8] S. Quoilin, A. Desideri, J. Wronski, I. H. Bell and V. Lemort. 'ThermoCycle: A Modelica library for the simulation of thermodynamic systems'. In: *Proceedings of the 10th International Modelica Conference*. Lund, Sweden: Modelica Association, 2014.

[9] A. Tafone, J. Wronski, A. D. Pascale and L. Branchini. 'Theoretical Investigation On Advanced ORCs'. In: *ASME-ORC 2013 – 2nd International Seminar on ORC Power Systems*. 2013.

[10] J. Wronski and K. Fredslund. 'Developing a New Expander'. In: *International Symposium on Advanced Waste Heat Valorisation Technologies*. Ed. by B. Vanslambrouck and M. van den Broek. 13–14th September 2012, Kortrijk, Belgium: Howest-Ghent University Association, 2012.

[11] J. Wronski, T. S. Ommen, W. B. Markussen and F. Haglind. 'Numerical and Experimental Analysis of Brazed Plate Heat Exchangers for Evaporators in Small-scale Organic Rankine Cycle Units'. In: *Submitted to ASME ORC 2015 the 3rd International Seminar on ORC Power Systems*. Brussels, Belgium, 2015.

[12] J. Wronski, J. F. Oudkerk and F. Haglind. 'Modelling Of A Small Scale Reciprocating ORC Expander For Cogeneration Applications'. In: *ASME-ORC 2013 – 2nd International Seminar on ORC Power Systems*. 2013.

[14] J. Wronski, M. J. Skovrup, B. Elmegaard, H. N. Rislå and F. Haglind. 'Design and Modelling of a Novel Compact Power Cycle for Low Temperature Heat Sources'. In: *Proceedings of ECOS 2012*. Ed. by U. Desideri, G. Manfrida and E. Sciubba. Perugia, Italy: Firenze University Press, June 2012.

Appendix B

Computational Performance

B.1 Average Execution Time

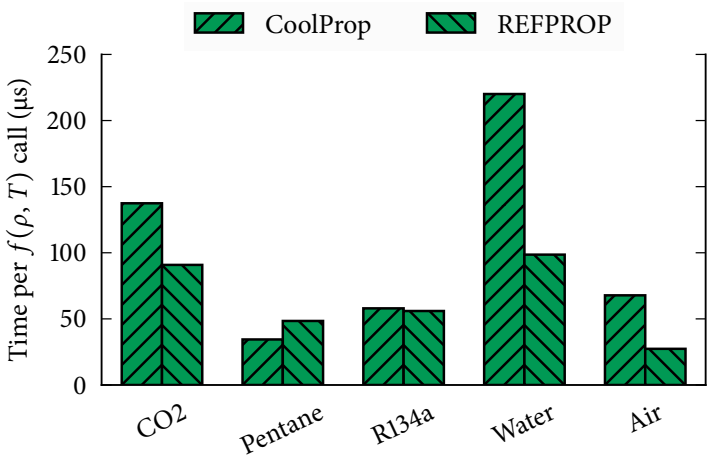

Figure B.1: Average execution times of calls to $f(\rho, T)$ using different fluids from CoolProp and REFPROP.

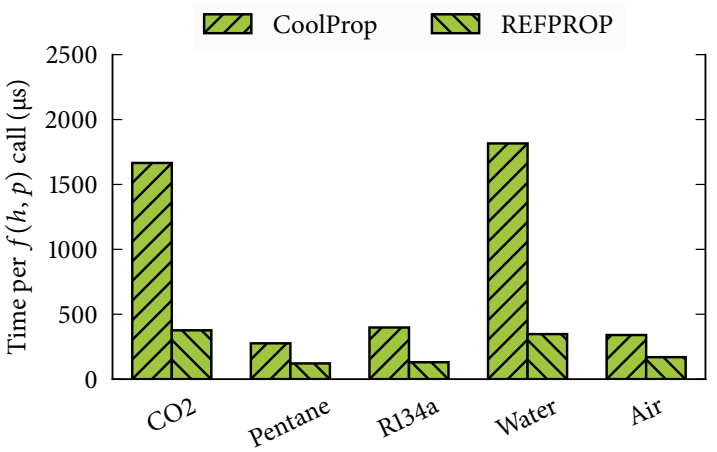

Figure B.2: Average execution times of calls to $f(h,p)$ using different fluids from CoolProp and REFPROP.

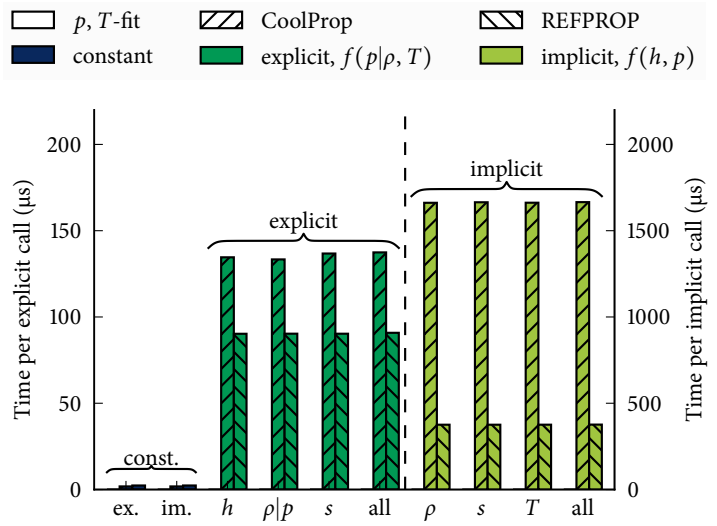

Figure B.3: Average execution times of calls to get the constant $T_{\max}$, $f(\rho,T)$ and $f(h,p)$ for CO_2 from CoolProp and REFPROP.

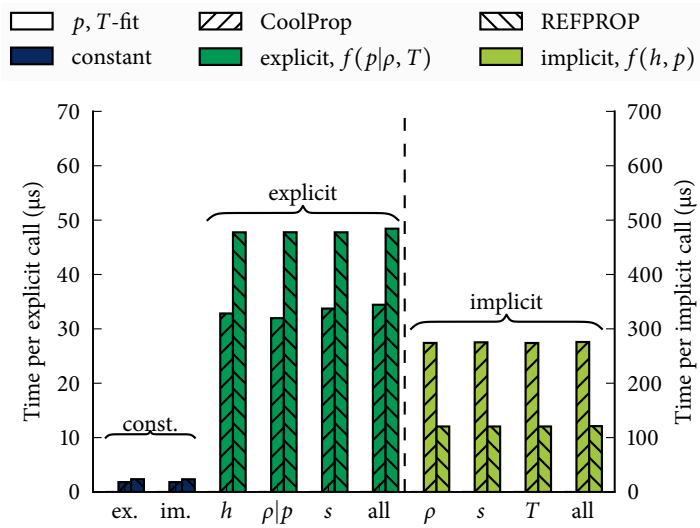

Figure B.4: Average execution times of calls to get the constant $T_{\max}$, $f(\rho, T)$ and $f(h, p)$ for n-pentane from CoolProp and REFPROP.

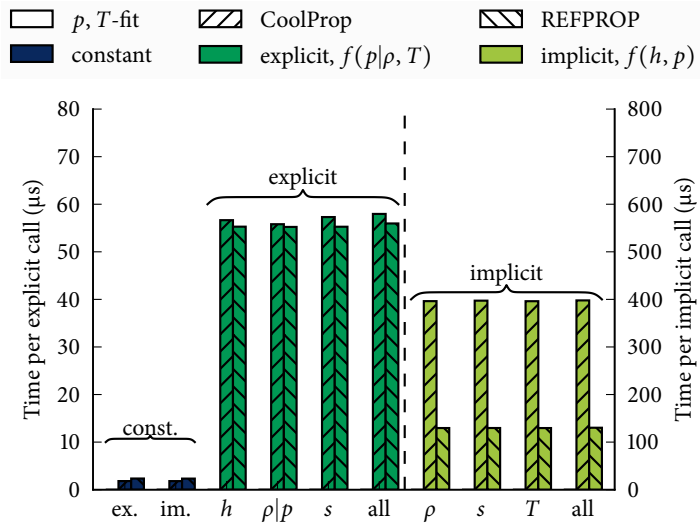

Figure B.5: Average execution times of calls to get the constant $T_{\max}$, $f(\rho, T)$ and $f(h, p)$ for R134a from CoolProp and REFPROP.

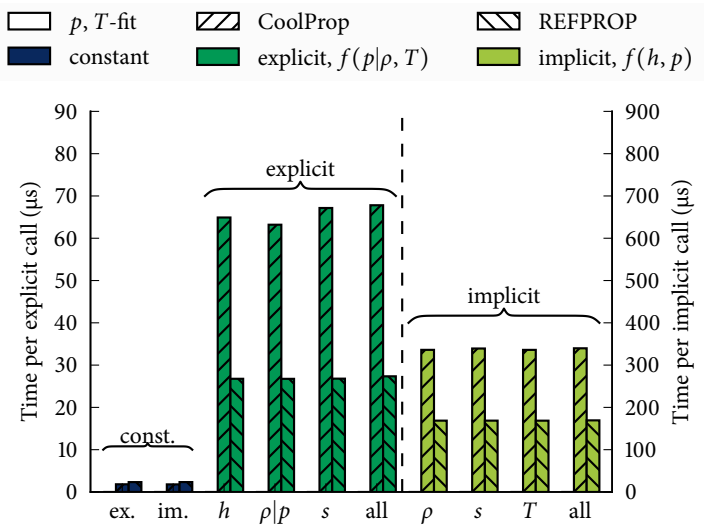

Figure B.6: Average execution times of calls to get the constant $T_{\max}$, $f(\rho, T)$ and $f(h, p)$ for air from CoolProp and REFPROP.

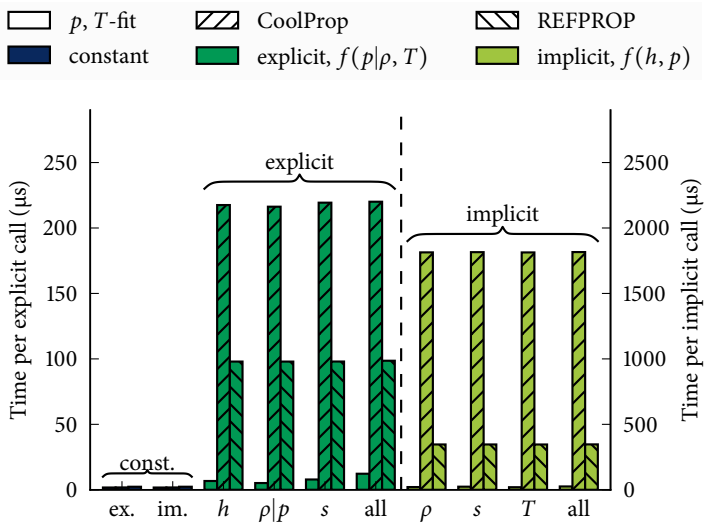

Figure B.7: Average execution times of calls to get the constant $T_{\max}$, $f(\rho, T)$ and $f(h, p)$ for water from CoolProp and REFPROP.

B.2 Execution Time Distribution

Enthalpy and Pressure Calls

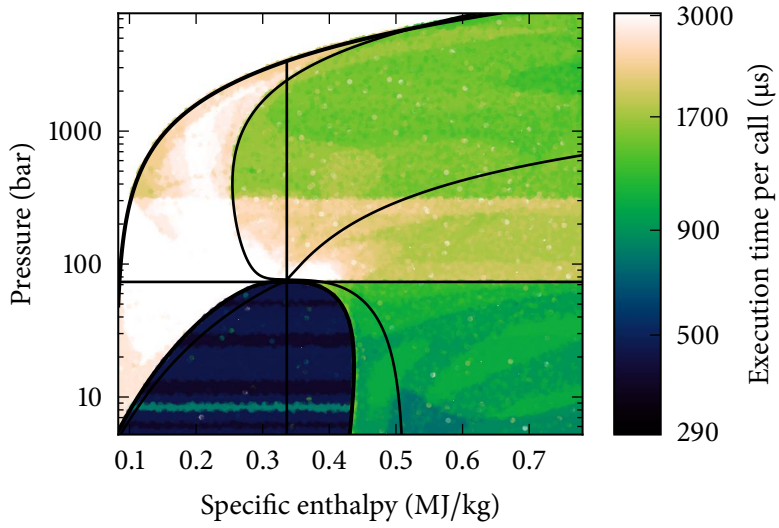

(a) CO_2 from CoolProp.

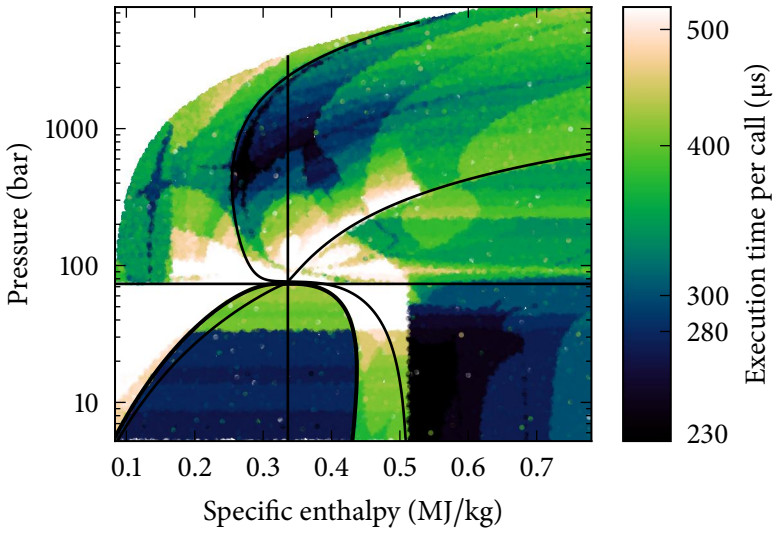

(b) CO_2 from REFPROP.

Figure B.8: Execution times of calls to $f(h, p)$ for CO_2 using different implementations of the same EOS.

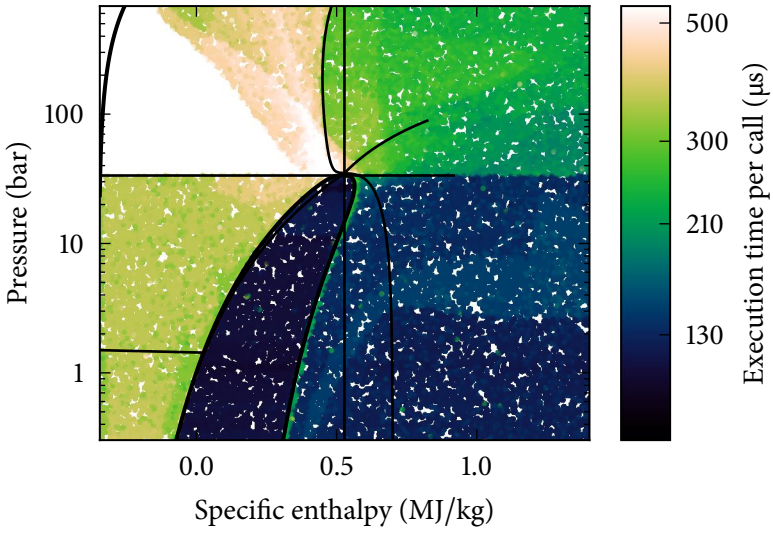

(a) n-pentane from CoolProp.

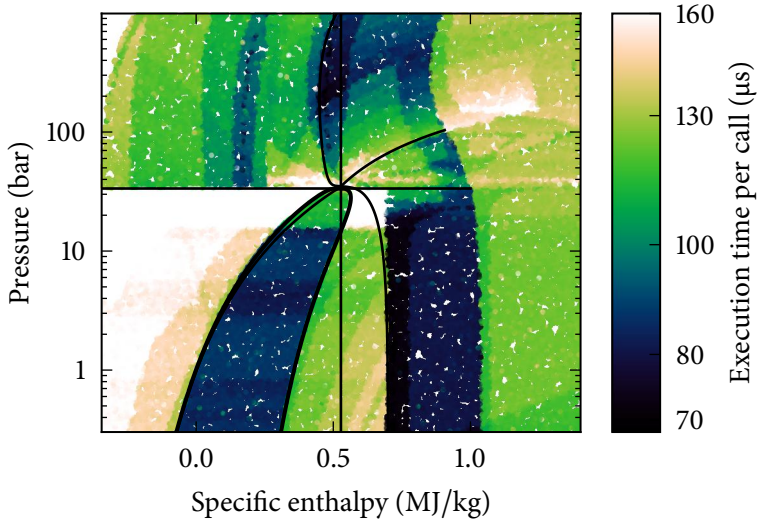

(b) n-pentane from REFPROP.

Figure B.9: Execution times of calls to $f(h, p)$ for n-pentane using different implementations of the same EOS.

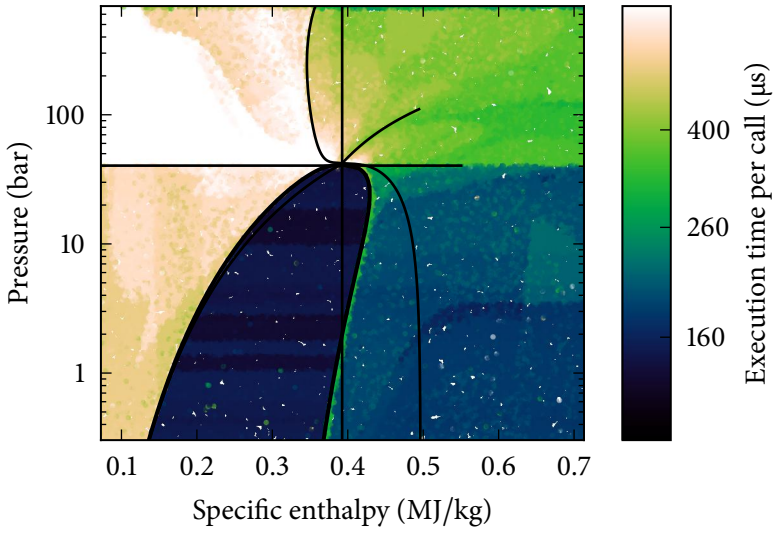

(a) R134a from CoolProp.

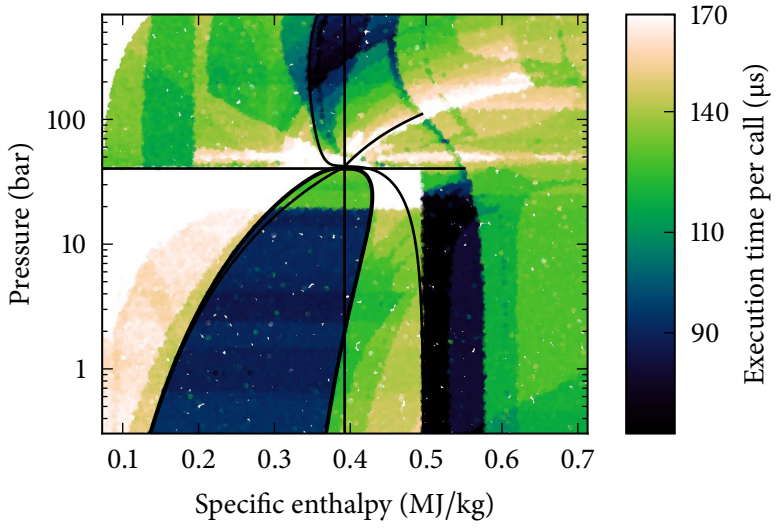

(b) R134a from REFPROP.

Figure B.10: Execution times of calls to $f(h, p)$ for R134a using different implementations of the same EOS.

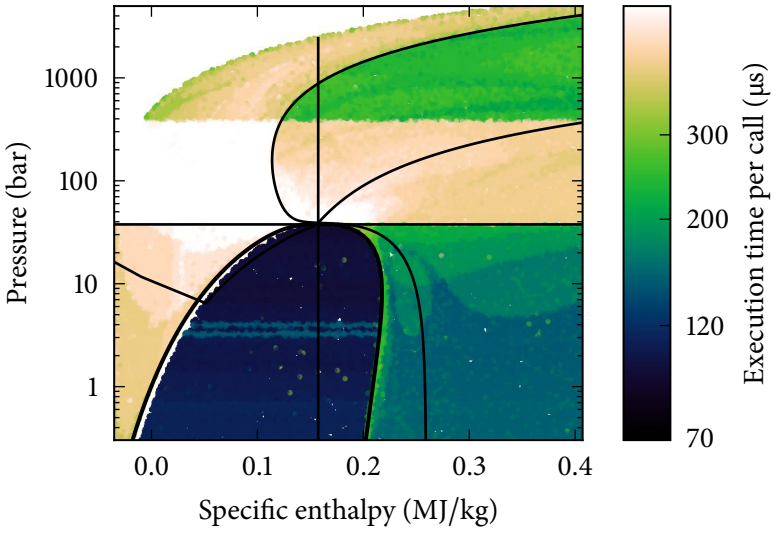

(a) air from CoolProp.

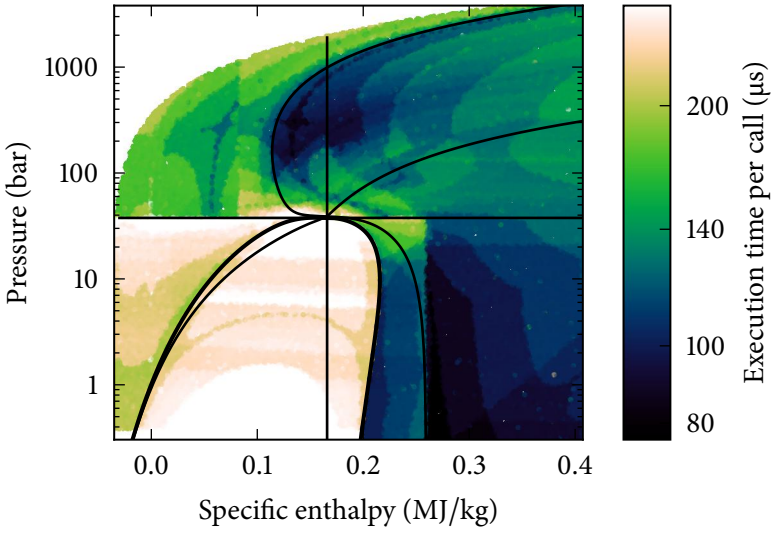

(b) air from REFPROP.

Figure B.11: Execution times of calls to $f(h, p)$ for air using different implementations of the same EOS.

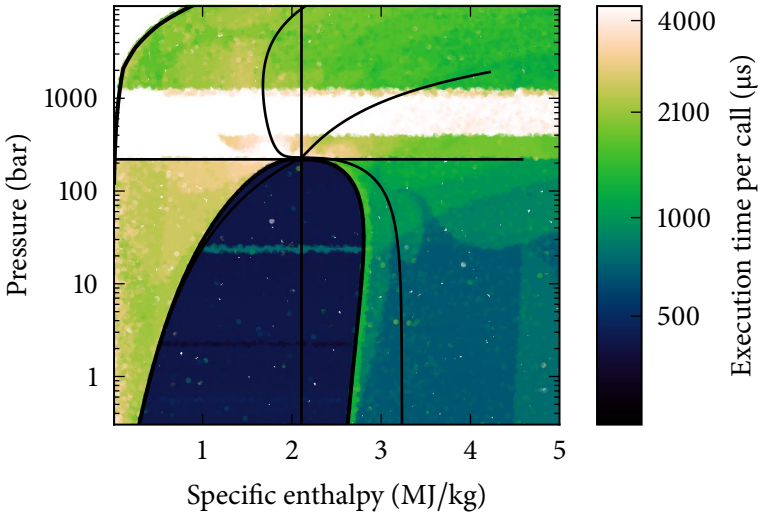

(a) water from CoolProp.

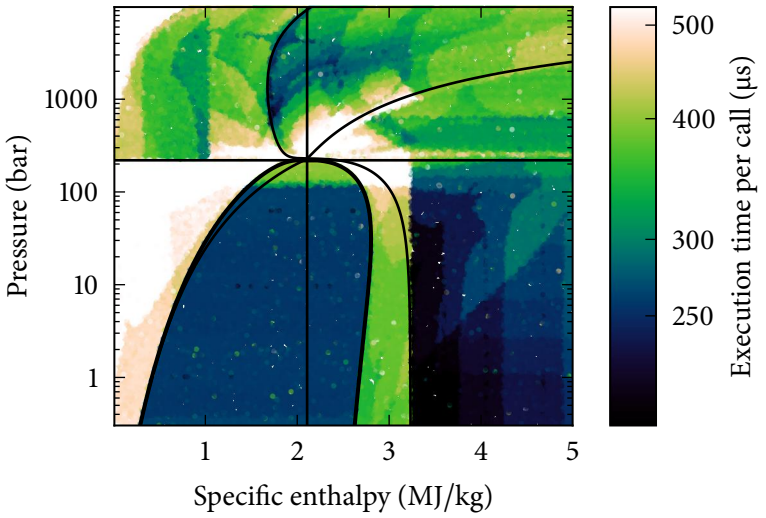

(b) water from REFPROP.

Figure B.12: Execution times of calls to $f(h, p)$ for water using different implementations of the same EOS.

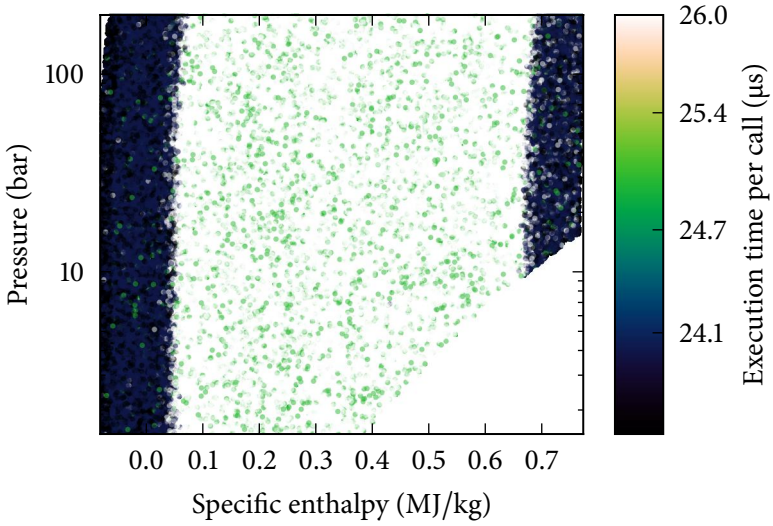

(a) water from CoolProp.

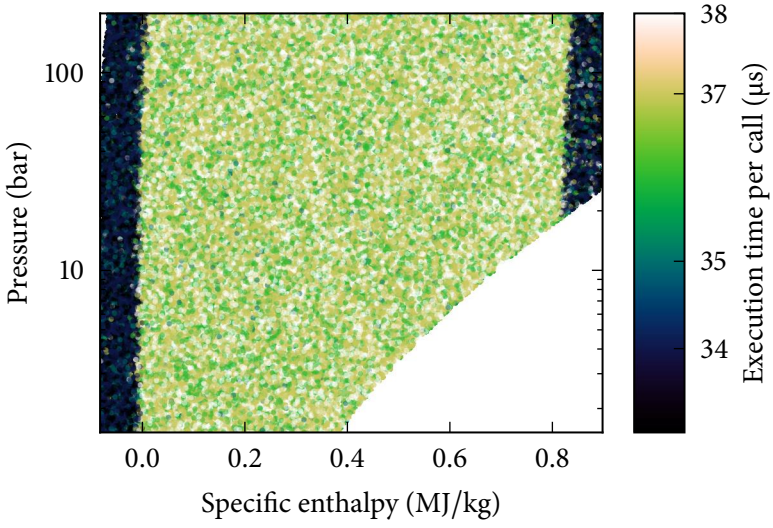

(b) LiBr (aq) from CoolProp.

Figure B.13: Execution times of calls to $f(h, p)$ for different incompressible fluids from the CoolProp library.

Explicit Calls

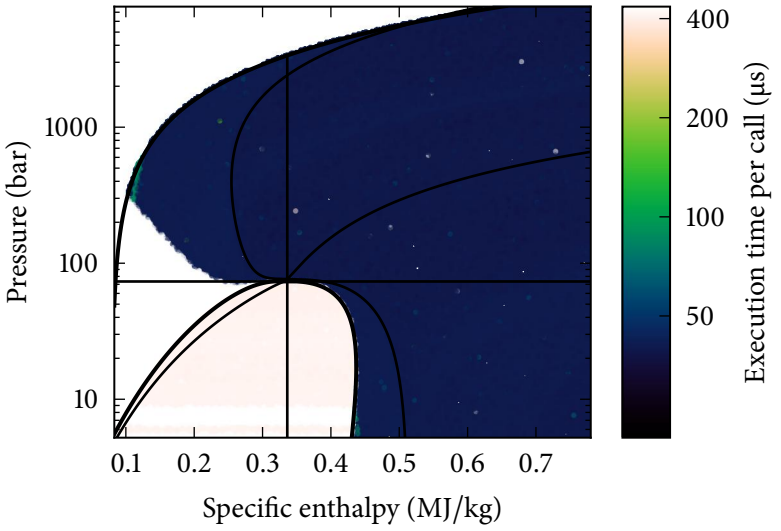

(a) CO_2 from CoolProp.

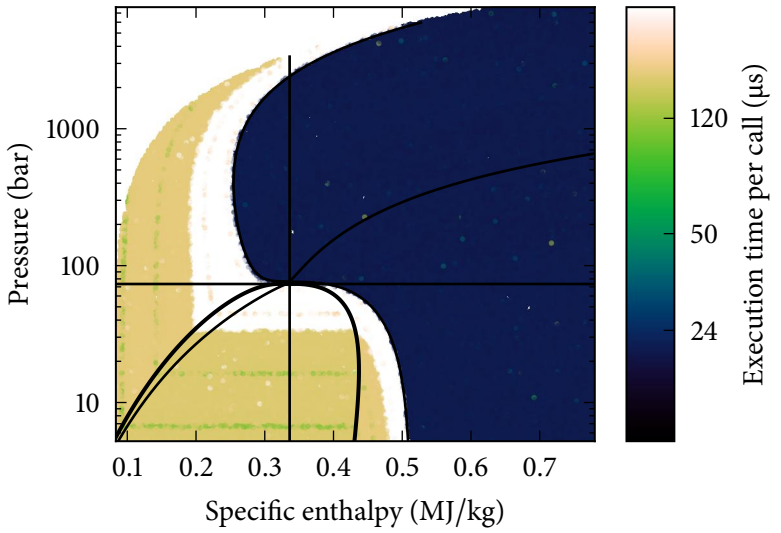

(b) CO_2 from REFPROP.

Figure B.14: Execution times of calls to $f(\rho, T)$ for CO_2 using different implementations of the same EOS.

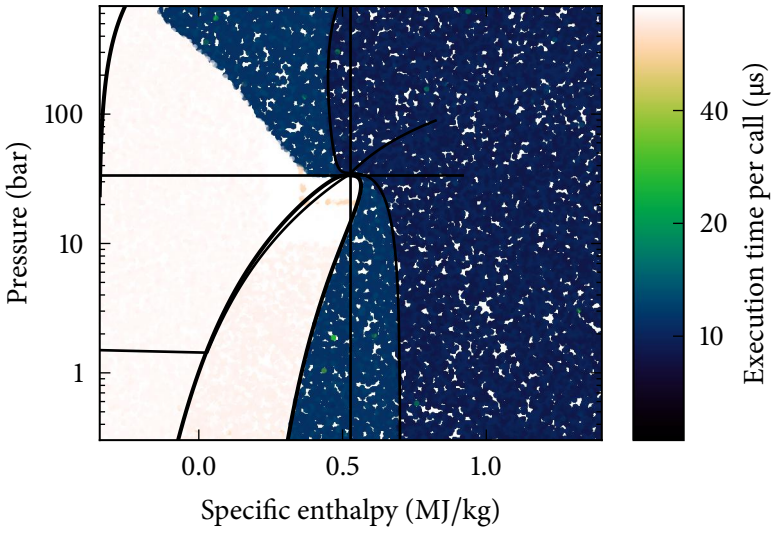

(a) n-pentane from CoolProp.

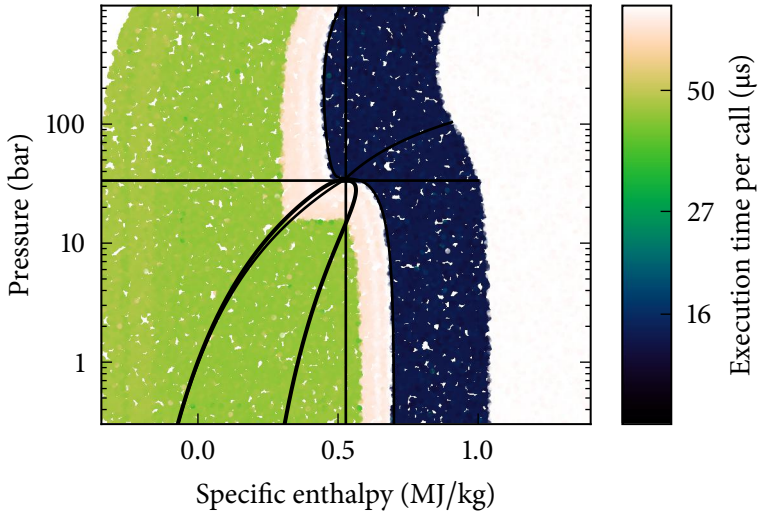

(b) n-pentane from REFPROP.

Figure B.15: Execution times of calls to $f(\rho, T)$ for n-pentane using different implementations of the same EOS.

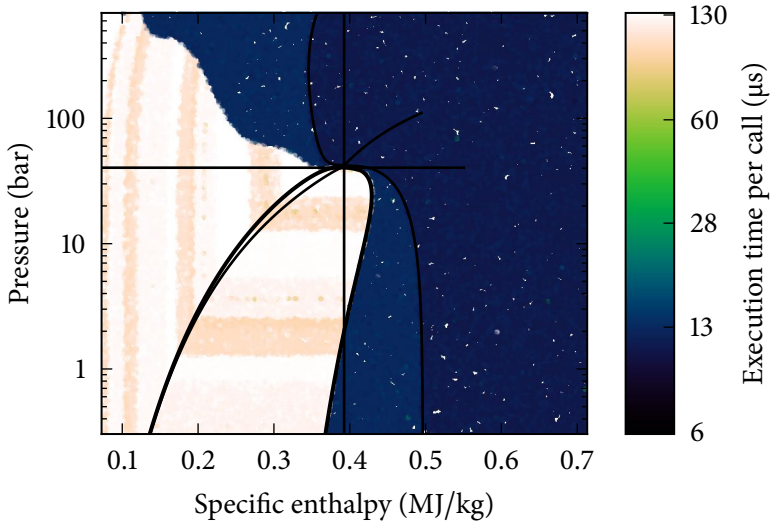

(a) R134a from CoolProp.

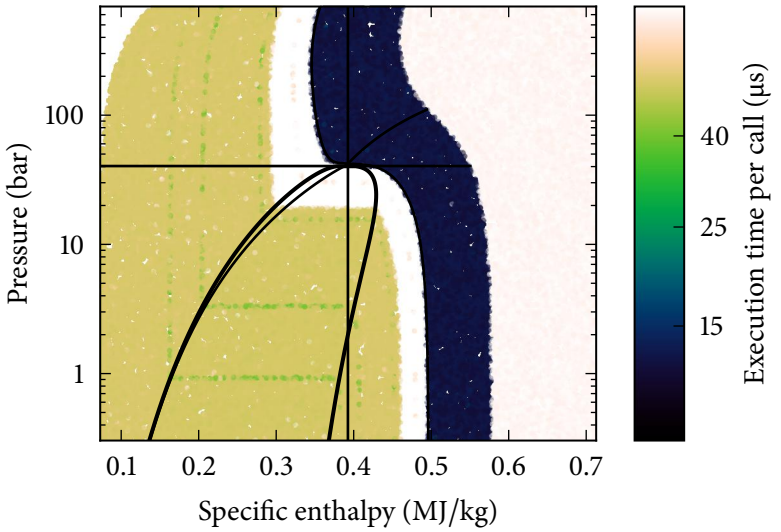

(b) R134a from REFPROP.

Figure B.16: Execution times of calls to $f(\rho, T)$ for R134a using different implementations of the same EOS.

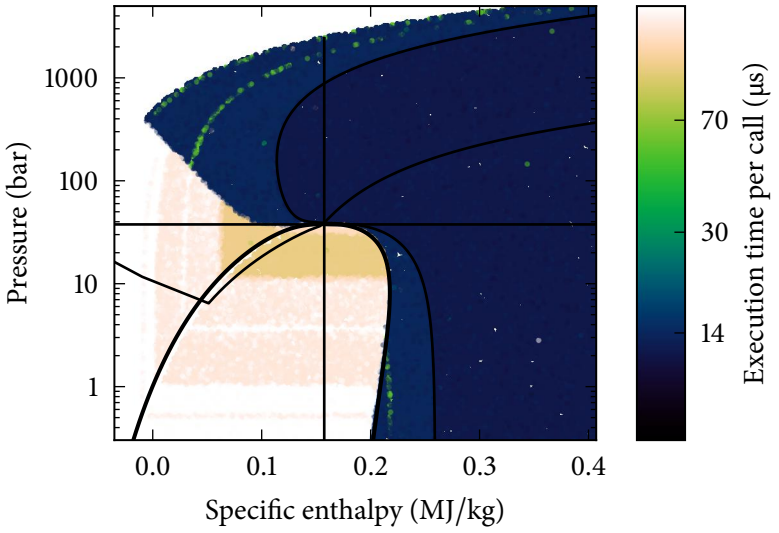

(a) air from CoolProp.

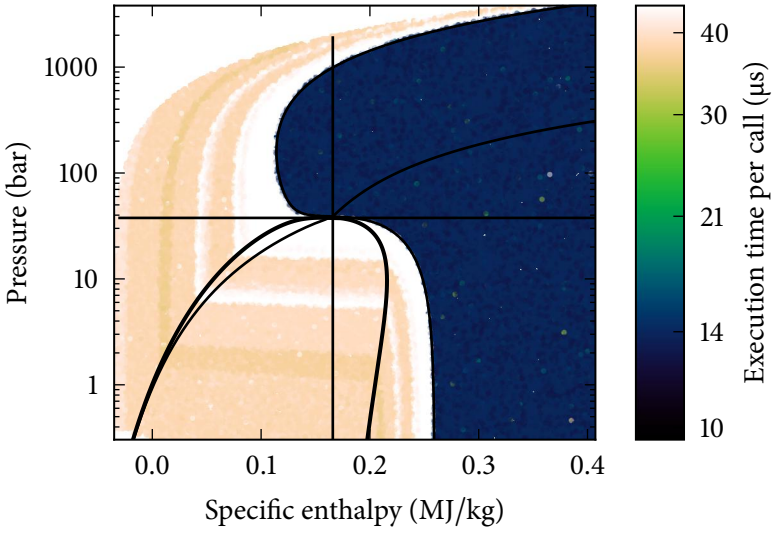

(b) air from REFPROP.

Figure B.17: Execution times of calls to $f(\rho, T)$ for air using different implementations of the same EOS.

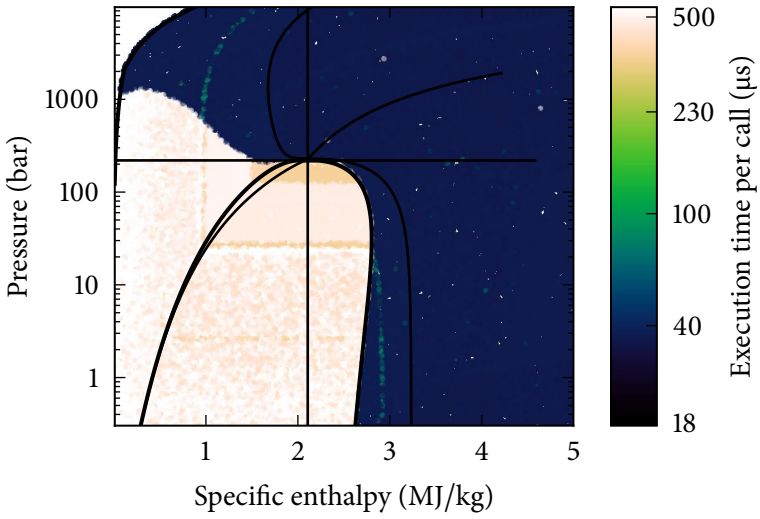

(a) water from CoolProp.

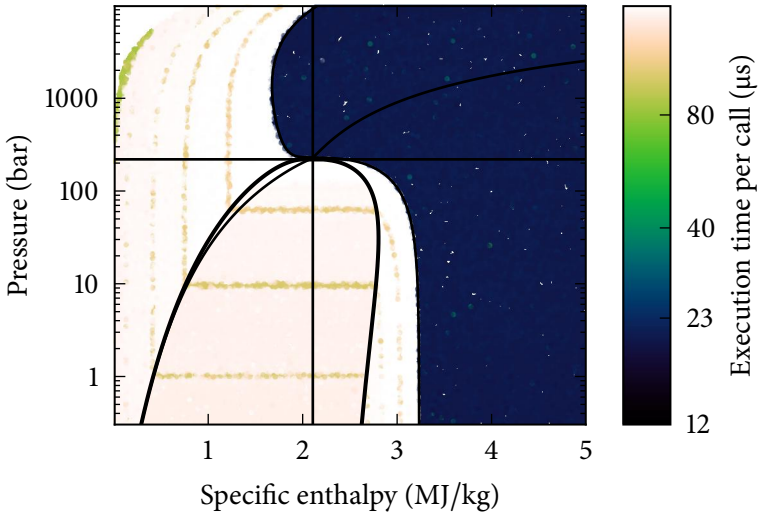

(b) water from REFPROP.

Figure B.18: Execution times of calls to $f(\rho, T)$ for water using different implementations of the same EOS.

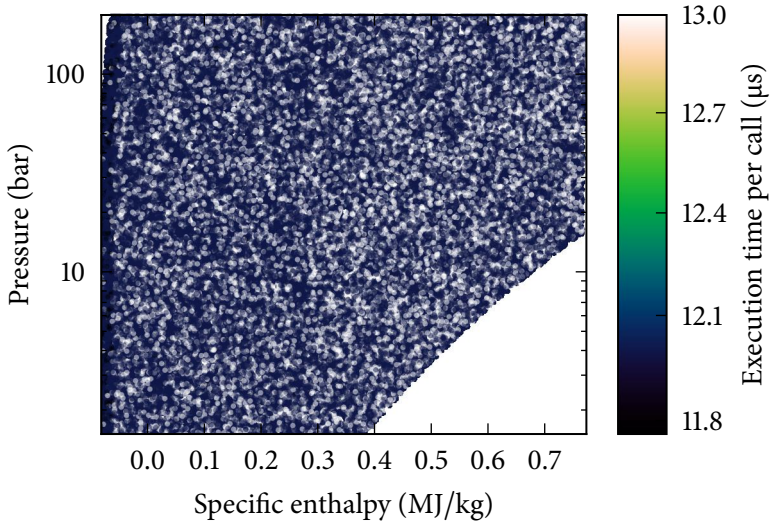

(a) water from CoolProp.

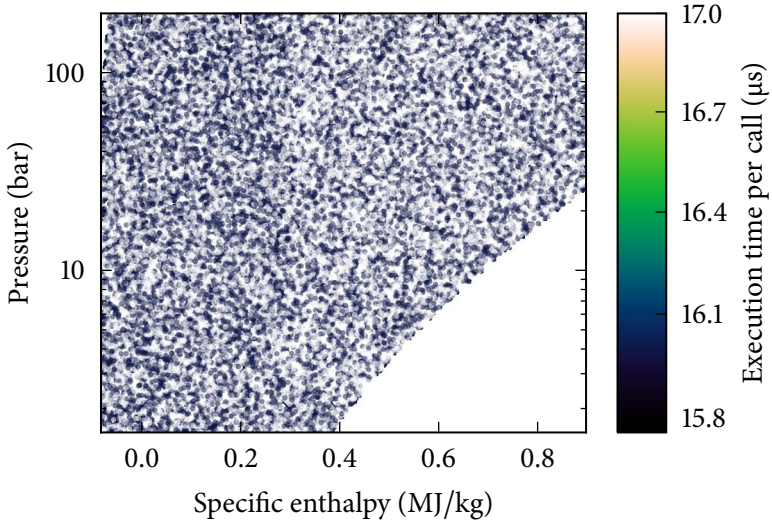

(b) LiBr (aq) from CoolProp.

Figure B.19: Execution times of calls to $f(p, T)$ for different incompressible fluids from the CoolProp library.

Appendix C

Incompressible Fluids

C.1 Fitting Procedures

This section describes the basic linear algebra for multidimensional polynomial fitting. We are going to use Python examples to illustrate how the coefficients are found to represent multi-dimensional (nD) data sets by means of simple polynomials.

Starting with a one-dimensional (1D) case, we use a vector $\boldsymbol{z}$ with measured data of the quantity z to determine a vector of polynomial coefficients $\boldsymbol{c}$ from the independent variable $\boldsymbol{x}$. To do so, we first build the Vandermonde Matrix $\boldsymbol{V}$ of the independent variable x. This matrix holds the powers of the vector of independent data points $\boldsymbol{x}^i \forall\, i \in 0..n$ with n denoting the desired order of the polynomial. Using the system of orthogonal equations given by $\boldsymbol{V}^{\mathrm{T}}\boldsymbol{V} \cdot \boldsymbol{c} = \boldsymbol{V}^{\mathrm{T}} \cdot \boldsymbol{z}$ rather than equating $\boldsymbol{V} \cdot \boldsymbol{c} = \boldsymbol{z}$ directly allows us to use more data points than variables and the solution automatically yields the minimised squared error $\epsilon_x(\boldsymbol{c}) = \sqrt{\sum(\boldsymbol{z} - \boldsymbol{V} \cdot \boldsymbol{c})^2}$. Employing Python tools, we leave the details to the software and implement the compact function shown in Listing C.1, lines 5 to 13.

We can extend the whole procedure to two dimensions, given that we have a solution matrix $\boldsymbol{Z}$ instead of a vector. Since this potentially involves a large number of coefficients, we disregard the higher order terms to avoid overfitting. This is done by discarding terms with a sum of exponents higher than the largest single exponent. The pair of exponents for the independent elements x and y, i and j, has to satisfy $i + j \leq \max(k, l)$ with k and l being the highest exponents in x and y direction, respectively. The matrix of exponent pairs $\boldsymbol{V}_2$ for each data tuple (x, y) with $k < l$ is defined as

$$\boldsymbol{V}_2 = \begin{pmatrix} (0,0) & (0,1) & \cdots & \cdots & \cdots & (0,l) \\ (1,0) & \ddots & & & (1,l-1) & (0,0) \\ \vdots & & & \iddots & \iddots & \vdots \\ (k,0) & \cdots & (k,l-k) & (0,0) & \cdots & (0,0) \end{pmatrix}. \tag{C.1}$$

Using $k = 2$ and $l = 4$, the approach presented above yields a matrix with three unused entries in the lower right corner

$$\boldsymbol{V}_2 = \begin{pmatrix} (0,0) & (0,1) & (0,2) & (0,3) & (0,4) \\ (1,0) & (1,1) & (1,2) & (1,3) & (0,0) \\ (2,0) & (2,1) & (2,2) & (0,0) & (0,0) \end{pmatrix}. \tag{C.2}$$

Strictly following the matrix notation would result in a four-dimensional (4D) functional matrix from the Cartesian product of all elements of $\boldsymbol{V}_2$ and the input vectors $\boldsymbol{x}$ and $\boldsymbol{y}$, see Listing C.1, lines 15 to 37. However, having many linear algebra solvers available for two-dimensional (2D) systems, it is more practical to manually reduce the dimensionality of the problem to two. We create a new matrix $\boldsymbol{A}$ with rows obtained from the flattened $\boldsymbol{V}_2$ and each element of the Cartesian product of the input vectors $\boldsymbol{x}$ and $\boldsymbol{y}$. Every row of $\boldsymbol{A}$ can be mapped to an entry in the solution matrix $\mathbf{Z}$ based on its unique (x, y)-tuple. A data set consisting of 10 entries in x and 20 entries in y requires $\boldsymbol{Z}$ to have 200 elements and $\boldsymbol{A}$ to have 200 rows. The example given above, $k = 2$ and $l = 4$, then leads to 12 columns in $\boldsymbol{A}$. After minimizing $\epsilon_{x,y}$, information from $\boldsymbol{V}_2$ can be used to convert the coefficient vector $\boldsymbol{c}$ to a matrix to be used with two-dimensional polynomials, as shown in lines 15 to 52 of Listing C.1.

A test run with the small data set from Listing C.2 produces the figures plotted in Figure C.1. The abscissa holds temperature information in Kelvin and the second axis of the bottom plain represents mass fractions of ethanol in an aqueous solution. Density information is shown as a scatter plot together with a 2D fit of the whole data range and a 1D fit at a concentration of 5 % ethanol as produced by the code from Listing C.2 on page 210.

```
## Linear algebra for multidimensional polynomial fitting
import numpy as np
from numpy.polynomial.polynomial import polyval, polyval2d

# 1d functions
def getCoeffs1d(x,z,order):
    if (len(x)<order+1):
        raise ValueError("You have only {0} elements and try to fit {1}
            coefficients, please reduce the order.".format(len(x),order
            +1))
    A = np.vander(x,order+1)[:,::-1]
    Anew = np.dot(A.T,A)
    znew = np.dot(A.T,z)
    coeffs = np.linalg.solve(Anew, znew)
    return coeffs #

# 2d function
def getCoeffs2d(x_in,y_in,z_in,x_order,y_order):
    x_order += 1; y_order += 1
    x_exp = range(x_order); y_exp = range(y_order)
    limit = max(x_order,y_order) # avoid overfitting
    xy_exp = [] # Construct the upper left triangle of coefficients
    for i in x_exp:
        for j in y_exp:
            if((i+j)<limit): xy_exp.append((i,j))
    x_num = len(x_in); y_num = len(y_in)
    cols = len(xy_exp)
    eqns = x_num * y_num
    if (x_num<x_order):
        raise ValueError("You have only {0} x-entries and try to fit {1}
             x-coefficients, please reduce the x_order.".format(x_num,
            x_order))
    if (y_num<y_order):
        raise ValueError("You have only {0} y-entries and try to fit {1}
             y-coefficients, please reduce the y_order.".format(y_num,
            y_order))
    #Create functional matrix
    #A = np.zeros((x_num,y_num,x_order,y_order))
    #for i in range(x_num):
    #    for j in range(y_num):
    #        for (xk,yk) in xy_exp:
    #            A[i][j][xk][yk] = x_in[i]**xk * y_in[j]**yk
    #raise NotImplementedError("No 4-dimensional solver implemented") #
    # Construct input pairs
    xx, yy = np.meshgrid(x_in,y_in,indexing='ij')
    xx.shape = (eqns,); yy.shape = (eqns,)
    zz = np.ravel(z_in) # Do not modify data!
    # Build the functional matrix
    A = np.zeros((eqns,cols))
    for i in range(eqns): # row loop
        for j, (xj,yj) in enumerate(xy_exp): # makes columns
            A[i][j] = xx[i]**xj * yy[i]**yj
    coeffs = np.linalg.lstsq(A, zz)[0]
    #Rearrange coefficients to a matrix shape
    C = np.zeros((x_order,y_order))
    for i, (xi,yi) in enumerate(xy_exp): # makes columns
        C[xi][yi] = coeffs[i]
    return C #
```

Listing C.1: Polynomial fitting function implemented in Python.

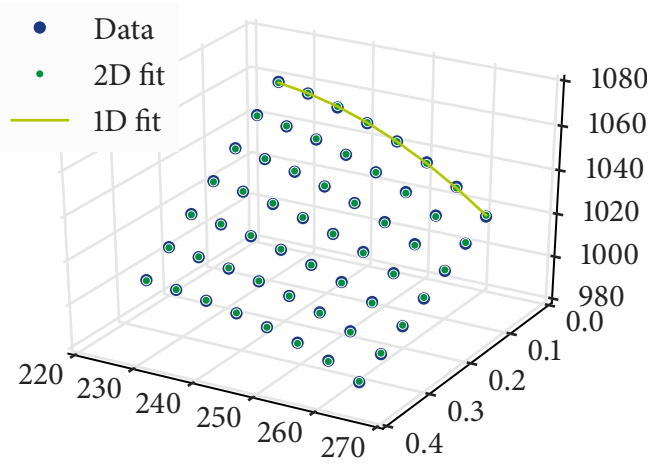

Figure C.1: Data points and function from fitted 1D and 2D polynomials.

```
# A data set
T_in = np.array([-45, -40, -35, -30, -25, -20, -15, -10])+273.15 # K
x_in = np.array([  5,  10,  15,  20,  25,  30,  35])/100.0 # mass frac
rho_in = np.array([
  [1064.0, 1054.6, 1045.3, 1036.3, 1027.4, 1018.6, 1010.0],
  [1061.3, 1052.1, 1043.1, 1034.3, 1025.6, 1017.0, 1008.6],
  [1057.6, 1048.8, 1040.1, 1031.5, 1023.1, 1014.8, 1006.7],
  [1053.1, 1044.6, 1036.2, 1028.0, 1019.9, 1012.0, 1004.1],
  [1047.5, 1039.4, 1031.5, 1023.7, 1016.0, 1008.4, 1000.9],
  [1040.7, 1033.2, 1025.7, 1018.4, 1011.2, 1004.0,  997.0],
  [1032.3, 1025.3, 1018.5, 1011.7, 1005.1,  998.5,  992.0],
  [1021.5, 1015.3, 1009.2, 1003.1,  997.1,  991.2,  985.4]]) # kg/m3

xorder = 2; yorder = 4
x1d  = T_in
y1d  = np.zeros_like(x1d)+x_in[0]
z1d  = rho_in[:,0]
c1d  = getCoeffs1d(x1d,z1d,xorder)
zf1d = polyval(x1d,c1d)
x2d = T_in; y2d = x_in; z2d = rho_in
c2d = getCoeffs2d(x2d,y2d,z2d,xorder,yorder)
x2d, y2d = np.meshgrid(x2d,y2d,indexing='ij')
x2d = np.ravel(x2d)
y2d = np.ravel(y2d)
z2d = np.ravel(z2d)
zf2d = polyval2d(x2d,y2d,c2d)
```

Listing C.2: Calling the fitting function from Python.

C.2 Pure Fluids

Name	Description	Reference	T_{min} (°C)	T_{max} (°C)	T_{base} (K)
AS10, p. 215	Aspen Temper -10, Potassium acetate/formate	[49, 55]	−10.00	30.00	273.15
AS20, p. 216	Aspen Temper -20, Potassium acetate/formate	[49, 55]	−20.00	30.00	273.15
AS30, p. 217	Aspen Temper -30, Potassium acetate/formate	[49, 55]	−30.00	30.00	273.15
AS40, p. 218	Aspen Temper -40, Potassium acetate/formate	[49, 55]	−40.00	30.00	273.15
AS55, p. 219	Aspen Temper -55, Potassium acetate/formate	[49, 55]	−55.00	30.00	273.15
DEB, p. 220	Diethylbenzene mixture - Dowtherm J	[39]	−80.00	100.00	0.00
DowJ, p. 221	DowthermJ	[52]	−80.00	345.00	405.65
DowJ2, p. 222	Dowtherm J, Diethylbenzene mixture	[49, 52]	−73.00	315.00	394.15
DowQ, p. 223	DowthermQ	[52]	−35.00	360.00	435.65
DowQ2, p. 224	Dowtherm Q, Diphenylethane/alkylated aromatics	[49, 52]	−35.00	330.00	420.65
HC10, p. 225	Dynalene HC10	[58]	−10.00	218.00	377.15
HC20, p. 226	Dynalene HC20	[58]	−20.00	210.00	368.15
HC30, p. 227	Dynalene HC30	[58]	−30.00	210.00	363.15
HC40, p. 228	Dynalene HC40	[58]	−40.00	200.00	353.15
HC50, p. 229	Dynalene HC50	[58]	−50.00	210.00	353.15
HCB, p. 230	Hydrocarbon blend - Dynalene MV	[39]	−80.00	100.00	0.00
HCM, p. 231	Hydrocarbon mixture - Gilotherm D12	[39]	−80.00	100.00	0.00
HFE, p. 232	Hydrofluoroether - HFE-7100 3M Novec	[39]	−80.00	100.00	0.00
HFE2, p. 233	HFE-7100, Hydrofluoroether	[49, 63]	−80.33	64.27	265.12
HY20, p. 234	HYCOOL 20, Potassium formate	[62]	−20.00	50.00	273.15
HY30, p. 235	HyCool 30, Potassium formate	[62]	−30.00	50.00	273.15
HY40, p. 236	HyCool 40, Potassium formate	[62]	−40.00	20.00	273.15

HY45, p. 237	HyCool 45, Potassium formate	[62]	−45.00	20.00	273.15
HY50, p. 238	HyCool 50, Potassium formate	[62]	−50.00	20.00	273.15
NBS, p. 239	NBS, Water	[46, 49]	1.00	100.00	323.65
NaK, p. 240	Nitrate salt, 0.6 NaNO3 and 0.4 KNO3	[74]	300.00	600.00	273.15
PCL, p. 241	Paracryol, Aliphatic Hydrocarbon	[49, 60]	−40.00	180.00	343.15
PCR, p. 242	Paratherm CR	[65]	−100.00	220.00	333.15
PGLT, p. 243	Paratherm GLT	[65]	−15.00	315.00	423.15
PHE, p. 244	Paratherm HE	[65]	0.00	330.00	438.15
PHR, p. 245	Paratherm HR	[65]	−15.00	370.00	450.65
PLR, p. 246	Paratherm LR	[65]	−85.00	230.00	345.65
PMR, p. 247	Paratherm MR	[65]	−40.00	315.00	410.65
PMS1, p. 248	Polydimethylsiloxan 1 - Baysilone KT3	[39]	−80.00	100.00	0.00
PMS2, p. 249	Polydimethylsiloxan 2 - Syltherm XLT	[39]	−80.00	100.00	0.00
PNF, p. 250	Paratherm NF	[65]	−10.00	315.00	425.65
PNF2, p. 251	Paratherm NF, Hydrotreated mineral oil	[49, 65]	−10.00	320.00	428.15
SAB, p. 252	Synthetic alkyl benzene - Marlotherm X	[39]	−80.00	100.00	0.00
T66, p. 253	Therminol66	[66]	0.00	380.00	463.15
T72, p. 254	Therminol72	[66]	−10.00	380.00	458.15
TCO, p. 255	Citrus oil terpene - d-Limonene	[39]	−80.00	100.00	0.00
TD12, p. 256	TherminolD12	[66]	−85.00	230.00	345.65
TVP1, p. 257	TherminolVP1	[66]	12.00	397.00	477.65
TVP1869, p. 258	Thermogen VP 1869	[49, 59]	−80.00	20.00	273.15
TX22, p. 259	Texatherm22	[56]	0.00	350.00	448.15
TY10, p. 260	Tyfoxit 1.10, Potassium Acetate	[49, 61]	−10.00	40.00	288.15
TY15, p. 261	Tyfoxit 1.15, Potassium Acetate	[49, 61]	−20.00	40.00	283.15
TY20, p. 262	Tyfoxit 1.20, Potassium Acetate	[49, 61]	−40.00	40.00	273.15
TY24, p. 263	Tyfoxit 1.24, Potassium Acetate	[49, 61]	−55.00	40.00	265.65

Water, p. 264	Fit of EOS from 1 bar to 100 bar	[27, 67]	0.00	200.00	373.15
XLT, p. 265	SylthermXLT	[52]	−100.00	260.00	353.15
XLT2, p. 266	Syltherm XLT, Polydimethylsiloxan	[49, 52]	−100.00	260.00	353.15
ZS10, p. 267	Zitrec S10, Potassium formate/Sodium propionate	[49, 64]	−8.00	90.00	314.15
ZS25, p. 268	Zitrec S25, Potassium formate/Sodium propionate	[49, 64]	−23.00	90.00	306.65
ZS40, p. 269	Zitrec S40, Potassium formate/Sodium propionate	[49, 64]	−38.00	90.00	299.15
ZS45, p. 270	Zitrec S45, Potassium formate/Sodium propionate	[49, 64]	−43.00	90.00	296.65
ZS55, p. 271	Zitrec S55, Potassium formate/Sodium propionate	[49, 64]	−55.00	90.00	290.65

Fitted functions for AS10

Description:	Aspen Temper -10, Potassium acetate/formate		
Source:	*Technical Data Sheet* [55]		
	Skovrup [49]		
Temperature:	-10.0 °C to 30.0 °C	Th. Cond.:	coefficients to polynomial (2, 1)
Composition:	pure fluid	Viscosity:	coefficients to polynomial (4, 1)
Density:	coefficients to polynomial (4, 1)	Psat:	no information
Spec. Heat:	coefficients to polynomial (3, 1)	Tfreeze:	no information

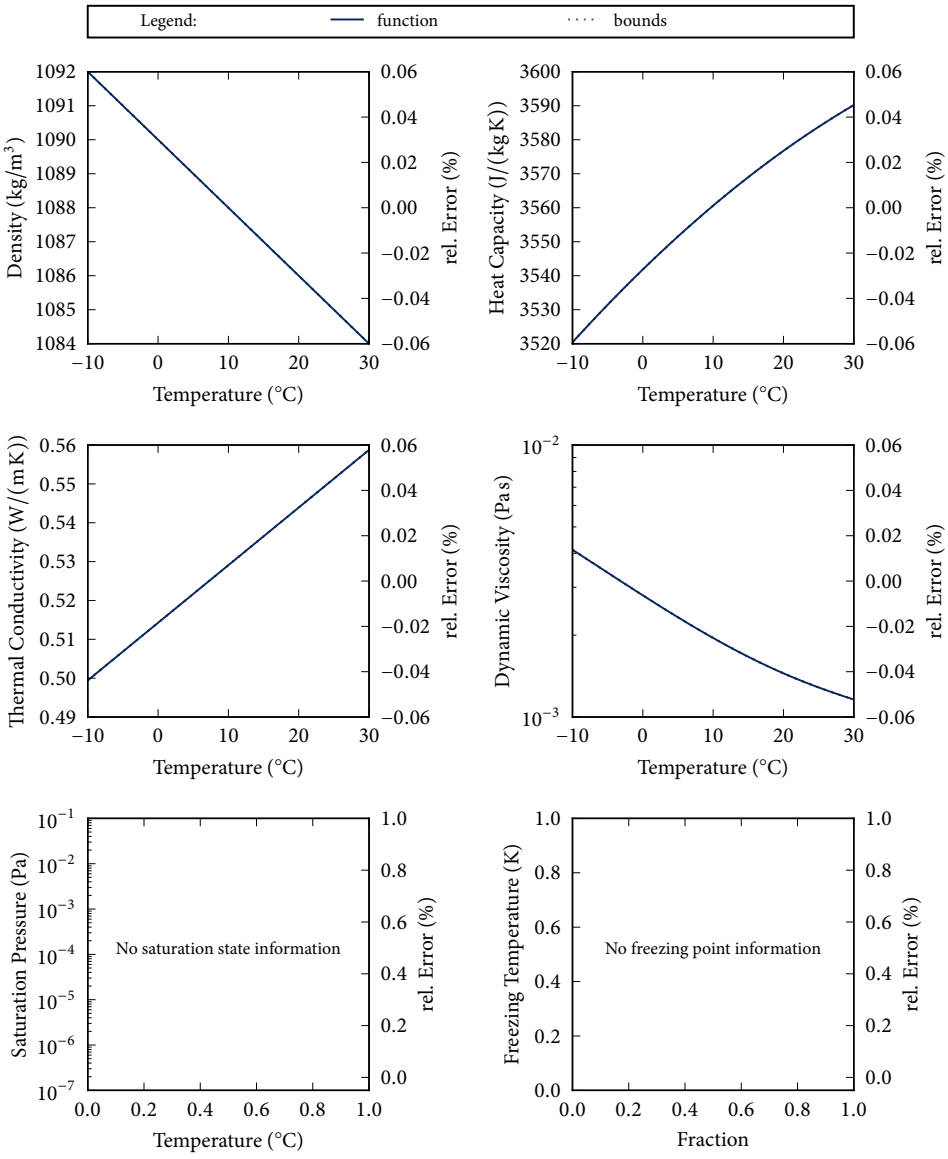

Fitted functions for AS20

Description:	Aspen Temper -20, Potassium acetate/formate		
Source:	*Technical Data Sheet* [55]		
	Skovrup [49]		
Temperature:	-20.0 °C to 30.0 °C	Th. Cond.:	coefficients to polynomial (2, 1)
Composition:	pure fluid	Viscosity:	equation to exppolynomial (4, 1)
Density:	coefficients to polynomial (4, 1)	Psat:	no information
Spec. Heat:	coefficients to polynomial (3, 1)	Tfreeze:	no information

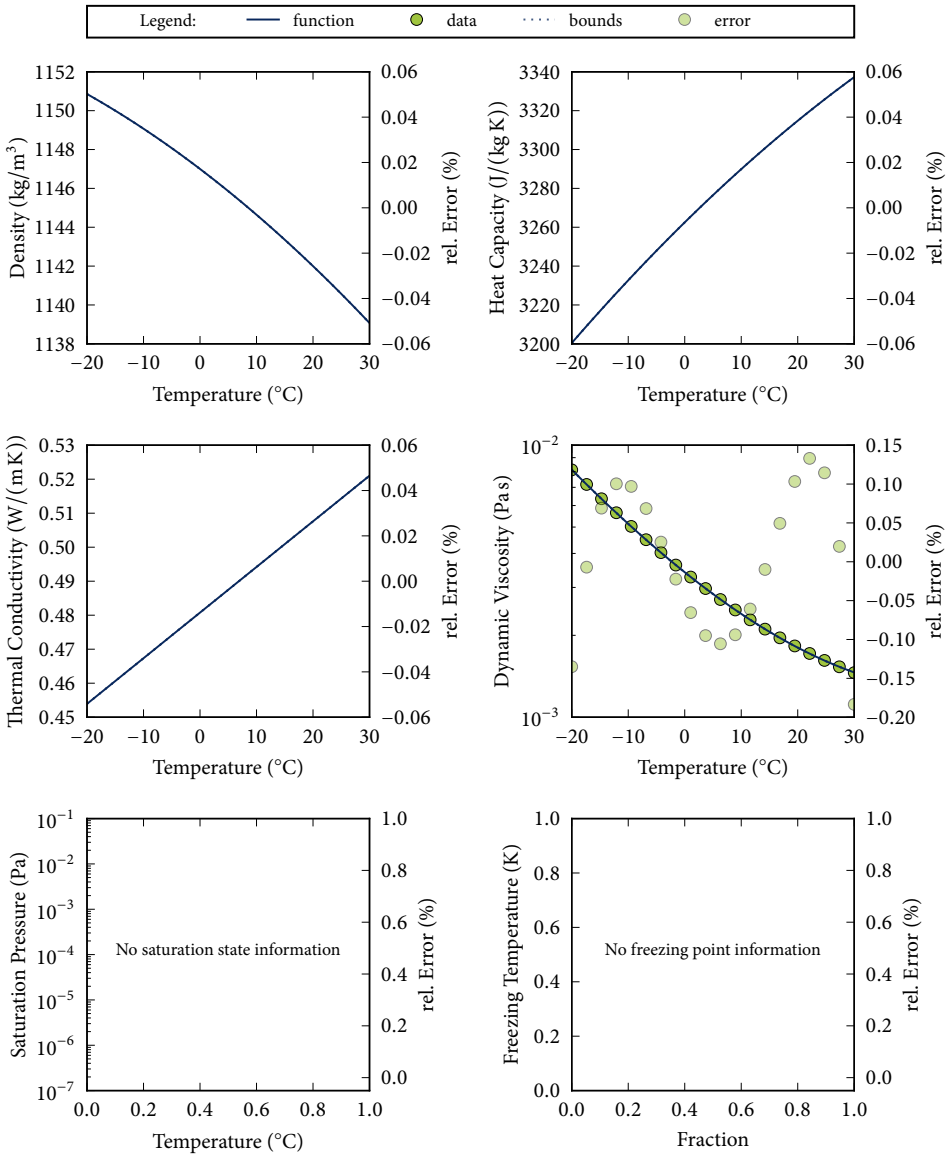

Fitted functions for AS30

Description:	Aspen Temper -30, Potassium acetate/formate		
Source:	*Technical Data Sheet* [55]		
	Skovrup [49]		
Temperature:	-30.0 °C to 30.0 °C	Th. Cond.:	coefficients to polynomial (2, 1)
Composition:	pure fluid	Viscosity:	equation to exppolynomial (4, 1)
Density:	coefficients to polynomial (4, 1)	Psat:	no information
Spec. Heat:	coefficients to polynomial (3, 1)	Tfreeze:	no information

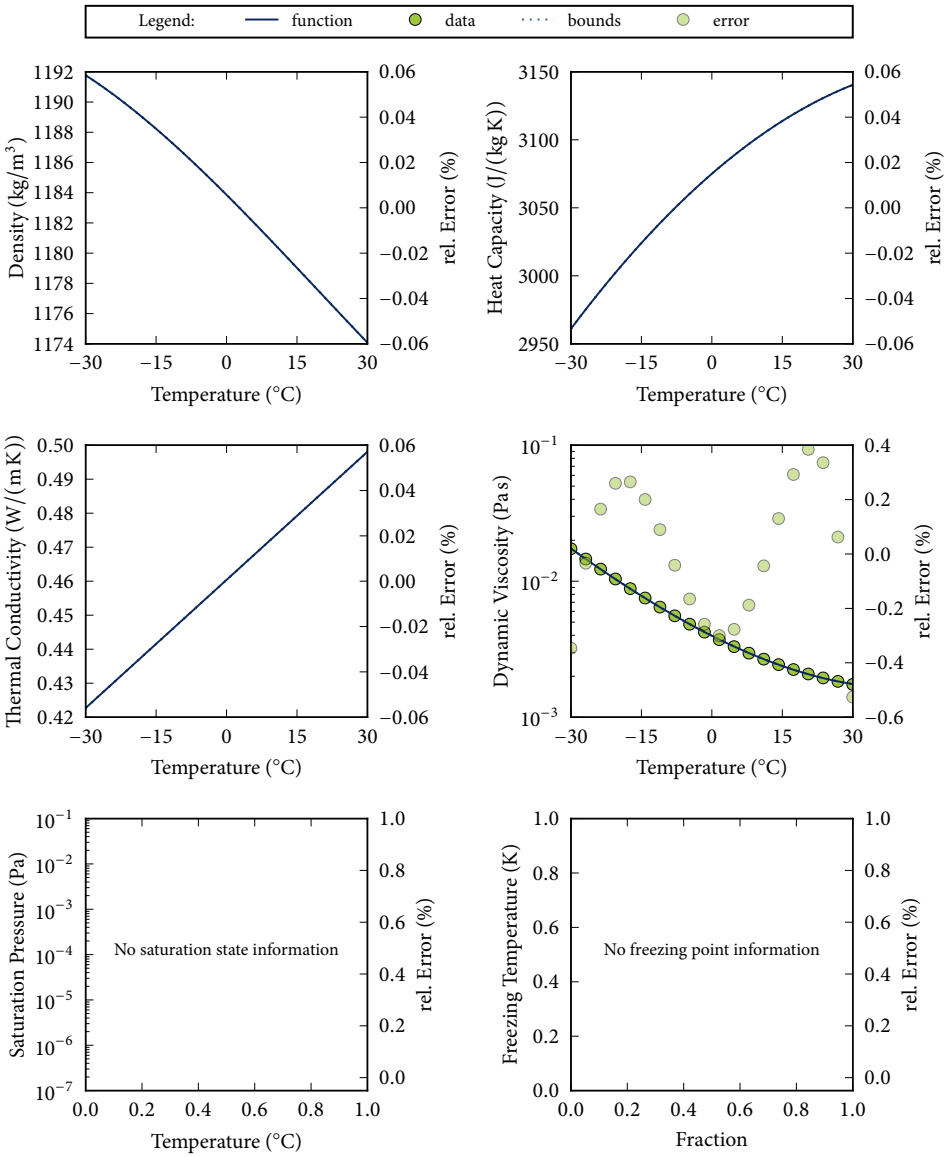

Fitted functions for AS40

Description:	Aspen Temper -40, Potassium acetate/formate		
Source:	*Technical Data Sheet* [55]		
	Skovrup [49]		
Temperature:	-40.0 °C to 30.0 °C	Th. Cond.:	coefficients to polynomial (2, 1)
Composition:	pure fluid	Viscosity:	equation to exppolynomial (4, 1)
Density:	coefficients to polynomial (4, 1)	Psat:	no information
Spec. Heat:	coefficients to polynomial (3, 1)	Tfreeze:	no information

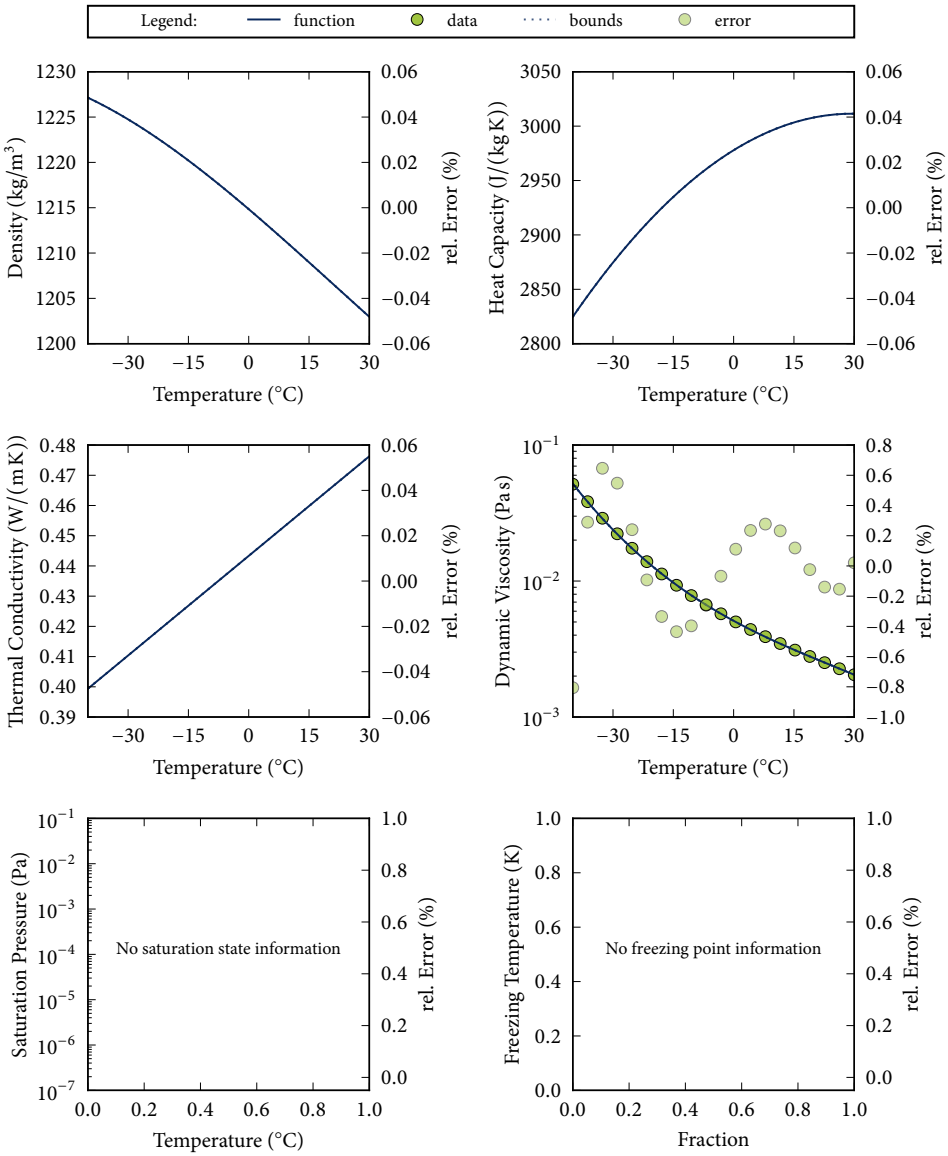

Fitted functions for AS55

Description:	Aspen Temper -55, Potassium acetate/formate		
Source:	*Technical Data Sheet* [55]		
	Skovrup [49]		
Temperature:	-55.0 °C to 30.0 °C	Th. Cond.:	coefficients to polynomial (3, 1)
Composition:	pure fluid	Viscosity:	equation to exppolynomial (4, 1)
Density:	coefficients to polynomial (4, 1)	Psat:	no information
Spec. Heat:	coefficients to polynomial (3, 1)	Tfreeze:	no information

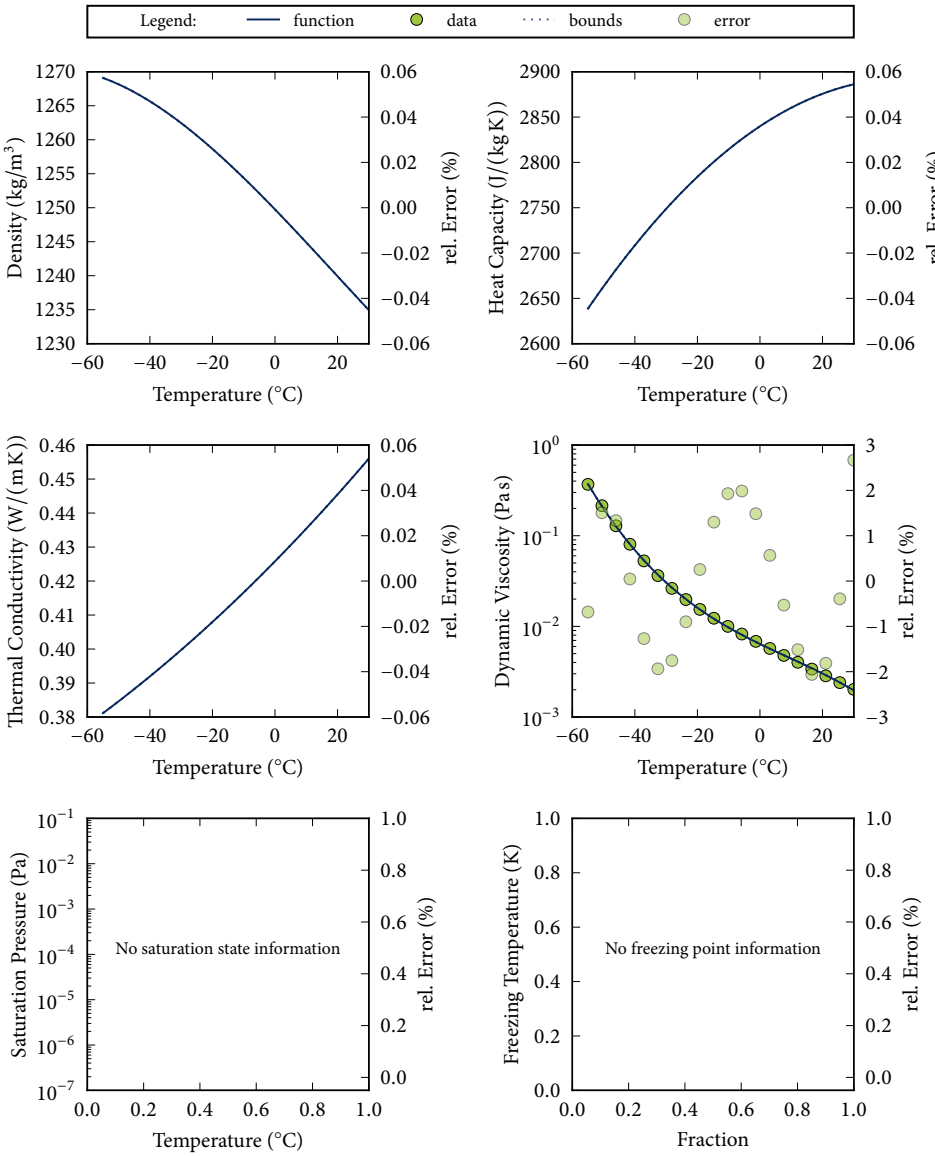

Fitted functions for DEB

Description: Diethylbenzene mixture - Dowtherm J
Source: Melinder [39]

Temperature:	-80.0 °C to 100.0 °C	Th. Cond.:	coefficients to polynomial (2, 1)
Composition:	pure fluid	Viscosity:	coefficients to exppolynomial (3, 1)
Density:	coefficients to polynomial (2, 1)	Psat:	no information
Spec. Heat:	coefficients to polynomial (2, 1)	Tfreeze:	no information

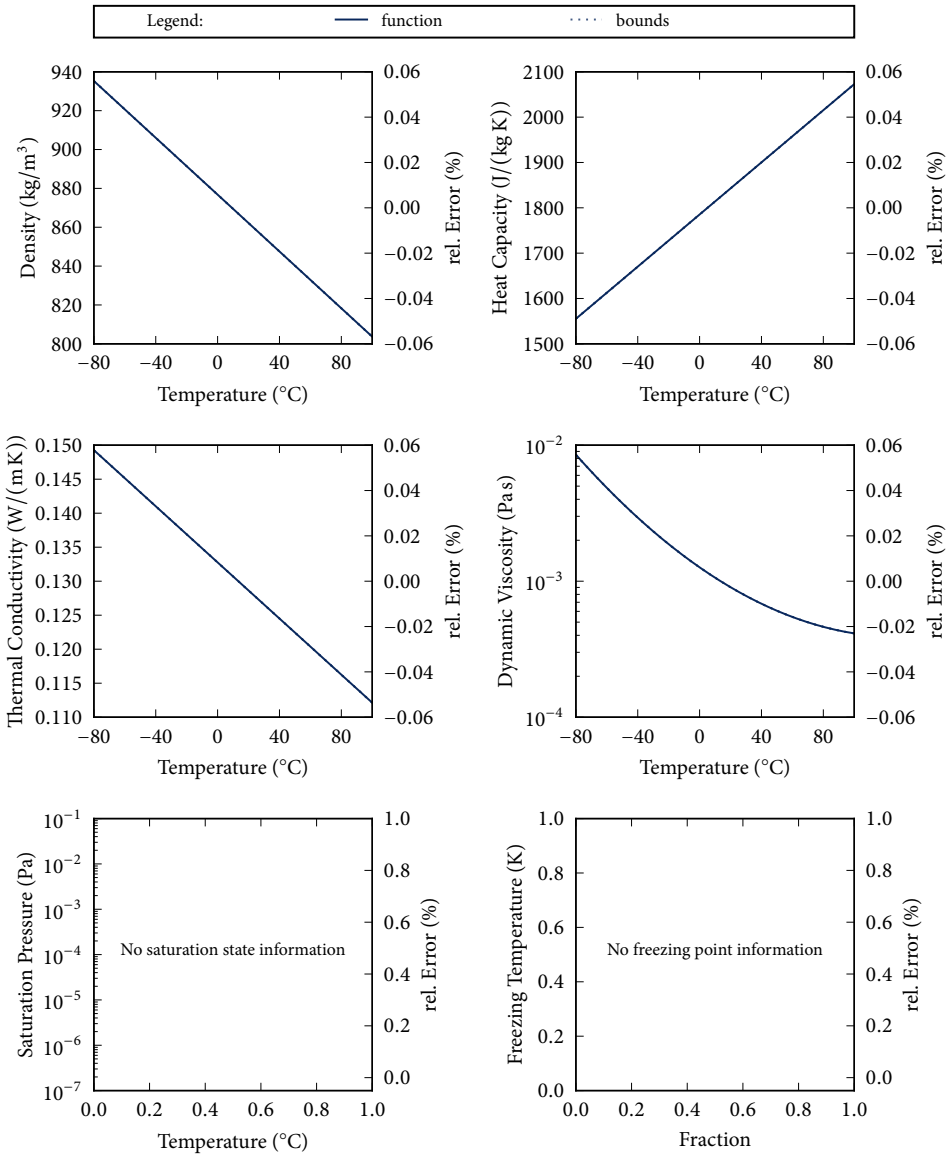

Fitted functions for DowJ

Description: DowthermJ
Source: *Technical Data Sheet* [52]

Temperature:	-80.0 °C to 345.0 °C	Th. Cond.:	data to polynomial (4, 1)
Composition:	pure fluid	Viscosity:	data to exponential (3,)
Density:	data to polynomial (4, 1)	Psat:	data to logexponential (3,)
Spec. Heat:	data to polynomial (4, 1)	Tfreeze:	no information

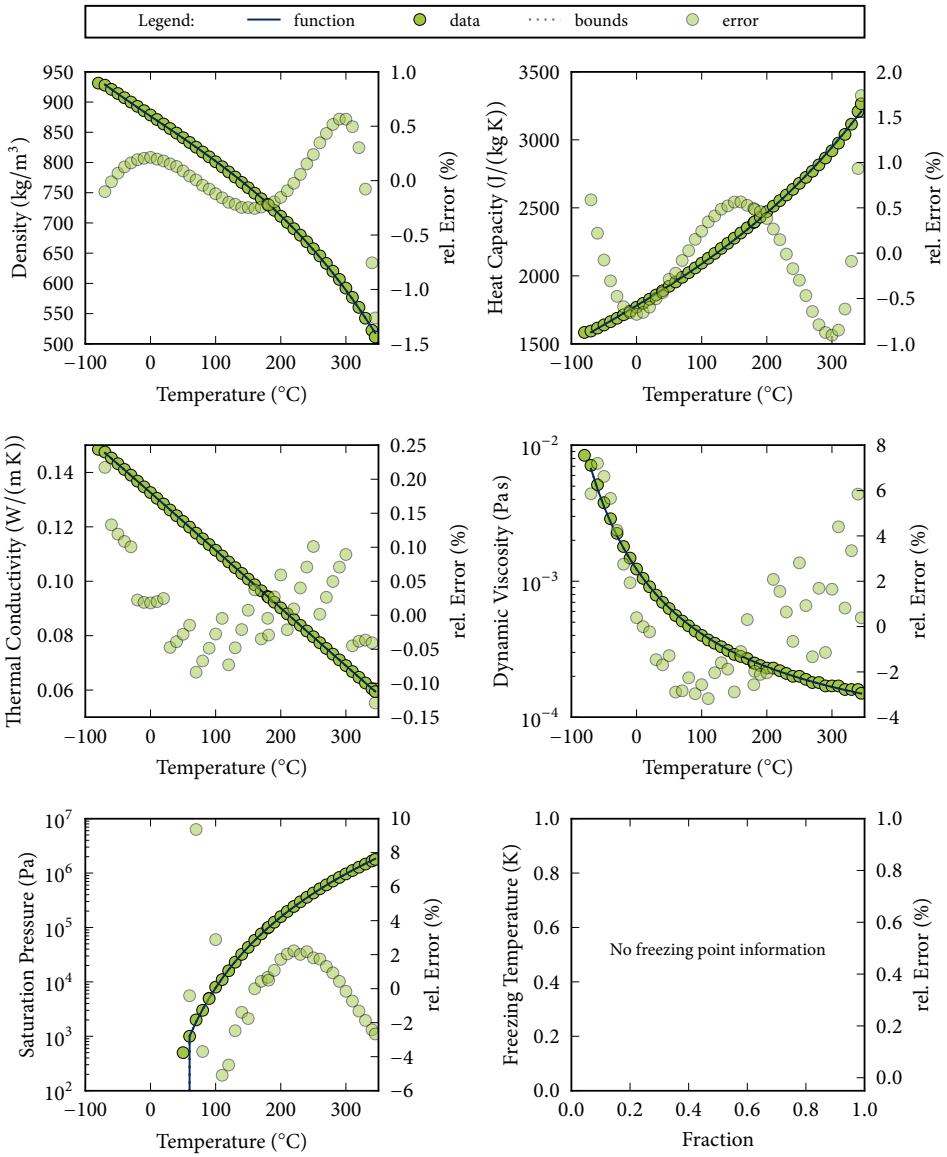

Fitted functions for DowJ2

Description:	Dowtherm J, Diethylbenzene mixture		
Source:	*Technical Data Sheet* [52]		
	Skovrup [49]		
Temperature:	-73.0 °C to 315.0 °C	Th. Cond.:	data to polynomial (4, 1)
Composition:	pure fluid	Viscosity:	data to exponential (3,)
Density:	data to polynomial (4, 1)	Psat:	no information
Spec. Heat:	data to polynomial (4, 1)	Tfreeze:	no information

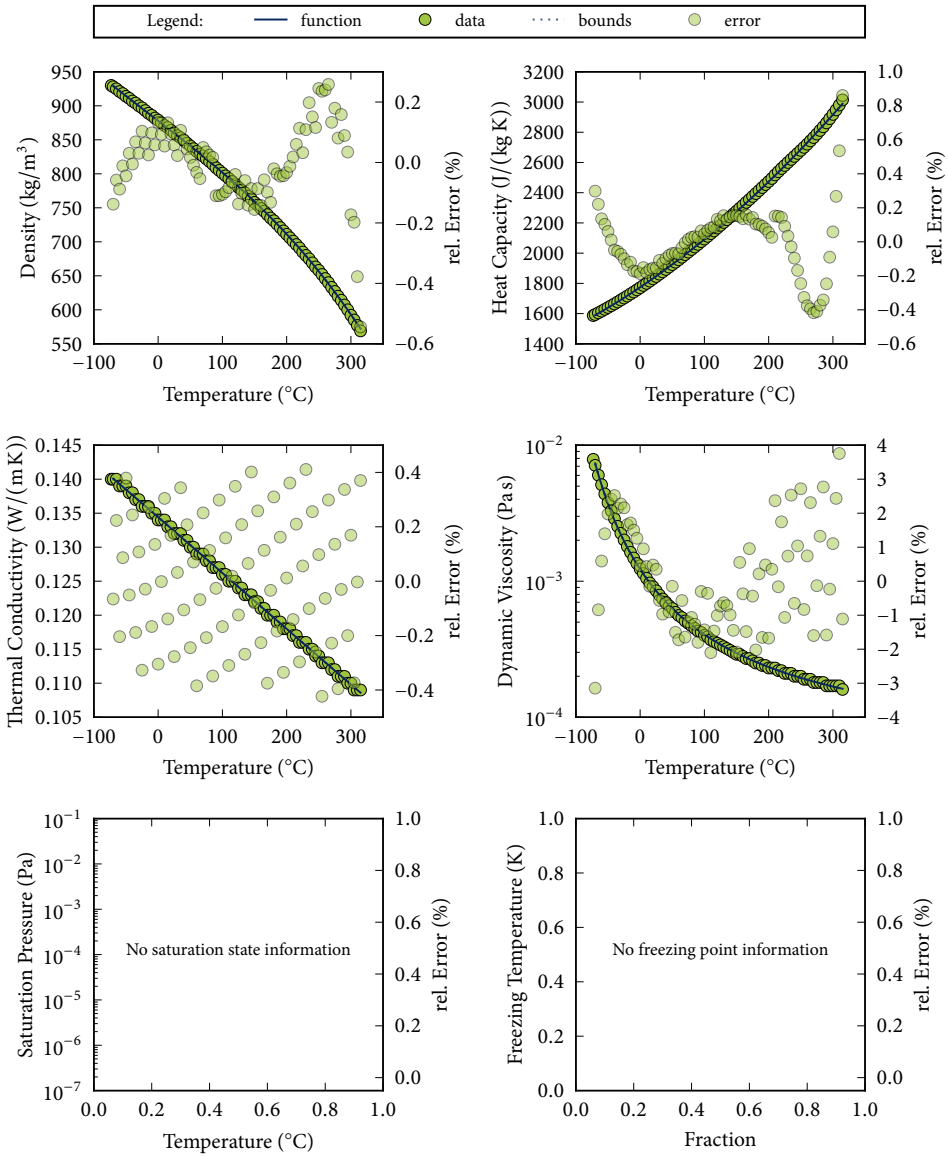

Fitted functions for DowQ

Description: DowthermQ
Source: *Technical Data Sheet* [52]

Temperature:	-35.0 °C to 360.0 °C	Th. Cond.:	data to polynomial (4, 1)
Composition:	pure fluid	Viscosity:	data to exponential (3,)
Density:	data to polynomial (4, 1)	Psat:	data to logexponential (3,)
Spec. Heat:	data to polynomial (4, 1)	Tfreeze:	no information

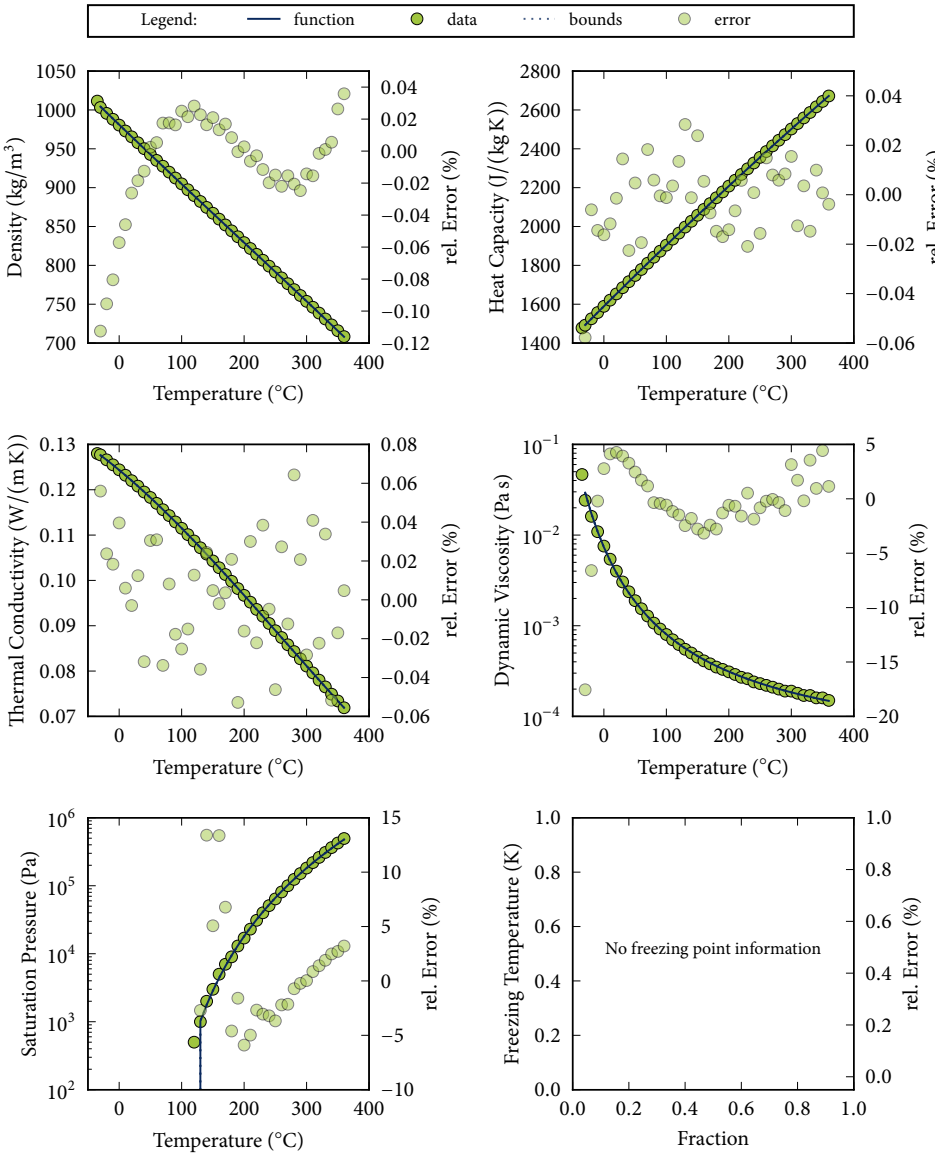

Fitted functions for DowQ2

Description:	Dowtherm Q, Diphenylethane/alkylated aromatics		
Source:	*Technical Data Sheet* [52]		
	Skovrup [49]		
Temperature:	-35.0 °C to 330.0 °C	Th. Cond.:	data to polynomial (4, 1)
Composition:	pure fluid	Viscosity:	data to exponential (3,)
Density:	data to polynomial (4, 1)	Psat:	no information
Spec. Heat:	data to polynomial (4, 1)	Tfreeze:	no information

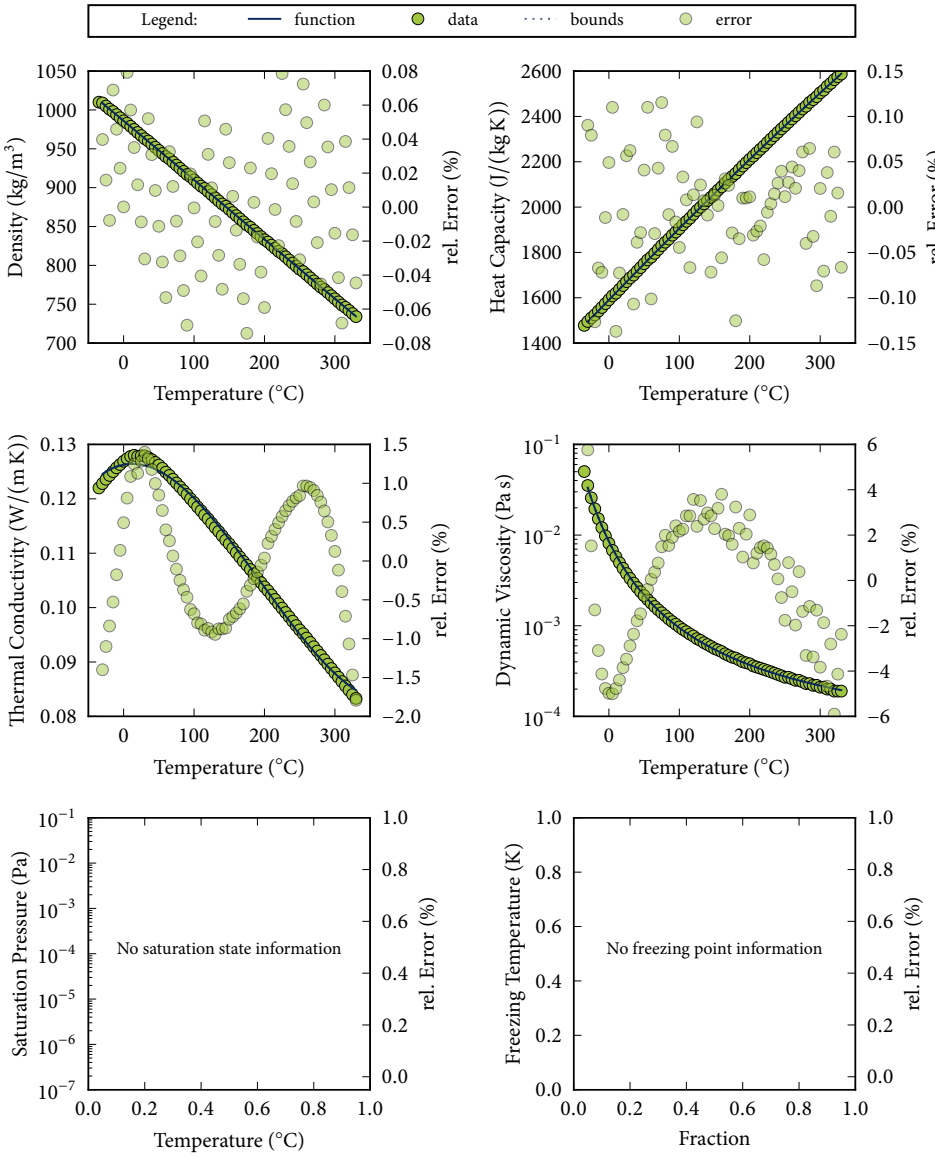

Fitted functions for HC10

Description: Dynalene HC10
Source: *Technical Data Sheet* [58]

Temperature:	-10.0 °C to 218.0 °C	Th. Cond.:	data to polynomial (4, 1)
Composition:	pure fluid	Viscosity:	data to exponential (3,)
Density:	data to polynomial (4, 1)	Psat:	data to exppolynomial (4, 1)
Spec. Heat:	data to polynomial (4, 1)	Tfreeze:	no information

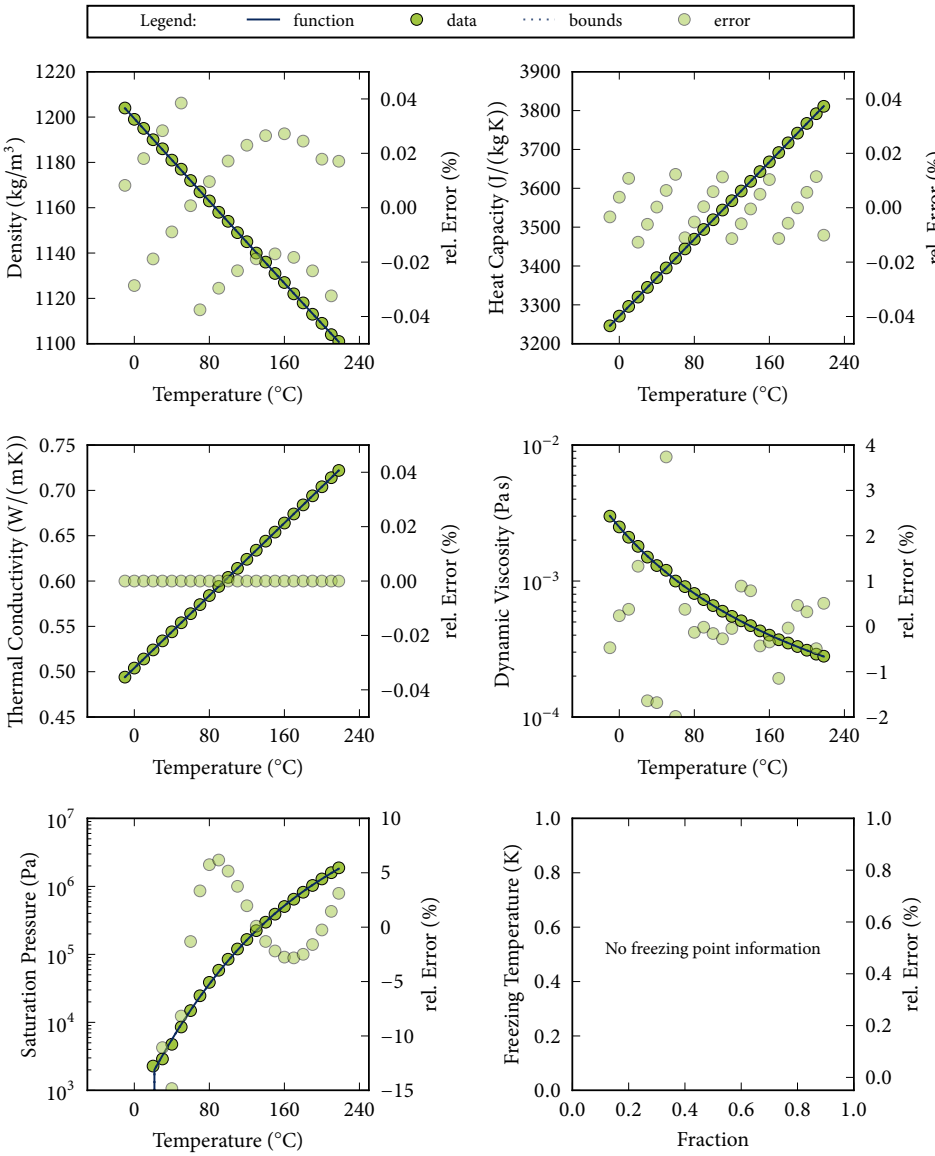

Fitted functions for HC20

Description: Dynalene HC20
Source: *Technical Data Sheet* [58]

Temperature:	-20.0 °C to 210.0 °C	Th. Cond.:	data to polynomial (4, 1)
Composition:	pure fluid	Viscosity:	data to exponential (3,)
Density:	data to polynomial (4, 1)	Psat:	data to exppolynomial (4, 1)
Spec. Heat:	data to polynomial (4, 1)	Tfreeze:	no information

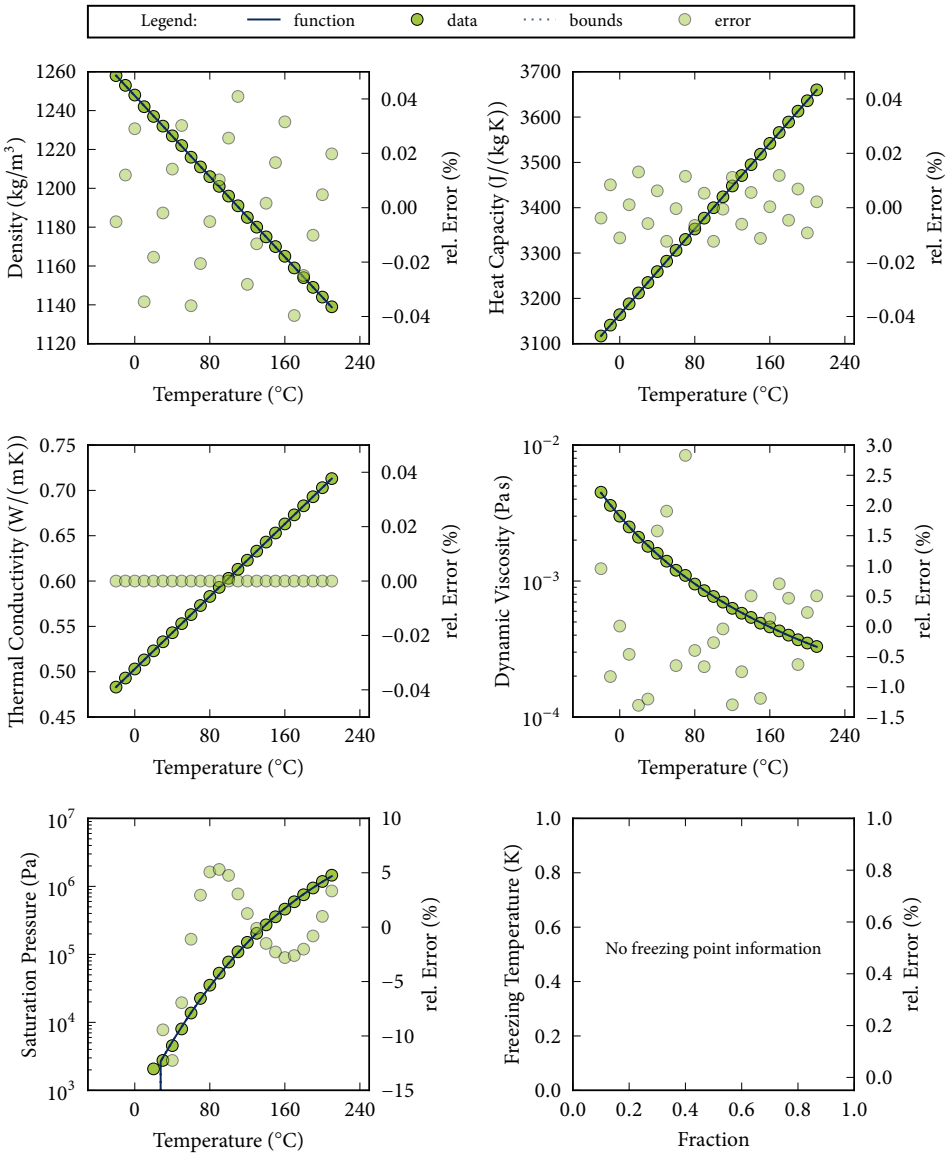

Fitted functions for HC30

Description: Dynalene HC30
Source: *Technical Data Sheet* [58]

Temperature:	-30.0 °C to 210.0 °C	Th. Cond.:	data to polynomial (4, 1)
Composition:	pure fluid	Viscosity:	data to exponential (3,)
Density:	data to polynomial (4, 1)	Psat:	data to exppolynomial (4, 1)
Spec. Heat:	data to polynomial (4, 1)	Tfreeze:	no information

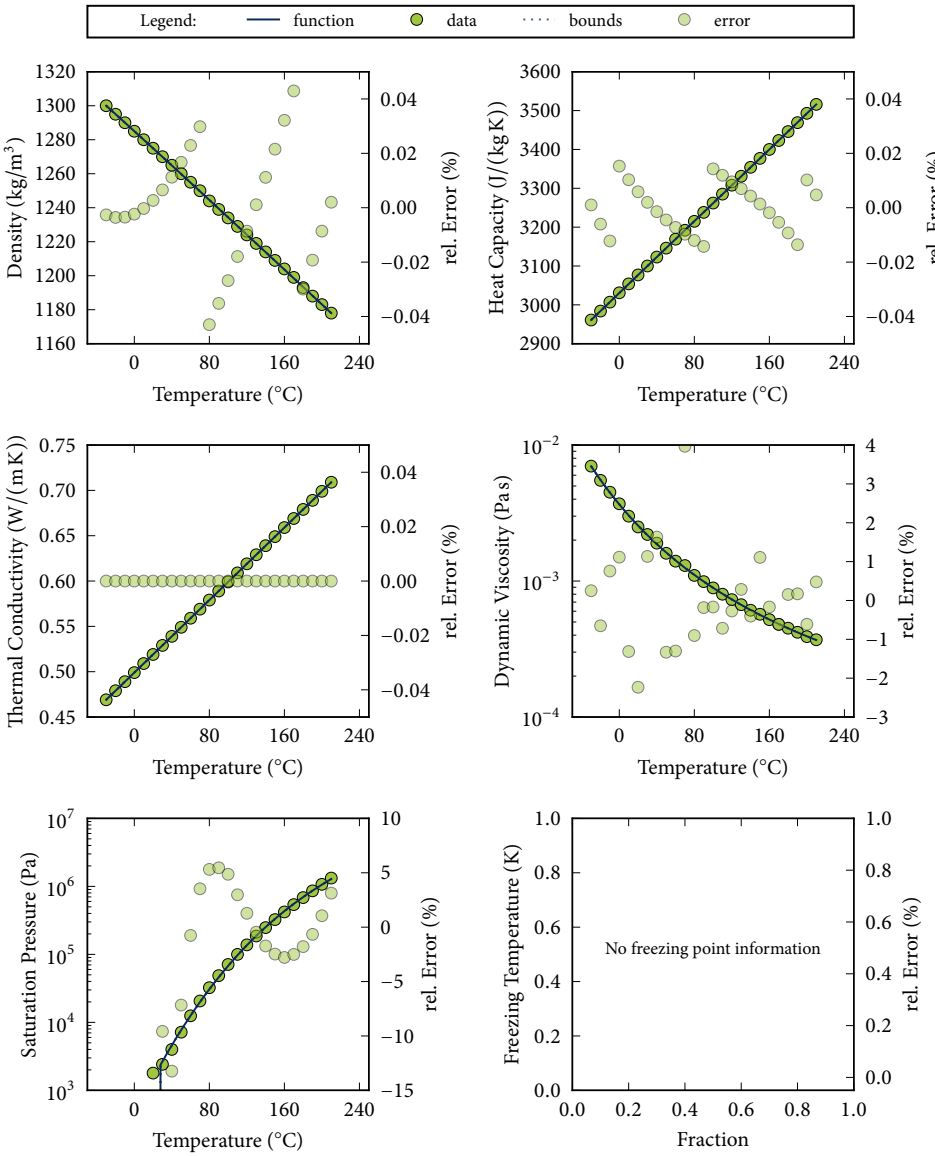

Fitted functions for HC40

Description: Dynalene HC40
Source: *Technical Data Sheet* [58]

Temperature:	-40.0 °C to 200.0 °C	Th. Cond.:	data to polynomial (4, 1)
Composition:	pure fluid	Viscosity:	data to exponential (3,)
Density:	data to polynomial (4, 1)	Psat:	data to exppolynomial (4, 1)
Spec. Heat:	data to polynomial (4, 1)	Tfreeze:	no information

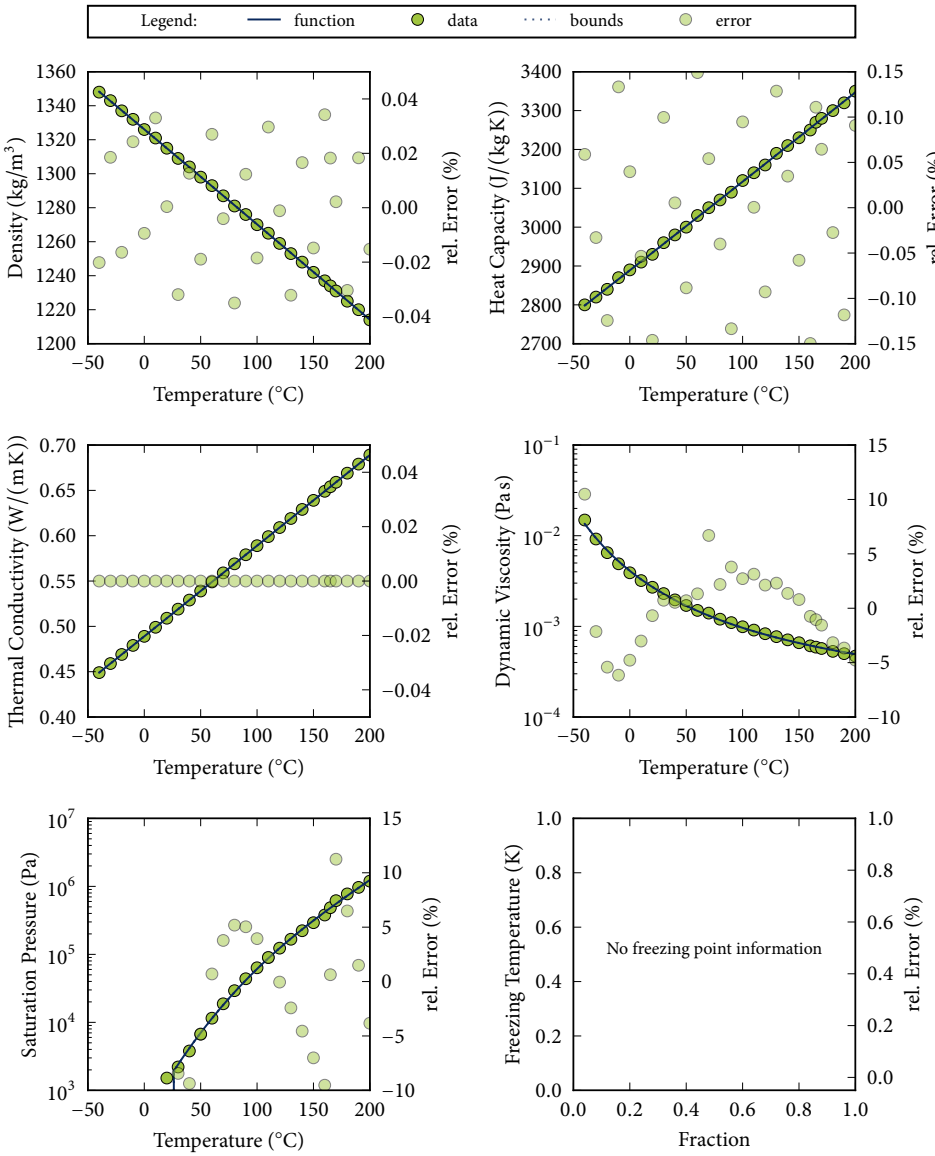

Fitted functions for HC50

Description: Dynalene HC50
Source: *Technical Data Sheet* [58]

Temperature:	-50.0 °C to 210.0 °C	Th. Cond.:	data to polynomial (4, 1)
Composition:	pure fluid	Viscosity:	data to exponential (3,)
Density:	data to polynomial (4, 1)	Psat:	data to exppolynomial (4, 1)
Spec. Heat:	data to polynomial (4, 1)	Tfreeze:	no information

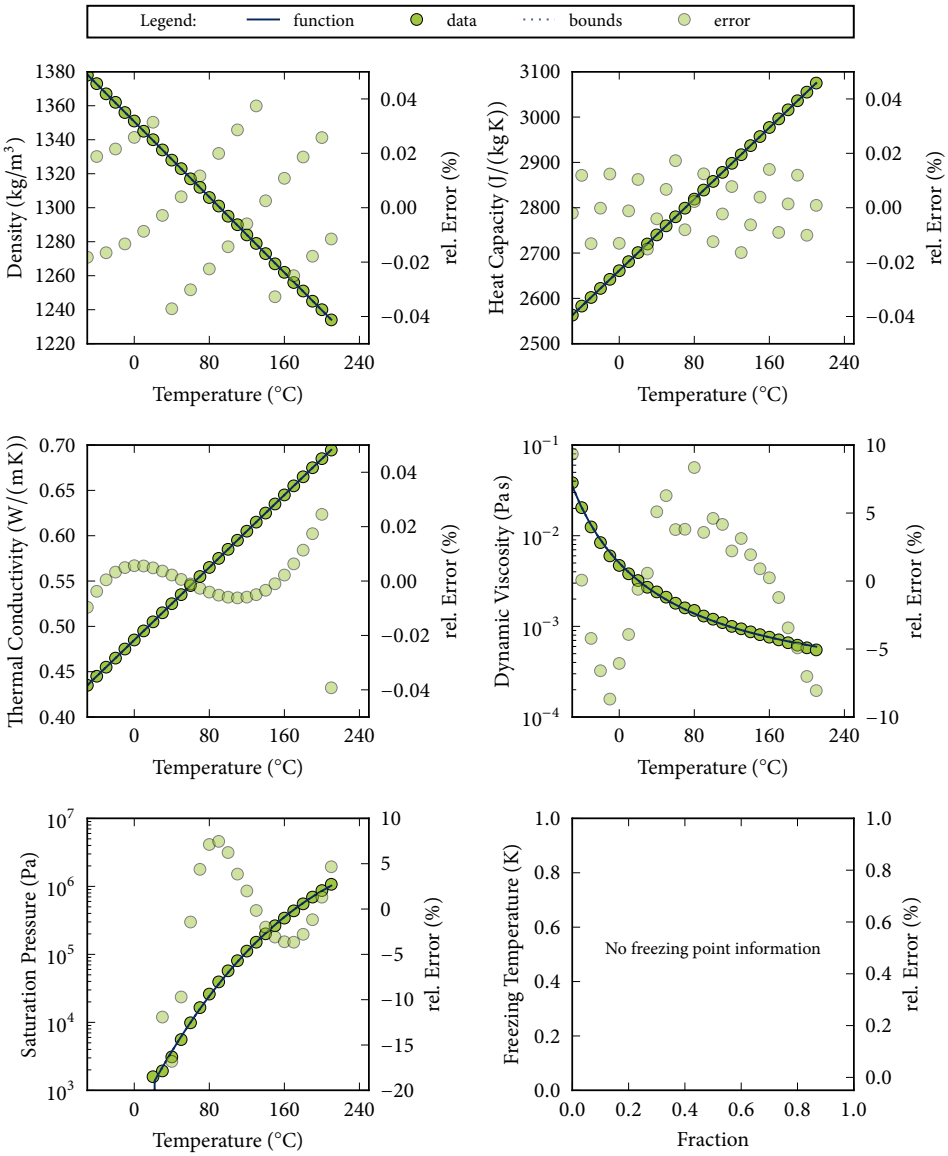

Fitted functions for HCB

Description: Hydrocarbon blend - Dynalene MV
Source: Melinder [39]

Temperature:	-80.0 °C to 100.0 °C	Th. Cond.:	coefficients to polynomial (2, 1)
Composition:	pure fluid	Viscosity:	coefficients to exppolynomial (3, 1)
Density:	coefficients to polynomial (2, 1)	Psat:	no information
Spec. Heat:	coefficients to polynomial (2, 1)	Tfreeze:	no information

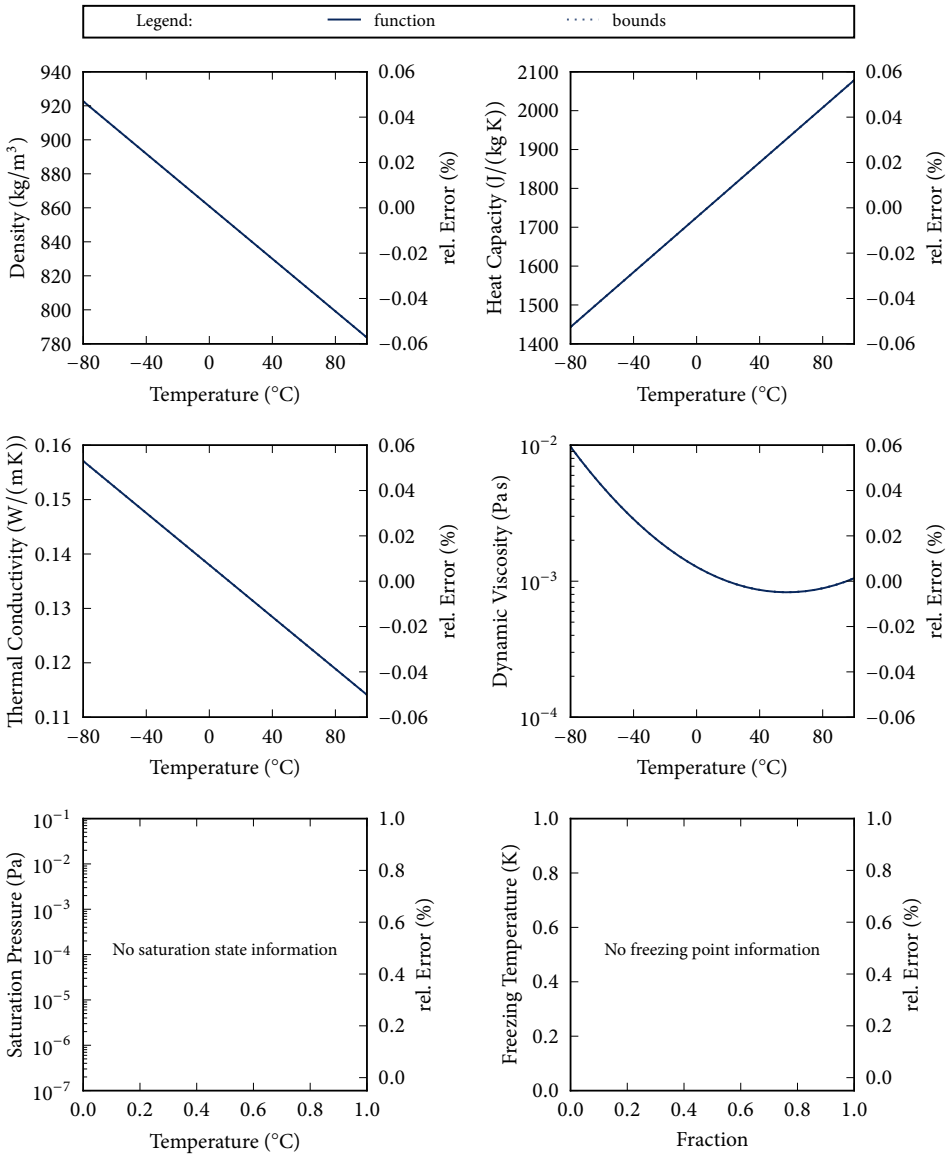

Fitted functions for HCM

Description: Hydrocarbon mixture - Gilotherm D12
Source: Melinder [39]

Temperature:	-80.0 °C to 100.0 °C	Th. Cond.:	coefficients to polynomial (2, 1)
Composition:	pure fluid	Viscosity:	coefficients to exppolynomial (3, 1)
Density:	coefficients to polynomial (2, 1)	Psat:	no information
Spec. Heat:	coefficients to polynomial (2, 1)	Tfreeze:	no information

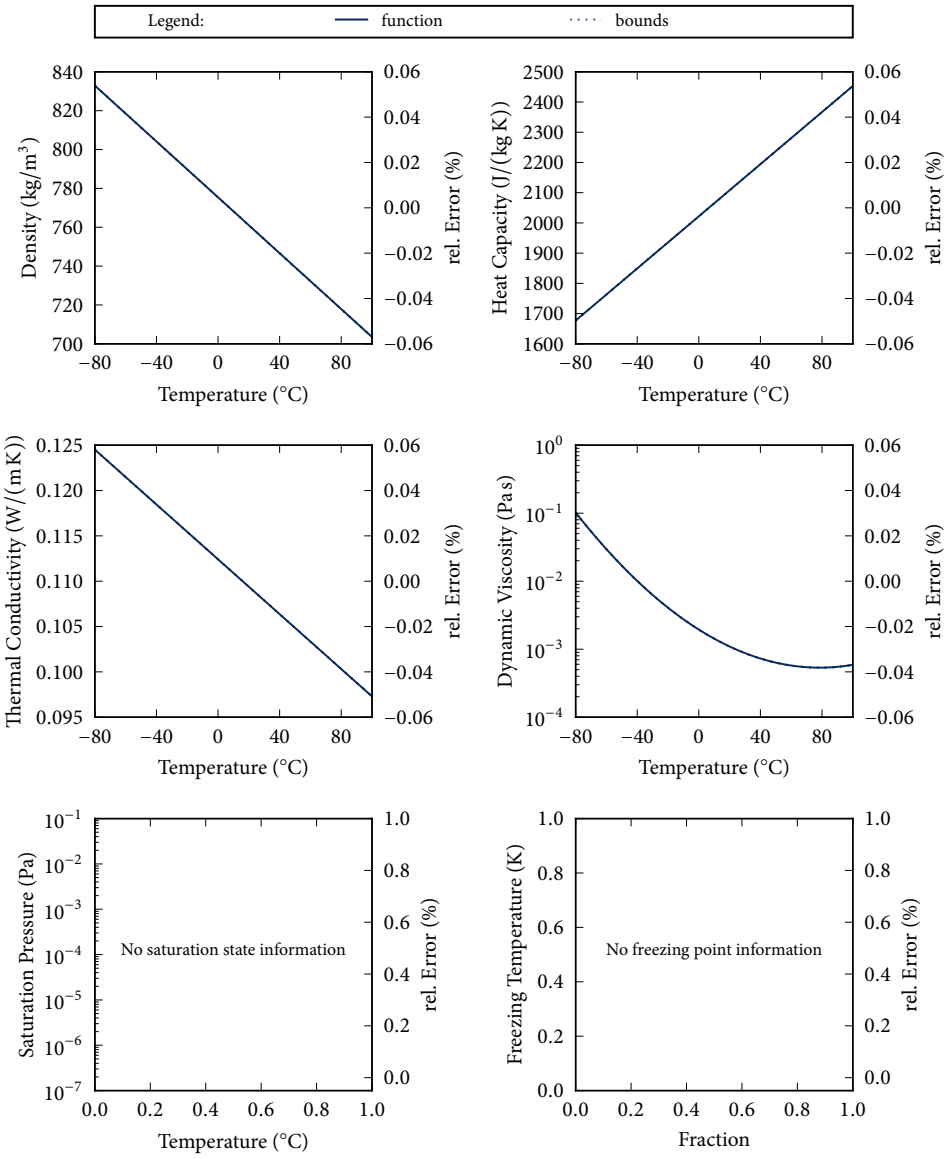

Fitted functions for HFE

Description: Hydrofluoroether - HFE-7100 3M Novec
Source: Melinder [39]

Temperature:	-80.0 °C to 100.0 °C	Th. Cond.:	coefficients to polynomial (2, 1)
Composition:	pure fluid	Viscosity:	coefficients to exppolynomial (3, 1)
Density:	coefficients to polynomial (2, 1)	Psat:	no information
Spec. Heat:	coefficients to polynomial (2, 1)	Tfreeze:	no information

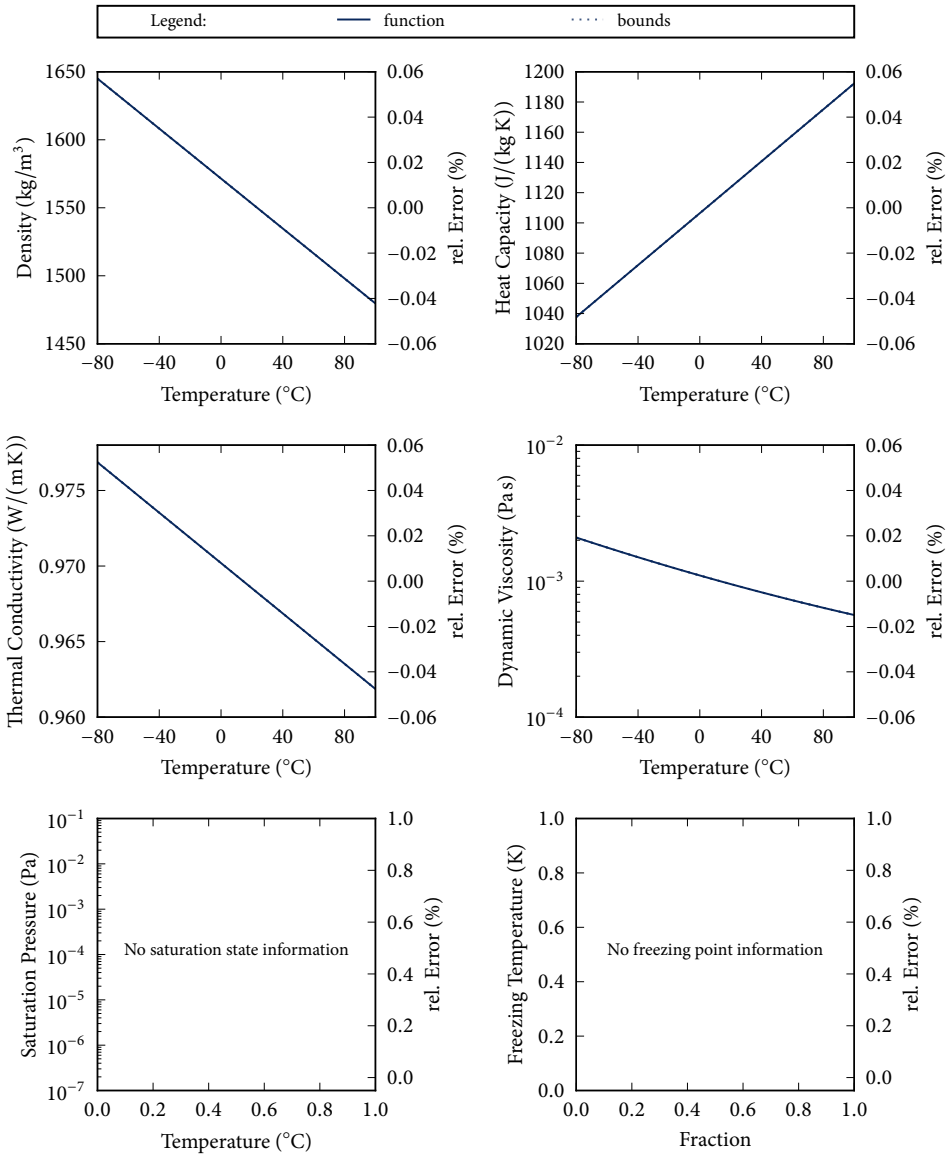

Fitted functions for HFE2

Description:	HFE-7100, Hydrofluoroether		
Source:	*Technical Information* [63]		
	Skovrup [49]		
Temperature:	-80.33 °C to 64.27 °C	Th. Cond.:	data to polynomial (4, 1)
Composition:	pure fluid	Viscosity:	data to exponential (3,)
Density:	data to polynomial (4, 1)	Psat:	no information
Spec. Heat:	data to polynomial (4, 1)	Tfreeze:	no information

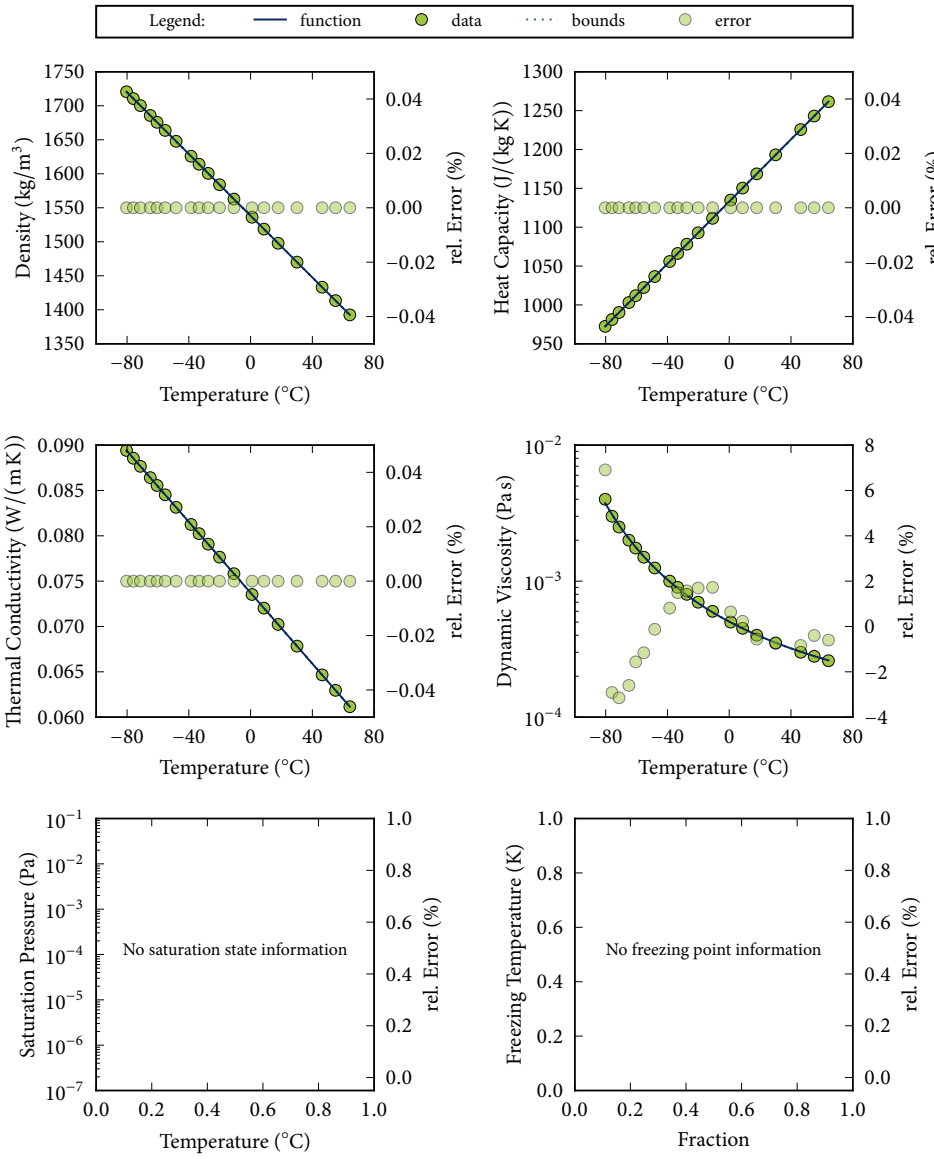

Fitted functions for HY20

Description: HYCOOL 20, Potassium formate
Source: *Technical Information* [62]

Temperature:	-20.0 °C to 50.0 °C	Th. Cond.:	equation to polynomial (4, 1)
Composition:	pure fluid	Viscosity:	equation to exponential (3,)
Density:	coefficients to polynomial (2, 1)	Psat:	no information
Spec. Heat:	coefficients to polynomial (2, 1)	Tfreeze:	no information

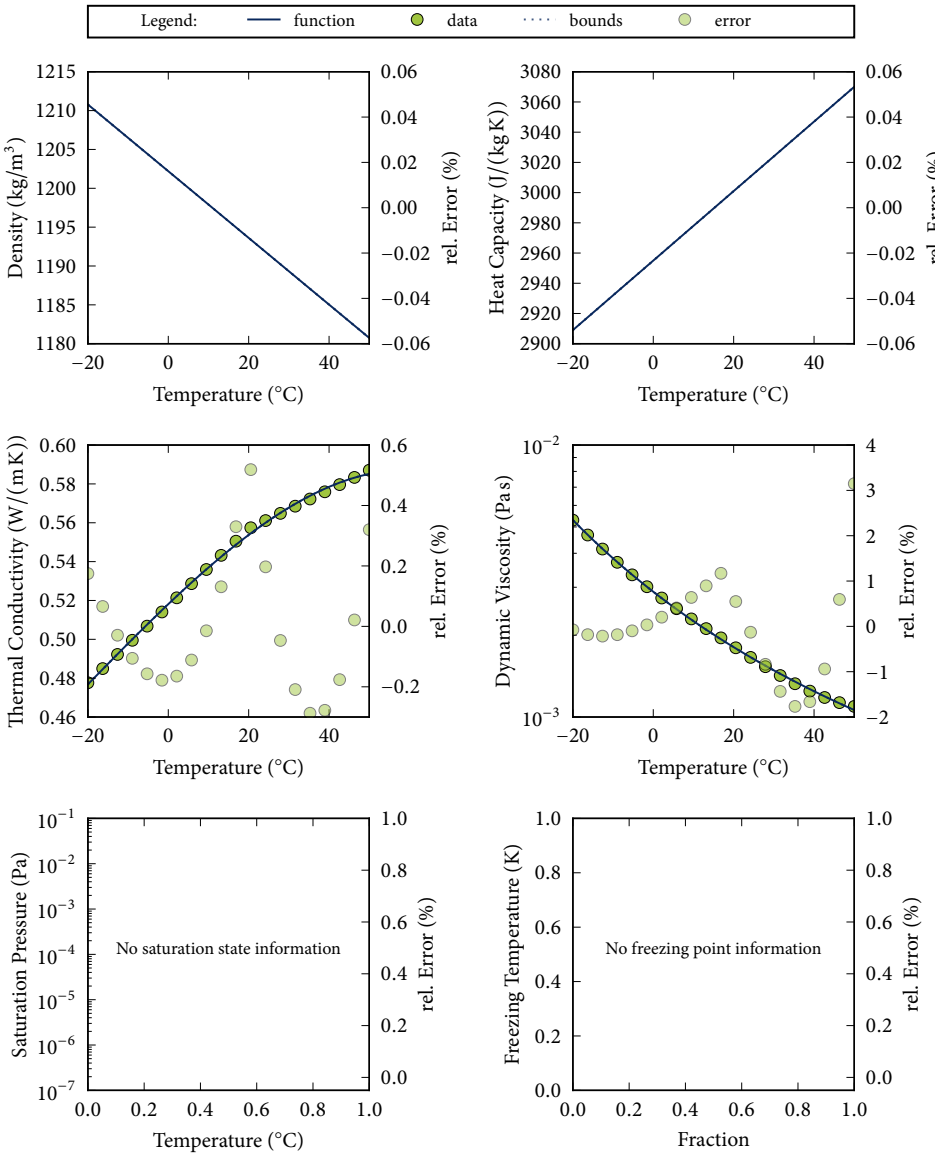

Fitted functions for HY30

Description: HyCool 30, Potassium formate
Source: *Technical Information* [62]

Temperature:	-30.0 °C to 50.0 °C	Th. Cond.:	equation to polynomial (4, 1)
Composition:	pure fluid	Viscosity:	equation to exponential (3,)
Density:	coefficients to polynomial (2, 1)	Psat:	no information
Spec. Heat:	coefficients to polynomial (2, 1)	Tfreeze:	no information

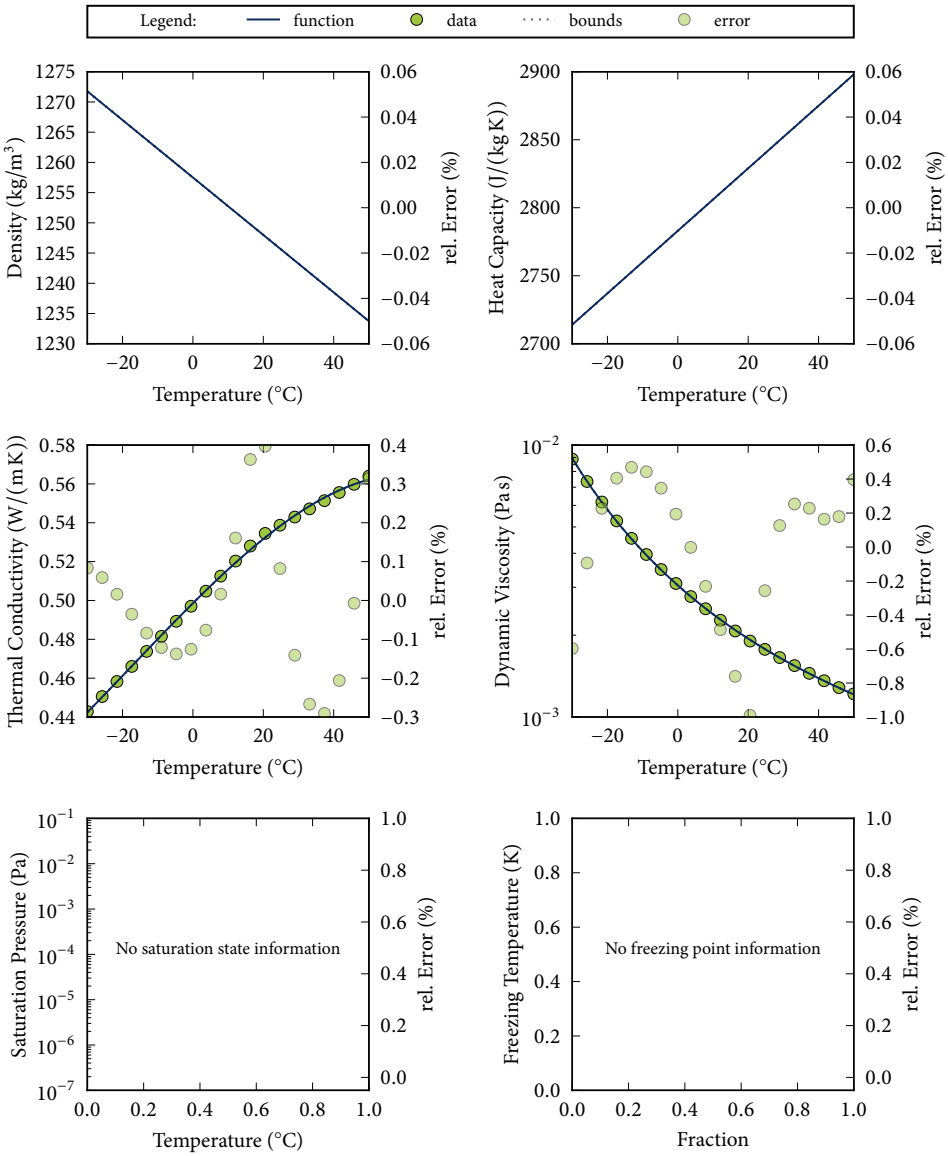

Fitted functions for HY40

Description: HyCool 40, Potassium formate
Source: *Technical Information* [62]

Temperature:	-40.0 °C to 20.0 °C	Th. Cond.:	coefficients to polynomial (2, 1)
Composition:	pure fluid	Viscosity:	equation to exponential (3,)
Density:	coefficients to polynomial (2, 1)	Psat:	no information
Spec. Heat:	coefficients to polynomial (2, 1)	Tfreeze:	no information

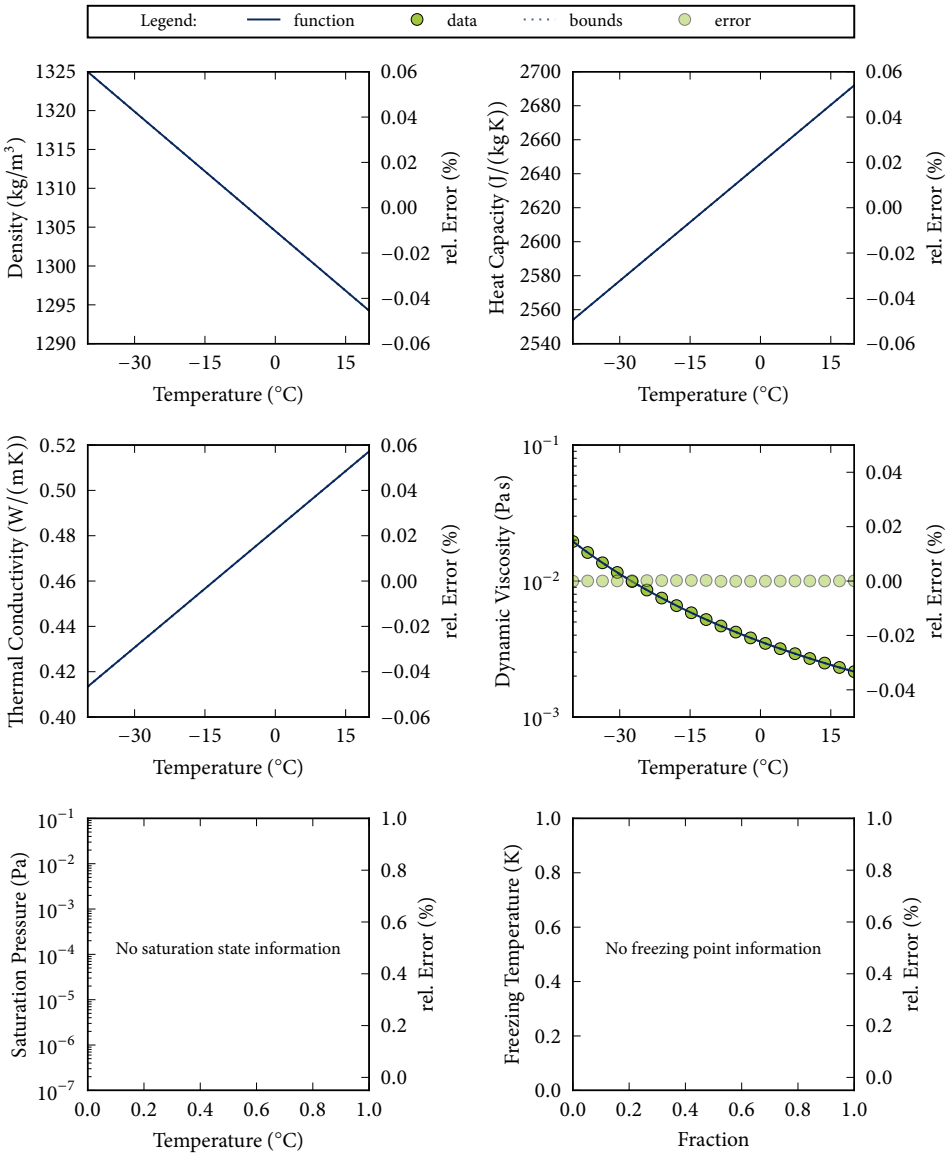

Fitted functions for HY45

Description: HyCool 45, Potassium formate
Source: *Technical Information* [62]

Temperature:	-45.0 °C to 20.0 °C	Th. Cond.:	coefficients to polynomial (2, 1)
Composition:	pure fluid	Viscosity:	equation to exponential (3,)
Density:	coefficients to polynomial (2, 1)	Psat:	no information
Spec. Heat:	coefficients to polynomial (2, 1)	Tfreeze:	no information

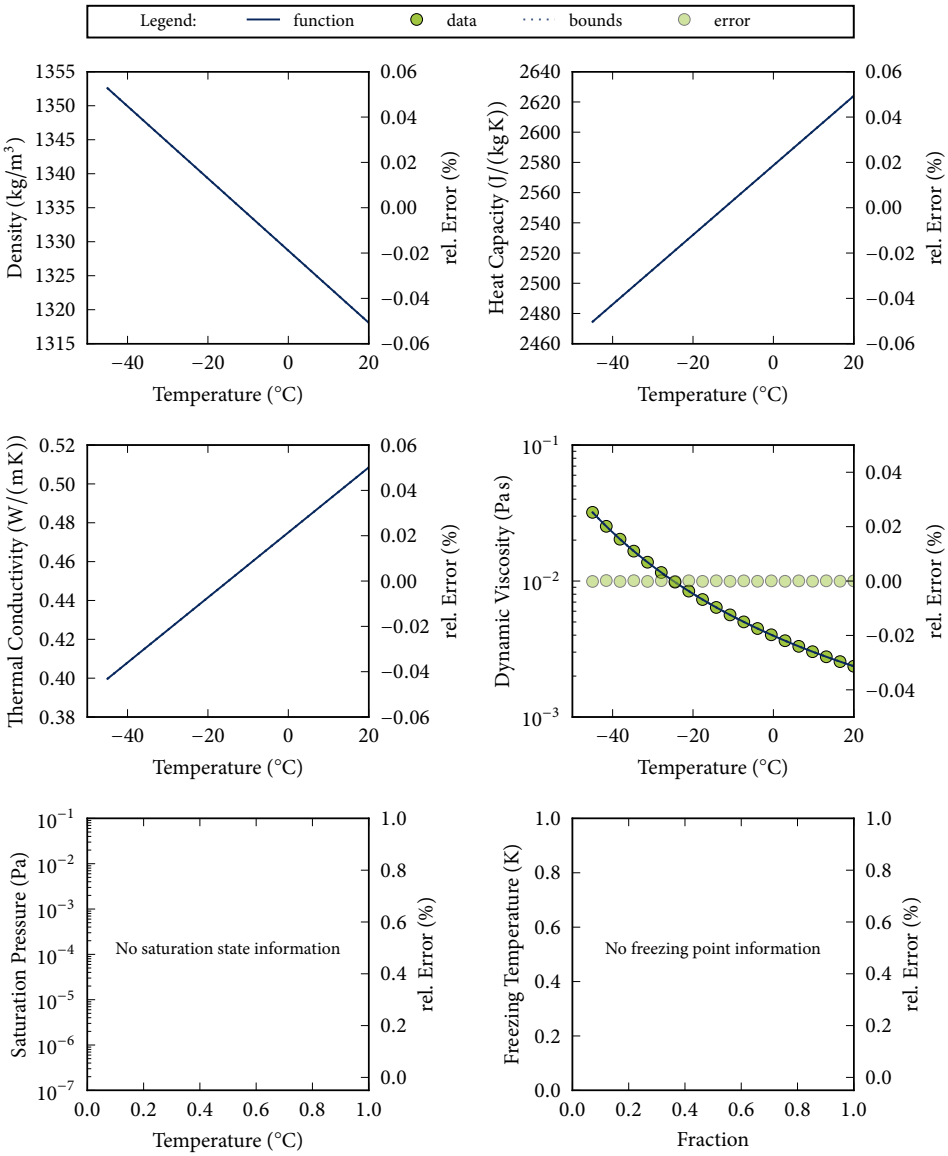

Fitted functions for HY50

Description: HyCool 50, Potassium formate
Source: *Technical Information* [62]

Temperature:	-50.0 °C to 20.0 °C	Th. Cond.:	coefficients to polynomial (2, 1)
Composition:	pure fluid	Viscosity:	equation to exponential (3,)
Density:	coefficients to polynomial (2, 1)	Psat:	no information
Spec. Heat:	coefficients to polynomial (2, 1)	Tfreeze:	no information

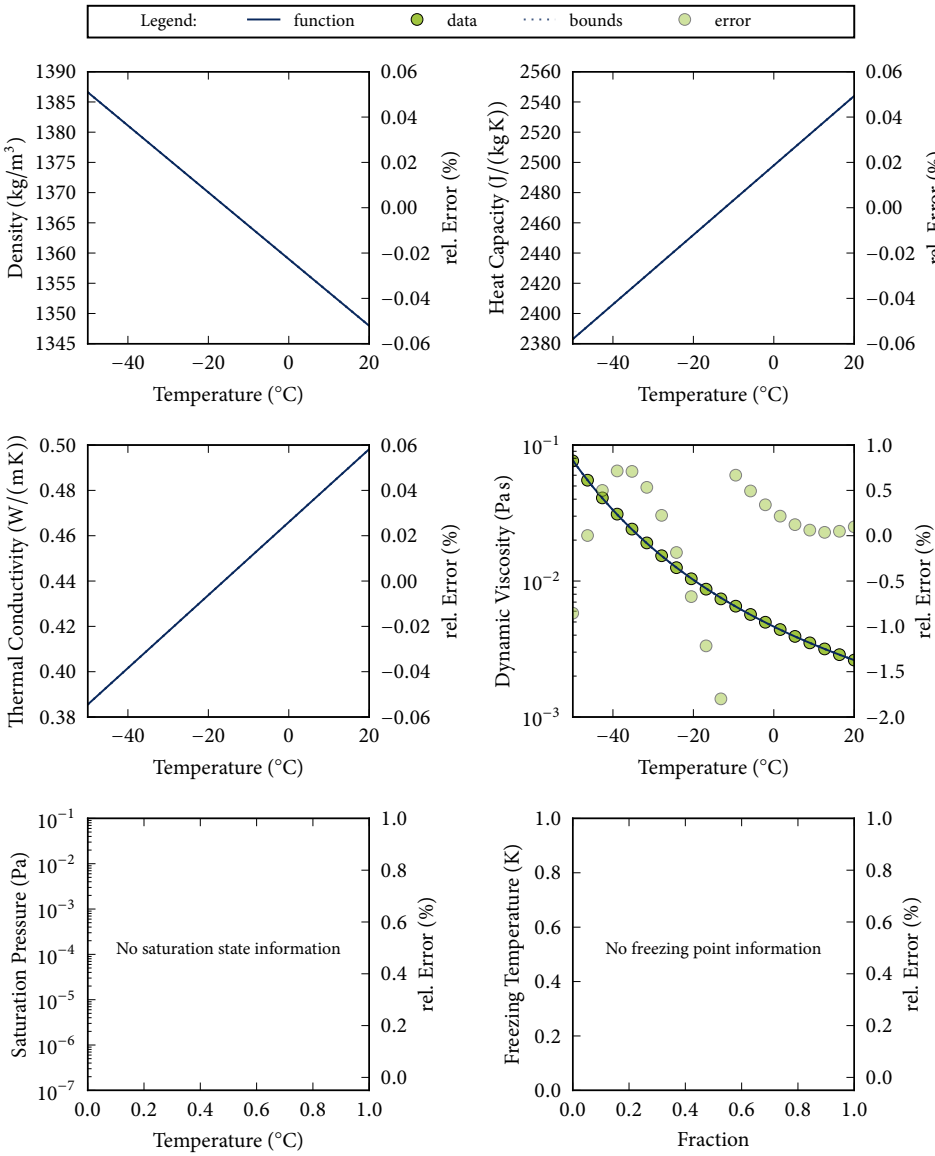

Fitted functions for NBS

Description:	NBS, Water		
Source:	Schmidt [46]		
	Skovrup [49]		
Temperature:	1.0 °C to 100.0 °C	Th. Cond.:	data to polynomial (4, 1)
Composition:	pure fluid	Viscosity:	data to exponential (3,)
Density:	data to polynomial (4, 1)	Psat:	no information
Spec. Heat:	data to polynomial (4, 1)	Tfreeze:	no information

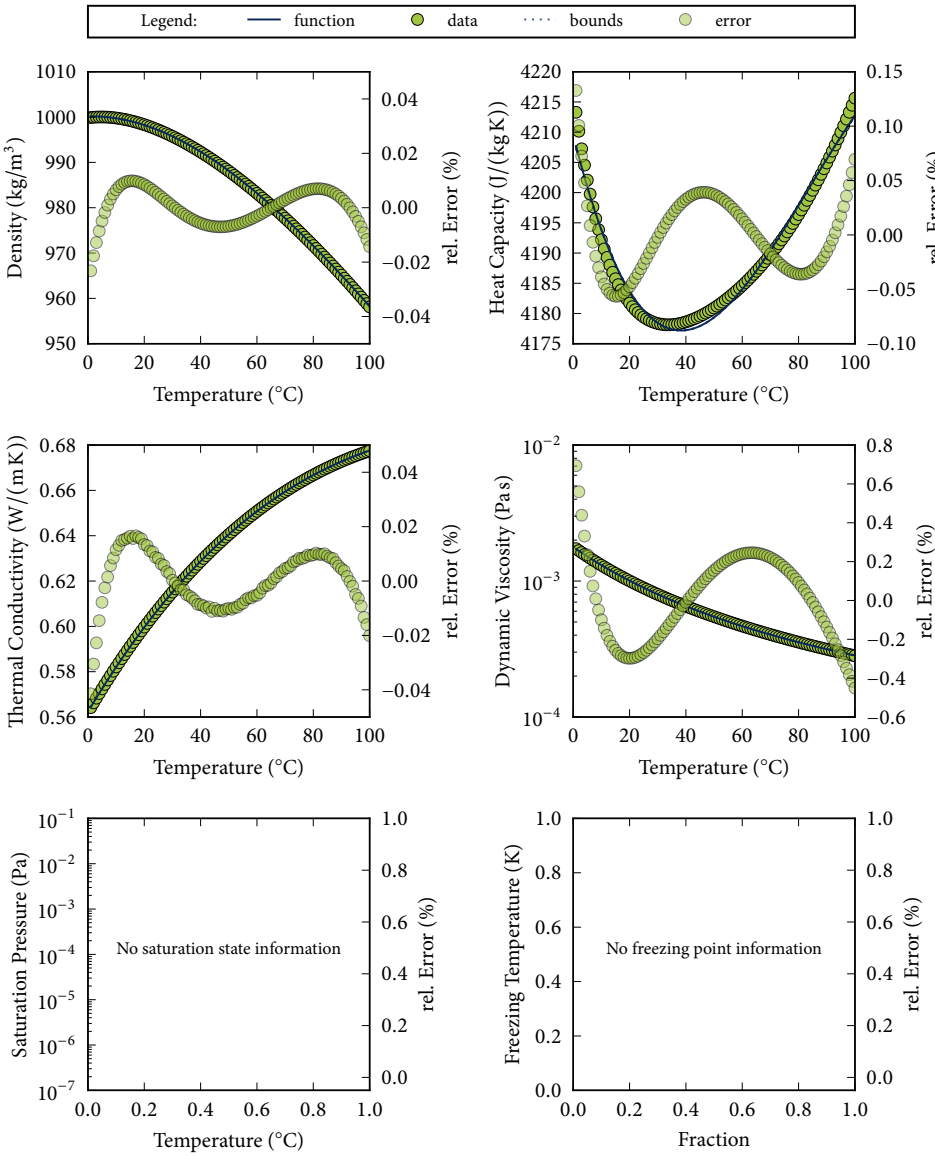

Fitted functions for NaK

Description: Nitrate salt, 0.6 NaNO3 and 0.4 KNO3
Source: Zavoico [74]

Temperature:	300.0 °C to 600.0 °C	Th. Cond.:	coefficients to polynomial (2, 1)
Composition:	pure fluid	Viscosity:	coefficients to polynomial (4, 1)
Density:	coefficients to polynomial (2, 1)	Psat:	no information
Spec. Heat:	coefficients to polynomial (2, 1)	Tfreeze:	no information

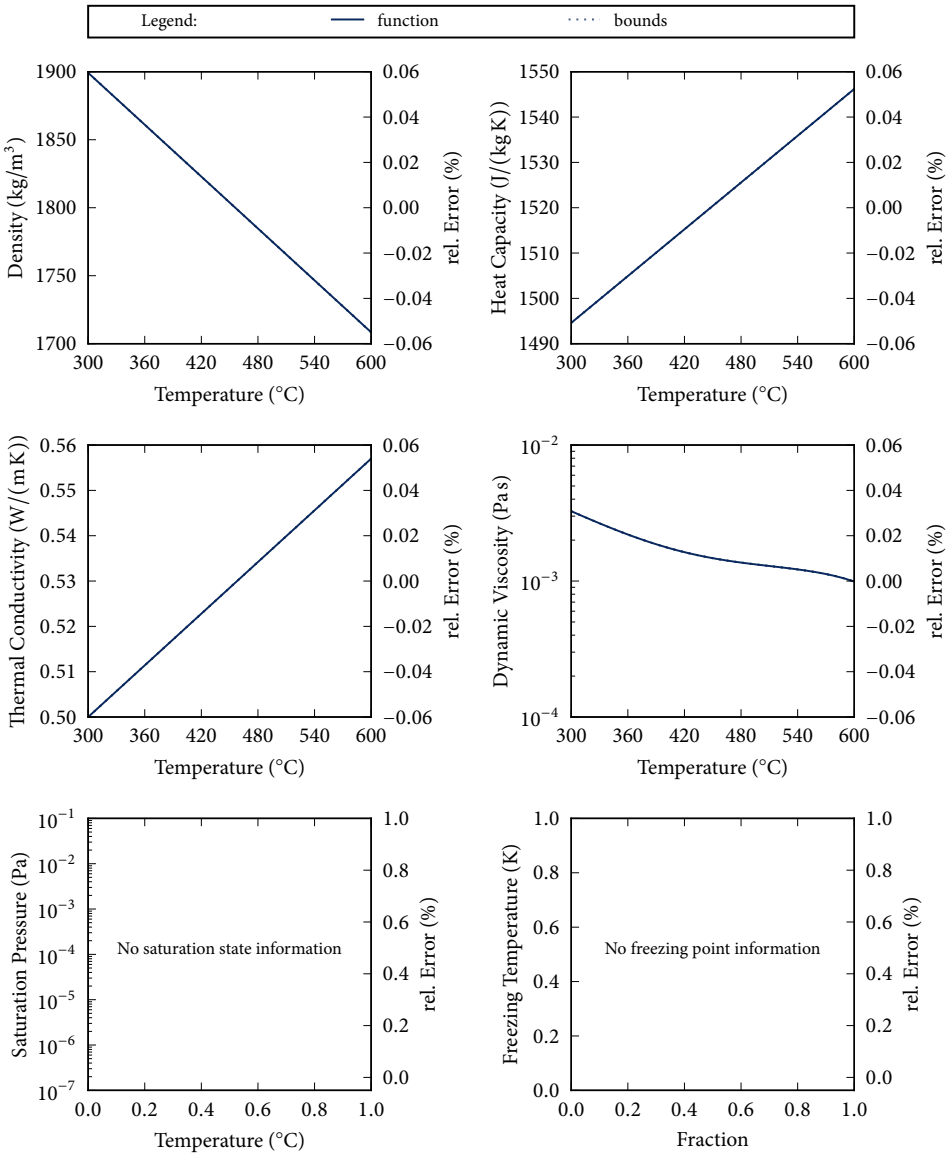

Fitted functions for PCL

Description:	Paracryol, Aliphatic Hydrocarbon		
Source:	*Technical Information* [60]		
	Skovrup [49]		
Temperature:	-40.0 °C to 180.0 °C	Th. Cond.:	data to polynomial (4, 1)
Composition:	pure fluid	Viscosity:	data to exponential (3,)
Density:	data to polynomial (4, 1)	Psat:	no information
Spec. Heat:	data to polynomial (4, 1)	Tfreeze:	no information

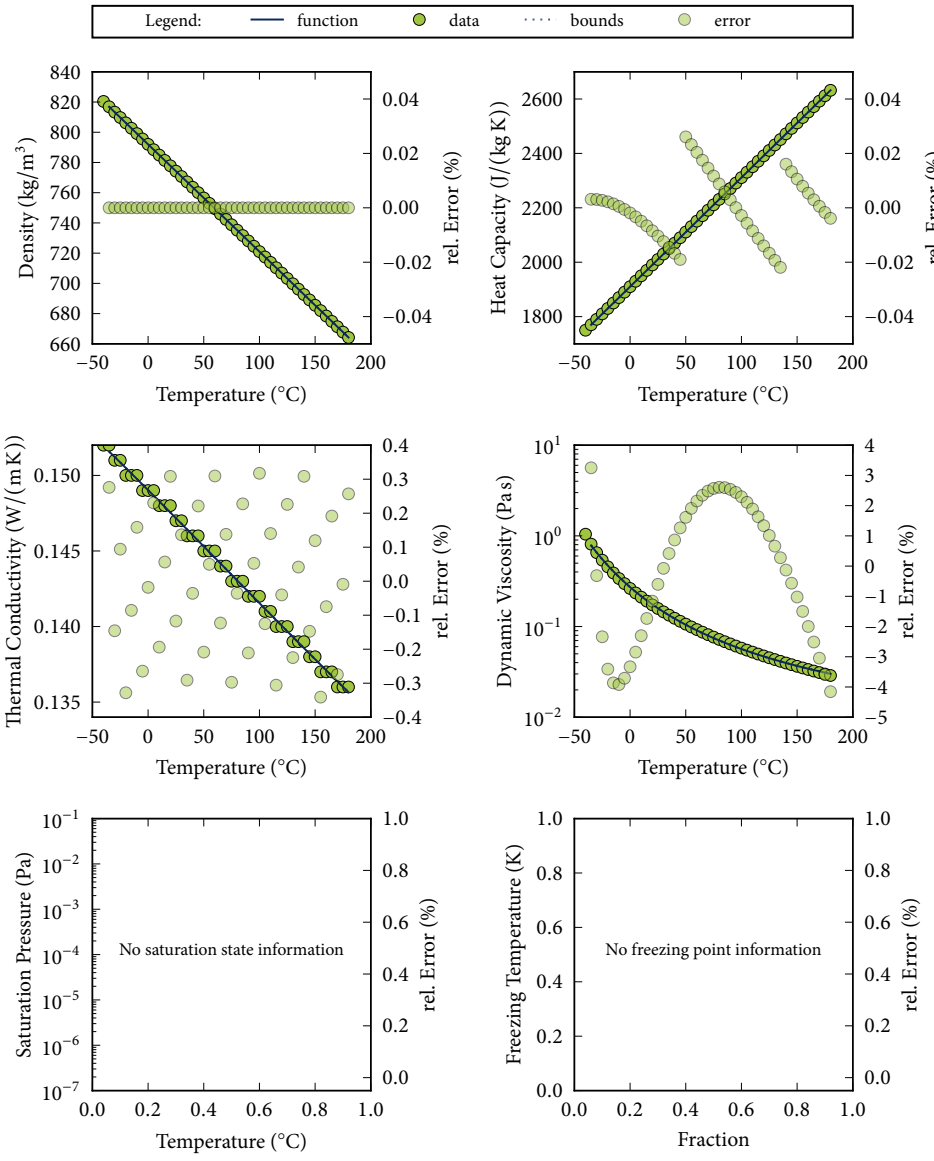

Fitted functions for PCR

Description: Paratherm CR
Source: *Thermal Properties Calculator v6.4* [65]

Temperature:	-100.0 °C to 220.0 °C	Th. Cond.:	data to polynomial (4, 1)
Composition:	pure fluid	Viscosity:	data to exponential (3,)
Density:	data to polynomial (4, 1)	Psat:	data to logexponential (3,)
Spec. Heat:	data to polynomial (4, 1)	Tfreeze:	no information

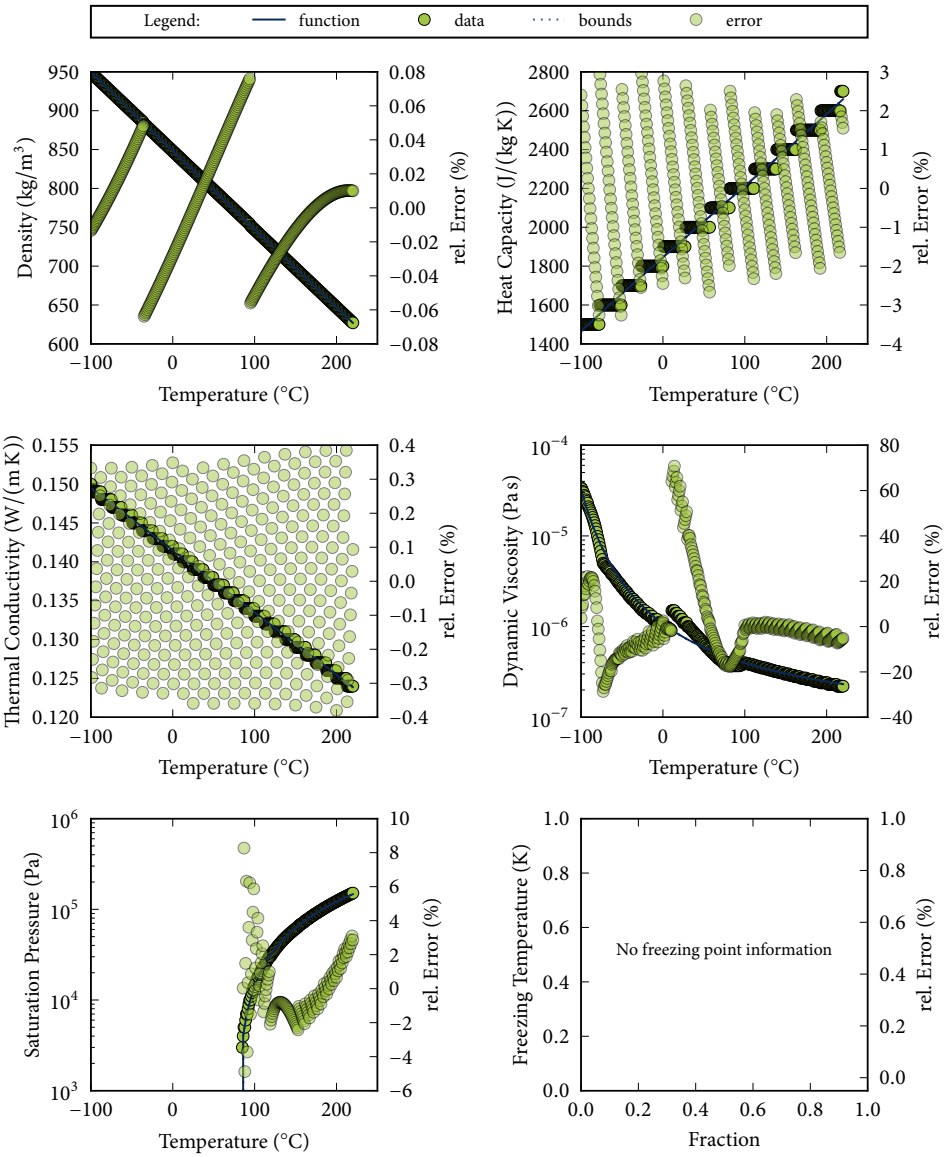

Fitted functions for PGLT

Description: Paratherm GLT
Source: *Thermal Properties Calculator v6.4* [65]

Temperature:	-15.0 °C to 315.0 °C	Th. Cond.:	data to polynomial (4, 1)
Composition:	pure fluid	Viscosity:	data to exponential (3,)
Density:	data to polynomial (4, 1)	Psat:	data to exppolynomial (4, 1)
Spec. Heat:	data to polynomial (4, 1)	Tfreeze:	no information

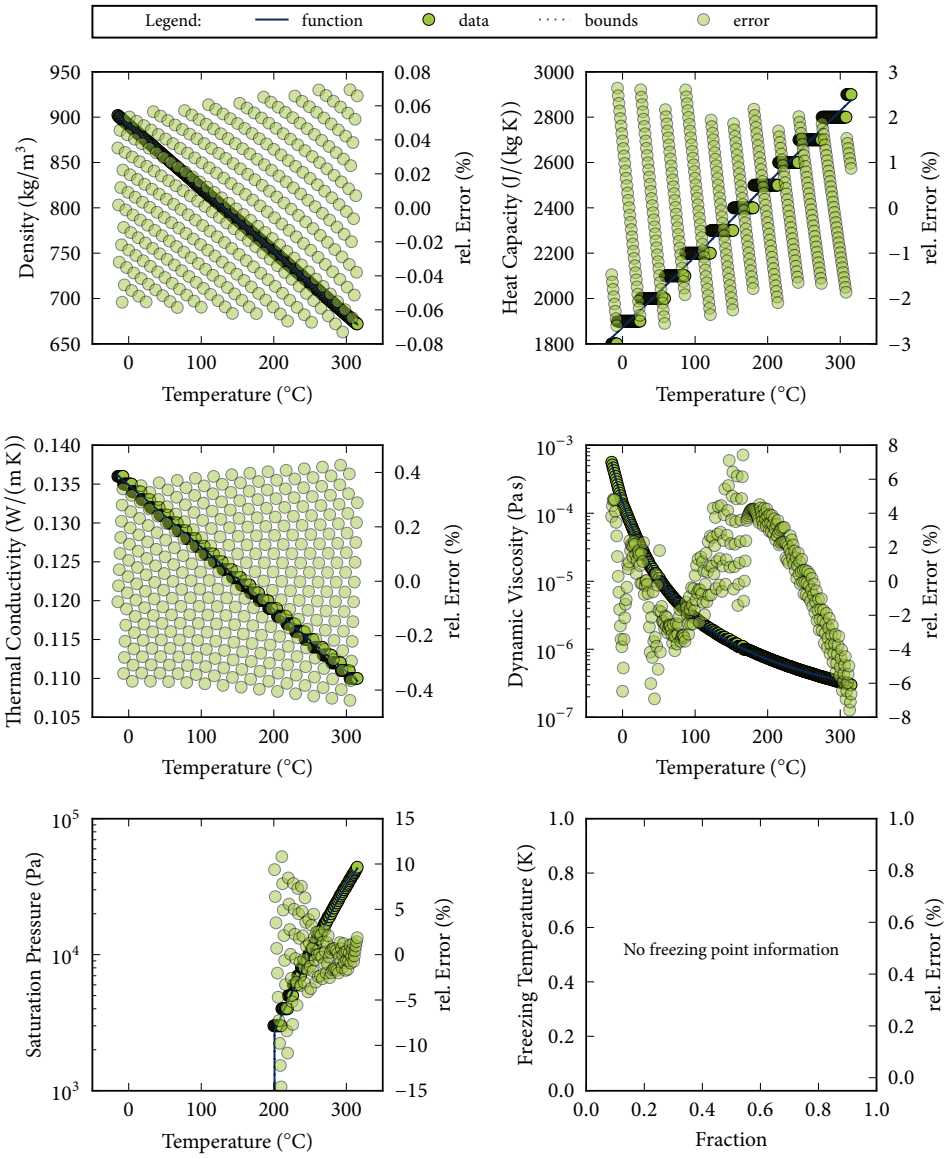

Fitted functions for PHE

Description: Paratherm HE
Source: *Thermal Properties Calculator v6.4* [65]

Temperature:	0.0 °C to 330.0 °C	Th. Cond.:	data to polynomial (4, 1)
Composition:	pure fluid	Viscosity:	data to exponential (3,)
Density:	data to polynomial (4, 1)	Psat:	data to exppolynomial (4, 1)
Spec. Heat:	data to polynomial (4, 1)	Tfreeze:	no information

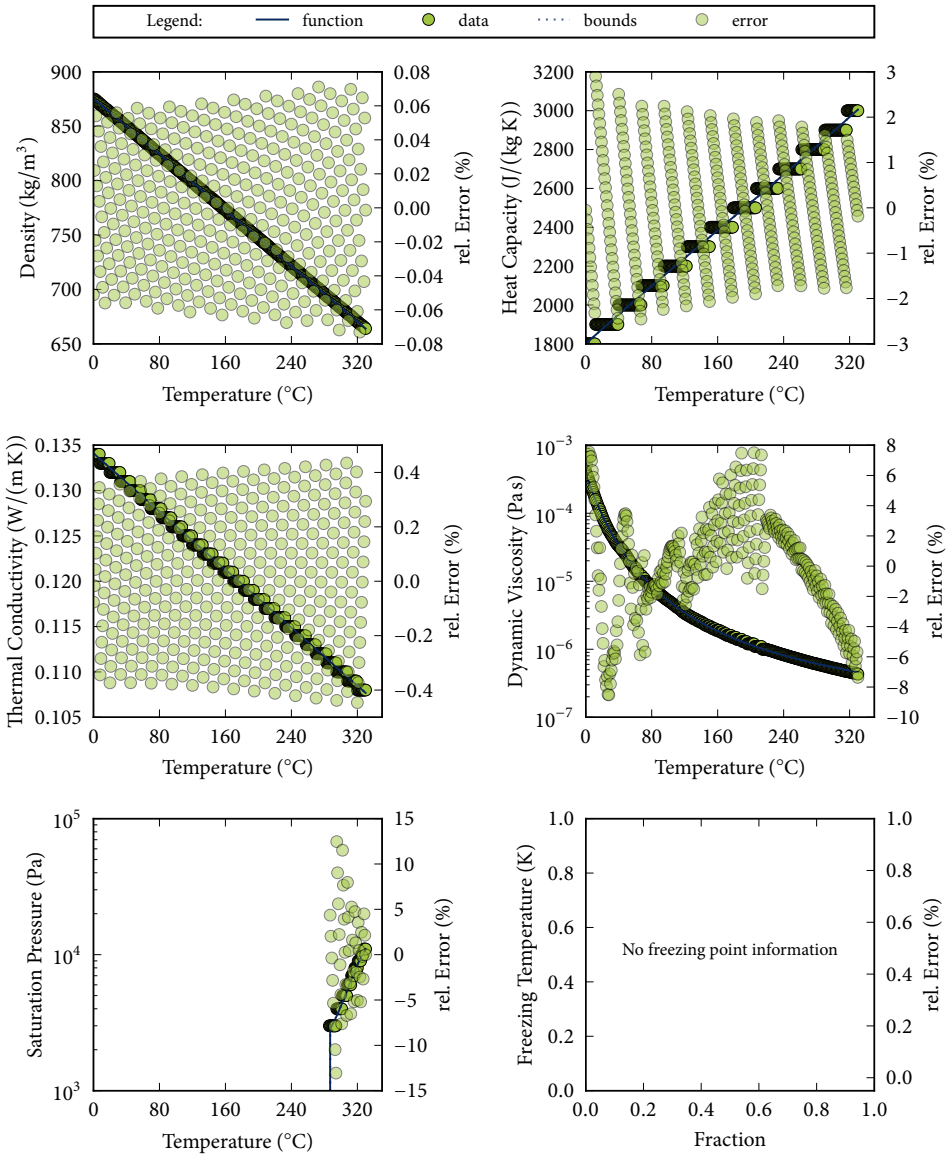

Fitted functions for PHR

Description: Paratherm HR
Source: *Thermal Properties Calculator v6.4* [65]

Temperature:	-15.0 °C to 370.0 °C	Th. Cond.:	data to polynomial (4, 1)
Composition:	pure fluid	Viscosity:	data to exponential (3,)
Density:	data to polynomial (4, 1)	Psat:	data to exppolynomial (4, 1)
Spec. Heat:	data to polynomial (4, 1)	Tfreeze:	no information

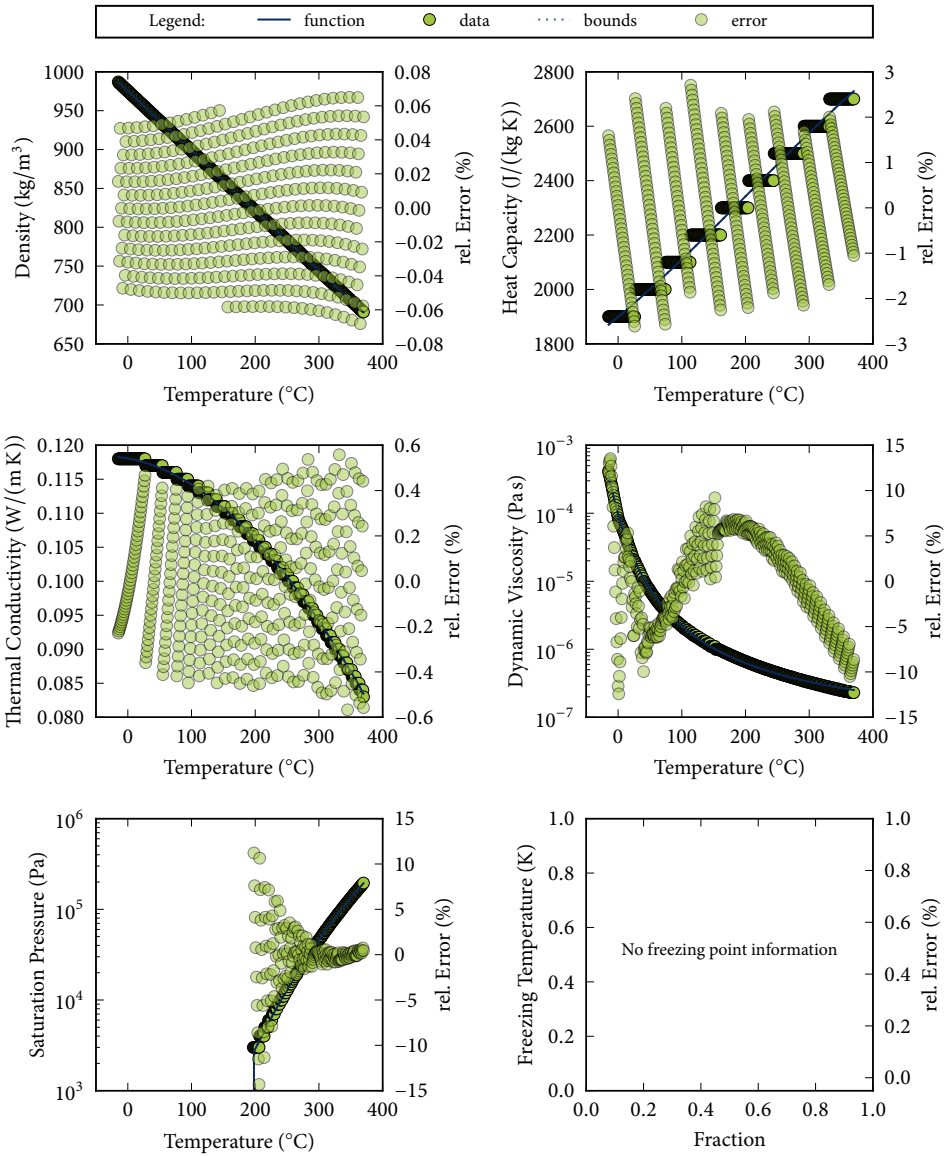

Fitted functions for PLR

Description: Paratherm LR
Source: *Thermal Properties Calculator v6.4* [65]

Temperature:	-85.0 °C to 230.0 °C	Th. Cond.:	data to polynomial (4, 1)
Composition:	pure fluid	Viscosity:	data to exponential (3,)
Density:	data to polynomial (4, 1)	Psat:	data to exppolynomial (4, 1)
Spec. Heat:	data to polynomial (4, 1)	Tfreeze:	no information

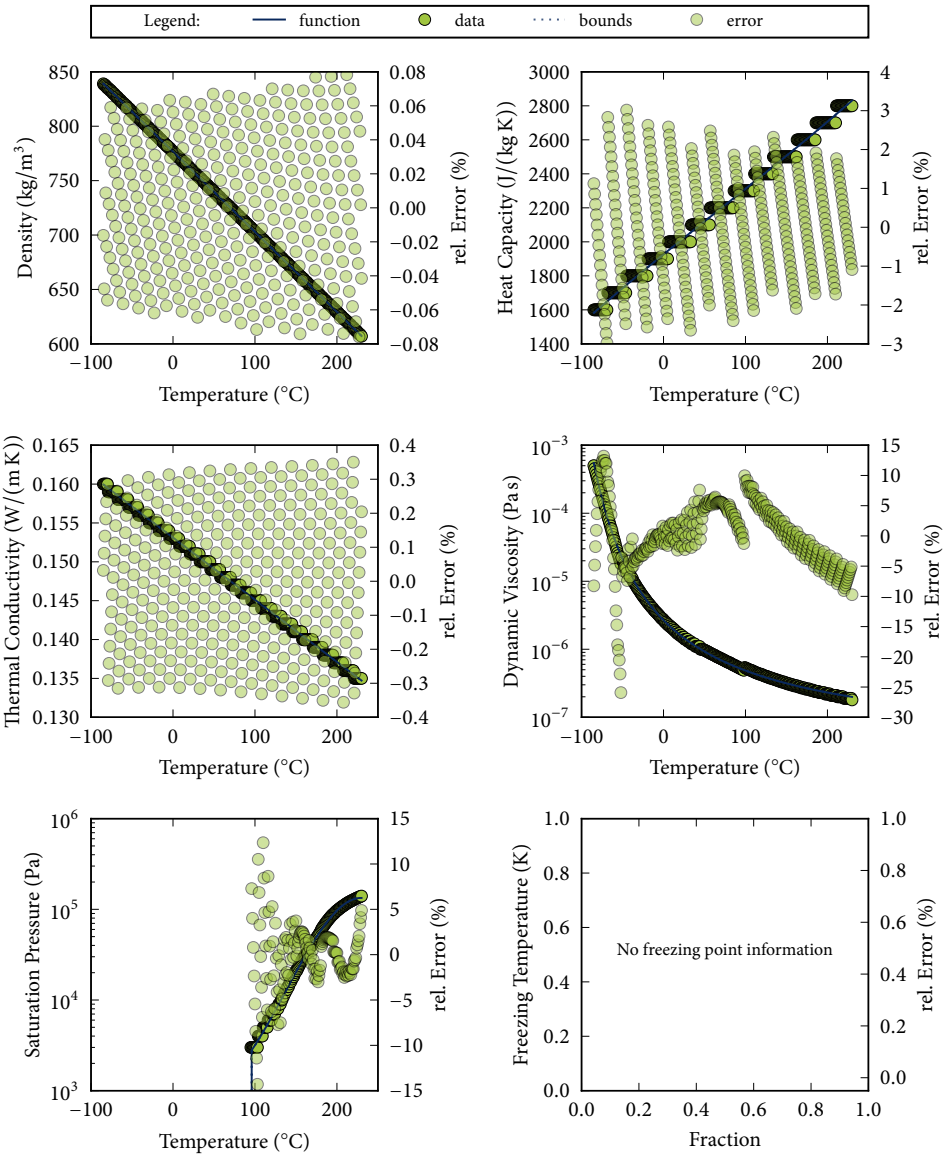

Fitted functions for PMR

Description: Paratherm MR
Source: *Thermal Properties Calculator v6.4* [65]

Temperature:	-40.0 °C to 315.0 °C	Th. Cond.:	data to polynomial (4, 1)
Composition:	pure fluid	Viscosity:	data to exponential (3,)
Density:	data to polynomial (4, 1)	Psat:	data to exppolynomial (4, 1)
Spec. Heat:	data to polynomial (4, 1)	Tfreeze:	no information

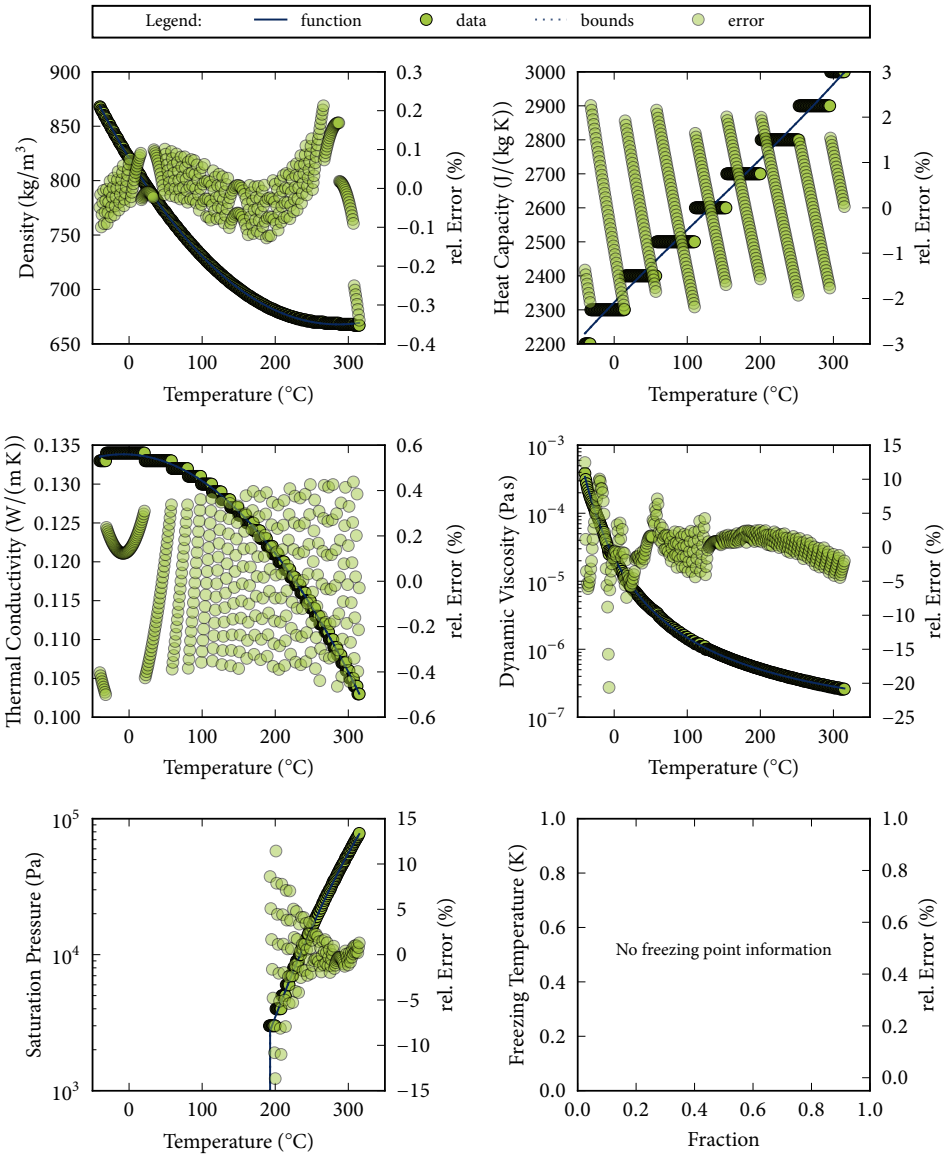

Fitted functions for PMS1

Description: Polydimethylsiloxan 1 - Baysilone KT3
Source: Melinder [39]

Temperature:	-80.0 °C to 100.0 °C	Th. Cond.:	coefficients to polynomial (2, 1)
Composition:	pure fluid	Viscosity:	coefficients to exppolynomial (3, 1)
Density:	coefficients to polynomial (2, 1)	Psat:	no information
Spec. Heat:	coefficients to polynomial (2, 1)	Tfreeze:	no information

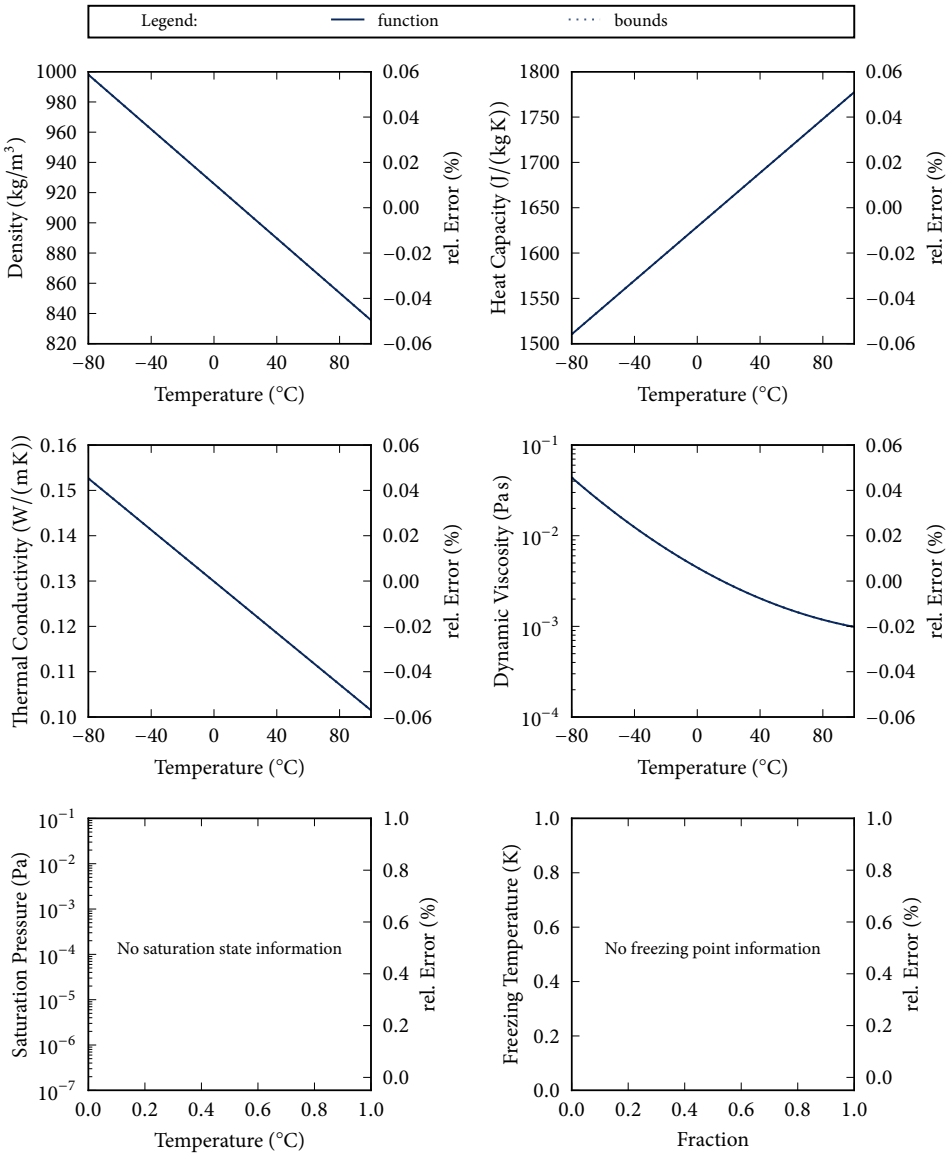

Fitted functions for PMS2

Description: Polydimethylsiloxan 2 - Syltherm XLT
Source: Melinder [39]

Temperature:	-80.0 °C to 100.0 °C	Th. Cond.:	coefficients to polynomial (2, 1)
Composition:	pure fluid	Viscosity:	coefficients to exppolynomial (3, 1)
Density:	coefficients to polynomial (2, 1)	Psat:	no information
Spec. Heat:	coefficients to polynomial (2, 1)	Tfreeze:	no information

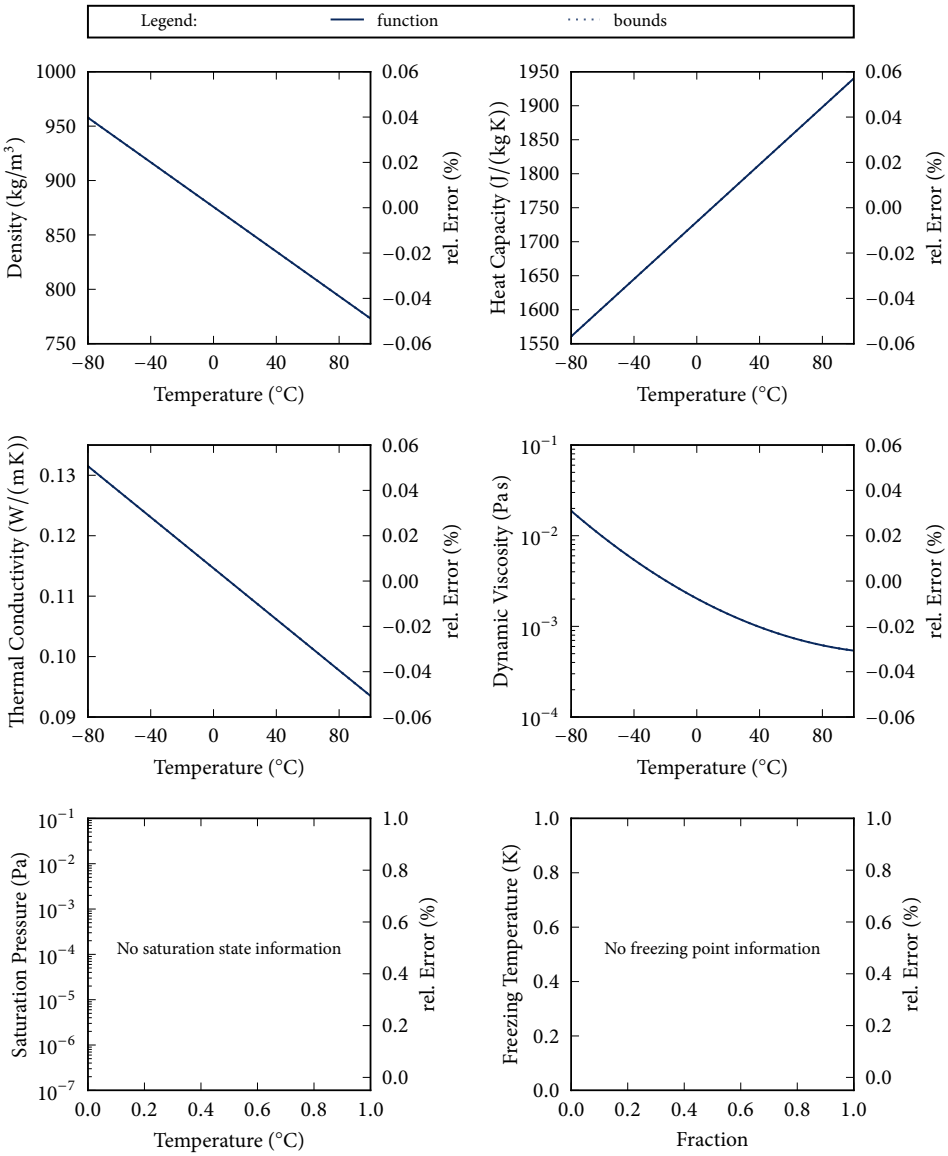

Fitted functions for PNF

Description: Paratherm NF
Source: *Thermal Properties Calculator v6.4* [65]

Temperature:	-10.0 °C to 315.0 °C	Th. Cond.:	data to polynomial (4, 1)
Composition:	pure fluid	Viscosity:	data to exppolynomial (4, 1)
Density:	data to polynomial (4, 1)	Psat:	data to exppolynomial (4, 1)
Spec. Heat:	data to polynomial (4, 1)	Tfreeze:	no information

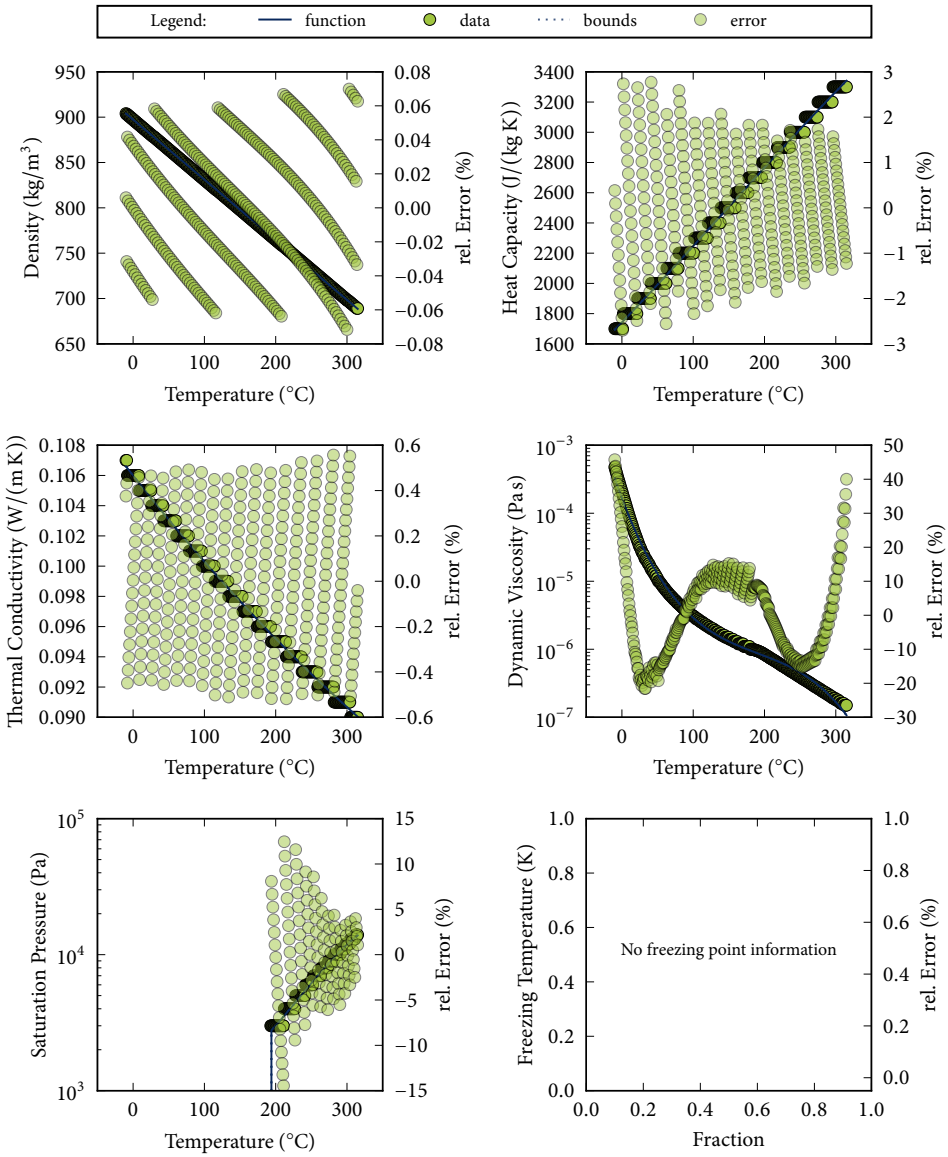

Fitted functions for PNF2

Description:	Paratherm NF, Hydrotreated mineral oil		
Source:	*Thermal Properties Calculator v6.4* [65] Skovrup [49]		
Temperature:	-10.0 °C to 320.0 °C	Th. Cond.:	data to polynomial (4, 1)
Composition:	pure fluid	Viscosity:	data to logexponential (3,)
Density:	data to polynomial (4, 1)	Psat:	no information
Spec. Heat:	data to polynomial (4, 1)	Tfreeze:	no information

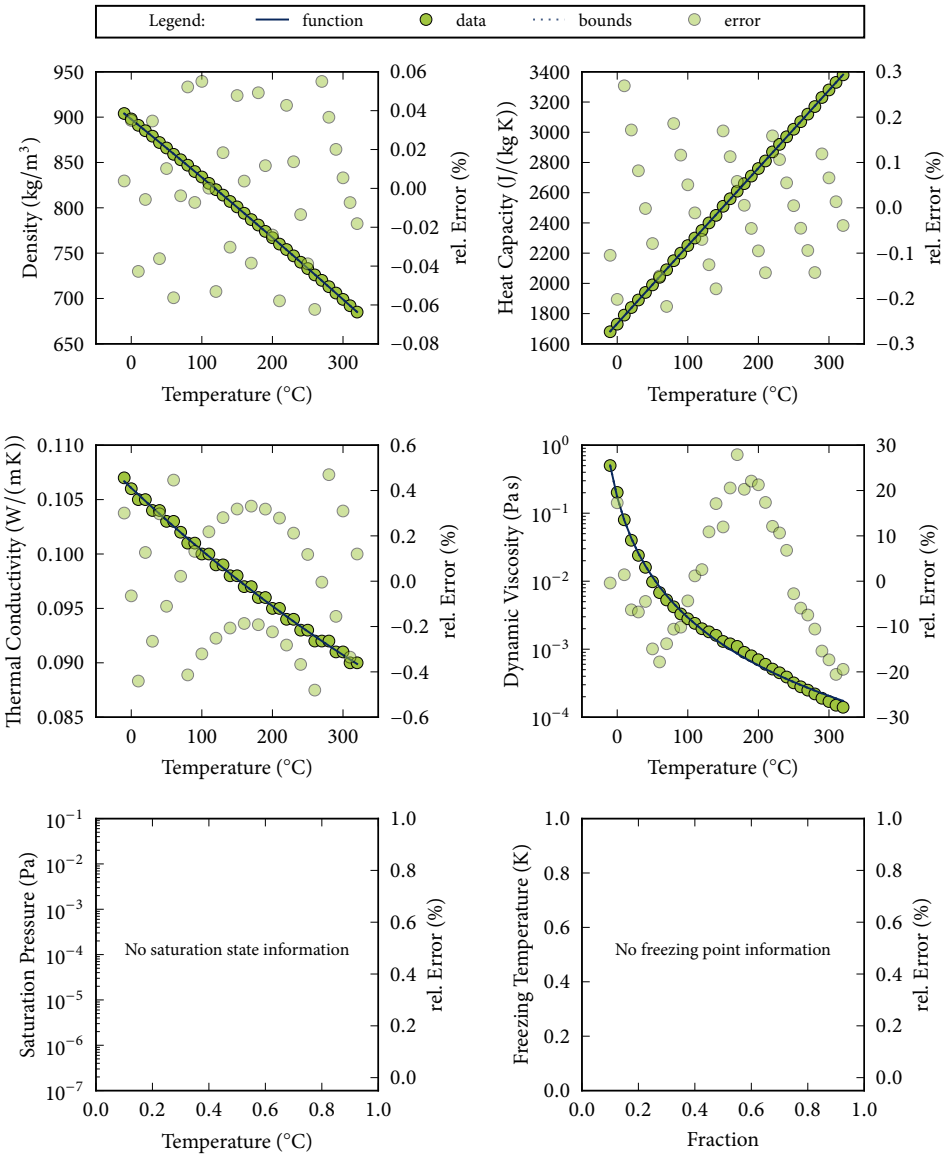

Fitted functions for SAB

Description: Synthetic alkyl benzene - Marlotherm X
Source: Melinder [39]

Temperature:	-80.0 °C to 100.0 °C	Th. Cond.:	coefficients to polynomial (2, 1)
Composition:	pure fluid	Viscosity:	coefficients to exppolynomial (3, 1)
Density:	coefficients to polynomial (2, 1)	Psat:	no information
Spec. Heat:	coefficients to polynomial (2, 1)	Tfreeze:	no information

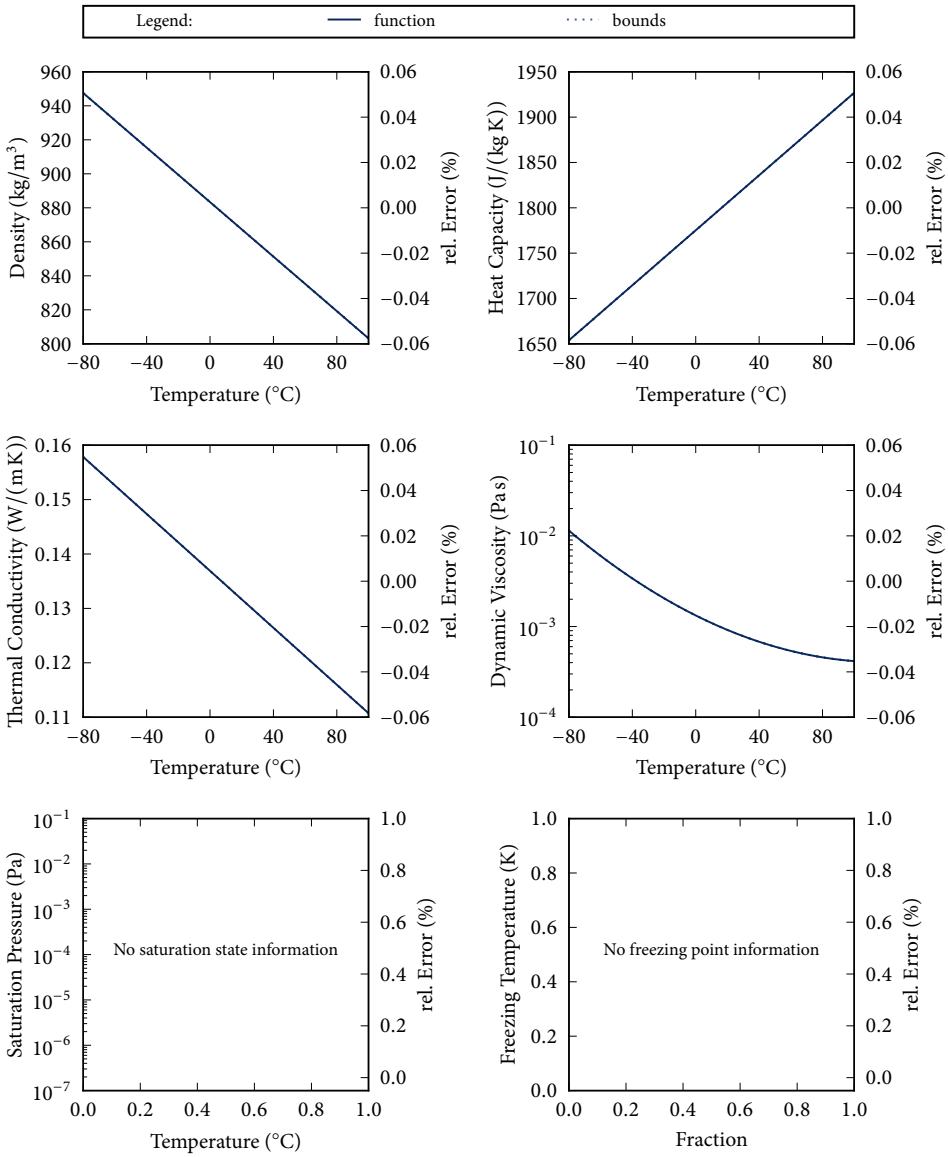

Fitted functions for T66

Description: Therminol66
Source: *Therminol Heat Transfer Reference Disk v5.1* [66]

Temperature:	0.0 °C to 380.0 °C	Th. Cond.:	data to polynomial (4, 1)
Composition:	pure fluid	Viscosity:	data to exponential (3,)
Density:	data to polynomial (4, 1)	Psat:	data to exponential (3,)
Spec. Heat:	data to polynomial (4, 1)	Tfreeze:	no information

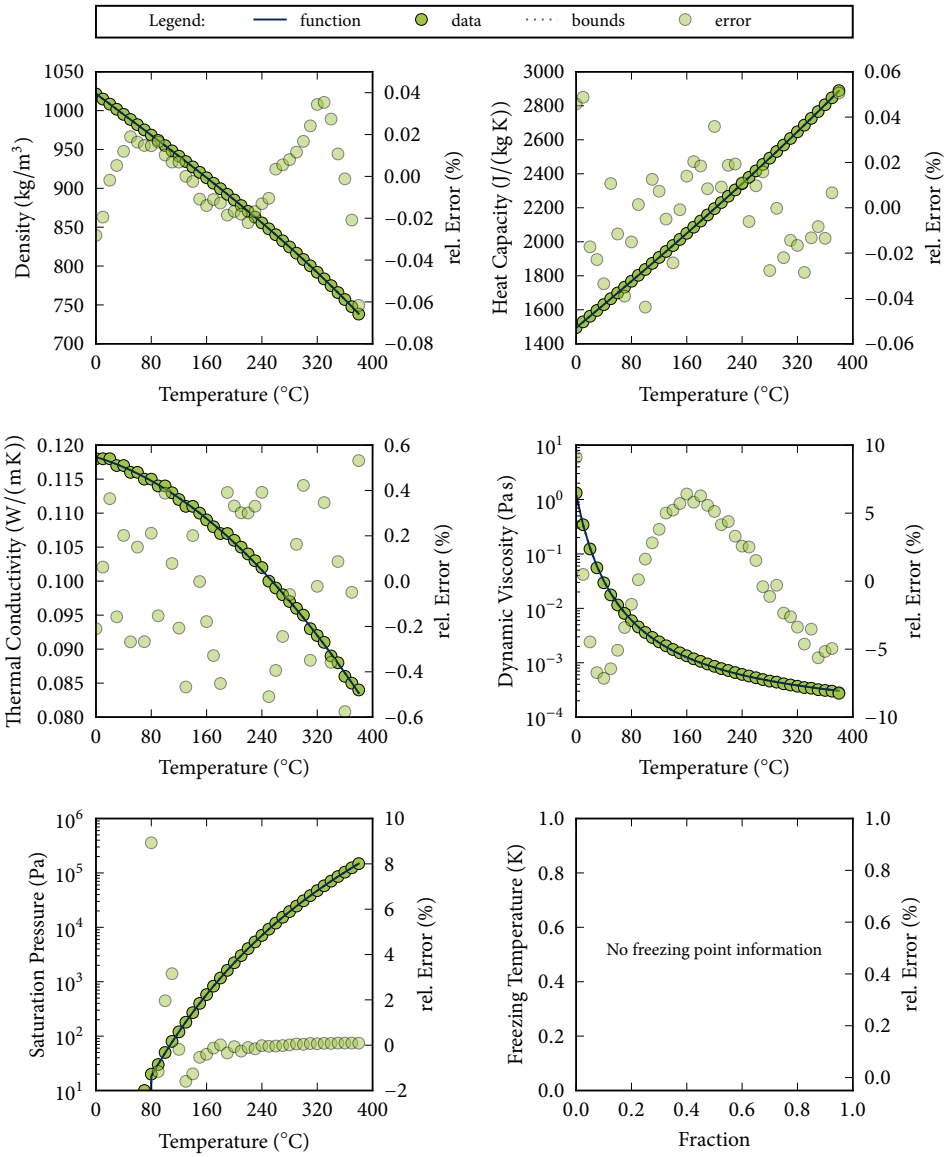

Fitted functions for T72

Description: Therminol72
Source: *Therminol Heat Transfer Reference Disk v5.1* [66]

Temperature:	-10.0 °C to 380.0 °C	Th. Cond.:	data to polynomial (4, 1)
Composition:	pure fluid	Viscosity:	data to logexponential (3,)
Density:	data to polynomial (4, 1)	Psat:	data to exppolynomial (4, 1)
Spec. Heat:	data to polynomial (4, 1)	Tfreeze:	no information

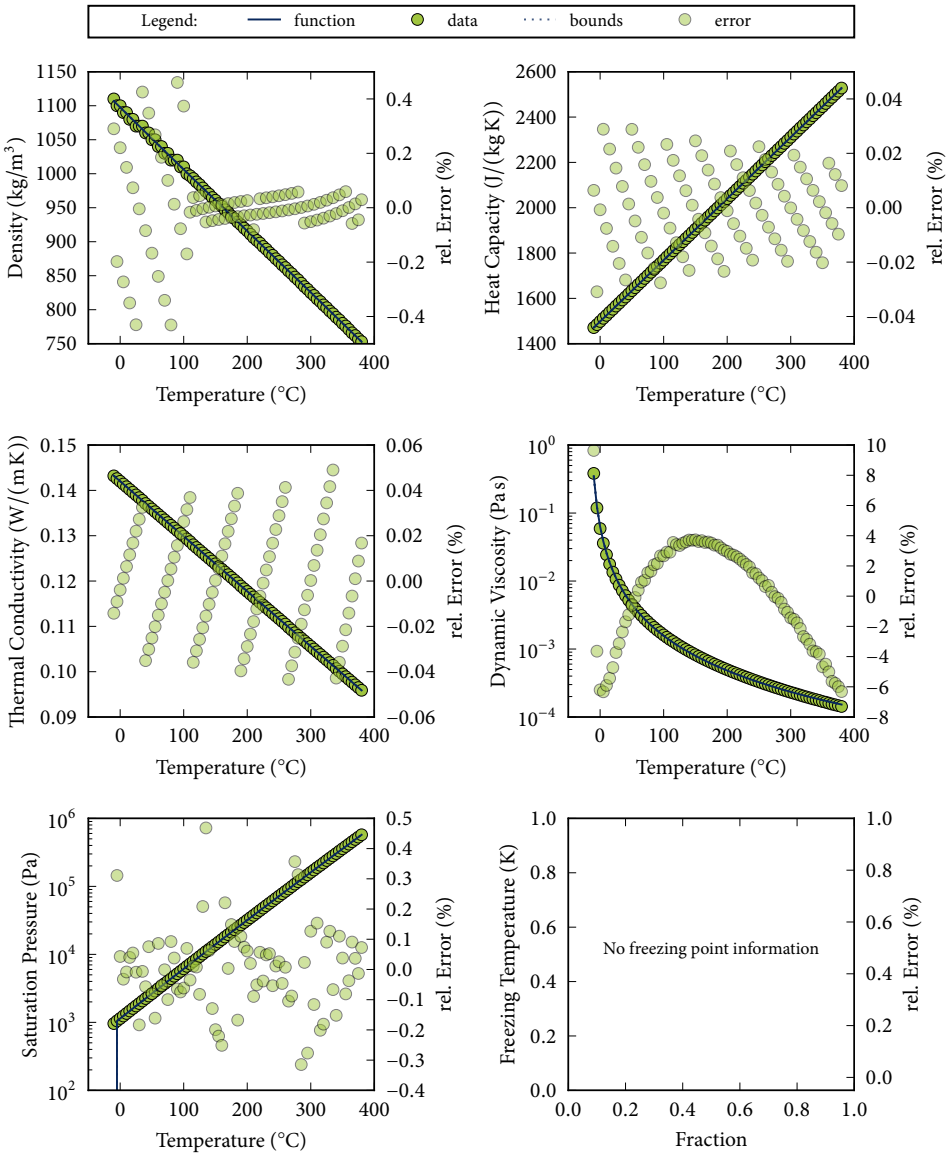

Fitted functions for TCO

Description: Citrus oil terpene - d-Limonene
Source: Melinder [39]

Temperature:	-80.0 °C to 100.0 °C	Th. Cond.:	coefficients to polynomial (2, 1)
Composition:	pure fluid	Viscosity:	coefficients to exppolynomial (3, 1)
Density:	coefficients to polynomial (2, 1)	Psat:	no information
Spec. Heat:	coefficients to polynomial (2, 1)	Tfreeze:	no information

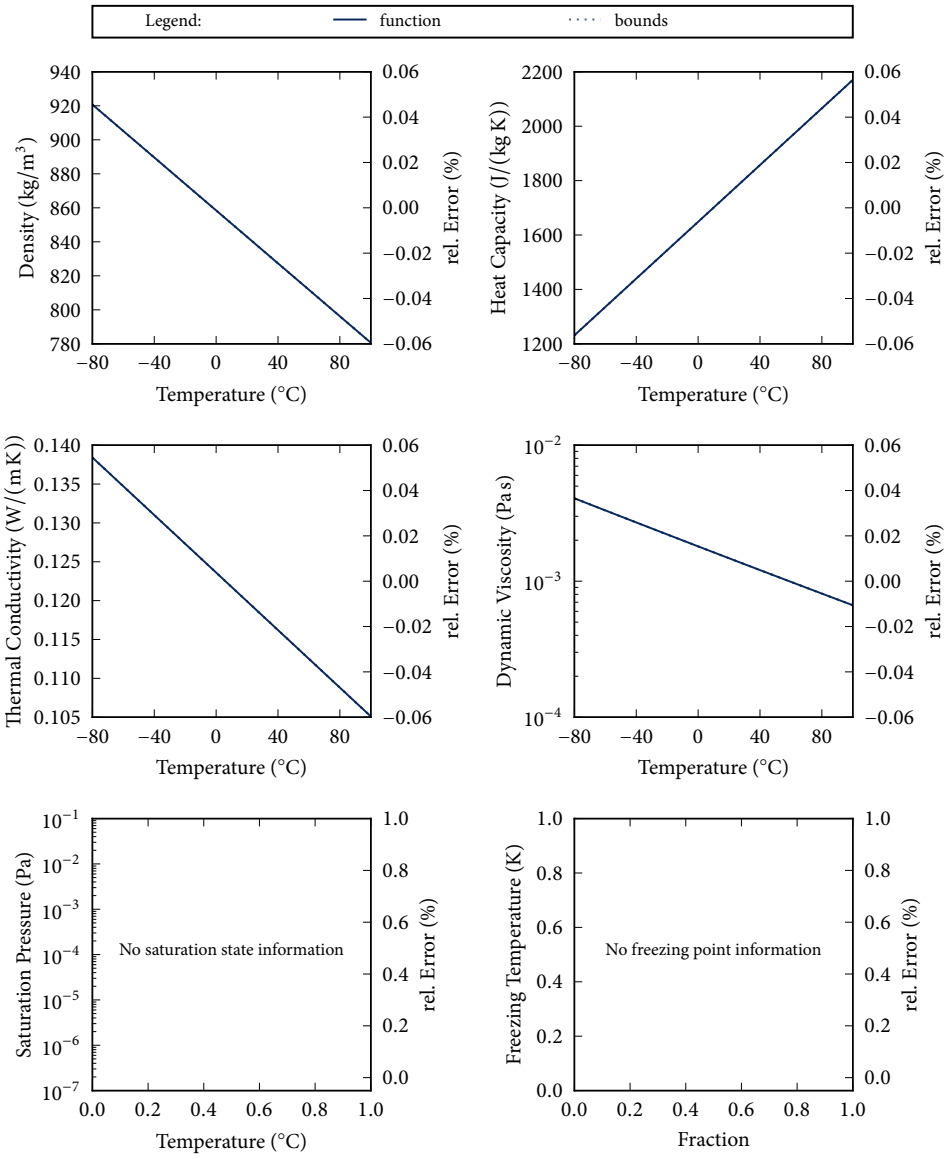

Fitted functions for TD12

Description: TherminolD12
Source: *Therminol Heat Transfer Reference Disk v5.1* [66]

Temperature:	-85.0 °C to 230.0 °C	Th. Cond.:	data to polynomial (4, 1)
Composition:	pure fluid	Viscosity:	data to exponential (3,)
Density:	data to polynomial (4, 1)	Psat:	data to exponential (3,)
Spec. Heat:	data to polynomial (4, 1)	Tfreeze:	no information

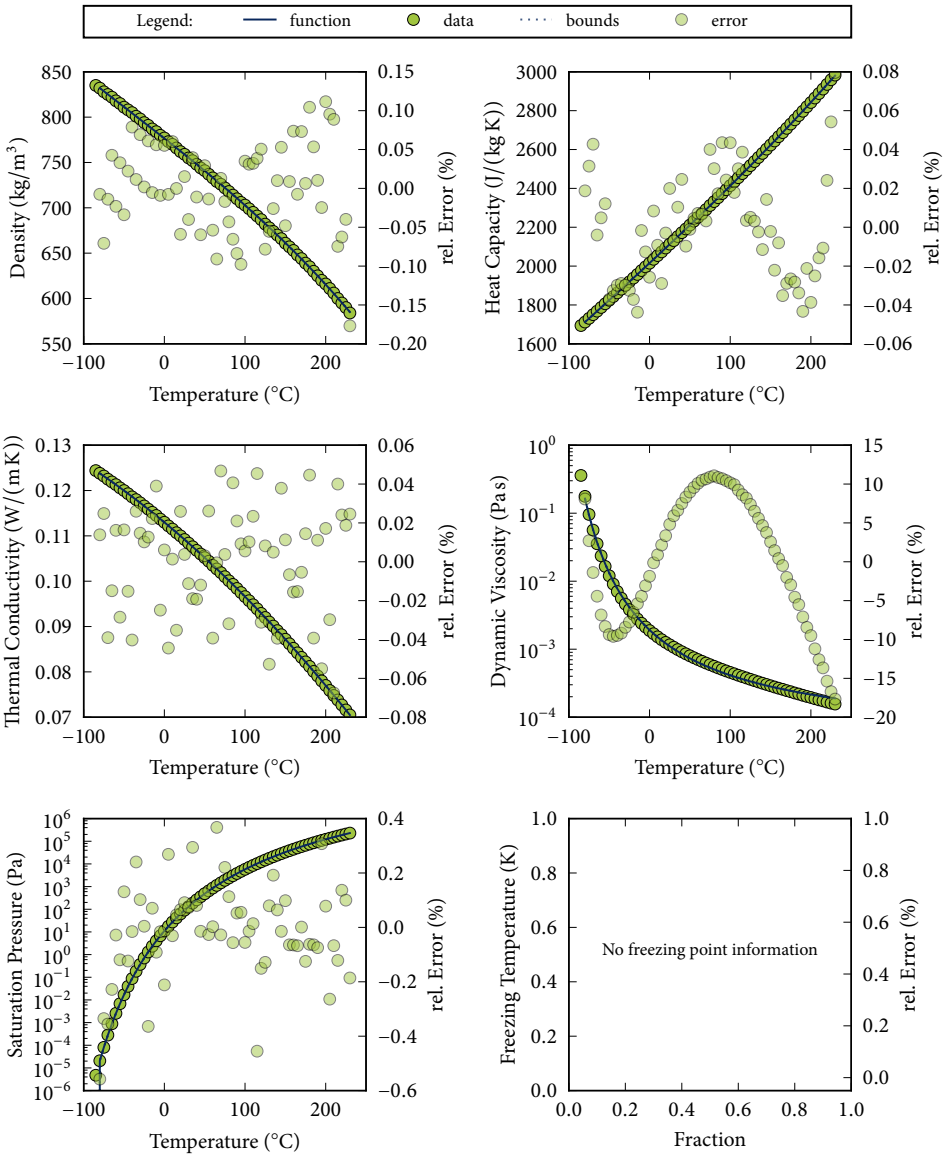

Fitted functions for TVP1

Description: TherminolVP1
Source: *Therminol Heat Transfer Reference Disk v5.1* [66]

Temperature:	12.0 °C to 397.0 °C	Th. Cond.:	data to polynomial (4, 1)
Composition:	pure fluid	Viscosity:	data to exponential (3,)
Density:	data to polynomial (4, 1)	Psat:	data to exponential (3,)
Spec. Heat:	data to polynomial (4, 1)	Tfreeze:	no information

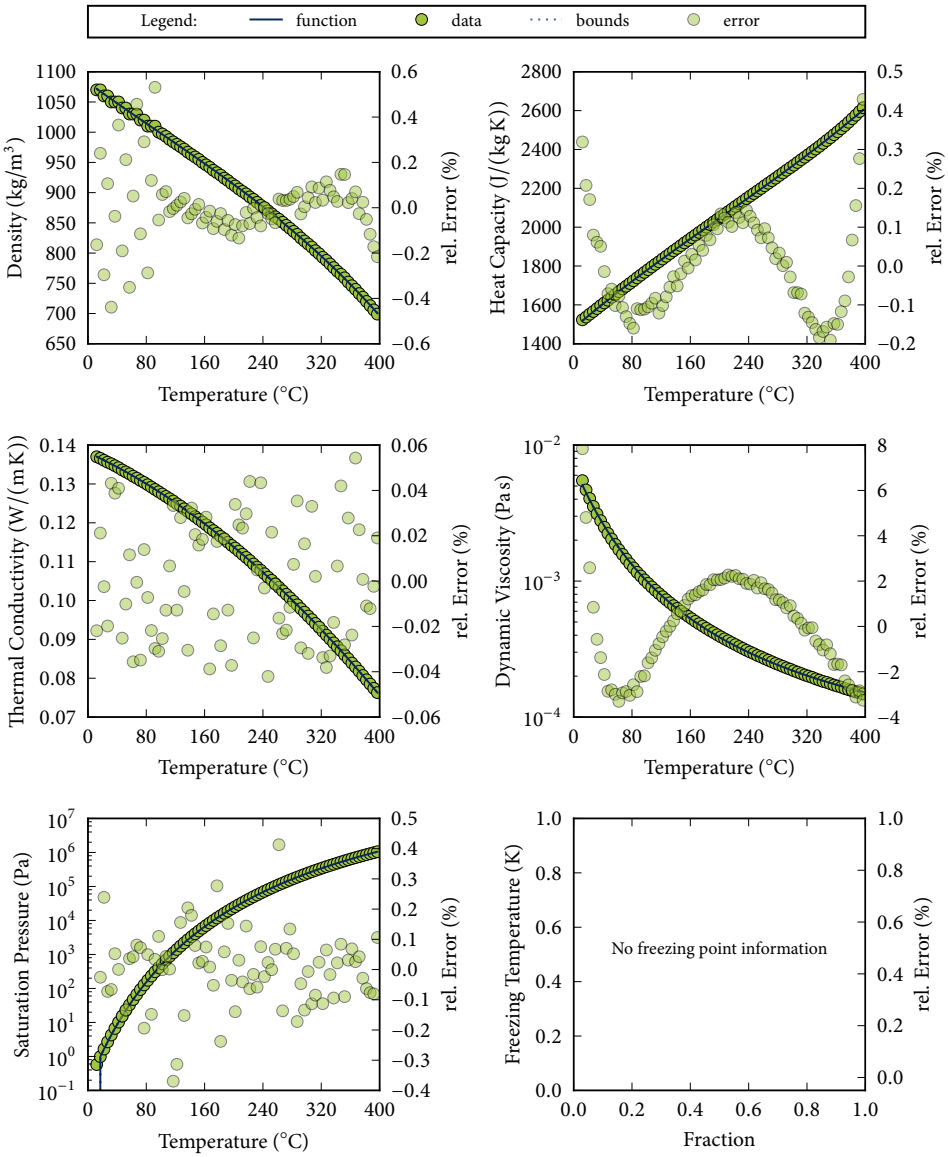

Fitted functions for TVP1869

Description:	Thermogen VP 1869		
Source:	*Technical Information* [59] Skovrup [49]		
Temperature:	-80.0 °C to 20.0 °C	Th. Cond.:	coefficients to polynomial (2, 1)
Composition:	pure fluid	Viscosity:	equation to exppolynomial (4, 1)
Density:	coefficients to polynomial (2, 1)	Psat:	no information
Spec. Heat:	coefficients to polynomial (2, 1)	Tfreeze:	no information

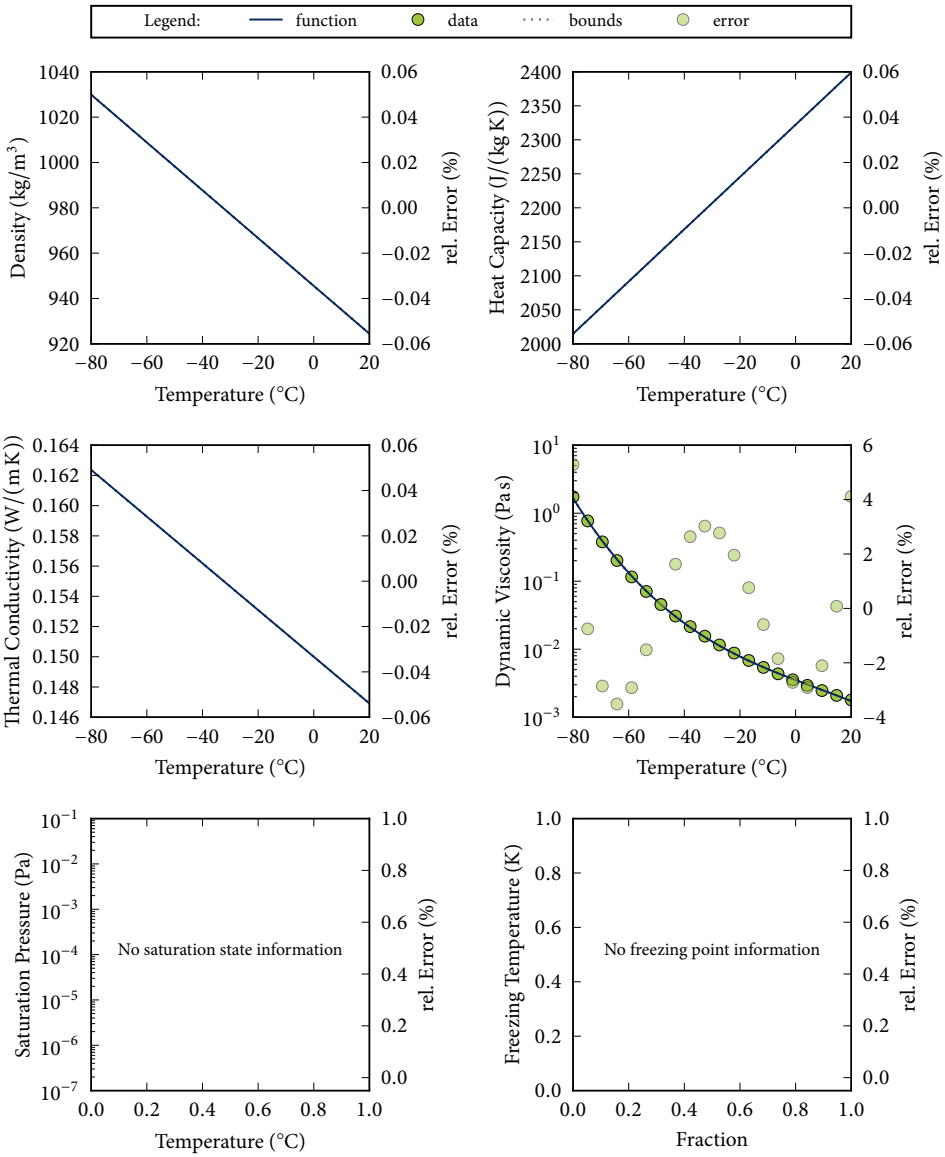

Fitted functions for TX22

Description: Texatherm22
Source: *Technical Data Sheet* [56]

Temperature:	0.0 °C to 350.0 °C	Th. Cond.:	data to polynomial (4, 1)
Composition:	pure fluid	Viscosity:	data to exponential (3,)
Density:	data to polynomial (4, 1)	Psat:	data to exppolynomial (4, 1)
Spec. Heat:	data to polynomial (4, 1)	Tfreeze:	no information

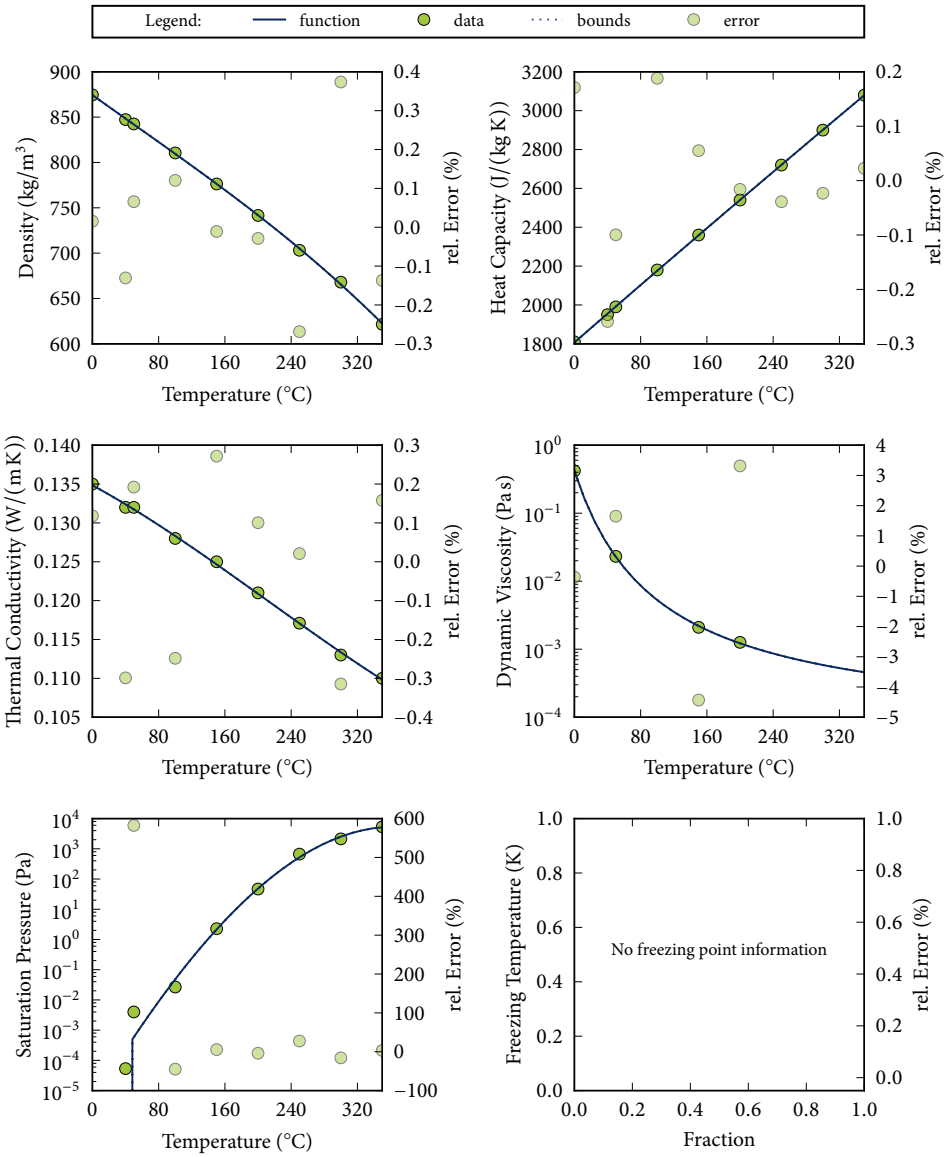

Fitted functions for TY10

Description:	Tyfoxit 1.10, Potassium Acetate		
Source:	*Technical Information* [61]		
	Skovrup [49]		
Temperature:	-10.0 °C to 40.0 °C	Th. Cond.:	data to polynomial (4, 1)
Composition:	pure fluid	Viscosity:	data to exponential (3,)
Density:	data to polynomial (4, 1)	Psat:	no information
Spec. Heat:	data to polynomial (4, 1)	Tfreeze:	no information

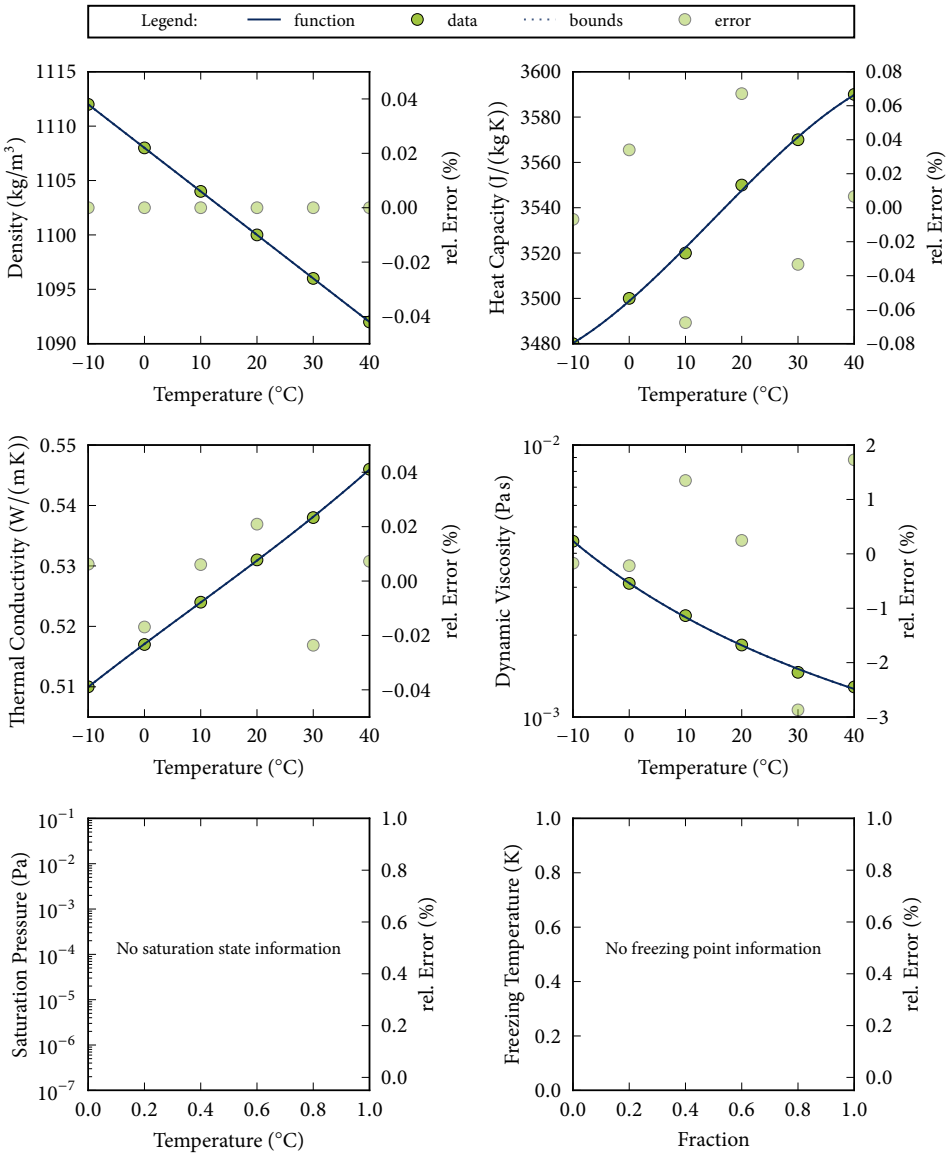

Fitted functions for TY15

Description:	Tyfoxit 1.15, Potassium Acetate		
Source:	*Technical Information* [61]		
	Skovrup [49]		
Temperature:	-20.0 °C to 40.0 °C	Th. Cond.:	data to polynomial (4, 1)
Composition:	pure fluid	Viscosity:	data to exponential (3,)
Density:	data to polynomial (4, 1)	Psat:	no information
Spec. Heat:	data to polynomial (4, 1)	Tfreeze:	no information

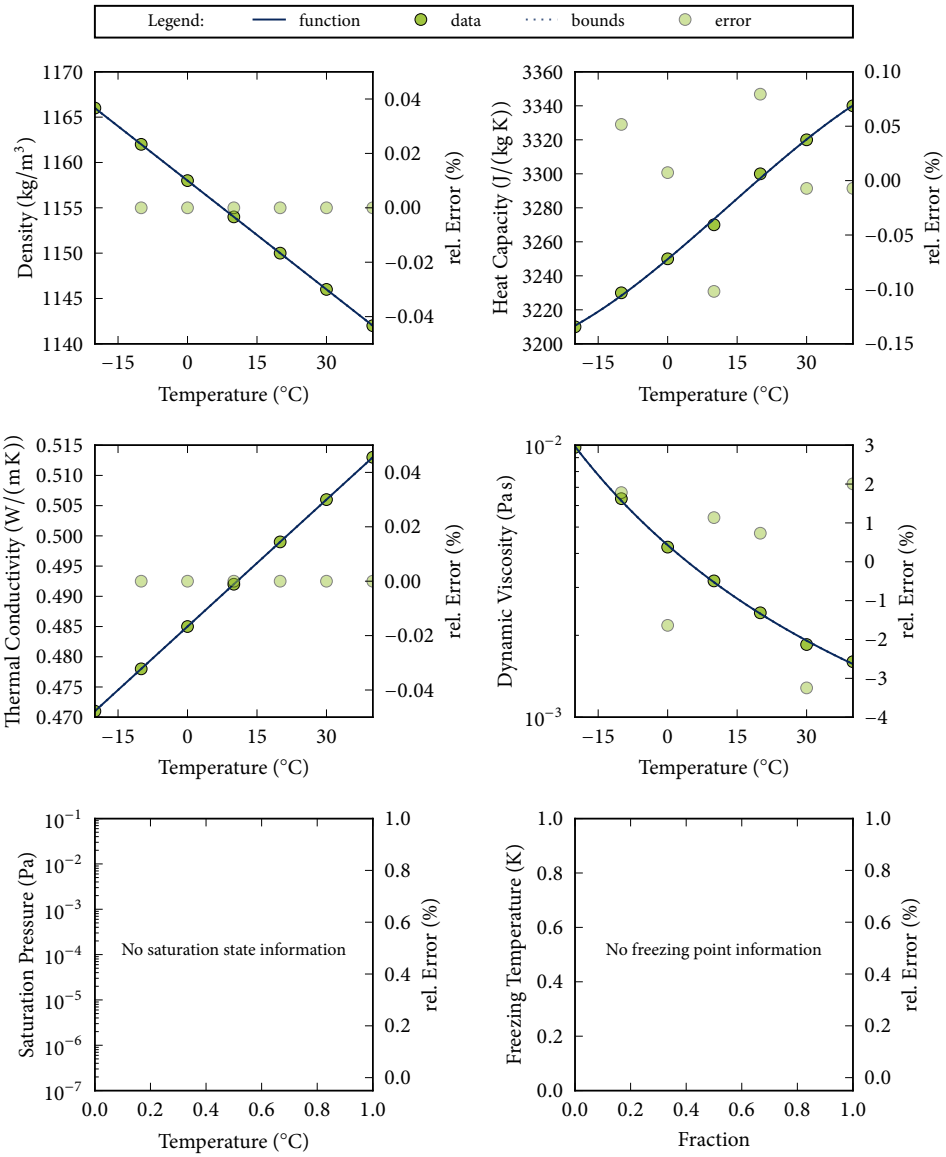

Fitted functions for TY20

Description:	Tyfoxit 1.20, Potassium Acetate		
Source:	*Technical Information* [61]		
	Skovrup [49]		
Temperature:	-40.0 °C to 40.0 °C	Th. Cond.:	data to polynomial (4, 1)
Composition:	pure fluid	Viscosity:	data to exponential (3,)
Density:	data to polynomial (4, 1)	Psat:	no information
Spec. Heat:	data to polynomial (4, 1)	Tfreeze:	no information

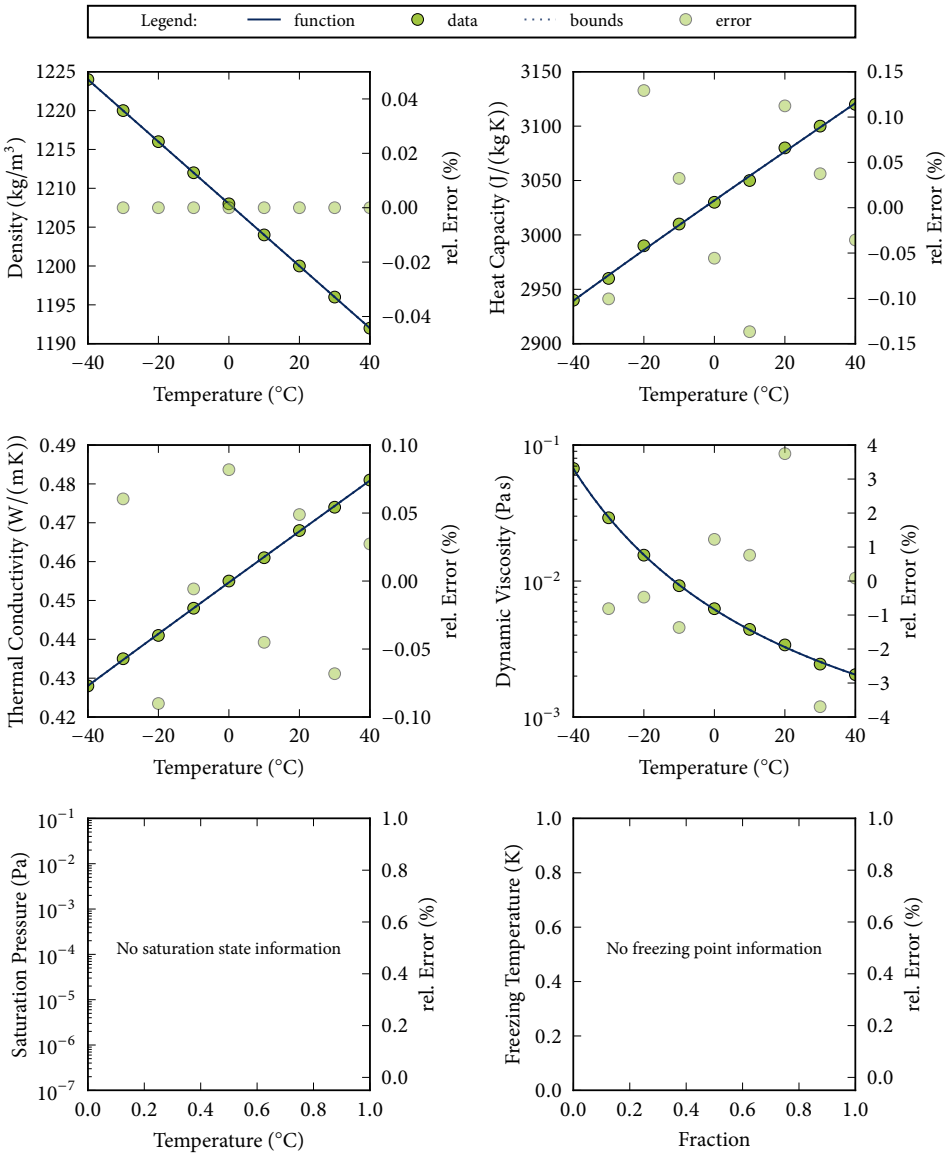

Fitted functions for TY24

Description:	Tyfoxit 1.24, Potassium Acetate		
Source:	*Technical Information* [61]		
	Skovrup [49]		
Temperature:	-55.0 °C to 40.0 °C	Th. Cond.:	data to polynomial (4, 1)
Composition:	pure fluid	Viscosity:	data to exponential (3,)
Density:	data to polynomial (4, 1)	Psat:	no information
Spec. Heat:	data to polynomial (4, 1)	Tfreeze:	no information

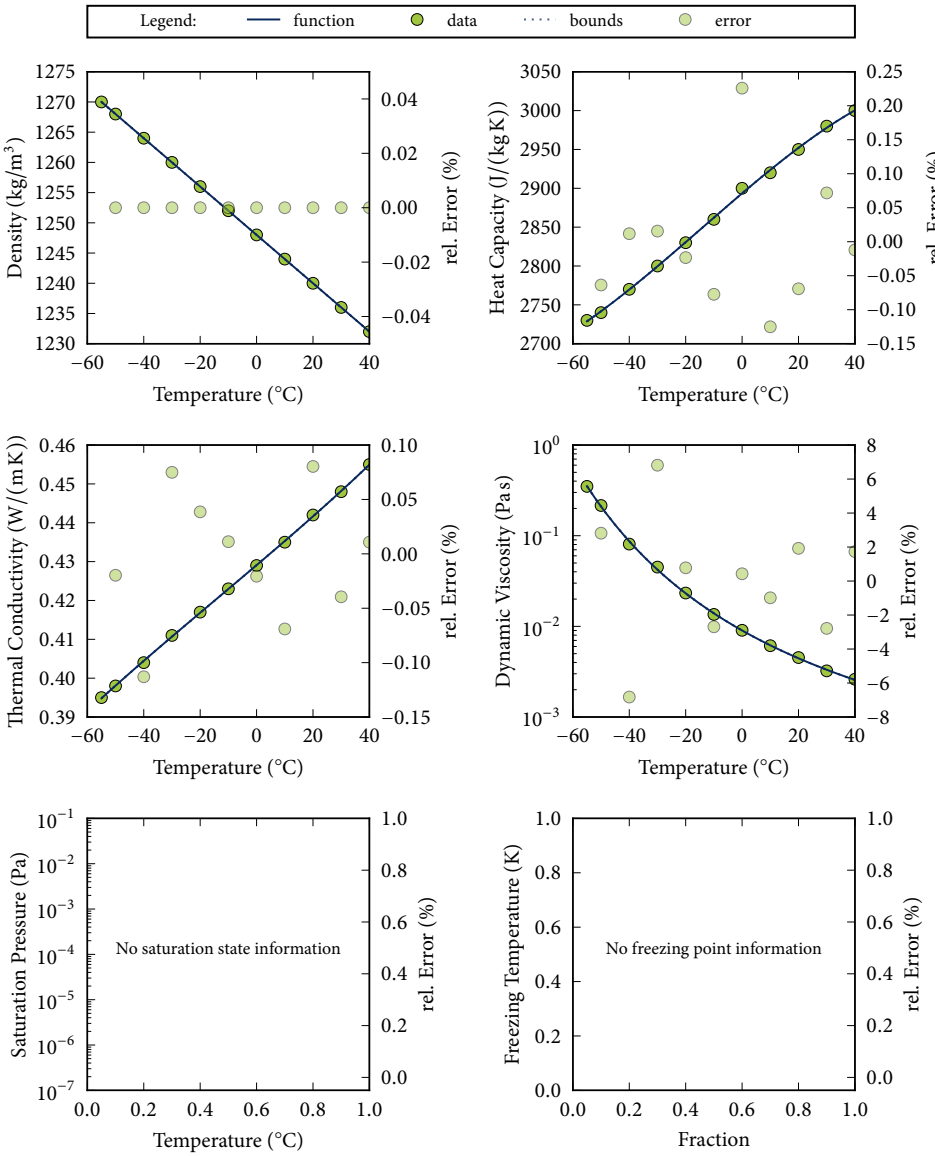

Fitted functions for Water

Description:	Fit of EOS from 1 bar to 100 bar		
Source:	Wagner and Pruss [67]		
	Huber et al. [27]		
Temperature:	0.0 °C to 200.0 °C	Th. Cond.:	data to polynomial (4, 1)
Composition:	pure fluid	Viscosity:	data to exponential (3,)
Density:	data to polynomial (4, 1)	Psat:	data to exponential (3,)
Spec. Heat:	data to polynomial (4, 1)	Tfreeze:	no information

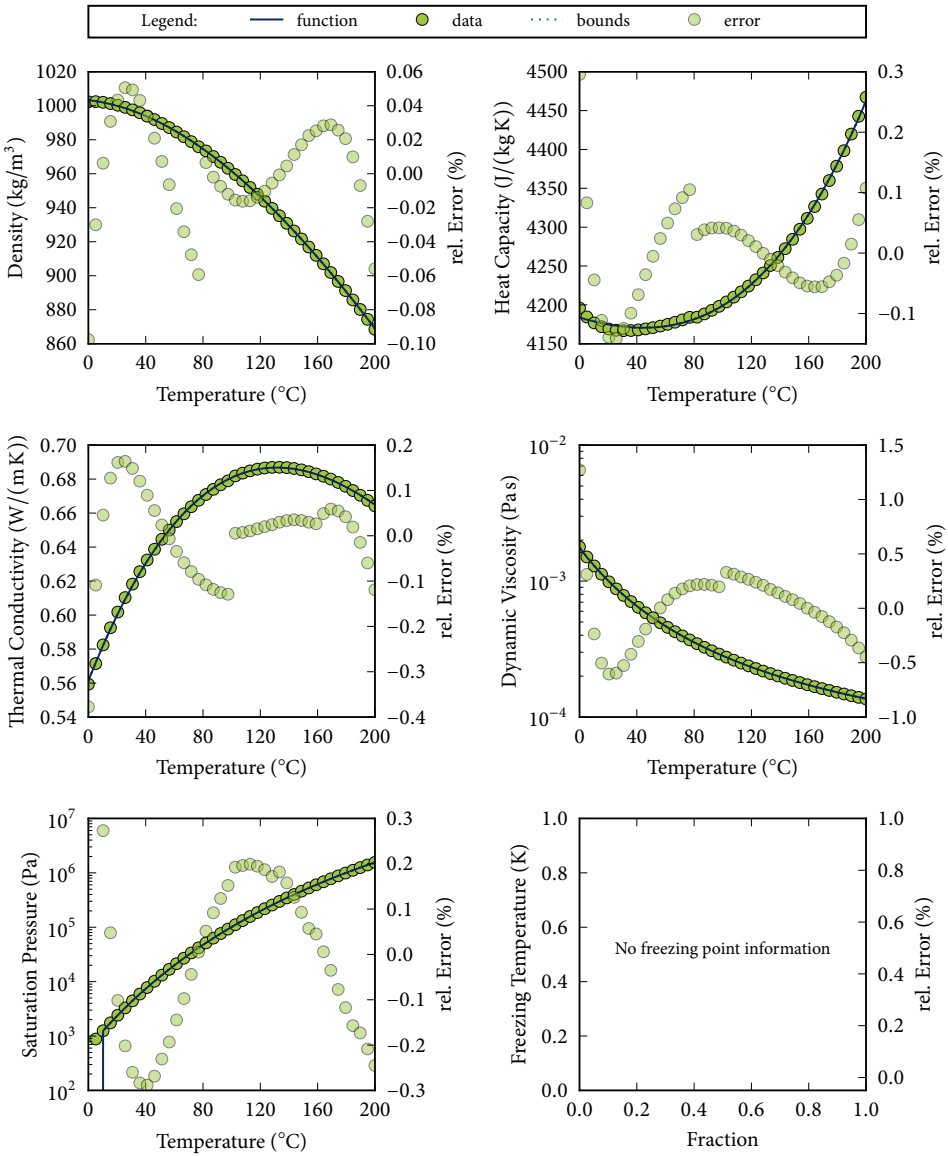

Fitted functions for XLT

Description: SylthermXLT
Source: *Technical Data Sheet* [52]

Temperature:	-100.0 °C to 260.0 °C	Th. Cond.:	data to polynomial (4, 1)
Composition:	pure fluid	Viscosity:	data to exponential (3,)
Density:	data to polynomial (4, 1)	Psat:	no information
Spec. Heat:	data to polynomial (4, 1)	Tfreeze:	no information

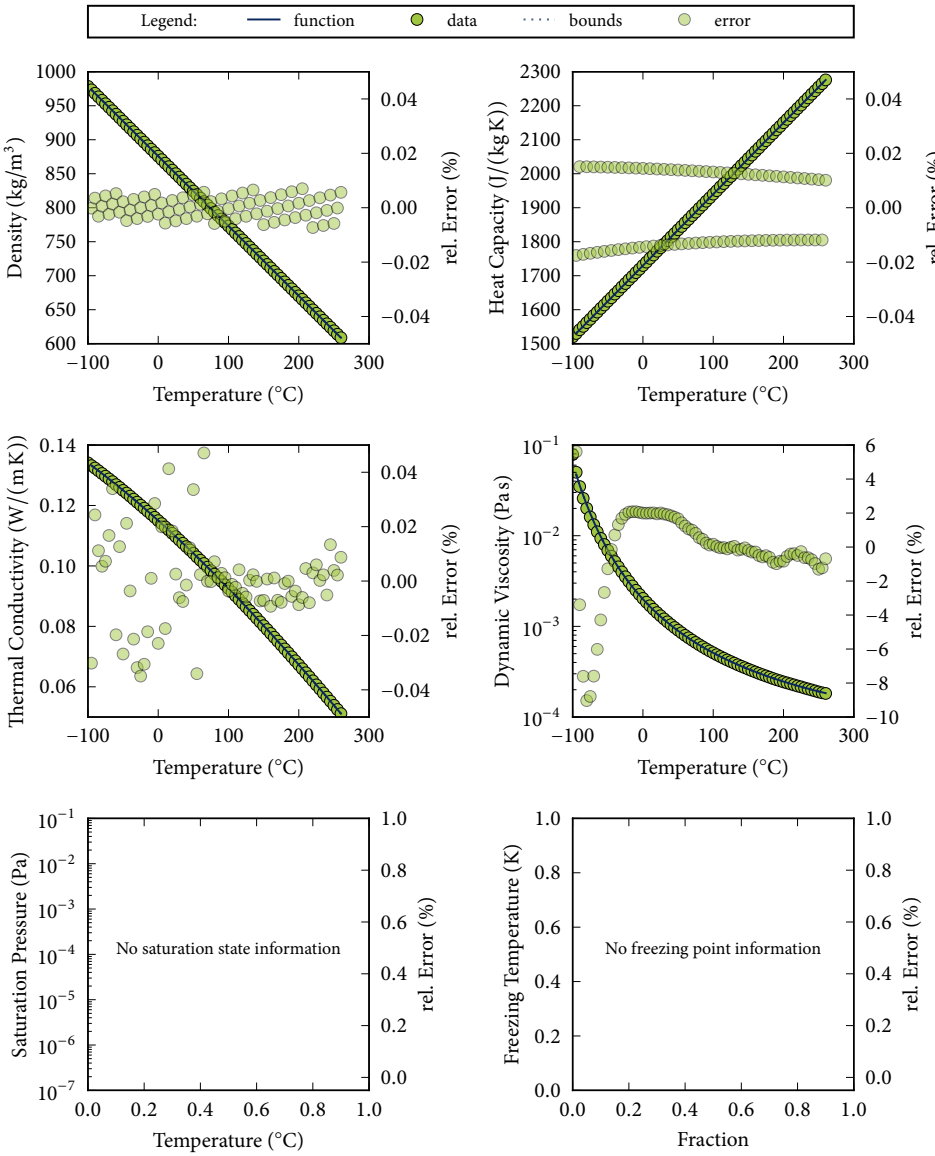

Fitted functions for XLT2

Description:	Syltherm XLT, Polydimethylsiloxan		
Source:	*Technical Data Sheet* [52]		
	Skovrup [49]		
Temperature:	-100.0 °C to 260.0 °C	Th. Cond.:	data to polynomial (4, 1)
Composition:	pure fluid	Viscosity:	data to exponential (3,)
Density:	data to polynomial (4, 1)	Psat:	no information
Spec. Heat:	data to polynomial (4, 1)	Tfreeze:	no information

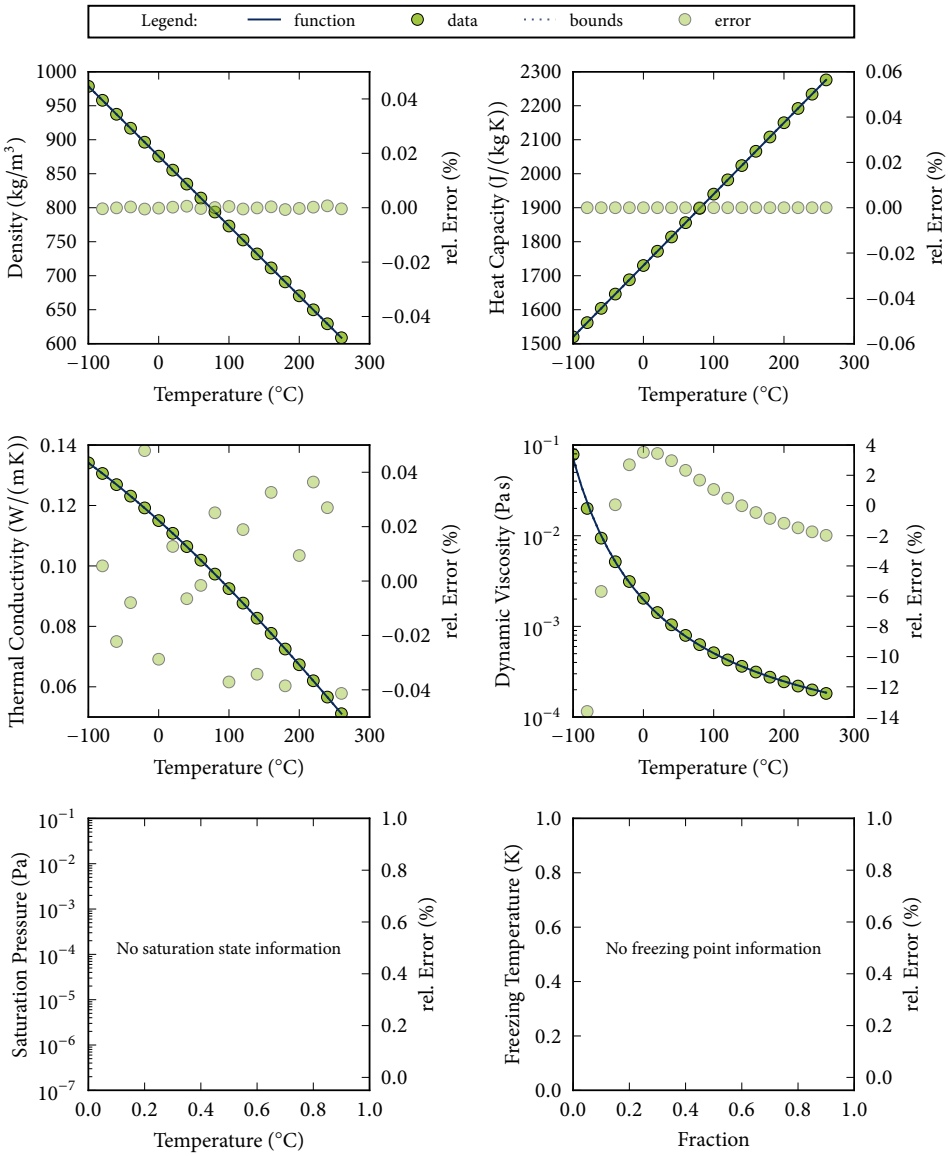

Fitted functions for ZS10

Description:	Zitrec S10, Potassium formate/Sodium propionate		
Source:	*Technical Information* [64]		
	Skovrup [49]		
Temperature:	-8.0 °C to 90.0 °C	Th. Cond.:	data to polynomial (4, 1)
Composition:	pure fluid	Viscosity:	data to exponential (3,)
Density:	data to polynomial (4, 1)	Psat:	no information
Spec. Heat:	data to polynomial (4, 1)	Tfreeze:	no information

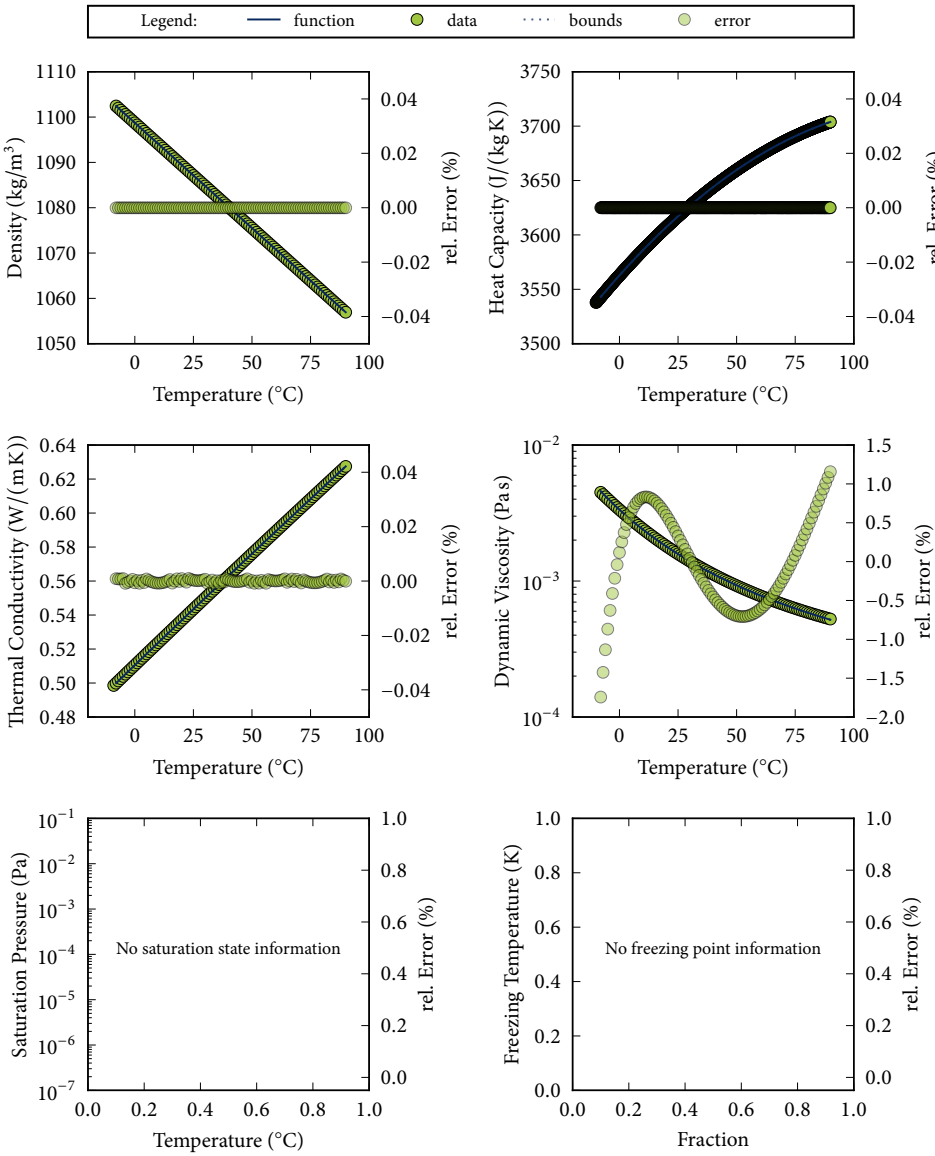

Fitted functions for ZS25

Description:	Zitrec S25, Potassium formate/Sodium propionate		
Source:	*Technical Information* [64]		
	Skovrup [49]		
Temperature:	-23.0 °C to 90.0 °C	Th. Cond.:	data to polynomial (4, 1)
Composition:	pure fluid	Viscosity:	data to exponential (3,)
Density:	data to polynomial (4, 1)	Psat:	no information
Spec. Heat:	data to polynomial (4, 1)	Tfreeze:	no information

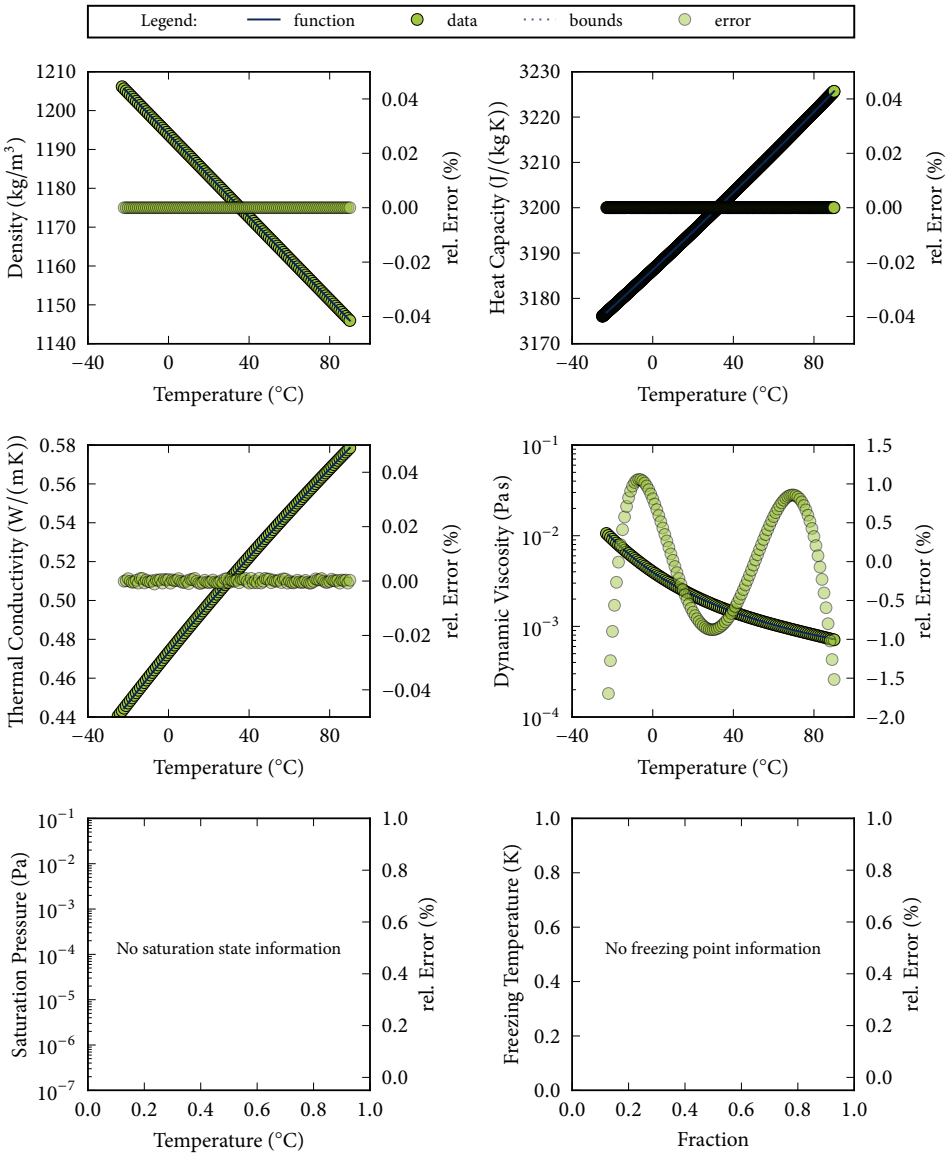

Fitted functions for ZS40

Description:	Zitrec S40, Potassium formate/Sodium propionate		
Source:	*Technical Information* [64]		
	Skovrup [49]		
Temperature:	-38.0 °C to 90.0 °C	Th. Cond.:	data to polynomial (4, 1)
Composition:	pure fluid	Viscosity:	data to exponential (3,)
Density:	data to polynomial (4, 1)	Psat:	no information
Spec. Heat:	data to polynomial (4, 1)	Tfreeze:	no information

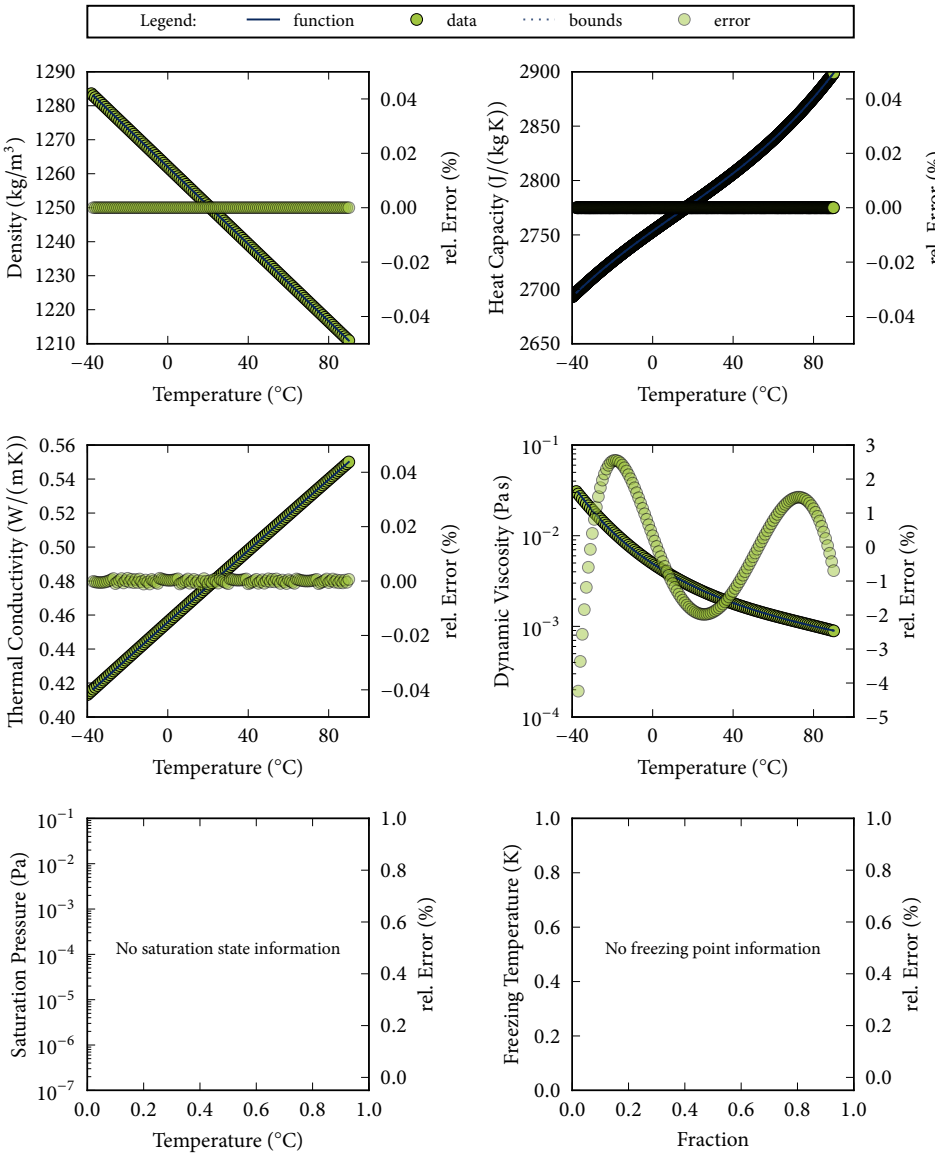

Fitted functions for ZS45

Description:	Zitrec S45, Potassium formate/Sodium propionate		
Source:	*Technical Information* [64]		
	Skovrup [49]		
Temperature:	-43.0 °C to 90.0 °C	Th. Cond.:	data to polynomial (4, 1)
Composition:	pure fluid	Viscosity:	data to exponential (3,)
Density:	data to polynomial (4, 1)	Psat:	no information
Spec. Heat:	data to polynomial (4, 1)	Tfreeze:	no information

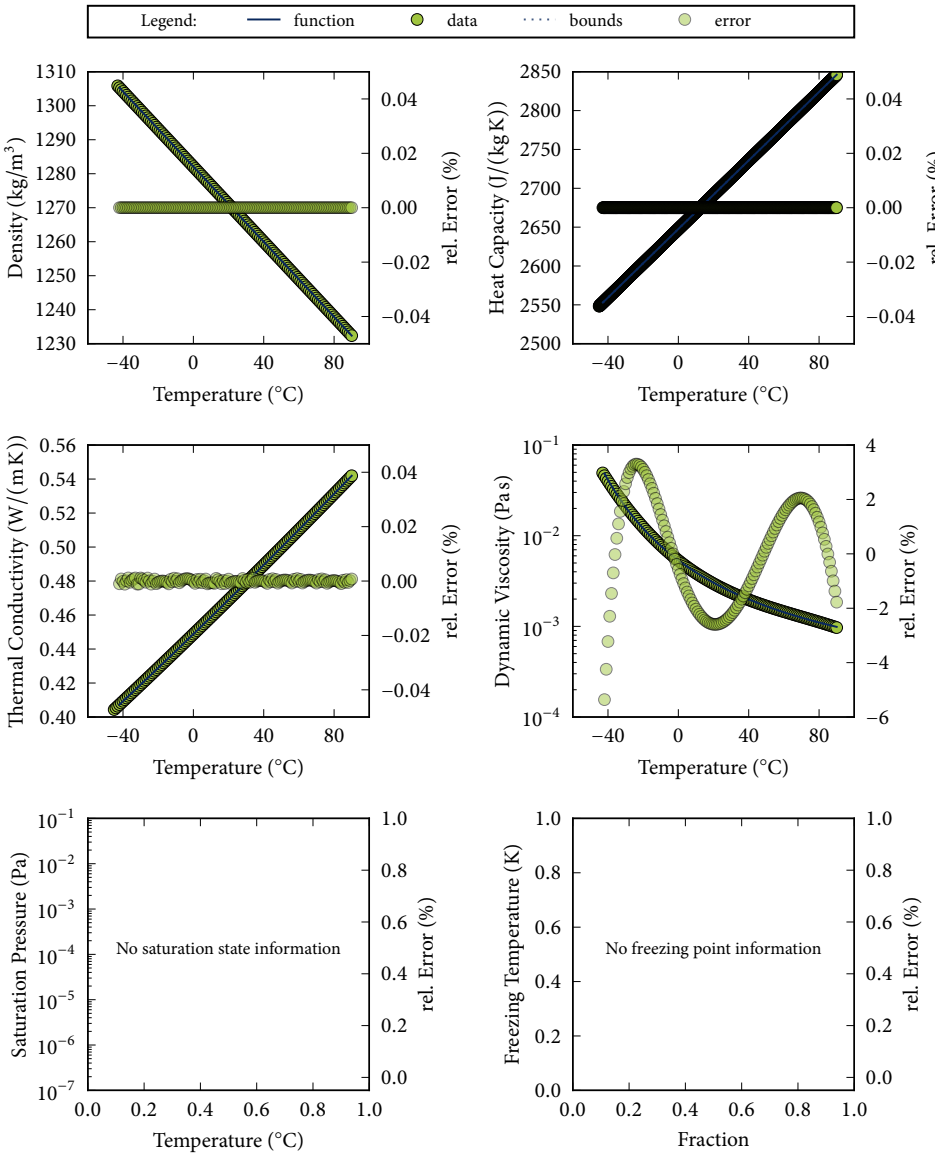

Fitted functions for ZS55

Description:	Zitrec S55, Potassium formate/Sodium propionate		
Source:	*Technical Information* [64]		
	Skovrup [49]		
Temperature:	-55.0 °C to 90.0 °C	Th. Cond.:	data to polynomial (4, 1)
Composition:	pure fluid	Viscosity:	data to exppolynomial (4, 1)
Density:	data to polynomial (4, 1)	Psat:	no information
Spec. Heat:	data to polynomial (4, 1)	Tfreeze:	no information

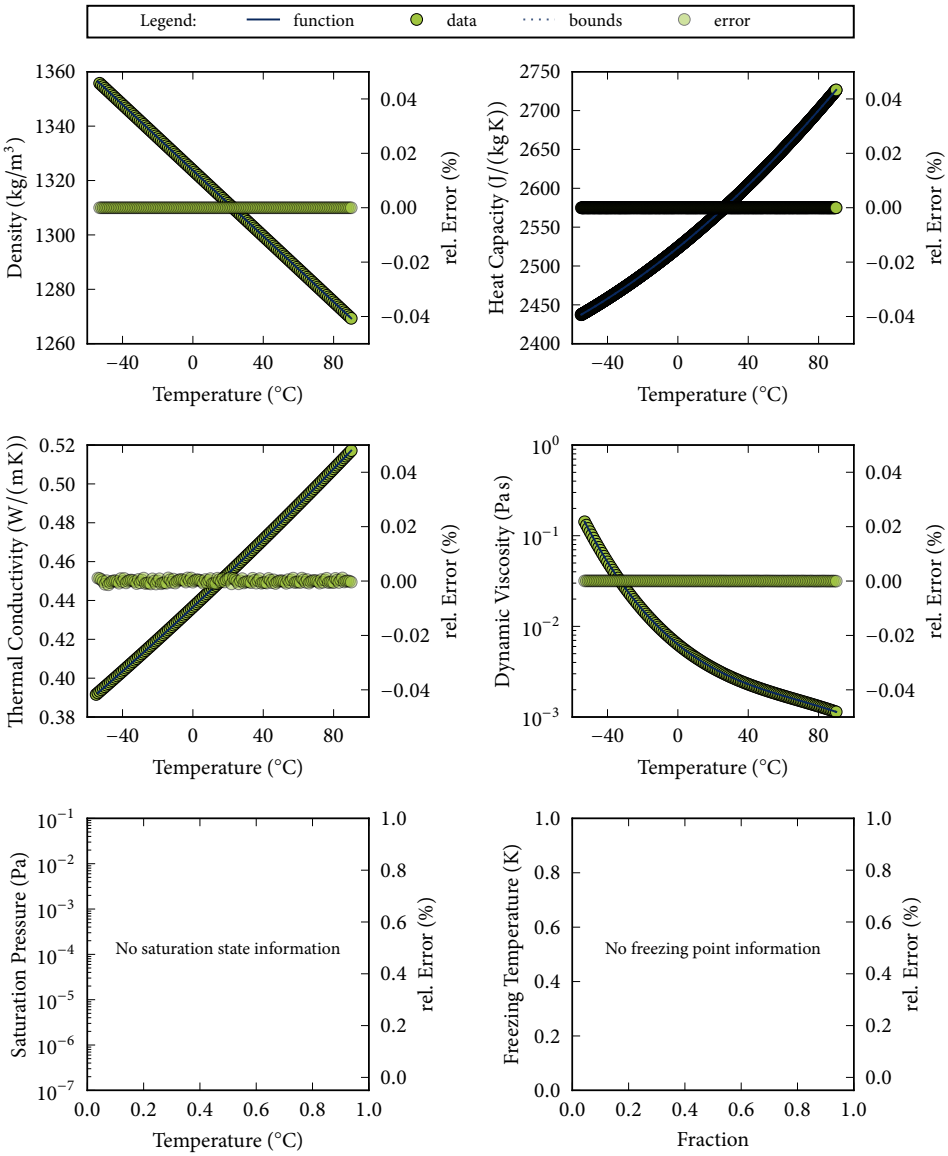

C.3 Mass-based Fluids

Name	Description	Reference	T_{min} (°C)	T_{max} (°C)	T_{base} (K)	x_{min}	x_{max}
FRE, p. 275	Freezium, Potassium Formate	[49, 53]	−40.15	39.85	273.15	0.19	0.50
IceEA, p. 276	Ice slurry with Ethanol	[32, 49]	−33.15	−8.15	252.50	0.05	0.35
IceNA, p. 277	Ice slurry with NaCl	[32, 49]	−18.15	−3.15	262.50	0.05	0.35
IcePG, p. 278	Ice slurry with Propylene Glycol	[32, 49]	−43.15	−8.15	247.50	0.05	0.35
LiBr, p. 279	Lithium-bromide solution - aq	[42]	−0.15	226.85	386.50	0.00	0.75
MAM, p. 280	Ammonia (NH3) - aq	[39]	−100.00	30.00	268.50	0.00	0.30
MAM2, p. 281	Melinder, Ammonia	[39, 49]	−49.00	20.00	258.65	0.08	0.24
MCA, p. 282	Calcium Chloride (CaCl2) - aq	[39]	−100.00	40.00	280.68	0.00	0.30
MCA2, p. 283	Melinder, Calcium Chloride	[39, 49]	−44.00	30.00	266.15	0.09	0.29
MEA, p. 284	Ethyl Alcohol (Ethanol) - aq	[39]	−100.00	40.00	281.31	0.00	0.60
MEA2, p. 285	Melinder, Ethanol	[39, 49]	−44.00	20.00	261.15	0.11	0.60
MEG, p. 286	Ethylene Glycol - aq	[39]	−100.00	100.00	304.88	0.00	0.60
MEG2, p. 287	Melinder, Ethylene Glycol	[39, 49]	−44.00	40.00	271.15	0.00	0.56
MGL, p. 288	Glycerol - aq	[39]	−100.00	40.00	282.06	0.00	0.60
MGL2, p. 289	Melinder, Glycerol	[39, 49]	−40.00	40.00	273.15	0.20	0.63
MKA, p. 290	Potassium Acetate (CH3CO2K) - aq	[39]	−100.00	40.00	279.93	0.00	0.45
MKA2, p. 291	Melinder, Potassium Acetate	[39, 49]	−44.00	30.00	266.15	0.11	0.41
MKC, p. 292	Potassium Carbonate (K2CO3) - aq	[39]	−100.00	40.00	284.39	0.00	0.40
MKC2, p. 293	Melinder, Potassium Carbonate	[39, 49]	−35.00	30.00	270.65	0.00	0.39
MKF, p. 294	Potassium Formate (CHKO2) - aq	[39]	−100.00	40.00	279.04	0.00	0.48
MLI, p. 295	Lithium Chloride (LiCl) - aq	[39]	−100.00	40.00	274.64	0.00	0.24
MMA, p. 296	Methyl Alcohol (Methanol) - aq	[39]	−100.00	40.00	276.69	0.00	0.60

MMA2, p. 297	Melinder, Methanol	[39, 49]	−50.00	20.00	258.15	0.08	0.47
MMG, p. 298	MgCl2 - aq	[39]	−100.00	40.00	282.47	0.00	0.30
MMG2, p. 299	Melinder, Magnesium Chloride	[39, 49]	−30.00	30.00	273.15	0.00	0.20
MNA, p. 300	Sodium Chloride (NaCl) - aq	[39]	−100.00	40.00	285.77	0.00	0.23
MNA2, p. 301	Melinder, Sodium Chloride	[39, 49]	−20.00	30.00	278.15	0.00	0.23
MPG, p. 302	Propylene Glycol - aq	[39]	−100.00	100.00	305.86	0.00	0.60
MPG2, p. 303	Melinder, Propylene Glycol	[39, 49]	−45.00	40.00	270.65	0.15	0.57
VCA, p. 304	VDI, Calcium Cloride	[43, 49]	−55.00	20.00	255.65	0.15	0.30
VKC, p. 305	VDI, Potassium Carbonate	[43, 49]	−35.00	20.00	265.65	0.13	0.39
VMA, p. 306	VDI, Methanol	[43, 49]	−80.00	0.00	233.15	0.10	0.90
VMG, p. 307	VDI, Magnesium Chloride	[43, 49]	−33.00	20.00	266.65	0.07	0.21
VNA, p. 308	VDI, Sodium Chloride	[43, 49]	−21.00	20.00	272.65	0.07	0.23

Fitted functions for FRE

Description:	Freezium, Potassium Formate		
Source:	*Technical Data Sheet* [53]		
	Skovrup [49]		
Temperature:	-40.15 °C to 39.85 °C	Th. Cond.:	coefficients to polynomial (2, 2)
Composition:	19.0 % to 50.0 %, mass	Viscosity:	equation to exppolynomial (4, 6)
Density:	coefficients to polynomial (2, 3)	Psat:	no information
Spec. Heat:	equation to polynomial (4, 6)	Tfreeze:	equation to polynomial (1, 6)

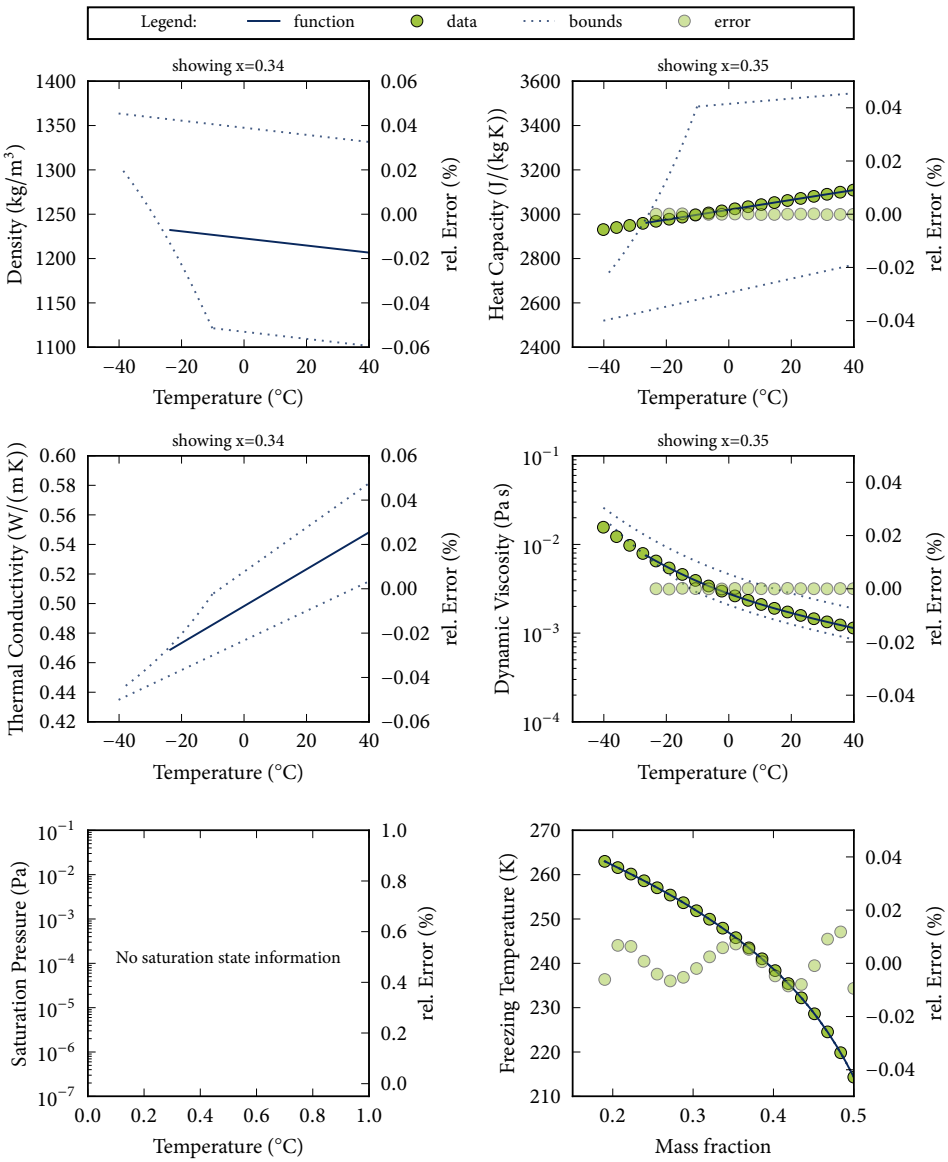

Fitted functions for IceEA

Description:	Ice slurry with Ethanol		
Source:	Kauffeld [32]		
	Skovrup [49]		
Temperature:	-33.15 °C to -8.15 °C	Th. Cond.:	data to polynomial (4, 6)
Composition:	5.0 % to 35.0 %, mass	Viscosity:	data to exppolynomial (4, 6)
Density:	data to polynomial (4, 6)	Psat:	no information
Spec. Heat:	data to polynomial (4, 6)	Tfreeze:	no information

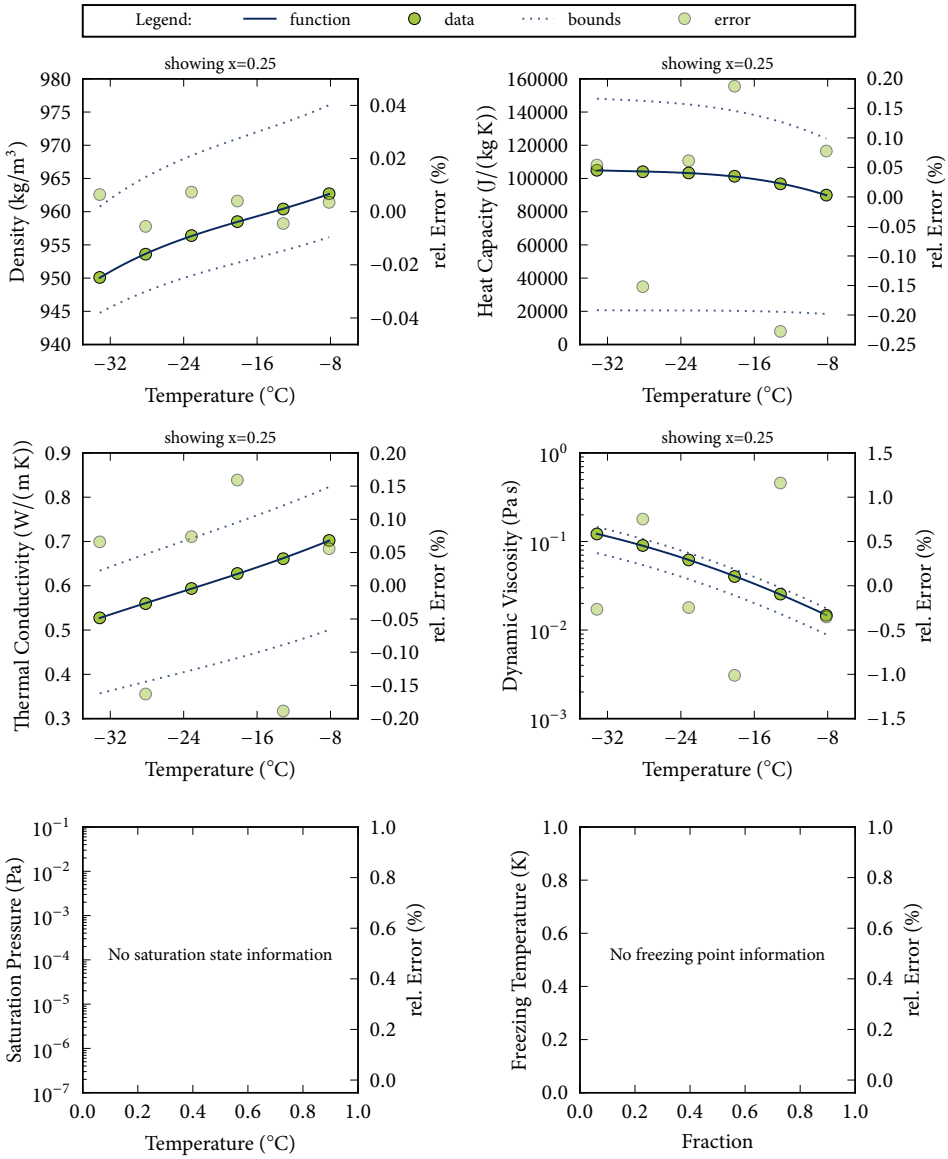

Fitted functions for IceNA

Description:	Ice slurry with NaCl		
Source:	Kauffeld [32]		
	Skovrup [49]		
Temperature:	-18.15 °C to -3.15 °C	Th. Cond.:	data to polynomial (4, 6)
Composition:	5.0 % to 35.0 %, mass	Viscosity:	data to exppolynomial (4, 6)
Density:	data to polynomial (4, 6)	Psat:	no information
Spec. Heat:	data to polynomial (4, 6)	Tfreeze:	no information

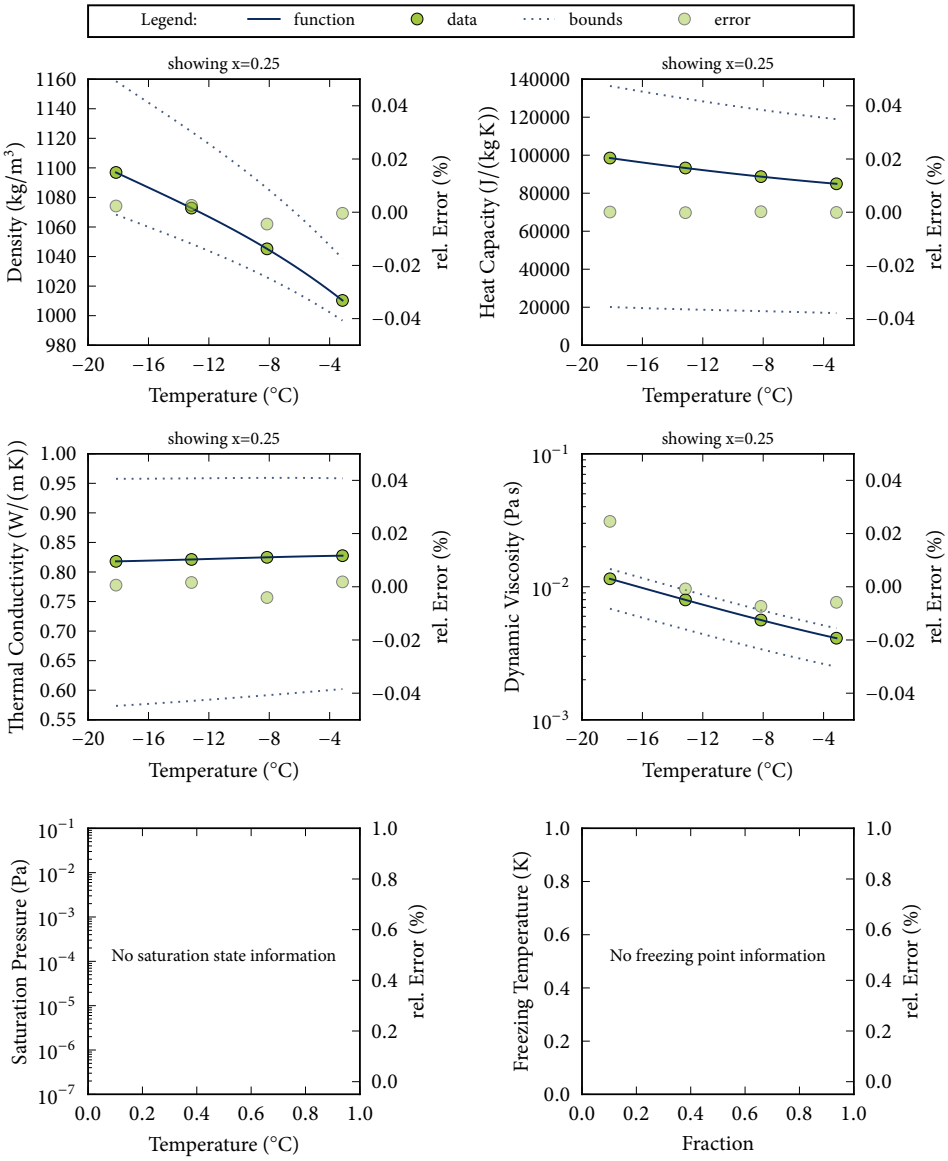

Fitted functions for IcePG

Description:	Ice slurry with Propylene Glycol		
Source:	Kauffeld [32]		
	Skovrup [49]		
Temperature:	-43.15 °C to -8.15 °C	Th. Cond.:	data to polynomial (4, 6)
Composition:	5.0 % to 35.0 %, mass	Viscosity:	data to exppolynomial (4, 6)
Density:	data to polynomial (4, 6)	Psat:	no information
Spec. Heat:	data to polynomial (4, 6)	Tfreeze:	no information

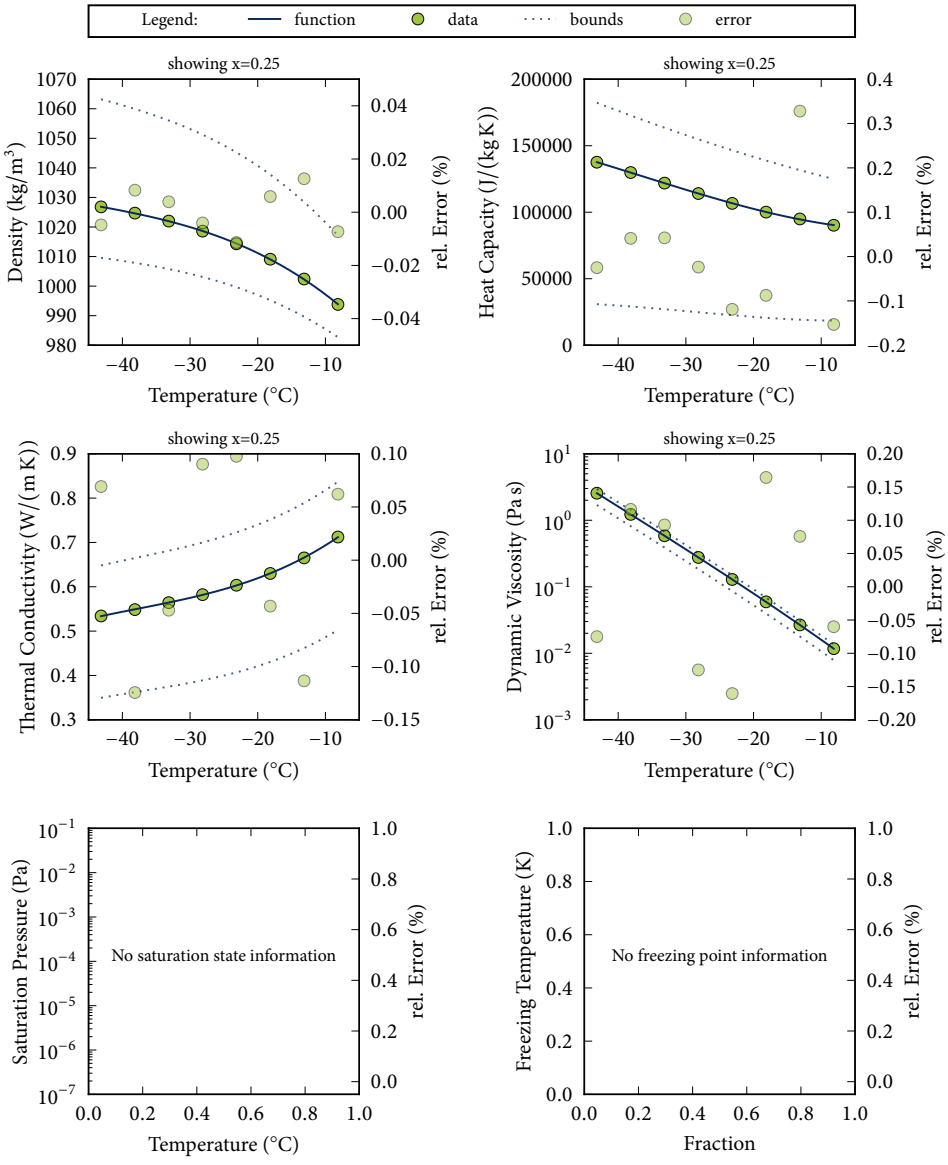

Fitted functions for LiBr

Description: Lithium-bromide solution - aq
Source: Pátek and Klomfar [42]

Temperature:	-0.15 °C to 226.85 °C	Th. Cond.:	no information
Composition:	0.0 % to 75.0 %, mass	Viscosity:	no information
Density:	equation to polynomial (4, 6)	Psat:	equation to exppolynomial (4, 6)
Spec. Heat:	equation to polynomial (4, 6)	Tfreeze:	no information

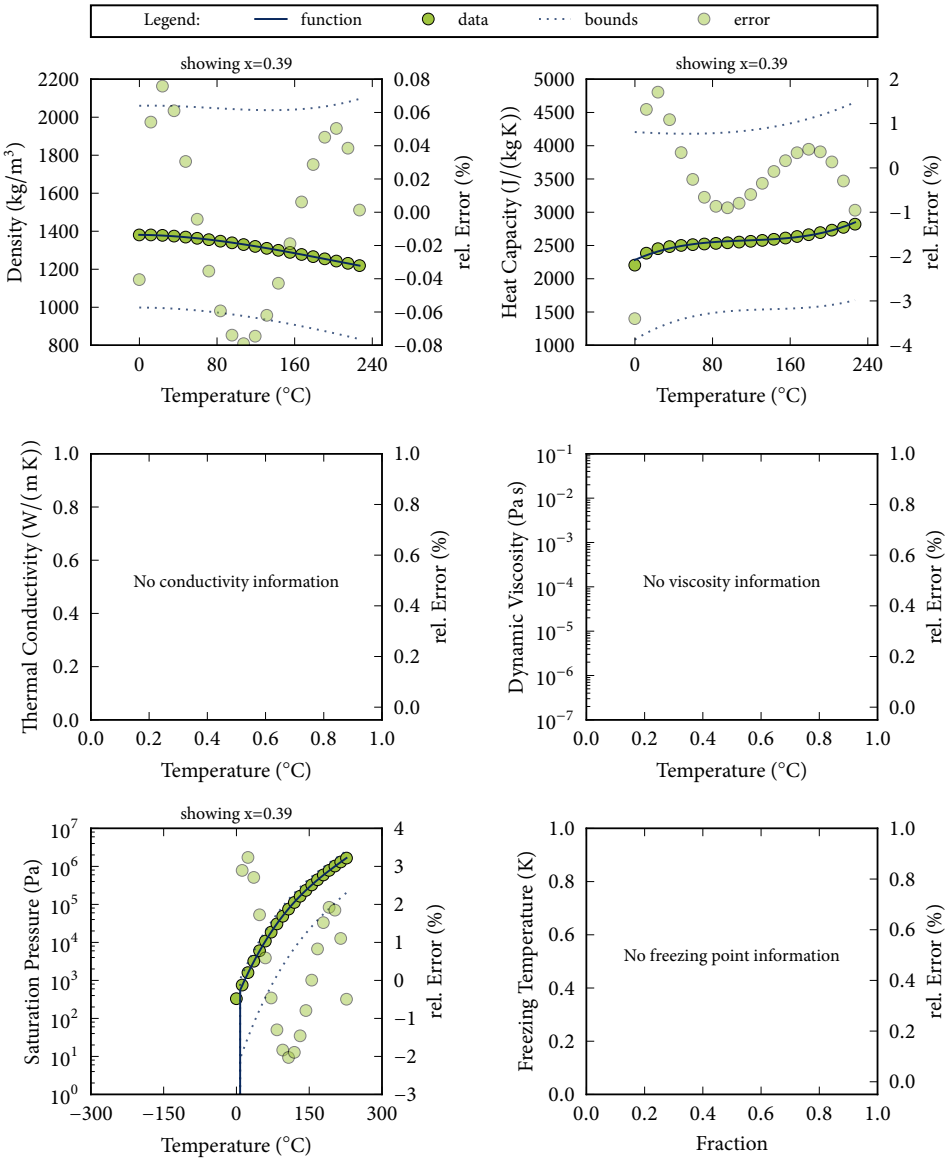

Fitted functions for MAM

Description: Ammonia (NH3) - aq
Source: Melinder [39]

Temperature:	-100.0 °C to 30.0 °C	Th. Cond.:	coefficients to polynomial (4, 6)
Composition:	0.0 % to 30.0 %, mass	Viscosity:	coefficients to exppolynomial (4, 6)
Density:	coefficients to polynomial (4, 6)	Psat:	no information
Spec. Heat:	coefficients to polynomial (4, 6)	Tfreeze:	coefficients to polynomial (1, 6)

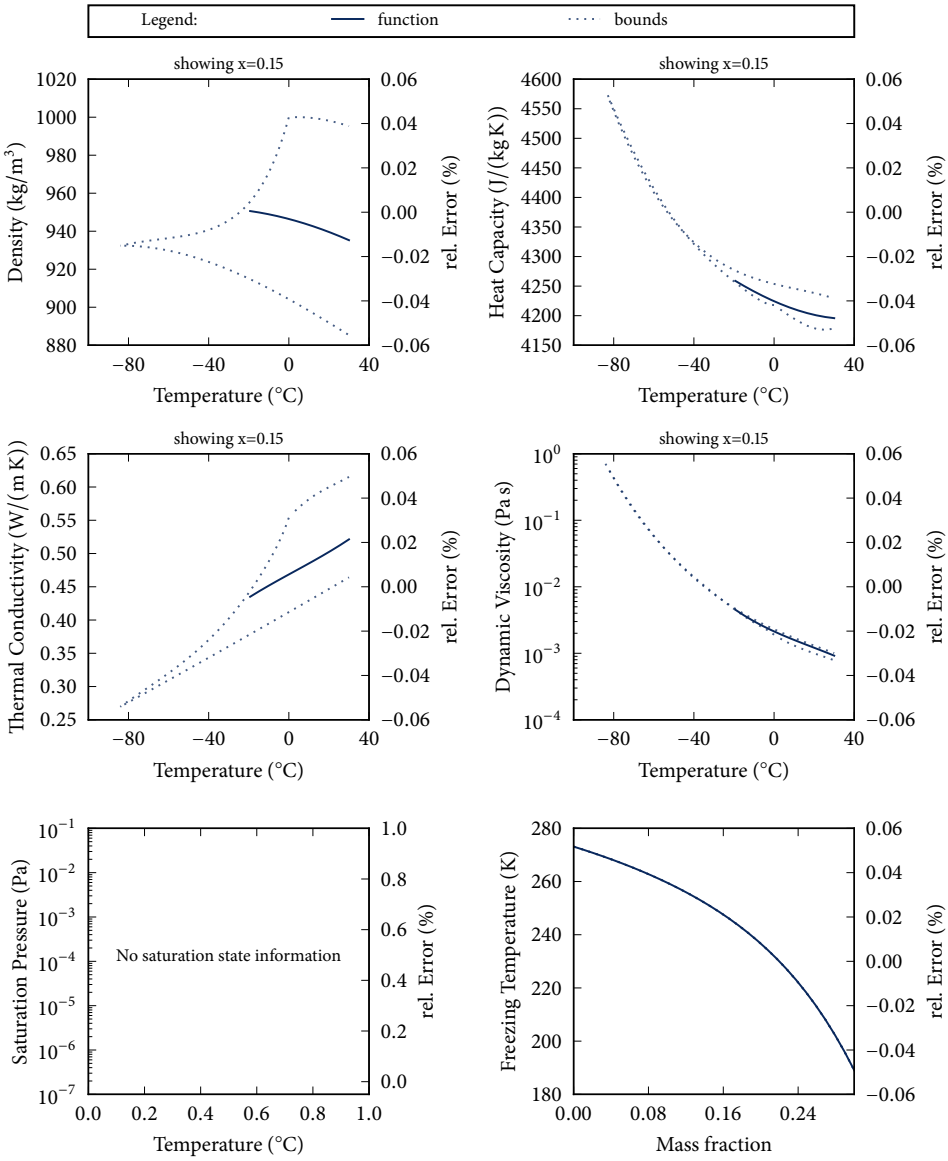

Fitted functions for MAM2

Description:	Melinder, Ammonia		
Source:	Melinder [39]		
	Skovrup [49]		
Temperature:	-49.0 °C to 20.0 °C	Th. Cond.:	data to polynomial (4, 5)
Composition:	7.8 % to 23.6 %, mass	Viscosity:	data to exppolynomial (4, 5)
Density:	data to polynomial (4, 5)	Psat:	no information
Spec. Heat:	data to polynomial (4, 5)	Tfreeze:	data to exppolynomial (1, 5)

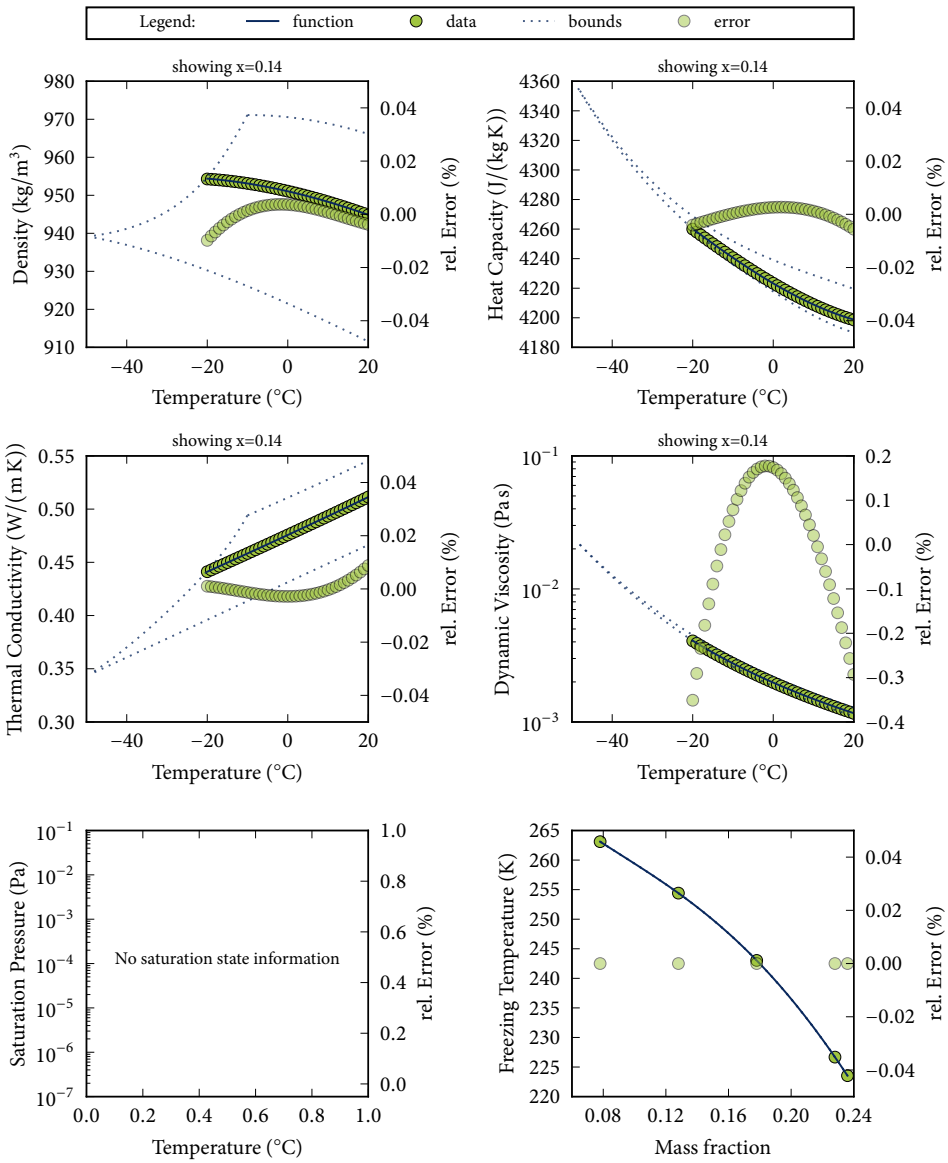

Fitted functions for MCA

Description: Calcium Chloride (CaCl2) - aq
Source: Melinder [39]

Temperature:	-100.0 °C to 40.0 °C	Th. Cond.:	coefficients to polynomial (4, 6)
Composition:	0.0 % to 30.0 %, mass	Viscosity:	coefficients to exppolynomial (4, 6)
Density:	coefficients to polynomial (4, 6)	Psat:	no information
Spec. Heat:	coefficients to polynomial (4, 6)	Tfreeze:	coefficients to polynomial (1, 6)

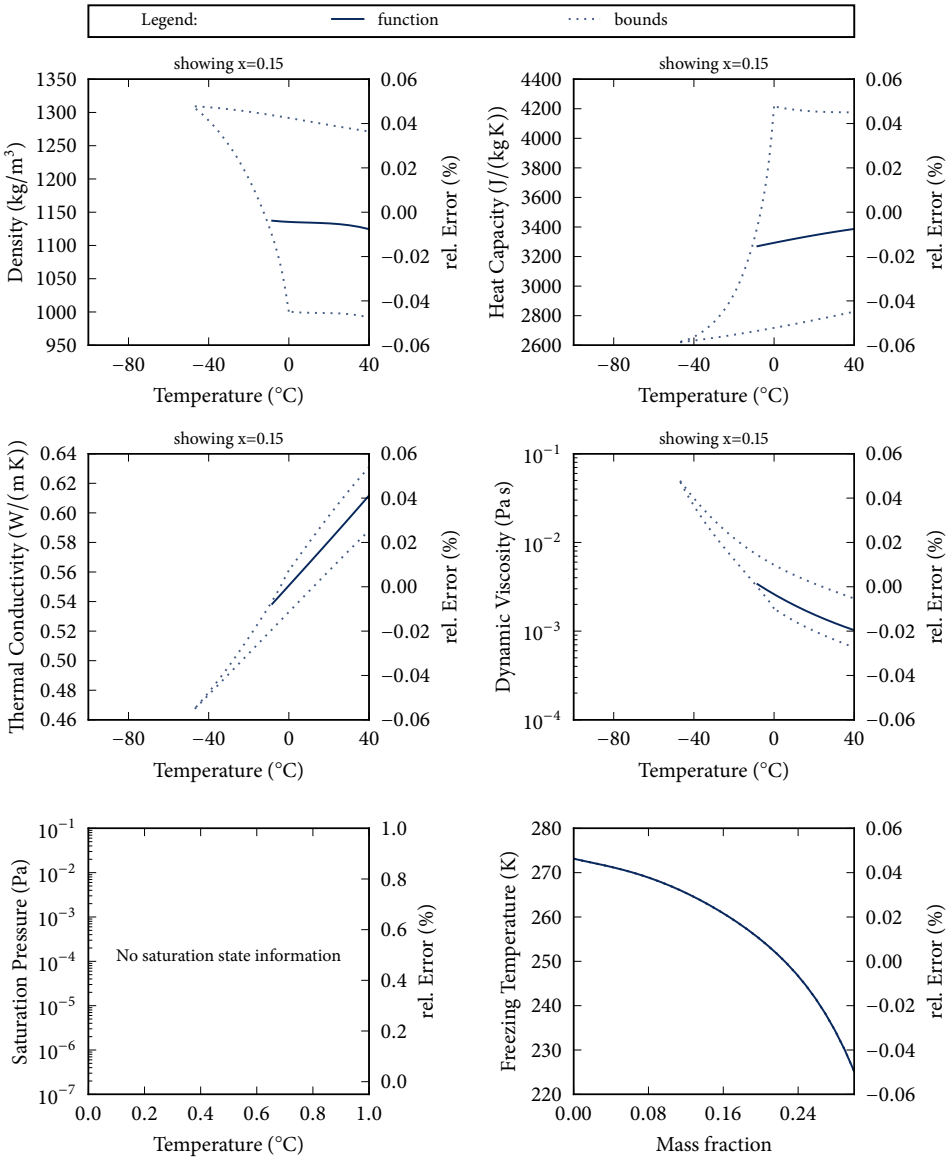

Fitted functions for MCA2

Description:	Melinder, Calcium Chloride		
Source:	Melinder [39]		
	Skovrup [49]		
Temperature:	-44.0 °C to 30.0 °C	Th. Cond.:	data to polynomial (4, 6)
Composition:	9.0 % to 29.4 %, mass	Viscosity:	data to exppolynomial (4, 6)
Density:	data to polynomial (4, 6)	Psat:	no information
Spec. Heat:	data to polynomial (4, 6)	Tfreeze:	data to exppolynomial (1, 6)

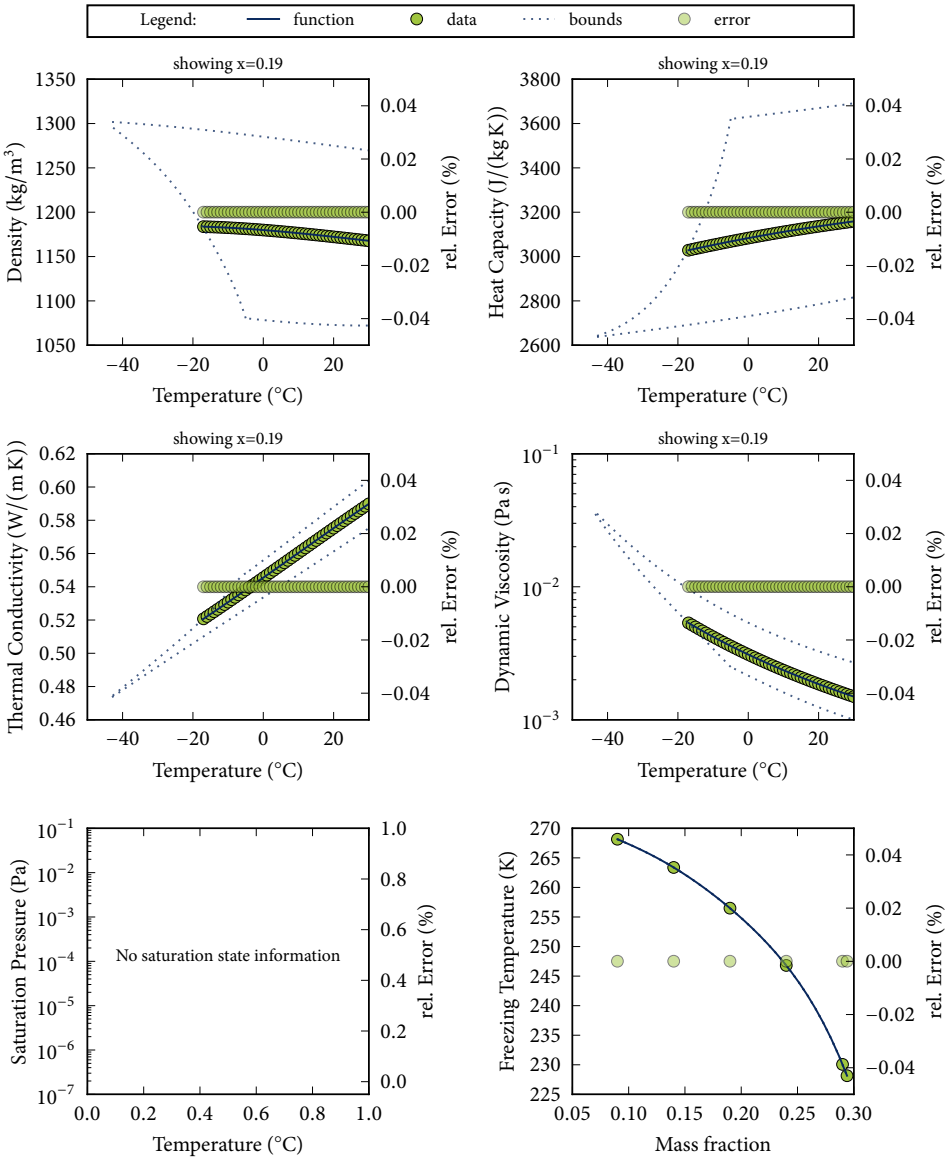

Fitted functions for MEA

Description: Ethyl Alcohol (Ethanol) - aq
Source: Melinder [39]

Temperature:	-100.0 °C to 40.0 °C	Th. Cond.:	coefficients to polynomial (4, 6)
Composition:	0.0 % to 60.0 %, mass	Viscosity:	coefficients to exppolynomial (4, 6)
Density:	coefficients to polynomial (4, 6)	Psat:	no information
Spec. Heat:	coefficients to polynomial (4, 6)	Tfreeze:	coefficients to polynomial (1, 6)

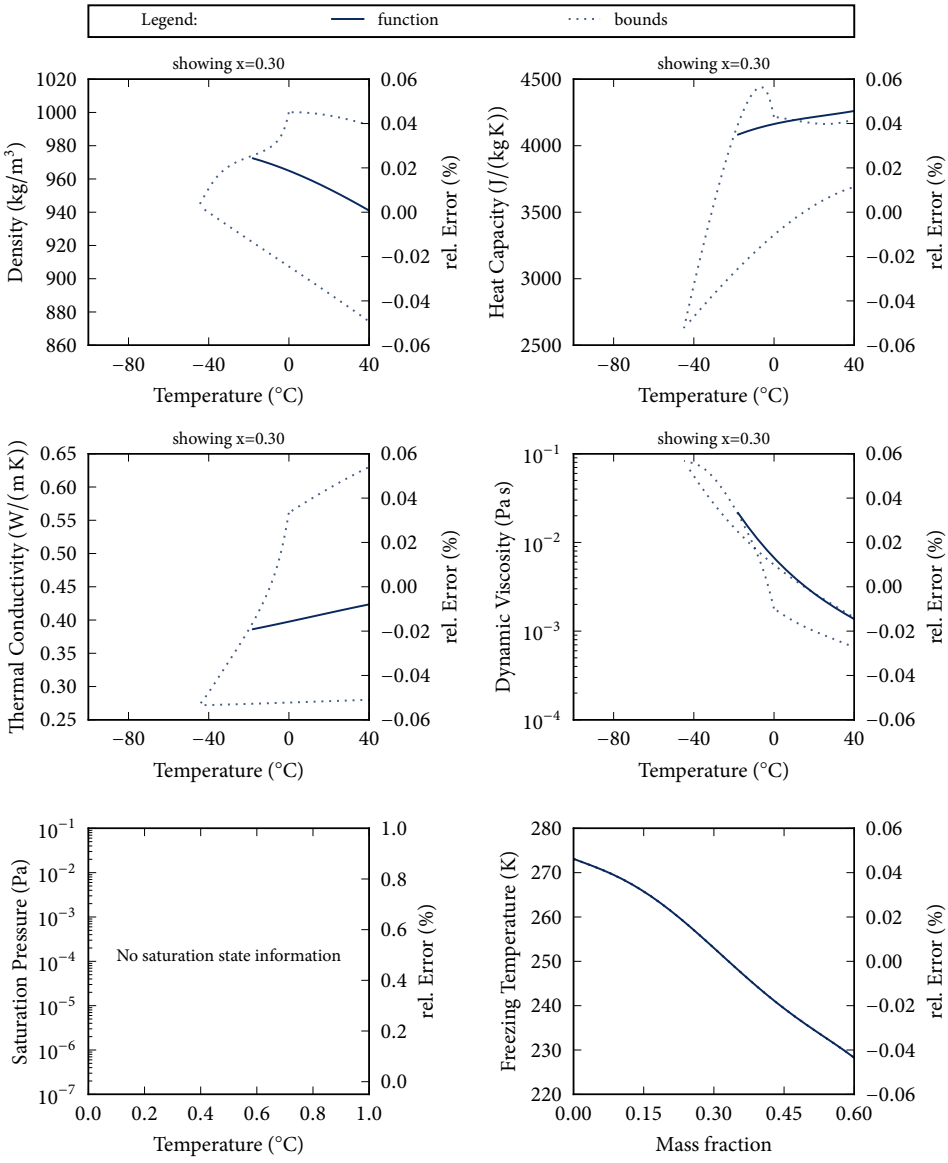

Fitted functions for MEA2

Description:	Melinder, Ethanol		
Source:	Melinder [39]		
	Skovrup [49]		
Temperature:	-44.0 °C to 20.0 °C	Th. Cond.:	data to polynomial (4, 6)
Composition:	11.0 % to 60.0 %, mass	Viscosity:	data to exppolynomial (4, 6)
Density:	data to polynomial (4, 6)	Psat:	no information
Spec. Heat:	data to polynomial (4, 6)	Tfreeze:	data to exppolynomial (1, 6)

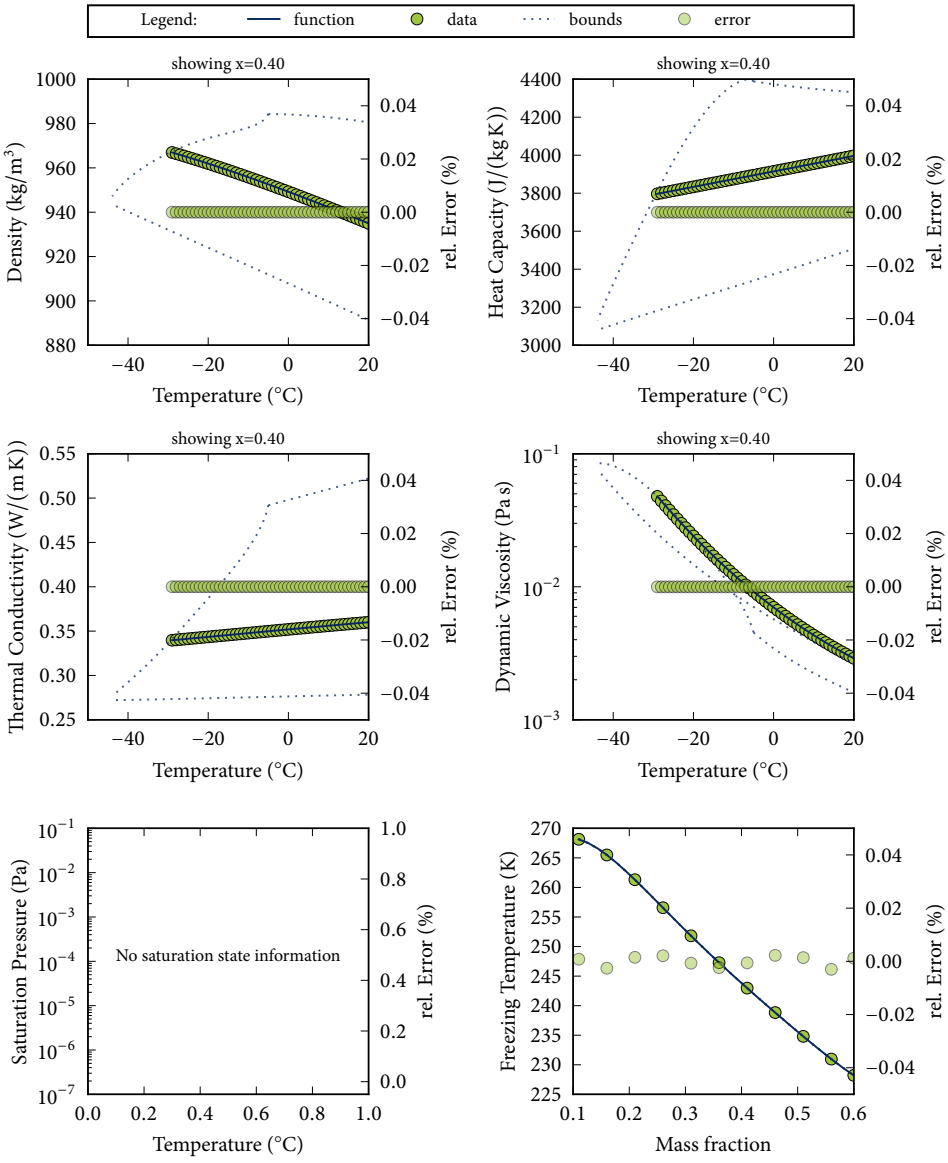

Fitted functions for MEG

Description: Ethylene Glycol - aq
Source: Melinder [39]

Temperature:	-100.0 °C to 100.0 °C	Th. Cond.:	coefficients to polynomial (4, 6)
Composition:	0.0 % to 60.0 %, mass	Viscosity:	coefficients to exppolynomial (4, 6)
Density:	coefficients to polynomial (4, 6)	Psat:	no information
Spec. Heat:	coefficients to polynomial (4, 6)	Tfreeze:	coefficients to polynomial (1, 6)

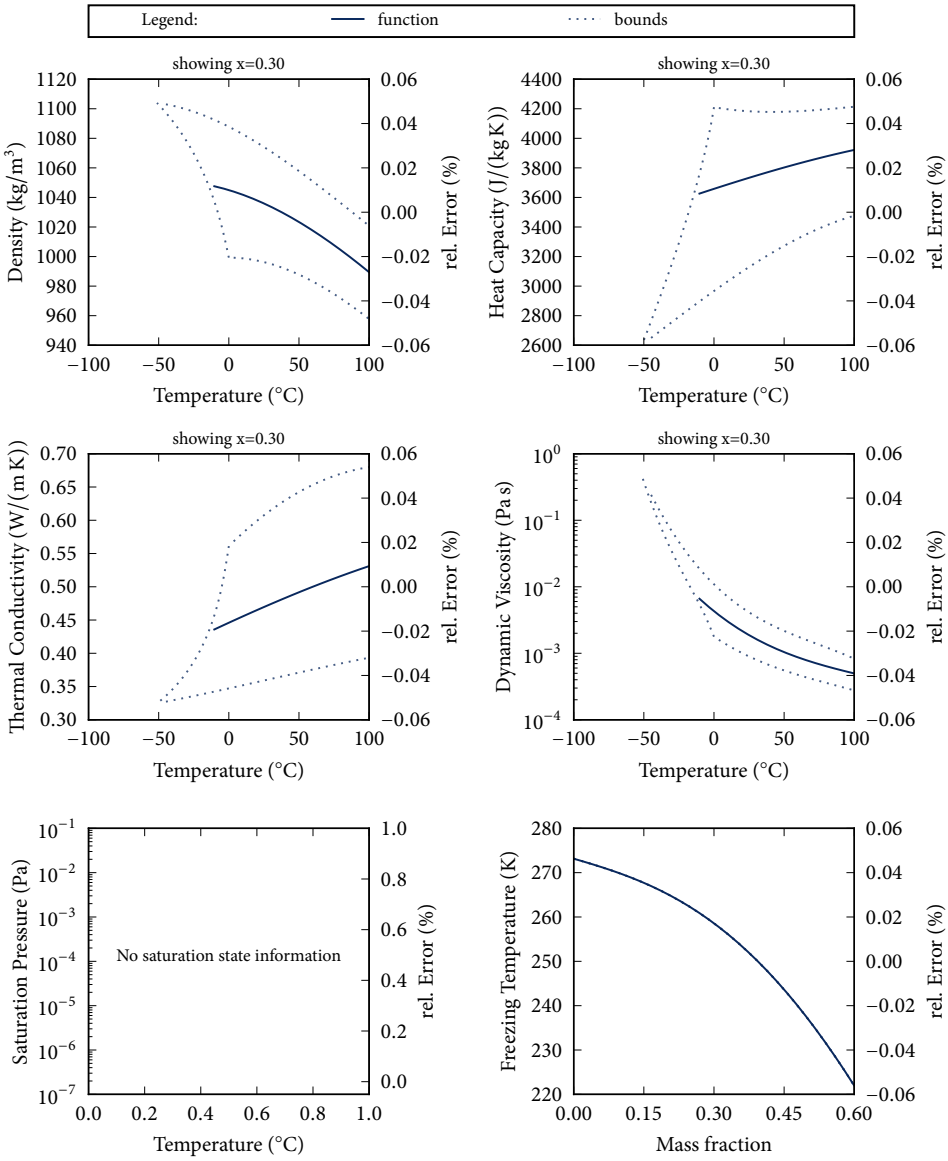

Fitted functions for MEG2

Description:	Melinder, Ethylene Glycol		
Source:	Melinder [39]		
	Skovrup [49]		
Temperature:	-44.0 °C to 40.0 °C	Th. Cond.:	data to polynomial (4, 6)
Composition:	0.0 % to 56.0 %, mass	Viscosity:	data to exppolynomial (4, 6)
Density:	data to polynomial (4, 6)	Psat:	no information
Spec. Heat:	data to polynomial (4, 6)	Tfreeze:	data to exppolynomial (1, 6)

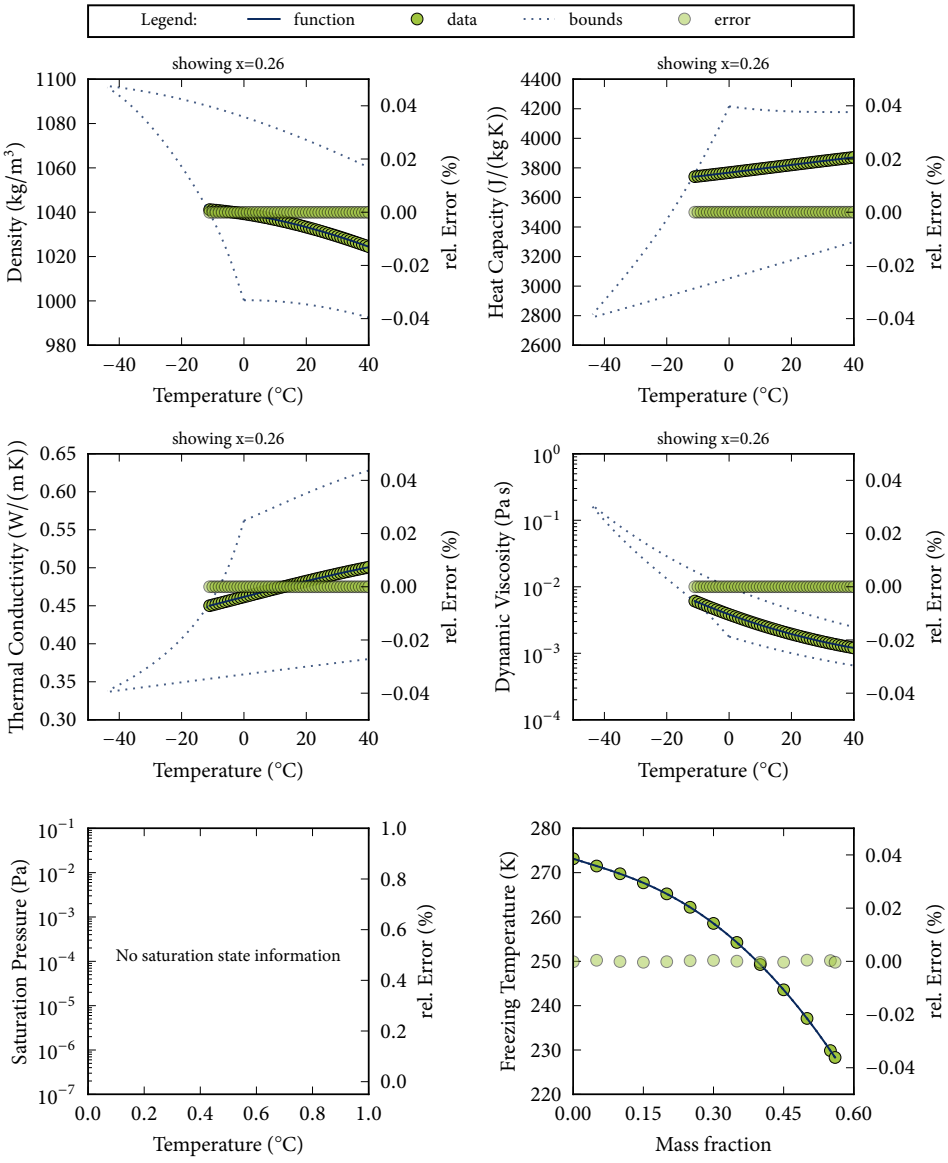

Fitted functions for MGL

Description: Glycerol - aq
Source: Melinder [39]

Temperature:	-100.0 °C to 40.0 °C	Th. Cond.:	coefficients to polynomial (4, 6)
Composition:	0.0 % to 60.0 %, mass	Viscosity:	coefficients to exppolynomial (4, 6)
Density:	coefficients to polynomial (4, 6)	Psat:	no information
Spec. Heat:	coefficients to polynomial (4, 6)	Tfreeze:	coefficients to polynomial (1, 6)

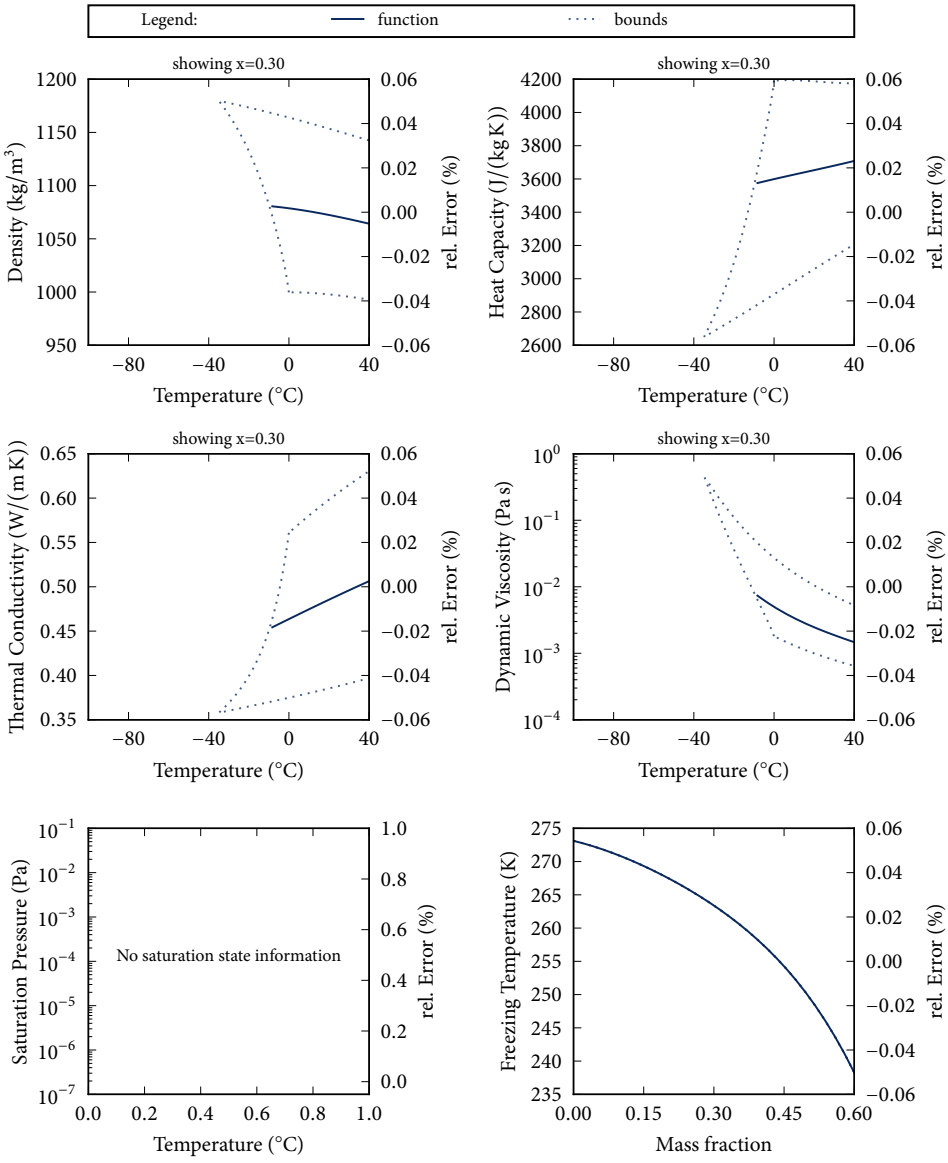

Fitted functions for MGL2

Description:	Melinder, Glycerol		
Source:	Melinder [39]		
	Skovrup [49]		
Temperature:	-40.0 °C to 40.0 °C	Th. Cond.:	data to polynomial (4, 6)
Composition:	19.5 % to 63.0 %, mass	Viscosity:	data to exppolynomial (4, 6)
Density:	data to polynomial (4, 6)	Psat:	no information
Spec. Heat:	data to polynomial (4, 6)	Tfreeze:	data to exppolynomial (1, 6)

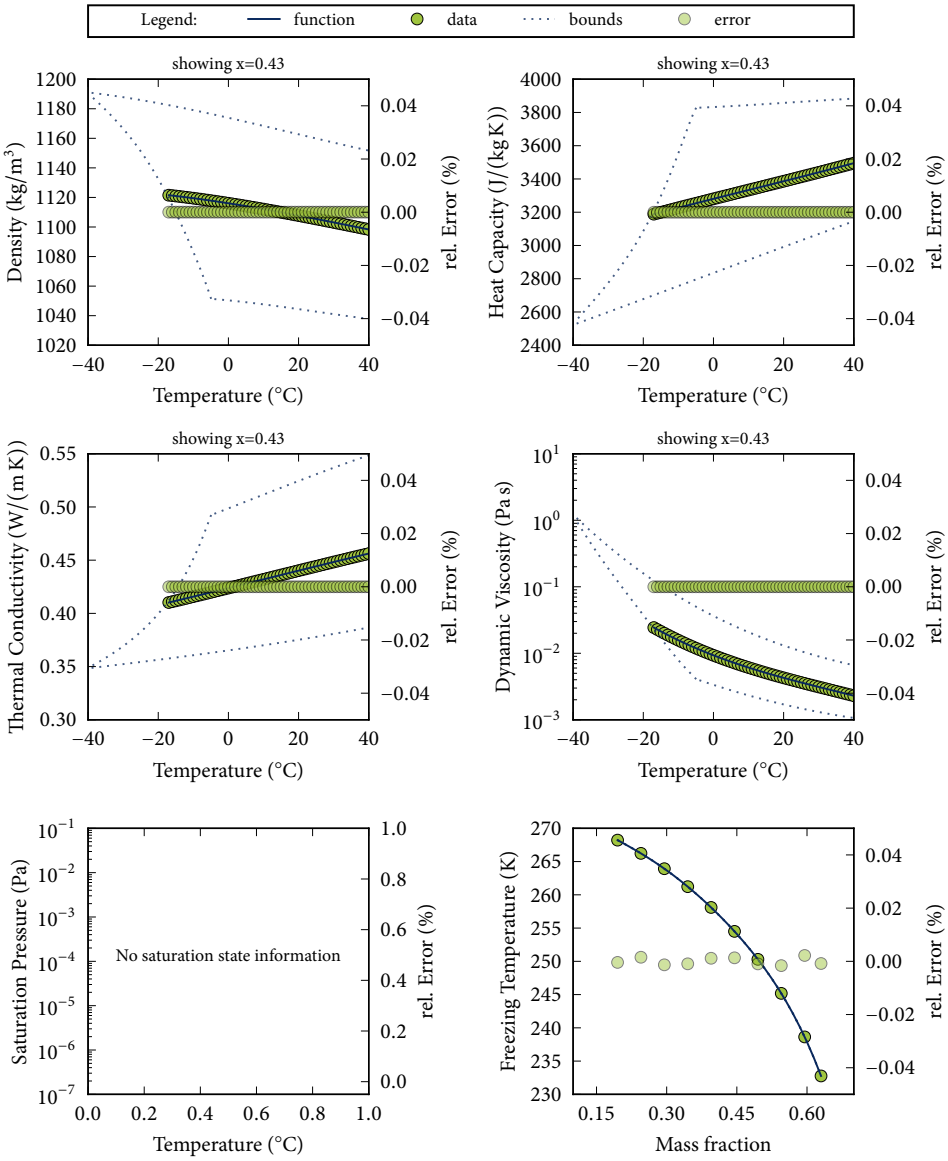

Fitted functions for MKA

Description: Potassium Acetate (CH3CO2K) - aq
Source: Melinder [39]

Temperature:	-100.0 °C to 40.0 °C	Th. Cond.:	coefficients to polynomial (4, 6)
Composition:	0.0 % to 45.0 %, mass	Viscosity:	coefficients to exppolynomial (4, 6)
Density:	coefficients to polynomial (4, 6)	Psat:	no information
Spec. Heat:	coefficients to polynomial (4, 6)	Tfreeze:	coefficients to polynomial (1, 6)

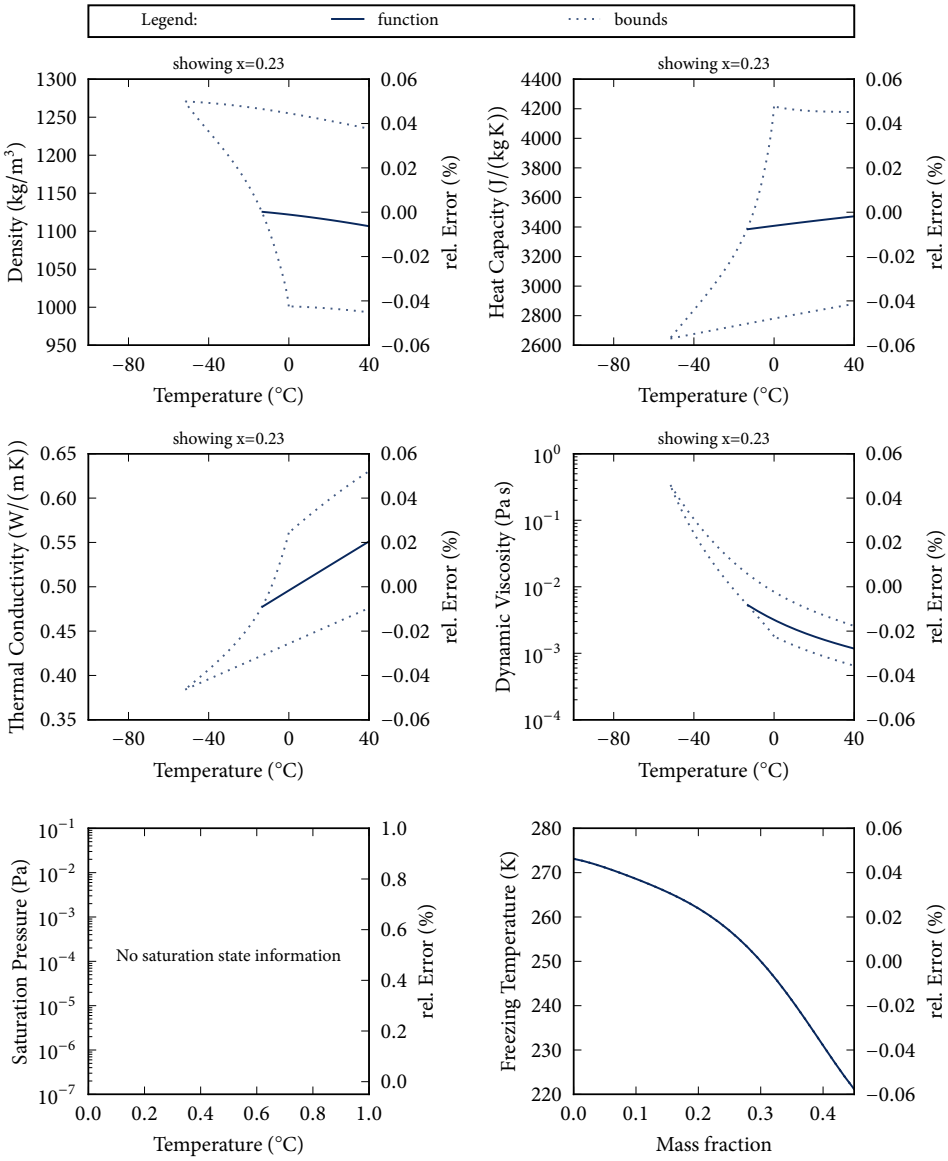

Fitted functions for MKA2

Description:	Melinder, Potassium Acetate		
Source:	Melinder [39]		
	Skovrup [49]		
Temperature:	-44.0 °C to 30.0 °C	Th. Cond.:	data to polynomial (4, 6)
Composition:	11.0 % to 41.0 %, mass	Viscosity:	data to exppolynomial (4, 6)
Density:	data to polynomial (4, 6)	Psat:	no information
Spec. Heat:	data to polynomial (4, 6)	Tfreeze:	data to exppolynomial (1, 6)

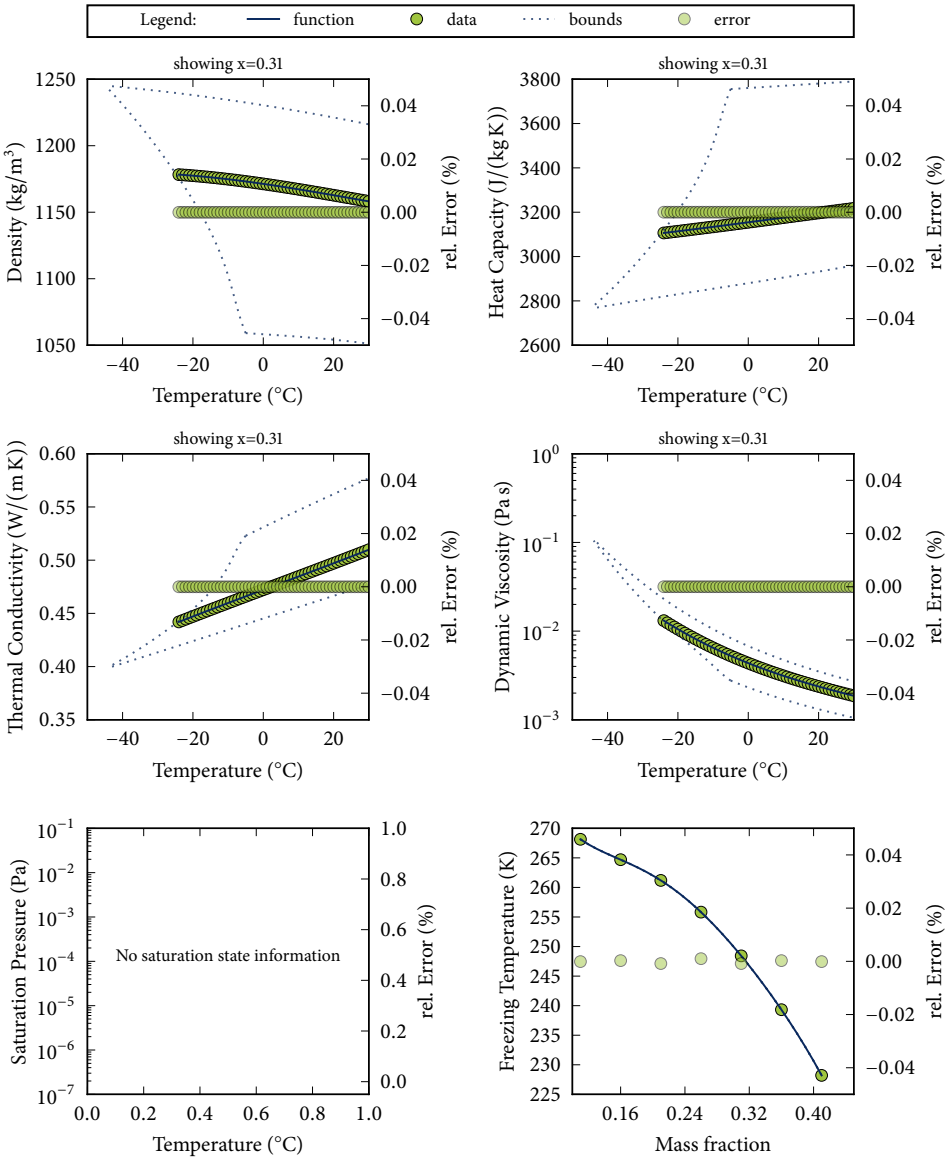

Fitted functions for MKC

Description: Potassium Carbonate (K2CO3) - aq
Source: Melinder [39]

Temperature:	-100.0 °C to 40.0 °C	Th. Cond.:	coefficients to polynomial (4, 6)
Composition:	0.0 % to 40.0 %, mass	Viscosity:	coefficients to exppolynomial (4, 6)
Density:	coefficients to polynomial (4, 6)	Psat:	no information
Spec. Heat:	coefficients to polynomial (4, 6)	Tfreeze:	coefficients to polynomial (1, 6)

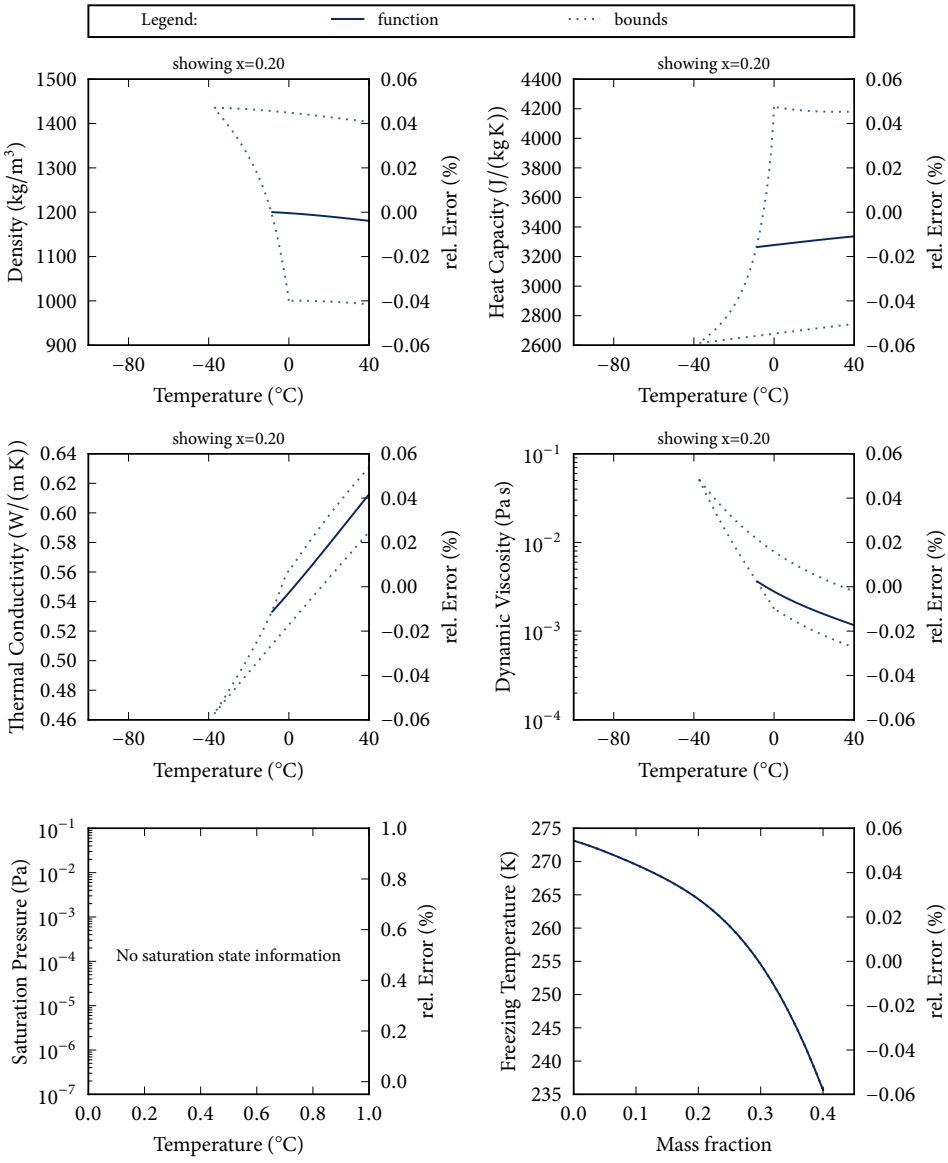

Fitted functions for MKC2

Description:	Melinder, Potassium Carbonate		
Source:	Melinder [39]		
	Skovrup [49]		
Temperature:	-35.0 °C to 30.0 °C	Th. Cond.:	data to polynomial (4, 6)
Composition:	0.0 % to 39.0 %, mass	Viscosity:	data to exppolynomial (4, 6)
Density:	data to polynomial (4, 6)	Psat:	no information
Spec. Heat:	data to polynomial (4, 6)	Tfreeze:	data to exppolynomial (1, 6)

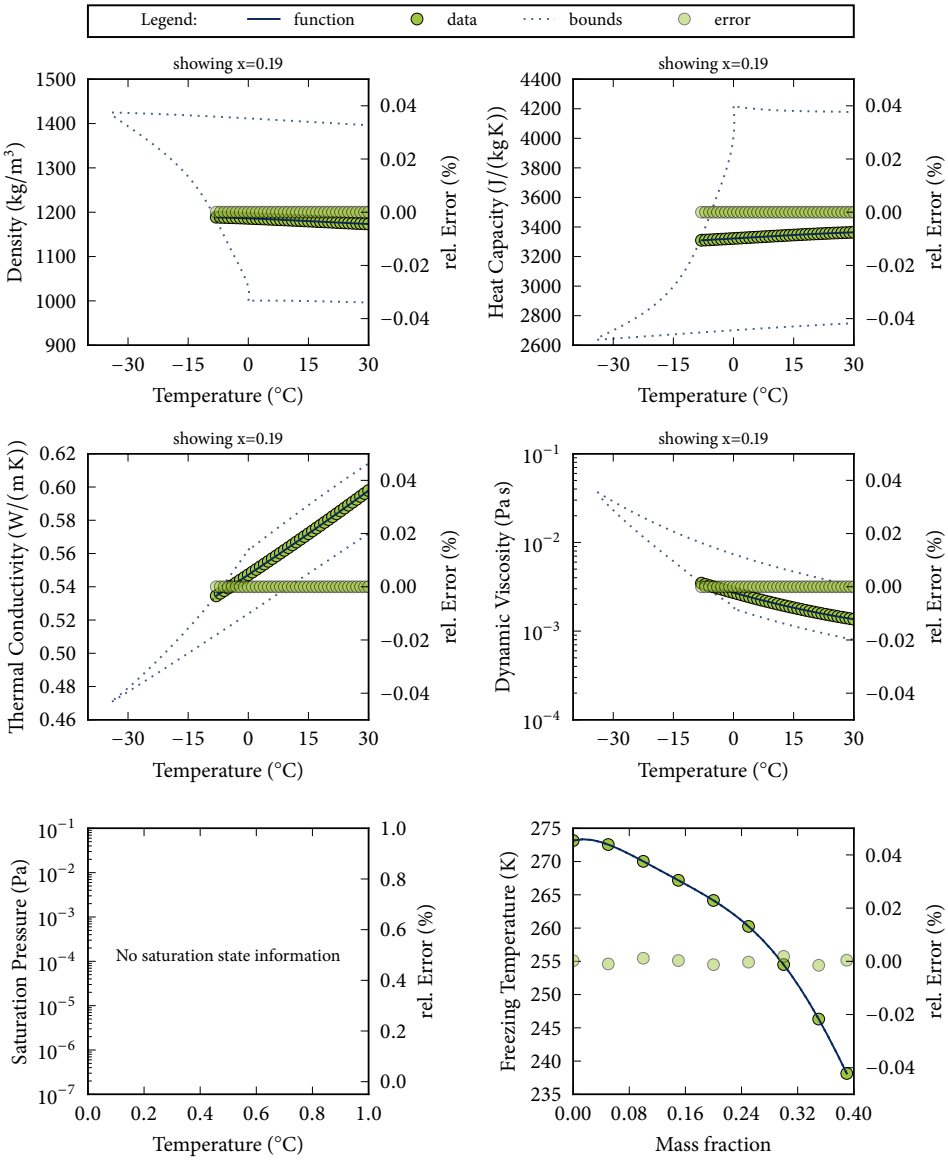

Fitted functions for MKF

Description: Potassium Formate (CHKO2) - aq
Source: Melinder [39]

Temperature:	-100.0 °C to 40.0 °C	Th. Cond.:	coefficients to polynomial (4, 6)
Composition:	0.0 % to 48.0 %, mass	Viscosity:	coefficients to exppolynomial (4, 6)
Density:	coefficients to polynomial (4, 6)	Psat:	no information
Spec. Heat:	coefficients to polynomial (4, 6)	Tfreeze:	coefficients to polynomial (1, 6)

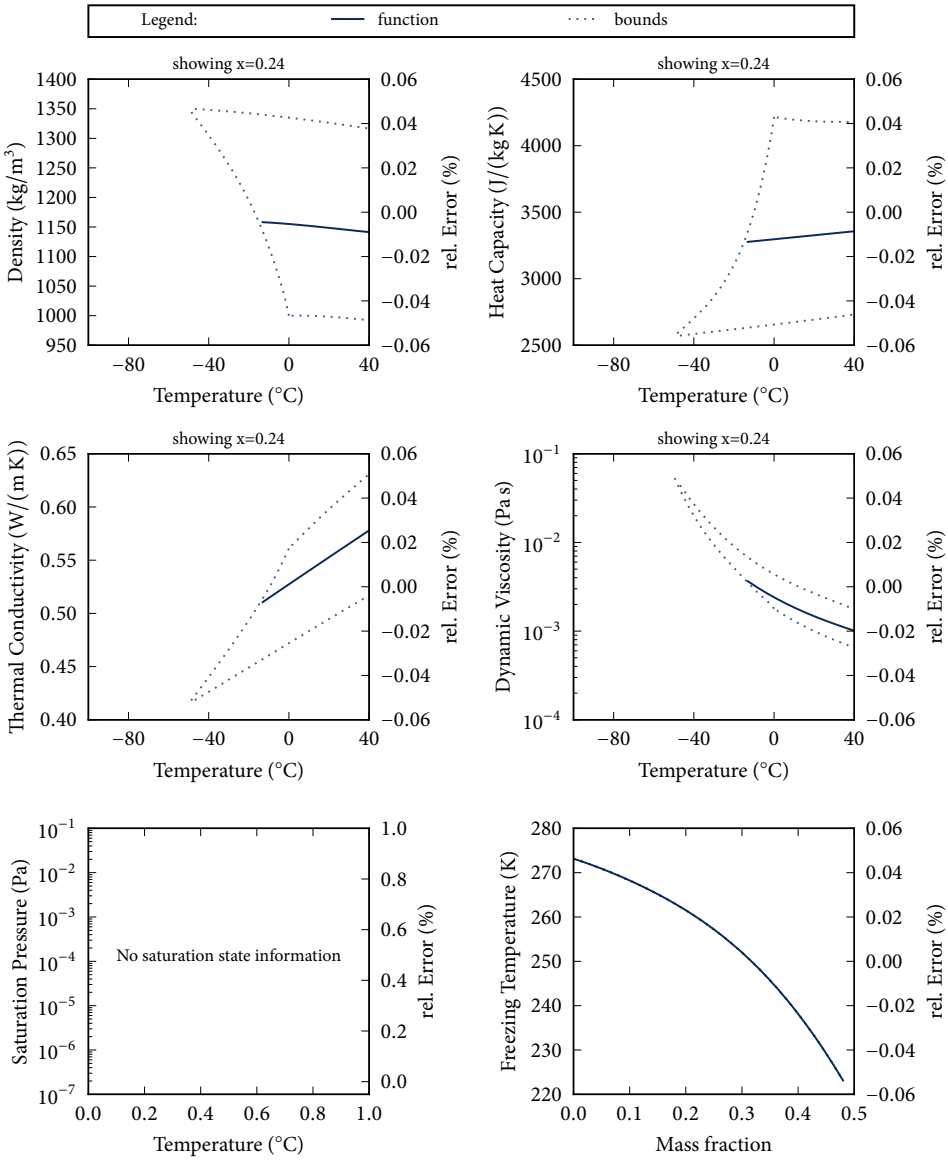

Fitted functions for MLI

Description: Lithium Chloride (LiCl) - aq
Source: Melinder [39]

Temperature:	-100.0 °C to 40.0 °C	Th. Cond.:	coefficients to polynomial (4, 6)
Composition:	0.0 % to 24.0 %, mass	Viscosity:	coefficients to exppolynomial (4, 6)
Density:	coefficients to polynomial (4, 6)	Psat:	no information
Spec. Heat:	coefficients to polynomial (4, 6)	Tfreeze:	coefficients to polynomial (1, 6)

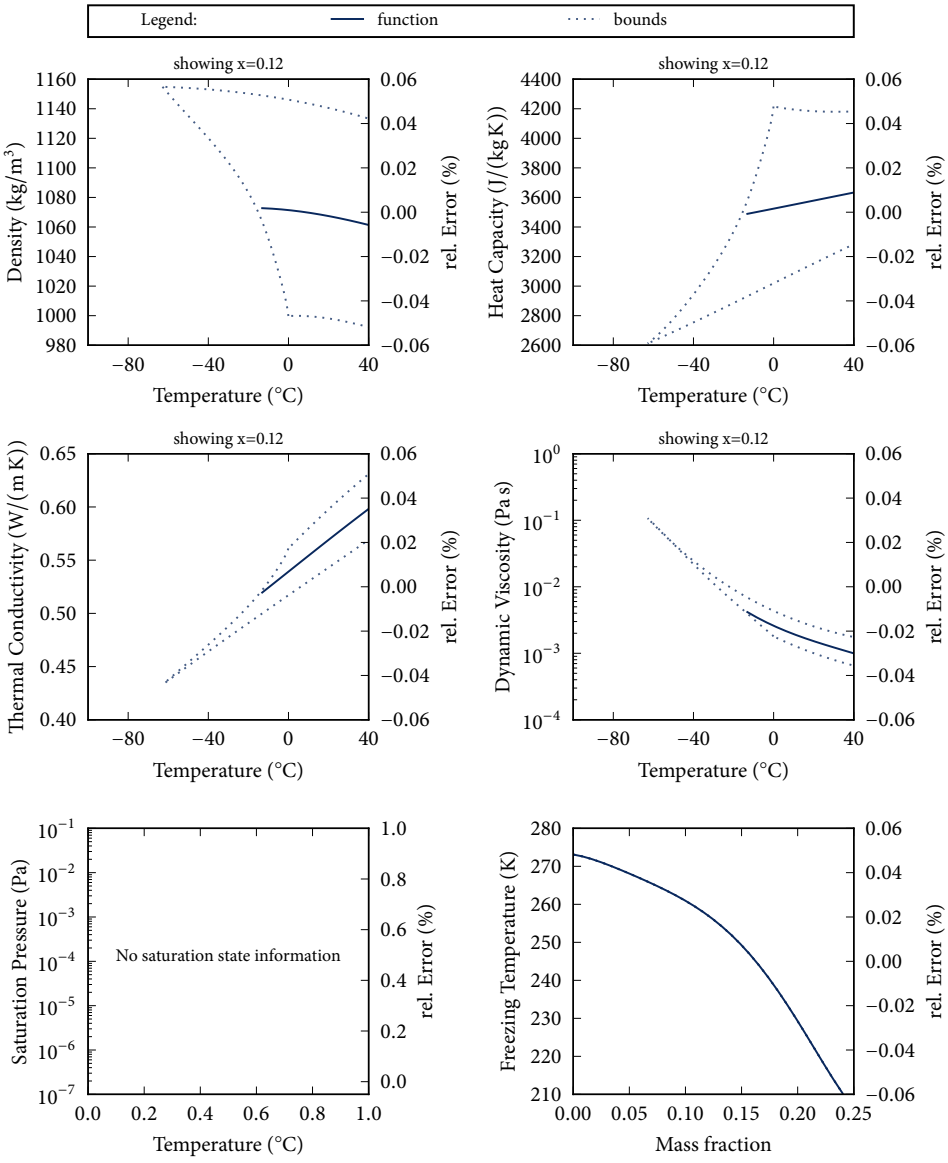

Fitted functions for MMA

Description: Methyl Alcohol (Methanol) - aq
Source: Melinder [39]

Temperature:	-100.0 °C to 40.0 °C	Th. Cond.:	coefficients to polynomial (4, 6)
Composition:	0.0 % to 60.0 %, mass	Viscosity:	coefficients to exppolynomial (4, 6)
Density:	coefficients to polynomial (4, 6)	Psat:	no information
Spec. Heat:	coefficients to polynomial (4, 6)	Tfreeze:	coefficients to polynomial (1, 6)

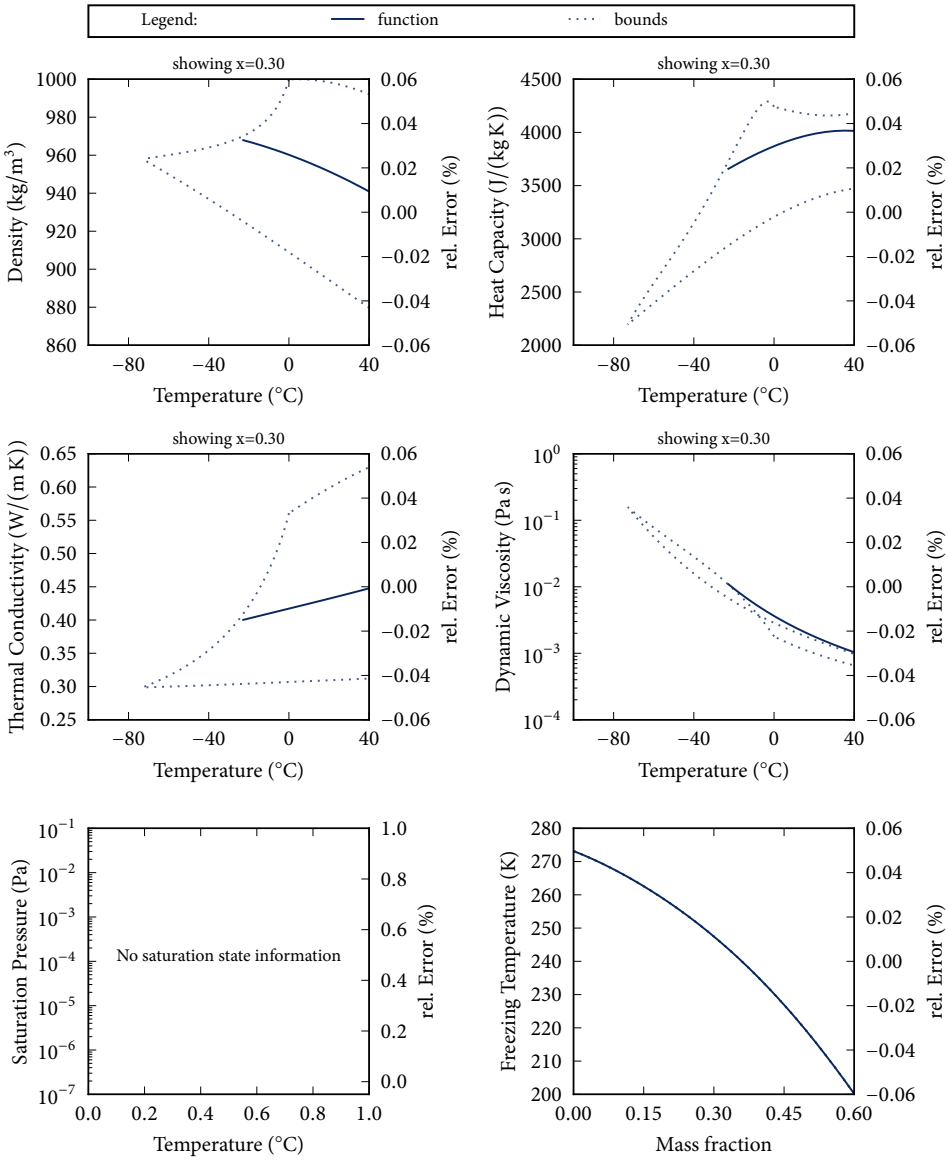

Fitted functions for MMA2

Description:	Melinder, Methanol		
Source:	Melinder [39]		
	Skovrup [49]		
Temperature:	-50.0 °C to 20.0 °C	Th. Cond.:	data to polynomial (4, 6)
Composition:	7.8 % to 47.4 %, mass	Viscosity:	data to exppolynomial (4, 6)
Density:	data to polynomial (4, 6)	Psat:	no information
Spec. Heat:	data to polynomial (4, 6)	Tfreeze:	data to exppolynomial (1, 6)

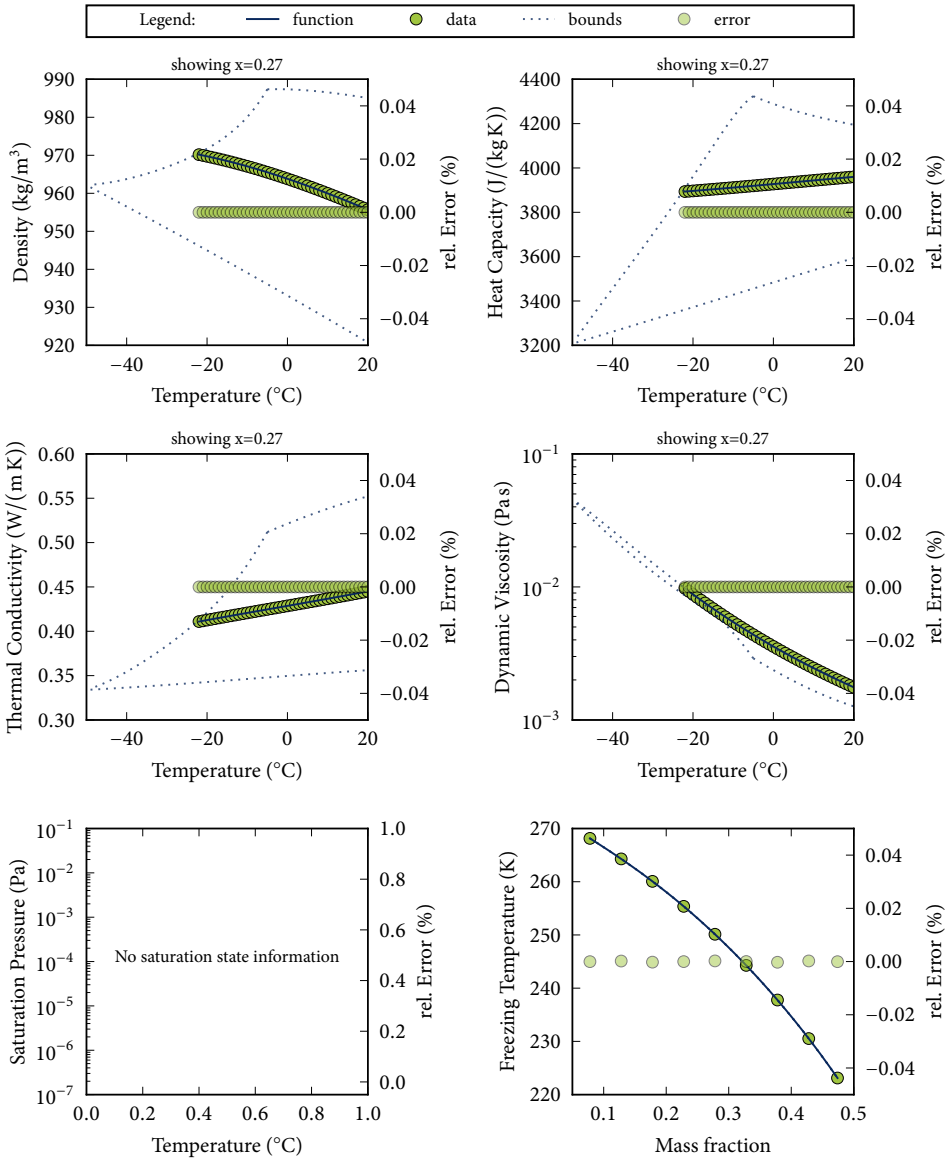

Fitted functions for MMG

Description: MgCl2 - aq
Source: Melinder [39]

Temperature:	-100.0 °C to 40.0 °C	Th. Cond.:	coefficients to polynomial (4, 6)
Composition:	0.0 % to 30.0 %, mass	Viscosity:	coefficients to exppolynomial (4, 6)
Density:	coefficients to polynomial (4, 6)	Psat:	no information
Spec. Heat:	coefficients to polynomial (4, 6)	Tfreeze:	coefficients to polynomial (1, 6)

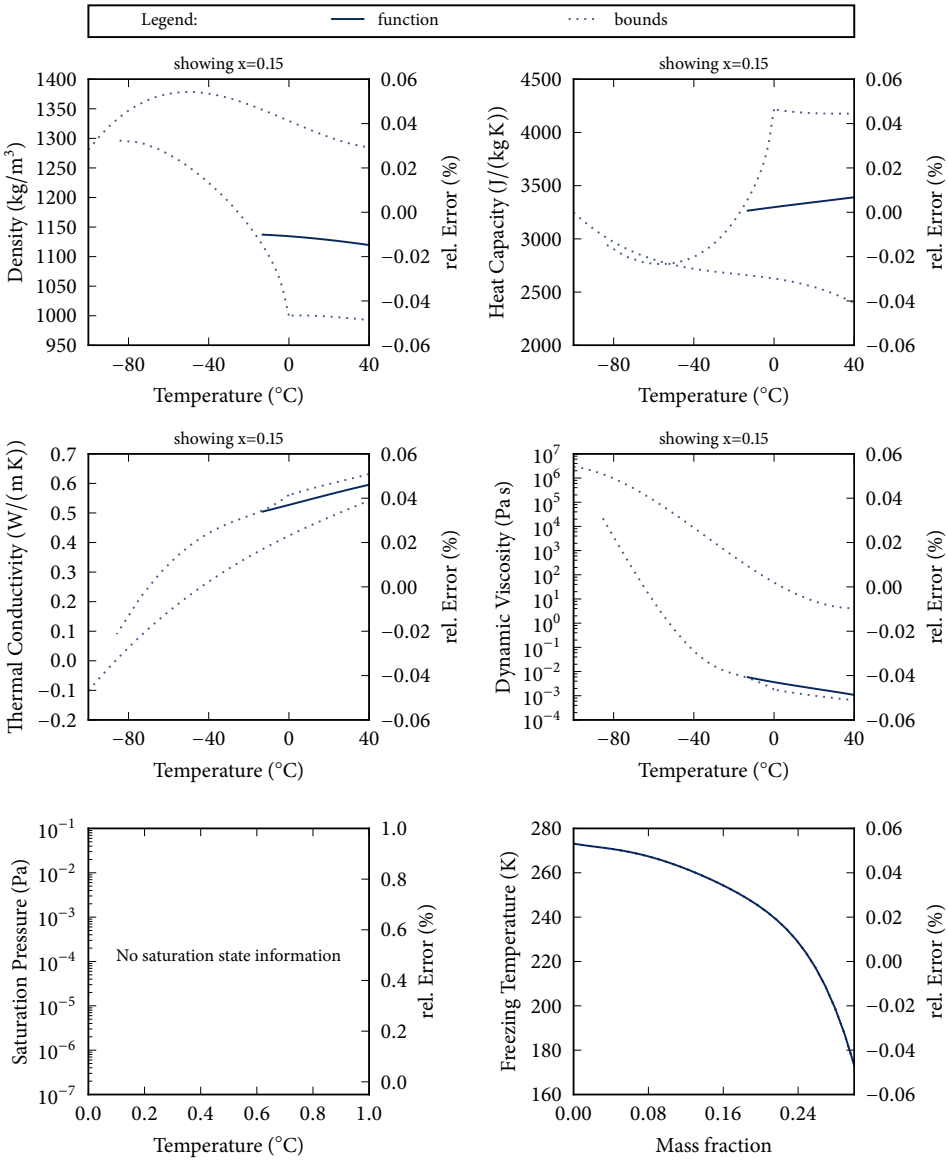

Fitted functions for MMG2

Description:	Melinder, Magnesium Chloride		
Source:	Melinder [39]		
	Skovrup [49]		
Temperature:	-30.0 °C to 30.0 °C	Th. Cond.:	data to polynomial (4, 6)
Composition:	0.0 % to 20.5 %, mass	Viscosity:	data to exppolynomial (4, 6)
Density:	data to polynomial (4, 6)	Psat:	no information
Spec. Heat:	data to polynomial (4, 6)	Tfreeze:	data to exppolynomial (1, 6)

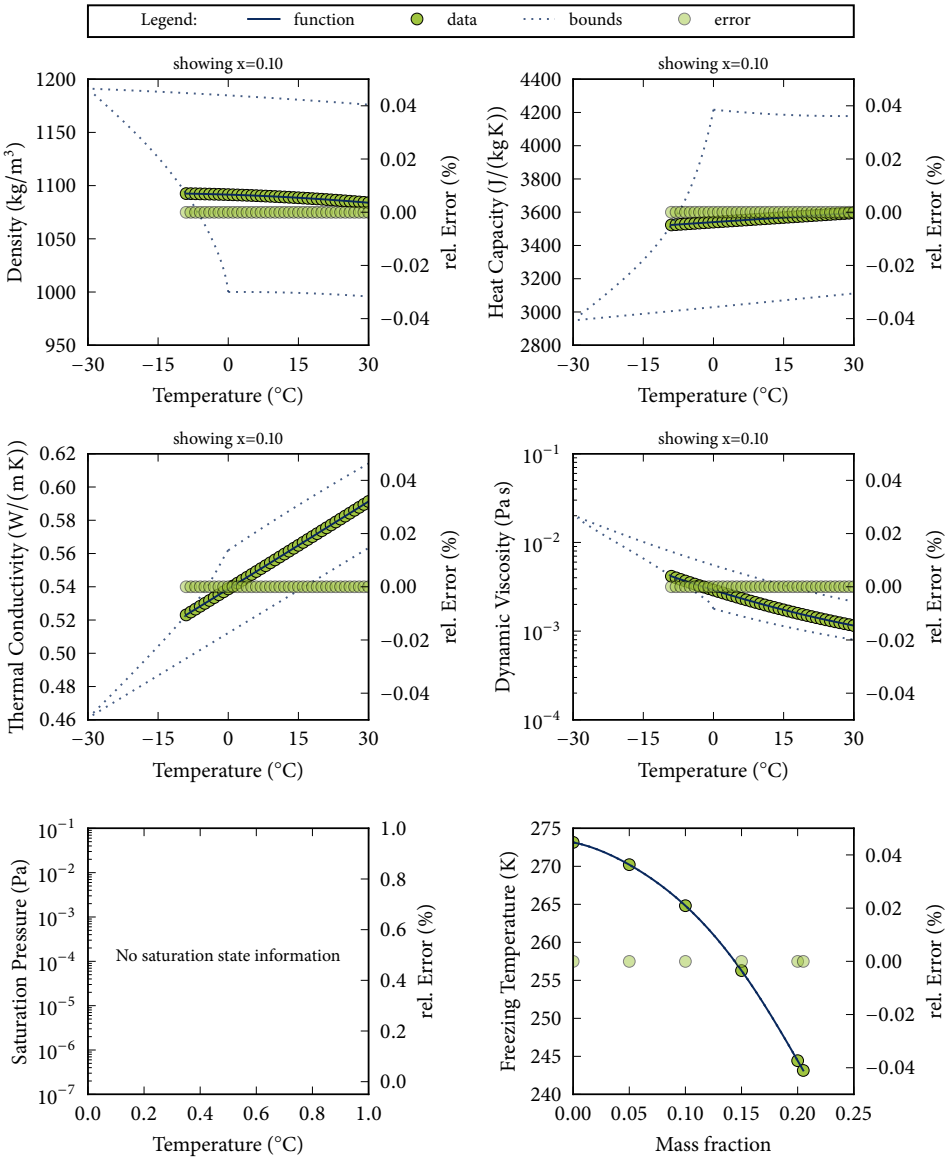

Fitted functions for MNA

Description: Sodium Chloride (NaCl) - aq
Source: Melinder [39]

Temperature:	-100.0 °C to 40.0 °C	Th. Cond.:	coefficients to polynomial (4, 6)
Composition:	0.0 % to 23.0 %, mass	Viscosity:	coefficients to exppolynomial (4, 6)
Density:	coefficients to polynomial (4, 6)	Psat:	no information
Spec. Heat:	coefficients to polynomial (4, 6)	Tfreeze:	coefficients to polynomial (1, 6)

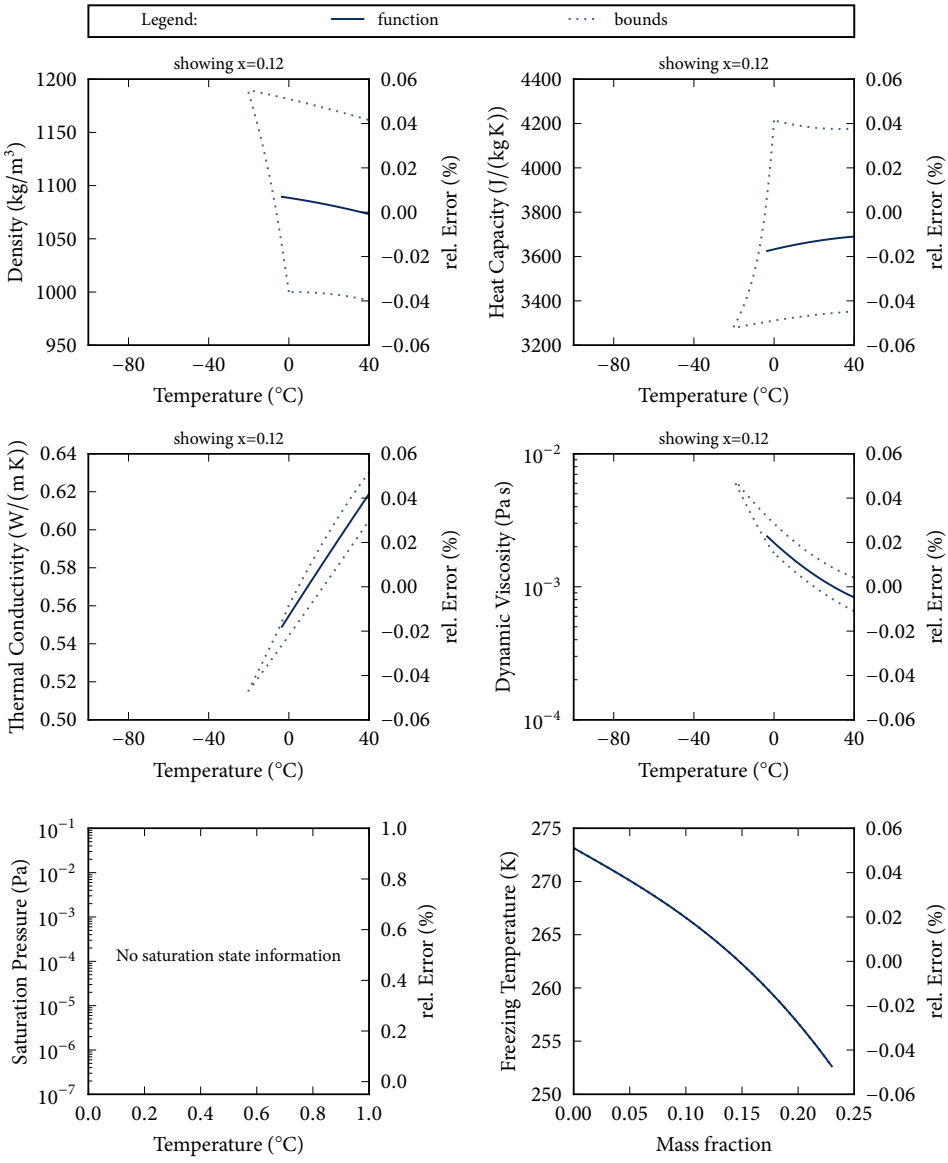

Fitted functions for MNA2

Description:	Melinder, Sodium Chloride		
Source:	Melinder [39]		
	Skovrup [49]		
Temperature:	-20.0 °C to 30.0 °C	Th. Cond.:	data to polynomial (4, 6)
Composition:	0.0 % to 23.0 %, mass	Viscosity:	data to exppolynomial (4, 6)
Density:	data to polynomial (4, 6)	Psat:	no information
Spec. Heat:	data to polynomial (4, 6)	Tfreeze:	data to exppolynomial (1, 6)

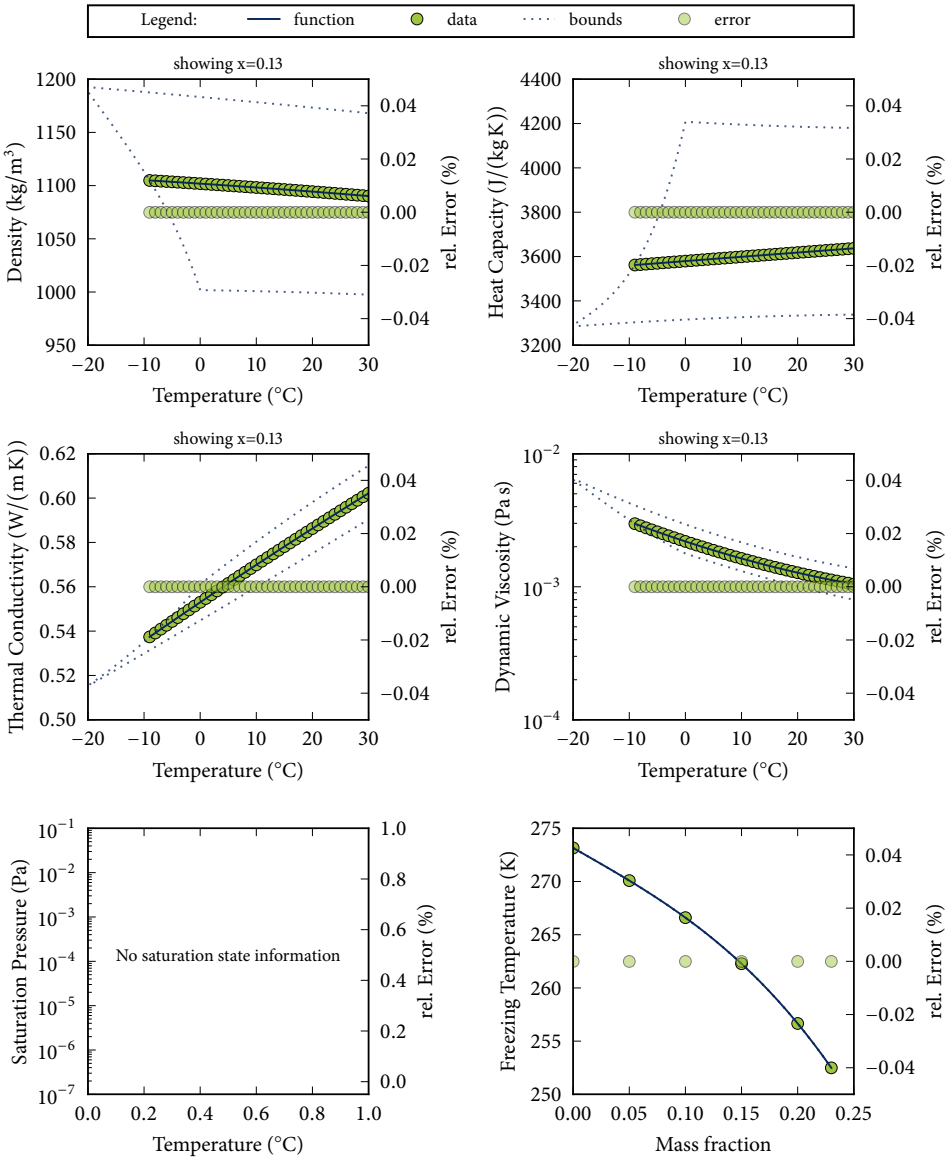

Fitted functions for MPG

Description: Propylene Glycol - aq
Source: Melinder [39]

Temperature:	-100.0 °C to 100.0 °C	Th. Cond.:	coefficients to polynomial (4, 6)
Composition:	0.0 % to 60.0 %, mass	Viscosity:	coefficients to exppolynomial (4, 6)
Density:	coefficients to polynomial (4, 6)	Psat:	no information
Spec. Heat:	coefficients to polynomial (4, 6)	Tfreeze:	coefficients to polynomial (1, 6)

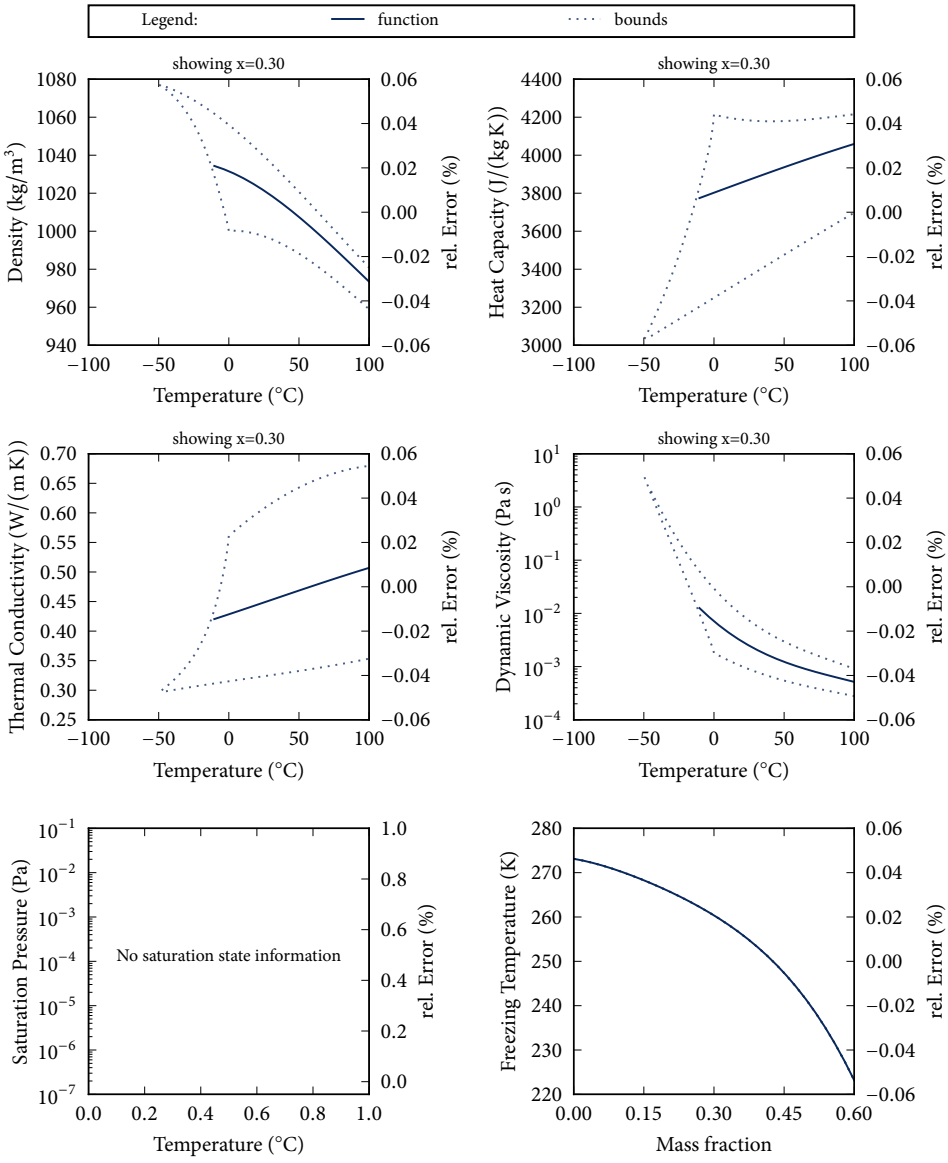

Fitted functions for MPG2

Description:	Melinder, Propylene Glycol		
Source:	Melinder [39]		
	Skovrup [49]		
Temperature:	-45.0 °C to 40.0 °C	Th. Cond.:	data to polynomial (4, 6)
Composition:	15.0 % to 57.0 %, mass	Viscosity:	data to exppolynomial (4, 6)
Density:	data to polynomial (4, 6)	Psat:	no information
Spec. Heat:	data to polynomial (4, 6)	Tfreeze:	data to exppolynomial (1, 6)

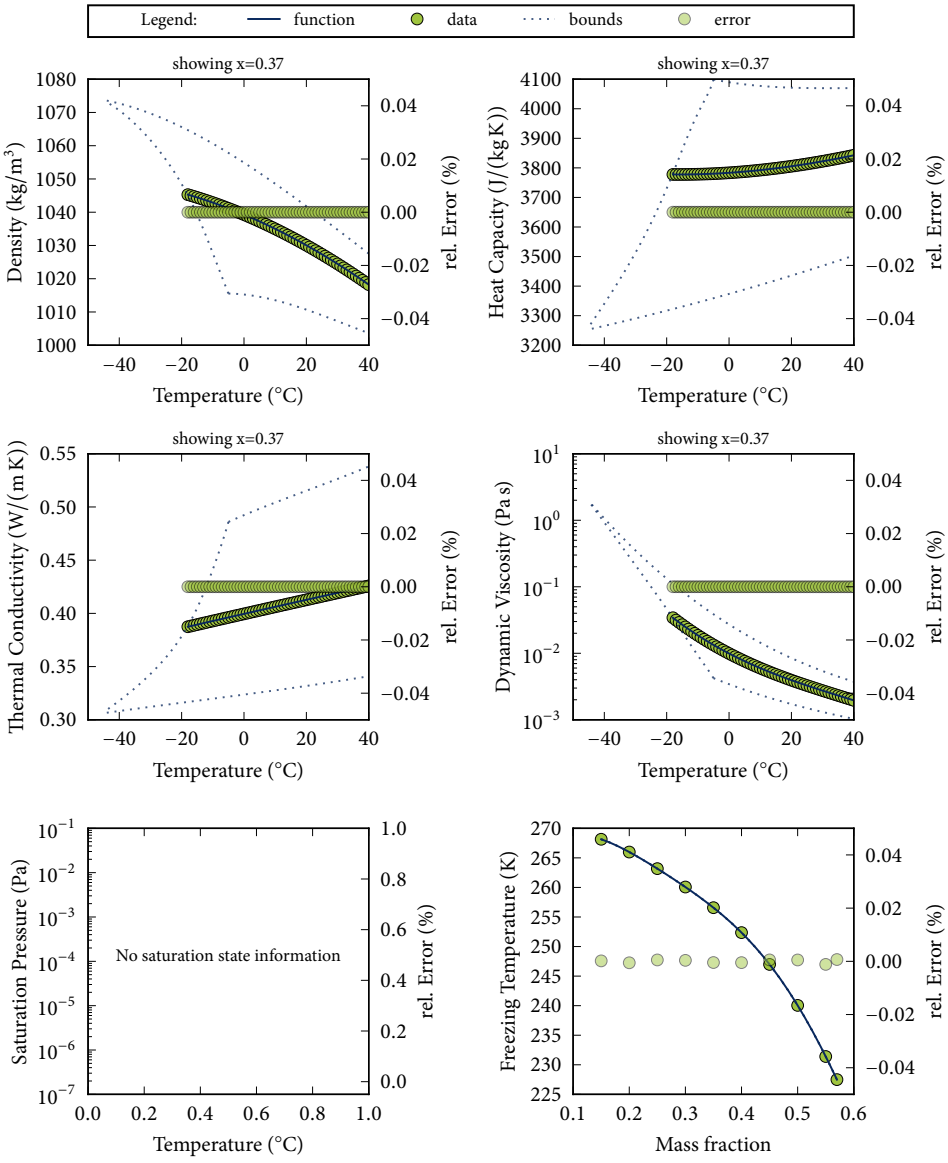

Fitted functions for VCA

Description:	VDI, Calcium Cloride		
Source:	Preisegger et al. [43]		
	Skovrup [49]		
Temperature:	-55.0 °C to 20.0 °C	Th. Cond.:	data to polynomial (4, 5)
Composition:	14.7 % to 29.9 %, mass	Viscosity:	data to exppolynomial (4, 5)
Density:	data to polynomial (4, 5)	Psat:	no information
Spec. Heat:	data to polynomial (4, 5)	Tfreeze:	data to exppolynomial (1, 5)

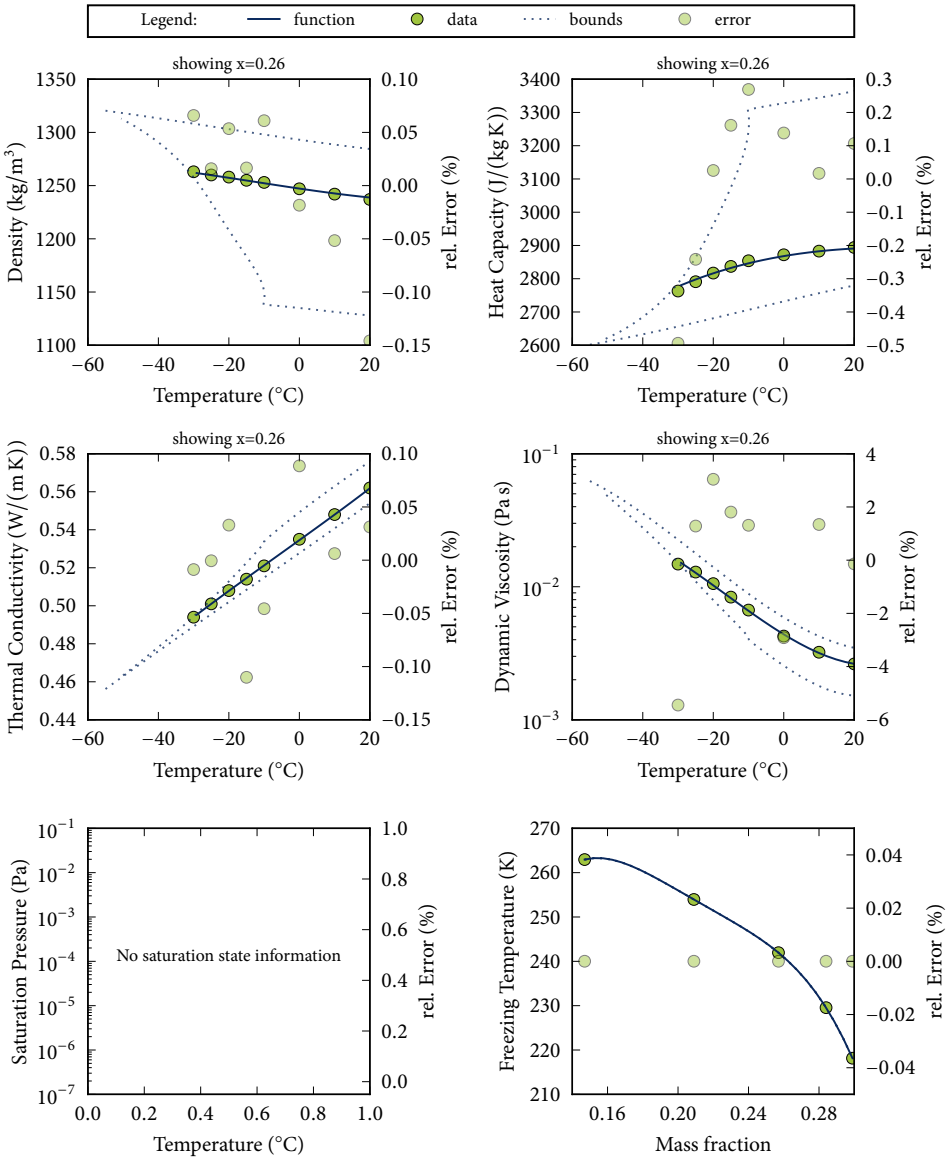

Fitted functions for VKC

Description:	VDI, Potassium Carbonate		
Source:	Preisegger et al. [43]		
	Skovrup [49]		
Temperature:	-35.0 °C to 20.0 °C	Th. Cond.:	data to polynomial (4, 6)
Composition:	12.8 % to 38.9 %, mass	Viscosity:	data to exppolynomial (4, 6)
Density:	data to polynomial (4, 6)	Psat:	no information
Spec. Heat:	data to polynomial (4, 6)	Tfreeze:	data to exppolynomial (1, 6)

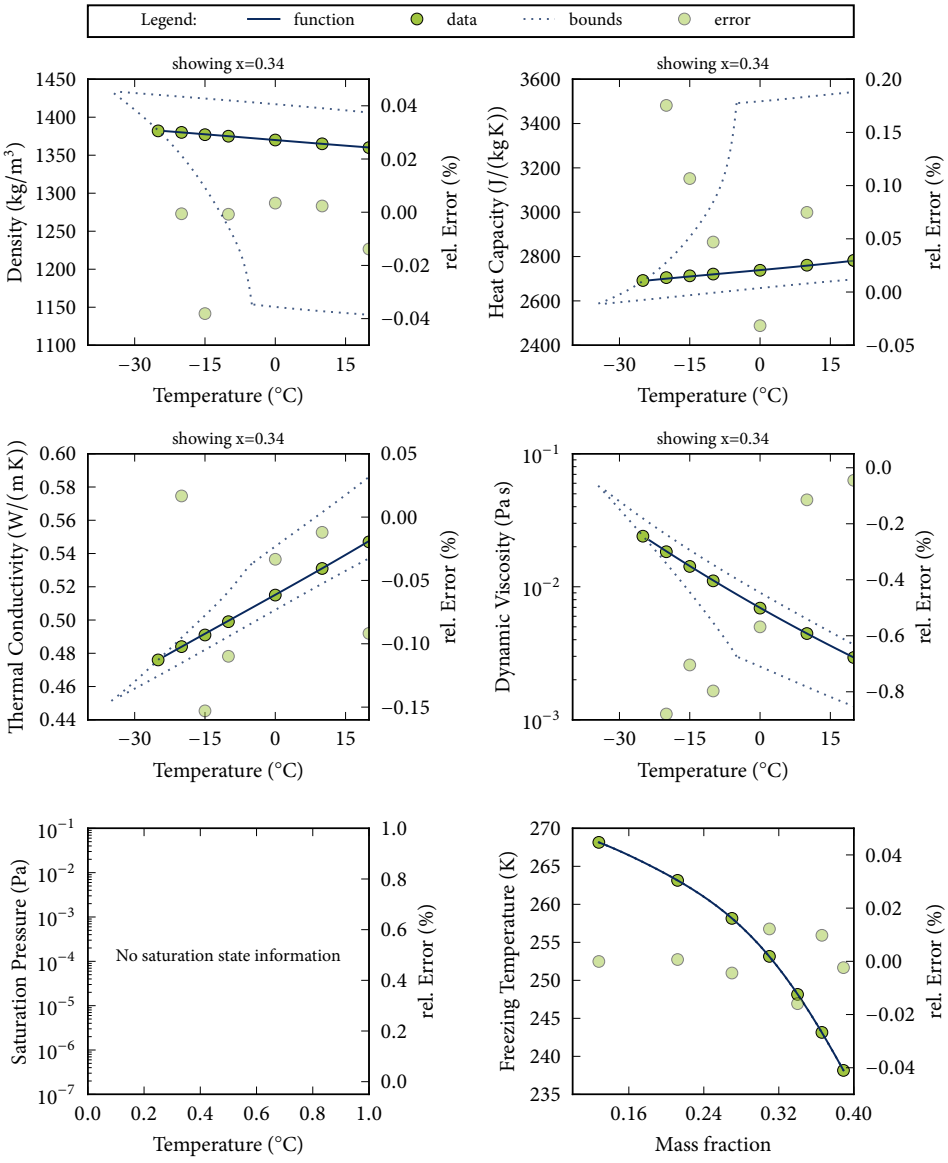

Fitted functions for VMA

Description:	VDI, Methanol		
Source:	Preisegger et al. [43]		
	Skovrup [49]		
Temperature:	-80.0 °C to 0.0 °C	Th. Cond.:	data to polynomial (4, 6)
Composition:	10.0 % to 90.0 %, mass	Viscosity:	data to exppolynomial (4, 6)
Density:	data to polynomial (4, 6)	Psat:	no information
Spec. Heat:	data to polynomial (4, 6)	Tfreeze:	data to exppolynomial (1, 6)

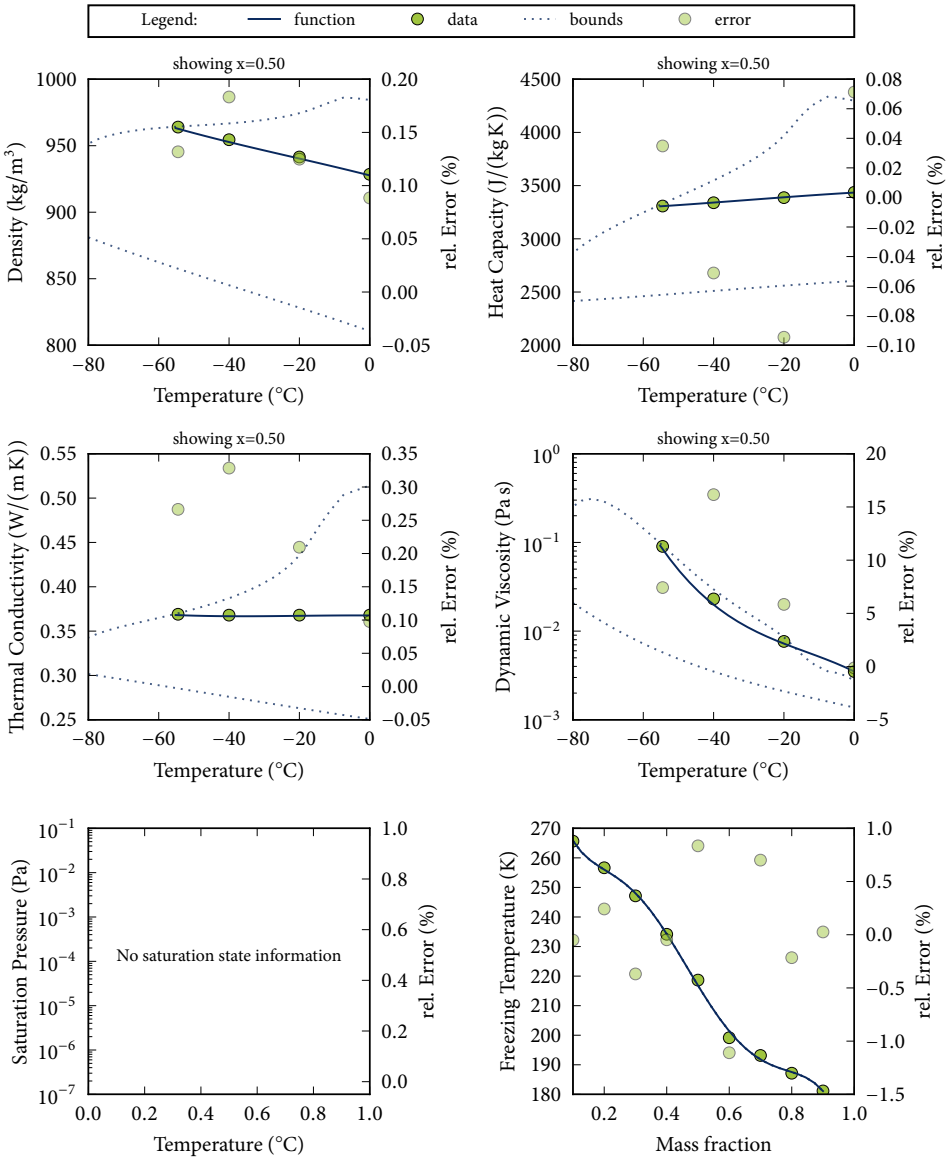

Fitted functions for VMG

Description:	VDI, Magnesium Chloride		
Source:	Preisegger et al. [43]		
	Skovrup [49]		
Temperature:	-33.0 °C to 20.0 °C	Th. Cond.:	data to polynomial (4, 5)
Composition:	7.2 % to 20.6 %, mass	Viscosity:	data to exppolynomial (4, 5)
Density:	data to polynomial (4, 5)	Psat:	no information
Spec. Heat:	data to polynomial (4, 5)	Tfreeze:	data to exppolynomial (1, 5)

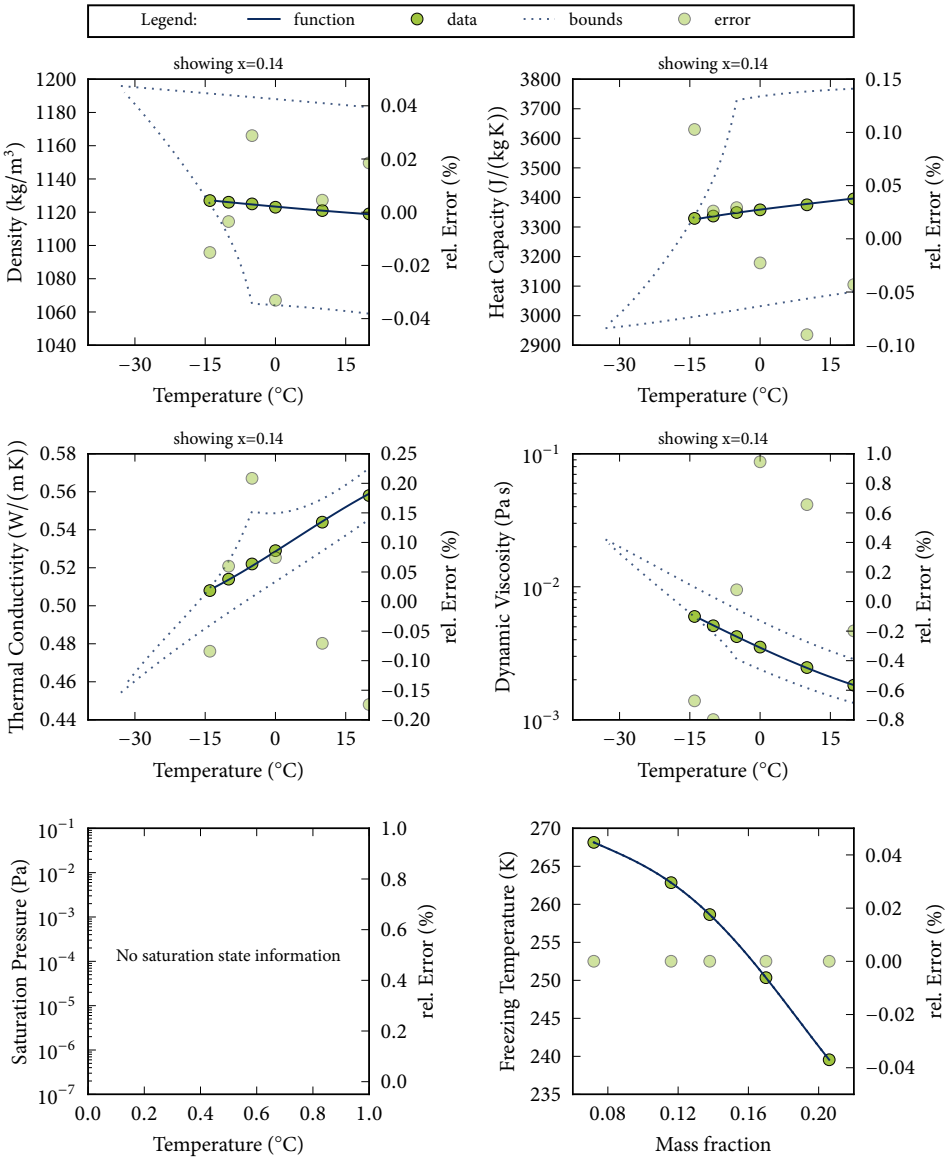

Fitted functions for VNA

Description:	VDI, Sodium Chloride		
Source:	Preisegger et al. [43]		
	Skovrup [49]		
Temperature:	-21.0 °C to 20.0 °C	Th. Cond.:	data to polynomial (4, 6)
Composition:	7.0 % to 23.1 %, mass	Viscosity:	data to exppolynomial (4, 6)
Density:	data to polynomial (4, 6)	Psat:	no information
Spec. Heat:	data to polynomial (4, 6)	Tfreeze:	data to exppolynomial (1, 6)

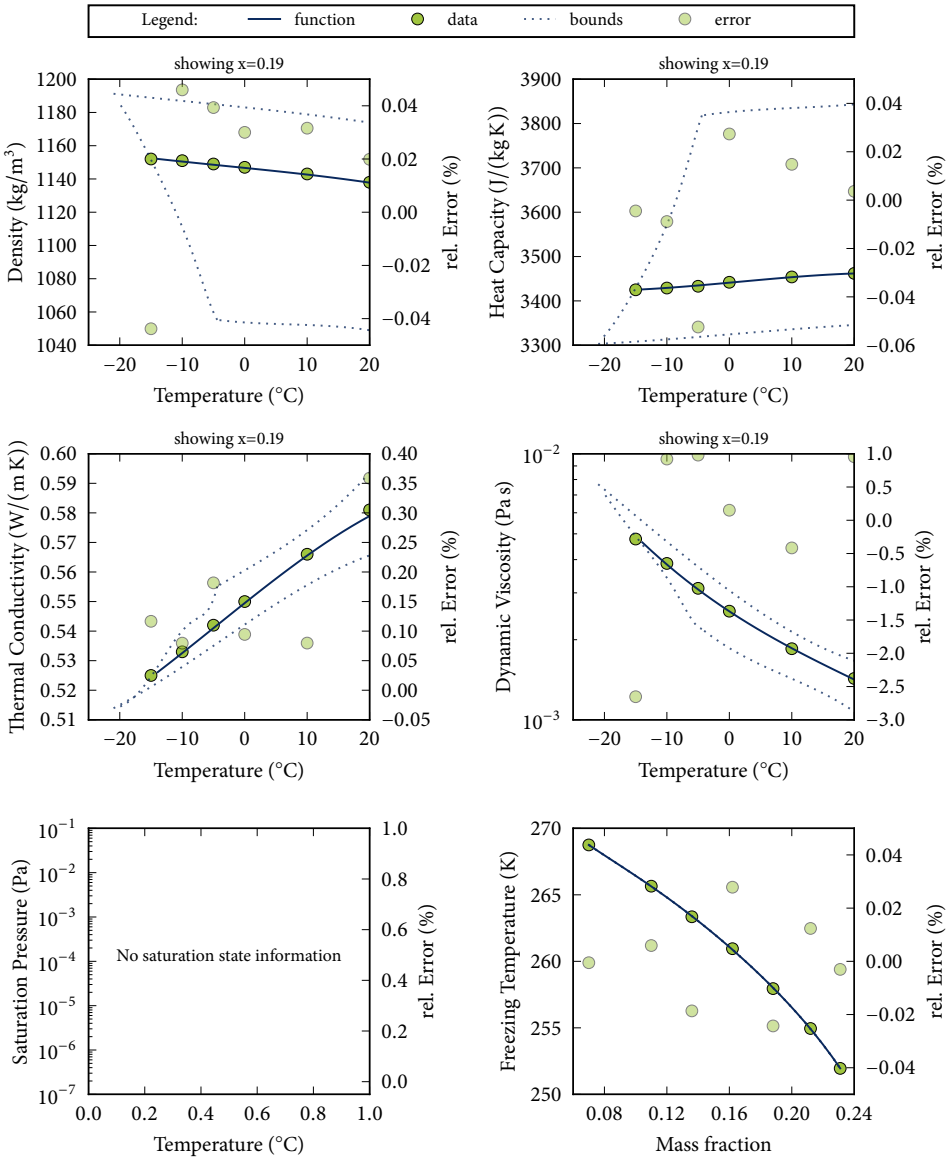

C.4 Volume-based Fluids

Name	Description	Reference	T_{min} (°C)	T_{max} (°C)	T_{base} (K)	x_{min}	x_{max}
AEG, p. 311	ASHRAE, Ethylene Glycol	[2, 49]	−35.00	100.00	305.65	0.10	0.60
AKF, p. 312	Antifrogen KF, Potassium Formate	[49, 54]	−40.00	50.00	278.15	0.40	1.00
AL, p. 313	Antifrogen L, Propylene Glycol	[49, 54]	−40.00	80.00	293.15	0.10	0.60
AN, p. 314	Antifrogen N, Ethylene Glycol	[49, 54]	−40.00	80.00	293.15	0.10	0.60
APG, p. 315	ASHRAE, Propylene Glycol	[2, 49]	−35.00	100.00	305.65	0.10	0.60
GKN, p. 316	Glykosol N, Ethylene Glycol	[49, 57]	−53.00	100.00	296.65	0.10	0.60
PK2, p. 317	Pekasol 2000, K acetate/formate	[49, 57]	−62.00	100.00	292.15	0.30	1.00
PKL, p. 318	Pekasol L, Propylene Glycol	[49, 57]	−49.00	100.00	298.65	0.10	0.60
ZAC, p. 319	Zitrec AC, Corrosion Inhibitor	[49, 64]	0.00	100.00	323.15	0.06	0.50
ZFC, p. 320	Zitrec FC, Propylene Glycol	[49, 64]	−40.00	100.00	303.15	0.30	0.60
ZLC, p. 321	Zitrec LC, Propylene Glycol	[49, 64]	−50.00	100.00	298.15	0.30	0.70
ZM, p. 322	Zitrec M, Ethylene Glycol	[49, 64]	−50.00	120.00	308.15	0.00	1.00
ZMC, p. 323	Zitrec MC, Ethylene Glycol	[49, 64]	−50.00	110.00	303.15	0.30	0.70

Fitted functions for AEG

Description:	ASHRAE, Ethylene Glycol		
Source:	American Society of Heating, Refrigerating and Air-Conditioning Engineers [2] Skovrup [49]		
Temperature:	-35.0 °C to 100.0 °C	Th. Cond.:	data to polynomial (4, 6)
Composition:	10.0 % to 60.0 %, volume	Viscosity:	data to exppolynomial (4, 6)
Density:	data to polynomial (4, 6)	Psat:	no information
Spec. Heat:	data to polynomial (4, 6)	Tfreeze:	data to exppolynomial (1, 6)

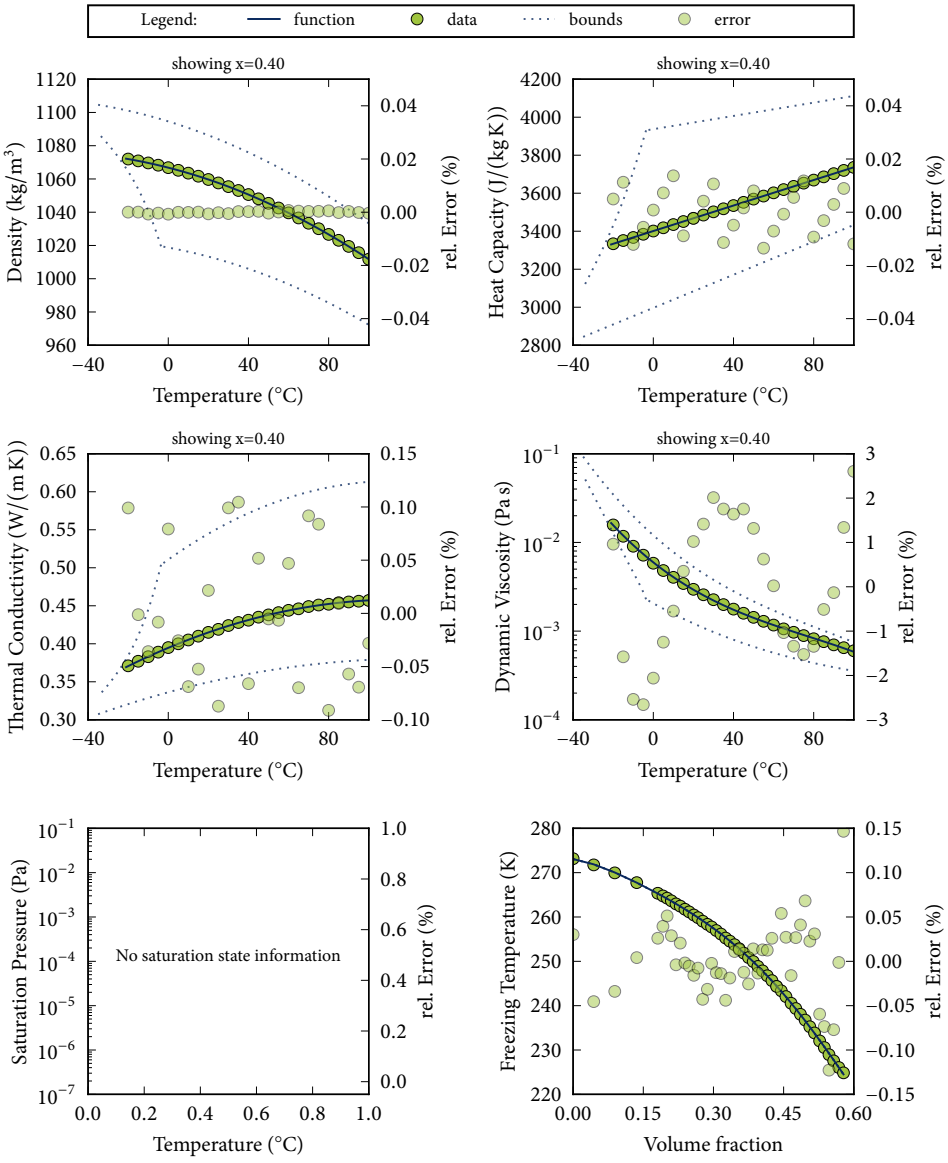

Fitted functions for AKF

Description:	Antifrogen KF, Potassium Formate		
Source:	*Technical Data Sheet* [54]		
	Skovrup [49]		
Temperature:	-40.0 °C to 50.0 °C	Th. Cond.:	data to polynomial (4, 6)
Composition:	40.0 % to 100.0 %, volume	Viscosity:	data to exppolynomial (4, 6)
Density:	data to polynomial (4, 6)	Psat:	no information
Spec. Heat:	data to polynomial (4, 6)	Tfreeze:	data to exppolynomial (1, 6)

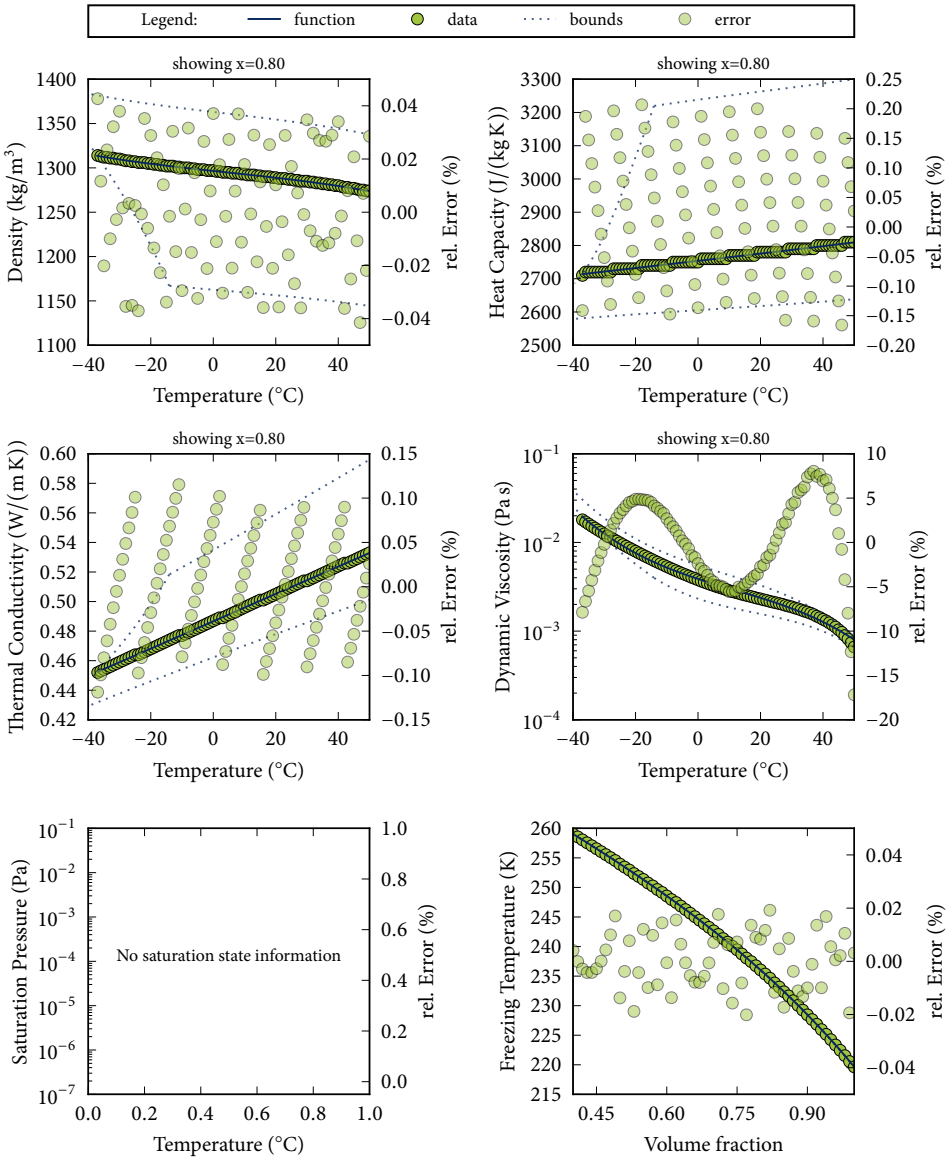

Fitted functions for AL

Description:	Antifrogen L, Propylene Glycol		
Source:	*Technical Data Sheet* [54]		
	Skovrup [49]		
Temperature:	-40.0 °C to 80.0 °C	Th. Cond.:	data to polynomial (4, 6)
Composition:	10.0 % to 60.0 %, volume	Viscosity:	data to exppolynomial (4, 6)
Density:	data to polynomial (4, 6)	Psat:	no information
Spec. Heat:	data to polynomial (4, 6)	Tfreeze:	data to exppolynomial (1, 6)

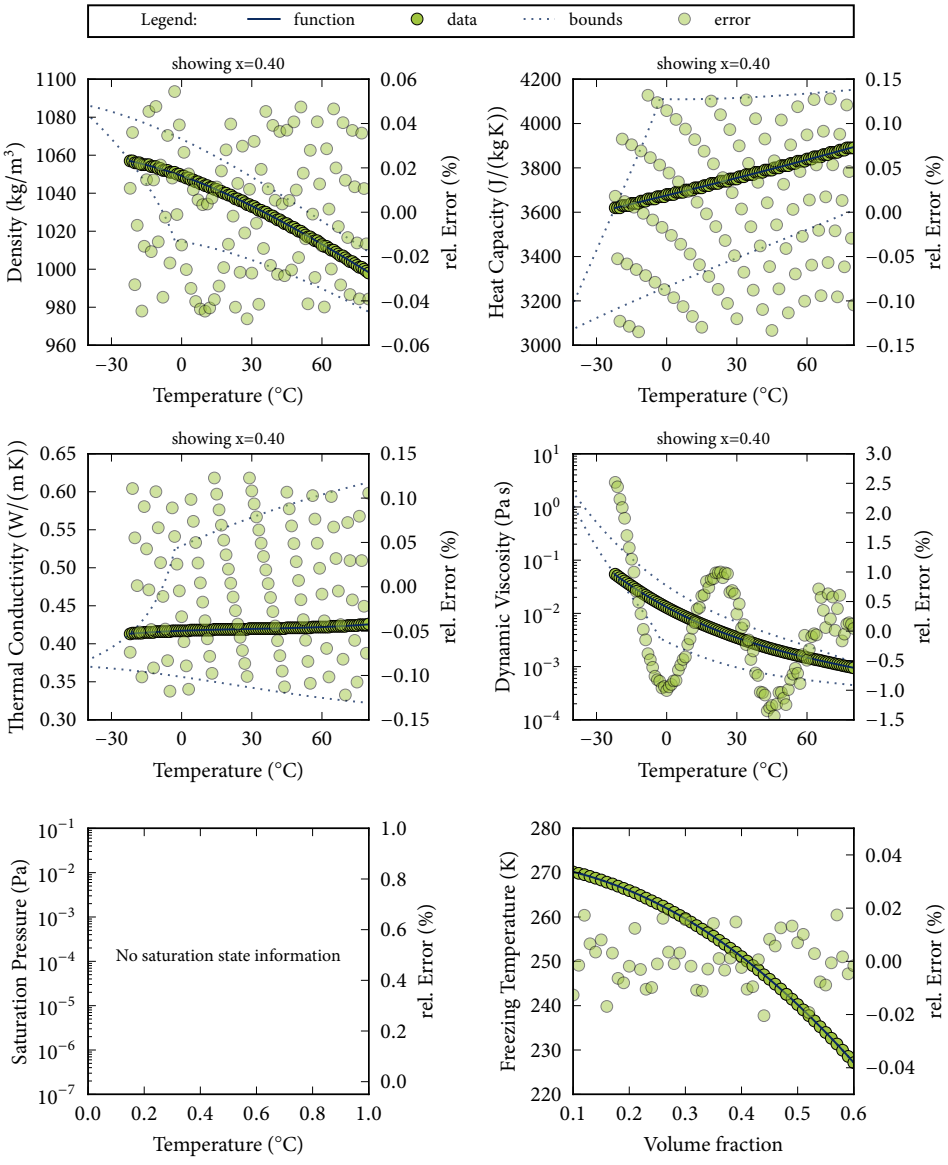

Fitted functions for AN

Description:	Antifrogen N, Ethylene Glycol		
Source:	*Technical Data Sheet* [54]		
	Skovrup [49]		
Temperature:	-40.0 °C to 80.0 °C	Th. Cond.:	data to polynomial (4, 6)
Composition:	10.0 % to 60.0 %, volume	Viscosity:	data to exppolynomial (4, 6)
Density:	data to polynomial (4, 6)	Psat:	no information
Spec. Heat:	data to polynomial (4, 6)	Tfreeze:	data to exppolynomial (1, 6)

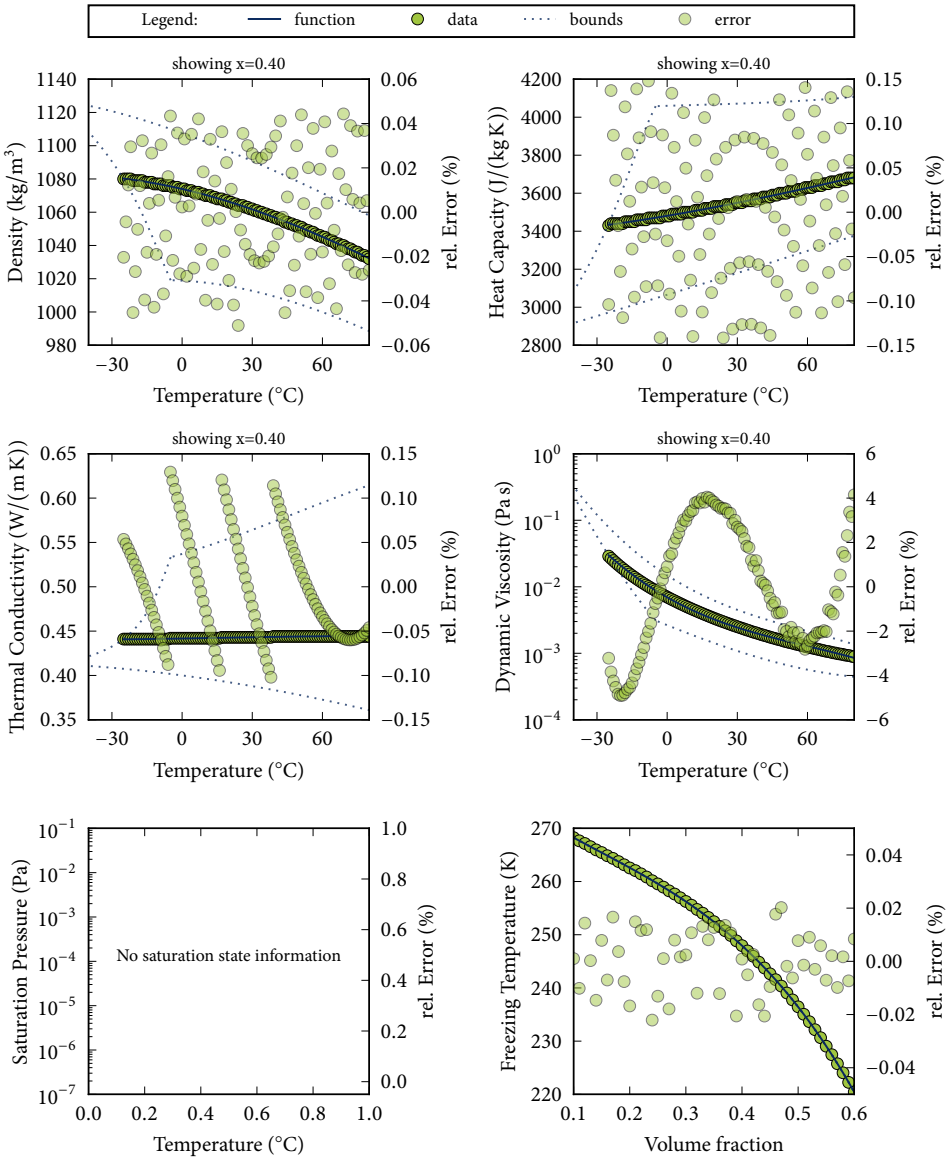

Fitted functions for APG

Description:	ASHRAE, Propylene Glycol		
Source:	American Society of Heating, Refrigerating and Air-Conditioning Engineers [2] Skovrup [49]		
Temperature:	-35.0 °C to 100.0 °C	Th. Cond.:	data to polynomial (4, 6)
Composition:	10.0 % to 60.0 %, volume	Viscosity:	data to exppolynomial (4, 6)
Density:	data to polynomial (4, 6)	Psat:	no information
Spec. Heat:	data to polynomial (4, 6)	Tfreeze:	data to exppolynomial (1, 6)

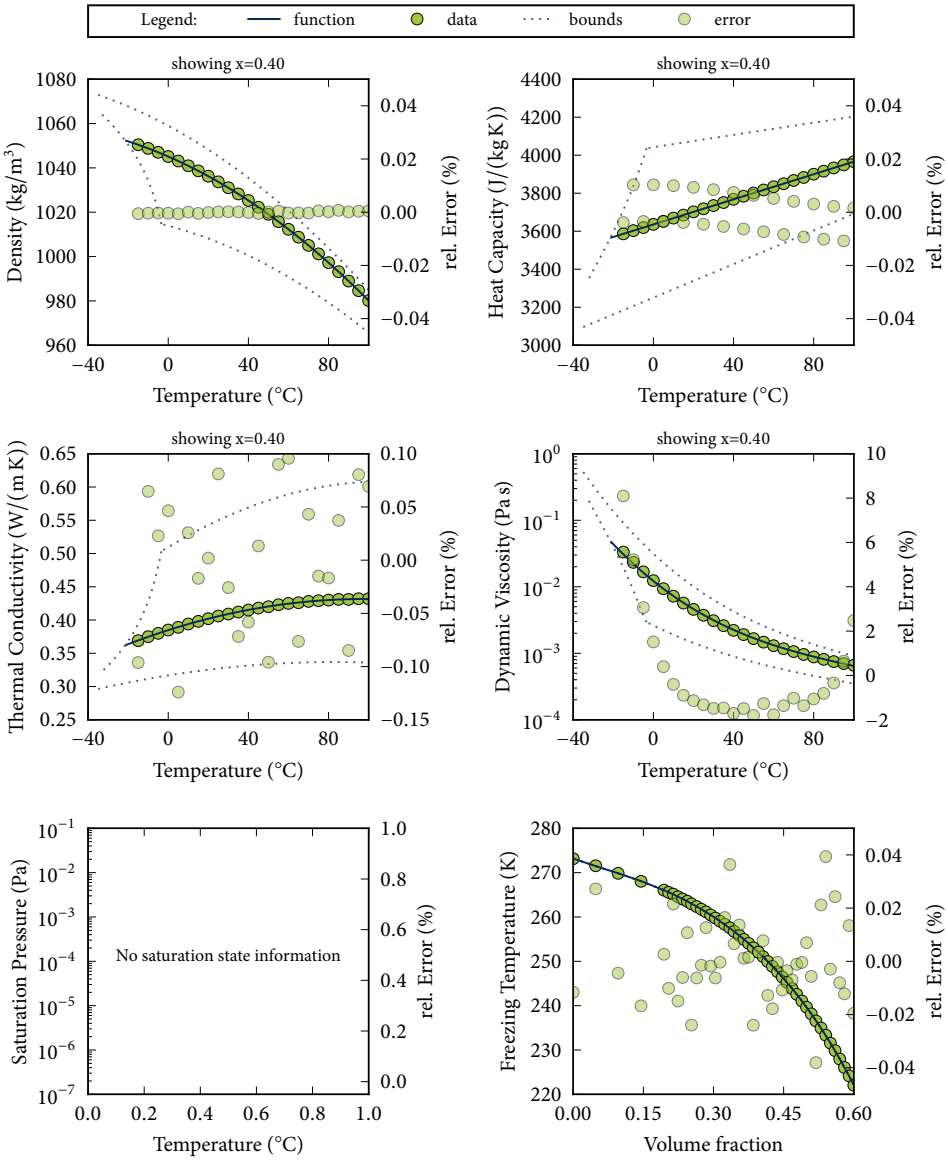

Fitted functions for GKN

Description:	Glykosol N, Ethylene Glycol		
Source:	*Technical Data Sheet* [57]		
	Skovrup [49]		
Temperature:	-53.0 °C to 100.0 °C	Th. Cond.:	data to polynomial (4, 6)
Composition:	10.0 % to 60.0 %, volume	Viscosity:	data to exppolynomial (4, 6)
Density:	data to polynomial (4, 6)	Psat:	no information
Spec. Heat:	data to polynomial (4, 6)	Tfreeze:	data to exppolynomial (1, 6)

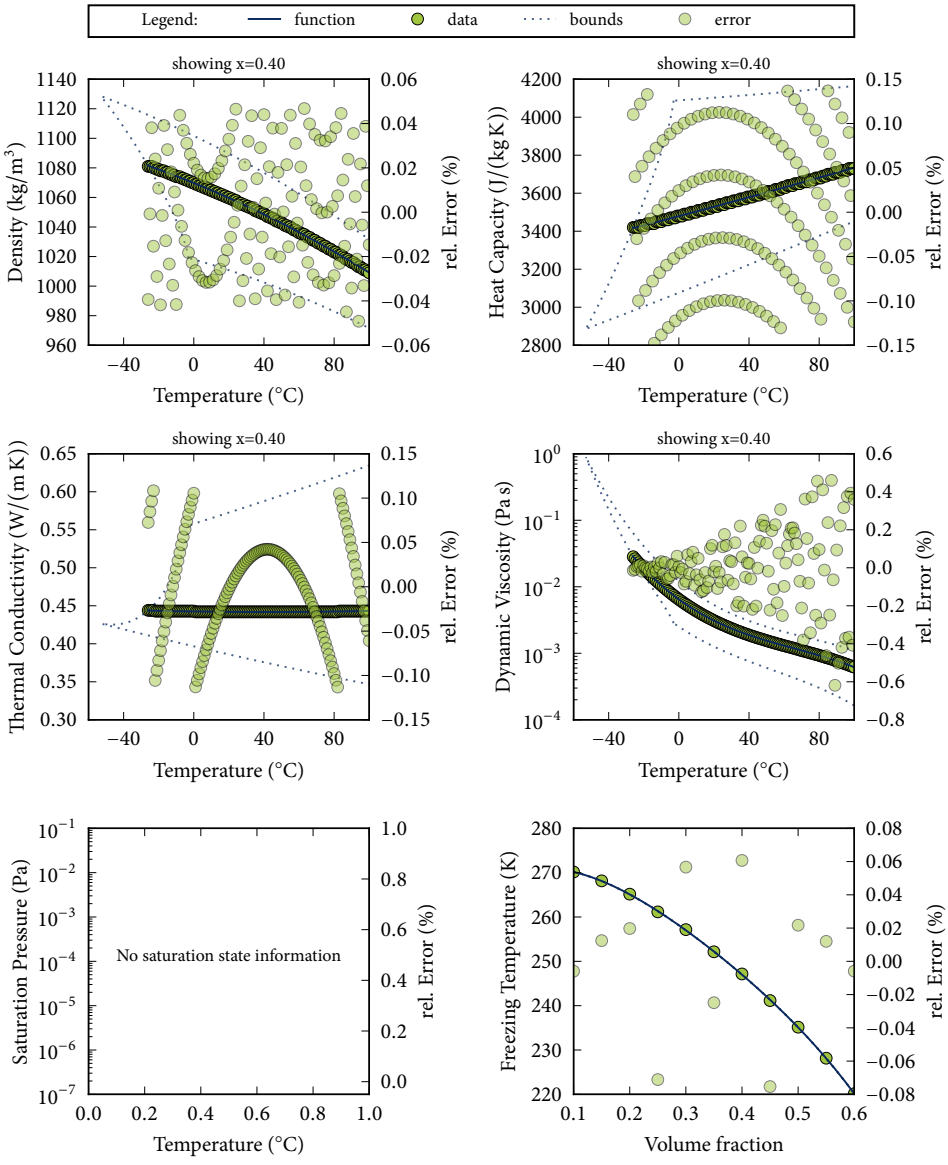

Fitted functions for PK2

Description:	Pekasol 2000, K acetate/formate		
Source:	*Technical Data Sheet* [57]		
	Skovrup [49]		
Temperature:	-62.0 °C to 100.0 °C	Th. Cond.:	data to polynomial (4, 6)
Composition:	30.0 % to 100.0 %, volume	Viscosity:	data to exppolynomial (4, 6)
Density:	data to polynomial (4, 6)	Psat:	no information
Spec. Heat:	data to polynomial (4, 6)	Tfreeze:	data to exppolynomial (1, 6)

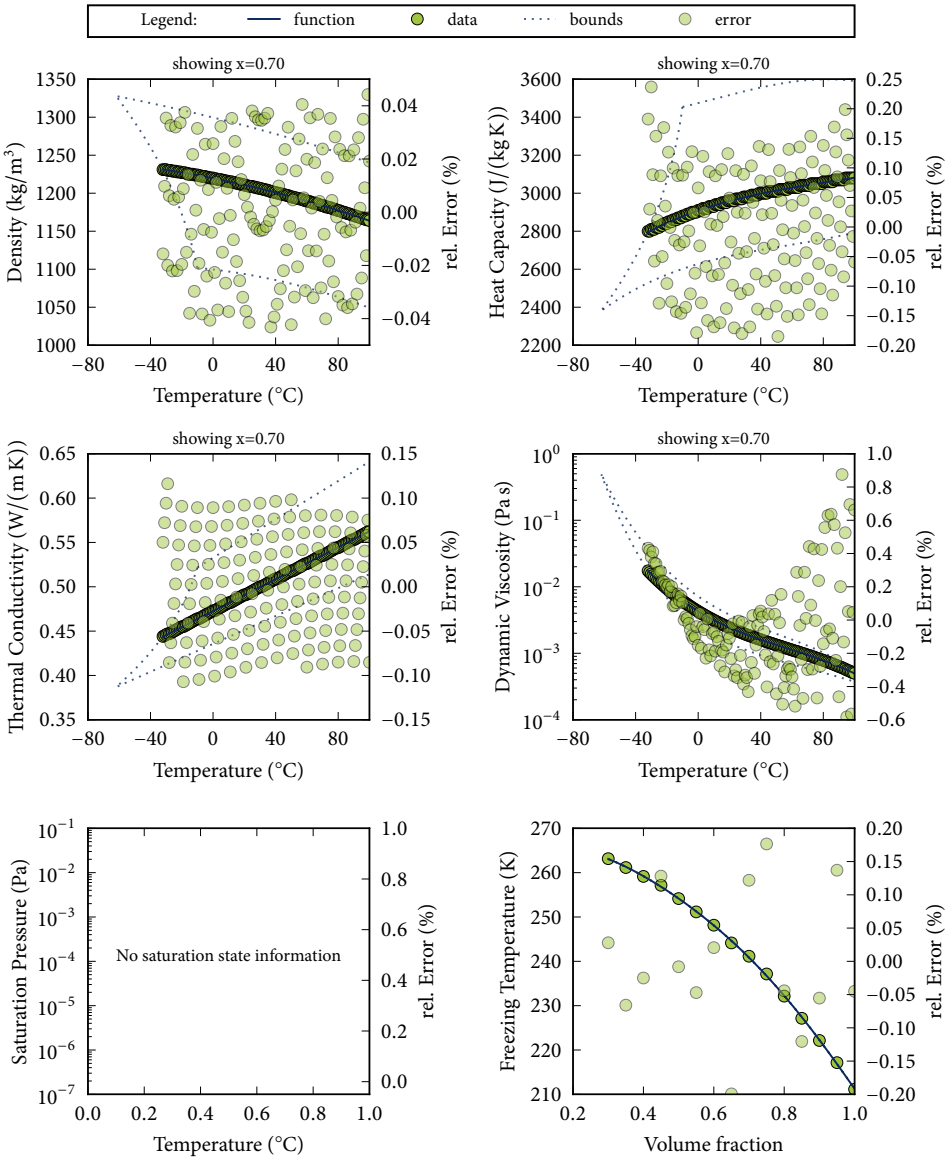

Fitted functions for PKL

Description:	Pekasol L, Propylene Glycol		
Source:	*Technical Data Sheet* [57]		
	Skovrup [49]		
Temperature:	-49.0 °C to 100.0 °C	Th. Cond.:	data to polynomial (4, 6)
Composition:	10.0 % to 60.0 %, volume	Viscosity:	data to exppolynomial (4, 6)
Density:	data to polynomial (4, 6)	Psat:	no information
Spec. Heat:	data to polynomial (4, 6)	Tfreeze:	data to exppolynomial (1, 6)

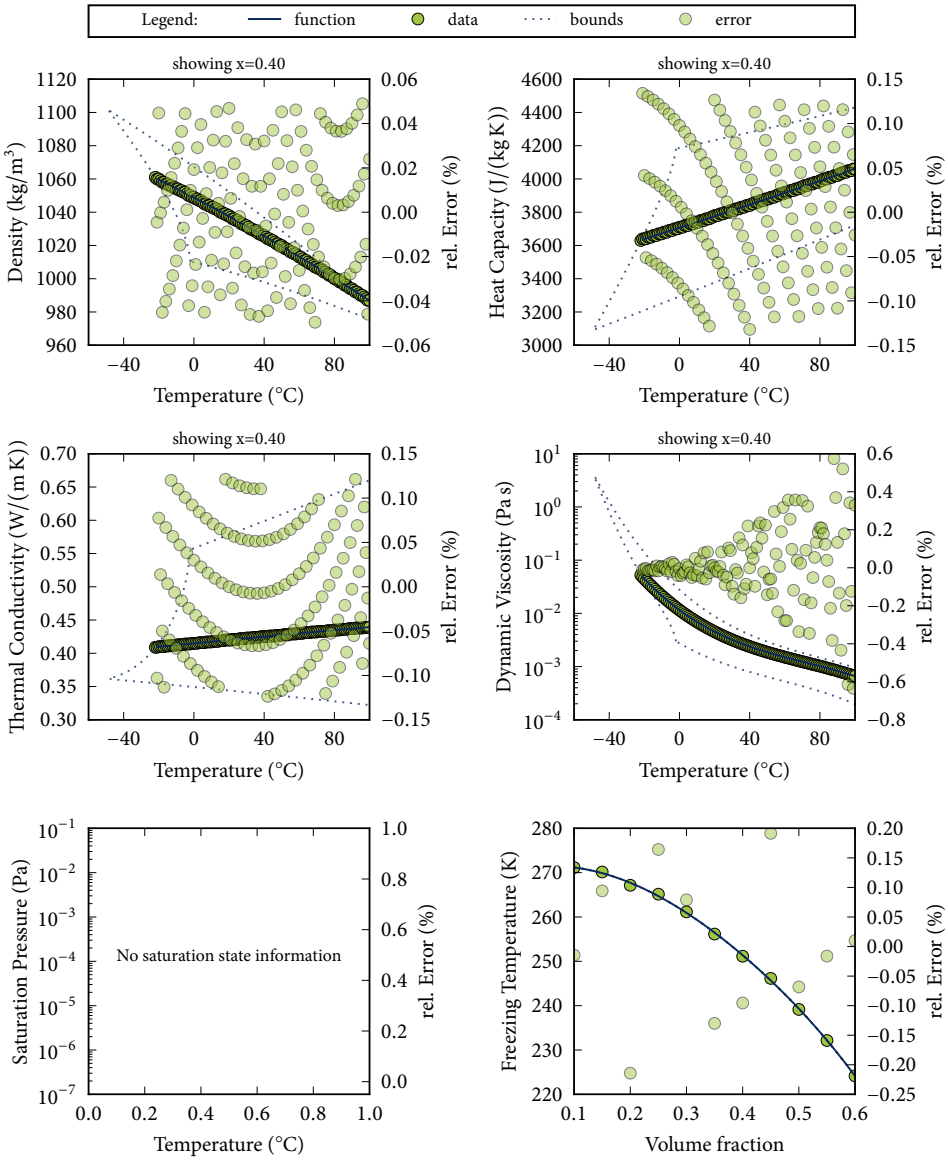

Fitted functions for ZAC

Description:	Zitrec AC, Corrosion Inhibitor		
Source:	*Technical Information* [64]		
	Skovrup [49]		
Temperature:	0.0 °C to 100.0 °C	Th. Cond.:	data to polynomial (4, 6)
Composition:	6.0 % to 50.0 %, volume	Viscosity:	data to exppolynomial (4, 6)
Density:	data to polynomial (4, 6)	Psat:	no information
Spec. Heat:	data to polynomial (4, 6)	Tfreeze:	data to exppolynomial (1, 6)

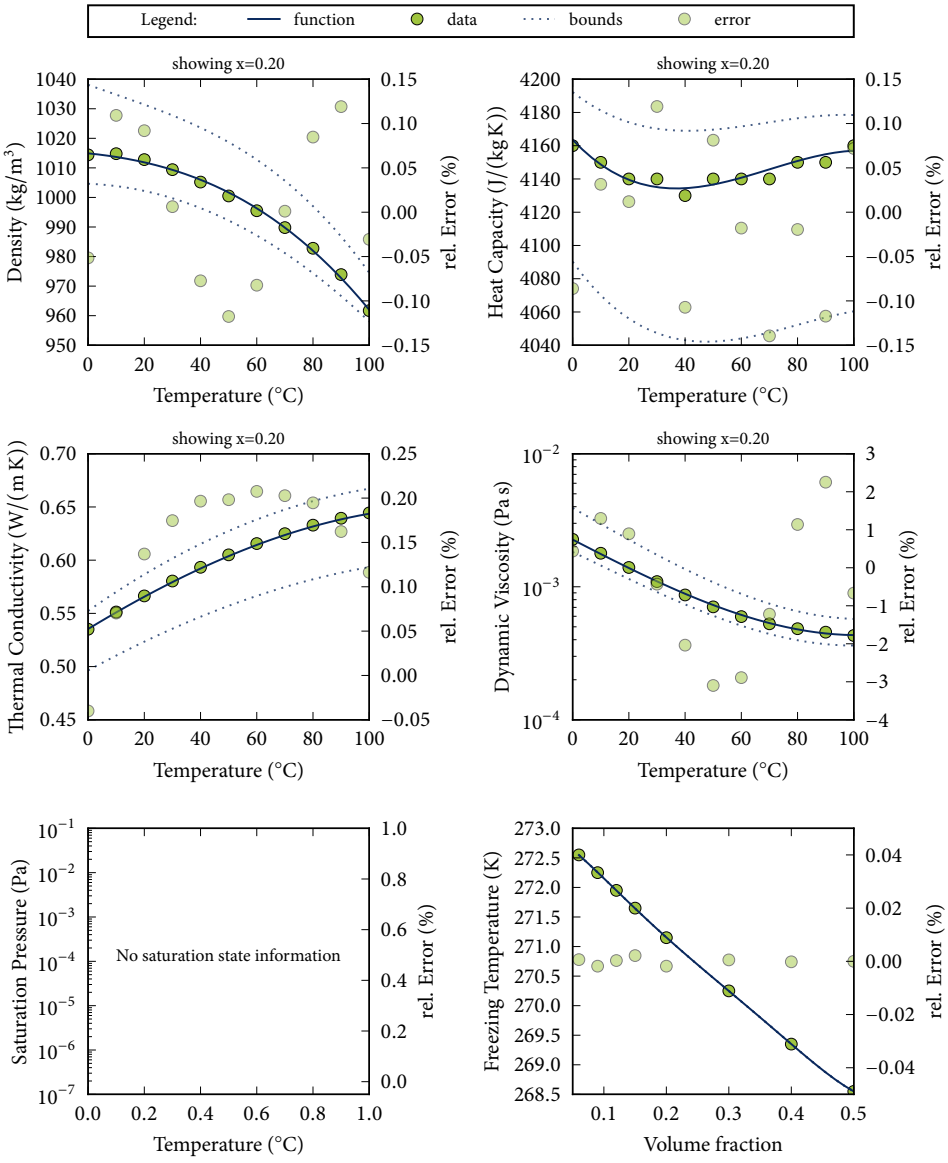

Fitted functions for ZFC

Description:	Zitrec FC, Propylene Glycol		
Source:	*Technical Information* [64]		
	Skovrup [49]		
Temperature:	-40.0 °C to 100.0 °C	Th. Cond.:	data to polynomial (4, 4)
Composition:	30.0 % to 60.0 %, volume	Viscosity:	data to exppolynomial (4, 4)
Density:	data to polynomial (4, 4)	Psat:	no information
Spec. Heat:	data to polynomial (4, 4)	Tfreeze:	data to exppolynomial (1, 4)

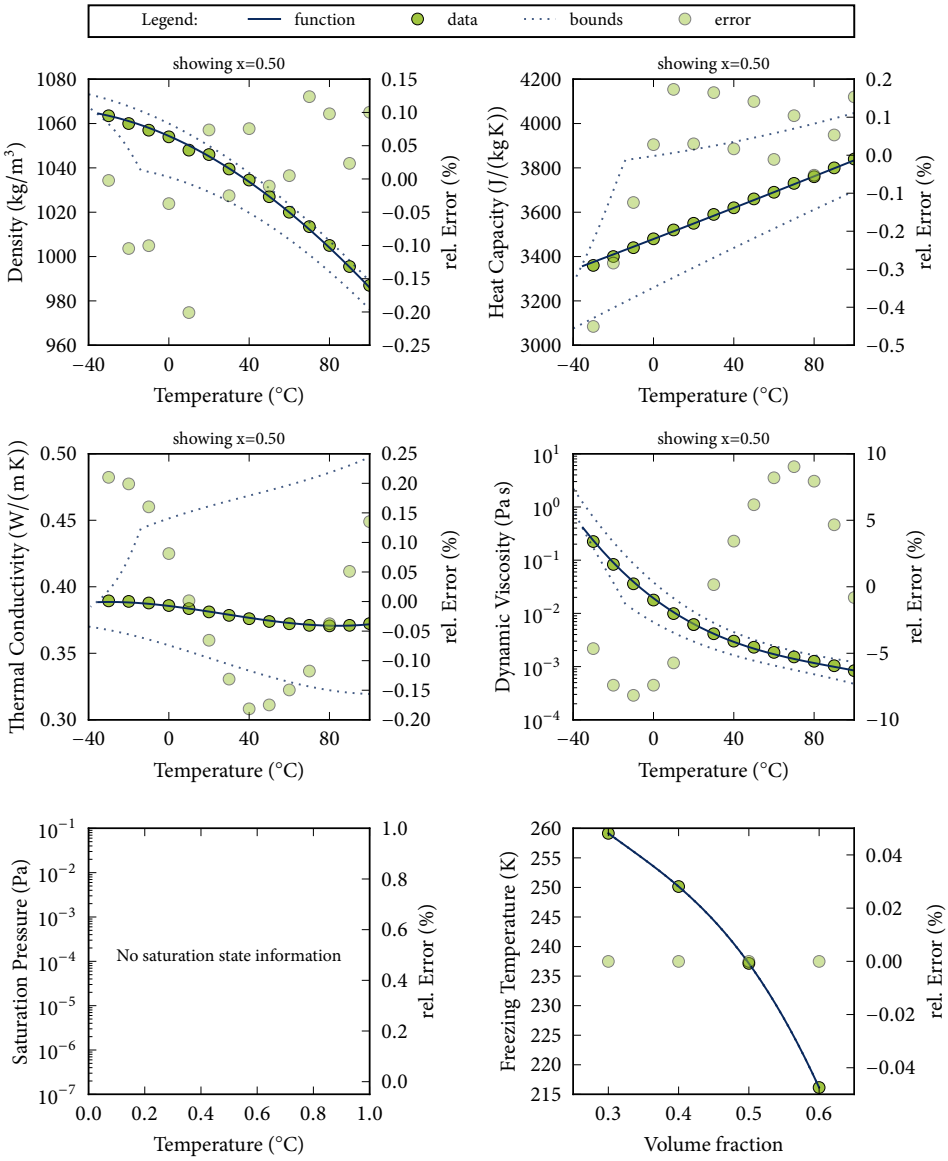

Fitted functions for ZLC

Description:	Zitrec LC, Propylene Glycol		
Source:	*Technical Information* [64]		
	Skovrup [49]		
Temperature:	-50.0 °C to 100.0 °C	Th. Cond.:	data to polynomial (4, 5)
Composition:	30.0 % to 70.0 %, volume	Viscosity:	data to exppolynomial (4, 5)
Density:	data to polynomial (4, 5)	Psat:	no information
Spec. Heat:	data to polynomial (4, 5)	Tfreeze:	data to exppolynomial (1, 5)

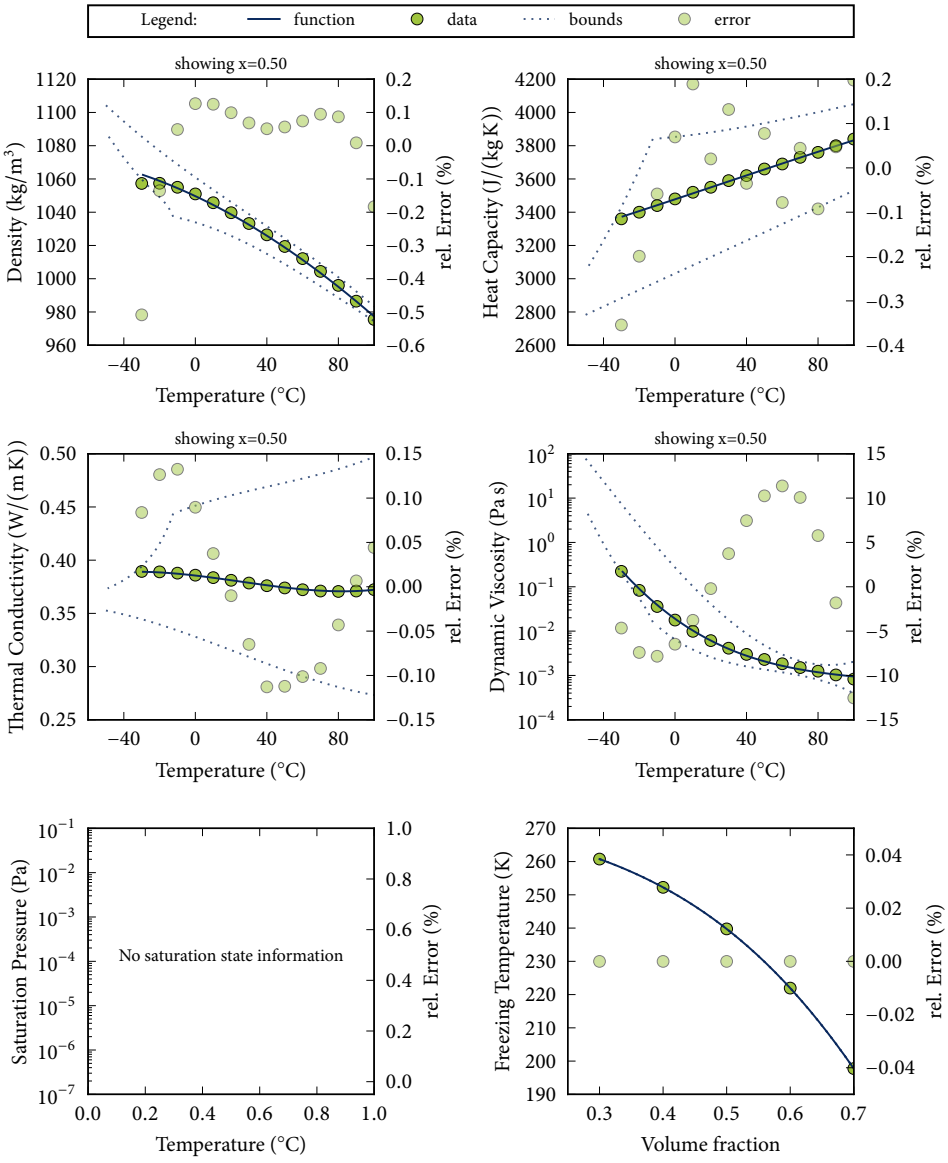

Fitted functions for ZM

Description:	Zitrec M, Ethylene Glycol		
Source:	*Technical Information* [64]		
	Skovrup [49]		
Temperature:	-50.0 °C to 120.0 °C	Th. Cond.:	data to polynomial (4, 6)
Composition:	0.0 % to 100.0 %, volume	Viscosity:	data to exppolynomial (4, 6)
Density:	data to polynomial (4, 6)	Psat:	no information
Spec. Heat:	data to polynomial (4, 6)	Tfreeze:	data to exppolynomial (1, 6)

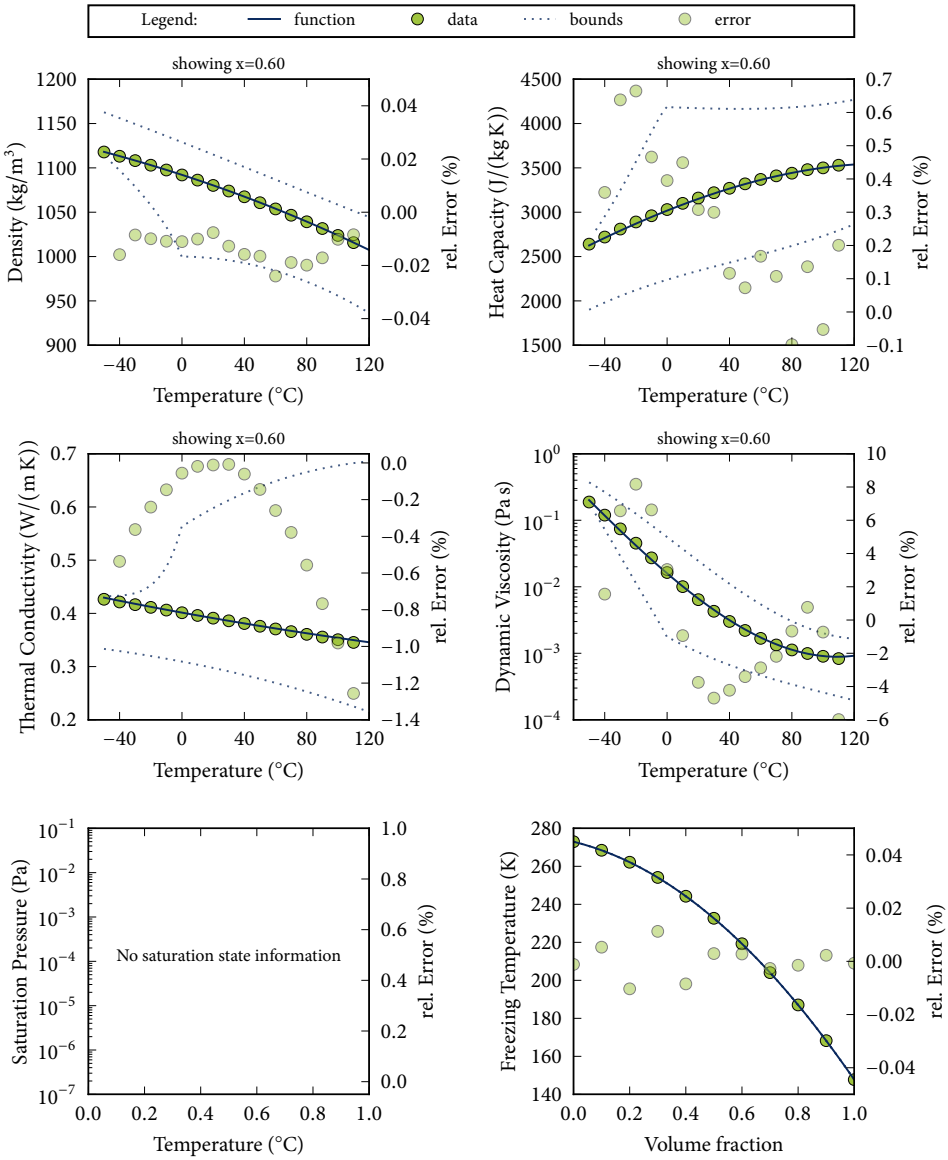

Fitted functions for ZMC

Description:	Zitrec MC, Ethylene Glycol		
Source:	*Technical Information* [64]		
	Skovrup [49]		
Temperature:	-50.0 °C to 110.0 °C	Th. Cond.:	data to polynomial (4, 5)
Composition:	30.0 % to 70.0 %, volume	Viscosity:	data to exppolynomial (4, 5)
Density:	data to polynomial (4, 5)	Psat:	no information
Spec. Heat:	data to polynomial (4, 5)	Tfreeze:	data to exppolynomial (1, 5)

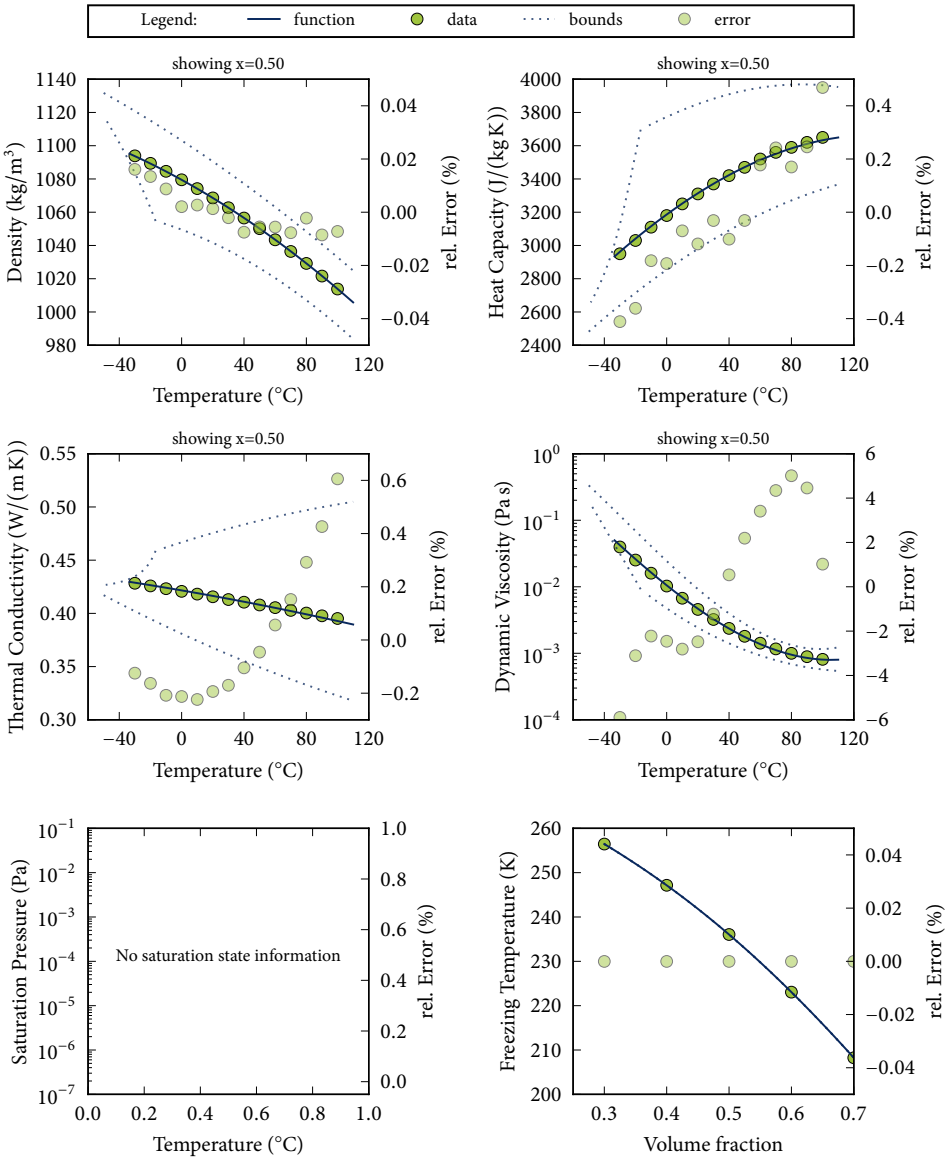

Appendix D

In-cylinder Heat Transfer Graphs

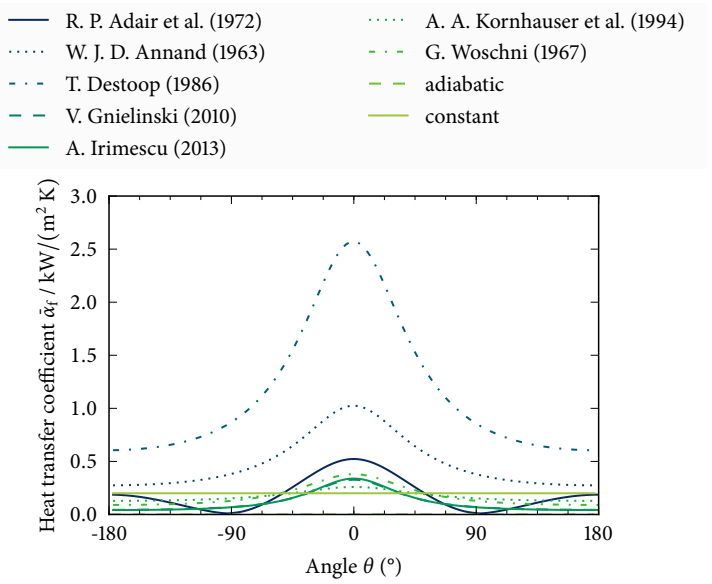

Figure D.1: Heat transfer coefficient for one revolution of an air-filled gas spring.

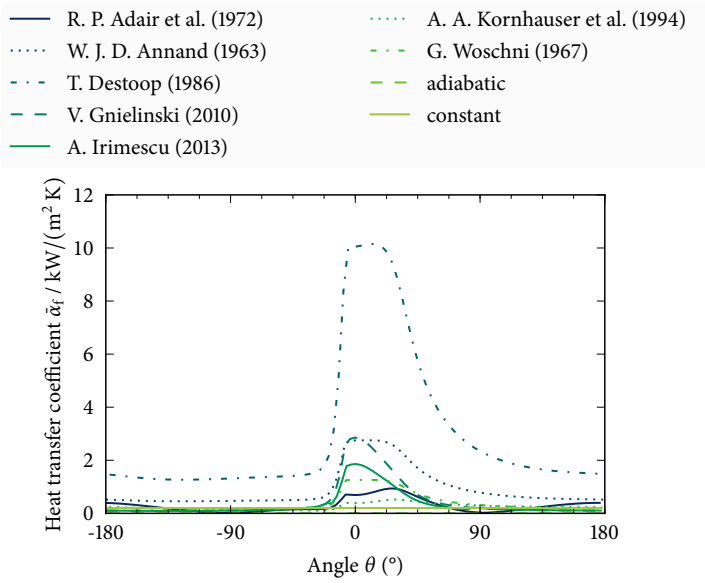

Figure D.2: Heat transfer coefficient for one revolution of an n-pentane expander.

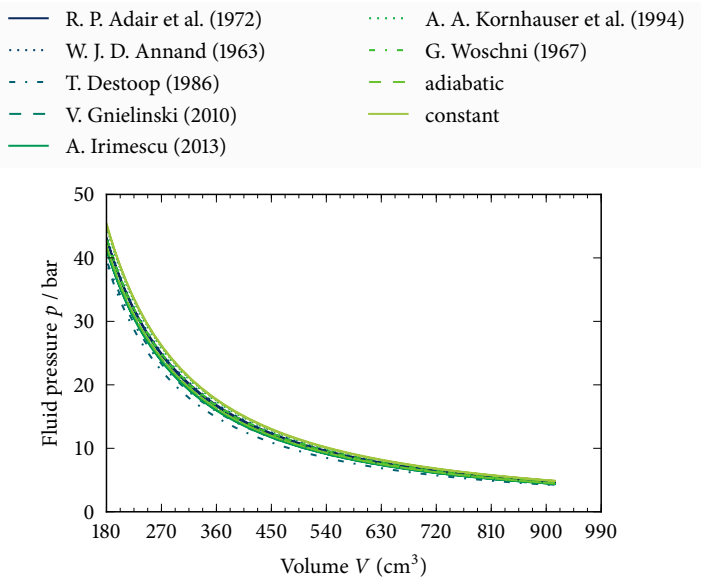

Figure D.3: Pressure over volume for one revolution of an air-filled gas spring.

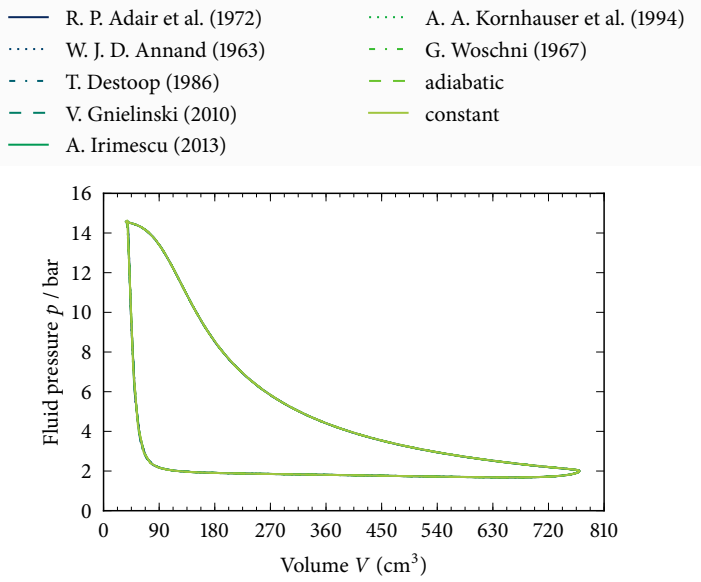

Figure D.4: Pressure over volume for one revolution of an n-pentane expander.

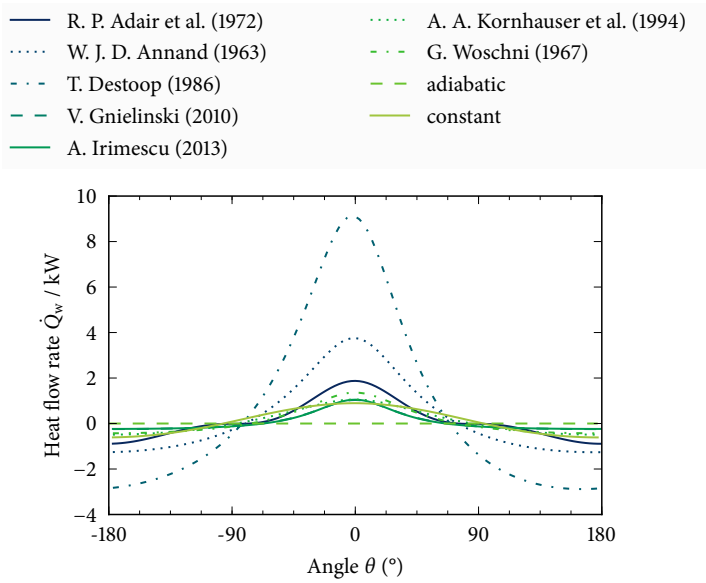

Figure D.5: Wall heat transfer during one revolution of an air-filled gas spring.

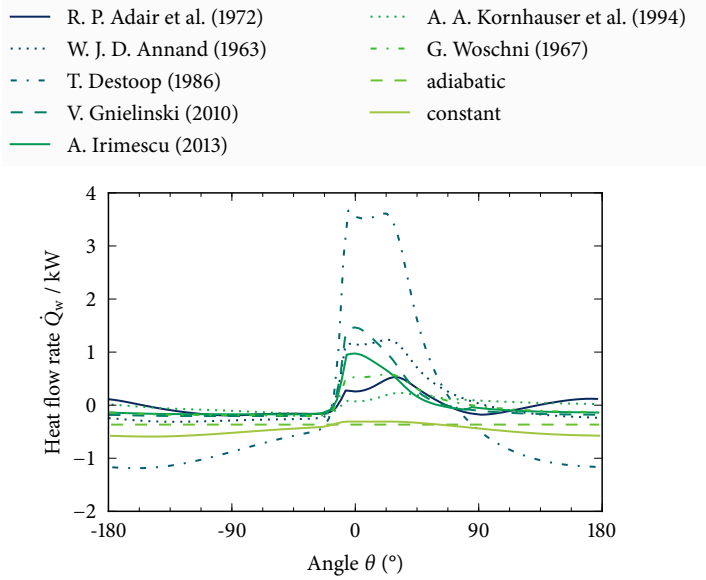

Figure D.6: Wall heat transfer during one revolution of an n-pentane expander.

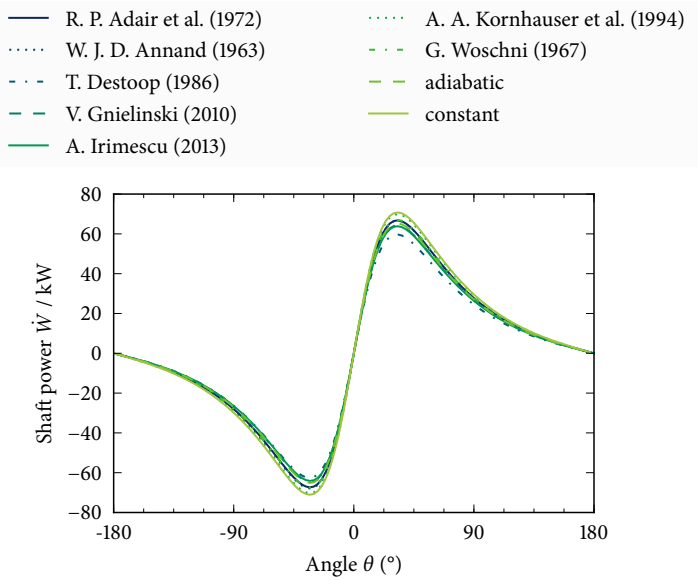

Figure D.7: Crankshaft power during one revolution of an air-filled gas spring.

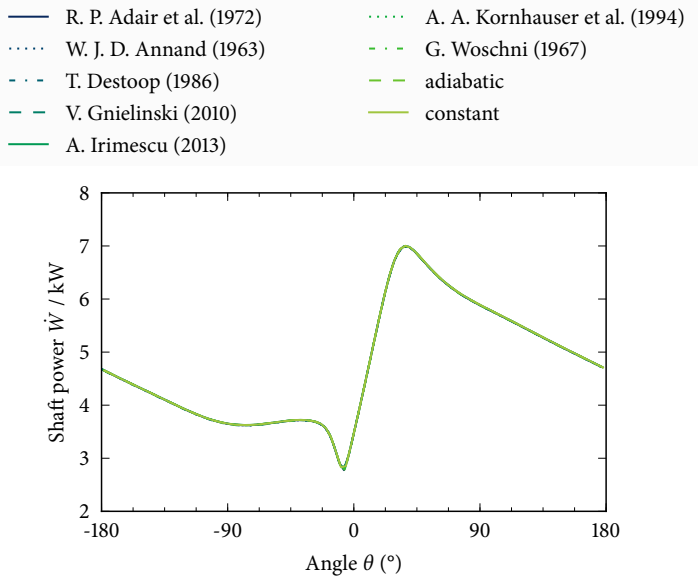

Figure D.8: Crankshaft power during one revolution of an n-pentane expander.

Appendix E

Heat Transfer Models

E.1 Implemented Correlations

Single-phase Operation

Muley

A special correlation for single-phase heat transfer in plate heat exchangers (PHEs) was provided by Muley and Manglik [40]. Looking at plate angles $30° \leq \phi \leq 60°$, they defined a polynomial-based correlation for Nusselt number (Nu)

$$\begin{aligned} \mathrm{Nu} = &\left(2.668 \times 10^{-1} - 6.967 \times 10^{-3}\phi + 7.244 \times 10^{-5}\phi^2\right) \\ &\cdot \left(2.078 \times 10^{1} - 5.094 \times 10^{1}\Phi + 4.116 \times 10^{1}\Phi^2 - 1.015 \times 10^{1}\Phi^3\right) \\ &\cdot \mathrm{Re}^{(0.728+0.0543\sin(\pi\phi/45°+3.7))}\ \mathrm{Pr}^{1/3} \left(\frac{\mu}{\mu_\mathrm{w}}\right)^{0.14}. \end{aligned} \tag{E.1}$$

Equation (E.1) is valid for a Reynolds number (Re) ≥ 1000 and for enlargement factors Φ between 1 and 1.5, which is expected to cover all possible plate heat exchanger configurations [40]. For lower Re in the range from 30 to 400, Palm and Claesson [41] recommended to use

$$\mathrm{Nu} = 0.44 \left(\frac{\phi}{30°}\right)^{0.38} \mathrm{Re}^{1/2}\ \mathrm{Pr}^{1/3} \left(\frac{\mu}{\mu_\mathrm{w}}\right)^{0.14}, \tag{E.2}$$

which also originates from Muley and Manglik [40]. Both equations assume that ϕ is given in degrees and not in radians. The final implementation used in this work employed the transition function from Equation (3.12) to combine the calculated Nusselt numbers for laminar and turbulent flow in the transition interval $400 < \mathrm{Re} < 1000$.

Martin

Following up on the analytical approach to flow distribution presented by Bassiouny and Martin [4, 5] and Wang [68, 69], also the heat transfer itself has been investigated theoretically by Martin [35], who compared the general pipe flow theory of Lévêque

[34] to the processes in PHEs. The resulting equations for the analogy of pressure drop and heat transfer cover the whole Chevron angle range from 0° to 90° and Martin [36] extended them to express mass transfer as well. His equations are among the most frequently used correlations for single-phase heat transfer and they were also recommend by Palm and Claesson [41]. Also in the updated formulation from Martin [37], the hydraulic diameter d_{hyd} was defined as

$$d_{\mathrm{hyd}} = 4\hat{a}/\Phi, \tag{E.3}$$

which then yielded the friction coefficient

$$\xi_{\mathrm{hx}} = \frac{2\,\Delta p\,d_{\mathrm{hyd}}}{\rho\,w^2\,l_{\mathrm{hx}}}. \tag{E.4}$$

In this correlation, the flow velocity w was determined from the volume flow $\dot{V}$ per channel N_{f} and the average cross section area of the gap yielding

$$w = \frac{\dot{V}}{N_{\mathrm{f}}}\,\frac{1}{2\hat{a}\,d_{\mathrm{hx}}}. \tag{E.5}$$

To close the system of equations, one has to provide a second set of equations involving the frictional pressure drop coefficient ξ_{hx}. Here, Martin [37] approached the problem from the two limiting cases and for laminar and turbulent flow. The first limiting case for $\phi = 0°$ was assumed to be similar to pipe flow. The corrugations were perpendicular to the flow directions effectively forming separated channels. Hence, Martin [37] recommended to use the equations by Gnielinski [20, 21] and Kast et al. [31]

$$\xi_{\mathrm{hx},0°} = \begin{cases} 64/\,\mathrm{Re} & \text{if } \mathrm{Re} < 2000, \text{laminar} \\ (1.8\log(\mathrm{Re}) - 1.5)^{-2} & \text{if } \mathrm{Re} \geq 2000, \text{turbulent.} \end{cases} \tag{E.6}$$

The first factor 64 refers to real pipes, but is also an acceptable approximation for PHEs as shown by Fischer and Martin [16], which also gave advice on the calculation of exact values for various other geometries.

For the second limiting case, $\phi = 90°$, the relative position of the plates has a large impact. In this work, the plates were assumed to be aligned with a phase difference of 90°, which means that the channel had a constant cross-sectional area. For this case, Martin [37] referred to Focke, Zachariades and Olivier [17] and recommended

$$\xi_{\mathrm{hx},90°} = 3.8 \begin{cases} 597/\,\mathrm{Re} + 3.85 & \text{if } \mathrm{Re} < 2000, \text{laminar} \\ 39/\,\mathrm{Re}^{0.289} & \text{if } \mathrm{Re} \geq 2000, \text{turbulent.} \end{cases} \tag{E.7}$$

The coefficients used in Equation (E.7) were only determined for corrugation lengths l_{co} that were four times larger than the corrugation amplitude $\hat{a}$, but the results shown by Martin [35] suggest that they can be used for other geometries as well.

The publications by Martin [35–37] do not mention the transition from laminar to turbulent flow. However, the graphs presented in the aforementioned publications suggest that the original work used a piecewise definition of the friction factors. In this work, the smooth function from Richter [44], see Equation (3.12), was used to provide a continuous transition in the range of Re = 2000 ± 100. This increased the numerical stability of the correlation in dynamic simulations. It also agrees well with the works of Claesson [9] and Palm and Claesson [41], who found that the change from laminar to turbulent flow had a limited impact on heat transfer and pressure drop in PHEs.

Based on these two limits, the actual flow pattern was described by a combined ξ_{hx} calculated from the corrugation inclination angle by

$$\frac{1}{\sqrt{\xi_{hx}}} = \frac{\cos\phi_{co}}{\sqrt{0.18\tan\phi_{co} + 0.36\sin\phi_{co} + \xi_{hx,0°}/\cos\phi_{co}}} + \frac{1-\cos\phi_{co}}{\sqrt{\xi_{hx,90°}}}. \tag{E.8}$$

Having obtained an expression for the friction factor, the Hagen number (Hg) could be rewritten to

$$\mathrm{Hg} = \frac{\rho\ \Delta p\ d_{hyd}^3}{\mu^2\ l_{hx}} = \xi_{hx}\ \mathrm{Re}^2/2. \tag{E.9}$$

The last equation from Martin [37] connects the Hagen number (Hg) to the Nusselt number (Nu) and the fluid properties:

$$\mathrm{Nu} = 0.122\,\mathrm{Pr}^{1/3}\left(\mu/\mu_w\right)^{1/6}\left(2\,\mathrm{Hg}\ \sin(2\phi)\right)^{0.374} \tag{E.10}$$

Also here, coefficients occurred that might have to be adapted to the actual geometry of the heat exchanger. However, the values that Martin [35] extracted from empirical relations presented by Heavner, Kumar and Wanniarachchi [26] are a reasonable starting point and could approximate a number of different geometries [37].

Dittus-Boelter

Exploiting this relationship and assuming a fully developed turbulent flow, the well-know Dittus-Boelter [13], or McAdams [38, 70, 72], correlation

$$\mathrm{Nu} = 0.023\ \mathrm{Re}^{0.8}\ \mathrm{Pr}^{(\ )} \tag{E.11}$$

with $\mathrm{Pr}^{0.4}$ for heating and $\mathrm{Pr}^{0.33}$ for cooling could be used. However, the general nature and simplicity of this correlation limit the accuracy and one might question if altering Prandtl number (Pr) coefficient yields the desired accuracy gains [70].

Gnielinski

The second heat transfer correlation for single-phase flow in pipes is more detailed and was first presented by Gnielinski [18]. As already described in Section 3.5, Gnielinski [19] confirmed the general validity of the equations for fully turbulent flows, but also proposed some revisions of his original correlation in the form of an additional factor K to be multiplied with the basic expression

$$\mathrm{Nu}_{\mathrm{avg,turb}} = \frac{(\xi/8)\ (\mathrm{Re} - \Delta\,\mathrm{Re})\ \mathrm{Pr}}{1 + 12.7\sqrt{\xi/8}\ \left(\mathrm{Pr}^{2/3} - 1\right)} \left(1 + \left(\frac{d_{\mathrm{hyd}}}{l_{\mathrm{hx}}}\right)^{2/3}\right) K. \tag{E.12}$$

The additional factor is a correction term for the changing fluid properties between the boundary layer and the bulk fluid. Using a ratio to relate fluid properties at different temperatures is an established technique that has already been discussed by Gregorig [22, 23]. As explained by Hufschmidt and Burck [28] and Hufschmidt, Burck and Riebold [29] and Gnielinski [19] and Gnielinski [21], a modified K that uses the Pr ratio for liquids

$$K = \left(\mathrm{Pr}/\mathrm{Pr}_{\mathrm{w}}\right)^{0.11} \tag{E.13}$$

and the temperature ratio

$$K = \left(T/T_{\mathrm{w}}\right)^{0} \tag{E.14}$$

is expected to behave better than employing the viscosity ratio, which is another common approach to capture the effect of changing fluid properties. Using 0 as exponent disabled the correction factor as it yielded a value of unity at all times, which is recommended by Gnielinski [21] for cooling applications. For $T_{\mathrm{f}} < T_{\mathrm{w}}$, the exponent had to be found from experiments and the referenced publications only contain values for air (0.45, [19]), steam (−0.18, [21]) and CO_2 (0.12, [21]). However, the original work by Gregorig [22, 23] provided background information that enable the interested reader to estimate the exponent over a wide range of temperatures for liquid and gaseous fluids.

The most comprehensive discussion of Equation (E.12) is given by Gnielinski [21], which also provides means of modelling heat transfer in laminar flows. Following the suggestions of that work, the current implementation assumed a constant $K = 1$ and $\Delta\,\mathrm{Re} = 0$. The friction factor ξ for Equation (E.12) was defined as

$$\xi = \left(1.80 \log\left(\mathrm{Re}\right) - 1.50\right)^{-2} \tag{E.15}$$

with Re ≥ 10 000. For lower Re, values were calculated from three different contributions

$$\mathrm{Nu}_{\mathrm{lam},T,1} = 3.66, \tag{E.16}$$

$$\mathrm{Nu}_{\mathrm{lam},T,2} = 1.615\sqrt[3]{\mathrm{Re}\ \mathrm{Pr}\ d_{\mathrm{hyd}}/l_{\mathrm{hx}}} \text{ and} \tag{E.17}$$

$$\mathrm{Nu}_{\mathrm{lam},T,3} = \sqrt[6]{2/(1+22\,\mathrm{Pr})}\ \sqrt{\mathrm{Re}\ \mathrm{Pr}\ d_{\mathrm{hyd}}/l_{\mathrm{hx}}}, \tag{E.18}$$

which eventually yielded the average Nu for a laminar flow along a near-isothermal wall

$$\mathrm{Nu}_{\mathrm{lam},T} = \sqrt[3]{(\mathrm{Nu}^3_{\mathrm{avg},T,1} + 0.7^3 + (\mathrm{Nu}_{\mathrm{avg},T,2} - 0.7)^3 + \mathrm{Nu}^3_{\mathrm{avg},T,3}}. \tag{E.19}$$

The last step employed, again, the transition function from Richter [44] to combine the calculated Nusselt numbers for laminar and turbulent flow in the transition interval 2300 < Re < 10 000.

Boiling and Evaporation

Cooper

Palm and Claesson [41] recommended to multiply the correlation by Cooper [11] with a factor of $C_{\mathrm{hx}} = 1.5$,

$$\tilde{\alpha}_{\mathrm{tp}} = C_{\mathrm{hx}}\ 55\left(p^*\right)^{\left(0.12-0.2\log\left(10^6 R_{\mathrm{p}}\right)\right)}\ \left(-\log p^*\right)^{-0.55}\ \left(q''\right)^{0.67}\ \left(10^3 M\right)^{(-0.5)}, \tag{E.20}$$

to model boiling heat transfer in PHEs, but they did not mention the surface roughness that they used to model the brazed PHEs. However, in a later publication Cooper [10] himself proposes a simplified nucleate boiling correlation

$$\tilde{\alpha}_{\mathrm{tp}} = C_{\mathrm{hx}}\ 35\left(p^*\right)^{0.12}\ \left(-\log p^*\right)^{-0.55}\ \left(q''\right)^{0.67}\ \left(10^3 M\right)^{(-0.5)} \tag{E.21}$$

based several experimental data sets. Given the scatter of the experimental data, Cooper [10] concluded that either correlation can be used. In this work, the updated and simplified version was used since it does not require the roughness term. The correlation has originally been proposed to model the nucleate boiling part in a meta-correlation by Chen [7, 8] that also includes a convective part, but Palm and Claesson [41] do not mention the convective part and thus neglect it.

Gungor-Winterton

The correlation introduced by Gungor and Winterton [24] and simplified in Gungor and Winterton [25] is of the superposition type and the simplified form

$$\tilde{\alpha}_{\mathrm{tp}} = \tilde{\alpha}_{\mathrm{sp}}\ \psi \tag{E.22}$$

uses one additional equation

$$\psi = 1 + 3000\ \mathrm{Bo}^{0.86} + 1.12\ \left(\frac{x}{1-x}\right)^{0.75}\ \left(\frac{\rho'}{\rho''}\right)^{0.41} \begin{cases} (\mathrm{Fr}')^{0.1-2\ \mathrm{Fr}'} & \text{if } \mathrm{Fr}' < 0.05 \\ 1 & \text{if } \mathrm{Fr}' \geq 0.05 \end{cases} \tag{E.23}$$

to modify the liquid-only heat transfer coefficient $\bar{\alpha}_{\mathrm{sp}}$. For subcooled boiling, Gungor and Winterton [25] recommended to use the correlations from Chen [8].

Shah

The correlation proposed by Shah [47] is an enhancement approach that uses a piecewise definition of the ratio of heat transfer coefficients like Equation (E.22) with $\psi = \bar{\alpha}_{\mathrm{tp}}/\bar{\alpha}_{\mathrm{sp}}$ and the Convection number (Co)

$$\mathrm{Co} = \left(x^{-1} - 1\right)^{0.8}\ \sqrt{\rho'/\rho''}. \tag{E.24}$$

The liquid-only coefficient is based on the superficial Dittus-Boelter approach

$$\bar{\alpha}_{\mathrm{sp}} = 0.023\left(G\ (1-x)\ \Gamma/\mu'\right)^{0.8}\ \left(\mathrm{Pr}'\right)^{0.4}\ \lambda'/\Gamma. \tag{E.25}$$

The chart correlation uses the switching parameter

$$N = \begin{cases} \mathrm{Co} & \text{if } \mathrm{Fr}' > 0.04 \\ 0.38\ (\mathrm{Fr}')^{-0.3}\ \mathrm{Co} & \text{if } \mathrm{Fr}' \leq 0.04 \end{cases} \tag{E.26}$$

for horizontal tubes and $N = \mathrm{Co}$ for vertical tubes. For $N > 1$, ψ is equal to the larger of the nucleate boiling factor

$$\psi_{\mathrm{nb}} = \begin{cases} 230\ \sqrt{\mathrm{Bo}} & \text{if Bo} > 0.3 \times 10^{-4} \\ 1 + 46\ \sqrt{\mathrm{Bo}} & \text{if Bo} \leq 0.3 \times 10^{-4} \end{cases} \tag{E.27}$$

and the convective boiling factor

$$\psi_{\mathrm{cb}} = 1.8\ N^{-0.8}. \tag{E.28}$$

For smaller values of $0.1 < N \leq 1.0$ ψ is equal to the larger of the bubble suppression boiling factor

$$\psi_{\mathrm{bs}} = F\ \sqrt{\mathrm{Bo}}\ \exp\left(2.74\ N^{-0.1}\right) \tag{E.29}$$

and the result of Equation (E.28). Below $N \leq 0.1$, Equation (E.29) is modified to read

$$\psi_{\mathrm{bs}} = F\ \sqrt{\mathrm{Bo}}\ \exp\left(2.74\ N^{-0.15}\right) \tag{E.30}$$

with

$$F = \begin{cases} 14.7 & \text{if Bo} \geq 11 \times 10^{-4} \\ 15.43 & \text{if Bo} < 11 \times 10^{-4} \end{cases}. \tag{E.31}$$

E.2 Detailed Results

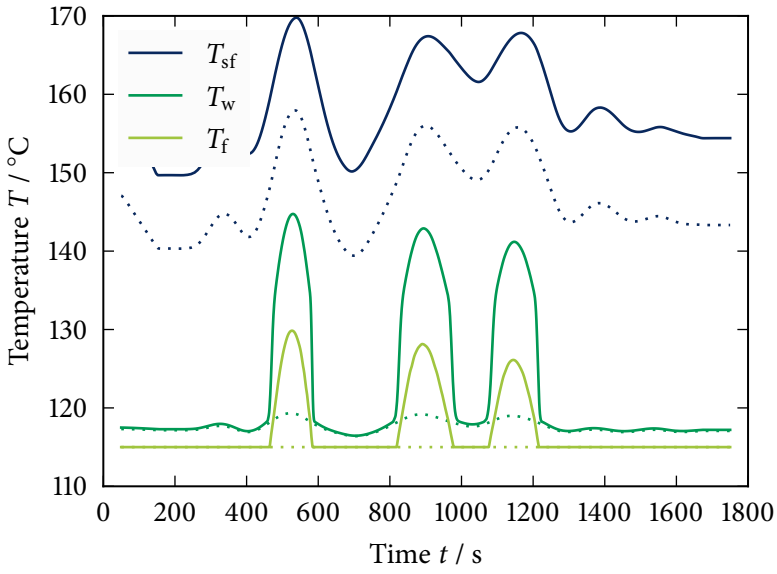

Figure E.1: Dotted in wf inlet and solid is wf outlet .

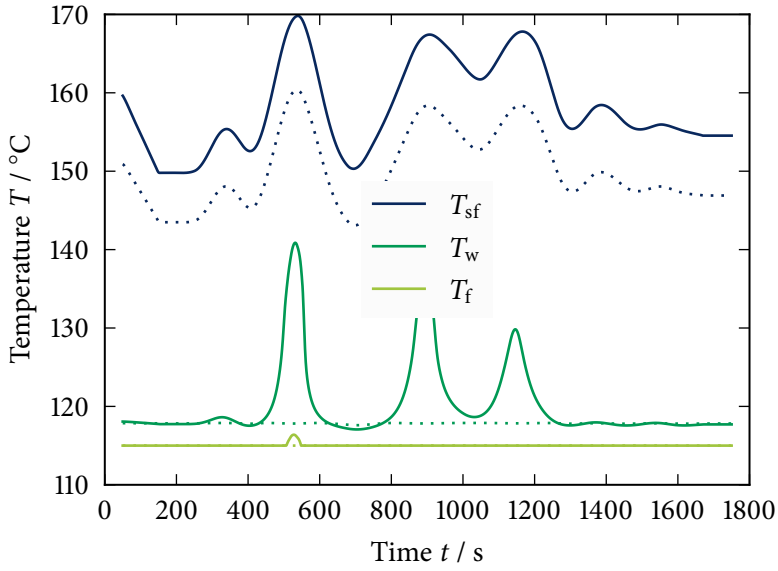

Figure E.2: Dotted in wf inlet and solid is wf outlet .

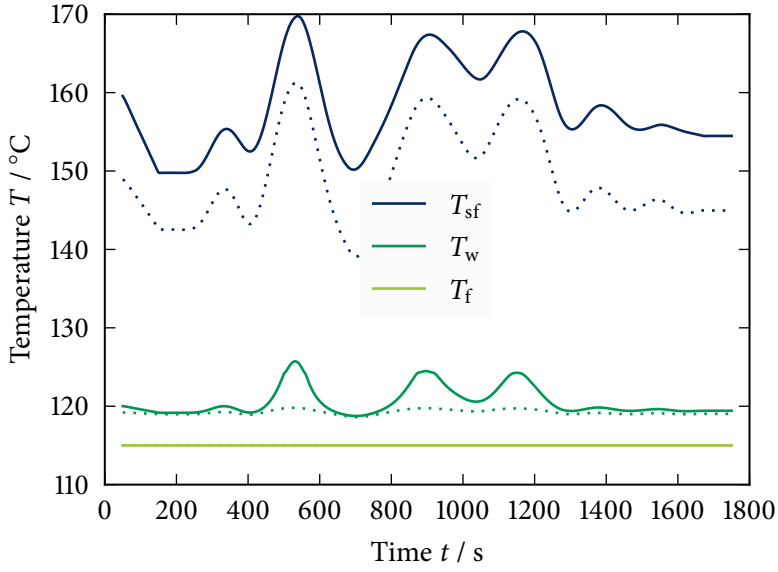

Figure E.3: Dotted in wf inlet and solid is wf outlet .

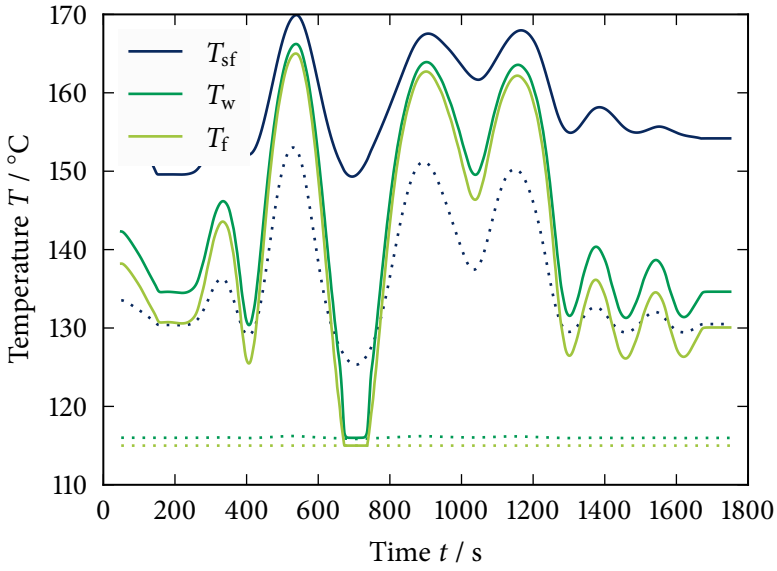

Figure E.4: Dotted in wf inlet and solid is wf outlet .

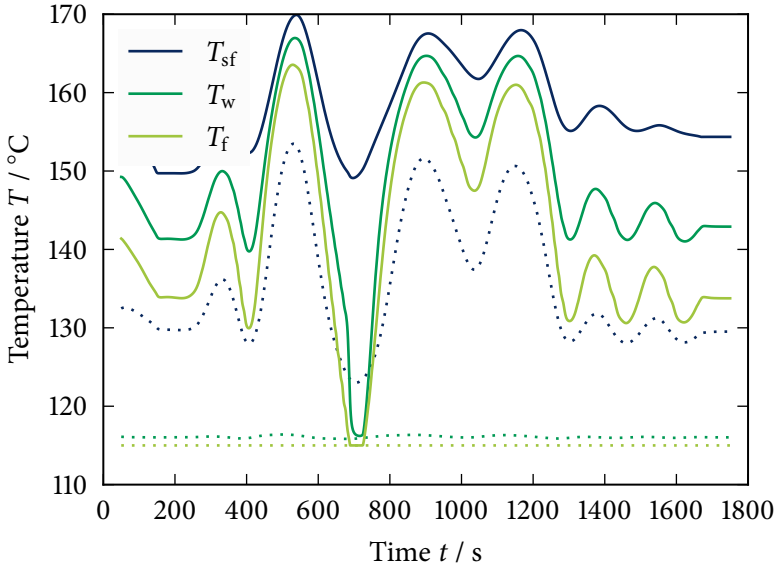

Figure E.5: Dotted in wf inlet and solid is wf outlet .

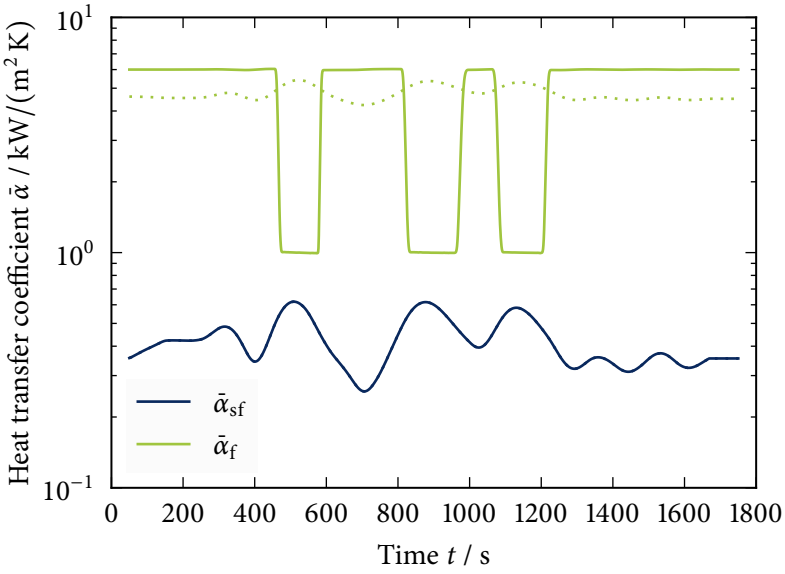

Figure E.6: Dotted in wf inlet and solid is wf outlet .

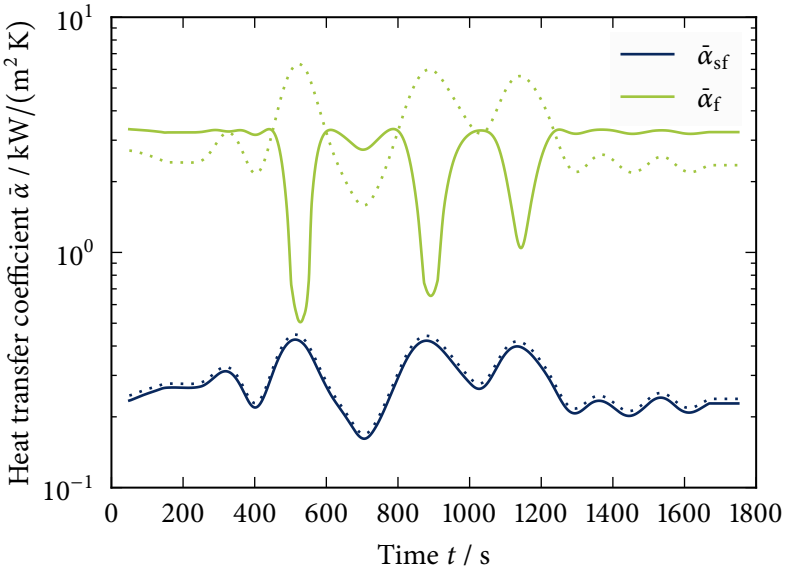

Figure E.7: Dotted in wf inlet and solid is wf outlet .

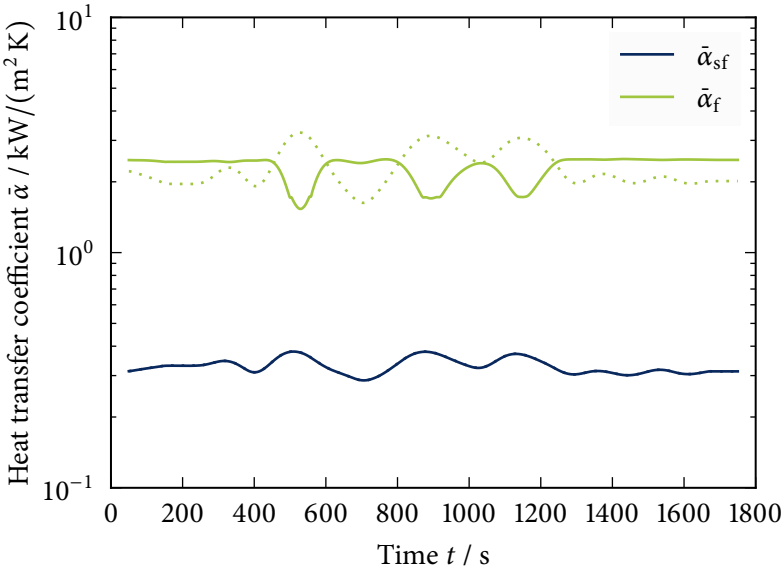

Figure E.8: Dotted in wf inlet and solid is wf outlet .

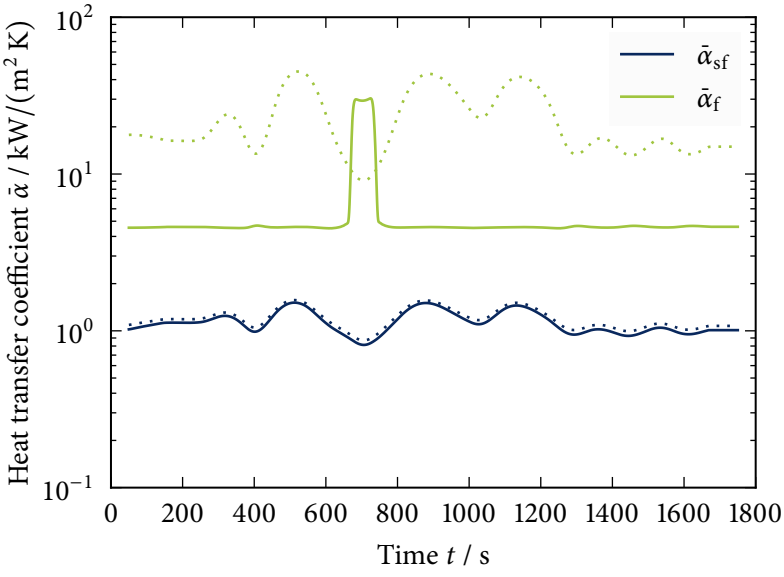

Figure E.9: Dotted in wf inlet and solid is wf outlet .

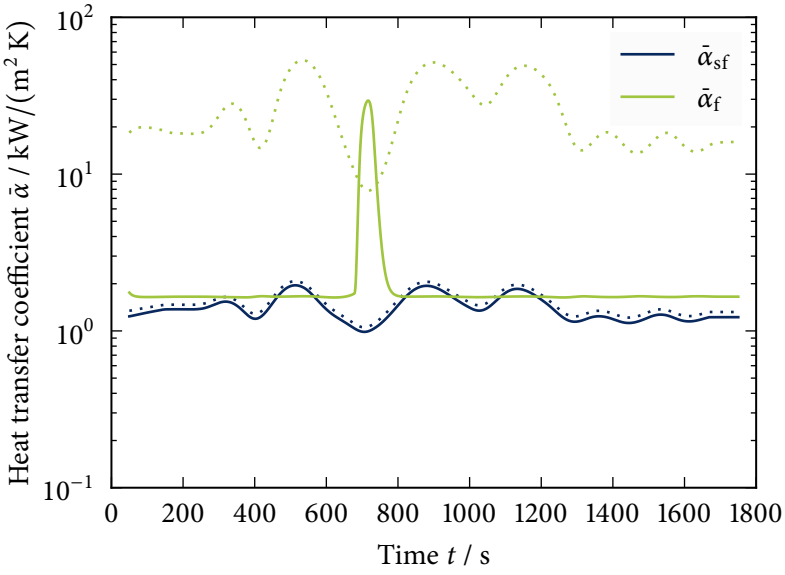

Figure E.10: Dotted in wf inlet and solid is wf outlet .

Appendix F

Heat Exchanger Tests

F.1 Processing Data

Considering two fluid streams that are separated by a wall, the typical engineering approach is to simplify the problem by introducing three heat transfer resistances R. Two of those connect the surface of the wall with the bulk working fluid, R_{f}, and the secondary fluid, R_{sf}, while the third resistance, R_{w}, represents the wall itself:

$$R_{\mathrm{hx}} = R_{\mathrm{f}} + R_{\mathrm{w}} + R_{\mathrm{sf}}. \tag{F.1}$$

The heat transfer area and the overall heat transfer coefficient are often used as one term. The total heat transfer coefficient UA_{hx}, which is the reciprocal value of the resistance

$$UA_{\mathrm{hx}} = 1/(R_{\mathrm{hx}}). \tag{F.2}$$

In the absence of phase change, this lumped parameter is directly linked to the heat transfer rate via logarithmic temperature difference ΔT_{lm}

$$\dot{Q}_{\mathrm{hx}} = UA_{\mathrm{hx}}\, \Delta T_{\mathrm{lm}}, \tag{F.3}$$

which itself is defined by

$$\Delta T_{\mathrm{lm}} = (\Delta T_1 - \Delta T_2) / \ln (\Delta T_1 / \Delta T_2). \tag{F.4}$$

The definitions of the internal differences ΔT_1 and ΔT_2 determine whether the heat exchange takes place in a co-current configuration

$$\Delta T_1 = T_{\mathrm{hot,in}} - T_{\mathrm{cold,in}} \text{ and } \Delta T_2 = T_{\mathrm{hot,out}} - T_{\mathrm{cold,out}} \tag{F.5}$$

or in a counter-current device

$$\Delta T_1 = T_{\mathrm{hot,in}} - T_{\mathrm{cold,out}} \text{ and } \Delta T_2 = T_{\mathrm{hot,out}} - T_{\mathrm{cold,in}}. \tag{F.6}$$

In the context of this work, only counter-current devices are considered and ΔT_{lm} is always defined using Equation (F.6). In cases that include phase change, the heat exchanger has to be divided into different sections to avoid an erroneous calculation

of the average temperature differences. Even though such an analysis is possible, it is not recommended to carry out measurements with a once-through heat exchanger that contains one or more single-phase parts and a two-phase zone on any of the sides. The changing values of $(\partial T/\partial h)_p$ violate the assumption of a close-to-linear temperature profile, which is required to apply Equation (F.4). Assuming that the heat exchanger only operates in either single-phase or two-phase on the primary side and in single-phase mode on the secondary side, the energy balance in terms of enthalpy

$$\dot{Q}_{\mathrm{hx},1} = \dot{m}_{\mathrm{f}} \left(h_{\mathrm{f,out}} - h_{\mathrm{f,in}} \right) \tag{F.7}$$

or in terms of specific heat capacities c_p

$$\dot{Q}_{\mathrm{hx},2} = \dot{m}_{\mathrm{sf}}\, c_{p,\mathrm{sf,avg}}\, \left(T_{\mathrm{sf,out}} - T_{\mathrm{sf,in}} \right) \tag{F.8}$$

can be used to check the measurements for consistency by comparing the heat release from one side to the heat uptake on the other side and the estimated heat loss to the environment. After passing this test, $\left| \dot{Q}_{\mathrm{hx},1} - \dot{Q}_{\mathrm{hx},2} \right| < \epsilon$, the heat transfer rate can be combined with Equation (F.3) to obtain R_{hx}. Knowing the value of R_{hx} or UA_{hx} allows us to proceed to the second step of the heat exchanger analysis as described below.

Single-phase heat transfer is often estimated with a relation based on Re and Pr. The explicit equation

$$\mathrm{Nu} = a\, \mathrm{Re}^{b}\, \mathrm{Pr}^{c} \tag{F.9}$$

can be used to characterise one side of the heat exchanger based on measurements of the total heat transfer. The original approach by Wilson [71] includes the fixed parameters $b = 0.8$ and $c = 0.3$, which leaves only a to be determined from experimental data. Given that the heat transfer resistance on one side can be held constant for all measurements, the convective heat transfer resistance and the conductive resistance in the wall can be lumped into a single parameter $C_1 = R_{\mathrm{f}} + R_{\mathrm{w}}$, while the remaining convective resistance is assumed to be proportional to Re^{-b} yielding

$$R_{\mathrm{hx}} = C_1 + C_2\ \mathrm{Re}^{-b}\,. \tag{F.10}$$

More details on this method are provided by the review of Fernández-Seara et al. [14] that also describes the extension of the method to work with changing conditions on both side of the wall. Considering only Equation (F.10), a linear regression may then be used to obtain the parameters. The coefficient a in Equation (F.9) is the found by

$$a^{-1} = C_2\, \mathrm{Pr}^{c}\, A_{\mathrm{hx}}\, \left(\lambda / d_{\mathrm{hyd}} \right) \tag{F.11}$$

with the thermal conductivity of the bulk fluid λ and the characteristic length d_{hyd} to convert between Nu and the heat transfer coefficient $\bar{\alpha}$. However, different heat

exchanger geometries and heat transfer fluids might require a modification of the parameter b as well. This modified Wilson plot involves and iterative procedure and an additional linearisation as introduced by Briggs and Young [6] and described by Fernández-Seara et al. [15]:

$$\ln\left(\left(R_{\mathrm{hx}} - C_1\right)^{-1}\right) = \ln C_2^{-1} + b\ \ln \mathrm{Re}\,. \tag{F.12}$$

The linearisation methods described above greatly simplify the solving process for the involved parameters. Even though contemporary non-linear solvers are able to fit Equation (F.9) directly, both Wilson plots are still suitable to provide a quick graphical representation of measured data helping to reveal unexpected operating conditions. Depending on which flavour of Wilson's method is employed, the process is subject to different possible sources of errors. Rose [45] provides general advice on the accuracy of experimentally determined heat-transfer coefficients and compares results from Wilson's method to other data. The publication by Sherbini, Joardar and Jacobi [48] shows detailed equations for error propagation and lists recommendations for optimal experimental design and data reduction.

The third and last step of the data processing involves the extraction of the primary side heat transfer coefficients. While the conditions on the primary should be held constant during the application of the Wilson method, this part of the analysis involves changing the mass flux on the primary side and usually covers different temperature and pressure ranges. The last bit of information needed to obtain the heat transfer coefficient on the working fluid side is an expression for thermal resistance of the metal wall R_{w}. For plate heat exchangers, it is common practice to estimate this value based on the plate thickness and the properties of the wall material since the contribution to the total heat transfer resistance is limited. Typical materials for small heat exchangers are stainless steel and titanium, which both have a thermal conductivity λ_{w} of approximately $20\,\mathrm{W/(m\,K)}$. Even for heavy plates with a thickness l_{w} of 1 mm, the final heat transfer resistance from

$$R_{\mathrm{w}} = l_{\mathrm{w}} / \left(\lambda_{\mathrm{w}}\, A_{\mathrm{w}}\right) \tag{F.13}$$

is orders of magnitude lower than the convection resistances in the fluid boundary layers. Rearranging Equation (F.1) and inserting Equation (F.2) then gives us the primary heat transfer coefficient as a function of the temperature difference and the transferred heat

$$\frac{1}{\bar{\alpha}_{\mathrm{f}}} = \frac{\Delta T_{\mathrm{lm}}\, A_{\mathrm{hx}}}{\dot{Q}_{\mathrm{hx}}} - \frac{l_{\mathrm{w}}}{\lambda_{\mathrm{w}}} - \frac{1}{\bar{\alpha}_{\mathrm{sf}}} \tag{F.14}$$

with $\bar{\alpha}_{\mathrm{sf}}$ from Equation (F.9).

F.2 Test Rig 2013

Installation Description

The initial attempt to construct a heat exchanger test rig was based on the old expander test bed and consisted of to small plate heat exchangers that were connected to the hot oil circuit and the working fluid loop. Additional sensors were mounted, but no control was added.

A sketch of the modified rig is shown in Figure F.1, which also contains the main components from the old installation. Starting at the air-driven pump in the lower left part of the sketch, the pressurised working fluid directly enters the added components. The main heat exchanger of the old rig is bypassed and the closed valves V1 and V2 cut off the heat transfer fluid and working medium lines. However, it is still possible to use the large main heat exchanger as an additional preheater if higher inlet temperatures are needed. After travelling through the mass flow meter and the first pressure sensor, the n-pentane enters the test section that consists of a preheater and an evaporator. The heat exchangers are connected in series and resistance temperature sensors are installed at the inlet and the outlet of both devices together with pressure difference measurement devices. On the secondary side, the heat transfer fluid enters the evaporator at the working fluid outlet in this counter-flow design and the oil temperatures are recorded in before the evaporator, between the PHEs and at the outlet of the preheater. Two turbine-based volume flow meters are mounted in the return line, but only the one closer to the heat exchanger is used since the flow rates during the tests are too low for the other flow meter.

The evaporated working fluid expands through a manually operated needle valve and reaches another measurement point for temperature and pressure. A condenser transfer the gaseous stream to the liquid state and the fluid is stored in liquid receiver feeding the pump. The condensation temperature can be adjusted by means of a three-way valve, which can be used to blend warm cooling water from the condenser into the cold stream returning from another heat exchanger (not shown in Figure F.1), which rejects heat to the main cooling water loop of the building. The water volume flow is measured downstream from the condenser and temperature is recorded at the inlet and at the outlet of the heat exchanger.

Reusing components from the expander tests described in Section 3.2 limits the operating domain of the heat exchanger test rig. The liquid receiver vessel has not been designed to withstand high pressures. The system has to operate with condenser temperatures below 30 °C to avoid pressures above atmospheric conditions when running with n-pentane. Thus the preheater has to deliver a lot of heat to lift the fluid temperature to a level relevant for organic Rankine cycle (ORC) evaporators. Targeting

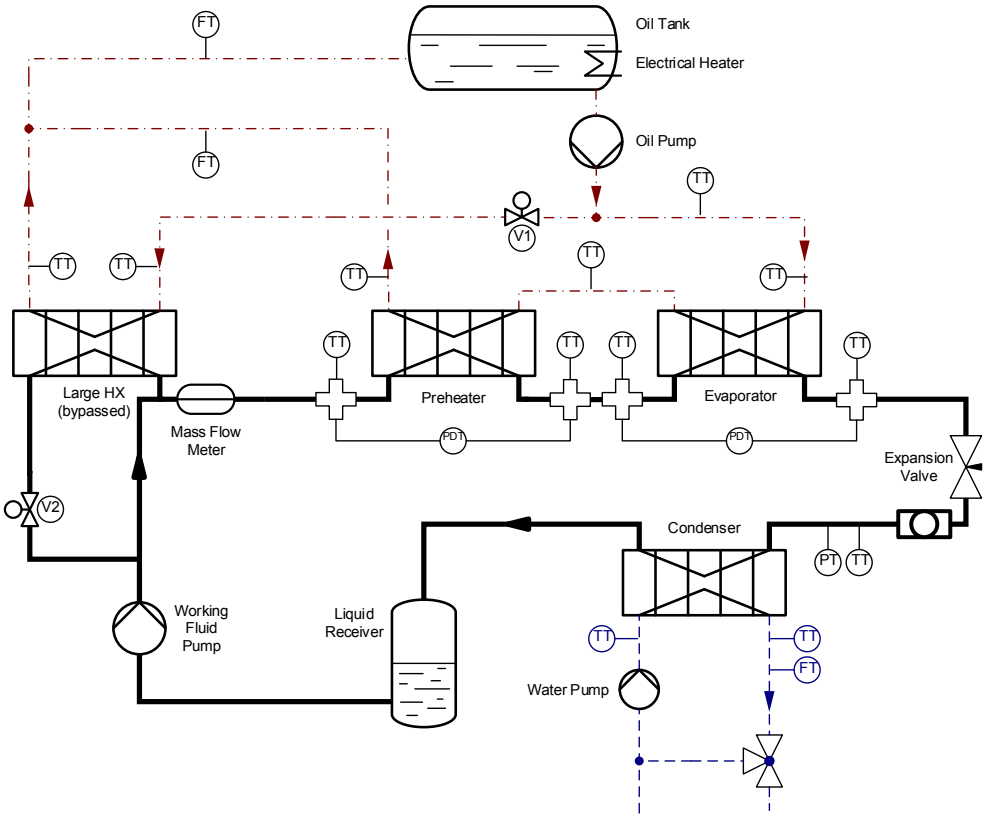

Figure F.1: ORC test rig modified for plate heat exchanger measurements.

evaporation temperatures between 80 °C and 140 °C at mass flow rates around 50 g/s, the design capacity for the preheater is 20 kW, while the evaporator is expected to transfer less than 10 kW. The standard brazed plate heat exchangers models BX8T and B12MT from SWEP International AB, Landskrona, Sweden (SWEP) are selected as preheater and evaporator, respectively. The detailed design calculations can be found Appendix F.2 and Table F.2 summarises the most important geometric features. Both models have a similar plate area, but the preheater needs twenty plates more to reach the desired capacity. Not all design details required for heat transfer modelling can be found in the product data sheets. However, the product information material describes the increase in device height as a function of the number of plates with a factor of 2.24 mm for BX8T [51] and 2.34 mm for B12MT [50]. It is thus assumed that 2 mm

Table F.2: Plate heat exchanger specifications, rig 2013.

Property	Preheater	Evaporator
Number of plates	50[a]	30[a]
Primary channels	24[a]	14[a]
Secondary channels	25[a]	15[a]
Flow length in mm	278[b]	234[c]
Flow width in mm	73[b]	118[c]
Total area in m^2	1.1[a]	0.812[a]
Weight in kg	5.9[a]	5.1[a]
Plate thickness in mm	0.24[b]	0.34[c]
Wave length in mm	7.5[d]	7.5[d]
Corrugation depth in mm	1.0[b]	1.0[c]
Chevron angle in °	65[d]	45[d]

[a] Based on design calculations, see also Appendix F.2.
[b] Based on the product data sheet for BX8T [51].
[c] Based on the product data sheet for B12MT [50].
[d] Approximate value based on manual measurements.

of both factors are caused by the corrugation pattern yielding $\hat{a} = 1$ mm and that the remainder represents the wall thickness l_w.

Before the heat transfer coefficients on the working fluid side can be determined, the secondary side has to be characterised. To apply the Wilson-plot technique introduced in Appendix F.1, the flow rate on the primary side has to be kept constant while the flow rate on the secondary side is varied. After adjusting the pumping power on the heat transfer fluid side, the system has to settle and reach steady state before data can be recorded. The 24 steady state data points presented below n-pentane cover mass flow rates from 39 g/s to 46 g/s and 34 g/s to 219 g/s for an oil-based heat transfer fluid by Chevron [56] (Texatherm 22). Depending on the operating conditions, the n-pentane inlet temperature to the preheater changes within the interval of 31 °C to 45 °C, while the oil temperature spans the range from 85 °C to 138 °C.

Measured Data

Each operating condition contributes to the linear fits that have to be constructed for each of the heat exchangers as described in Appendix F.1. Figure F.3 shows the results of Wilson's method and the modified Wilson approach for both heat exchangers. The

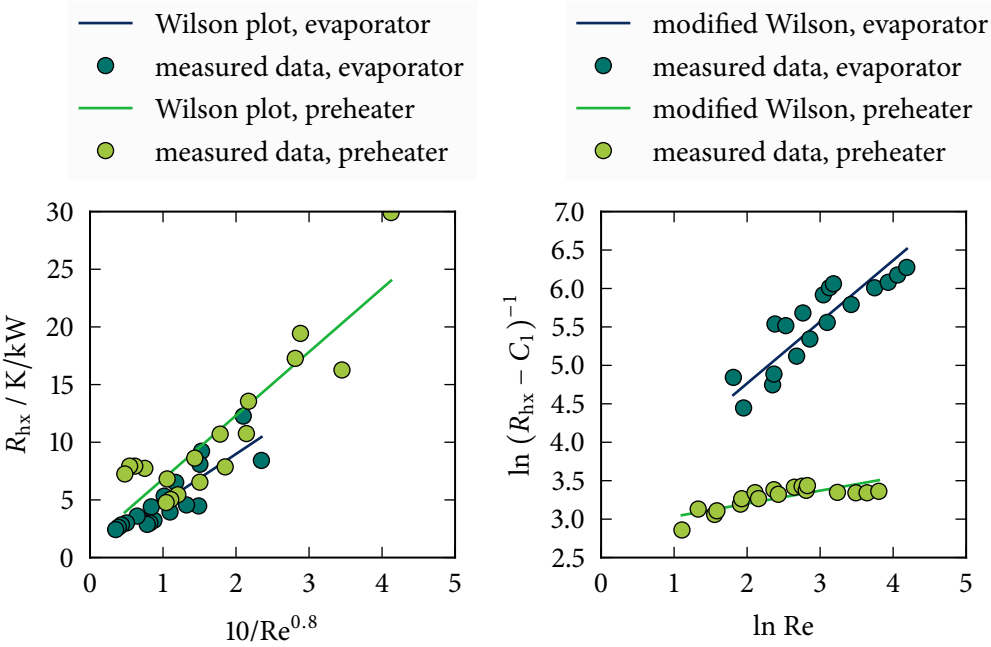

Figure F.3: Wilson plot and modified Wilson plot for the preheater and the evaporator in the first test rig.

points represent measured data, while the lines have been drawn using the coefficients obtained from the linearisation procedures.

The linear approximation of the heat transfer resistance is shown on the left hand side of Figure F.3. To obtain values for the modified Wilson plot, implicitly defined equations have to be solved. Stopping the iteration procedure for Equation (F.12) at a relative change of b of less than 0.5 % in two subsequent iterations yields the plot on the right hand side of Figure F.3. The resulting parameters are compiled in Table F.4. For the evaporator, the modified procedure does not lead to other paramaters because the already the first iteration resulted in a relative change of less than the threshold value.

The original Wilson plot on the left hand side of Figure F.3 has a reciprocal abscissa that shows high Reynolds numbers on the left of the axis while the logarithmically scaled abscissa of the modified Wilson plot puts the higher values to the right. Since similar modifications are made to the ordinates, both Wilson plots shows graphs that evolve from the lower left to the upper right, but with a reversed order of points.

Table F.4: Wilson plot parameters, rig 2013.

Plot type	C_1	C_2	a	b	c
original, Eq. F.10					
preheater	0.0013	0.0551	0.099	0.8	0.3
evaporator	0.0005	0.0422	0.204	0.8	0.3
modified, Eq. F.12					
preheater	-0.0274	0.0570	0.096	0.169	0.3
evaporator	0.0005	0.0422	0.204	0.8	0.3

The oil side of the evaporator has been tested at Re between 5 and 100 and for the preheater, the recorded Re regime covers the range from 2 to 50. The generally higher Reynolds numbers in the evaporator occur for two reasons: (i) the devices are connected in series and the oil is colder when it enters the preheater and (ii) the higher number of plates effectively compensates for the smaller flow width, which leads to an increased total flow area on the secondary side of the preheater and thus a lower mass flux for the same total mass flow rate.

The determined heat flow resistances are shown on the ordinates in Figure F.3. Despite the larger heat transfer area, the overall heat transfer resistance R_{hx} is larger in the preheater than in the evaporator, also at equal Reynolds numbers. Looking at all test runs, both heat exchangers have been operated with similar logarithmic temperature differences from 17 K to 45 K. The lower heat transfer resistance in the evaporator manifests itself in the resulting heat flow rate of 2.5 kW to 13 kW, which is higher than the heat flow rate of 1 kW to 5.5 kW that has been measured in the preheater.

By definition, both Wilson plot methods require that the heat transfer coefficient on the primary side is constant and that no phase change occurs on either side of the heat exchanger. Following these assumptions the figures presented above are based on the secondary side only. Including also the primary fluid in the investigation makes it possible to split the total heat flow rate into the part that is released from the heat transfer medium and the part that is received by the primary fluid. The first plot in Figure F.5 shows the heat transfer rates for both sides of the evaporator in darker colours and for the preheater in brighter colours. The secondary heat flow rates $\dot{Q}_{\mathrm{sf}}$ are higher in the evaporator than in the preheater. This is not the case for the calculated heat transfer on the primary side $\dot{Q}_{\mathrm{f}}$. According to the calculations, the working fluid does receive not more than 3 kW in the evaporator while the figures for the preheater lie between 1 kW and 6 kW.

Plotting only the differences in heat flow rates for both heat exchangers leads to Figure F.5. The presented data suggests an imbalance in the energy flows. Even though

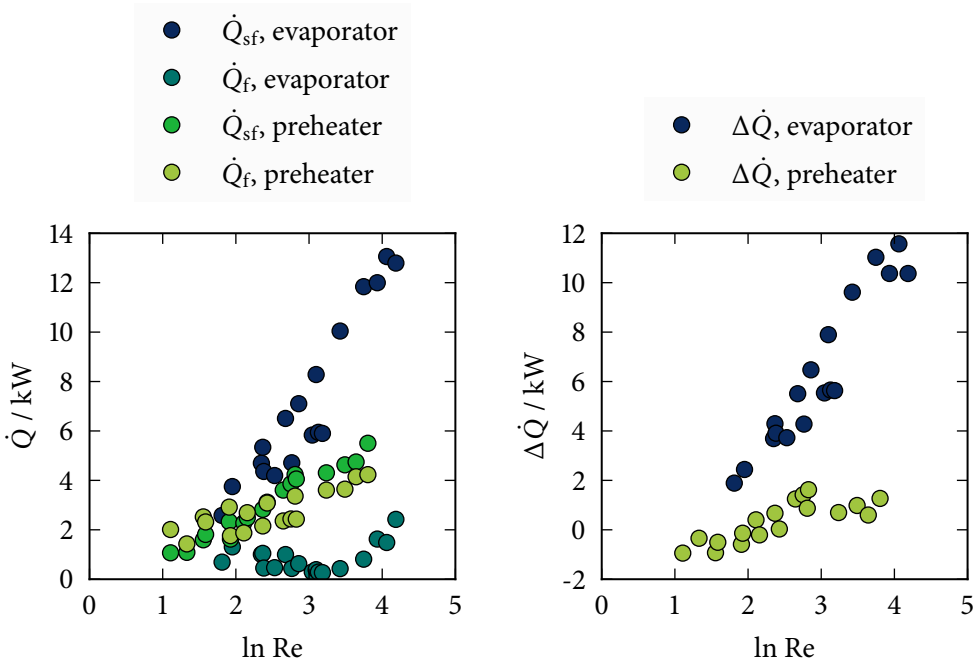

Figure F.5: Energy balance for the preheater and the evaporator in the first test rig with $\Delta\dot{Q} = \dot{Q}_{sf} - \dot{Q}_{f}$.

the installation only runs with little insulation, heat losses up to several kilowatts are unlikely to appear. Also the measurement uncertainty cannot explain deviations in such an order of magnitude. A possible explanation could be that evaporation takes place.

The working fluid pressure has been measured in the inlet pipes to the first heat exchanger and was recorded to be around 7.5 bar, which means that evaporation should not take place in any of the heat exchangers since the maximum n-pentane outlet temperature was determined to be 104 °C, which still is below the saturation temperature of 110 °C. However, the lower heat transfer resistance in the evaporator and the faulty energy balance could be explained with a partly evaporation in the second heat exchanger. Heat transfer increases during boiling lowering the heat transfer resistance and the energy balance is based on temperature and inlet pressure, which obviously leads to erroneous figures in case of evaporation.

Since the calibration of the pressure sensor confirmed its proper operation, one remaining is the internal averaging of the pressure signal. The data has not been

recorded at a high sampling rate. The data points used for Figure F.5 are average values obtained from intervals with the length of one or more minutes. The large swept volume of the reciprocating pump of over 300 cm^3 introduces pulsations into the system. In fact, assuming a subcooled condenser outlet stream with a density of 620 kg/m^3, one pump stroke delivers more than 0.18 kg of n-pentane, which corresponds to a pumping frequency of less than 0.3 Hz.

It is unlikely that the installed accumulators and expansion vessels are able to damp the flow variations completely. The changes in flow velocity and the associated variation in the time a certain portion of fluid spends in the heat exchangers could lead to the partly evaporation of the working fluid during operation.

Reusing the test facilities that were built to test the reciprocating expander prototypes described earlier has not produced satisfying results. Even though no bubbles were to be seen in the installed sight glasses, the energy balance suggests that partial evaporation took place during the tests. The control of the installation has proven to be a major challenge since the primary side of the heat exchanger could not be kept in single-phase operation.

It is thus recommended to carry out measurements with other equipment. Further analysis of the recorded data is not expected provide further insights due to the large imbalance in the energy flows. A dedicated rig should be equipped with a controller that minimises the number of possible error sources. Due to the findings presented above, the new test facilities described in Section 4.3 were built.

Preheater Data Sheet 2013

SINGLE PHASE - Design
Heat Exchanger : BX8Tx50

Fluid Side 1 : R601 (Pentane) (Liquid)
Fluid Side 2 : Therminol 66

Flow Type : Counter-Current

DUTY REQUIREMENTS		**Side 1**		**Side 2**
Heat load	kW		20.00	
Inlet temperature	°C	28.00		175.00
Outlet temperature	°C	165.00		125.00
Flow rate	kg/s	0.05365		0.1986
Max. pressure drop	kPa	50.0		50.0
Thermal length		3.578		1.306

PLATE HEAT EXCHANGER		**Side 1**		**Side 2**
Total heat transfer area	m²		1.10	
Heat flux	kW/m²		18.1	
Mean temperature difference	K		38.29	
O.H.T.C. (available/required)	W/m²,°C		493/502	
Pressure drop -total*	kPa	0.180		1.55
- in ports	kPa	0.0665		0.518
Port diameter	mm	16.0		16.0
Number of channels		24		25
Number of plates			50	
Oversurfacing	%		0	
Fouling factor	m²,°C/kW		-0.038	
Reynolds number		534.8		146.5
Port velocity	m/s	0.508		1.07

PHYSICAL PROPERTIES		**Side 1**	**Side 2**
Reference temperature	°C	105.13	151.80
Dynamic viscosity	cP	0.123	1.52
Dynamic viscosity - wall	cP	0.0917	2.01
Density	kg/m³	541.8	920.1
Heat capacity	kJ/kg,°C	2.721	2.014
Thermal conductivity	W/m,°C	0.08696	0.1099
Min. fluid temperature at wall	°C	28.00	
Max. fluid temperature at wall	°C		175.00
Film coefficient	W/m²,°C	897	1110
Minimum wall temperature	°C	130.80	131.14
Channel velocity	m/s	0.0283	0.0591
Shear stress	Pa	0.361	3.27

Totals		**Side 1**	**Side 2**
Total weight empty	kg	4.14	
Total weight filled	kg	5.54	
Hold-up volume, inner circuit	dm^3	0.936	
Hold-up volume, outer circuit	dm^3	0.975	
PortSize F1/P1	mm	16.0	
PortSize F2/P2	mm	16.0	
PortSize F3/P3	mm	16.0	
PortSize F4/P4	mm	16.0	
NND F1/P1	mm	16.0	
NND F2/P2	mm	16.0	
NND F3/P3	mm	16.0	
NND F4/P4	mm	16.0	
Carbon Footprint	kg	29.1	

DIMENSIONS

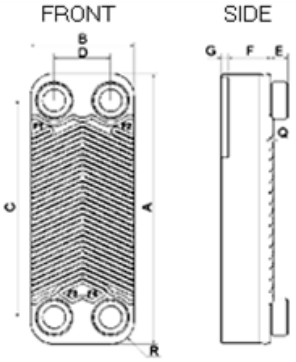

This is a schematic sketch. For correct drawings please use the order drawing function or contact your SWEP representaive.

A	mm	315 +/-2
B	mm	73 +/-1
C	mm	278 +/-1
D	mm	40 +/-1
E	mm	20 (opt. 48) +/-1
F	mm	109.50 +5%/-4.5%
G	mm	7 +/-1
Q	mm	2
R	mm	16

Evaporator Data Sheet 2013

EVAPORATOR - Design
Heat Exchanger : B12MTx30

Fluid Side 1 : R601 (Pentane)
Fluid Side 2 : Therminol 66

Flow Type : Counter-Current

DUTY REQUIREMENTS		**Side 1**		**Side 2**
Heat load	kW		9.500	
Inlet vapor quality		0.000		
Outlet vapor quality		1.000		
Inlet temperature	°C	165.00		200.00
Evaporation temperature (dew)	°C	165.00		
Superheating	K	0.00		
Outlet temperature	°C	165.00		175.00
Flow rate	kg/s	0.04988		0.1768
- inlet vapor	kg/s	0.0000		
Fluid vaporized	kg/s	0.04988		
Max. pressure drop	kPa	50.0		50.0

PLATE HEAT EXCHANGER		**Side 1**		**Side 2**
Total heat transfer area	m²		0.812	
Heat flux	kW/m²		11.7	
Mean temperature difference	K		20.76	
H.T.C. (available/required)	W/m²,°C		575/563	
Pressure drop -total*	kPa	0.813		0.289
- in ports	kPa	0.0297		0.0227
Pressure drop in fluid distribution	kPa	0.000 - 0.000		
Operating pressure - outlet	kPa	2050		
Number of channels		14		15
Number of plates			30	
Oversurfacing	%		2	
Fouling factor	m²,°C/kW		0.036	
Port diameter	mm	33.0/33.0 (up/down)		33.0
Recommended inlet connection diameter	mm	From 2.44 to 3.85		
Recommended outlet connection diameter	mm	From 6.21 to 13.9		
Reynolds number				214.2
Outlet port velocity	m/s	0.886		0.231

PHYSICAL PROPERTIES		Side 1	Side 2
Reference temperature	°C	165.01	187.61
Liquid - Dynamic viscosity	cP	0.0638	0.974
- Density	kg/m³	428.0	893.7
- Heat capacity	kJ/kg,°C	3.630	2.149
- Thermal conductivity	W/m,°C	0.06758	0.1067
Vapor - Dynamic viscosity	cP	0.0121	
- Density	kg/m³	65.79	
- Heat capacity	kJ/kg,°C	3.352	
- Thermal conductivity	W/m,°C	0.03558	
- Latent heat	kJ/kg	190.5	
Film coefficient	W/m²,°C	4650	785
Minimum wall temperature	°C	167.16	167.28
Channel velocity	m/s	0.240	0.0584

Totals		Side 1	Side 2
Total weight (no connections)	kg	4.93 - 6.85	
Hold-up volume, inner circuit	dm³	0.882	
Hold-up volume, outer circuit	dm³	0.945	
PortSize F1/P1	mm	33.0	
PortSize F2/P2	mm	33.0	
PortSize F3/P3	mm	33.0	
PortSize F4/P4	mm	33.0	
NND F1/P1	mm	36.0	
NND F2/P2	mm	36.0	
NND F3/P3	mm	36.0	
NND F4/P4	mm	36.0	
Carbon Footprint	kg	35.4	

DIMENSIONS

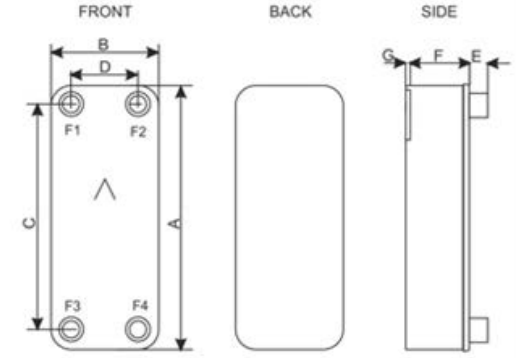

This is a schematic sketch. For correct drawings please use the order drawing function or contact your SWEP representative.

A	mm	287 to 290 +/-2
B	mm	117 to 119 +/-1
C	mm	234 +/-1
D	mm	63 +/-1
E	mm	27 (opt. 45) +/-1
F	mm	74.20 to 82.60 +/-2%
G	mm	2 to 6 +/-1
R	mm	22

F.3 Test Rig 2015

Temperature-Entropy Plots

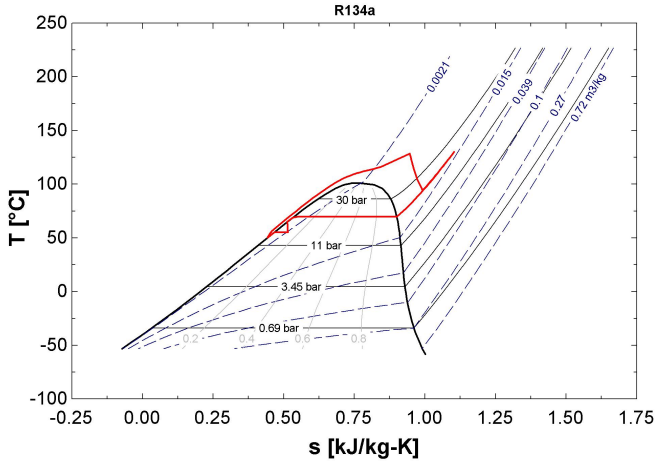

Figure F.6: *T*-*s* diagram of the targeted process with supercritical R134a.

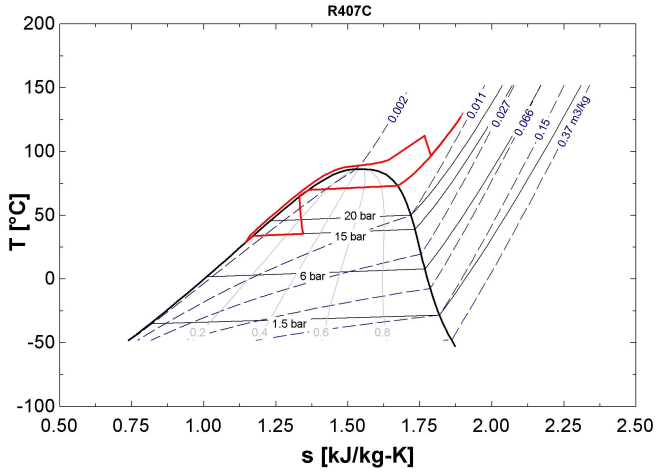

Figure F.7: *T*-*s* diagram of the targeted process with supercritical R407c.

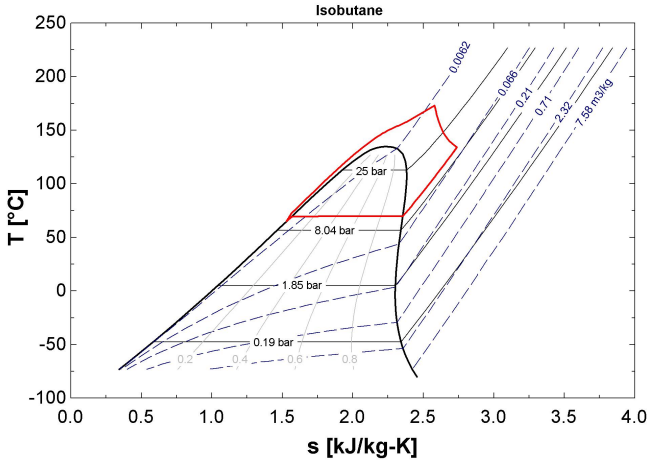

Figure F.8: *T*-*s* diagram of the targeted process with supercritical isobutane.

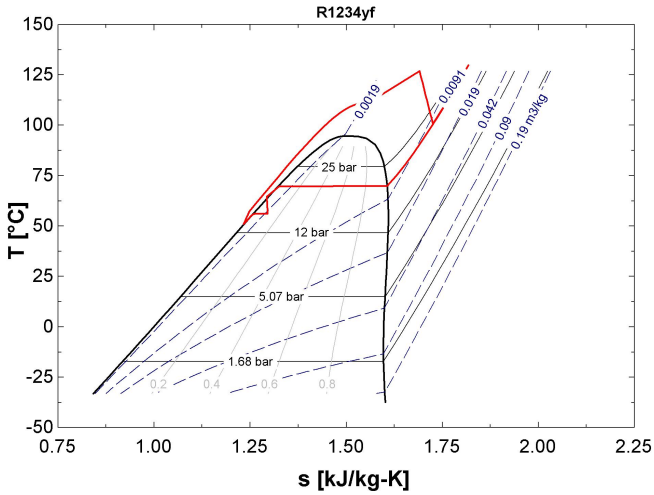

Figure F.9: *T*-*s* diagram of the targeted process with supercritical isobutane.

Sensors

Table F.10: Sensors installed on the working fluid side.

State	Type	N°	Range	Output	Supply	Comments	Connector	Sensor
a	DPT		5-40 mbar	4-20 mA	10.5-42 V DC	T max 120 °C	NPT ¼", female	Yokogawa EJX110A
c	DPT		5-40 mbar	4-20 mA	10.5-42 V DC	T max 120 °C	NPT ¼", female	Yokogawa EJX110A
0	PT		0-25 bar g	4-20 mA	12-30 V DC	Before pump	BSPP ½", male	VegaBar14
0	PT		0-25 bar g	4-20 mA	12-30 V DC	Before receiver	BSPP ½", male	VegaBar14
0	TT		-50-250 °C	TC, mV	-	Before pump	0.5 mm sheath	Omega TMTSS
0	TT		-50-250 °C	TC, mV	-	Before receiver	0.5 mm sheath	Omega TMTSS
0	TT‡		-50-250 °C	TC, mV	-	Before receiver	0.5 mm sheath	Omega TMTSS
1	FT		0-0.1 kg/s	4-20 mA	24 V AC/DC	Output channel 1	DN 15 flange	Siemens Mass 2100 DI6
1	DT		750-1500 kg/m^3	4-20 mA	-	Output channel 2	DN 15 flange	Siemens Mass 2100 DI6
1	FT‡		0-0.1 kg/s	4-20 mA	-	Output channel 3	DN 15 flange	Siemens Mass 2100 DI6
1	PT		0-50 bar g	4-20 mA	9.6-35 V DC		BSPP 1½", male	VegaBar82
1	TT		-50-250 °C	TC, mV	-		0.5 mm sheath	Omega TMTSS
2	TT		-50-250 °C	TC, mV	-		0.5 mm sheath	Omega TMTSS
2	TT‡		-50-250 °C	TC, mV	-		0.5 mm sheath	Omega TMTSS
4	TT		-50-250 °C	TC, mV	-		0.5 mm sheath	Omega TMTSS
4	TT‡		-50-250 °C	TC, mV	-		0.5 mm sheath	Omega TMTSS
4	PT‡*		10-50 bar	0.5-2.5 V	9-18 V DC	Static diagnostic setup	M5x0.5, male	OptrandAutoPSI
5	TT		-50-250 °C	TC, mV	-		0.5 mm sheath	Omega TMTSS
6	TT		-50-250 °C	TC, mV	-		0.5 mm sheath	Omega TMTSS
6	PT‡*		10-50 bar	0.5-2.5 V	9-18 V DC	Static diagnostic setup	M5x0.5, male	OptrandAutoPSI
6	TT‡		-50-250 °C	TC, mV	-		0.5 mm sheath	Omega TMTSS
7	PT		0-50 bar g	4-20 mA	9.6-35 V DC		BSPP 1½", male	VegaBar82
7	TT		-50-250 °C	TC, mV	-		0.5 mm sheath	Omega TMTSS
7	TT‡		-50-250 °C	TC, mV	-		0.5 mm sheath	Omega TMTSS
8	TT		-50-250 °C	TC, mV	-		0.5 mm sheath	Omega TMTSS
9	TT		-50-250 °C	TC, mV	-		0.5 mm sheath	Omega TMTSS

‡**= control sensors, *= output signal from PLC to DAQ as 4-20 mA**

Table F.11: Sensors installed on the secondary side.

Loop	State	Type	N°	Range	Output	Supply	Comments	Connector	Sensor
Oil	W	PT		Pressure	4-20 mA	10-28 V DC	P max = 25 bar	BSPP ½", male	Danfoss 4701
Oil	X	DT		500-1000 kg/m^3	4-20 mA	24 V AC/DC	Output channel 1	DN 15 flange	Siemens Mass 2100 DI15
Oil	X	FT		0-0.15 kg/s	0-10 kHz	6-30 V DC, I<100mA	Output channel 2	DN 15 flange	Siemens Mass 2100 DI15
Oil	A	TT		-50-250 °C	TC, mV	-		0.5 mm sheath	Omega TMTSS
Oil	A	TT		-50-250 °C	TC, mV	-		0.5 mm sheath	Omega TMTSS
Oil	A	FT		2-20 l/min	4-20 mA	8 - 28 V AC/DC	4 wire setup	BSPP ½", male	GL Lx and 101ai
Oil	B	TT		-50-250 °C	TC, mV	-		0.5 mm sheath	Omega TMTSS
Oil	B	TT		-50-250 °C	TC, mV	-		0.5 mm sheath	Omega TMTSS
Oil	B	FT		2-20 l/min	4-20 mA	8 - 28 V AC/DC	4 wire setup	BSPP ½", male	GL Lx and 101ai
Oil	C	TT		-50-250 °C	TC, mV	-		0.5 mm sheath	Omega TMTSS
Oil	C	TT		-50-250 °C	TC, mV	-		0.5 mm sheath	Omega TMTSS
Oil	G	TT		-50-250 °C	TC, mV	-		0.5 mm sheath	Omega TMTSS
Oil	G	TT		-50-250 °C	TC, mV	-		0.5 mm sheath	Omega TMTSS
Oil	d	DPT		0-74.6 mbar	4-20 mA	12-45 V DC	Low accuracy	NPT ¼", female	Rosemount 1151 DP3
Water	b	DPT		0-74.6 mbar	4-20 mA	12-45 V DC	Low accuracy	NPT ¼", female	Rosemount 1151 DP3
Water	Y	PT		Pressure	4-20 mA	10-28 V DC	P max = 25 bar	BSPP ½", male	Danfoss 4701
Water	D	TT		-50-250 °C	TC, mV	-		0.5 mm sheath	Omega TMTSS
Water	D	TT		-50-250 °C	TC, mV	-		0.5 mm sheath	Omega TMTSS
Water	D	FT		0-20 l/min	4-20 mA	230 V AC	NOT Ex approved	DN15 flange	Yokogawa RXF015G
Water	E	TT		-50-250 °C	TC, mV	-		0.5 mm sheath	Omega TMTSS
Water	E	TT		-50-250 °C	TC, mV	-		0.5 mm sheath	Omega TMTSS
Water	E	FT		0-20 l/min	4-20 mA	230 V AC	NOT Ex approved	DN15 flange	Yokogawa RXF015G
Water	F	TT		-50-250 °C	TC, mV	-		0.5 mm sheath	Omega TMTSS
Water	F	TT		-50-250 °C	TC, mV	-		0.5 mm sheath	Omega TMTSS
Water	G	TT		-50-250 °C	TC, mV	-		0.5 mm sheath	Omega TMTSS
Water	G	TT		-50-250 °C	TC, mV	-		0.5 mm sheath	Omega TMTSS

Preheater Data Sheet 2015

SINGLE PHASE - Design
Heat Exchanger : B8Tx8

Fluid Side 1 : R600a, liquid, 29bar
Fluid Side 2 : Texatherm 22

Flow Type : Counter-Current

DUTY REQUIREMENTS		**Side 1**		**Side 2**
Heat load	kW		3.671	
Inlet temperature	°C	70.00		140.00
Outlet temperature	°C	118.00		120.00
Flow rate	kg/s	0.02500		0.08031
Max. pressure drop	kPa	50.0		50.0
Thermal length		1.41		0.59

PLATE HEAT EXCHANGER		**Side 1**		**Side 2**
Total heat transfer area	m²		0.138	
Heat flux	kW/m²		26.6	
Mean temperature difference	K		34.11	
O.H.T.C. (available/required)	W/m²,°C		835/780	
Pressure drop -total*	kPa	1.55		8.37
- in ports	kPa	0.0113		0.0667
Port diameter	mm	17.5		17.5
Number of channels		3		4
Number of plates			8	
Oversurfacing	%		7	
Fouling factor	m²,°C/kW		0.074	
Reynolds number		2950		185
Port velocity	m/s	0.230		0.423

PHYSICAL PROPERTIES		**Side 1**	**Side 2**
Reference temperature	°C	94.00	130.00
Dynamic viscosity	cP	0.0773	2.98
Dynamic viscosity - wall	cP	0.0622	4.25
Density	kg/m³	452.1	789.8
Heat capacity	kJ/kg,°C	3.059	2.286
Thermal conductivity	W/m,°C	0.06950	0.1260
Min. fluid temperature at wall	°C	70.00	
Max. fluid temperature at wall	°C		140.00
Film coefficient	W/m²,°C	2180	1760
Minimum wall temperature	°C	109.81	110.35
Channel velocity	m/s	0.126	0.174
Shear stress	Pa	4.89	26.4

TOTALS

Total weight (no connections)	kg	1.41
Hold-up volume, inner circuit	dm^3	0.117
Hold-up volume, outer circuit	dm^3	0.156
PortSize F1/P1	mm	16.0
PortSize F2/P2	mm	16.0
PortSize F3/P3	mm	16.0
PortSize F4/P4	mm	16.0
NND F1/P1	mm	18.0
NND F2/P2	mm	18.0
NND F3/P3	mm	18.0
NND F4/P4	mm	18.0
Carbon Footprint	kg	9.90

DIMENSIONS

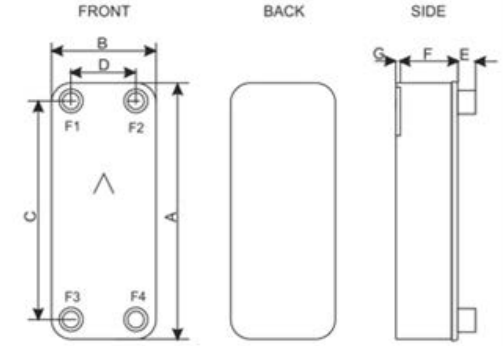

This is a schematic sketch. For correct drawings please use the order drawing function or contact your SWEP representative.

A	mm	317 +/-2
B	mm	76 +/-1
C	mm	278 +/-1
D	mm	40 +/-1
E	mm	20.10 +/-1
F	mm	21.90 +3.7%/-3.1%
G	mm	7 +/-1
R	mm	18

Evaporator Data Sheet 2015

EVAPORATOR - Design
Heat Exchanger : B8Tx10

Fluid Side 1 : R600a, two-phase
Fluid Side 2 : Texatherm 22

Flow Type : Counter-Current

DUTY REQUIREMENTS		**Side 1**		**Side 2**
Heat load	kW		4.100	
Inlet vapor quality		0.00		
Outlet vapor quality		1.00		
Inlet temperature	°C	115.76		160.00
Evaporation temperature (dew)	°C	115.76		
Superheating	K	9.00		
Outlet temperature	°C	124.76		140.00
Flow rate	kg/s	0.01926		0.08691
- inlet vapor	kg/s	0.0000		
Fluid vaporized	kg/s	0.01926		
Max. pressure drop	kPa	50.0		50.0

PLATE HEAT EXCHANGER		**Side 1**		**Side 2**
Total heat transfer area	m²		0.184	
Heat flux	kW/m²		22.3	
Mean temperature difference	K		32.19	
H.T.C. (available/required)	W/m²,°C		692/692	
Pressure drop -total*	kPa	3.37		6.20
- in ports	kPa	0.0452		0.0794
Pressure drop in fluid distribution	kPa	0.000 - 0.000		
Operating pressure - outlet	kPa	2630		
Number of channels		4		5
Number of plates			10	
Oversurfacing	%		0	
Fouling factor	m²,°C/kW		0.000	
Port diameter	mm	17.5/17.5 (up/down)		17.5
Recommended inlet connection diameter	mm	From 1.59 to 2.51		
Recommended outlet connection diameter	mm	From 3.52 to 7.87		
Reynolds number				211
Outlet port velocity	m/s	1.01		0.465

PHYSICAL PROPERTIES		Side 1	Side 2
Reference temperature	°C	115.80	147.91
Liquid - Dynamic viscosity	cP	0.0540	2.26
- Density	kg/m³	387.9	777.8
- Heat capacity	kJ/kg,°C	4.111	2.351
- Thermal conductivity	W/m,°C	0.06372	0.1247
Vapor - Dynamic viscosity	cP	0.0123	
- Density	kg/m³	79.10	
- Heat capacity	kJ/kg,°C	4.092	
- Thermal conductivity	W/m,°C	0.03803	
- Latent heat	kJ/kg	167.0	
Film coefficient	W/m²,°C	909	1720
Minimum wall temperature	°C	119.28	119.81
Channel velocity	m/s	0.417	0.153

TOTALS		
Total weight (no connections)	kg	1.56
Hold-up volume, inner circuit	dm³	0.156
Hold-up volume, outer circuit	dm³	0.195
PortSize F1/P1	mm	16.0
PortSize F2/P2	mm	16.0
PortSize F3/P3	mm	16.0
PortSize F4/P4	mm	16.0
NND F1/P1	mm	18.0
NND F2/P2	mm	18.0
NND F3/P3	mm	18.0
NND F4/P4	mm	18.0
Carbon Footprint	kg	11.0

DIMENSIONS

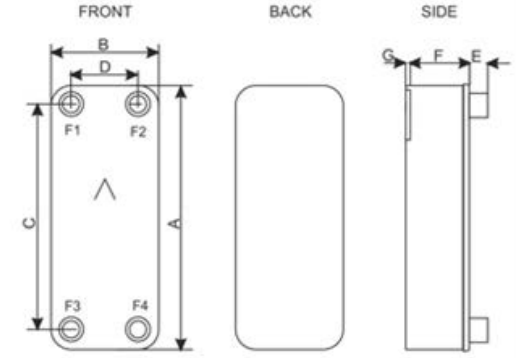

This is a schematic sketch. For correct drawings please use the order drawing function or contact your SWEP representative.

A	mm	317 +/-2
B	mm	76 +/-1
C	mm	278 +/-1
D	mm	40 +/-1
E	mm	20.10 +/-1
F	mm	26.40 +3.7%/-3.1%
G	mm	7 +/-1
R	mm	18

Desuperheater Data Sheet 2015

SINGLE PHASE - Design
Heat Exchanger : B8Tx16

Fluid Side 1 : R407C, vapour, 34bar
Fluid Side 2 : Water

Flow Type : Counter-Current

DUTY REQUIREMENTS		**Side 1**		**Side 2**
Heat load	kW		4.300	
Inlet temperature	°C	130.00		60.00
Outlet temperature	°C	73.00		110.00
Flow rate	kg/s	0.05464		0.02046
Max. pressure drop	kPa	50.0		50.0
Thermal length		3.51		3.08

PLATE HEAT EXCHANGER		**Side 1**		**Side 2**
Total heat transfer area	m²		0.322	
Heat flux	kW/m²		13.4	
Mean temperature difference	K		16.25	
O.H.T.C. (available/required)	W/m²,°C		817/822	
Pressure drop -total*	kPa	4.11		0.106
- in ports	kPa	0.188		3.54e-3
Port diameter	mm	17.5		17.5
Number of channels		7		8
Number of plates			16	
Oversurfacing	%		0	
Fouling factor	m²,°C/kW		-0.006	
Reynolds number		12600		210
Port velocity	m/s	1.75		0.0878

PHYSICAL PROPERTIES		**Side 1**		**Side 2**
Reference temperature	°C	101.50		85.00
Dynamic viscosity	cP	0.0170		0.334
Dynamic viscosity - wall	cP	0.0168		0.318
Density	kg/m³	129.9		968.7
Heat capacity	kJ/kg,°C	1.381		4.203
Thermal conductivity	W/m,°C	0.02372		0.6728
Min. fluid temperature at wall	°C	64.04		
Max. fluid temperature at wall	°C			114.76
Film coefficient	W/m²,°C	1190		3430
Minimum wall temperature	°C	89.40		89.18
Channel velocity	m/s	0.412		0.0181
Shear stress	Pa	12.4		0.324

TOTALS

Total weight (no connections)	kg	2.01
Hold-up volume, inner circuit	dm^3	0.273
Hold-up volume, outer circuit	dm^3	0.312
PortSize F1/P1	mm	16.0
PortSize F2/P2	mm	16.0
PortSize F3/P3	mm	16.0
PortSize F4/P4	mm	16.0
NND F1/P1	mm	18.0
NND F2/P2	mm	18.0
NND F3/P3	mm	18.0
NND F4/P4	mm	18.0
Carbon Footprint	kg	14.1

DIMENSIONS

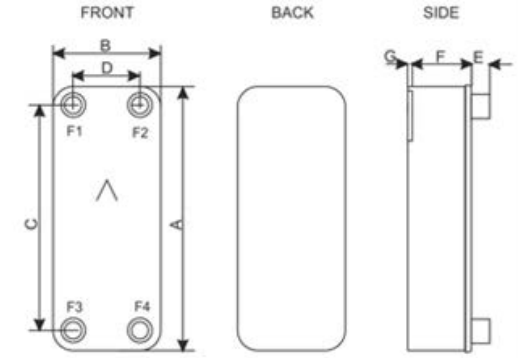

This is a schematic sketch. For correct drawings please use the order drawing function or contact your SWEP representative.

A	mm	317 +/-2
B	mm	76 +/-1
C	mm	278 +/-1
D	mm	40 +/-1
E	mm	20.10 +/-1
F	mm	39.80 +3.7%/-3.1%
G	mm	7 +/-1
R	mm	18

Appendix Bibliography

[1] R. P. Adair, E. B. Qvale and J. T. Pearson. 'Instantaneous Heat Transfer to the Cylinder Wall in Reciprocating Compressors'. In: *Proceedings of the International Compressor Engineering Conference*. 86. 1972, pp. 521–526.

[2] American Society of Heating, Refrigerating and Air-Conditioning Engineers. *2001 ASHRAE Handbook: Fundamentals*. Vol. 111. ASHRAE, 2001.

[3] W. J. D. Annand. 'Heat transfer in cylinders of reciprocating internal combustion engines'. In: *Proceedings of the Institution of Mechanical Engineers* 177.36 (1963), pp. 973–996.

[4] M. K. Bassiouny and H. Martin. 'Flow distribution and pressure drop in plate heat exchangers—I U-type arrangement'. In: *Chemical Engineering Science* 39.4 (1984), pp. 693–700. DOI: 10.1016/0009-2509(84)80176-1.

[5] M. K. Bassiouny and H. Martin. 'Flow distribution and pressure drop in plate heat exchangers—II Z-type arrangement'. In: *Chemical Engineering Science* 39.4 (1984), pp. 701–704. DOI: 10.1016/0009-2509(84)80177-3.

[6] D. E. Briggs and E. H. Young. 'Modified Wilson plot techniques for obtaining heat transfer correlations for shell and tube heat exchangers'. In: *Chemical engineering progress symposium series*. Vol. 65. 92. AIChE, New York, NY. 1969, pp. 35–45.

[7] J. C. Chen. 'Correlation for boiling heat transfer to saturated fluids in convective boiling'. In: *ASME paper* 63-HT-34 (1963).

[8] J. C. Chen. 'Correlation for boiling heat transfer to saturated fluids in convective boiling'. In: *Industrial & Engineering Chemistry Process Design and Development* 63-HT-34 (1966). DOI: 10.1021/i260019a023.

[9] J. Claesson. 'Thermal and Hydraulic Performance of Compact Brazed Plate Heat Exchangers Operating as Evaporators in Domestic Heat Pumps'. PhD Thesis. Royal Institute of Technology, 2004.

[10] M. G. Cooper. 'Flow boiling—the 'apparently nucleate′ regime'. In: *International Journal of Heat and Mass Transfer* 32.3 (1989), pp. 459–464. DOI: 10.1016/0017-9310(89)90133-6.

[11] M. G. Cooper. 'Heat Flow Rates in Saturated Nucleate Pool Boiling—A Wide-Ranging Examination Using Reduced Properties'. In: *Advances in Heat Transfer* 16 (1984), pp. 157–239. DOI: 10.1016/S0065-2717(08)70205-3.

[12] T. Destoop. 'Compresseurs volumetriques'. In: Techniques de l'ingénieur, 1986. Chap. B4220, pp. 1–27.

[13] F. W. Dittus and L. M. K. Boelter. 'Heat transfer in automobile radiators of the tubular type'. In: *University of California Publications in Engineering* 2 (1930), pp. 443–461.

[14] J. Fernández-Seara, F. J. Uhía, J. Sieres and A. Campo. 'A general review of the Wilson plot method and its modifications to determine convection coefficients in heat exchange devices'. In: *Applied Thermal Engineering* 27.17–18 (2007), pp. 2745–2757. DOI: 10.1016/j.applthermaleng.2007.04.004.

[15] J. Fernández-Seara, F. J. Uhía, J. Sieres and A. Campo. 'Experimental apparatus for measuring heat transfer coefficients by the Wilson plot method'. In: *European Journal of Physics* 26.3 (2005), N1–N11. DOI: 10.1088/0143-0807/26/3/N01.

[16] L. Fischer and H. Martin. 'Friction factors for fully developed laminar flow in ducts confined by corrugated parallel walls'. In: *International Journal of Heat and Mass Transfer* 40.3 (1997), pp. 635–639. DOI: 10.1016/0017-9310(96)00136-6.

[17] W. W. Focke, J. Zachariades and I. Olivier. 'The effect of the corrugation inclination angle on the thermohydraulic performance of plate heat exchangers'. English. In: *International Journal of Heat and Mass Transfer* 28.8 (1985), pp. 1469–1479.

[18] V. Gnielinski. 'New Equations For Heat And Mass-transfer In Turbulent Pipe And Channel Flow'. In: *International Chemical Engineering* 16.2 (1976), pp. 359–368.

[19] V. Gnielinski. 'On heat transfer in tubes'. In: *International Journal of Heat and Mass Transfer* 63 (2013), pp. 134–140. DOI: 10.1016/j.ijheatmasstransfer.2013.04.015.

[20] V. Gnielinski. 'Berechnung des Druckverlustes in glatten konzentrischen Ringspalten bei ausgebildeter laminarer und turbulenter isothermer Strömung'. In: *Chemie Ingenieur Technik* 79.1–2 (2007), pp. 91–95. DOI: 10.1002/cite.200600126.

[21] V. Gnielinski. 'VDI Heat Atlas'. In: ed. by P. Stephan. 2nd. Berlin Heidelberg: Springer, 2010. Chap. G1 Heat Transfer in Pipe Flow, pp. 691–700. DOI: 10.1007/978-3-540-77877-6_34.

[22] R. Gregorig. 'The effect of a nonlinear temperature dependent Prandtl-number on heat transfer of fully developed flow of liquids in a straight tube'. In: *Wärme- und Stoffübertragung* 9.2 (1976), pp. 61–72. DOI: 10.1007/BF01589459.

[23] R. Gregorig. 'Verallgemeinerter Ausdruck für den Einfluß temperaturabhängiger Stoffwerte auf den turbulenten Wärmeübergang'. In: *Wärme- und Stoffübertragung* 3.1 (1970), pp. 26–40. DOI: 10.1007/BF01881220.

[24] K. E. Gungor and R. H. S. Winterton. 'A general correlation for flow boiling in tubes and annuli'. In: *International Journal of Heat and Mass Transfer* 29.3 (1986), pp. 351–358. DOI: 10.1016/0017-9310(86)90205-X.

[25] K. E. Gungor and R. H. S. Winterton. 'Simplified general correlation for saturated flow boiling and ccomparison of correlations with data'. In: *Chemical Engineering Research and Design* 65 (1987), pp. 148–156.

[26] R. L. Heavner, H. Kumar and A. S. Wanniarachchi. 'Performance of an industrial plate heat exchanger: effect of chevron angle'. In: *AIChE symposium series* 89.295 (1993), pp. 262–267.

[27] M. L. Huber, R. A. Perkins, A. Laesecke, D. G. Friend, J. V. Sengers, M. J. Assael et al. 'New International Formulation for the Viscosity of H2O'. In: *J. Phys. Chem. Ref. Data* 38.2 (2009), pp. 101–125. DOI: 10.1063/1.3088050.

[28] W. Hufschmidt and E. Burck. 'Der Einfluss temperaturabhängiger Stoffwerte auf den Wärmeübergang bei turbulenter Strömung von Flüssigkeiten in Rohren bei hohen Wärmestromdichten und Prandtlzahlen'. In: *International Journal of Heat and Mass Transfer* 11.6 (1968), pp. 1041–1048.

[29] W. Hufschmidt, E. Burck and W. Riebold. 'Die Bestimmung örtlicher und mittlerer Wärmeübergangszahlen in Rohren bei hohen Wärmestromdichten'. In: *International Journal of Heat and Mass Transfer* 9.6 (1966), pp. 539–565.

[30] A. Irimescu. 'Convective heat transfer equation for turbulent flow in tubes applied to internal combustion engines operated under motored conditions'. In: *Applied Thermal Engineering* 50.1 (2013), pp. 536–545. DOI: 10.1016/j.applthermaleng.2012.06.051.

[31] W. Kast, H. Nirschl, E. S. Gaddis and K.-E. Wirth. 'VDI Heat Atlas'. In: ed. by P. Stephan. 2nd. Berlin Heidelberg: Springer, 2010. Chap. L1 Pressure Drop in Single Phase Flow, pp. 1053–1116. DOI: 10.1007/978-3-540-77877-6_70.

[32] M. Kauffeld. *RP-1166—Behavior of Ice Slurries in Thermal Storage Systems*. Tech. rep. Sponsored by ASHRAE Technical Committee 6.9 Thermal Storage. Danish Technological Institute, 2001.

[33] A. A. Kornhauser and J. L. Smith. 'Application of a complex Nusselt number to heat transfer during compression and expansion'. In: *Transactions of the ASME. Journal of Heat Transfer* 116.3 (1994), pp. 536–542. DOI: 10.1115/1.2910904.

[34] A. Lévêque. 'Les lois de la transmission de chaleur par convection'. In: *Annales des Mines ou Recueil de Mémoires sur l'Exploitation des Mines et sur les Sciences et les Arts qui s'y Rattachent* XIII.13 (1928), pp. 201–239.

[35] H. Martin. 'A theoretical approach to predict the performance of chevron-type plate heat exchangers'. In: *Chemical Engineering and Processing: Process Intensification* 35.4 (1996), pp. 301–310. DOI: 10.1016/0255-2701(95)04129-X.

[36] H. Martin. 'The generalized Lévêque equation and its practical use for the prediction of heat and mass transfer rates from pressure drop'. In: *Chemical Engineering Science* 57.16 (2002), pp. 3217–3223. DOI: 10.1016/S0009-2509(02)00194-X.

[37] H. Martin. 'VDI Heat Atlas'. In: ed. by P. Stephan. 2nd. Berlin Heidelberg: Springer, 2010. Chap. N6 Pressure Drop and Heat Transfer in Plate Heat Exchangers, pp. 1515–1522. DOI: 10.1007/978-3-540-77877-6_109.

[38] W. H. McAdams. *Heat Transmission*. 2nd. New York: McGraw-Hill, 1942.

[39] Å. Melinder. *Properties of Secondary Working Fluids for Indirect Systems*. International Institute of Refrigeration, 2010.

[40] A. Muley and R. M. Manglik. 'Experimental Study of Turbulent Flow Heat Transfer and Pressure Drop in a Plate Heat Exchanger With Chevron Plates'. In: *Journal of Heat Transfer* 121.1 (1999), pp. 110–117. DOI: 10.1115/1.2825923.

[41] B. Palm and J. Claesson. 'Plate heat exchangers: Calculation methods for single and two-phase flow'. In: *Heat Transfer Engineering* 27.4 (2006), pp. 88–98. DOI: 10.1080/01457630500523949.

[42] J. Pátek and J. Klomfar. 'A computationally effective formulation of the thermodynamic properties of LiBr-H2O solutions from 273 to 500 K over full composition range'. In: *International Journal of Refrigeration* 29.4 (2006), pp. 566–578. DOI: 10.1016/j.ijrefrig.2005.10.007.

[43] E. Preisegger, F. Flohr, G. Krakat, A. Glück and D. Hunold. 'D4 Properties of Industrial Heat Transfer Media'. English. In: *VDI Heat Atlas*. VDI-Buch. Berlin Heidelberg: Springer, 2010, pp. 419–512. DOI: 10.1007/978-3-540-77877-6_20.

[44] C. C. Richter. 'Proposal of New Object-Oriented Equation-Based Model Libraries for Thermodynamic Systems'. PhD thesis. Technical University Carolo-Wilhelmina Braunschweig, 2008.

[45] J. W. Rose. 'Heat-transfer coefficients, Wilson plots and accuracy of thermal measurements'. In: *Experimental Thermal and Fluid Science* 28.2–3 (2004). Ed. by G. P. Celata, S. Kandlikar, B. Thonon and A. Bontemps, pp. 77–86. DOI: 10.1016/S0894-1777(03)00025-6.

[46] E. Schmidt. *Properties of Water and Steam in SI-Units*. 2nd. Springer, 1979.

[47] M. M. Shah. 'Chart Correlation For Saturated Boiling Heat Transfer: Equations And Further Study'. In: *ASHRAE Transactions* 88 (1982), pp. 185–196.

[48] A. I. E. Sherbini, A. Joardar and A. M. Jacobi. 'Modified Wilson-plot Technique For Heat Exchanger Performance: Strategies For Minimizing Uncertainty In Data Reduction'. In: *Proceedings of the International Refrigeration and Air Conditioning Conference*. 627. 2004.

[49] M. J. Skovrup. *SecCool Properties v1.33*. IPU Refrigeration and Energy Technology. 2013.

[50] SWEP International AB. *Technical Information on B12*. http://www.swep.net/en/products_solutions/productfinder/Pages/B12.aspx. [Online; accessed 2015-5-9].

[51] SWEP International AB. *Technical Information on BX8T*. http://www.swep.net/en/products_solutions/productfinder/Pages/BX8T.aspx. [Online; accessed 2015-5-9].

[52] *Technical Data Sheet*. The Dow Chemical Company. 1997.

[53] *Technical Data Sheet*. Kemira Chemicals OY. 1998.

[54] *Technical Data Sheet*. Clariant GmbH. 2000.

[55] *Technical Data Sheet*. Aspen Petroleum AB. 2001.

[56] *Technical Data Sheet*. Chevron Products Company. 2004.

[57] *Technical Data Sheet*. pro Kühlsole GmbH. 2005.

[58] *Technical Data Sheet*. Dynalene Inc. 2014.

[59] *Technical Information*. Hoechst AG. 1995.

[60] *Technical Information*. Sulzer Chemtech AG. 1999.

[61] *Technical Information*. Tyforop Chemie Gmbh. 1999.

[62] *Technical Information*. Hydro Chemicals. 2000.

[63] *Technical Information*. 3M Company. 2007.

[64] *Technical Information*. Arteco NV/SA. 2010.

[65] *Thermal Properties Calculator v6.4*. Paratherm Ltd. 2013.

[66] *Therminol Heat Transfer Reference Disk v5.1*. Eastman Chemical Company. 2014.

[67] W. Wagner and A. Pruss. 'The IAPWS Formulation 1995 for the Thermodynamic Properties of Ordinary Water Substance for General and Scientific Use'. In: *J. Phys. Chem. Ref. Data* 31 (2002), pp. 387–535. DOI: 10.1063/1.1461829.

[68] J. Wang. 'Pressure drop and flow distribution in parallel-channel configurations of fuel cells: U-type arrangement'. In: *International Journal of Hydrogen Energy* 33.21 (2008), pp. 6339–6350. DOI: 10.1016/j.ijhydene.2008.08.020.

[69] J. Wang. 'Pressure drop and flow distribution in parallel-channel configurations of fuel cells: Z-type arrangement'. In: *International Journal of Hydrogen Energy* 35.11 (2010). 3rd Argentinean and 2nd Latin American Congress inHydrogen and Sustainable Energy Sources 3rd Argentinean and 2nd Latin American Congress inHydrogen and Sustainable Energy Sources, pp. 5498–5509. DOI: 10.1016/j.ijhydene.2010.02.131.

[70] W. C. Williams. 'If the Dittus and Boelter equation is really the McAdams equation, then should not the McAdams equation really be the Koo equation?' In: *International Journal of Heat and Mass Transfer* 54.7-8 (2010), pp. 1682–1683.

[71] E. E. Wilson. 'A basis of rational design of heat transfer apparatus'. In: *Journal of Heat Transfer* 37 (1915), pp. 47–70.

[72] R. H. S. Winterton. 'Where did the Dittus and Boelter equation come from?' In: *International Journal of Heat and Mass Transfer* 41.2-3 (1998), pp. 809–810.

[73] G. Woschni. *A Universally Applicable Equation for the Instantaneous Heat Transfer Coefficient in the Internal Combustion Engine*. Technical Paper 670931. Society of Automotive Engineers (SAE), Feb. 1967. DOI: 10.4271/670931.

[74] A. B. Zavoico. *Solar Power Tower Design Basis Document*. Tech. rep. Sandia National Laboratories, July 2001. DOI: 10.2172/786629.

DTU Mechanical Engineering
Section of Thermal Energy
Technical University of Denmark

Nils Koppels Allé, Bld. 403
DK- 2800 Kgs. Lyngby
Denmark
Phone (+45) 4525 4131
Fax (+45) 4588 4325
www.mek.dtu.dk

ISBN: 978-87-7475-432-9

DCAMM
Danish Center for Applied Mathematics and Mechanics

Nils Koppels Allé, Bld. 404
DK-2800 Kgs. Lyngby
Denmark
Phone (+45) 4525 4250
Fax (+45) 4593 1475
www.dcamm.dk
ISSN: 0903-1685